

# ACOUSTIC EMISSION



*Current Practice and  
Future Directions*

**Sachse/Roget/Yamaguchi**

*Editors*

**STP 1077**



**STP 1077**

# ***Acoustic Emission: Current Practice and Future Directions***

*Wolfgang Sachse, James Roget, and Kusuo Yamaguchi, editors*



ASTM  
1916 Race Street  
Philadelphia, PA 19103

## Library of Congress Cataloging-in-Publication Data

Acoustic emission: current practice and future directions/Wolfgang Sachse, James Roget, and Kusuo Yamaguchi, editors.

(STP ; 1077)

Papers presented at a symposium on world meeting on acoustic emission, held in Charlotte, NC, on 20-23 March 1989, and sponsored by AEWG.

"ASTM publication code number (PCN) 04-010770-22."

Includes bibliographical references and indexes.

ISBN 0-8031-1389-7

1. Acoustic emission testing. I. Sachse, Wolfgang, 1942-  
II. Roget, James, 1949- III. Yamaguchi, K. (Kusuo). IV. AEWG  
(Association). V. Series: ASTM special technical publication: 1077.  
TA418.84.A2573 : 1991

620.2--dc20

90-25872

CIP

Copyright © 1991 by the American Society for Testing and Materials. All rights reserved. No part of this publication may be reproduced, stored in a retrieval system, or transmitted, in any form or by any means, electronic, mechanical, photocopy, recording, or otherwise, without prior written permission of the publisher.

### NOTE

The Society is not responsible, as a body,  
for the statements and opinions  
advanced in this publication.

### Peer Review Policy

Each paper published in this volume was evaluated by three peer reviewers. The authors addressed all of the reviewers' comments to the satisfaction of both the technical editor(s) and the ASTM Committee on Publications.

The quality of the papers in this publication reflects not only the obvious efforts of the authors and the technical editor(s), but also the work of these peer reviewers. The ASTM Committee on Publications acknowledges with appreciation their dedication and contribution of time and effort on behalf of ASTM.

# Foreword

This publication, *Acoustic Emission: Current Practice and Future Directions*, contains papers presented at the symposium on World Meeting on Acoustic Emission held in Charlotte, NC on 20–23 March 1989. The symposium was sponsored by AEWG. Co-sponsoring groups were ASTM Committee E-7 on Nondestructive Testing, ASNT, IEEE, and SEM. Professor Wolfgang Sachse of Cornell University, Dr. James Roget of Nordon and CIE, and Professor Kusuo Yamaguchi of the University of Tokyo, presided as symposium chairman. They are also editors of this publication.

# Contents

<b>Overview</b> —W. SACHSE, K. YAMAGUCHI, AND J. ROGET	1
<b>AE SENSORS AND SYSTEMS</b>	
<b>The General Problems of AE Sensors</b> —Y. HIGO AND H. INABA	7
<b>Stress Wave Sensing—Affordable AE for Industry</b> —T. J. HOLROYD, T. E. TRACEY, N. RANDALL, AND S. D. KING	25
<b>Monitoring Electron Beam Welding Process Using Electro-Magnetic Acoustic Transducers (EMAT's)</b> —H. A. CROSTACK, H. J. STORP, AND P. BOHM	35
<b>AE SOURCES AND WAVE PROPAGATION</b>	
<b>Development and Future Aspects in AE Source Characterization</b> —M. ENOKI AND T. KISHI	47
<b>Joule Heating Line and Point AE Sources and the Adhesion of Thin Metal Films</b> —K. Y. KIM AND W. SACHSE	67
<b>A Calibration Source for Acoustic Emission Analysis</b> —C. R. HEIPLE, S. H. CARPENTER, AND S. S. CHRISTIANSEN	77
<b>Simultaneous Velocity Tomography and Source Location of Synthetic Acoustic Emission Data</b> —S. C. MAXWELL, R. P. YOUNG, AND D. A. HUTCHINS	86
<b>Acousto-Ultrasonics: An Update</b> —A. VARY	95
<b>Theoretical Basis of the Acousto-Ultrasonic Method</b> —M. T. KIERNAN AND J. C. DUKE, JR.	105
<b>SIGNAL PROCESSING APPROACHES</b>	
<b>Acoustic Emission Technology Using Multi-Parameter Analysis of Waveform and Application to GFRP Tensile Tests</b> —K. YAMAGUCHI, H. OYAIZU, J. JOHKAJI, AND Y. KOBAYASHI	123
<b>Acoustic Emission Detection of Crack Presence and Crack Advance During Flight</b> —S. L. MCBRIDE, M. D. POLLARD, J. D. MACPHAIL, P. S. BOWMAN, AND D. T. PETERS	146
<b>Structural Integrity Evaluation Using AE Techniques</b> —B. R. A. WOOD AND R. W. HARRIS	156
<b>Solving AE Problems by a Neural Network</b> —I. GRABEC, W. SACHSE, AND E. GOVEKAR	165
<b>STRUCTURAL MONITORING APPLICATIONS</b>	
<b>Periodic Inspection of Compressed Gas Cylinders and Transport Vessels by Using Acoustic Emission Testing</b> —H. M. BARTHÉLÉMY	185

<b>Detectability of Defects in Reactor Pressure Components by Location and Interpretation of AE-Sources—C. SKLARCZYK AND E. WASCHKIES</b>	199
---	-----

#### DEFORMATION STUDIES

<b>Effect of Pre-Exposure to Water on the Acoustic Emission Behavior of 2091-T3 Al-Li Alloy—F. ZEIDES AND I. ROMAN</b>	213
<b>Acoustic Emission During Tensile Deformation and Fracture in Austenitic Alloys—B. RAJ AND T. JAYAKUMAR</b>	218
<b>Relationship Between Acoustic Emission and Flaw Size in Si<sub>3</sub>N<sub>4</sub> Ceramics—Y. MORI AND T. KISHI</b>	242
<b>A Comparison of the Acoustic Emission Generated from the Fracture and Decohesion of Graphite Nodules with Theoretical Predictions—S. H. CARPENTER AND Z. ZHU</b>	252
<b>Evaluation of Fatigue Crack Growth Rate of Carburized Gear by Acoustic Emission Technique—Y. OBATA, H. KOBAYASHI, K. AOKI, T. YAMAGUCHI, AND K. SHIBATA</b>	261

#### NOVEL APPLICATIONS

<b>Characterisation of Dust Impact at Low Velocity by Acoustic Emission—D. J. BUTTLE AND C. B. SCRUBY</b>	273
<b>Applications of Acoustic Emission Techniques for Diagnosis of Large Rotating Machinery and Mass Production Products—I. SATO, T. YONEYAMA, K. SATO, T. TANAKA, M. YANAGIBASHI, AND K. TAKIKAWA</b>	287
<b>Cavitation Monitoring of Hydroturbines with RMS Acoustic Emission Measurement—O. DERAKHSHAN, J. R. HOUGHTON, R. K. JONES, AND P. A. MARCH</b>	305
<b>Tool Monitoring by Acoustic Emission—J. ROGET, P. SOUQUET, M. DESCHAMPS, AND N. GSIB</b>	316
<b>Monitoring of the Machining Process by Means of Acoustic Emission Sensors—D. A. DORNFELD</b>	328

#### GEOTECHNICAL APPLICATIONS

<b>Microseismics and Geotechnical Applications—M. OHTSU</b>	347
<b>Acoustic Emission/Microseismic Activity at Very Low Strain Levels—B. H. ARMSTRONG AND C. M. VALDES</b>	358
<b>Acoustic Emission Monitoring and Analysis Procedures Utilized During Deformation Studies on Geologic Materials—X. SUN, H. R. HARDY, JR., AND M. V. M. S. RAO</b>	365

<b>Acoustic Emission Analysis and Ultrasonic Velocity Imaging in the Study of Rock Failure—S. D. FALLS, T. CHOW, R. P. YOUNG, AND D. A. HUTCHINS</b>	381
<b>APPLICATIONS TO COMPOSITE MATERIALS</b>	
<b>Fracture Mechanism Studies of a Carbon Fiber-Peek Composite by Acoustic Emission—K. ONO, J. S. JENG, AND J. M. YANG</b>	395
<b>On the Correlation Between Acoustic Emission and Progression of Matrix Splitting in a Unidirectional Graphite/Epoxy Composite—S. GHAFARI AND J. AWERBUCH</b>	404
<b>Identification of Fatigue Failure Modes in Carbon Fibre Reinforced Composites with the Energy Discriminating Acoustic Emission Method—M. WEVERS, I. VERPOEST, P. DE MEESTER, AND E. AERNOUDT</b>	416
<b>Detection of Impact Damage in Composite Bi-Axial Test Specimens by Use of Thermally-Activated Acoustic Emission—J. W. WHITTAKER AND W. D. BROSEY</b>	424
<b>Acoustic Emission Monitoring of Contact Drying of Southern Pine Veneer—F. C. BEALL</b>	435
<b>Author Index</b>	445
<b>Subject Index</b>	447

## INTRODUCTION

Acoustic emission (AE) is the phenomenon in which elastic or stress waves are emitted from a rapid, localized change of strain energy in a material. AE as a technology has rapidly become accepted as a non-destructive methodology. It has become in recent years the basis of a number of recommended practices and inspection codes of several societies. The applications of AE which involves the detection of AE signals and possibly their characterization are diverse. Most commonly, they include the monitoring of manufacturing and other dynamical processes, the integrity of structural components as well as fundamental investigations of failure processes of engineering as well as geological materials.

In the last decade the science, technology and applications of AE progressed significantly. In order to provide a forum for reporting important, recent developments and to provide an opportunity to critically review the directions in which this field is moving, the *Acoustic Emission Working Group* with the endorsement of other technical societies, including ASTM Committee E-7, ASNT, IEEE, and SEM, organized the *World Meeting on Acoustic Emission* which was held 20-23 March 1989 in Charlotte, North Carolina. Eighty-seven papers from nineteen countries were presented at the conference. The thirty-four comprising this *ASTM Special Technical Publication (STP)* volume were selected for their topical content and international appeal.

The first section of this book focuses on AE sensors and systems. The calibration of AE sensors and AE systems using the pencil break and a reciprocity technique is discussed by Higo and Inaba. The development of an integrated AE sensor suitable for use in harsh, industrial environments and its use in diverse process monitoring applications is reported by Holroyd et al. The application of non-contact, electro-magnetic acoustic sensors (EMAT's) in an AE weld monitoring application is described by Crostack et al.

The second section of the book deals with fundamental investigations of AE sources and the propagation of simulated AE signals through a structure for materials characterization applications. The case of point sources modeling the formation of microcracks in brittle solids is reviewed by Enoki and Kishi while the signals from line sources are described in the paper by Kim and Sachse. Heiple et al. describes a study of the AE accompanying the fracture of boron particles in an aluminum matrix which may serve as an AE system calibration signal. The use of a point source generating broadband ultrasonic signals in a large number of directions in a material, forms the basis of tomographic technique described by Maxwell et al. to determine the velocity structure of a specimen which may find application in the future to image the distribution of stresses or cracks in materials. Another application utilizing simulated AE signals is in the so-called *acousto-ultrasonic*, or *AU* technique, which



## 2 ACOUSTIC EMISSION

was developed by Vary. In this volume he reviews recent developments and considers its further potential and some of its limitations. A theoretical foundation of the *AU* technique based on Lamb plate modes is described by Kiernan and Duke.

The next section contains four of the papers at the conference which dealt with new signal processing approaches for AE signals. Description of a high-performance AE system capable of rapidly extracting a number of waveform parameters from the detected signals is given by Yamaguchi et al. A similar approach, but based on an envelope processing of the AE signals, is the basis of an in-flight AE system reported by McBride et al. The application of expert systems to assist in interpreting AE data is considered by Wood and Harris. The last paper in this section by Grabec et al. reports the development of a neural-like processing procedure for extracting the location and characteristics of an AE source from the signals detected at a number of sensors.

The use of AE in structural monitoring applications is the focus of the following section. Included is a paper by Barthélémy describing an AE-based inspection procedure for evaluating the integrity of compressed gas cylinders used in transportation systems. The second paper in this section is by Sklarczyk and Waschkies who demonstrate that AE signal parameters such as risetime, provide a means for delineating between growing and non-growing defects in reactor pressure components.

Five papers comprise the section focusing on AE used in deformation studies and in investigations of environmental and cyclic loading effects. The results of an investigation of the effect of pre-exposure to water on the AE behavior of an aluminum-lithium alloy are summarized in the paper by Zeides and Roman. A study of AE generated during tensile deformation and fracture in austenitic alloys is described by Raj and Jayakumar. The use of AE to investigate the effect of flaw size on the fracture of  $\text{Si}_3\text{N}_4$  ceramics is reported by Mori and Kishi. A study of the AE from the fracture and decohesion of graphite nodules in ductile cast iron is reported by Carpenter and Zhu. The last paper in this section by Obata et al. describes the successful application of AE to monitor the growth of a fatigue crack in a carburized gear.

The next section of the book contains a number of papers reporting novel applications of AE measurements. Included here is the paper by Buttle and Scruby who apply quantitative AE techniques to determine the impact source and hence the sizes of small particles striking a plate. The development of a digital AE-based system for machinery diagnostics applications is described in the paper by Sat et al. Derakhshan et al. report the use of rms AE measurements to monitor cavitation-generated pressure pulses in a hydroturbine. The final two papers of this section deal with the application of AE to monitor metal machining processes. Roget et al. address the problems related to the application of AE measurements for delineating between tool breakage detection and tool wear monitoring. Dornfeld reviews the generation of AE and its use as a monitoring procedure during a metal cutting process. He explores the use of adaptive and neural processing

procedures for analyzing the detected AE signals.

Three papers comprise the section dealing with geotechnical applications of AE. A survey of AE source characterization studies yielding the moment tensor components and the ability of characterize the crack type and its orientation in geological specimens is described by Ohtsu. The use of AE to detect microstrains in the earth prior to an earthquake is considered by Armstrong and Valdes. The next paper in this section reports on the use of a novel amplitude analysis procedure to delineate between several deformation mechanisms in geological materials is described by Sun et al. The final paper in this section by Falls et al. describes the novel combination of AE source studies and ultrasonic tomographic imaging to investigate the failure mechanisms in rocks. If applied properly, such multi-measurement techniques can yield significantly more information about a process than when used individually.

The final section of the book focuses on the application of AE measurements for investigation failure processes in composite materials. The AE parameters that can be used to identify the failure mechanisms initiated by bending, flexure, and tensile tests of a thermoplastic carbon fiber-PEEK composite are reported by Ono et al. Ghaffari and Awerbuch describe the correlation they establish between AE and the initiation, accumulation and progression of matrix splitting in unidirectional graphite/epoxy specimens. Wevers et al. describe the use of an energy-related measure of the AE signals to monitor the damage development in a fatigue-loaded carbon fiber/epoxy laminate. Whittaker and Brosey describe the use of a cyclic thermal loadings to generate AE by which impact damage in Kevlar<sup>®</sup>-wound aluminum spheres can be detected. The last paper, written by Beall, reports the use of AE to monitor the contact drying process of a wood veneer.

The editors express their deep appreciation to the more than fifty reviewers who so carefully read all the manuscripts and provided critical reviews of them.

There were two sessions at the conference for which no papers are included in the book. A panel discussion was organized which was chaired by D. G. Eitzen (USA) and which was used to exchange information about the status of AE-related codes and standards in several countries. Other members of the panel included Y. Higo (Japan), J. Roget (France) and P. Tscheliesnig (Austria). Each panel member presented an overview of recent developments and trends in his country. It was agreed that a continuing exchange of information about the development of AE-related codes and standards among AE groups would be desirable and an important undertaking.

Unique to this conference was an evening discussion session focusing on the topics "Critical AE Problems for the Researcher," which was led by A. Pollock<sup>1</sup> (Physical Acoustics Corp.) and "Critical Instrumentation Issues," which was led by A. Beattie (Sandia National Laboratories).

---

<sup>1</sup>*Journal of Acoustic Emission* (1990). In Press.

## 4 ACOUSTIC EMISSION

The discussors identified the following issues for further investigation: (1) The development of a coherent, unified theory of acoustic emission to explain phenomena such as the Kaiser and Felicity effects for materials subjected to repeated loadings or load-hold tests; (2) The development of rational guidelines for the realistic stimulation of AE in structures which may be subjected to multi-dimensional states of thermal or mechanical stress in service; (3) The development of realistic artificial sources for AE system calibration application; and (4) Ways of obtaining more information from the detected acoustic signal, both by improved detection methods and by new or novel methods of signal processing.

A number of additional topics were identified by members of the audience for future investigation. These included: Study of AE signal cascades; Investigation of large amplitude AE burst-type emission before and during yield of some materials; Additional investigation of elastic waves in plates and shells for source location and characterization applications; Quantitative AE from frictional sources; Exploration of AE in conjunction with other NDT techniques; Absolute acoustic measurements; Application of chaos theory to AE; Application of neural networks to analyze AE signals; New and imaginative AE applications.

A note of thanks must be extended to the editorial staff of ASTM without whom this project could not have been undertaken. The efforts of Barbara Stafford, Therese Pravitz, and Kathy Greene deserve special recognition.

Wolfgang Sachse  
Cornell University  
Ithaca, NY USA

Kusuo Yamaguchi  
University of Tokyo  
Tokyo, Japan

James Roget  
Nordon & Cie  
Nancy, France

# **AE Sensors and Systems**

Yakichi Higo, and Hidehiro Inaba

## THE GENERAL PROBLEMS OF AE SENSORS

---

**REFERENCE:** Higo, Y. and Inaba, H., "The General Problems of AE Sensors," Acoustic Emission: Current Practice and Future Directions, ASTM STP 1077, W. Sachse, J. Roget, and K. Yamaguchi, Eds., American Society for Testing and Materials, Philadelphia 1991.

**ABSTRACT:** The general problems of AE sensors are overviewed. The effects of mounting conditions of sensors on the sensitivity are discussed. Then the sensitivity measurement methods are compared. The results of a sensor's sensitivity, obtained by NBS and by the Hatano method show that there is very little difference between them.

The convenient calibration method for sensor sensitivities, especially the "acoustic pressure method" and the "pencil lead fracture method" are discussed. The characteristics of lead, specially standard pencil lead from JAEWG which produce very stable reproducible AE signals, was demonstrated. The characteristics of the lead is quite similar to the lead produced in 1975. Then sensor sensitivities were obtained by the standard lead and are compared with the results of the reciprocal method.

**KEYWORDS:** AE, sensor sensitivity, sensor mounting condition, acoustic pressure method, pencil lead

The technology and equipment of AE have been progressed significantly in the past ten years. Especially, the AE analysis methods, both in the time and frequency domain, have progressed and are widely applied not only to the fundamental research but also to the evaluation of the actual structure and equipments.

Dr. Higo is an Associate Professor of Materials Science Division, the Research Laboratory of Precision Machinery and Electronics, Tokyo Institute of Technology, Nagatsuta, Midoriku, Yokohama, 227, Japan; Mr. Inaba is a research scientist of the Fuji Ceramics Co., Ltd., Sannomiya, Hujinomiya-shi, 418-01, Japan.

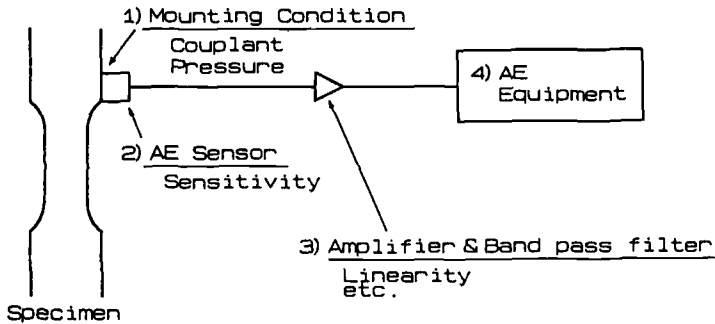


Fig.1 -- Basic AE measurement system

The basic AE measurement system consists of an AE sensor, amplifier and AE signal analyzing equipment, as schematically shown in Figure 1. Some phenomenon occurs in the specimen and it emits AE. Then an AE wave propagates through the specimen and is detected by the AE sensor, where the AE changes from an elastic wave to an electrical signal. Then, the AE signals are processed by using electronic devices and technology. The AE sensor is the most important part of the AE equipment. However, the AE sensor has many kinds of unclarified problems to be solved. The general problems of the sensor are;

- a) Effect of mounting condition on sensitivity,
- b) Sensor sensitivity,
- c) Degradation of the sensitivity and its method of evaluation.

These factors mentioned above affect detected AE signals, and change the peak voltage, duration time and so on. Therefore, even if the same sensor and AE equipment are used under the same measurement conditions, the results of AE event count may be changed depending on the mounting condition. This leads to difficulty in exchanging and comparing actual AE signal data among different research groups using different equipments and sensors, even if sensor sensitivities have been calibrated. Thus, it is quite important to find some solution to make it possible to compare AE data and for producing an AE data base in the near future.

In this paper, the following subjects are mentioned and discussed.

- a) Effect of mounting condition (couplant, mounting pressure and so on) on sensitivity (amplitude and phase components),
- b) Sensor sensitivity and its measurement methods,
- c) Degradation of the sensitivity and convenient methods for its calibration.

## MOUNTING CONDITION OF AE SENSORS

The factors of mounting condition which strongly relate to the sensitivity are thought to be 1) the couplant material between the sensor and AE wave propagation medium, 2) mounting pressure (mechanical force to hold the sensor against the structure or the specimen) and 3) surface condition of the specimen. These factors affect not only the resonance frequency but also phase component of the AE sensor's sensitivity. The phase component directly affects to the receiving AE wave form. Therefore, when AE waves are analyzed in time domain, the most important thing is to know the characteristics and the reproducibility of the mounting condition. Because, this condition affects not only the peak voltage but also the number of event counts, arrival time and so on.

### Measuring method

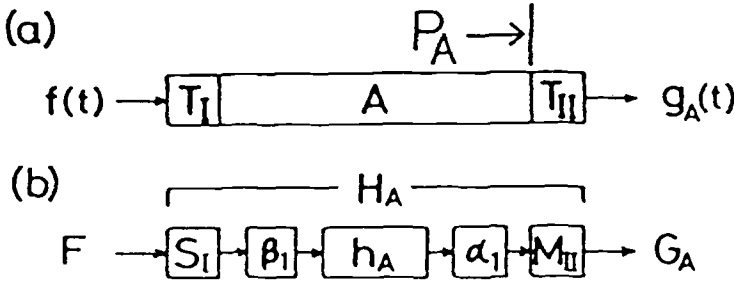


Fig.2 -- the schematic diagram showing the transmitting input signal to the transmitting sensor  $T_I$ .  $g_A(t)$  is the output signal of the receiving sensor  $T_{II}$ .

Figure 2 is a schematic diagram showing the transmitting input signal,  $f(t)$ , to the transmitting sensor  $T_I$ .  $g_A(t)$  is the output signal of the receiving sensor  $T_{II}$  [1,2]. The system in Fig.2(a) can be described using the transfer functions in frequency domain as shown in Fig.2(b) according to their components. The transfer function through the whole system,  $H_A$ , in Fig.2(b) is expressed as follows;

$$\frac{G_A}{F} = H_A = S_I \beta_I h_A \alpha_I M_{II} \quad (1)$$

where  $F$  and  $G_A$  are the Fourier transform of  $f(t)$  and  $g_A(t)$  respectively;  $S_I$ ,  $M_{II}$  and  $h_A$  are the transfer function of the transmitting and the receiving sensor and the wave propagation medium respectively;  $\beta_I$  and  $\alpha_I$  are the transfer functions representing the coupling condition between the sensor and the propagation medium.

Firstly, the voltage sensitivity of receiving sensor,  $M_{II}$ , is obtained by the reciprocity calibration procedure developed by Hatano, Mori [3] and Breckenridge et al. [4]. Then the acoustic pressure spectral density function at the surface,  $A$ , is obtained as follows.

$$P_A = \frac{F H_A}{\alpha_I M_{II}} = \frac{G_A}{\alpha_I M_{II}} \quad (2)$$

If the signal  $F$  has good reproducibility, and if the same transfer system is used except for  $M_{II}$  and  $\alpha_I$ , then it is possible to identify  $P_A$ . Therefore, when the same sensors and propagation medium are used and the mounting condition is changed, the difference of mounting condition,  $\Delta\alpha_n$ , is expressed as follows;

$$\Delta\alpha_n = \frac{H_n}{H_A} = \frac{G_n}{G_A} = \frac{\alpha_n}{\alpha_A} \quad (3)$$

$\Delta\alpha_n$  includes not only amplitude but also phase component.

The signal used for the measurement was periodic pseudo-random noise, which was synthesized by a computer using the equation (4) and (5) [5,6,7].

$$f(t) = \sum_{k=1}^{512} A \cos\left(\frac{2\pi k}{3072} t - \Phi_k\right), \quad m \Delta T \leq t < (m+1) \Delta T \quad (4)$$

where  $T$  is the repeat period ( $T = 3072 \Delta T$ ),  $m$  is an integer from 1 to 3072, and  $\Phi_k$  is a random number between 0 and  $2\pi$ . The Fourier transform of  $f(t)$  is  $F(\omega_k)$ , where Fig.3 shows an example of both  $f(t)$  and  $F(\omega)$ .

$$|F(\omega_k)|^2 = \frac{1}{4} \left\{ \frac{\sin\left(\frac{\omega_k \Delta T}{2}\right)}{\frac{\omega_k \Delta T}{2}} \right\}^2 \times \left\{ \sum_{h=1}^{512} A(\delta_{h,k+3072n} + \delta_{h,-k+3072n}) \right\}, \quad \omega_k = \frac{2\pi k}{t} \quad (5)$$

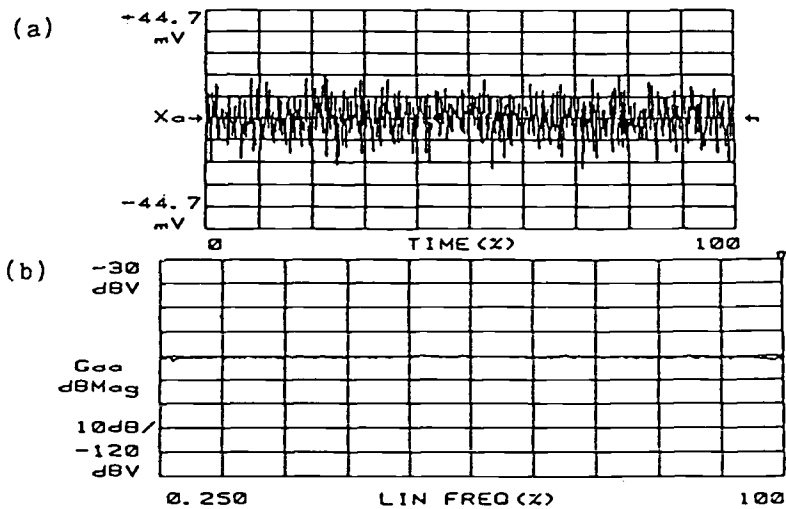


Fig.3 -- Pseudo-random noise ; time domain (a) and frequency spectrum (b).



The characteristics of the signal are that the power is flat in both the time and frequency domain, and the power and phase of each frequency are completely identified [6]. In addition of these characteristics, the important thing is its very precise reproducibility. The block diagram of the measuring system is shown in Fig.4.

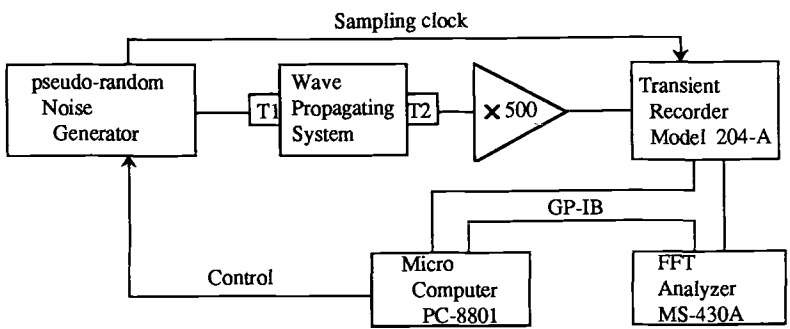


Fig.4 -- Block diagram of the measuring system.

Effect of mounting pressure

In order to obtain good coupling conditions for detecting AE, mechanical force is applied to hold the sensor against the structure or the specimen. This pressure should be greater than 0.7MPa for a dry contact according to ASTM E650-85. When using W-400 grease (mentioned later), the relationship between receiving sensitivity of a 20mmφ flat type sensor (frequency range was 100kHz to 5MHz) and the pressure is shown in Fig.5. The power spectrum of receiving signals are indicated for each 1MHz range ( shown by different symbols in the figure). The sensitivity increases with increasing pressure.

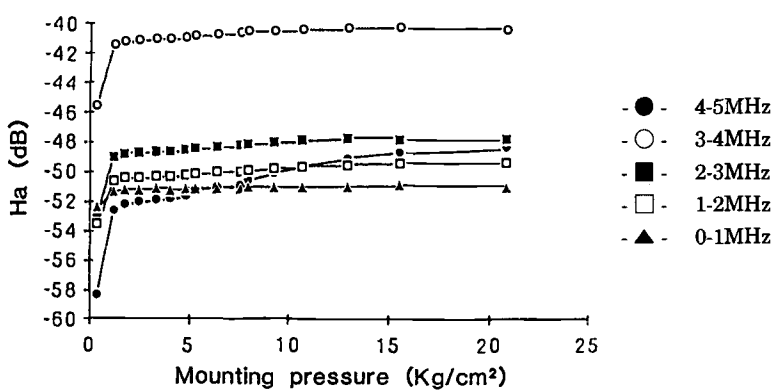
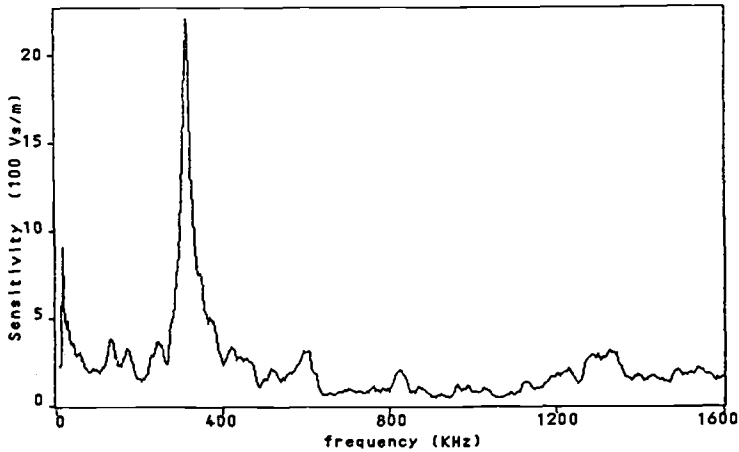


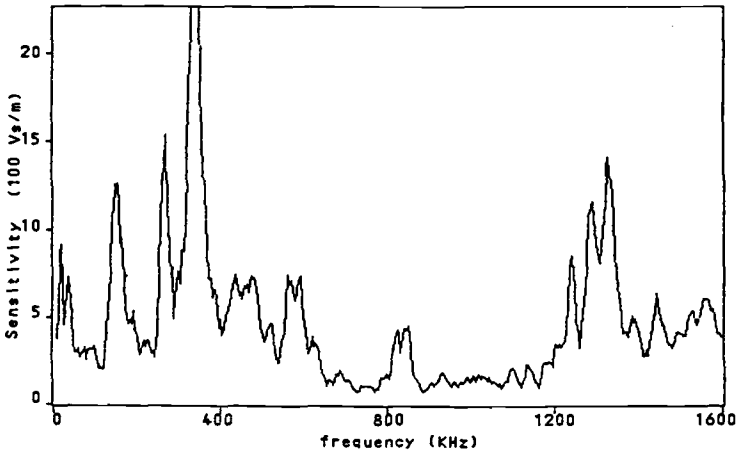
Fig.5 -- Relationship between receiving sensitivity of a 20mmφ flat type sensor (frequency range was 100kHz to 5MHz) and the pressure. The power spectrum of receiving signals are indicated for each 1MHz range ( shown by different symbols in the figure).

When the detecting frequency range is up to 2MHz, 300g/mm (0.03MPa) of applied force is sufficient. However, to detect over 4MHz, more than 10Kg/mm (1MPa) is required [8].

#### Effect of couplant on sensitivity



(a)



(b)

Fig.6 -- The effect of couplant on sensor sensitivity obtained by the reciprocal method; (a) is for a poorly coupled sensor with air babbles in the couplant and (b) is carefully mounted using cyanoacrylate.

Figure 6(a) shows the voltage sensitivity for longitudinal wave of a sensor obtained by the reciprocity calibration procedure using three similar sensors. The resonant frequency of each sensor is almost the same, and is about 350KHz [1]. We assumed that the  $\alpha_n$  and  $\alpha_1$  are the same. In this study, the sensors were carefully bonded to the propagation medium. However, it is not always to maintain the couplant condition between the sensor and the propagation medium. When the couplant is looser because of included bubbles and so on, the output of the receiving sensor will be changed even if the acoustic pressure spectral density function and the voltage sensitivity of the sensor itself are exactly the same. Figure 6(b) demonstrates the effect of a loose couplant condition [1].

For comparison, the sensor was rightly attached to the AE propagation medium with cyanoacrylate. The sensor was carefully mounted, then the sensitivity was measured (Fig.6a). The result shown in Fig.6(b) was obtained for a poorly coupled sensor. There is a tremendous difference between the two mounting conditions.

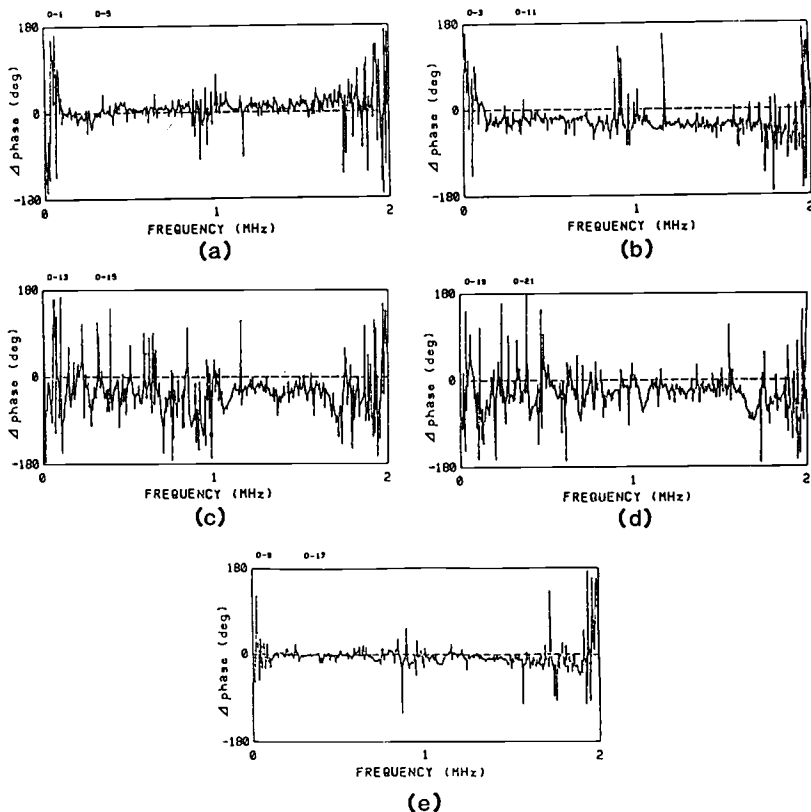


Fig.7 -- The effect of couplant material on the reproducibility of phase component of sensitivity,  $\Delta\alpha_n$ . (a,b,c,d and e) The couplants used were silicone oil, silicon grease, mixture of silicone grease and oil, pine resin base wax and W-400 respectively.

Effect of couplant material on phase component of sensitivity

When a sensor was carefully mounted with various couplants and the sensitivity measured and compared with Fig.6(a), the reproducibility of amplitude component of sensitivity is not so bad. However, the reproducibility of the phase component of the sensitivity is strongly related to the material of the couplant. Figure 7 shows the effect of couplant material on the reproducibility of phase component,  $\Delta\alpha_n$  of equation (3) [2]. Solid or higher viscosity couplants such as pine-resin, glue or silicon grease gave bad results, especially in low frequency range. This range most affects the detected AE wave form. Thus, the analyzed results of AE parameter might be changed. The best results at room temperature were obtained with W-400 couplant [2]. However, the

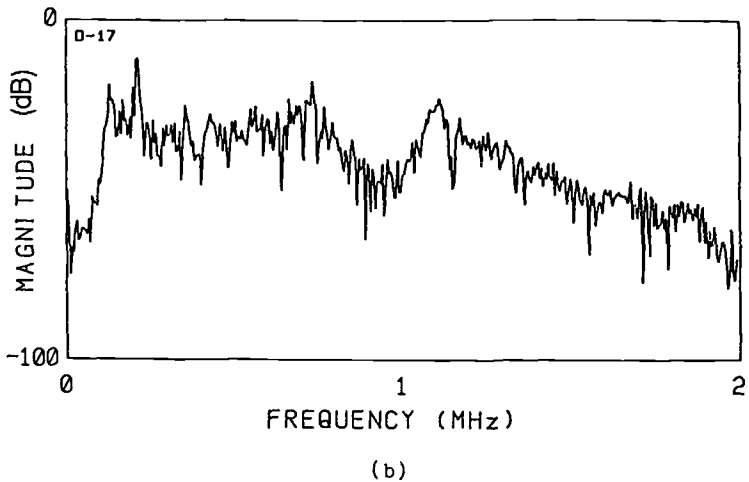
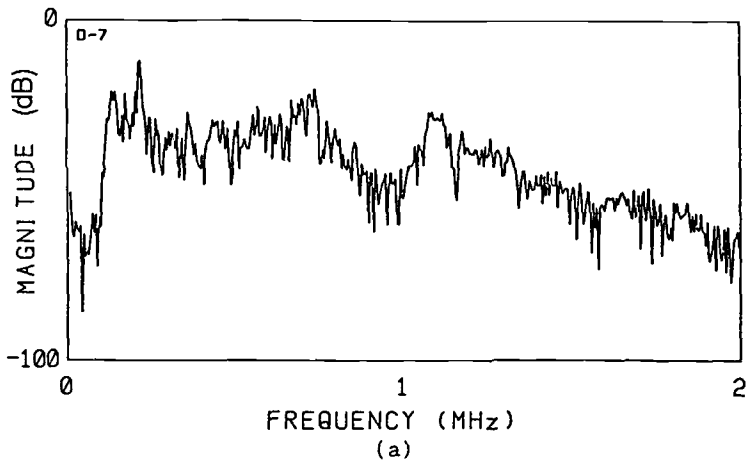


Fig.8 -- The power spectrum of receiving signals detected using silicon grease (a) and W-400 couplant (b).

powerspectrum of receiving signals detected using silicon grease and W-400 couplant were almost same, as shown in Fig.8 [2]. Therefore, in this study, W-400 was the best. However, couplant materials select carefully for AE wave analysis in time domain.

## SENSOR SENSITIVITIES AND ITS MEASUREMENT METHODS

Many methods to measure the sensor sensitivities have been proposed in the last twenty years. Typical methods to obtain the quantitative sensitivity are two, proposed by NBS [4,9] and Hatano et al [3].

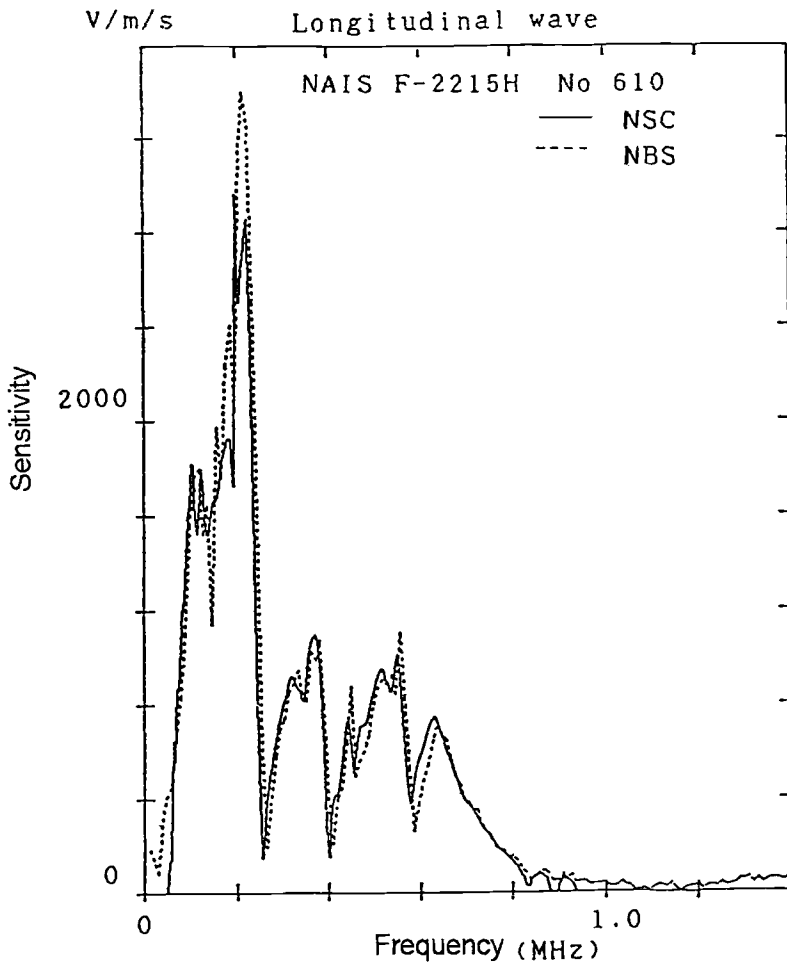


Fig.9 -- Sensor sensitivities obtained by NBS and Nippon Steel (Hatano's Method).

In 1982, the results of both methods were compared using same sensors [4]. Figure 9 shows one of the results. At that time, it was concluded that there was little difference between them, but in details, such as the peak height of the resonant frequency are slightly different. The reason for the difference was mainly thought to be the mounting

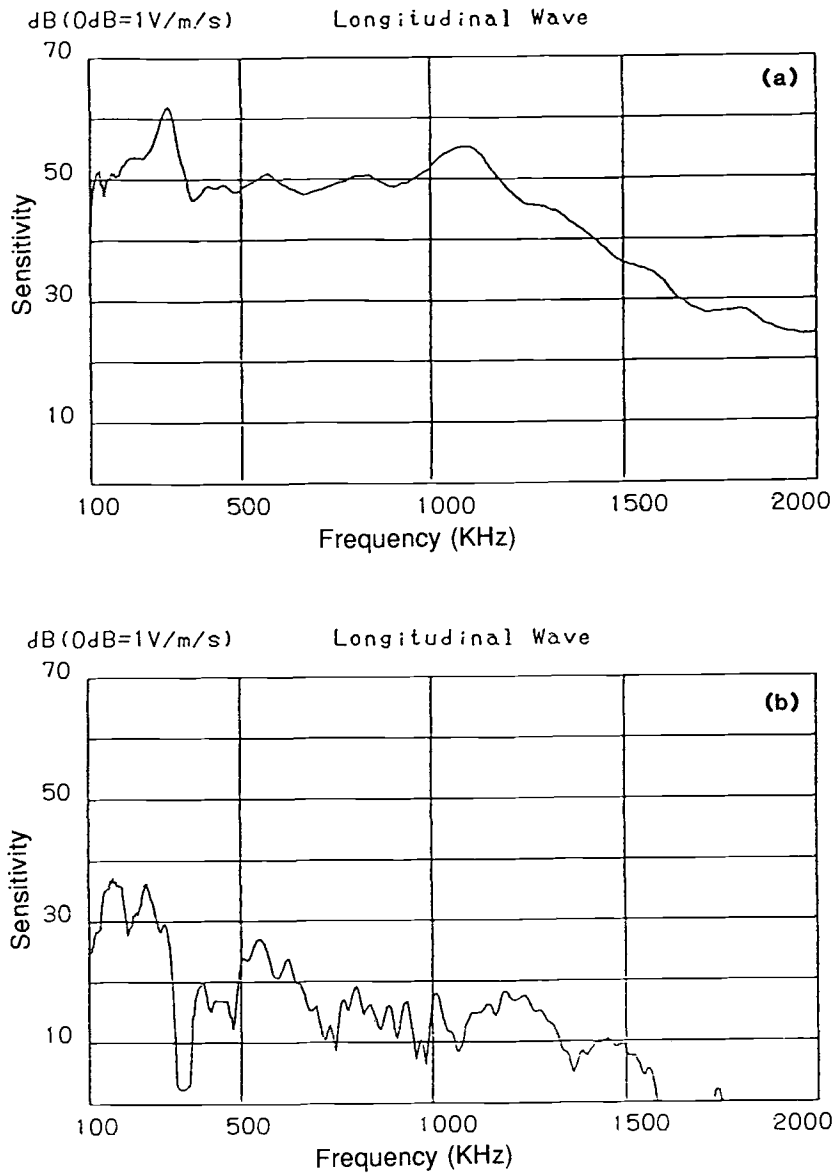


Fig.10 -- (a) is the sensitivity of the sensor before applying thermal cycles and (b) is after the cycles.

and the surface condition of the AE wave propagating medium. However, There are some limitation on both methods, caused by

- 1) size and the alignment of AE sensor with the specimen,
- 2) material characteristics (elastic constant etc.) on which sensor mounted,
- 3) accuracy of the distances between AE sensor, reference AE sensor and quasi AE source on NBS method,
- 4) transmitting characteristics of AE sensor on Hatano's method.

## DEGRADATION OF THE SENSITIVITY AND A METHOD FOR ITS CONVENIENT CALIBRATION

We quite often experience a degradation of sensor sensitivity, especially when the AE method is applied to measure the characteristics of super conducting materials or monitor the super conducting magnet at liquid He temperature. The AE sensor experiences thermal cycles. During the cycle, degradation of sensitivity occurs because of the thermal expansion coefficient of sensor component materials are different. If the sensor is significantly damaged, it is very easy to find the degradation. However, when the degradation is not so obvious, it is quite difficult to find it. Figure 10 shows the former case [10]. Before the thermal cycles, the sensitivity was measured (Fig.10(a)). Then thermal cycles were applied five times, and the sensitivity was measured (Fig.10(b)). The sensitivity decreased about 30dB. However, for the latter case, we need some simple, quick and convenient calibration method to know the characteristics of degradation.

### Convenient calibration method (Acoustic pressure method)

As mentioned in a previous section, we have a method for mounting the sensor to obtain good reproducibility. Using a periodic pseudo-random noise, sensor sensitivity,  $M_n$ , is derived from equation (2) as follows [1],

$$M_n = \frac{G_n}{P_A} \quad (6)$$

The sensitivity difference between before,  $M_{nb}$ , and after thermal cycles,  $M_{na}$ , is

$$\Delta M_{nba} = \frac{M_{na}}{M_{nb}} \quad (7)$$

Figure 11 demonstrates the small degradation of sensitivity after 5 thermal cycles, obtained by the method. Figure 11(a) is the sensitivity of the sensor before applying thermal cycles, (b) is after the cycles and (c) is the difference between them.

### Convenient calibration method (Pencil lead fracture method)

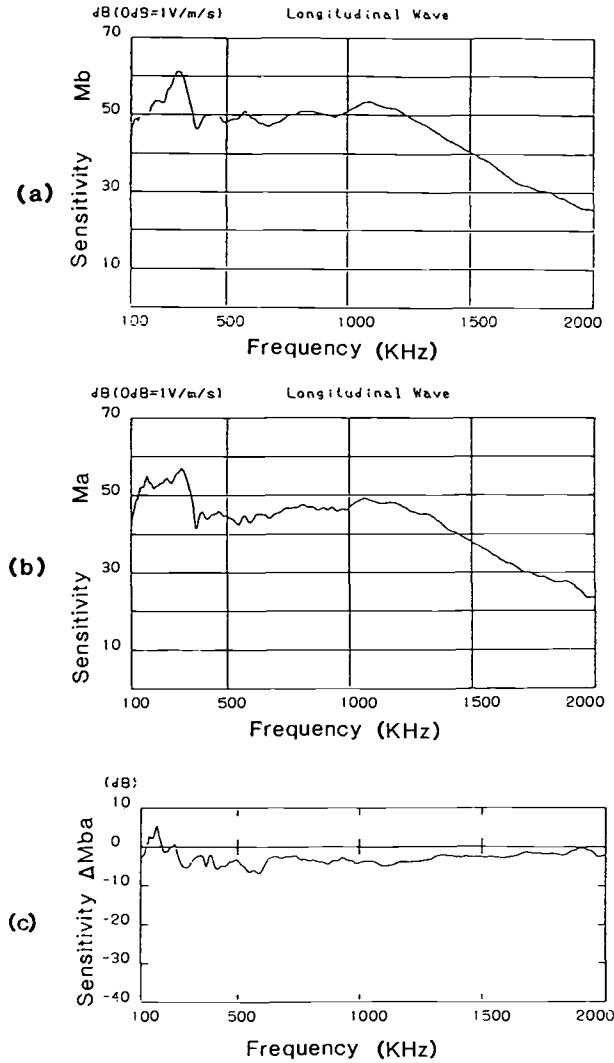


Fig.11 -- (a) is the sensitivity of the sensor before applying thermal cycles, (b) is after the cycles and (c) is the difference between them.

The two methods mentioned above, NBS and NSC, are suitable for measuring the precise sensitivities, but they are not convenient for general use, because the system is heavy in weight and also very costly in price. Thus some alternative convenient methods have been proposed, such as, the helium gas jet or pencil lead fracture method. The pencil lead fracture method (PLF) has been proposed by Dr. Hsu (NBS) in 1975. This method is popular, ASTM has adopted it as a standard method [11]. PLF used to use Pentel 2H 0.5mm lead as a standard. However, the size of the lead changed to 0.3mm



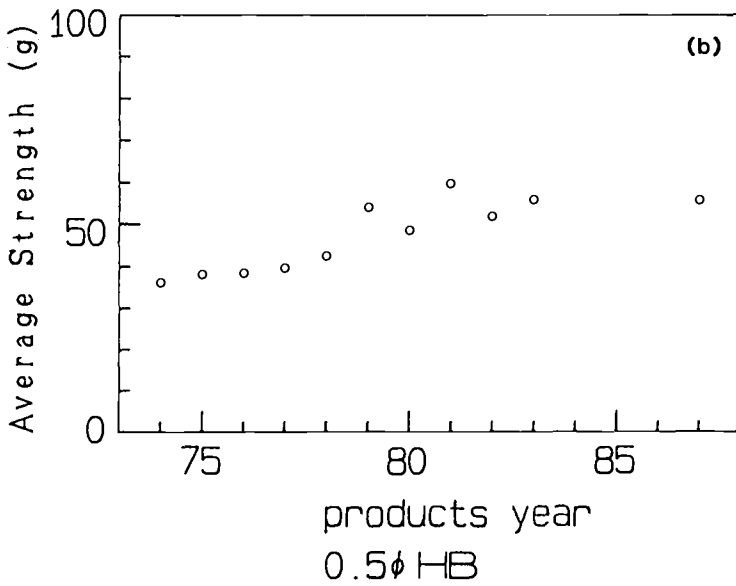
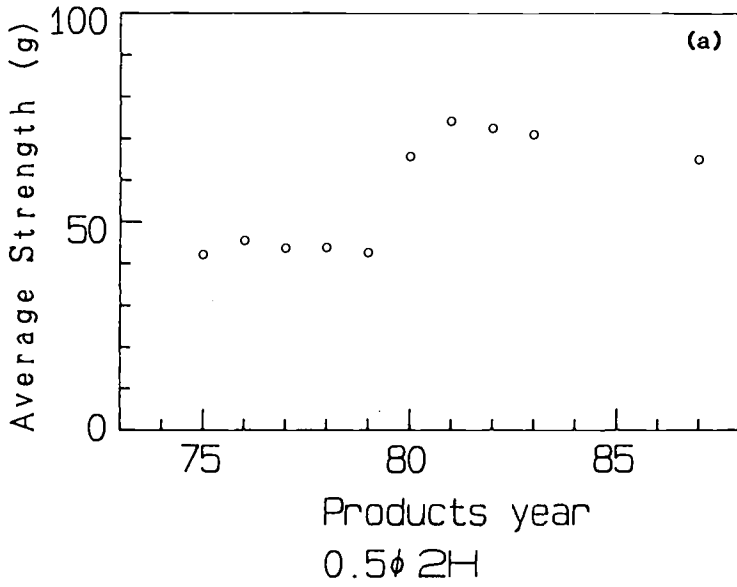


Fig.12 -- Average strength (g) of the lead produced each year from 1974 to 1978, measured by three points bending (span was 40 mm).

[12]. Figure 12 shows the historical change of strength of Pentel 0.5mm 2H and HB [13]. The characteristics and manufacturing method of lead has been changed since 1980. During the period, the strength of the lead was improved and doubled. Therefore the characteristics of AE, emitted by the fracture of it, were also changed. The most important characteristics of the lead are the reproducibility of fracture strength (Weibull Coefficient) and of the AE wave. A measurement system for AE waves emitted by pencil lead fracture is schematically shown in Fig.13 [13]. Figure 14 shows the peak voltage of AE emitted by the pencil lead manufactured from 1974 to 1988, corresponding to Fig.12. Peak voltage showed much more scatter with 0.5mm 2H.

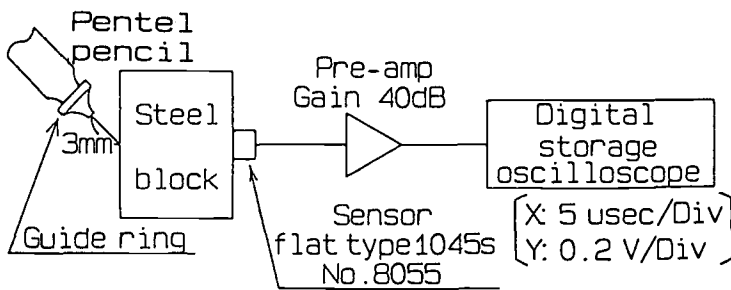


Fig.13 -- Measurement system for AE wave emitted due to the pencil lead fracture.

The pencil lead which is sold at ordinary stationary shops have a Weibull Coefficient (WC) of about 10 and the reproducibility of AE is quite bad. The WC in 1975 was about 20. JAEWG tried producing and supplying standard pencil lead which has very similar characteristics of strength and AE signals as the lead produced in 1975.

The WC of standard lead is above 40 and it gives extremely high reproducibility of AE waves [13,14]. Figure 15 shows the signal emitted due to the lead fracture and the sensitivity of the sensor used for the signal measurement.

When the pencil lead is fractured, the lead is gripped in the mechanical pencil with teflon guide ring at the tip. The ring is very important factor for obtaining good reproducibility of AE waves. Figure 16(a) shows the shape of the most widely used ring. However, if the collar of the ring is very weak, it deforms very easily when the lead is fractured, and causes a decrease in reproducibility of AE. Figure 16(b) shows the modified guide ring with more stiffness at the collar. Also a special mechanical pencil for AE was manufactured to avoid scratching the pencil lead surface. The reproducibility of the signal was so good that the sensor sensitivity can be obtained using the signal as follows(6)

Figure 17 demonstrates the sensor sensitivity obtained by the standard pencil lead fracture method (Fig.17(a)), and by the reciprocal method (Fig.17( b)). Both results agree.

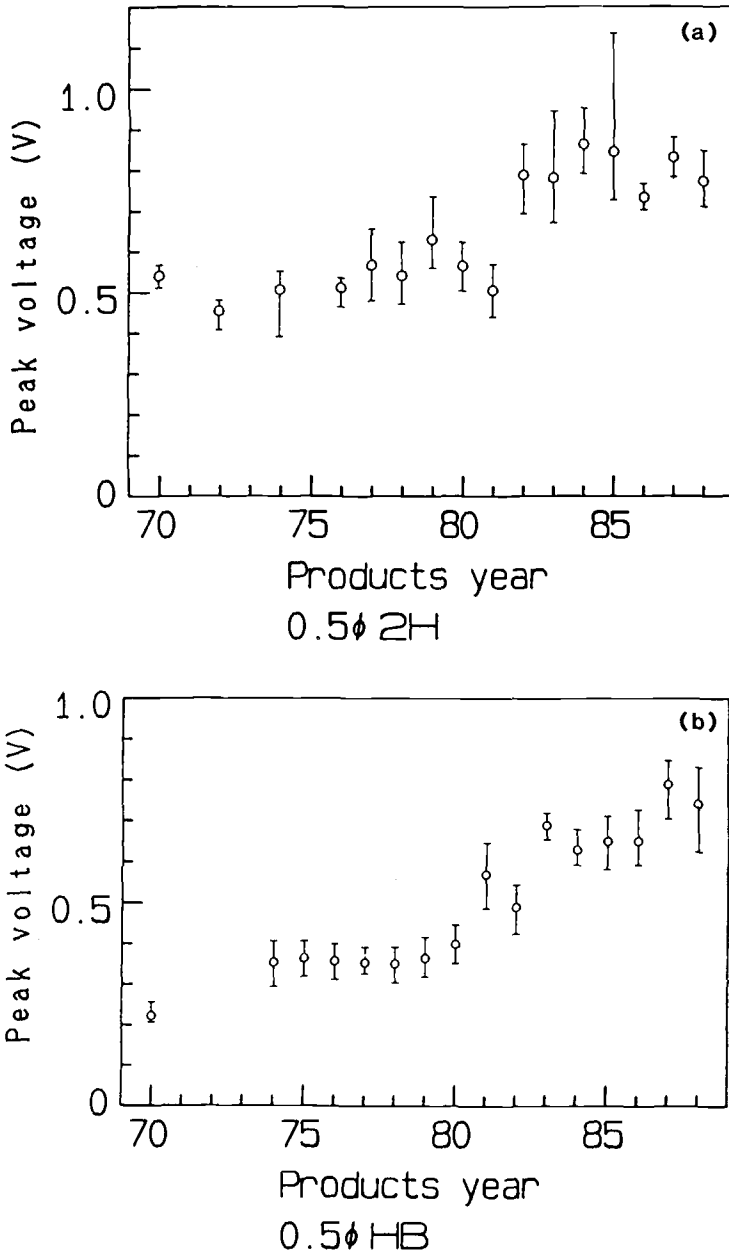


Fig.14 -- Relation between the peak voltage of AE emitted due to the pencil lead fracture of 0.5mm 2H (a) and 0.5mm HB (b), and manufactured year, corresponding to Fig.12. Scatter bands of peak voltage are shown by bars with the mean value by open circle.

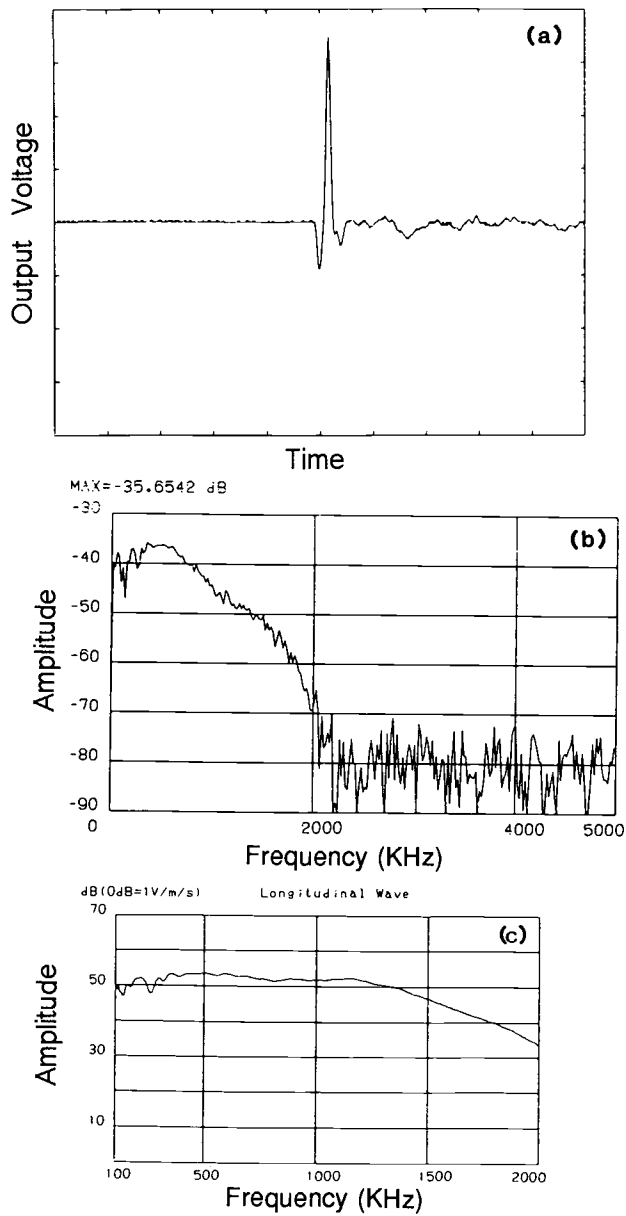


Fig.15 -- The signal emitted from a standard pencil lead fracture. (a) is in time domain (Vertical axis; 0.2V/Div, Horizontal axis; 5  $\mu$ m sec/Div), (b) is power spectrum of (a), and (c) is the sensor sensitivity for the signal measurement.

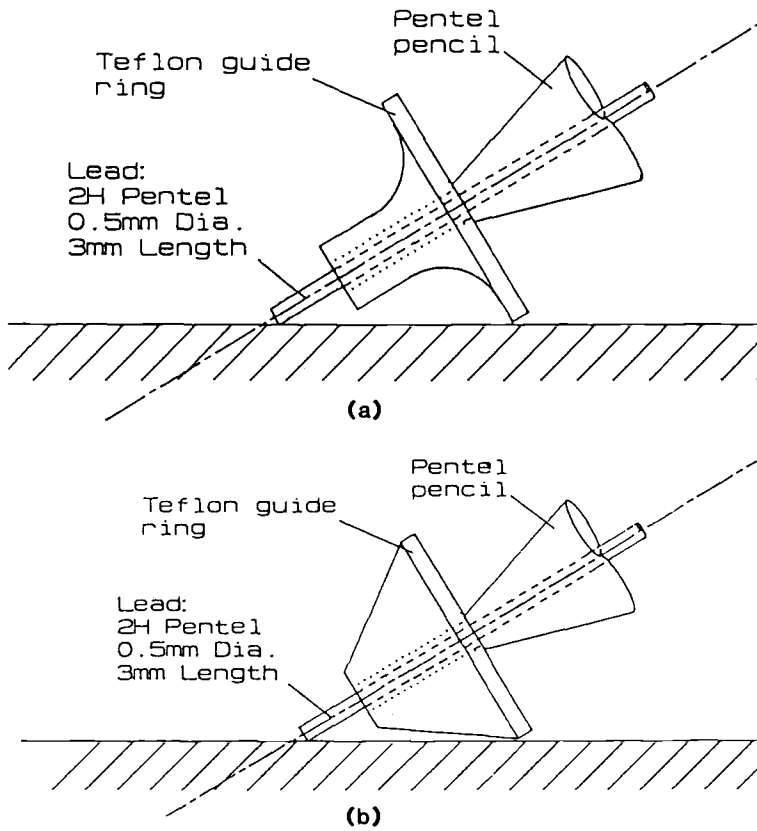


Fig.16 -- Traditional shape of a teflon guide ring (a) and a modified one (b).

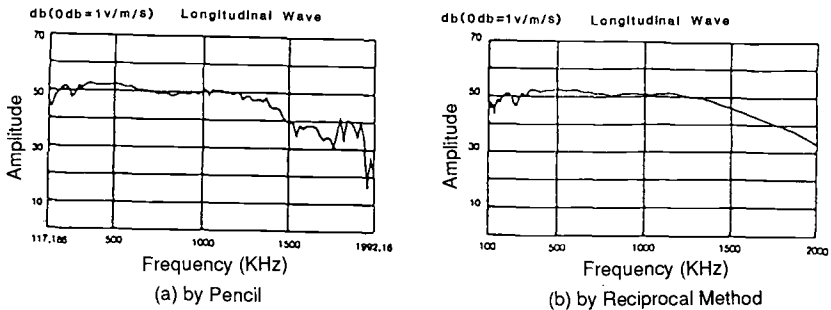


Fig.17 -- The sensor sensitivity obtained by the standard pencil lead fracture method (a), and by the reciprocal method (b).

## CONCLUSION

The general problems of AE sensors were reviewed. The effects of mounting condition of the sensor on the sensitivity were discussed and the sensitivity measurement methods were compared. The results of sensor's sensitivity, obtained by the NBS and by the Hatano method showed that they yielded very similar results.

The convenient calibration methods for sensor sensitivities, especially the "acoustic pressure method" and the "pencil lead fracture method" were discussed. The characteristics of lead, specially standard pencil lead of JAEWG which result in stable reproducibility of generating AE signals, was demonstrated. The characteristics of the lead are quite similar to that produced in 1975. Then sensor sensitivities obtained by the standard lead and the reciprocal method were compared.

## REFERENCES

- [1] Ono, M., Higo, Y. et al., Progress in Acoustic Emission, vol. 2, 1984, pp.343 - 350.
- [2] Higo, Y., Ono, M. et al., Progress in Acoustic Emission, vol. 3, 1986 pp.685 - 691.
- [3] Hatano, H. and Mori, E., Journal of Acoustic Society America, vol.59, 1976, pp.344 - 349.
- [4] Breckenridge, F., Watanabe, T. and Hatano, H., Progress in Acoustic Emission, vol. 1, 1982, pp.448 - 458.
- [5] Hushimi, Y. and Wada, A., Japan Journal of Applied Physics, vol. 16, 1976, pp.230 - 238.
- [6] Nakamura, H. and Wada, A., Applied Physics, vol. 13, 1978, pp.407 - 451. (in Japanese).
- [7] Higo, Y., Takashima, K., Nunomura, S., Nakamura, H. and Wada, A., Proceeding of 5th International Acoustic Emission Symposium, 1980, pp.103 - 114.
- [8] Higo, Y. and Kazama, S. and Nunomura, S., Proceeding of the 2nd Symposium on Nondestructive Evaluation for New Materials, JSNDI, Tokyo, 1988, pp.131-137.
- [9] ASTM standard E1106-86.
- [10] Ninomiya, A., Higo, Y. et al., Proceeding of Japan Electric Society Spring Meeting, Japan, 1989, pp.7-141.
- [11] ASTM standard E1067-85, E976-84 and others.
- [12] ASME Boiler and Pressure Vessel Code (1983) and others.
- [13] Higo, Y. and Inaba, H., Progress in Acoustic Emission, vol. 4, 1988, pp.164 - 169.
- [14] Higo, Y. and Inaba, H., Journal for Acoustic Emission, vol. 18, 1989, pp.s24 - 27.

Trevor J. Holroyd, Timothy E. Tracey, Neil Randall and Simon D King

## STRESS WAVE SENSING - AFFORDABLE AE FOR INDUSTRY

---

REFERENCE: Holroyd, T. J., Tracey, T. E., Randall, N. and King, S. D., "Stress Wave Sensing - Affordable AE for Industry", Acoustic Emission: Current Practice and Future Directions, ASTM STP 1077, W. Sachse, J. Roget and K. Yamauchi, Eds, American Society for Testing and Materials, Philadelphia 1991.

ABSTRACT: A fully integrated stress wave sensor has been created which incorporates the basic functions of an AE system. The sensor is mounted in a robust and easy to install housing which greatly simplifies the sensing of stress wave activities in the industrial environment. The use of signal enveloping techniques in the sensor eases the subsequent handling of its outputs whilst retaining the useful information in the detected stress wave signal. A number of applications are discussed to illustrate the versatility of the approach described.

KEYWORDS: integrated sensor, industrial applications, thick-film hybrid, stress wave sensor, stress wave sensing

## INTRODUCTION

The industrial requirements of AE hardware have been critically reappraised and a shift in emphasis from a non-destructive testing role to a general sensing role has been identified. This shift requires 'AE systems' which are radically different to conventional AE systems in terms of their appearance and performance, as well as mode of use. In view of this it is felt appropriate to rename the approach presently being pursued (SWS) 'Stress Wave Sensing' to avoid confusion with conventional (AE) Acoustic Emission. The label Stress Wave Sensing has been chosen due to the almost universal use of the term stress waves to describe propagating activity detected

Dr Holroyd is Technical Director, Mr Tracey is Analogue Systems Engineer, Mr Randall is Product Development Specialist and Mr King is Applications Specialist, Stresswave Technology Limited, Ravenstor Rd, Wirksworth, Derbyshire, DE4 4FY, UK.

by AE transducers irrespective of the operative causal mechanisms (ie a pressure sensor senses pressure, a load sensor senses load and a stress wave sensor senses stress waves). According to this definition, therefore, Acoustic Emission activity is regarded as a specific category of stress wave activity.

#### THE STRESS WAVE SENSOR CONCEPT

The potential for monitoring the wider physical world using AE hardware has been illustrated over the years in a number of papers which have broadened the horizons of the technique from the defect detection, location and characterisation technique which has been its main thrust since the sixties. All too often these pockets of research aimed at various process and condition monitoring applications have not been fully developed and applied as a result of the high cost of AE hardware and its all too apparent laboratory origins. Taking these considerations into account the concept of applying AE as a simple sensor was developed in which the measurand was stress wave activity whatever its origin as discussed in [1].

For such applications the users primary requirements of the hardware are reliability, ruggedness and ease of installation since these all affect both the viability and cost effectiveness of an application. There are also ample opportunities for trading off certain aspects of performance against cost as discussed in detail in [2]. These considerations led to the concept of a fully integrated AE system or stress wave sensor. Such a sensor should be easy to install on industrial machinery and provide a readily usable output.

#### REALISATION OF THE STRESS WAVE SENSOR

At its heart an AE system consists of a transducer, amplification and signal processing. In a stress wave sensor these functions need to be integrated into a common housing. To achieve this in a physically acceptable package size it was necessary to use thick-film hybridisation techniques in addition to component efficient designs. In doing this a major breakthrough has been the integration of the transducer into the hybrid circuit in the midst of its conditioning and processing electronics. Such a design takes advantage of the compatible acoustic properties of the alumina substrate used in the construction of the hybrid circuit and the piezoelectric element which forms the transducer element. The transducer has a mechanical resonance at the working frequency and the output from the transducer element is amplified within a narrow bandwidth centred on the transducer resonance. This results in a combined transducer and amplifier response which takes a simple form, as shown in Figs 1 & 2. In view of the resonant detection there is little to be gained from analysing the frequency content of the raw signal. Furthermore in view of the random nature of the source processes and the variables and uncertainties in the propagation path there will be no usable



information in the phase of the signal. Hence, the usable part of the signal resides solely in its amplitude (both its absolute level and the nature of its variations). In view of this enveloping has been used as the primary signal processing method. Since the envelope of the signal is generated by an analogue circuit there is a decision to be made concerning the value of the time constant over which the smoothing process is to be carried out. A long time constant output (ie a slowly responding voltage signal) is convenient in that it can be easily read from a meter display or plotted on a chart recorder, for example, whilst a short time constant output (ie a rapidly responding voltage signal) is convenient for analysing fine structure and timing measurements (eg via an oscilloscope or other instrumentation system). In order to satisfy these two conflicting needs the design of the present stress wave sensor incorporates a dual enveloping circuit having fast (100  $\mu$ sec) and slow (1 sec) time constants.

As well as reducing size the incorporation of the transducer into the electronics gives considerable benefits in terms of ruggedness and cost. The resulting hybrid element which forms the heart of the integrated stress wave sensor is shown in Fig 3 and measures only 32mm by 32mm. This is mounted in a rugged housing to make it easier to handle and in order to protect it from the environment although in principle it could be bonded to any surface to provide an 'AE' monitoring function. The casing material is cast stainless steel in order to give mechanical strength, resistance to chemical attack, electromagnetic shielding and the necessary acoustic properties. A photograph of the sensor is presented in Fig 4.

The use of a tab mounting design represents a radical departure from traditional AE design practice. Whereas a typical AE transducer has a (quite delicate) face which is coupled to the workpiece of interest, the stress wave sensor housing as a whole reverberates in response to stress wave excitation. In other words the sensor is designed from a diffuse field standpoint. The sensor housing is excited at some point or in some region and this causes a complex field of stress waves to evolve which can be described statistically via a measurement at any point on the housing.

Considering the baseplate of the sensor therefore this means that it is possible to quantitatively relate the activity detected at the sensitive piezoelectric element to that at the point of sensor housing attachment even though it is at a remote (and in principle arbitrary) position. Whilst in principle this approach has disadvantages in terms of the limit of detection and the temporal resolution of activity, neither of these present a practical problem for the intended use of these sensors. Firstly, with regard to sensitivity, for many industrial applications the limit of detection is set by other interfering stress wave activity not the sensitivity and electronic noise level of the transducer. Under these circumstances a small reduction of sensitivity caused by distancing the transducer element from the workpiece is largely irrelevant. Secondly, the theoretical loss of temporal resolution through the choice of a 'diffuse-field housing' is also irrelevant provided the enveloping time constant is comparable to, or larger than, that of the housing.

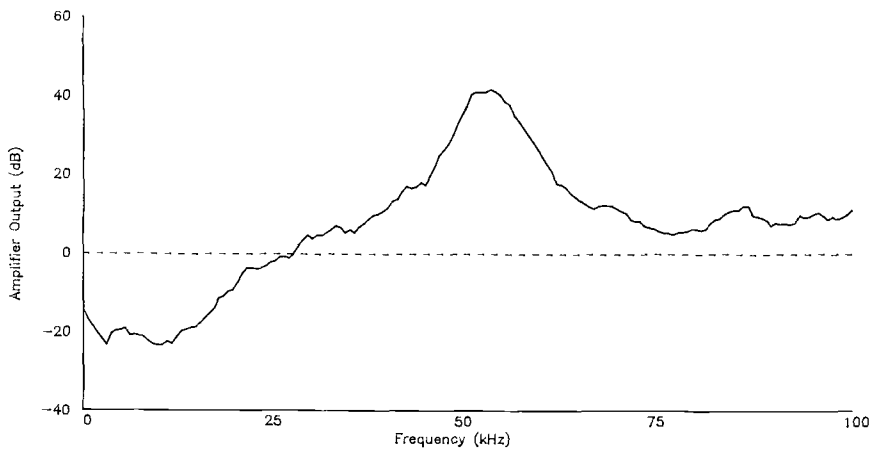


FIG 1 COMBINED RESPONSE OF CRYSTAL & AMPLIFIER (LF)

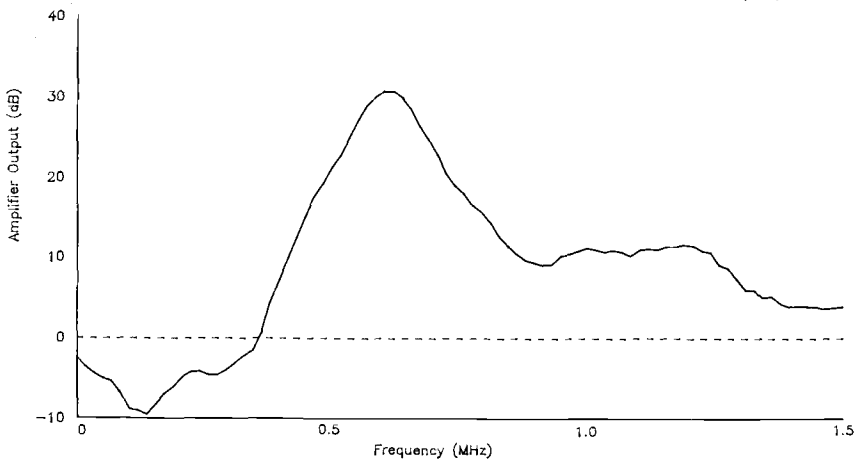


FIG 2 COMBINED RESPONSE OF CRYSTAL & AMPLIFIER (HF)

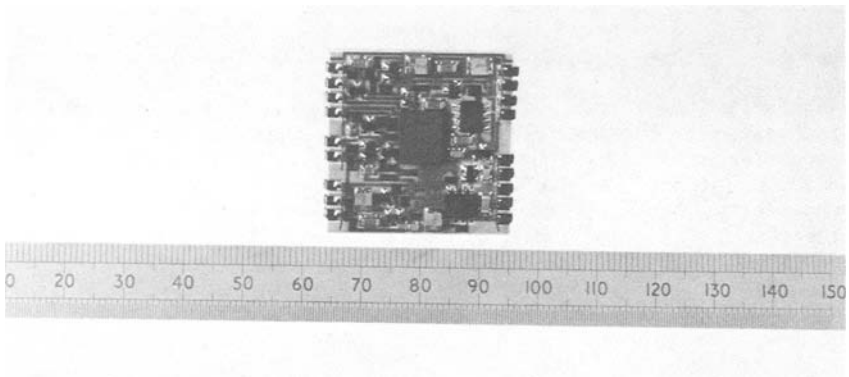


FIG 3 HYBRID CIRCUIT USED IN STRESS WAVE SENSOR

Of course the great advantage of the bolt-on housing design is the increased protection of the sensitive piezoelectric element from accidental mechanical damage (eg due to rough handling) and the elimination of possible sensor damage due to overtightening during installation or uneven mounting surfaces. Indeed high coupling forces can be positively encouraged in view of the resulting improvement in coupling efficiency and stability which results.

#### APPLICATION OF THE STRESS WAVE SENSOR

The resulting sensor is aimed at general use and is intended to be applied alongside, and in a similar manner to, a temperature or load sensor for example. In this general purpose role the stress wave sensor has the advantage (in common with all AE measurements) of sensitivity to a variety of source processes, non-invasive detection, fast response and global monitoring.

Whilst industry in general has shown a ready acceptance of the resulting stress wave sensors it is to be expected that the immediate reaction of an AE practitioner to the above developments may well include some scepticism: 'is tab mounting acceptable?'; 'has too much detection sensitivity been sacrificed?'; 'over what range of applications can enveloping provide useful data?' etc. Experience gained in the application of such sensors to a wide range of industrial processes and plant suggests that these concerns are all too easily overstated. For brevity the examples which will be cited to back up this claim are arbitrarily restricted to those concerning fluid related source processes.

The purpose of a valve for example is to restrict the flow of fluids and in doing so it presents an obstruction to the flow which (subject to the flow conditions) is likely to induce flow anomalies such as turbulence and cavitation. Such anomalies give rise to energy loss in the flow and part of this loss takes the form of stress wave activity. The transient and localised pressure changes which accompany eddies and bubble collapse, for example, cause the activity to be broadband. When a stress wave sensor is used to monitor the activity from a valve then the detected signal level is dependent upon the intensity of the source processes present. If a valve is fully open then it presents the minimum restriction to the flow and therefore gives rise to a low signal level. If the valve is progressively closed the increasing restriction to the flow increases the detected signal level as shown in Fig 5 for the case of a water valve (ie decreasing flow rate gives increasing stress wave level). If, on the other hand, a valve is left open at a fixed setting and the flow rate is remotely altered then the energy loss due to the restriction of the valve or any other flow obstruction increases as the flow rate increases and therefore gives rise to an increasing stress wave level as shown in Fig 6 for steam flowing through an orifice plate.

Caution must be exercised in extrapolating from these findings. Whilst the signal level can readily provide information on the

presence/absence of flow and the consistency of flow (rate, material and geometry) it is not reasonable to expect to obtain a calibrated flow meter simply by bolting a stress wave sensor onto a valve in view of the large range of fluid properties and valve designs. Another area in need of investigation for an accurate flow rate measurement is the long term consistency of the turbulence levels associated with a valve since the possibilities of surface scoring and scale build up need to be borne in mind. Clearly if extreme sensitivity to these secondary effects was observed this could be of great practical significance from a maintenance viewpoint in certain applications.

If the flow at the inlet to a pump is being restricted then cavitation can be induced by the reduced fluid pressure. This is illustrated in Fig 7 where a characteristic increase in stress wave activity occurs as the (NPSHa) Nett Positive Suction Head available reduces. Using the industry standard procedure for interpreting the NPSHa vs head rise curve for this system suggests that significant cavitation should occur when  $NPSHa < 3$ . The monitoring of stress wave activity provides a more direct indication of the presence and relative extent of cavitation which can be of particular benefit in system components with variable geometry and, being non-invasive, in sterile/hygienic systems.

In a diesel engine it is important to its efficient operation that the fuel injectors of the different cylinders are 'balanced' (ie the injection process occurs at the same point relative to the engine cycle in each cylinder). When spring return valves are used it is necessary to balance the different spring return forces by the use of shims. Furthermore, following prolonged operation of the engine it is likely that the spring force will begin to reduce at an unpredictable rate. As this happens the engine efficiency reduces.

To investigate the effects of this on the generated stress wave signal a stress wave sensor was bolted onto a six cylinder diesel engine which was run at a variety of engine speeds. Starting from a well-balanced condition the spring return force of one of the injector valves was deliberately weakened by the removal of a shim such that it opened and closed at approximately 230 psi rather than the normal 270 psi. The complex stress wave signal was analysed with respect to the engine cycle in order to isolate the injection pulse associated with each cylinder. The width of these pulses for an engine operating at 2400 rpm is plotted in Fig 8 from which it can be seen that a broader injection pulse is associated with the cylinder which had a weakened spring return force. The variability of the pulse widths from the other cylinders is probably indicative of the difficulty in balancing such injectors. The sensor used for this trial had a maximum operating temperature of  $70^{\circ}\text{C}$  and therefore a waveguide was used to keep it within its operating range.

In certain types of pump there is a large swept area of rotor/stator contact and this is lubricated by the fluid being pumped. It is therefore critically important that the pump does not dry run since this can rapidly cause serious damage to the stator. It has been found that a stress wave sensor can provide an instant indication of dry running from the reduction in the pumping process

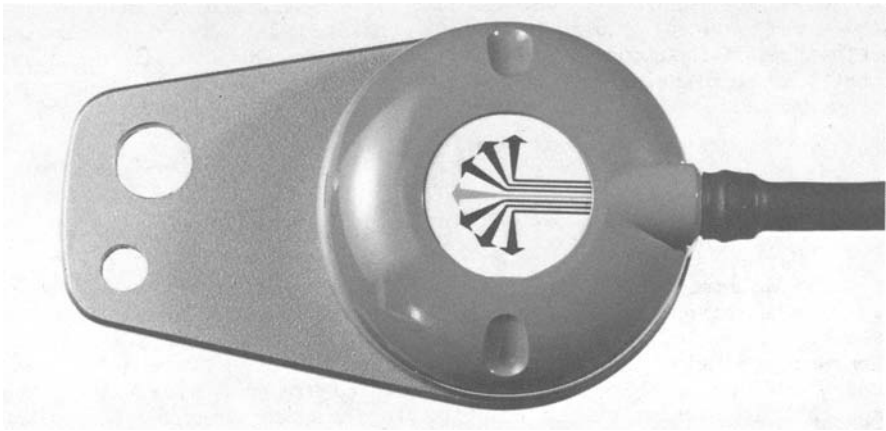


FIG 4 STRESS WAVE SENSOR (SAME SCALE AS FIG 3)

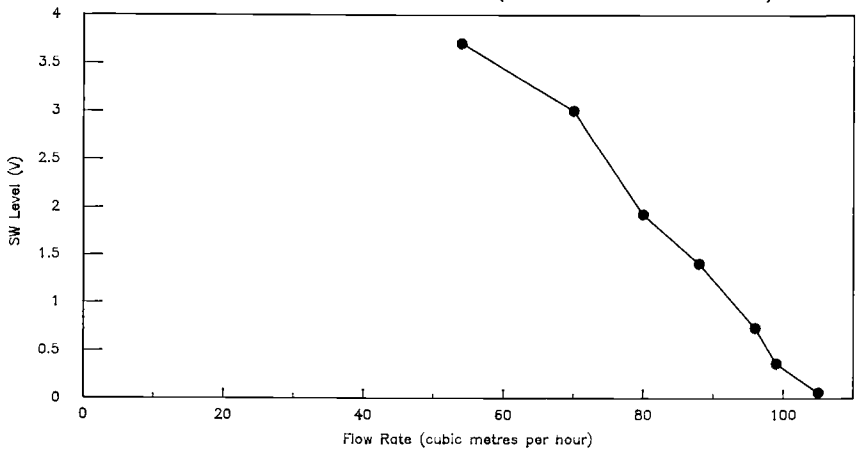


FIG 5 EFFECT ON SW LEVEL OF CLOSING VALVE

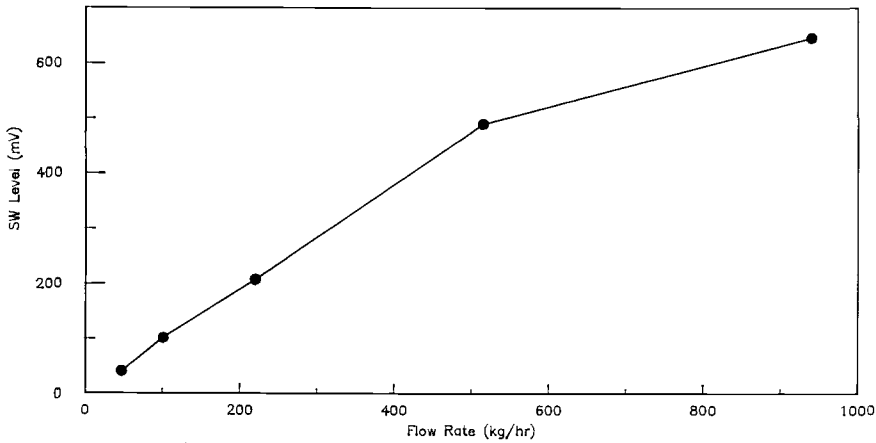


FIG 6 EFFECT OF FLOW RATE ON SW LEVEL AT ORIFICE PLATE

noise as dry running occurs and this is illustrated by the plot of the sensor output shown in Fig 9. This finding is of particular relevance to the food and chemical industries where it is important that the fluid being pumped does not become contaminated by damaged stator debris.

## DISCUSSION

The abilities of AE technology and the requirements of industry in general have been reappraised and a new type of general purpose sensor has been created. The adoption of an integrated sensor approach greatly simplifies the application of AE technology and therefore provides increased opportunities for its wider use. The approach is particularly attractive in those applications where the source processes of interest are dominant since it will then usually be possible to act directly on the output of the sensor using, for example, a standard control system. Quite apart from the unit cost of the sensor the removal of the need for a dedicated AE instrument and the simplification of system specification and installation increases the affordability and accessibility of the technology. Even in the more complex application areas where the signal from the stress wave sensor needs to be further processed to identify the features of specific interest then there is considerable scope for reduction in hardware costs since the specification with regard to bandwidth and inherent noise level can be relaxed without any knock-on effect.

In particular the outputs from the stress wave sensor can be fed via an A to D converter into an appropriate microprocessor for further processing and decision making. This approach has been used successfully to allow more sophisticated discrimination and control functions to be performed in an affordable manner and without the need for operator controls. Alternatively using generally available interface cards and software packages it is possible to input the stress wave sensor output into a PC in order to give the investigative user the maximum flexibility.

Finally, attention is drawn to the broader application of stress wave sensing than for the purely fluid related processes which have been described for brevity. The sensors are equally useful for monitoring frictional, impact and machining type processes as well as for certain structural stability/integrity applications. In this way stress wave sensing can provide a very versatile approach to both condition monitoring and process monitoring/control.

## CONCLUSIONS

- a) The concept of (SWS) Stress Wave Sensing has broad applicability to the monitoring and control of processes and the monitoring of machinery and structural condition.

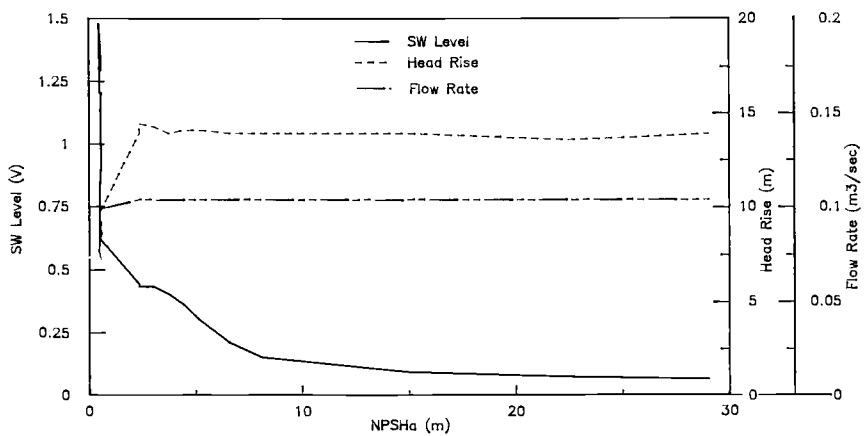


FIG 7 RELATIONSHIP BETWEEN NPSHa & SW LEVEL

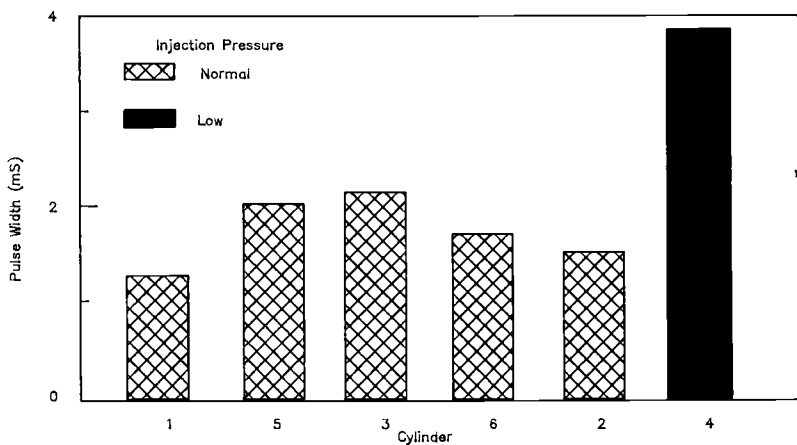


FIG 8 SW PULSE WIDTH ASSOCIATED WITH INJECTION PROCESS

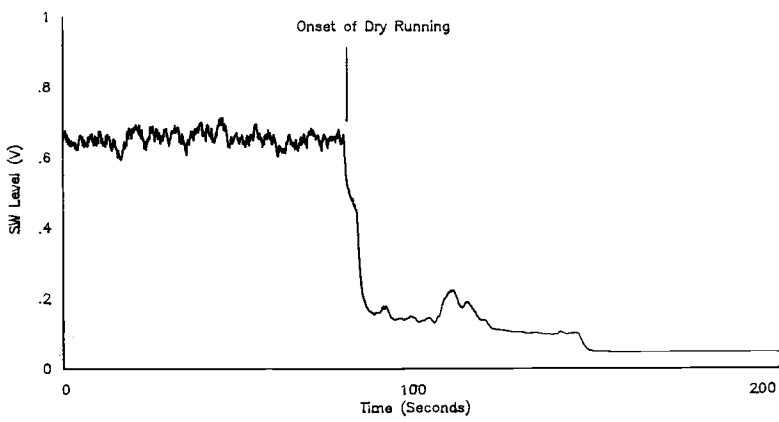


FIG 9 EFFECT OF DRY RUNNING ON SW LEVEL

- b) The stress wave sensor approach offers AE-like capability in an affordable and easy to use package which is appropriate to the industrial environment.
- c) Stress wave sensor outputs are suitable for further processing in either microprocessor based instrumentation or PC's.

#### REFERENCES

- [1] Holroyd, T. J., "AE as a Simple Sensor", Proceedings of the Fifth National Conference on Condition Monitoring, London, 26th November 1985 pp. 5.1, 5.11.
- [2] Holroyd, T. J., "AE from an Industrial Applications Viewpoint", Proceedings of IAES 9, Kobe, Japan, 14-17th November 1988.



Horst A. Crostack, Hermann J. Storp, and Peter Bohm

MONITORING ELECTRON BEAM WELDING PROCESS USING ELECTRO-  
MAGNETIC ACOUSTIC TRANSDUCERS (EMAT's)

-----

**REFERENCE:** Crostack, H. A., Storp, H. J., and Bohm, P.,  
"Monitoring Electron Beam Welding Process Using Electro-  
Magnetic Acoustic Transducers (EMAT's)," Acoustic  
Emission: Current Practice and Future Directions, ASTM  
STP 1077, W. Sachse, J. Roget, and K. Yamaguchi, Eds.,  
American Society for Testing and Materials,  
Philadelphia, 1991.

**ABSTRACT:** This paper describes the use of acoustic emission analysis (AEA) to monitor and control an electron beam welding process. For this to be successful requires that the signals emitted during the welding process be detected and that a good correlation can be established between the welding parameters and the acoustic signals. Weld monitoring applications place special requirements on both the electronic system as well as the sensor used to detect the AE signals. These requirements include a good directional selectivity and a capability for operation at high-temperatures which limits the use of piezoelectric sensors. In this paper the application of non-contact, electromagnetic acoustic transducers is described. The operation of such a sensor to detect the acoustic emissions accompanying an electron beam welding process is demonstrated and their application in a weld-monitoring system is described.

**KEYWORDS:** electron beam welding, process monitoring, process control, electromagnetic-acoustic transducer

Dr. Storp and Mr. Bohm are research scientists, Professor Crostack is director at Fachgebiet Qualitätskontrolle, Universität Dortmund, 46 Dortmund 60, Germany

## INTRODUCTION

The non-destructive investigation of welds imposes particularly high requirements on the test methods. Traditional non-destructive methods often detect flaws in welded seams only with difficulty, according to size and position.

In addition, all methods have in common that welding flaws are generally checked only on the finish-welded component; tests during welding are not yet common. Improvements can therefore only be made afterwards. Here, the acoustic emission analysis offers the advantage, that flaws can be registered directly as they occur, i.e. during welding, so that welding parameters can therefore be corrected at once.

During welding, difficulties arise in the use of the acoustic emission analysis because not only various useful signals, but also very high interference noise may occur. Furthermore, in many welding methods, the acoustic emission of heating and cooling procedures are overlaid. Additional measurements are therefore necessary to suppress interference and separate different sound sources and these measures must be adapted according to the welding process /1,2,3/. This is demonstrated by the following example of electron beam welding.

## FUNDAMENTAL CORRELATION BETWEEN ELECTRON - BEAM (EB) WELDING PROCESS AND DATA OF ACOUSTIC-EMISSION ANALYSIS

During EB welding, noise occurs both during welding and during the cooling phase, Fig. 1. When the sound is registered parallel to the welding current, three different types of noise occur. During welding, continuous acoustic emission occurs together with high amplitudes which become a bundle of smaller amplitudes on turning off the welding current. Burst pulses can then occasionally be observed for a long time.



Fig. 1 : Acoustic emission from EB welding

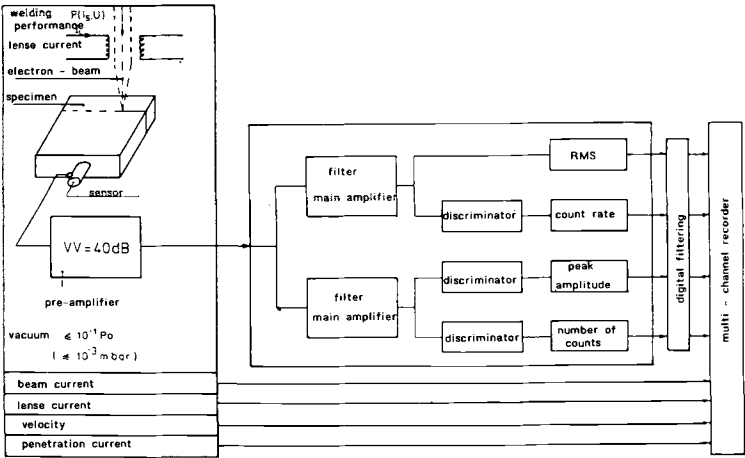


Fig. 2 : Schematic diagram of acoustic emission analysis during EB welding

Whereas the correlations between the characteristic features of the acoustic signals and the sound sources during the cooling phase of the weld seams are satisfactorily clarified, the evaluation of the signals emitted by the process is far more complex /4/. To investigate this testing problem, the experiment shown in Fig. 2 was set up.

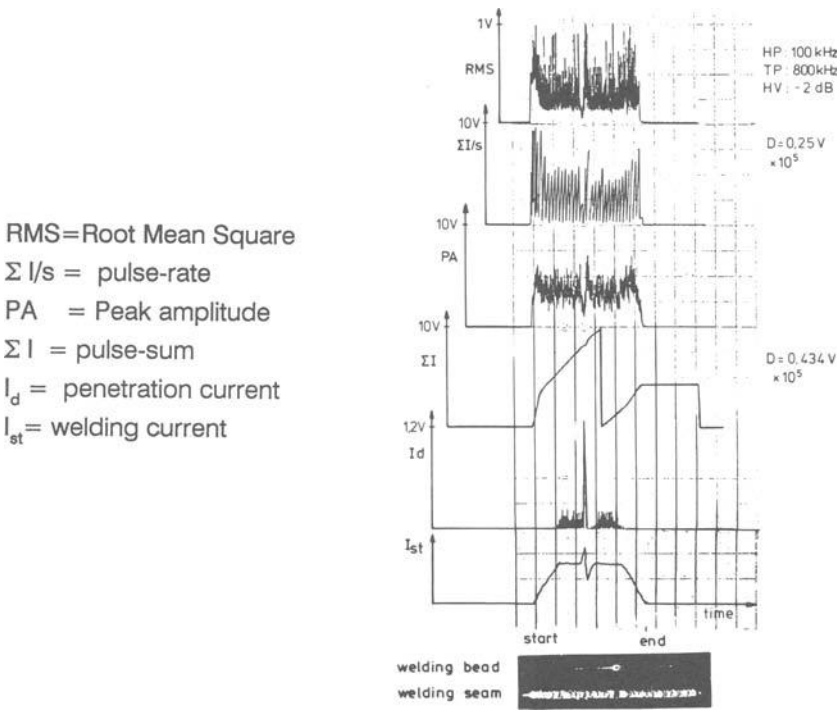


Fig. 3 : Influence of welding process on AEA

Measurements on a 20 mm thick specimen (material 10 CrMo 9 10) show good means of identification of welding current, melting bath motion and acoustic signals, Fig. 3.

The welding parameters beam current, lens current, drive speed and the penetration current can be monitored. The penetration current represents a measure for the number of electrons which come out on the rear side of the component with opened seam channel and which can thus directly be correlated to the welding process.

The acoustic signals were acquired using various high-temperature resistant piezoceramics at centre frequencies between 140 and 600 kHz were used.

An RMS voltmeter, a pulse-sum counter, a pulse-rate counter and a peak amplitude detector were used for the identification of the received signals. The signals are digitally filtered and then plotted on a multi-channel recorder and evaluated.

Thus all four analysis methods used show an increase in sound activity up to maximum at the beginning of the welding process with an increasing opening of the seam channel. The open seam channel presses the sound-active slag out of the passage. The amplitudes of the RMS value, the peak amplitude and also the pulse-rate amplitude accordingly drop, and/or the gradient of the pulse-sum curve is reduced. When the beam current is taken down at completion of the welding process, the RMS meter shows the expected temporary increase in amplitudes. The welding current was temporarily increased in addition to the simulation of flaws. The sudden wide opening of the seam passage leads to the corresponding drop in sound intensity and an increase in amplitudes of the penetration current.

After the pulse-like increase in intensity, the welding current was taken down too strongly, which can be seen from the corresponding curve course of the acoustic signals and/or characteristic break in the pulse-sum curve during the acoustic signal analysis.

Compared to the registration of the penetration current, the acoustic emission hence allows process monitoring even with closed steam passage, thus enabling an early access to the welding process. This is a particularly interesting approach for possible process control.

The large scattering range of the AE-signals is due to the integrally measuring acoustic transducer which also receives signals from the cooling seams in addition to the process noise. In order to exclude the scattering influence on the welding process control, an increased location selectivity of the acoustic transducer with regard to the interesting seam regions should result in a considerable increase in AE sensitivity for a separate monitoring of the welding process and the cooling weld seam.

## OPTIMIZATION OF THE AEA BY USE OF ELECTRODYNAMIC TRANSDUCERS

This problem can be resolved by a face-to-face arrangement of acoustic emission transducer and electron beam. Further increase in the direction selectivity requires the application of the transducer in the near vicinity of the electron beam, whereby the transducer is subjected to high temperatures during the welding process. The experimental problem thus requires contact-free detection of the acoustic emission signals. At present the only possible solution is the use of electrodynamic and/or permanent dynamic transducers. The electrodynamic transducer consists of a coil and a superimposed electric or permanent magnet. Its function as receiving transducer is that an ultrasonic wave within the region of the coil leads to a modulation of the static magnet field according to the wave frequency. An alternating current voltage is thus induced in the coil whose amplitudes can be correlated directly to the height of the particle deflection in the component.

Depending on the geometry of the coil (in this case a meander-shaped coil) and the direction of the magnetic field lines (normal or parallel to the surface) the transducer may be made to favor the detection of shear, longitudinal or Rayleigh-waves, Fig.4.

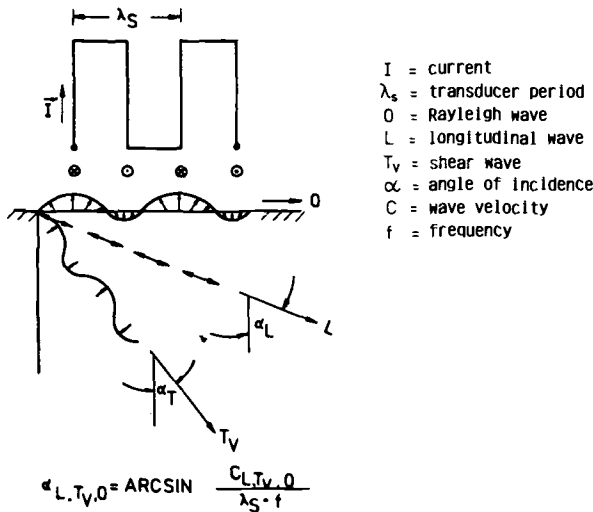


Fig. 4 : Geometry of a meander coil for sending and detecting different kinds of waves by an electromagnetic sensor

The correlation between the transducer period  $s$ , the test frequency  $f$ , the wave velocity and the soundfield characteristic features is of particular importance for the electrodynamic transducer prepared with a meander-shaped coil. After fixing the transducer period, the determination of the test frequency at a narrow-band range result in a particularly clear directional sensitivity of the transducer in the axial direction for each kind of wave mode.

To increase the lateral resolution, the sides of the meander can be additionally arranged in a circular segment around a chosen focus point, Fig. 5 (a).

To show the influence of the coil geometry on its lateral resolution, an acoustic source was moved transverse to the focus point. The detection of the sound source either by a focus or the conventional sensor and plotting the coil voltages over the path of the sound source show a strong

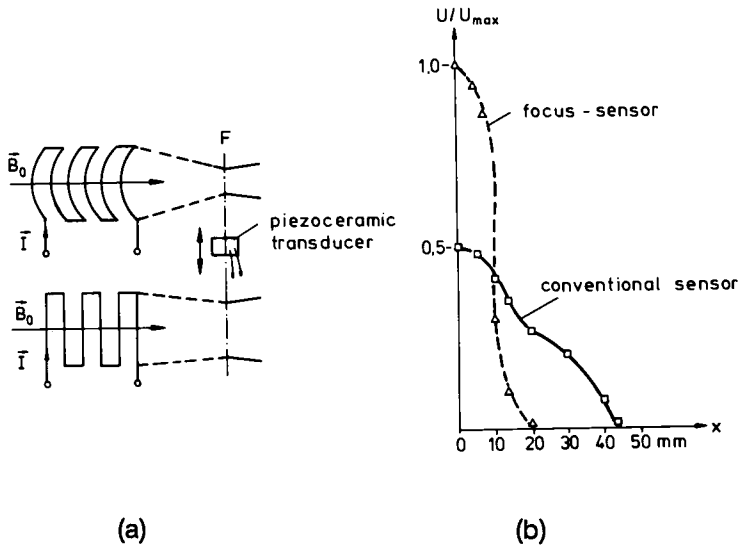


Fig. 5 : Comparison of the directional characteristics of focus and conventional sensor

increased directional selectivity of the focus transducer in comparison with a conventional transducer (5 (a)). In addition, the significantly higher absolute sensitivity of the focus sensor becomes evident. The above mentioned

method thus contributes to an increase in sensitivity of the electrodynamic transducers.

Measurements up to now thus show that the direction selectivity of an electrodynamic transducer can be directly controlled in axial and radial direction.

After completion of the optimization of the transducer system, initial measurements during welding are performed in practice. The schematic diagram of the experimental set-up is illustrated in Fig. 6.

The permanent magnet dynamic transducer was installed on the specimen surface and its design was to receive ultrasound waves from the surface-near zone for its response frequency of 500 kHz. A piezoelectric transducer was additionally arranged on the front side of the specimen. For simplified illustration, the signals received were digitally filtered and plotted on the recorder, Fig. 7.

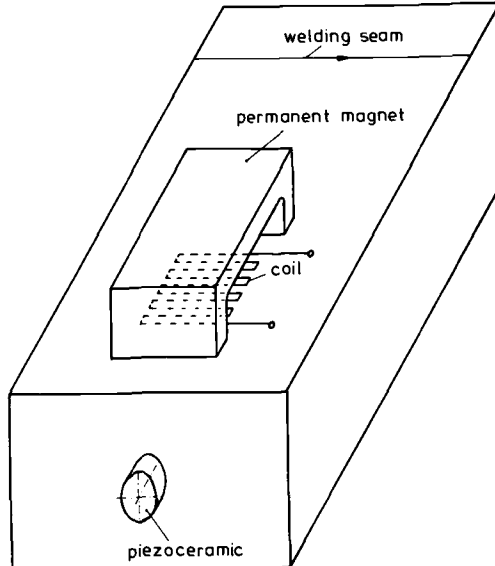


Fig. 6: Position of piezoceramic and electromagnetic sensor for monitoring welding process



The comparison of both curves shows that the received maximum signal height of the permanent dynamic transducer was reached when the welding beam was in the region of the focusing point of the transducer. The measured results hence show that the employment of electrodynamic transducers allow the detection of acoustic signals from the weld seam. More over there are clear advantages over conventional transducers owing to the transducer-specific location selectivity.

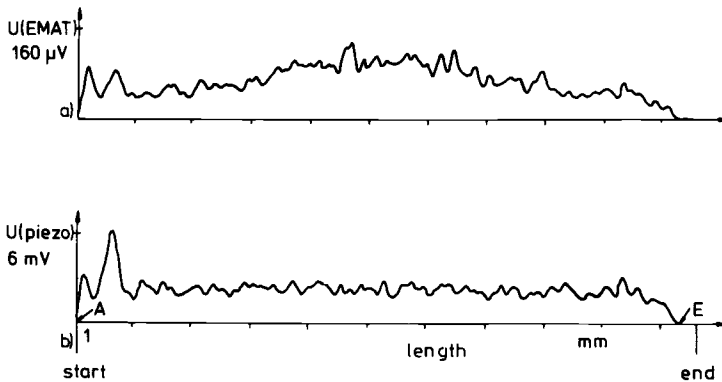


Fig. 7 : Acoustic emission amplitudes detected by EMAT and piezoceramic sensor

## CONCLUSIONS

The measurements show that the acoustic emission signals can directly be correlated with weld beam position in material. Therefore AEA is an interesting method for monitoring and regulating welding process. One weak point in the process regulating line is the piezoelectric acoustic transducer which generally dispose of broad soundfield edges so that the direction of an acoustic event can not be determined accurately. This problem can be solved by introducing permanent dynamic transducers into the process. Compared to the piezoelectric transducer, this sensor has the following advantages:

## CONCLUSIONS

AE measurements can be used to monitor and control a number of welding processes. When sources of emission are to be located during the weld process for control applications, the broad directivity exhibited by conventional, piezoelectric acoustic transducers results in poor angular resolution which complicates the location procedures. This problem can be overcome by using appropriately designed, permanent magnet, electromagnetic acoustic transducers. Our measurements with non-contacting electromagnetic acoustic transducers to detect AE signals during electron beam welding show that the signals can be directly correlated with the position of the weld beam in a test piece. When compared to conventional piezoelectric transducers, such transducers have the following advantages:

- The non-contact detection of acoustic signals permits their use at high temperatures.
- A suitable transducer geometry results in improvements in locating sources of emission both in the axial and radial directions.

It must however be pointed out that the absolute sensitivity of the electrodynamic transducer is approximately 30 dB lower than a piezoceramic transducer. This sensitivity is further reduced if the gap between the coil and the test piece is increased. Hence the application of electromagnetic transducers as AE sensors is restricted to applications in which the generated acoustic signals are of sufficiently high amplitude.

## REFERENCES

- [1] Crostack, H.-A. and Storp, H.-J.: "Acoustic Emission Analysis-An Integral Method for Process Control during Welding" in "Acoustic Emission," edited by J. Eisenblätter, DGM Informationsgesellschaft, Oberusel, 1988.
- [2] Crostack, H.-A., Steffens, H.-D., Kern, H., and Morlo, H.: Untersuchungen zur Anwendung der Schallemissionsanalyse für die zerstörungsfreie Prüfung von Abbreinstumpfschweißverbindungen, "Schweißen und Schneiden 40 (1988), Heft 10.
- [3] Prine, D. W.: "Acoustic Emission Monitoring during Welding, a Powerful NDT Tool," 5th. Intern. Acoustic Emission Symp., Tokyo, 1980.
- [4] Steffens, H.-D., Jüptner, W., and Crostack, H.-A.: Anwendung der Schallemissionsanalyse zur Überwachung des Elektronenstrahlschweißprozesses, Strahltechnik VII, DVS-Berichte Band 34, 1975.

# **AE Sources and Wave Propagation**

DEVELOPMENT AND FUTURE ASPECTS IN AE SOURCE CHARACTERIZATION

---

REFERENCE: Enoki, M. and Kishi, T., "Development and Future Aspects in AE Source Characterization," Acoustic Emission: Current Practice and Future Directions, ASTM STP 1077, W. Sachse, J. Roget, and K. Yamaguchi, Eds., American Society for Testing and Materials, Philadelphia, 1991.

ABSTRACT: The acoustic emission (AE) source characterization has been developed to understand the dynamic process of microfracture in metals, ceramics and composites. The development of AE source characterization can be summarized firstly. This paper is concerned with the theoretical background of AE source characterization. An infinitesimal deformation in a material can be represented as a moment tensor by the 'eigenstrain method' of micromechanics. In this treatment a microcracking can be modeled as a dislocation source with moment tensor components. AE signals can be represented as the convolution integral of the source function due to microcracking, the dynamic Green's function of the media and the transfer function of the measuring system. Secondly, our method of AE source characterization is described. We developed the advanced analysis system to evaluate AE signals quantitatively. Source location of each AE is determined from the signals recorded using six transducers. Each dynamic Green's function of the compact tension specimen concerning each source location is calculated by a finite difference method. The transfer function of the measuring system is calibrated by the breaking pencil lead method. Moment tensor components are determined by the developed deconvolution algorithm. Then the size, fracture mode, orientation and nucleation time of microcracks are obtained from the moment tensor. This analysis system was applied to the fracture toughness tests in various materials. Finally, the future aspects in AE source characterization will be discussed.

KEYWORDS: acoustic emission, source characterization, microcrack, microfracture, micromechanics, quantitative nondestructive evaluation, dynamic Green's function, deconvolution, inverse problem.

Dr. Enoki is a research associate and Dr. Kishi is a professor of Research Center for Advanced Science and Technology, The University of Tokyo, 4-6-1 Komaba, Meguro-ku, Tokyo 153, Japan.

## METHODS OF AE SOURCE CHARACTERIZATION

In the fields of micromechanics and seismology the deformations such as microcracks have been formulated analytically. Those deformations in materials can be generally represented as nonelastic 'eigenstrain' in micromechanics[1]. We have to establish the relationship between microcracking and eigenstrain (or deformation moment tensor). Also we have to develop the method to obtain the moment tensor. An acoustic emission (AE) technique has been used as an almost unique method to detect dynamic deformation and fracture of materials with high sensitivity. Some studies have attempted to characterize AE sources quantitatively on the analogy of seismology[2]. In this paper we summarize the development of AE source characterization firstly. Secondly we mention the theory of AE, which was described in detail in [9], and the experimental and analysis system. Finally some examples of analysis and the future aspects will be discussed.

The development of AE source characterization can be summarized as shown in Table 1, and described as follows.

Single Deconvolution Method

In order to determine the deformation moment tensor and characterize the AE sources, the multiple deconvolution must be carried out in multiple convolution equation by using the recorded AE waveform with more than six channels, as mentioned below. However, if the mode of microcracking is the tensile type, this equation can be reduced to a simple linear convolution equation, and then only the size of microcracking is the unknown parameter and measuring with one channel can determine the size and generation velocity of microcracking. Wadley et al. [3] determined the volume and generation velocity of the cleavage and intergranular microcracks in a mild steel and electrolytic iron by using a capacitance transducer, which can measure the displacement of the surface, and the Yobell specimen, to which the theoretical Green's function can be applied, and then by carrying out the single deconvolution method in the time domain. Kishi et al. [4], on the other hand, also independently applied the simple deconvolution method and characterized intergranular microcracks in Ni-Cr-Mo steel by using the response function, which includes both the transfer function of the measuring system and the Green's function of specimen and can be experimentally calibrated by a breaking pencil lead. Their method could characterize the AE sources by general transducers and specimens.

Table 1 -- The history of AE source characterization.

Year	Author(s)	Channel	Green function	Deconvolution
1981	Kishi, Ohno & Kuribayashi[4]	1	experimental	o
1981	Wadley, Scruby & Shrimpton[3]	1	half-space	o
1985	Ohira & Pao[5]	6	plate	$\Delta$
1986	Enoki & Kishi[9]	6	finite-body	o
1986	Scruby, Stacey & Baldwin[6]	6	half-space	-
1986	Kim & Sachse[8]	6	plate	$\Delta$
1988	Ohtsu	6	half-space	-

o: perfectly carried out,  $\Delta$ : partially carried out, -: not carried out

### Simplified Amplitude Method

The deformation moment tensor has to be determined to obtain the mode and orientation of microcracking. However, various simplified methods have been proposed in this problem to avoid solving the convolution equation directly. Ohira et al. [5] determined the moment tensor in A533B steel from the ratio of amplitudes between longitudinal and transverse waves, by comparing with the ratio which is calculated from the Green's function of an infinite plate. They obtained the time function of the moment tensor by using the single deconvolution method under the assumption that the components of the moment tensor have the same time function. Scruby et al. [6] carried out the analysis by using the strength of the first arrival pulse which is defined as multiplication of the first peak amplitude and time. As the Green's function of media, they used the far-field term of the longitudinal wave of the theoretical Green's function in an infinite medium under the consideration of the reflection at the surface, that is, they used the far-field term of the Green's function in a semifinite medium. They determined the moment tensor in 7010 Al alloy by comparing the pulse strength and this far-field term. Ohtsu [7] used only the first peak amplitude and simplified the Scruby's method in the result. He determined the ratio of the moment tensor, however the absolute value of the moment tensor and time function is not determined by his method. Kim et al. [8] determined the strength and time function of dipoles due to a thermal crack in glass by comparing the epicentral normal response and the Green's function in an infinite plate and by using the single deconvolution method. They determined the radiation pattern of the moment tensor from the peak amplitude of the first longitudinal wave under the assumption that longitudinal wave amplitude is proportional to the surface displacement.

### Multiple Deconvolution Method

The authors [9] determined the moment tensor in A470 steel by solving the convolution equation directly. Firstly, the source location of each acoustic emission was determined from the signals recorded by six multi-transducers. Secondly, each dynamic Green function of the compact tension specimen concerning each source location was calculated by a finite difference method [10]. Finally, the transfer function of the measuring system was calibrated by a pencil breaking lead [11, 12], and then both deconvolution algorithms in time domain and in frequency domain were developed and all the moment tensor components were determined.

## THEORY OF ACOUSTIC EMISSION

### Deformation Moment Tensor

Let  $V$  denote an elastic domain occupied by a given three dimensional body and  $\epsilon_{mn}^*(\mathbf{x}, t)$  denote an eigenstrain tensor in  $V$ . If the dimension of region occupied by eigenstrain  $\epsilon_{mn}^*(\mathbf{x}, t)$  is small compared with distance between the position  $\mathbf{x}$  and  $\mathbf{x}'$ , and the shortest wavelength due to  $\epsilon_{mn}^*(\mathbf{x}, t)$ , then the point source approximation can be applied. Then we can state the displacement field due to  $\epsilon_{mn}^*(\mathbf{x}, t)$  as [1, 9]

$$u_i(\mathbf{x}', t) = G_{ij,k}(\mathbf{x}', \mathbf{x}, t) * D_{jk}(\mathbf{x}, t), \quad (1)$$

where

$G_{ij}(\mathbf{x}', \mathbf{x}, t)$  = the displacement field in the direction  $x_i$  at position  $\mathbf{x}'$  at the time  $t$  due to an impulsive force in the direction  $x_j$  at  $\mathbf{x}$  at time 0,

and the comma indicates a differentiation and  $*$  means a convolution integral with respect to time. The deformation moment tensor  $D_{jk}(\mathbf{x}, t)$ , which is the quantity to represent an infinitesimal deformation, is defined as, for an isotropic material,

$$\begin{aligned} D_{jk}(\mathbf{x}, t) &= C_{jkmn} \epsilon_{mn}^*(\mathbf{x}, t) dV \\ &= (\lambda \epsilon_{mm}^* \delta_{jk} + 2\mu \epsilon_{jk}^*) dV, \end{aligned} \quad (2)$$

where

$C_{jkmn}$  = the elastic stiffness tensor,  
 $\delta_{jk}$  = Kronecker's delta,  
 $dV$  = the volume of deformation domain,  
 $\lambda$  and  $\mu$  = the Lamé's constants.

The deformation moment tensor  $D_{jk}(\mathbf{x}, t)$  is a symmetry tensor of a second order, which is represented by mode and intensity of an infinitesimal deformation. Equation 2 shows that independent six quantities of  $D_{jk}$  are represented by seven quantities of  $\epsilon_{mn}^*$  and  $dV$ .

Let us consider the eigenvalue problem of  $D_{jk}$  because  $D_{jk}$  is a symmetry tensor of a second order. We can calculate three invariants  $J_1$ ,  $J_2$  and  $J_3$  respectively

$$\begin{aligned} J_1 &= D_{ii} = (3\lambda + 2\mu) \epsilon_{ii}^* dV, \\ J_2 &= [(3\lambda^2 + 4\lambda\mu + 2\mu^2)(\epsilon_{ii}^*)^2 - 2\mu^2(\epsilon_{ij}^* \epsilon_{ij}^*)](dV)^2, \\ J_3 &= (1/3)[(3\lambda^3 + 6\lambda^2\mu + 6\lambda\mu^2 + 4\mu^3)(\epsilon_{ii}^*)^3 \\ &\quad - (6\lambda\mu^2 + 12\mu^3)\epsilon_{kk}^*(\epsilon_{ij}^* \epsilon_{ij}^*) \\ &\quad + 8\mu^3 \epsilon_{ij}^* \epsilon_{jk}^* \epsilon_{ki}^*](dV)^3. \end{aligned} \quad (3)$$

Eigenvalues  $D$  are three solutions of the following equation,

$$D^3 - J_1 D^2 + J_2 D - J_3 = 0. \quad (4)$$

### Microcracking Model

It is well known that the generation of microcrack can be modeled as the discontinuity of displacement on the faulting surface like a dislocation[1]. Eigenstrain  $\epsilon_{ij}^*(\mathbf{x}, t)$  due to the discontinuity of displacement can be represented as

$$\epsilon_{ij}^*(\mathbf{x}, t) = (1/2)\{[u_i(\mathbf{x}, t)] \nu_j(\mathbf{x}) + [u_j(\mathbf{x}, t)] \nu_i(\mathbf{x})\} \delta(A - \mathbf{x}), \quad (5)$$

where

$[u_i(\mathbf{x}, t)]$  = the discontinuity of displacement on a surface  $A$ ,  
 $\nu_i(\mathbf{x})$  = the normal to surface  $A$ ,

$\delta(A - \mathbf{x})$  = two dimensional delta function on surface A.

The deformation moment tensor is, from Eq 2,

$$D_{jk}(\mathbf{x}, t) = \{\lambda [u_m] \nu_m \delta_{jk} + \mu ([u_j] \nu_k + [u_k] \nu_j)\} \Delta A, \quad (6)$$

where

$\Delta A$  = the area of surface A.

This  $D_{jk}(\mathbf{x}, t)$  is called a seismic moment tensor in seismology[2].

Substituting Eq 5 into Eq 3, we can calculate three invariants  $J_1$ ,  $J_2$  and  $J_3$ , and obtain three eigenvalues  $D^{(1)}$ ,  $D^{(2)}$  and  $D^{(3)}$  of  $D_{jk}$  from Eq 4 as

$$\begin{aligned} D^{(1)} &= ((\lambda + \mu) [u_m] \nu_m + \mu [u]) \Delta A, \\ D^{(2)} &= \lambda [u_m] \nu_m \Delta A, \\ D^{(3)} &= ((\lambda + \mu) [u_m] \nu_m - \mu [u]) \Delta A, \end{aligned} \quad (7)$$

where

$$[u] = ([u_m] [u_m])^{1/2}.$$

Three eigenvectors  $\mathbf{x}^{(1)}$ ,  $\mathbf{x}^{(2)}$  and  $\mathbf{x}^{(3)}$  are respectively represented as

$$\begin{aligned} x_i^{(1)} &= [u_i] + [u] \nu_i, \\ x_i^{(2)} &= \epsilon_{ijk} [u_j] \nu_k, \\ x_i^{(3)} &= [u_i] - [u] \nu_i, \end{aligned} \quad (8)$$

where

$\epsilon_{ijk}$  = the permutation tensor.

This result shows that  $\mathbf{x}^{(1)}$  is the vector in the direction of isometric angle between  $[u]$  and  $\nu$ ,  $\mathbf{x}^{(2)}$  is the vector in the direction of normal to the plane given by  $[u]$  and  $\nu$ , and  $\mathbf{x}^{(3)}$  which is on the plane given by  $[u]$  and  $\nu$  is normal to  $\mathbf{x}^{(1)}$ . Consequently the generation of displacement discontinuity  $[u]$  on the surface A with the normal  $\nu$  is equivalent to the generation of moment with magnitude  $D^{(1)}$ ,  $D^{(2)}$  and  $D^{(3)}$ , and with direction  $\mathbf{x}^{(1)}$ ,  $\mathbf{x}^{(2)}$  and  $\mathbf{x}^{(3)}$  respectively, which is called a vector dipole which has the same direction of arm and force.

Using the trace of moment tensor, the volume  $\Delta V$  of microcrack and the angle  $\theta$  between  $[u_i]$  and  $\nu_i$  can be represented as respectively

$$\Delta V = [u_m] \nu_m \Delta A = D_{ii} / (3\lambda + 2\mu), \quad (9)$$

$$\cos \theta = [u_m] \nu_m / ([u_k] [u_k])^{1/2}. \quad (10)$$

Assuming that a microcrack is a disc-like crack subject to a normally applied stress  $\sigma$ , we can state the crack volume as[13]

$$\Delta V = 16 a^3 \sigma (1 - \nu^2) / 3E, \quad (11)$$

where



$a$  = the crack radius,  
 $E$  = the Young's modulus,  
 $\nu$  = Poisson's ratio.

The crack radius  $a$  is, from Eqs 9 and 11,

$$a = \{3 (1 - 2\nu) D_{ii} / 16 (1 - \nu^2) \sigma\}^{1/3}. \quad (12)$$

The nucleation velocity of microcracking  $v$  can be defined as

$$v = a / \Delta t, \quad (13)$$

where

$\Delta t$  = the nucleation time of microcracking.

### Acoustic Emission Signals

The detected signals of acoustic emission are generally different from the displacement field because of the response function of the measuring system, which is shown in Fig. 1. Denoting the response function in the  $i$ -direction at the position  $\mathbf{x}$  on the surface by  $S_i(\mathbf{x}, t)$ , the detected signals  $V(\mathbf{x}', t)$  due to moment tensor  $D_{jk}(\mathbf{x}, t)$  can be expressed as[4], from Eq 1,

$$V(\mathbf{x}', t) = S_i(\mathbf{x}', t) * G_{ij,k}(\mathbf{x}', \mathbf{x}, t) * D_{jk}(\mathbf{x}, t). \quad (14)$$

### EXPERIMENTAL SYSTEM OF AE SOURCE CHARACTERIZATION

Figure 2 shows the block diagram of the multichannel AE detection and recording system.

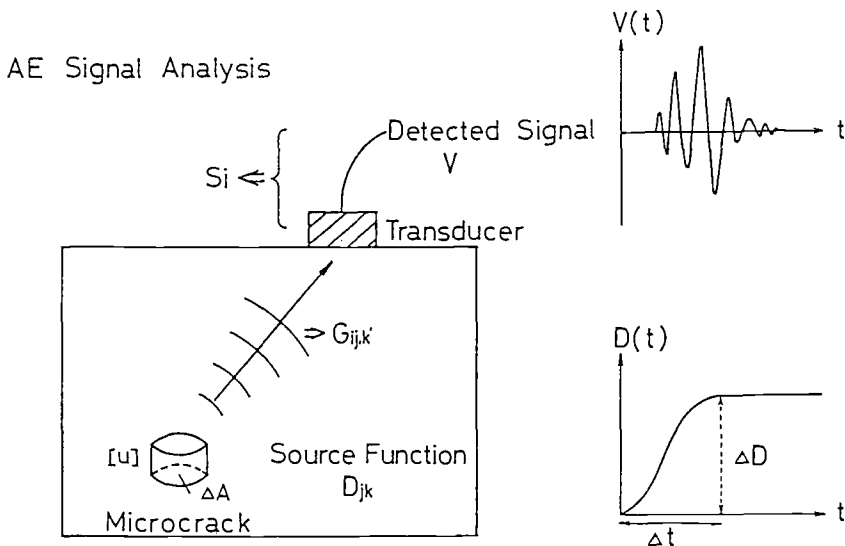


FIG. 1 --The relation between source function  $D_{jk}$  and detected signal  $V$  in acoustic emission signal processing, where  $G_{ij,k}$  is a dynamic Green's Function and  $S_i$  is a response function of measuring system.

### Transducers

The transducer P50 (PAC) has a piezoelectric element of about 1 mm and a broad-band response up to 2 MHz.

### Preamplifier

The output from each transducer is amplified 20 or 40 dB by the low noise type preamplifier 9913 (NF) with a frequency response, DC-20MHz.

### Wave Memory

And then digitized and stored by the wave memory AE9620 (NF) with the maximum sampling rate of 20 MHz, resolution of 10 bits and the record length of 2048 points.

### Computer

Data from the wave memory are transferred via a GP-IB interface and stored on magnetic disc in the model 350 computer (HP). The transducers and measuring system are calibrated using a breaking pencil lead[11, 12]. The AE analyzer AE9600 (NF) is also used to measure the conventional AE parameters of events and peak amplitude. The output from the transducer P50 (PAC) is fed into the AE analyzer AE9600 and the conventional AE parameters are stored on magnetic disc in a model 216 computer (HP) with the external parameters of load and crack opening displacement (COD). Each dynamic Green's function of the

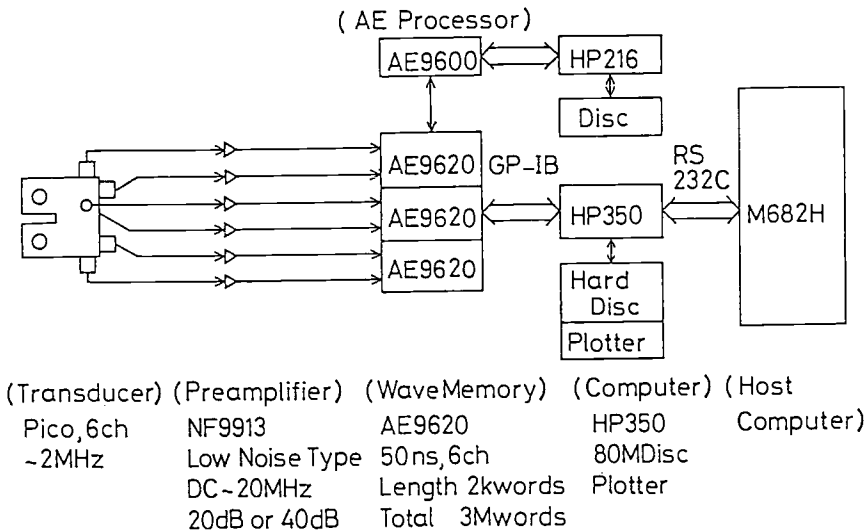


FIG. 2 -- The block diagram of the multichannel acoustic emission detection and recording system.

compact tension specimen concerning each source location which is calculated by a finite difference method, are transferred via a RS-232C interface and stored on magnetic disc in the model 350 computer (HP).

### Fracture Toughness Tests

Fracture toughness tests are carried out at a constant crosshead speed and AE signals are recorded during testing. Source location of each acoustic emission is determined from the waveform recorded using six transducers.

### ANALYSIS SYSTEM OF AE SOURCE CHARACTERIZATION

#### Source Location

Figure 3 shows the developed analysis system for AE source characterization. Accurate source location is required in order to understand fracture processes. The location of each source event is determined by measuring the differences in the wave arrival time between two transducers[14]. Suppose that  $\Delta t_{ij}$  is the difference in the wave arrival time between  $i$ -th and  $j$ -th transducers. Let  $r_i$  denote the transducer positions ( $1 \leq i \leq P$ ) and  $r$  denote the location of the source, where  $P$  is the total number of channels. We can represent the general equation for source location as

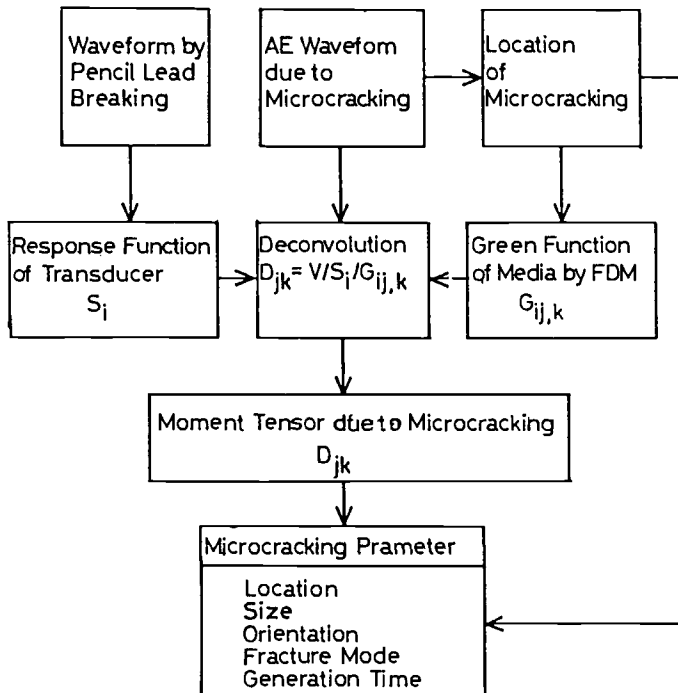


FIG. 3 -- The developed analysis system for AE source characterization.

$$\Delta t_{ij} = |r - r^i| / v^e(r, r^i) - |r - r^j| / v^e(r, r^j), \quad (15)$$

where

$v^e(r, r^i)$  = the energy velocity of  $r^i$ - $r$  direction.

This equation can be reduced as, for an isotropic materials,

$$\alpha \Delta t_{iP} = |r - r^i| - |r - r^P|, \quad 1 \leq i \leq P-1, \quad (16)$$

where

$\alpha$  = the longitudinal velocity of material.

If  $P \geq 4$ , then a nonlinear least-square method can be used to solve the Eq 16 for source location  $r$ . Figure 4 shows the typical positions of six P50 transducers which are attached to the compact tension specimen.

### Green's Function of Media

The analytical[15], experimental[4] or numerical researches on Green's function of media have been investigated. However, the Green's function which has the complex boundary conditions can be obtained only by the numerical simulation method. We simulate the dynamic Green's function of compact tension specimen by a finite difference method[10].

The equations of wave motion in an elastic, isotropic and homogeneous medium in vector form are:

$$\rho \partial^2 U / \partial t^2 = \mu \nabla^2 U + (\lambda + \mu) \nabla (\nabla \cdot U), \quad (17)$$

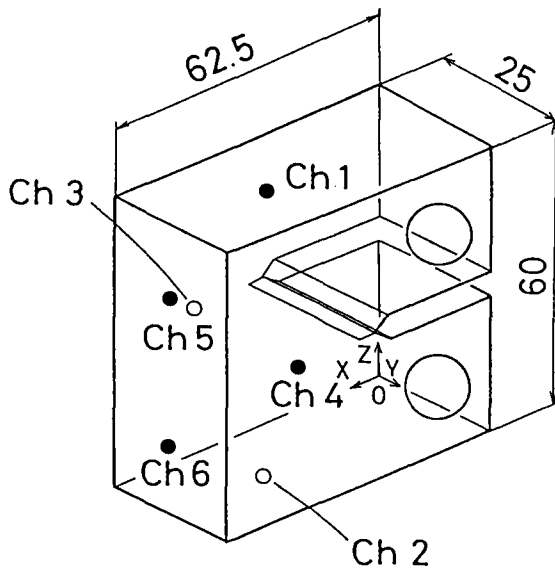


FIG. 4 -- Geometry of compact tension specimen and configuration of six P50 AE transducers.

where

$U$  = the displacements,  
 $\rho$  = the mass density of the material.

In order to obtain the Green's function for a CT specimen, the specimen is modeled by a rectangular parallelepiped with a macrocrack as shown in Fig. 5. The pinholes are disregarded since the effect of a reflection wave from them on the AE source characterization is minimal for the sensor locations used in Fig. 4. The boundary conditions are that all tractions on the free surfaces are zero. On the upper surface shown by the shaded portion in Fig. 5, for example, we get the following formulations as boundary conditions:

$$\begin{aligned}\sigma_{zz} &= (\lambda + 2\mu)U_{z,z} + \lambda(U_{x,x} + U_{y,y}) = 0, \\ \sigma_{zx} &= \mu(U_{x,z} + U_{z,x}) = 0, \\ \sigma_{zy} &= \mu(U_{y,z} + U_{z,y}) = 0.\end{aligned}\quad (18)$$

The boundary conditions for the other free surfaces and crack surfaces can be formulated in the same way. The free surfaces are shown by solid lines in Fig. 6. The length of a crack is represented by AA'. The initial conditions are

$$U = \partial U / \partial t = 0 \quad \text{for } t \leq 0. \quad (19)$$

Let us consider the input function for moment tensors,  $D_{jk}(\mathbf{x})r(t)$ , at an inner point  $\mathbf{x}$ , where  $D_{jk}(\mathbf{x})$  is the moment resulting from the product of the force in the  $j$ -direction with the arm in the  $k$ -direction, and  $r(t)$  is a nondimensional time function with some rise time. Here, a force is applied at each of the two points  $\mathbf{x}^{k+}$  and  $\mathbf{x}^{k-}$ ,

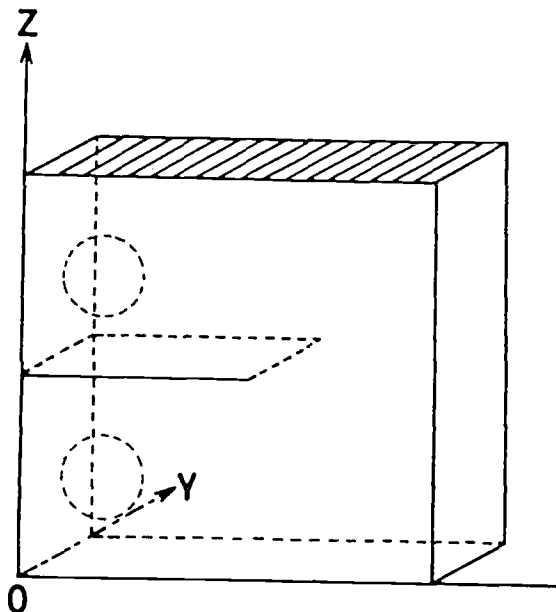


FIG. 5 -- A model of LTCT specimen.

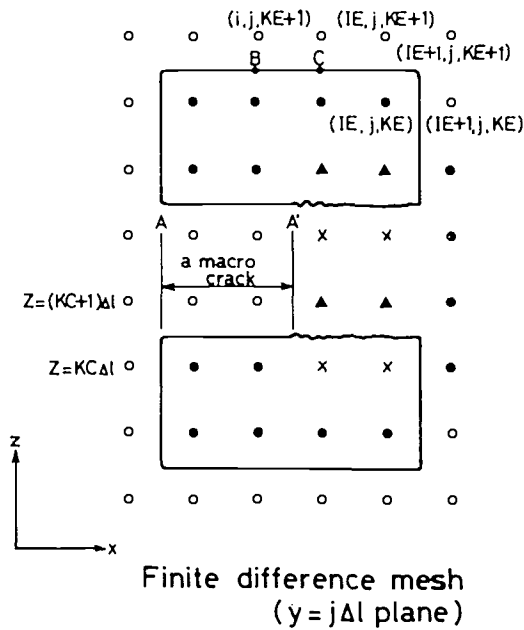


FIG. 6 -- Finite difference mesh around the free surfaces and crack surfaces.

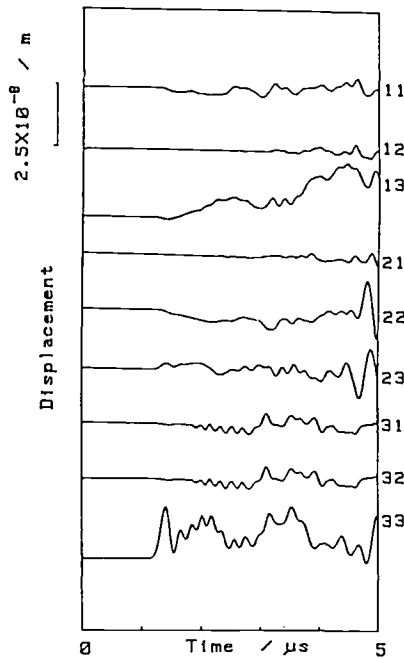


FIG. 7 -- The example of the response function  $G_{ij,k}$  at the position of transducers which are simulated by a finite difference method.

where the size of each force  $F$  is  $D_{jk}(\mathbf{x})/\Delta l$ , and their directions are opposite. By considering the equation of motion containing the body forces at two points,  $\mathbf{x}^{k+}$  and  $\mathbf{x}^{k-}$ , the following equations result:

$$\begin{aligned}\rho \partial^2 U_j(\mathbf{x}^{k+}) / \partial t^2 &= \mu \nabla^2 U_j(\mathbf{x}^{k+}) + (\lambda + \mu) U_{j,j}(\mathbf{x}^{k+}) + F \cdot \mathbf{r}(t) / \Delta l^3, \\ \rho \partial^2 U_j(\mathbf{x}^{k-}) / \partial t^2 &= \mu \nabla^2 U_j(\mathbf{x}^{k-}) + (\lambda + \mu) U_{j,j}(\mathbf{x}^{k-}) - F \cdot \mathbf{r}(t) / \Delta l^3.\end{aligned}\quad (20)$$

Nine different forms of the moment tensor may exist, where the sign of force is defined to be positive if it acts along the positive direction of the axis.

Let us take the same increments  $\Delta l$  in the  $x$ ,  $y$  and  $z$ -directions in Eq 17, and take an increment  $\Delta t$  in time.  $U(i,j,k,p)$  represents the approximate components of displacement at a grid point  $(i\Delta l, j\Delta l, k\Delta l)$  at time  $p\Delta t$ . For simplicity we denote the point by  $(i, j, k)$ . Here  $i, j, k$  and  $p$  are integers  $0 \leq i \leq IE, 0 \leq j \leq JE, 0 \leq k \leq KE$ , where  $IE, JE$ , and  $KE$  represent the total numbers of the mesh points in  $x, y$  and  $z$ -directions, respectively. The stability condition of these equations is

$$L = \Delta t / \Delta l \leq (\alpha^2 + 2\beta^2)^{-1/2}, \quad (21)$$

where

$$\begin{aligned}\alpha^2 &= (\lambda + 2\mu) / \rho, \\ \beta^2 &= \mu / \rho.\end{aligned}$$

It is well known that the discretized formulation generally converges to the exact solution of Eq 17, as  $\Delta l$  is decreased while keeping the value of  $L$  constant.

In the application of the acoustic emission method, detection and evaluation of microcracks nucleated at the macrocrack tip are essential. Thus, the interest of this paper is to obtain the Green's function of finite medium which includes a macrocrack. The Green's functions of a one inch compact tension (1CT) type specimen shown in Fig. 4 are simulated using the present FDM. The material is steel with the material constants,  $\lambda = 1.07 \times 10^{11}$  Pa,  $\mu = 7.67 \times 10^{10}$  Pa, and  $\rho = 7.87 \times 10^3$  kg/m<sup>3</sup>. In order to obtain the Green's functions, the nine couples of moment are applied to the three-dimensional localized points. The response functions at the six points of transducers are simulated. An example of the results at a transducer point on the surface is given in Fig. 7, where the input point is one of the experimentally localized points. With consideration given to a reasonable amount of computer memory utilization, the values  $\Delta l = 0.5$  mm,  $\Delta t = 0.05$   $\mu$ s and rise time  $t_r = 0.5$   $\mu$ s are used.

### Response Function of Measuring System

The transducers and measuring system are calibrated using a breaking pencil lead. Before the fracture toughness testing, the waveform data due to the breaking pencil lead at the surface of specimen are recorded. The Green's function corresponding to the braking pencil lead is calculated by a finite difference method [10]. Then the response function of the measuring system is obtained from the result of the deconvolution with the known source function of the pencil breaking lead [12] and the above Green's function.

Deconvolution in Time Domain

Equation 14, which is a convolution integral equation in time domain, can be written as

$$u^i(t) = \sum_{j=1}^J g^{ij}(t) * d^j(t), \quad i=1, \dots, I, \quad j=1, \dots, J. \quad (22)$$

where

- $u^i(t)$  = the waveform data due to microcracking,
- $g^{ij}(t)$  = the transfer function which is convoluted by the transfer function of measuring system and Green's function of media,
- $d^j(t)$  = the unknown moment tensor.

Assuming that the components of the microcracking moment tensor have the same time function  $T(t)$ , Eq 22 is written as

$$u^i(t) = \sum_{j=1}^J c^j g^{ij}(t) * T(t). \quad (23)$$

The problem of source characterization is then to simultaneously determine  $T(t)$  and  $c^j$  ( $1 \leq j \leq J$ ), given  $u^i(t)$  and  $g^{ij}(t)$  over a finite time interval [16]. Let  $N$  be the value of  $n$  which corresponds to the maximum time for which  $u^i(t)$  and  $g^{ij}(t)$  are specified. The convolution integral in Eq 23 reduces to a summation as

$$u^i(n) = \sum_{j=1}^J \sum_{k=1}^N c^j g^{ij}(n - k + 1) T(k) \Delta t, \quad 1 \leq n \leq N. \quad (24)$$

We develop the iterative algorithm to solve this nonlinear equations as follows:

1. The  $c_0^j$  coefficients and  $T_0(n)$  are set to nonzero initial values.
2. Using these  $c_0^j$ , the  $T_1(n)$  are calculated from Eq 24.
3. These  $T_1(n)$  are used to calculate the improved  $c_0^j$  from Eq 24.
4. The more improved  $c_1^j$ ,  $T_1(n)$  are obtained by averaging.
5. These procedure of alternately calculating  $c_M^j$  and  $T_M(n)$  can be continued until the  $c_M^j$  and  $T_M(n)$  converge to fixed values.

Deconvolution in Frequency Domain

Applying Laplace transform to this equation, we can find a discrete convolution integral equation in frequency domain as [17]

$$\tilde{u}_n^i = \sum_{j=1}^J \tilde{g}_n^{ij} \tilde{d}_n^j, \quad i=1, \dots, I, \quad n=1, \dots, N, \quad (25)$$

where  $\sim$  means Laplace transform. The algorithm to obtain moment tensor components is developed as follows:

1. The Laplace transform is carried out. Both  $u^i(t)$  and  $g^{ij}(t)$  are converted into  $\tilde{u}_n^i$  and  $\tilde{g}_n^{ij}$ , respectively.
2. Solving the linear Eq 25,  $\tilde{d}_n^j$  is calculated.
3. Using inverse Laplace transform, a moment tensor  $d_k^j$  is obtained



from  $\hat{a}_n^j$ .

In connection with the Laplace transform the time function has to be multiplied with  $e^{-\delta t}$ , so the discrete convolution error can be neglected if one chooses a suitable value for  $\delta$ . As both transforms are performed by using the algorithm of the fast Fourier transform (FFT), the calculation time of deconvolution can be shorter than that of the algorithm in time domain.

## RESULTS AND DISCUSSION

### Source Location

Figure 8 shows both the results of optical observation and the location results by AE of the SiC fiber reinforced glass composite using a half size of a standard 1 inch thickness compact tension specimen with 2.85 mm and the notch of 0.1 mm width. The results were in good agreement with the observation and the location by AE. Figure 9 shows the location data of Al-Li alloy in fracture toughness test with 1TCT specimen of TL direction. AE events can be classified two groups. Figure 9 shows that source events under the low applied load are generated at the back of the fatigue precrack tip, while those under the high applied load are generated in front. It can be concluded that the former is due to cleavage at the precrack tip and the latter is due to separation crack in front by the observation of scanning electron microscope, which is clearly shown in Fig. 14 later. The errors of source location are given by a sampling rate, positions of transducers and dimensions of transducers. A sampling rate of 20 MHz and a

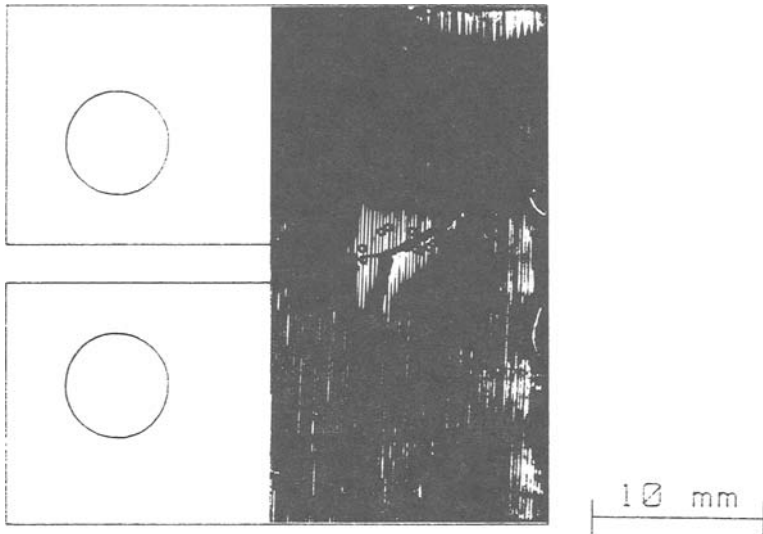


FIG. 8 -- The results of location of AE sources detected during fracture toughness test in the SiC glass composite.

longitudinal velocity in Al-Li alloy give the maximum error of about 0.6 mm in source location. Although the size of the piezoelectric element is about 1 mm, the error of positions in attachment of transducers is smaller than this. Then the experimental error on each coordinate is estimated to be approximately 1 mm.

#### Single Deconvolution Method

The AE waveform with more than six channels must be recorded and the multiple deconvolution must be carried out in Eq 14 to determine the deformation moment tensor and characterize the AE sources. However, if the mode of microcracking is the tensile type, Eq 14 can be reduced to a simple linear convolution equation, and then only the size of microcracking is the unknown parameter and measuring with one channel can determine the size and nucleation velocity of microcracking[4]. From the moment obtained by the single deconvolution method, a radius and nucleation velocity of microcracking can be calculated using Eqs 12 and 13. Figures 10 and 11 show the relations between radius  $a$  and velocity  $v$  in the SiC fiber reinforced glass composite and Al-Li alloy, respectively. The values of mean radius and mean nucleation of microcrack were evaluated from the moment obtained by the single deconvolution method, which were 240  $\mu\text{m}$  and 200 m/s in the SiC fiber reinforced glass composite, and 45  $\mu\text{m}$  and 50 m/s in Al-Li alloy, respectively.

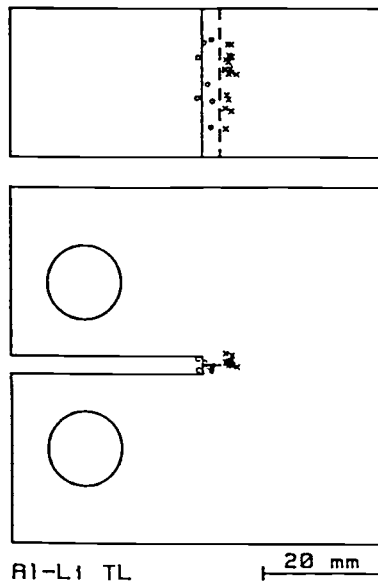


FIG. 9 -- The results of location of A sources detected during fracture toughness test in Al-Li alloy, where o indicates AE under the low applied load and x indicates AE under the high applied load.

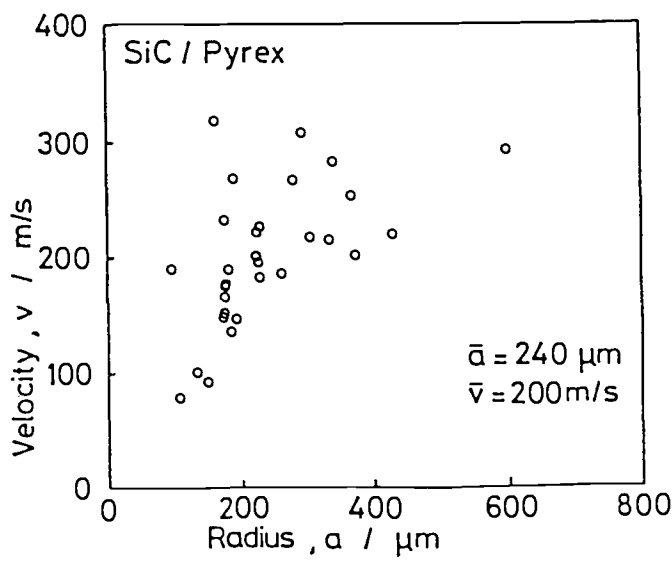


FIG. 10 -- The relations between radius and velocity of microcracking in the SiC glass composite.

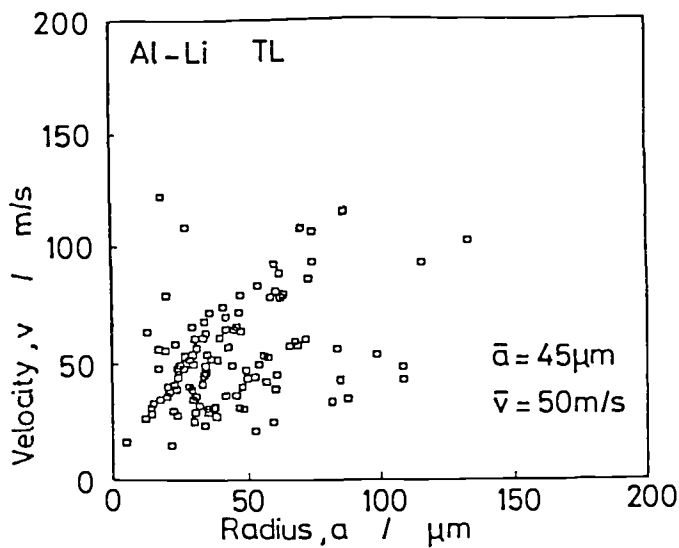


FIG. 11 -- The relations between radius and velocity of microcracking in Al-Li alloy.

### Multiple Deconvolution Method

The deformation moment tensor has to be determined to obtain the mode and orientation of microcracking. We have presented the multiple deconvolution method to determine the moment tensor [9, 17]. Moment tensor  $D_{jk}$  is determined by the frequency deconvolution method using some time points from longitudinal wave arrival. Figure 12 shows an example of moment tensor  $D_{jk}$  due to microcracking in Al-Li alloy. As shown in Fig. 12, a microcrack is generated with a rise time of about  $0.4 \mu\text{s}$ . Applying the nonlinear least-square method to Eq. 6, the displacement discontinuity  $[u_i]$  and the normal  $\nu_i$  are obtained from the determined moment tensor  $D_{jk}$ . Figure 13 indicates that the inclination of the microcrack plane to the main crack surface is  $106^\circ$  and the inclination of the microcrack plane to the direction of the displacement discontinuity is  $83^\circ$ . This result has demonstrated that a microcracking occurs in mixed mode of tensile and shear, but the shear component is stronger. The crack radius  $a$  is estimated as  $156 \mu\text{m}$  from Eq. 12 by assuming  $\sigma = 3\sigma_{ys}$ . Figure 14 shows the microscopic fracture surface by scanning electron microscope. The estimated value of radius  $a$  agrees well with the size of the separation crack which is observed at the location of source event in front of the precrack tip. It can be concluded that the recorded AE events due to microcracking are identified as the separation cracks in front of the precrack. The value of the crack radius from the multiple deconvolution method is about 10 % larger than that value from the single deconvolution method. This result demonstrates that the size of cracking with any mode can be obtained within about 10 % error by the single deconvolution method.

### SUMMARY

We have presented a theoretical consideration for an infinitesimal deformation in accordance with the method of micromechanics. We also developed the experimental and analysis system by using AE waveforms in

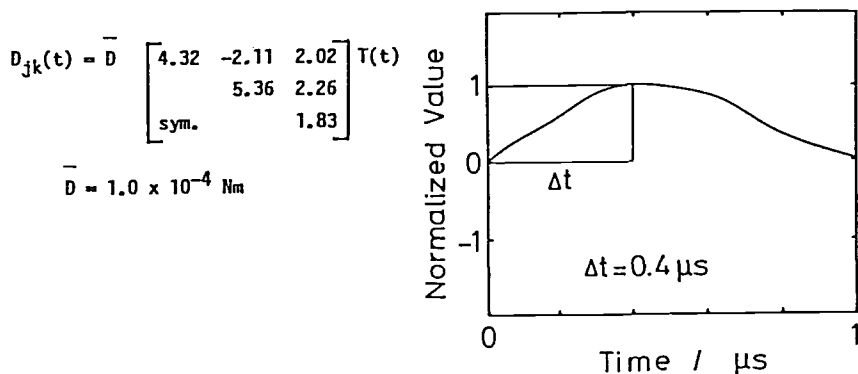


FIG. 12 -- The obtained result of moment tensor due to a microcracking in Al-Li alloy.

order to evaluate this microcracking quantitatively. In this paper we applied this method to fracture toughness testing of the SiC fiber reinforced glass composite and Al-Li alloy, the following conclusions could be drawn.

1. The experimental and analysis system for AE source characterization, which can determine the moment tensor components in microcracking, was developed. This method is remarkable for the dynamic Green's function of finite media by finite difference computer simulation and for the deconvolution with multiple Green's function in frequency domain.

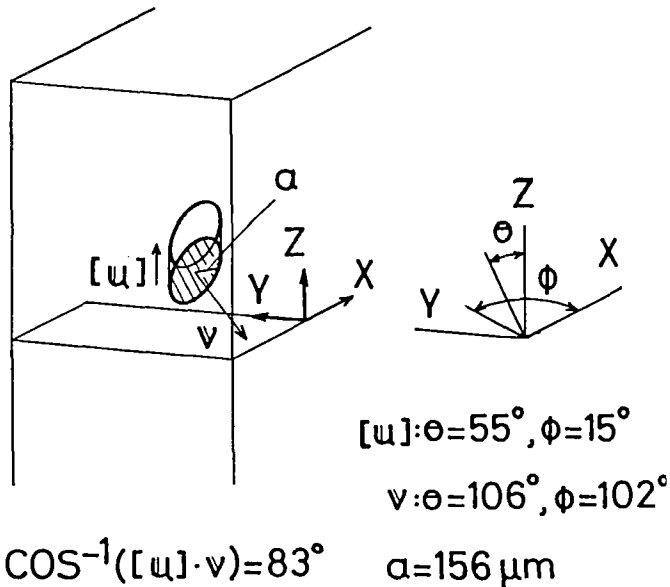


FIG. 13 -- The results of the orientation, fracture mode and size of the microcrack in Al-Li alloy.

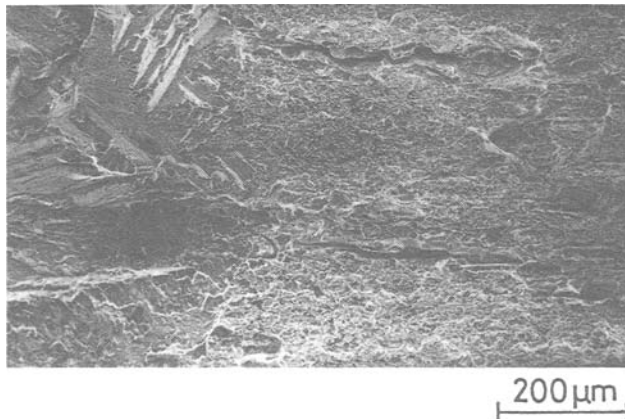


FIG. 14 -- The microscopic fracture surface in Al-Li alloy.

2. The results in SiC fiber reinforced glass composite were in good agreement with the observation and the location by AE, and means the AE source location possesses high potential. The AE source location could clear that AE source events under the low applied load due to cleavage were generated at the back of the fatigue precrack tip, while those under the high applied load due to separation crack were generated in front in Al-Li alloy.

3. The values of mean radius and mean nucleation of microcrack were evaluated from the moment obtained by the single deconvolution method, which were 240  $\mu\text{m}$  and 200 m/s in the SiC fiber reinforced glass composite, and 45  $\mu\text{m}$  and 50 m/s in Al-Li alloy, respectively.

4. From the obtained result of moment tensor by the multiple deconvolution method, size, inclination of microcrack surface and fracture mode of microcrack were quantitatively evaluated. The observation by scanning electron microscope verified that these AE sources were identified as the separation crack in front of the precrack in Al-Li alloy, which have a size of about 300  $\mu\text{m}$ .

#### FUTURE ASPECTS

It has been well-known that the AE waveform is strongly influenced by the transducer response. It is obvious from the Eq 14 that the effect of transducer characteristic must be considered. In the study of AE source characterization, the absolute sensitivity, the respective sensitivity between transducers and the frequency band of AE sources become more important. The transducer must be calibrated in any way and the frequency band of the transducer must be checked also. The analysis neglecting the effect of the transducer cannot be applicable.

In the case that the geometry of the specimen is a plate and an AE source location is fixed, such as Kim et al. used, the simplified amplitude method may be applicable under some restraint. However, in the case that the distances between transducers and source are not necessarily the same, care is needed when applying this method because the rise time of time function can change the first peak amplitude as well as the first peak time[18], that is, the moment tensor with the same components and the different time function may be failed to evaluate by the simplified amplitude method. In the case that the AE source occur near the crack tip, such as for a compact tension specimen, the effect of crack in the Green's function must be considered because the existence of a crack gives a strong influence on emitted waves. In this case, theoretical Green's function cannot be applicable. In the above respects, the author's method may be the most general analysis method because transducer characteristics are calibrated and the Green's function is calculated numerically in the geometry of specimen with the effect of an existing crack. This method may be complicated and it may take more longer time than any other method to carry out the analysis.

However, as the future method of the AE source characterization, the analysis method which is based on this multiple deconvolution method must be developed with the consideration of the data base technique or intelligent expert system. The computer aided system will become more important as well as another measuring system[19].

## REFERENCES

- [1] Mura, T., Micromechanics of Defects in Solids, Martinus Nijhoff Publishers, The Hague, 1982.
- [2] Aki, K. and Richards, P. G., Quantitative Seismology Vol.1, W. H. Freeman and Company, San Francisco, 1980.
- [3] Wadley, H. N. G., Scruby, C. B. and Shrimpton, G., "Quantitative Acoustic Emission Source Characterization during Low Temperature Cleavage and Intergranular Fracture," Acta Metallurgica, Vol. 29, 1981, pp. 399-414.
- [4] Kishi, T., Ohno, K. and Kuribayashi, K., "Acoustic Emission Source Wave Analysis for Dynamic Information on Micro Crack Formation," Journal of JSNDI, Vol. 30, 1981, pp. 911-917. (in Japanese)
- [5] Ohira, T. and Pao, Y. H., "Acoustic Emission Source Characterization of Microcracking in A533B Steel," in Solid Mechanics Research for Quantitative Non-Destructive Evaluation Martinus Nijhoff Publishers, Dordrecht, 1987, pp. 411-423.
- [6] Scruby, C. B., Stacey, K. A. and Baldwin, G. R., "Defect Characterisation in Three Dimensions by Acoustic Emission," Journal of Physics D, Vol.19, 1986, pp. 1597-1612.
- [7] Ohtsu, M., "Source Inversion Procedure for Acoustic Emission," in Progress in Acoustic Emission IV, JSNDI, 1988, pp. 67-74.
- [8] Kim, K. Y. and Sachse, W., "Characteristics of an Acoustic Emission Source from a Thermal Crack in Glass," International Journal of Fracture, Vol. 31, 1986, pp. 211-231.
- [9] Enoki, M. and Kishi, T., "Theory and Analysis of Deformation Moment Tensor due to Microcracking," International Journal of Fracture, Vol. 38, 1988, pp.295-310.
- [10] Fukunaga, Y., Enoki, M., Kishi, T. and Kihara, J., "Dynamic Green's Function of Finite Media by Finite Difference Method," Journal of Vibration, Acoustics, Stress, and Reliability in Design, (to be published).
- [11] Hsu, N. N., Simmons, J. A. and Hardy, S. C., "An Approach to Acoustic Emission Signal Analysis," Materials Evaluation, Vol. 35, 1977, pp. 100-106.
- [12] Ohisa, N. and Kishi, T., "Response Characterization of Piezo-electric Transducers and Wave Media for Acoustic Emission Source Wave Analysis," in Proceedings of the 1982 Joint Conference on Experimental Mechanics, Society for Experimental Stress Analysis, 1982, pp. 359-364.
- [13] Hutchinson, J. W., "Crack Tip Shielding by Micro-cracking in Brittle Solids," Acta Metallurgica, Vol. 35, 1987, pp.1605-1619.
- [14] Scruby, C. B. and Baldwin, G. R., "Three-Dimensional Crack Location by AE," Journal of AE, Vol. 3, 1984, pp. 182-188.
- [15] Ceranoglu, A. N. and Pao, Y. H., "Propagation of Elastic Pluses and Acoustic Emission in a Plate," Journal Applied Mechanics, Vol. 48, 1981, pp. 125-147.
- [16] Michaels, J. E. and Pao, Y. H., "The Inverse Source Problem for an Oblique Force on an Elastic Plate," Journal Acoustical Society of America, Vol. 77, 1985, pp. 2005-2011.
- [17] Enoki, M. and Kishi, T., "A Study for Analysis System of Acoustic Emission Source Characterization," in Progress in Acoustic Emission IV, JSNDI, 1988, pp. 140-147.
- [18] Enoki, M. and Kishi, T., "On the Determination of Moment Tensor from Acoustic Emission Waveform", (to be published).
- [19] Sachse, W., "The Processing of AE Signals," in Progress in Acoustic Emission IV, JSNDI, 1988, pp. 26-38.

## JOULE HEATING LINE AND POINT AE SOURCES AND THE ADHESION OF THIN METAL FILMS

---

**REFERENCE:** Kim, K. Y. and Sachse, W., "Joule Heating Line and Point AE Sources and the Adhesion of Thin Metal Films," Acoustic Emission: Current Practice and Future Directions, STP 1077, W. Sachse, J. Roget, and K. Yamaguchi, Eds., American Society for Testing and Materials, Philadelphia, 1991.

**ABSTRACT:** This paper describes a novel approach for generating line and point sources of ultrasound from a thin metal film attached to an insulating substrate. Both line and point sources are generated by a transient, electrical Joule heating of a long- and a short section of the thin film of narrow width, respectively. It is shown that the line and point sources are of dipolar type. By deconvolving the detected ultrasonic signals it is found that a current pulse of short duration generates a step source with risetime approximately equal to that of an input power pulse while a current pulse of long duration produces a linear ramp source resembling the temporal behavior of the temperature rise in the heated thin film. It is also shown that the failure of the film can be detected in the generated ultrasonic signals as well as in the measured electrical resistance of the film. By suitably processing these signals, information on the adhesion strength of the film to its substrate can be found.

**KEYWORDS:** Quantitative AE, thermoelastic source, thermoelastic generation, point source, line source, Green's functions, thin-film testing, film adhesive strength, metal coatings

## INTRODUCTION

The generation of acoustic or thermoelastic waves by the transient heating of a localized region of a specimen and its use for imaging and characterizing materials are rapidly coming into widespread use. In most cases, the transient heating is obtained by Q-pulsed laser beams, but other sources include high energy

Dr. Kwang Yul Kim is Senior Research Associate and Professor Wolfgang Sachse is a professor in the Department of Theoretical and Applied Mechanics at Cornell University in Ithaca, New York - 14853 U S A.



electron beams or intense pulses of synchrotron-generated x-rays. In this paper another method of generating thermoelastic waves is described which is based on the electrical Joule heating of a segment of a thin metal film of narrow width which has been directly deposited on an insulating substrate [1]. It is demonstrated that both point- and line sources of ultrasound are generated by heating short and long sections of the film, respectively. The heating is obtained by sending a current pulse of various magnitudes and durations through the film.

The advantage of using an electrical power pulse lies in its simplicity and versatility in generating elastic waves of various shapes and amplitudes through control of the risetime, duration and magnitude of the current pulse and also its relatively low cost in comparison with other methods. It should also be possible to generate a variety of thermoelastic waves associated with different source types by a proper layout of the thin film on the substrate. This can be realized with modern semiconductor fabrication techniques.

## THEORY

A thin metal film, heated by the resistance to the flow of an electrical current, will expand freely in the absence of a substrate. However, when the film is attached to a substrate, the thermal expansion of the film is constrained by the film/substrate interface. The temperature rise of the film and the boundary of the substrate in contact with it, is given by  $\theta$ . If the linear coefficients of thermal expansion of the metal film and a glass substrate are denoted by  $\alpha_f$  and  $\alpha_g$ , respectively, then the force per unit length exerted by the film on the glass at the interface is given by

$$f = \frac{Ed}{1 - \nu_f} (\alpha_f - \alpha_g) \theta \quad (1)$$

where  $E$ ,  $\nu_f$  and  $d$  are the Young's modulus, Poisson's ratio and the thickness of the film, respectively. This outward force acts in a direction perpendicular to the film strip at both edges of the film, thus constituting a horizontal dipole force.

If the  $x$ -axis of a coordinate system is perpendicular to the length of the film and the  $y$ -axis is aligned along its length, then a horizontal dipole associated with a point source having a short section of the film length,  $\Delta l$ , located at  $y$ , can be written as

$$D_{xx}(y, t) \Delta l = f w \Delta l = \frac{Ewd\Delta l}{1 - \nu_f} (\alpha_f - \alpha_g) \theta(t). \quad (2)$$

where  $w$  is the width of the thin film strip. Then the normal displacement  $u_z^P(\mathbf{r}, t)$  at location  $\mathbf{r}$  and at time  $t$ , resulting from a point dipole  $D_{xx}(t) \Delta l$ , can be expressed by a Green's function according to [2]

$$u_z^P(\mathbf{r}, t) = \int_0^t D_{xx}(y, t) \Delta l G_{xx,z}^P(\mathbf{r}, y; t - \tau) d\tau = D_{xx}(t) \Delta l * G_{xx,z}^P(\mathbf{r}, y; t) \quad (3)$$

where  $G^P$  represents the Green's tensor associated with a point source and '\*' denotes a convolution integral in time. The displacement  $u_z^L(\mathbf{r}, t)$  resulting

from a line source of length,  $\ell$ , is given by

$$\begin{aligned} u_z^\ell(\mathbf{r}, t) &= \int_0^\ell D_{zz}(t) * G_{zz,z}^P(\mathbf{r}, y; t) dy \\ &= D_{zz}(t) * G_{zz,z}^\ell(\mathbf{r}, t) \end{aligned} \quad (4)$$

where

$$G_{zz,z}^\ell(\mathbf{r}, t) \equiv \int_0^\ell G_{zz,z}^P(\mathbf{r}, y; t) dy$$

When  $\ell$  is sufficiently long,  $G_{zz,z}^\ell(\mathbf{r}, t)$  can be approximated by  $G_{zz,z}^\infty(\mathbf{r}, t)$ , which is the Green's function corresponding to that of an infinitely long line source. If the time of interest is limited to the arrival time,  $\tau_P^\ell$ , corresponding to the first  $P$ -(longitudinal) ray emanating from the ends of the line source, then,

$$G_{zz,z}^\ell(\mathbf{r}, t) = G_{zz,z}^\infty(\mathbf{r}, t) \quad (5)$$

for  $0 \leq t \leq \tau_P^\ell$ .

To maximize  $\tau_P^\ell$  in an experiment, the acoustic sensors should be placed at points equidistant from the ends of the film. In our experiments, this corresponded to a value of  $\tau_P^\ell$  of approximately  $9 \mu\text{sec}$  for the epicentral receiver.

Algorithms for computing the point-source Green's function of the plate appearing in the above equations have been developed for the near field of a source by Ceranoglu and Pao [3] using generalized ray theory. To compute the values of  $G_{zz,z}^\ell$ , Eq. (4) can be used, even though using Eq. (5) would be more convenient for times less than  $\tau_P^\ell$  if  $G_{zz,z}^\infty$  were available. Calculated waveforms for a short and a 10 cm long thin strip source on a glass substrate with the receiver located on the opposite side are shown in Figs. 1(a) - (c).

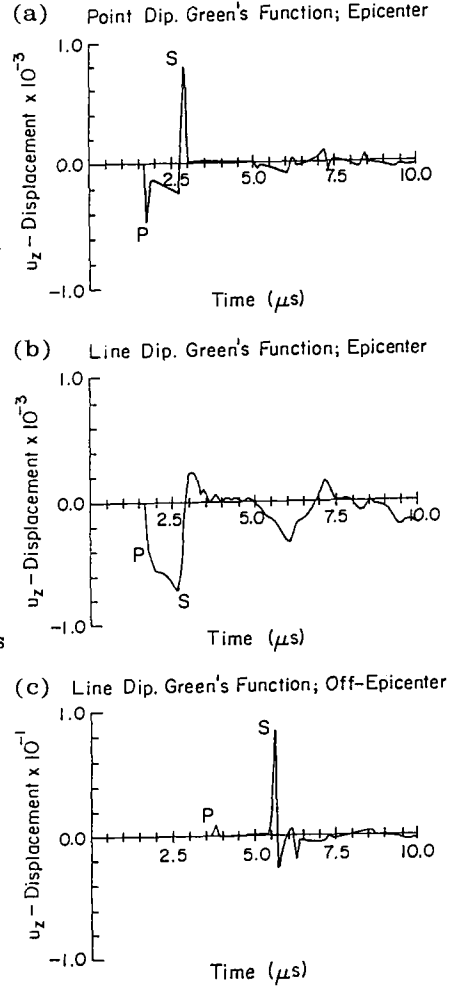


Figure 1: Green's functions of a plate 0.968 cm thick ( $c_P = 0.582 \text{ cm}/\mu\text{s}$ ;  $c_S = 0.350 \text{ cm}/\mu\text{s}$ ) for a horizontal dipole source. (a) Point source, receiver at epicenter; (b) Line source, receiver at epicenter; (c) Line source, receiver at  $2H$  from epicenter.

## MEASUREMENTS

The thin metal films were deposited as strips on one side of a glass plate approximately 15 cm long, 15 cm wide and 0.968 cm thick. The initial experiments were conducted on two film materials which were chosen for their high electrical conductivity so that the total electrical resistance was minimized to maximize the current and hence the power which could be applied to the thin film. It should, however, also be possible to use films possessing lower conductivities, such as chromium, nickel, titanium.

The results to be described were obtained on two thin film specimens. One was silver, 2 mm wide and  $0.5\text{ }\mu\text{m}$  thick, which was deposited by sputtering. The other was aluminum, 1.5 mm wide and  $1\text{ }\mu\text{m}$  thick obtained by evaporation. Two small, polished brass plates were attached to the ends of the film strips with a silver epoxy cement. The spacing between the end pieces on the silver film was 2 mm giving an approximate point source while on the aluminum film they were separated by about 10 cm to give a line source. Each brass plate had two electrodes on it, one for the current excitation and the other for the potential measurement.

The excitation was obtained using a current pulse generator capable of delivering a maximum power of 20 kW in pulses of nearly constant amplitude for a time interval ranging from  $2\text{ }\mu\text{s}$  to  $500\text{ }\mu\text{s}$  and operating with a repetition rate of 10 pulses/second. The measurement system is shown in Fig. 2.

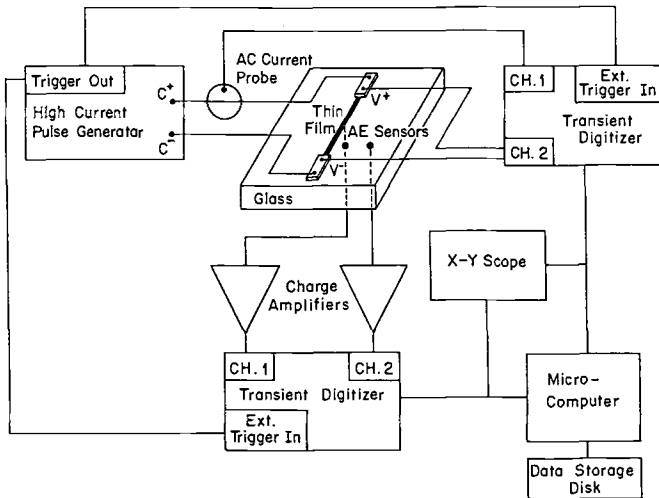


Figure 2: Electronic block diagram of line and point-source AE generation and the detection system.

The normal surface motions of the elastic waves were detected on the side opposite to the films by two, miniature high-fidelity capacitive transducers, one mounted at epicenter and the other at  $2H$  away from the epicenter [4]. Both sensors were located midway between the ends of a thin film segment. To obtain

a ground plane for the capacitive transducers, the entire bottom side of each specimen was coated with a  $0.3\text{ }\mu\text{m}$  thick film of chromium. The signal from each capacitive transducer was amplified by a charge amplifier whose bandwidth extended from 10 kHz to 10 MHz.

The measurements were carried out with current pulses of magnitude ranging from several to 100 Amperes with duration ranging from a few to  $100\text{ }\mu\text{s}$ . The magnitude of current flowing through the film was measured by an AC current probe whose bandwidth was 120 Hz to 60 MHz. The signals from the current probe and the voltage across the thin film were fed into a two-channel transient recorder operating at a sampling rate of 30 MHz and 10 bits. The output of the charge amplifier was measured by a second waveform recorder operating similarly as the first. Both recorders operated under control of an interactive minicomputer-based data acquisition and processing system.

## RESULTS

### Short-duration Excitations

In Fig. 3(a) is shown the measured excitation current pulse which was applied to the 2 mm wide, 2 mm long, and  $0.5\text{ }\mu\text{m}$  thick silver film. This relatively short length of film acts as a point source of ultrasound when excited by the current pulse. The dipole source time function  $D_{xx}(t)$  obtained from Eq. (4) by deconvolving the displacement signal measured at epicenter with the Green's function shown in Fig. 1(a) is called the magnitude of the source and this is plotted in arbitrary units on the ordinate axis in Fig. 3(b). The source-time function is a step function with a risetime of about  $1.0\text{ }\mu\text{sec}$  which approximately equals that of the input power pulse. This suggests that the temperature rise and hence the thermal dilatation of the film instantaneously follows the input power increment associated with the rising portion of the power curve, whereas the generally flat portion of the source-time function after the ramp may be the result of the slow thermal diffusion after the input power begins to decrease abruptly.

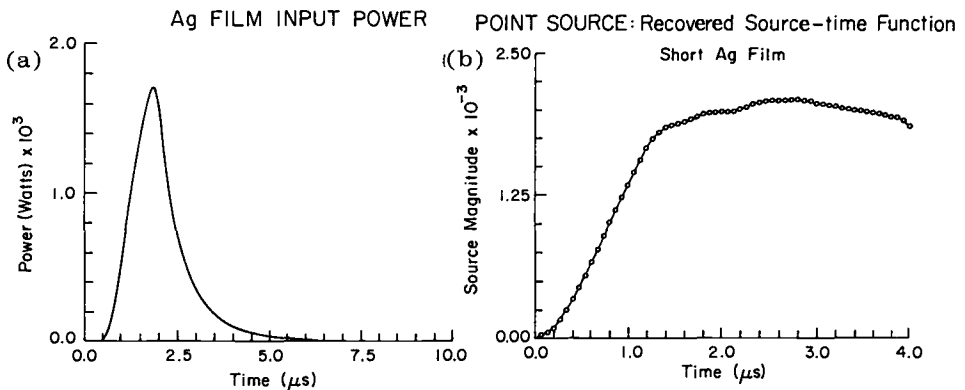


Figure 3: Short-duration excitation, short section of silver film. (a) Electrical Power; (b) Point dipole source time function.

The line source responses of an aluminum film 1.5 mm wide, 10 cm long and  $1.0\text{ }\mu\text{m}$  thick to which a short-duration pulse of maximum power of about 15 kW was applied were analyzed similarly using the Green's functions shown in Figs. 1(b) and (c). It was found that the source-time function determined from the epicentral response was again a ramp-step function whose risetime equalled that of the input power pulse. Once the source-time function was known, synthetic waveforms were reconstructed and compared to those measured. The agreement in all cases was very good. Hence, regardless of source type, be it a point or a line source, the short pulse excitation produces essentially the same type of source-time function since it is principally determined by the temporal response of the thermal dilatation of the film.

#### Long-duration Excitations

A sample result obtained on an aluminum film which was heated with a 23 Ampere current pulse  $17\text{ }\mu\text{s}$  in duration is shown in Figs. 4(a)-(c). Shown in Fig. 4(a) is the time function of the line dipole source which was obtained by deconvolving the measured epicentral displacement signal shown as a solid line in Fig. 4(b) with the Green's function shown in Fig. 1(b). A small parabolic contribution is buried in this source-time function. A comparison between the experimental waveform measured at epicenter and that computed theoretically using Eq. (3) with the source strength shown in Fig. 4(a) for the aluminum film line source on a glass substrate is also shown in Fig. 4(b). A similar comparison is made for the case of the off-epicentral responses in Fig. 4(c). In every case the agreement between the measured and computed waveforms is found to be excellent.

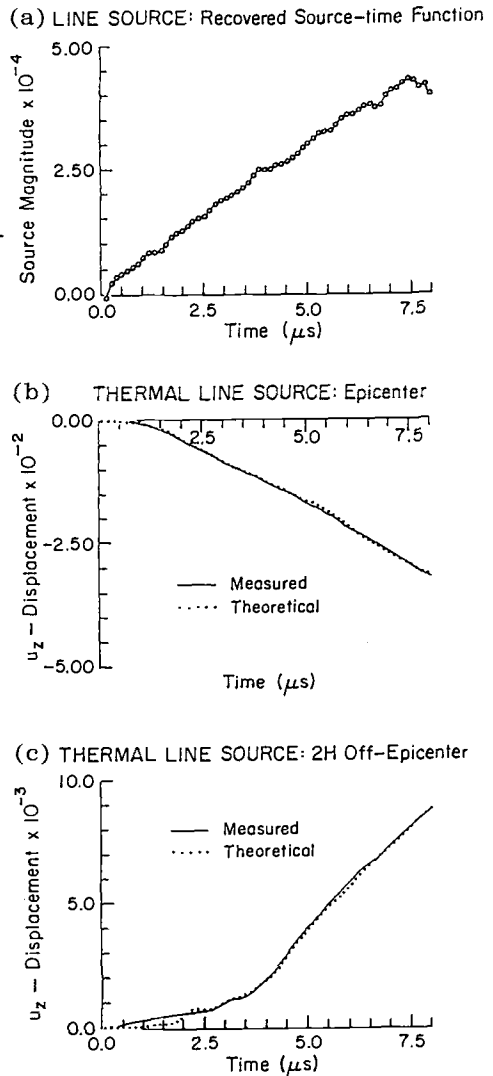


Figure 4: (a) Line dipole time function associated with the current pulse of long-duration; (b) Observed and recovered waveforms at epicenter; (c) Observed and recovered waveforms at  $2H$  off-epicenter.

The actual temperature rise in the thin film can be obtained from dynamically measured electrical resistance data. The resistance of the film,  $R$ , as a function of its temperature rise  $\theta$ , is expressed as

$$R(t) = R_0 [1 + \gamma \theta(t)] \quad (6)$$

where  $R_0$  is the initial resistance of the film and  $\gamma$  is the temperature coefficient of unit resistance. Such measurements show that there is a sharp initial impedance transient which is followed by an slow increase in the resistance corresponding to the rise in film temperature until the current decreases abruptly at the end of the pulse. Between the two impedance transients at both ends of the pulse lies the contribution of the pure resistance whose temporal behavior can be fit with a quadratic polynomial determined by a least-squares method. The polynomial is extrapolated to the time of the arrival of the excitation pulse so that the initial electrical resistance  $R_0$  of the film can be determined. In all cases, the determined value of  $R_0$  was found to be in good agreement with the value determined via a static DC measurement. Knowing the coefficient of resistance,  $\gamma$ , of the film material, the temperature rise of the film can be computed by solving for  $\theta(t)$  in Eq. (6) for any instant during the excitation. For example, for a short, thin film of silver on glass to which was applied a long-duration pulse of 22 Amperes, a temperature increase of  $23.7^\circ\text{C}$  was determined at  $t = 17 \mu\text{sec}$  just before the excitation pulse dropped to zero.

The resistance measurements showed that the temperature increase and hence the thermal dilatation of the metal films were almost linear with time with only a small parabolic term present. This is in agreement with the source-time functions found for the AE signals from the pulse-heated films.

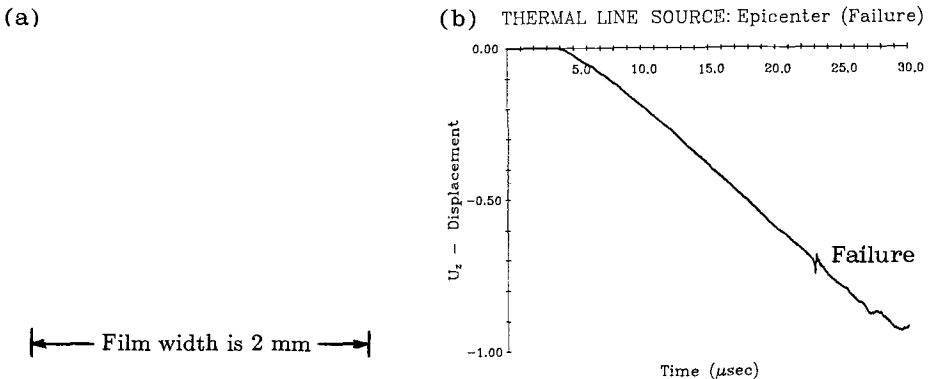


Figure 5: Failure of a  $0.5 \mu\text{m}$  thick silver film from a glass substrate. (a) Failed region; (b) Epicentral AE displacement signal exhibiting film failure.

### Film Debonding

The debonding of the thin film from its substrate as a result of the accumulated thermal biaxial normal stresses at the interface is shown in Fig. 5(a). A

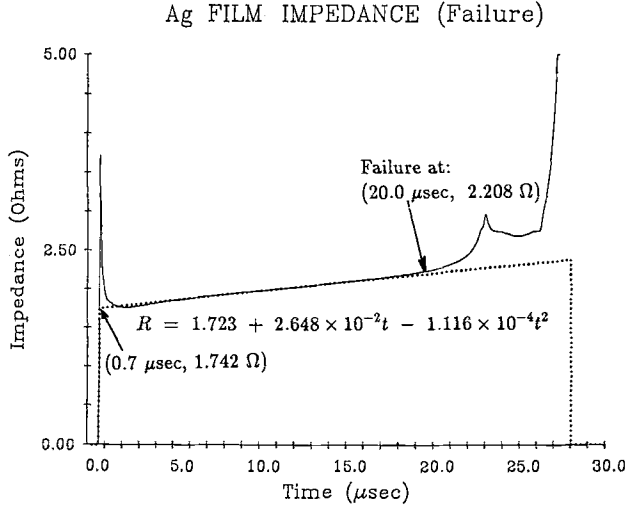


Figure 6: Electrical resistance characteristics of the silver film showing film failure.

clear indication of the film failure can also be observed in the emitted ultrasonic signals. The off-epicentral signal detected by a receiver  $2H$  from a silver film source is shown in Fig. 5(b). It should be possible to deconvolve this signal which corresponds to Eq. (4) to determine the dipole source strength at the instant of film failure. Knowing this, the normal stress in the film at the instant of failure can be found according to

$$\sigma_{zz} = \sigma_{yy} = \frac{D_{zz}}{wd} \quad (7)$$

Because of the correspondence between the temperature rise of the film and the dipole source strength, an alternative procedure is based on processing the emitted ultrasonic signals to determine the temperature of the film at the instant,  $t^*$ , of its failure,  $\theta(t^*)$ . From this, the failure stress at the interface can be found

$$\sigma_{zz} = \sigma_{yy} = \frac{E}{1 - \nu_f} (\alpha_f - \alpha_g) \theta(t^*) \quad (8)$$

Alternatively, the temperature at film failure can be determined from the measured electrical resistance characteristics. The case of the silver film is shown in Fig. 6. Clearly evident in the data is the instant when the film begins to debond from the substrate. The magnitude of the current measured when debonding occurred was about 30 Amperes. The value of resistance measured at the instant of failure was  $2.208 \Omega$  while the initial resistance obtained by extrapolation to the time of the pulse arrival at  $0.7 \mu\text{sec}$  was  $1.742 \Omega$ . Using the value of  $\gamma$  equal to  $4.1 \text{ m}\Omega/\Omega/^\circ\text{K}$  and Eq. (6) the temperature rise of the silver film was calculated to be  $65.2^\circ\text{C}$ . Once this temperature is known, the debonding stress acting at the interface can be obtained from Eq. (8). For the silver film this was  $64.1 \text{ MPa}$ .

More difficult than the above procedures, would be the extraction of that portion of the generated ultrasonic signal which corresponds to the failure of the film. But this is far more difficult, hence the work to date has been based on dynamic resistance measurements as described in the previous paragraph [5,6].

## CONCLUSIONS

Based on this work, the following conclusions can be drawn about thermoelastic waves generated by Joule heating sources: (1) A localized, transient Joule heating generates a thermoelastic pulse whose source-type is characterized by a dipole; (2) A short-duration current pulse generates a source whose time function is characterized as a ramp-step for which the risetime is approximately equal to that of an input power pulse; (3) A long-duration current pulse excites a source whose time function corresponds to the temperature increase of the thin film, exhibiting an almost linear behavior in time with a small non-linear contribution; (4) The ultrasonic source characterization method can be used to study thermal properties of materials and to predict the temperature rise of a heated conductor; (5) The line source generation from the metal thin film can be used to determine the adhesion strength of a thin conductive film on a substrate.

## ACKNOWLEDGEMENTS

This work has been supported by the Office of Naval Research (Physical Acoustics Program). Use of the facilities of the Materials Science Center at Cornell University is also acknowledged.

## REFERENCES

- [1] Kim, K. Y. and Sachse, W., "Generation of Elastic Waves from Line and Point Sources by a High-current Pulse Method", *Journal of the Acoustical Society of America*, Vol. 86, 1989, pp. 875-884.
- [2] Aki, K. and Richards, P. G., *Quantitative Seismology: Theory and Methods*, Vol. I, Freeman, San Francisco, 1980, Chapt. 3.
- [3] Ceranoglu, A. N. and Pao, Y. H., "Propagation of Elastic Pulses and Acoustic Emission in a Plate: Part I. Theory; Part II. Epicentral Response; Part III. General Responses", *Transactions ASME, Journal of Applied Mechanics*, Vol. 48, 1981, pp. 125-147.
- [4] Kim, K. Y., Niu, L., Castagnede, B. and Sachse, W., "Miniaturized Capacitive Transducer for Detection of Broadband Ultrasonic Displacement Signals", *Review of Scientific Instruments*, Vol. 60, 1989, pp. 2785-2788.
- [5] Kim, K. Y. and Sachse, W., "Thin-film Acoustics: Line and Point Source Generation and Testing of Thin Films", in *Progress in Acoustic Emission IV*, K. Yamaguchi, I. Kimpara and Y. Higo, Eds., Japanese Society of Non-destructive Inspection, Tokyo, 1988, pp. 98-105.



- [6] Sachse, W., Kim, K. Y. and Conway, H. D., "Determination of the Bond Strength of a Metal Coating on a Substrate", in *Interfaces Between Polymers, Metals and Ceramics*, B. M. DeKoven, A. J. Gellman and R. Rosenberg, Eds., Vol. 153, MRS Symposium Proceedings Series, Materials Research Society, Pittsburgh, PA, 1989, pp. 249-259.

Clinton R. Heiple, Steve H. Carpenter, and Scott S. Christiansen

## A CALIBRATION SOURCE FOR ACOUSTIC EMISSION ANALYSIS

---

REFERENCE: Heiple, C. R., Carpenter, S. H., and Christiansen, S. S., "A Calibration Source for Acoustic Emission Analysis," Acoustic Emission: Current Practice and Future Directions, ASTM STP 1077, W. Sachse, J. Roget, and K. Yamaguchi, Eds., American Society for Testing and Materials, Philadelphia, 1991.

ABSTRACT: Acoustic emission produced by the fracture of boron particles in 2219 aluminum during tensile deformation was measured and characterized. The boron particles were introduced into the aluminum using a powder metallurgy approach. The response of an rms voltmeter to individual acoustic emission bursts was found to be proportional to the energy of the burst (integral of the squared signal voltage). The energy released by fracture of the boron particles was estimated from elasticity theory using measured diameters of the individual fractures. The energy of the acoustic emission signals produced by boron particle fracture was found to be proportional to the energy released by the particle fractures. This relation can be used to estimate the energy released by other comparable acoustic emission sources in samples of similar geometry from their acoustic emission signals.

KEYWORDS: acoustic emission, calibration, inclusion fracture, signal energy

The fracture of boron particles in an aluminum matrix was proposed by Hamstad as a potential well-defined acoustic emission source [1]. Boron particles were incorporated into 2219 aluminum tensile bars using a powder metallurgy approach. Since the mechanical properties of boron and aluminum are well known, the energy release from fracture of the boron particles can be calculated from expressions which have been derived for the fracture of an

Dr. Heiple is an associate scientist, Professor Carpenter (University of Denver) is a consultant, and Mr. Christiansen is a Senior Development Engineer at EG&G Rocky Flats, Inc., Box 464, Golden CO 80402-0464.

elastic inclusion in an infinite matrix [2]. The correlation between the elastic energy released and the resulting acoustic emission signal is useful both for calibration purposes and for estimating the energy released by other sources from their acoustic emission signals.

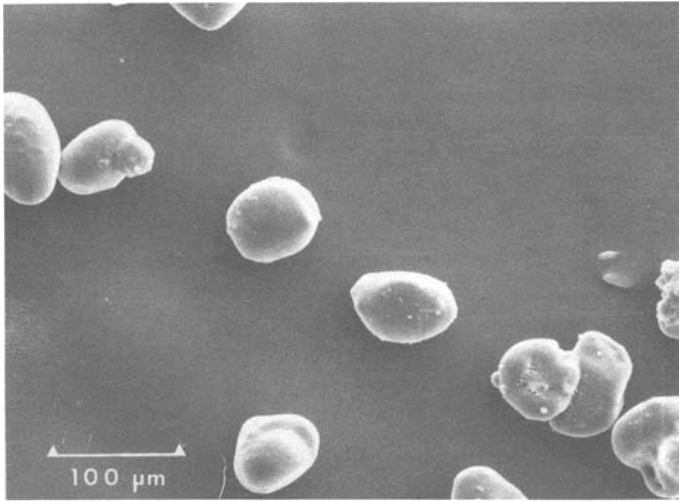
#### EXPERIMENTAL PROCEDURE

Aluminum alloy 2219 was chosen as the matrix material for two reasons. First, no burst emission is produced during deformation, and the level of continuous emission is very low - particularly in the peak-aged condition. Second, this alloy is age hardenable to fairly high strengths for aluminum alloys, so it was expected that sufficient stress to produce fracture of the boron particles would be developed during plastic deformation of the aluminum matrix.

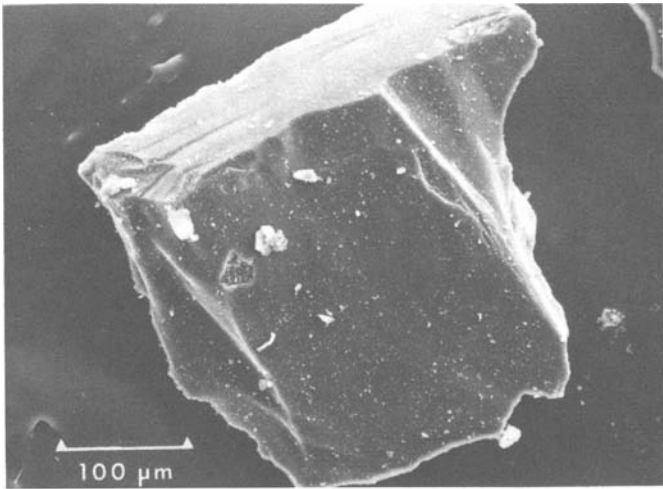
A block of 2219 aluminum was milled into small chips. Boron particles were mixed by hand with the chips and the mixture cold pressed. The resulting compact was vacuum hot pressed (430 °C, 20,000 psi). There was no detectable porosity in the resulting pressing. Samples were fabricated using 250-350  $\mu\text{m}$  boron particles, 60-90  $\mu\text{m}$  boron particles, and with no boron particles added. Scanning electron micrographs of typical small and large boron particles are shown in Figure 1. The pressings were hot-swaged (450-460 °C) into rod, and tensile bars machined from the rod. The tensile bars were solution heat treated (550 °C, 1.5 hr) and aged to peak strength (190 °C for 30 hr after a room temperature hold).

Acoustic emission was detected with a Dunegan-Endevco S140 transducer (resonant piezoelectric type, 140 kHz nominal resonant frequency). Transducer output was amplified with a Panametrics 5050AE-160A preamplifier. The amplified signals were characterized with an Acoustic Emission Associates Phoenix acoustic emission signal characterization system, recorded directly with a Soltec SDA2000 transient recorder, and measured with a Hewlett-Packard 3400A rms voltmeter.

Following tensile testing, one tensile bar containing large boron particles was examined in detail metallographically. The aluminum matrix was gradually removed by electropolishing and the boron particles were photographed individually in a scanning electron microscope as they were uncovered. Particles in both the grip and gauge sections were examined. A similar, but less extensive, examination was carried out on a tensile bar with small boron particles. The metallographic examination determined the number of particles fractured during deformation, estimated the size of the fractures, and verified that the fractures occurred during tensile testing - not during sample fabrication.



(a)



(b)

Figure 1. Scanning secondary electron micrograph of boron particles added to 2219 aluminum. (a) 60-90  $\mu\text{m}$  particles. (b) 250-350  $\mu\text{m}$  particle.

## RESULTS

An example of a large boron particle fractured during deformation is shown in Figure 2. The fracture surfaces are nearly parallel, close together, and approximately perpendicular to the tensile axis. Fractures with these characteristics were found only in the gauge section, never in the grips. About half of the particles in the gauge section contained fractures of this type, and a few particles had multiple fractures.

Some particles were completely intact; an example is shown in Figure 3. Other particles were crushed during processing; fractures of this type were found in both the grip and gauge sections. For the crushed particles, the pieces were more widely separated, the fracture faces were generally not parallel or perpendicular to the tensile axis, and there was often aluminum between the broken pieces. An example of such a particle is shown in Figure 4.

A sample without boron particles was fabricated and tensile tested to verify that the fabrication procedure did not affect the basic acoustic emission behavior of the material. The acoustic emission behavior of the powder-processed material was identical to that of wrought 2219 aluminum [3]. No burst emissions were detected and there was no continuous emission detectable at 110 dB total amplification. Thus, aluminum oxide and any other microstructural modifications introduced by the powder processing do not contribute detectable acoustic emission.

Burst-type acoustic emission began in the boron-containing samples in the macroscopically elastic region near yield and continued through and well beyond yield. No continuous emission was observed at yield or during macroscopic plastic flow. The number of acoustic emission bursts detected greatly exceeded the number of boron particles in the sample gage length, particularly for the large particle samples. Most of the events were relatively small, and these small events are attributed to decohesion of the particles from the matrix. If only the largest events are considered, i.e. those large enough to individually produce a spike on the rms voltmeter, then the number of these events is comparable to the number of boron particle fractures observed in the sample gage length. As expected, the amplitude of the signals from the small-particle samples was less than from the large-particle samples.

One property of each acoustic emission burst which can be calculated using the transient recorder is its "energy", that is a point by point integration of the signal waveform squared. The resultant quantity, with units of  $\text{volt}^2\text{sec}$ , is proportional to energy, but is not actually an energy unit. The energy was calculated in this way for all of the larger signals from a large-particle and small-particle tensile bar. The time at which each signal occurred is also recorded by the transient recorder, so a direct comparison can be made of each acoustic emission signal and the response of the rms voltmeter to it. A comparison of the calculated energy in each of the acoustic emission signals with the height of the rms voltmeter spike produced is shown in Figure 5

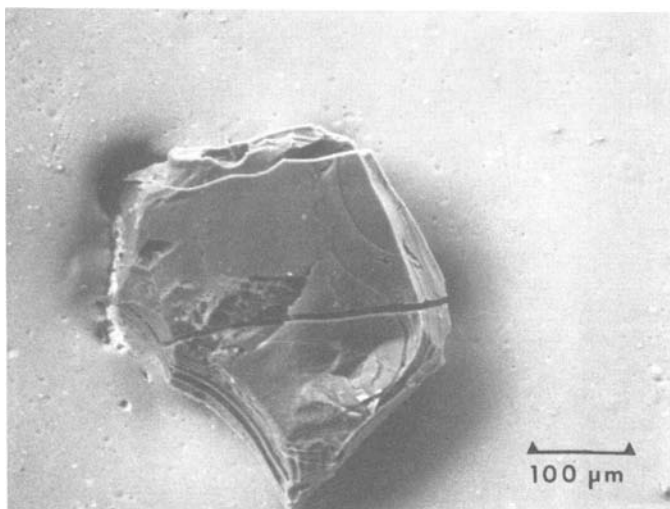


Figure 2. Scanning secondary electron micrograph of a large boron particle fractured during tensile deformation. The tensile axis is vertical.

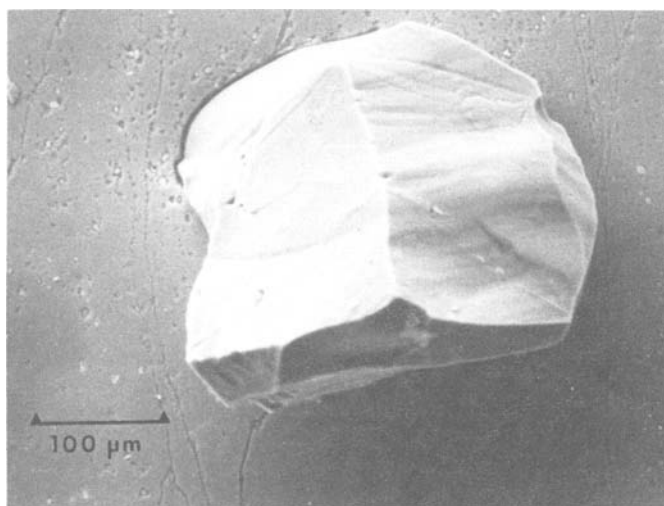


Figure 3. Scanning secondary electron micrograph of an intact large boron particle (following deformation) in the tensile bar gauge length.

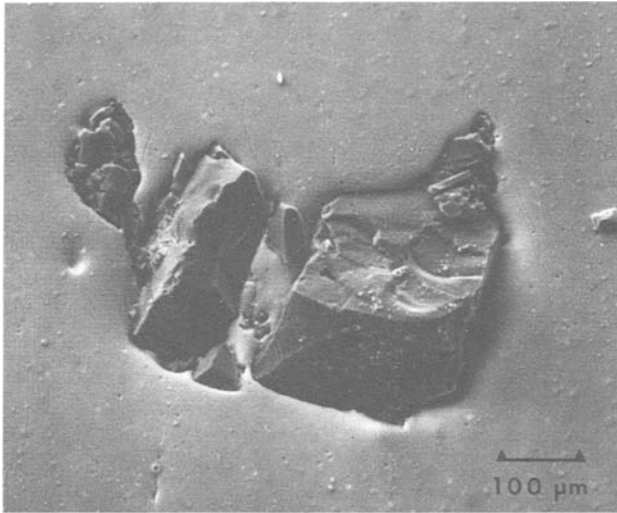


Figure 4. Scanning secondary electron micrograph of a boron particle crushed during sample material fabrication. The tensile axis is vertical.

and Figure 6. As expected, the rms voltmeter response is proportional to signal energy. No noise correction is required because the actual signal during the time that the spike is produced exceeds background by at least two orders of magnitude. It should be noted that the correlation between signal peak amplitude and rms meter response isn't nearly as good as with signal energy, because the signal shape is quite variable. Thus signals with quite different energies can have similar peak amplitudes.

An expression for the strain energy released from cracking a spherical inclusion in an infinite matrix when the inclusion has elastic properties different from the matrix has been calculated by Kant [2] and reproduced in Reference 4. The energy released is proportional to the radius of the fracture cubed, the applied stress squared, and is also a function of the elastic constants of the matrix and inclusion. The radius of each boron-particle crack resulting from tensile deformation of the large-particle tensile bar was estimated from the scanning electron micrographs and the energy release then calculated. The calculated fracture energy releases were ordered from largest to smallest. They were plotted against the measured acoustic emission signal energies (similarly ordered) for the 32 signals large enough to individually produce a spike on the rms voltmeter. The resultant plot is given in Figure 7. This plot serves as a calibration from which the elastic energy released by a real acoustic emission source in a sample of useful geometry can be estimated from the acoustic emission signal produced.

Estimates of the energy released by martensitic transformations in Au-47.5 at% Cd and in plutonium, by twin formation in uranium, and

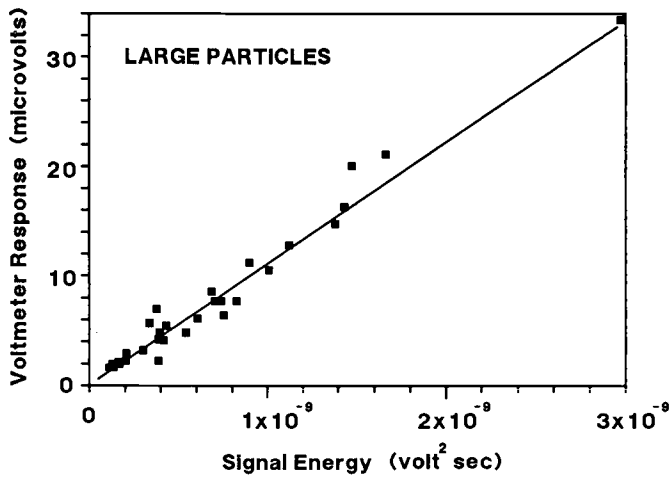


Figure 5. RMS voltmeter response versus acoustic emission signal energy for large-particle sample. Values referenced to transducer output.

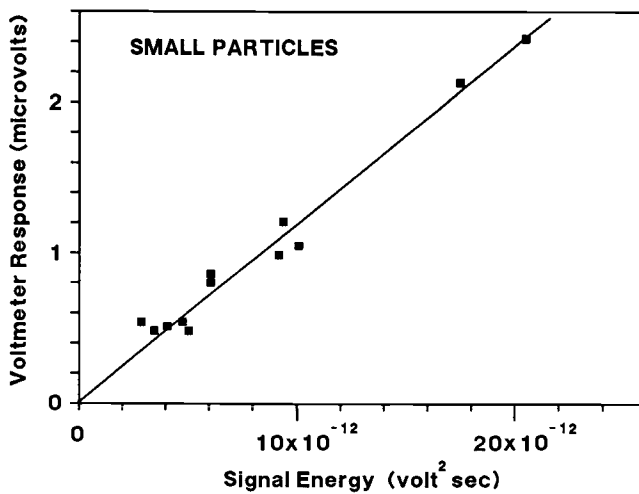


Figure 6. RMS voltmeter response versus acoustic emission signal energy for small-particle sample. Values referenced to transducer output.



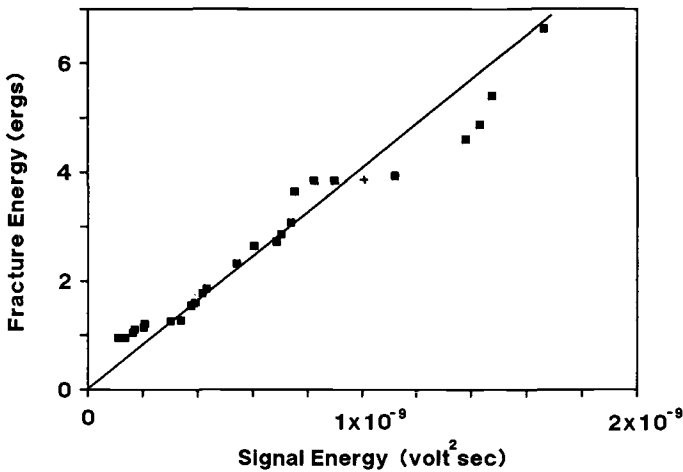


Figure 7. Boron particle fracture energy versus acoustic emission signal energy, referred to transducer output. The point plotted with a + is from a particle with a branching crack. The calculated fracture energy for this particle was taken to be the sum of the energies for the two branches.

by dislocation motion in beryllium were made from their acoustic emission signals. Details of these estimates are given elsewhere [5]. The estimates are in reasonable agreement with other available data.

## CONCLUSIONS

Samples where the only source of acoustic emission is the decohesion and fracture of second phase particles with known mechanical properties have been successfully fabricated and tested. The material used was 2219 aluminum, with boron particle additions, prepared using a powder metallurgy approach. The acoustic emission from this material has been measured and characterized. The response of an rms voltmeter to a single event is proportional to the signal energy, over a wide range, where the signal energy is the integral of the voltage squared. When the acoustic emission signal energies are correlated with the energy releases calculated for the observed boron particle fractures, a linear relation is found. From this relation, an estimate in absolute energy units can be made of the energy released in a sample by an acoustic emission source from the acoustic emission signal observed, provided the source velocity and sample geometry are similar to the boron particle fractures.

## ACKNOWLEDGMENT

This work was supported by the Department of Energy, Albuquerque Operations Office. Their support is gratefully acknowledged.

## REFERENCES

- [1] Hamstad, M. A., University of Denver, Unpublished Research.
- [2] Kant, R., "The Elastostatic Axisymmetric Problem of Cracked Sphere Embedded in a Dissimilar Matrix," Doctoral Thesis, University of California, Berkeley, CA, 1979.
- [3] Heiple, C. R., Carpenter, S. H., and Carr, M. J., "Acoustic Emission from Dislocation Motion in Precipitation-Strengthened Alloys," Metal Science, Vol. 15, Nov.-Dec. 1981, pp. 587-598.
- [4] Heiple, C. R., and Carpenter, S. H., "Acoustic Emission Produced by Deformation of Metals and Alloys - A Review: Part II," Journal of Acoustic Emission, Vol. 6, No. 4, Oct.-Dec., 1987, pp. 215-237.
- [5] Heiple, C. R., Carpenter, S. H., and Christiansen, S. S., "Fracture of Boron Particles in 2219 Aluminum as a Known Acoustic Emission Source," Accepted for publication in Acta Metallurgica, 1990.

Shawn C. Maxwell, R. Paul Young, and David A. Hutchins

SIMULTANEOUS VELOCITY TOMOGRAPHY AND SOURCE LOCATION OF SYNTHETIC ACOUSTIC EMISSION DATA

---

REFERENCE: Maxwell, S.C., Young, R.P., and Hutchins, D.A., "Simultaneous Velocity Tomography and Source Location of Synthetic Acoustic Emission Data," Acoustic Emission: Current Practice and Future Directions, ASTM STP 1077, W. Sasche, J. Roget, K. Yamaguchi, Eds., American Society for Testing and Materials, Philadelphia, 1991.

ABSTRACT: A method is proposed to simultaneously determine source locations, and passively image the velocity structure of a deformed sample. The method utilizes arrival time data measured from recordings of induced acoustic emissions. Images of the velocity structure are sensitive to the state of stress in a sample, and can be used to map spatial variations in stress induced changes. This study documents the first phase of a passive imaging research project. Synthetic arrival time data were used to attempt to passively image a velocity model, using both spatially uniform and restricted event coverage. In both cases, the actual model was reproduced, however the restricted event coverage resulted in some loss of resolution. Sequential passive imaging should prove to be a powerful tool for imaging the evolving in-situ stress field using only basic monitoring instrumentation.

KEYWORDS: ultrasonic imaging, passive tomography, acoustic emission, source location

INTRODUCTION

Ultrasonic velocity imaging has been successfully used to study the effects of changing stress fields and map stress concentrations in

Mr. Maxwell and Professor Young are with the Rock Physics and Engineering Seismology Laboratory, Department of Geological Sciences, Queen's University, Kingston, Canada K7L 3N6. Professor Hutchins is in the Department of Physics at Queen's.

deformed rock samples [1]. This is an active technique, in that the recorded waveforms of artificial ultrasonic sources are used to measure travel times through the sample. The travel times are then used to reconstruct or image the spatial variations of velocity, which are sensitive to the state of stress within the sample. Similarly, active seismic velocity imaging using artificial seismic sources has been utilized in the delineation of stress concentrations, and mapping of other geotechnical properties of in-situ rockmasses [2,3]. Furthermore, concurrent monitoring of induced activity and active imaging has proven to be a useful tool in examining failure mechanisms in both laboratory acoustic emission and in-situ induced microseismic activity studies [1,3]. Passive imaging is a logical extension of concurrent monitoring of induced activity and active imaging, since velocity images may be generated by exploitation of information contained in arrival time data sets of the recorded activity. This study examines the application of passive imaging techniques, for ultrasonic velocity imaging using arrival time data from acoustic emission monitoring.

Passive ultrasonic imaging involves simultaneous determination of the source location and velocity structure by inversion of acoustic emissions arrival time data. Generally, source locations are calculated assuming a constant velocity. By accounting for velocity heterogeneities, more accurate source locations can be determined. Improved source locations are important since they are one of the most fundamental results of an acoustic emission experiment. Further, velocity imaging can provide additional information for the study of the failure characteristics of rock samples in the laboratory.

Late stages of mining in brittle rock types are occasionally plagued by the occurrence of rockbursts, mining induced seismic events which result in damage to the mine workings, equipment, and in some cases loss of life. To develop and test methodologies to be used in the investigation of rockbursts in the mining environment, controlled laboratory experiments of deforming rock samples were performed. As part of this research strategy, a research project has been undertaken to examine the application of passive imaging techniques in the investigation of rockbursts, by first applying the techniques to acoustic emissions recorded in the laboratory. This study documents the first phase in this research project, an examination of synthetic data sets, which were used to calibrate and test a passive imaging algorithm.

## PASSIVE IMAGING

A linearized inversion method to simultaneously determine the three-dimensional velocity structure and source locations was used. The method was originally developed to invert local earthquake arrival times [4]. Fermat's principle is used to linearize arrival times residuals of  $n$  events recorded at  $m$  stations as

$$T = Av + Bh, \quad (1)$$

where  $T$  is a  $mn$  vector of arrival time residuals calculated from an initial parameterized velocity model and source locations;  $v$  is a  $p$  vector of velocity model perturbations, and  $A$  is the corresponding  $mn \times p$  matrix of travel time partial derivatives; and  $h$  is a  $4m$  vector of hypocenter perturbations, and  $B$  is the corresponding  $mn \times 4m$  matrix of travel time partial derivatives. The residuals are calculated assuming some initial parameters. This equation is simply a combination of the standard direct velocity tomography and source location equations. Nonlinearity of the problem generally requires an iterative method, with ray tracing to account for ray bending effects.

A least squares solution of the problem results in two "normal equations",

$$A^T T = A^T A v + A^T B h \quad (2)$$

$$B^T T = B^T A v + B^T B h$$

Solving these simultaneous equations for  $v$  and  $h$  gives,

$$\begin{aligned} h &= (B^T B)^{-1} (B^T T - B^T A v), \\ v &= (OA)^{-1} OT, \end{aligned} \quad (3)$$

where,

$$O = A^T - A^T B (B^T B)^{-1} B^T.$$

The solution to Eq. 3 requires the inversion of the  $p \times p$  matrix  $(OA)$  and the  $4m \times 4m$  matrix  $(B^T B)$ , usually with some damping to ensure linearity and avoid singularity in the matrices.  $(B^T B)$  is a block diagonal matrix, and the calculation of its inverse can easily be computed by the individual inversion of the  $m-4 \times 4$  block submatrices. Computationally, the solution is the same as a least-squares tomography solution in addition to  $m$  least-squares source location solutions. A tapered singular value decomposition method was used to invert the matrices [5].

## SYNTHETIC EXAMPLES

The synthetic model used is shown in Figure 1. A cube was parameterized with  $5 \times 5 \times 5$  constant velocity blocks, creating 125 independent velocity parameters. The size of the cube was normalized to be 5 units in each dimension. The center ( $y = 3$ ) plane of blocks was modeled as a high velocity feature, with a 5% velocity contrast compared to the constant velocity background, which was normalized to

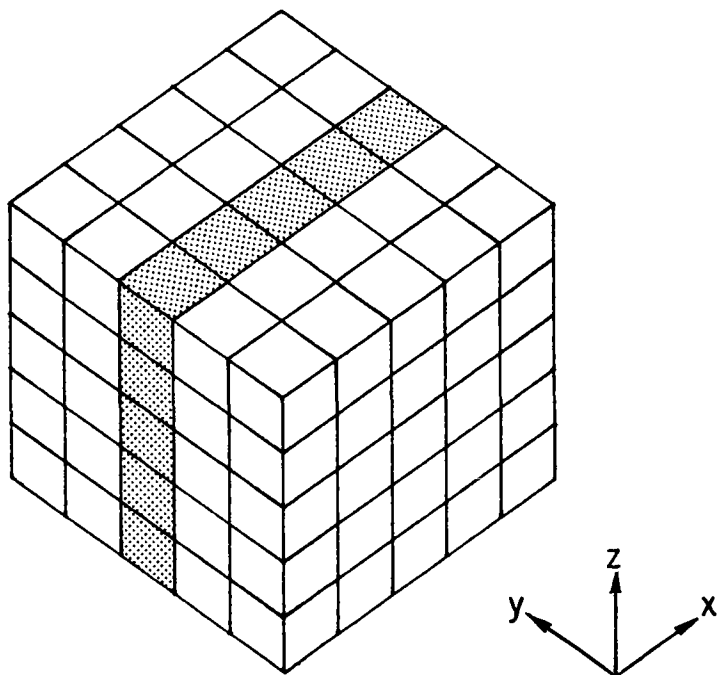


FIGURE 1 Physical model for the three-dimensional velocity structure.

unity. A plan view of a single layer of the velocity model in a plane perpendicular to the  $z$ -axis is shown in Figure 2. The synthetic model is identical in each such layer corresponding to a horizontal slice through the model, perpendicular to the  $z$ -axis.

Calculation of the synthetic arrival times utilized straight ray paths. Sensors were assumed to be located at each of the 8 vertices of the cube, although surface mounting is more practical in real experiments. Events were simply modeled as point sources, with equidirectional radiation patterns and zero rise times. No errors were included in the arrival times. Although this is an oversimplification of real data, it is intended to isolate and analyze the resulting resolution in the final images caused by restricted spatial distributions of source and sensor locations. Initial parameters in the simultaneous inversion were a constant background velocity and associated least squares source locations. Corrections to these initial parameters were then computed by solving Eq. 3. Two examples were considered, each with distinct event spatial coverage. The first example assumes spatially uniform event coverage, with 125 events located at the center of each cell. The second case considers more realistic event distributions, with 50 events confined to the sides of the high velocity layer.

In the case of the first example, with spatially uniform event coverage, two iterations were required to reproduce the velocity model

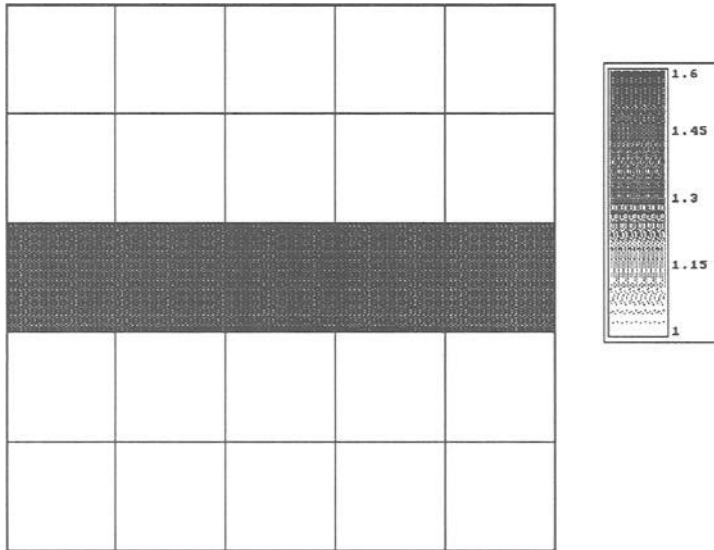


FIGURE 2 Plan view, or horizontal slice perpendicular to the z-axis, of the velocity model used in the synthetic study.

parameters to a precision of within 0.01%. The resulting image contained identical results for each horizontal layer in the model. Figure 3 shows a plan view of a horizontal layer in the resulting velocity image. The imaged model appears identical to the actual velocity model (Fig. 2).

Figure 4 shows a plan view of the event relocations. Location errors were reduced from up to 10% of a unit cell, to less than 0.01% after the inversion. Notice that due to the symmetry of the model, events in the high velocity zone were not originally mislocated. However, simple constant velocity source locations were biased for most events. Further, mislocations would be relatively larger for larger velocity variations.

The first case, with spatially uniform event coverage is obviously not realistic. Therefore, a second example is documented with restricted event coverage. In this case, events were confined to the center of the cell boundaries on each side of the high velocity  $y=3$  layer. The 50 events were located at the center of each cell boundary. Conceptually the model could represent a stress concentration, inducing localized failure along forming or preexisting microfractures.

Figure 5 shows a plan view of the velocity model produced by two

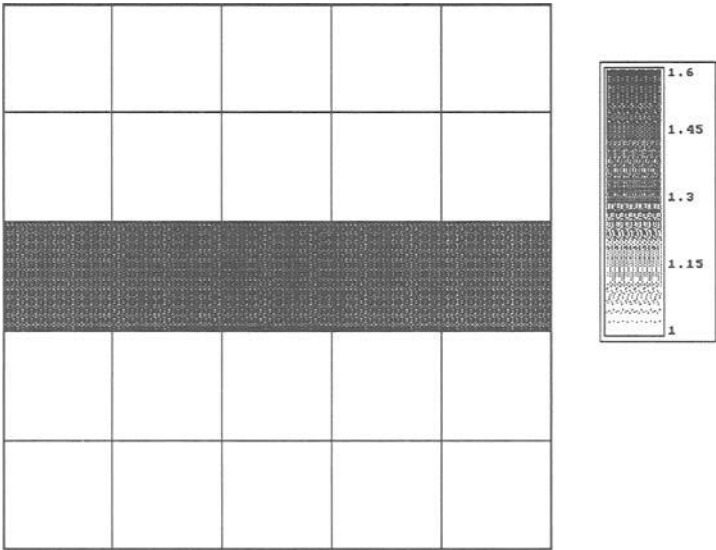


FIGURE 3 Plan view of the passively imaged velocity structure with spatially uniform event coverage.

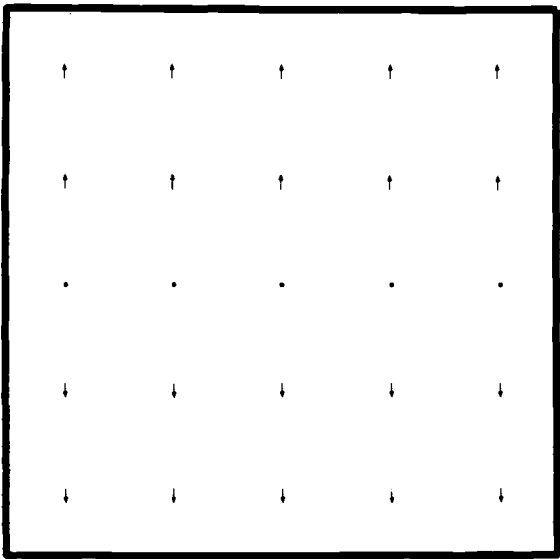


FIGURE 4 Plan view of event relocations, corresponding to the velocity model in Figure 3. Arrows point from constant velocity half-space locations, to locations determined by passive imaging.



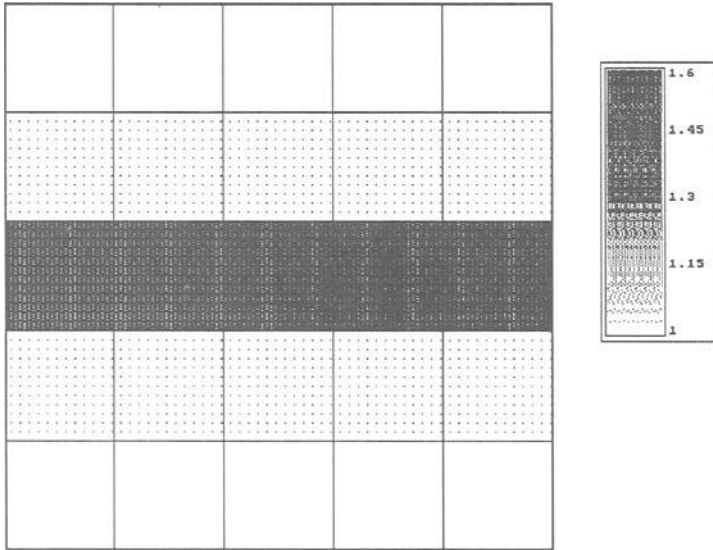


FIGURE 5 Plan view of the passively imaged velocity structure with spatially restricted event coverage.

iterations of the simultaneous inversion method. In this example there existed some subtle variation between x-y layers. The image of the  $z=2$  layer is shown in Figure 5, which is representative of the average resolution. Compared to the first example, the ray coverage is not uniform, so that some cells were not transversed by a single ray. This caused the matrix OA to be singular, and damping had to be applied to quell the influence of near zero singular values. The damping caused some loss of resolution, so that errors of about 0.5% in the high velocity zone resulted.

#### REAL DATA

As previously mentioned, this study simply documents the development and testing of a proposed technique to passively image the velocity structure of a deformed sample. The next phase of the project will be to invert a real data set. The data set will consist of arrival times measured from whole waveforms digitized on 16 channels, an expanded version of the system described in reference [1]. The data will be collected on a hydraulic fracturing experiment in the laboratory, where a crystalline rock is injected with high

pressure fluids. Concurrent monitoring of the induced acoustic emissions and active imaging of the rock sample will be performed. The results of a passive imaging calculation of the monitored acoustic emissions can then be compared to the results of a conventional active image, to validate the passively imaged velocity structure.

The simplified assumptions of the source characteristics and the wave propagation made in the synthetic data set, will now be discussed in relation to the real data set. Errors exist from the hypocenter point source location approximation to the finite sized event, the relative significance of which varies with the actual size of the fracture surface. Directional variations in the radiation pattern of the event will tend to increase the probability of arrival time picking errors as the signal-to-noise ratio decreases for raypaths close to nodal directions. However, a more significant contribution to the errors in the arrival time data results from the non-zero rise times. The finite rise times of real events increases along the raypath as energy is attenuated. For ultrasonic frequency propagation in crystalline rocks, dispersion along the raypath results in long rise times. This makes the actual arrival times difficult to measure, and more susceptible to errors. The effect of arrival time errors on the velocity images will be to degrade the accuracy of the imaged parameters. These errors ultimately control the minimum velocity contrast that can be imaged. In order to quantify the accuracy of the inverted parameters, the covariance matrix should be examined. Further, the resolution matrix should be examined to access the significance of the inverted parameters [6].

## CONCLUSIONS

From the second example, it is interesting to note that with the actual event locations spatially restricted to the velocity anomaly, the anomaly could still be reproduced. This suggests that in stress monitoring using sequential passive imaging, the evolving effects of the stress field can be imaged by monitoring the induced acoustic emissions. The locations of the induced activity will be coupled to zones of anomalous stress states, and hence velocity variations. Passive imaging of the recorded arrival time data of the activity should be able to resolve these spatial velocity variations, and to map stress related changes in the rock.

In these synthetic models, straight ray theory has been applied. However, for more pronounced velocity contrasts ray tracing methods are required to account for ray bending effects. Iterative inversion steps with intermediate ray tracing are then required to converge to the correct velocity structure and ray trajectory. More accurate ray directions also improve the accuracy of moment inversions and fault plane solutions [6]. Further, the isotropic velocity image may then be used for more extensive data analysis. These further analyses could include determining anisotropy effects and attenuation imaging, for supplemental information of the physical state of the rock.

Thus, passive imaging provides information on the spatial variation of the stress sensitive velocity structure, more accurate source locations, and ray directions for source mechanism studies. This method is particularly applicable to laboratory acoustic emissions and mining-induced seismicity, where monitors of arrival times of acoustical activity are already in place.

#### ACKNOWLEDGEMENTS

The authors gratefully acknowledge the assistance given by other members of the Queen's Rock Physics and Engineering Seismology Laboratory. Financial support was provided by NSERC and Queen's University.

#### REFERENCES

- [1] Falls, S. D., Chow, T., Young, R. P. and Hutchins, D. A., "Acoustic Emission Analysis and Ultrasonic Velocity Imaging in the Study of Rock Failure," Acoustic Emission : Current Practice and Future Development, ASTM STP 1076, J. Roget, K. Yamaguchi, and W. Sasche, Eds., American Society for Testing and Materials, Philadelphia, 1990.
- [2] Young, R. P., "Geotomography in the Study of Rockbursts and Seismicity in Mines," Proceedings of the Second International Symposium of Rockbursts and Seismicity in Mines, Minnesota, 1988, pp 122-141.
- [3] Young, R. P., Hutchins, D. A. and McGaughey, W. J., "Seismic Imaging Ahead of Mining in Rockburst Prone Ground," Proceedings of the Second International Symposium of Rockbursts and Seismicity in Mines, Minnesota, 1988, pp 122-141.
- [4] Spencer, C. and Gubbins D., "Travel Time Inversion for Simultaneous Earthquake Location and Velocity Structure Determination in Laterally Varying Media," Geophysical Journal of the Royal Astronomical Society, Vol. 63, 1980, pp 95-116.
- [5] Nolet, G., Ed., Seismic Tomography, D. Reidel Publishing Company, Dordrecht, 1987.
- [6] Thurber, C. H., "Seismic Structure and Tectonics of Kilauea Volcano, United States Geological Survey Professional Paper, No. 1350, 1987, pp 919-934.

Alex Vary

## ACOUSTO-ULTRASONICS: AN UPDATE

---

REFERENCE: Vary, A., "Acousto-Ultrasonics - An Update," Acoustic Emission: Current Practice and Future Directions, ASTM STP 1077, W. Sachse, J. Roget, and K. Yamaguchi. Eds., American Society for Testing and Materials, Philadelphia, 1991.

ABSTRACT: The acousto-ultrasonic technique was devised to assess diffuse flaw populations and any associated changes of the mechanical properties of composites and composite-like materials. Acousto-ultrasonics has been used to evaluate fiber reinforced composites, adhesive bonds, paper and wood products, cable and rope, and also human bone. The potentials and limitations of the technique are reviewed. Basic methods and guidelines are discussed. The underlying hypothesis for acousto-ultrasonic materials evaluation is stated and needs for theory and signal analysis development are indicated.

KEYWORDS: acousto-ultrasonics, stress waves, stress wave factor, composites, strength, adhesive strength

The acousto-ultrasonic approach uses simulated stress waves and stochastic wave propagation to detect and assess diffuse defect states, damage conditions, and variations of mechanical properties in fiber reinforced composites and composite-like materials [1]. The term acousto-ultrasonics denotes a combination of some aspects of acoustic emission signal analysis and ultrasonic materials characterization methodology. Unlike the usual acoustic emission practice, acousto-ultrasonics is not concerned with source location and characterization. Instead, acousto-ultrasonics deals primarily with the assessment of the integrated effects of diffuse defect states, thermo-mechanical degradation, and populations of subcritical flaws. These are factors that both singly and collectively influence acousto-ultrasonic measurements that, therefore, correlate with mechanical

Alex Vary heads the nondestructive evaluation group at the National Aeronautics and Space Administration's Lewis Research Center, 21000 Brookpark Road, Cleveland, OH 44135.

property variations and dynamic response. The acousto-ultrasonic technique has been demonstrated to be highly sensitive to interlaminar and adhesive bond strength variations. It has been shown useful to assess micro-porosity and/or microcracking produced by fatigue cycling.

This chapter reviews recent experimental findings and progress in the application of acousto-ultrasonics. Also, guidelines for making acousto-ultrasonic measurements are given along with limitations of the technique. Some current concepts of wave propagation modes that form the basis of the acousto-ultrasonic approach are reviewed.

## BACKGROUND

The seminal idea for the acousto-ultrasonic approach was derived from the work of Egle who investigated stress wave simulation using various excitation methods [2]. Egle and his colleagues were interested in simulating acoustic emission stress waves with the idea of improving methods for the characterization of acoustic emission signals and sources [3]. Vary and his colleagues [4,5] advanced the notion of using ultrasonically simulated stress waves and acoustic emission signal analysis methods to evaluate defect states and material properties. The term "acousto-ultrasonics" was coined to describe the close relation with acoustic emission and the internal acoustics of solids [6].

The original incentive for introducing the acousto-ultrasonic approach was the recognition of nondestructive testing needs peculiar to composite structures such as fiber reinforced composite laminates and filament-wound composite vessels. Acousto-ultrasonics was seen as a means for assessing factors that influence strength properties in principal load directions in these structures, e.g., "in-plane" parallel to fiber directions in composite laminates.

Another incentive was the need to go beyond detection of overt flaws like cracks, delaminations or inclusions. The idea was to deal with large populations of minute flaws where it is both impractical and unnecessary to image each individual discontinuity. Moreover, it was apparent that if a test piece has no dominant flaws, the objective should be the detection of global collections of subcritical flaws and material anomalies that diminish strength, stiffness, toughness, dynamic response, etc.

Acousto-ultrasonics belongs to a class of techniques that includes (coin) tap testing, dynamic resonance, and structural damping measurements. These are in addition to more directly related techniques like acoustic emission, pulse-echo, and guided Lamb wave methods. Sonic (coin) tap testing can be considered a primitive version of acousto-

ultrasonics, except that with acousto-ultrasonics "tapping" is usually done with a piezotransducer while "listening" is done with a second piezotransducer.

An acoustic emission system in its elementary form constitutes half of an acousto-ultrasonic system: passive listening but no active interrogation. The combination of an acoustic emission sensor with an active pulser forms the basis for an acousto-ultrasonic system. Calibration of acoustic emission sensors is conventionally done with lead pencil or glass capillary breaks, electric sparking, and also with piezotransducers. Conceptually, this comprises the first step toward an acousto-ultrasonic configuration.

It is worth considering the adoption of the idea that an acoustic emission system benefits from including pulsed transducers that help interrogate the condition of the material on which passive sensors are stationed. This combination can in theory be used to continually check changes in the background accumulation of material damage and diffuse flaws against which acoustic emission events are monitored. The true level of spontaneous activity in the material might be then taken as a function of the ratio of the acoustic emission rate versus the acousto-ultrasonic energy transmission level.

The leaky Lamb wave approach, like acousto-ultrasonics, utilizes two transducers, a sender and receiver. Instead of being attached to the test piece as in acousto-ultrasonics, the transducers in the leaky Lamb wave approach interrogate through water in a immersion tank. Using angle beams and immersion, the leaky Lamb wave approach excites waves that are similar to "in-plane" waves generated in plates by the acousto-ultrasonic approach. In either case, the waves are affected by the same microstructural and morphological factors that determine material quality.

## HYPOTHESIS

The general objective of acousto-ultrasonics is to rate the relative efficiency of stress wave propagation in a material. The basic attribute measured is stress wave energy loss, e.g., by scatter attenuation. For many fiber reinforced composites lower attenuation means better stress wave energy transfer and hence, better transmission and distribution of dynamic strain energy.

The working hypothesis is that more efficient strain energy transfer and strain redistribution during loading corresponds to increased strength and fracture resistance in composites. This hypothesis is based on the "stress wave interaction" concept which holds that spontaneous stress waves at the onset of fracture will promote rapid

macrocracking unless their energy is dissipated by other mechanisms, for example, plastic deformation or microcrack deflections [7]. In lieu of these mechanisms, prompt and efficient dissipation of stress wave energy away from crack nucleation sites is needed to assure that the energy is not focused or localized in a way that causes catastrophic fracture. One very important implication of the hypothesis is that the wave attenuation properties of a material are pivotal. For composites and adhesive bonds low attenuation will usually indicate high strength and impact resistance.

Experimental results have confirmed the ability of the acousto-ultrasonic approach to measure relative stress wave energy dissipation properties of composites. But, further work is needed to establish the above-stated hypothesis in connection with crack nucleation and damage accumulation mechanics in composites. Better understanding is needed of the connection between the attenuation of the benign ultrasonic waves used to interrogate composites and the attenuation of spontaneous stress waves during loading.

Acousto-ultrasonic interrogation can be used to assess morphological states just before or at the onset of fracture. Or, changes wrought by thermo-mechanical degradation can be measured. Acousto-ultrasonic measurements can also be applied to predict loci where failure might begin or how a material sample will react to loading.

There are currently no entirely satisfactory micro-mechanical or constitutive models for describing interactions of ultrasonic stress waves with factors that govern mechanical properties and dynamic response. Appropriate models should make it possible to specify the degree to which elastic properties, fiber-matrix bond quality, fiber fraction, and matrix void content, and similar factors will affect stress waves and material response to stress wave interactions.

## METHODOLOGY

Acousto-ultrasonics is a generalized approach to ultrasonic testing that uses a pair of ultrasonic piezoelectric probes in a send-receive configuration. A pulsed sending probe is optimized for wave generation while the receiving probe is optimized for signal sensing. The usual and often most convenient arrangement is to have the probes on the same surface of a test piece.

Acousto-ultrasonics differs from conventional ultrasonic methods primarily in the nature of the received signal. Instead of well-defined wave reflection and propagation paths, as in flaw detection, the acousto-ultrasonic approach requires that the received signal be the result of

multiple reflections and interactions with material microstructure in a volume of material between sending and receiving probes.

Bulk and guided waves and several types of plate waves can arise during acousto-ultrasonic testing [8]. Flexural Lamb waves will tend to dominate in composite panels. In these cases the wavelength will be comparable to or less than major dimensions of the sample, for example, thickness. But, pure plate or Lamb waves are unlikely because (1) wave generation is not long duration, single frequency but broadband pulsing, (2) lamina and fiber-matrix interfaces will break up the wave propagation paths. This produces stochastic wave propagation which is actually desirable because it ensures repeated wave interactions with key microstructural features and diffuse flaws. In composite panels this means that overlapping, scattered and mode-converted (longitudinal and transverse) signals will arrive at the receiver.

It has been observed that composite materials modulate and bandpass filter the acousto-ultrasonic signals. The signals arriving at the receiver probe often have spectra that indicate selective transmission of guided wave modes. For example, signals running parallel to the fibers in a unidirectional composite panel may exhibit a bi-modal frequency spectrum: (1) a low frequency component because of guided plate waves and (2) a high frequency component because of transmission by fibers.

Selection of the sending transducer center frequency and the receiving transducer bandwidth and sensitivity are pivotal in acousto-ultrasonics. For composite panels it is advantageous for the sender to produce wavelengths that are less than the thickness. This is to assure that there are multiple wave interactions with diffuse flaws and microstructural features within the test volume. This may also entail high ultrasonic frequencies that are quite strongly attenuated. The receiver must be very sensitive and have a bandwidth covering all frequencies passed by the sample.

## ANALYTICAL

In acousto-ultrasonics quantification of information contained in the simulated stress wave signals is done by calculating a stress wave factor (SWF). There are many ways to define and calculate the SWF. The definition of the SWF in any particular case depends on the nature of the signal; test piece (e.g., material, size, shape); and types of flaws, damage states, properties to be assessed.

Acousto-ultrasonic signals often resemble acoustic emission "burst" waveforms. In these cases it has been



found practical to use signal analysis methods based on acoustic emission practice. For example, time domain quantities such as rise time, peak voltage, voltage decay or ringdown count, and root-mean-square voltage values tend to correlate with defect states and material properties.

Statistical analysis of spectral mean values, second and third moments, and skewness can also form a basis for defining the SWF. These involve power spectrum analysis and spectral distribution functions. Cepstrum analysis offers further means for signal analysis and SWF quantification. In the future, advanced methods using inverse scattering theory, homomorphic and diffuse field analysis will undoubtedly emerge as tools for dealing with acousto-ultrasonic signals [9-11].

Although a number of approaches for quantifying the acousto-ultrasonic SWF have been successful, they have usually been based on somewhat unsophisticated signal analysis methods, for example, ringdown counts and root-mean-square voltages. In many instances these simple definitions for the SWF suffice. However, further studies are needed to specify and measure the SWF in terms of specific wave propagation modes that arise under various material conditions and geometries.

It is important to note that the SWF should not always be defined in terms of the entire waveform or spectrum. By selecting only certain portions of waveforms or spectra it is possible to greatly improve correlations between the SWF and specific material properties. This is because guided wave modes at specific frequencies may correspond closely to particular elastic and mechanical properties. Possibly, the best correlation between the SWF and a property or flaw condition will be obtained by measuring the least dominant rather than the most dominant part of the signal.

One underexplored area is that of diffuse field theory for dealing with signals where phase information has been lost due to stochastic scattering and multiple reflections. Experimental observations indicate that there are likely to be intermixed diffuse, bulk, plate, and guided modes. The effects of interplay of these modes need to be evaluated by appropriate analytical methods. Moreover, further work is needed to identify SWF quantification methods that relate directly to composite integrity, fiber-matrix bonding, and thermo-mechanical degradation effects.

## LIMITATIONS

Acousto-ultrasonics has the capabilities and also the limitations associated with other ultrasonic techniques. Acousto-ultrasonics certainly has limitations common to all

techniques that attempt to measure either absolute or relative attenuation and velocity. There is an essential difference with respect to ultrasonic techniques where the objective is only to detect the presence of overt flaws. By going beyond flaw detection, that is, by attempting to characterize defect states and subtle material anomalies, acousto-ultrasonics becomes vulnerable to material vagaries that affect probe sensitivity and signal reproducibility.

In addition to sample thickness and material variations all acousto-ultrasonic signals are affected by a number of factors associated with transducer-specimen attachment: applied pressure, type and amount of couplant, the specimen surface roughness, transducer alignment, the spacing and location of sending and receiving transducers, and so on. Properties of the transducers, i.e., bandwidth, resonance frequencies, internal damping, and inherent sensitivity, affect the material characteristics revealed [12,13].

To assure stochastic wave propagation and to sense the collective effects of minute discontinuities requires using the highest possible ultrasonic frequency bands that can be transmitted and sensed. The increased sensitivity gained imposes penalties because surface roughness effects, probe alignment and coupling, and associated factors impose variations on the signals transmitted by the bulk material. Signal validity and reproducibility in acousto-ultrasonics require the utmost care in the test set-up and procedure.

There are further problems after the previous factors have been dealt with. In practice, measurements must be repeated to map material variations. This requires scanning by lifting and recoupling the transducers or by using probes that can scan while remaining in contact with the surface. The latter can be accomplished by transducers stationed in the hubs of elastomer wheels that are rolled over the test surface, usually with dry coupling. Acousto-ultrasonics has also been successfully accomplished using probes encased in a squirter fixture where water jets couple the probes to a part and allow free scan movement.

The use of laser ultrasonics is being studied as an alternative to methods that rely on contact. Non-contact laser methods have problems associated with thermal-to-acoustic energy conversion, potential laser damage, the possible need for sacrificial layers, and the laser-optic (i.e., interferometric) detection of stress waves.

Using either laser beams or the water jet approach, noncontact acousto-ultrasonic methods should be able to accommodate the scanning of large areas and curved surfaces. However, the technique still requires a constant material thickness for comparative measurements of material property variations or defect states.

Although quite capable of detecting overt flaws, the

acousto-ultrasonic approach was devised primarily to assess the integrated effects of diffuse flaw populations, impact damage, and thermo-mechanical degradation. Applications that demand resolution of small isolated discontinuities are not readily handled by the technique. Other techniques such as pulse-echo or through transmission C-scanning are likely to be more appropriate for high spatial resolution flaw detection and imaging.

Acousto-ultrasonics does not lend itself to high resolution flaw imaging because of inherent constraints on transducer positioning and spacing. Generally, the technique demands that a relatively sizable volume of material be examined for each position on the test piece. This is determined in part by the size of the probes. A typical minimum probe spacing may be approximately one centimeter. With water jet fixtures and laser beams the spacing may be reduced. But, the spacing must not be so small that the volume of material interrogated does not allow a large number of multiple wave interactions.

## APPLICATIONS

The sensitivity of acousto-ultrasonics for detecting and measuring subtle but significant material property variations in composites has been amply demonstrated [1]. There are now numerous examples of successful and useful applications of acousto-ultrasonics. The technique has been used to measure variations of the interlaminar shear strength of composites, polymer composite cure state, filler content in wood and paper products, wire rope strength, and adhesive bond strength [14-18].

Among the most useful aspects of acousto-ultrasonics is the ability to locate weak areas and to assess degradation and diffuse flaw states in composites. Micro-cracking, fatigue and impact damage can be closely measured with the acousto-ultrasonic stress wave factor [19-22]. Acousto-ultrasonics currently appears to be an excellent technique for ranking fiber composite laminates and adhesive joints according to their strength variations [23,24]. This latter attribute is primarily due to in-plane shear waves generated in bond zones.

## CONCLUSION

Although practical field applications of acousto-ultrasonics exist, most of the uses reported to date have been with laboratory samples. As in the case of acoustic emission, acousto-ultrasonics is proving to be a valuable

tool in materials research. Acousto-ultrasonics should be considered for in-situ monitoring during proof testing and materials tests that are usually monitored by acoustic emission. This can help gauge material changes that affect acoustic emission signal characteristics and also assess concomitant material damage and degradation. The understanding gained during these test activities can aid in applying acousto-ultrasonics to the evaluation of the integrity and service life of structural composites.

#### REFERENCES

- [1] Acousto-Ultrasonics - Theory and Applications, Duke, J. C. Jr., Ed., Plenum Press, New York, 1988.
- [2] Egle, D. M. and Brown, A. E., Journal of Testing and Evaluation, Vol. 4, No. 3, 1976, pp. 196-199.
- [3] Egle, D. M., Journal of the Acoustical Society of America, Vol. 65, No. 5, 1979, pp. 1198-1203.
- [4] Vary, A., and Bowles, K. J., Proceedings, 11th Symposium on Nondestructive Evaluation, American Society for Non-destructive Testing, 1977, pp. 242-258.
- [5] Vary, A., and Lark, R. F., Journal of Testing and Evaluation, Vol. 7, No. 4, 1979, pp. 185-191.
- [6] Vary, A., Materials Evaluation, Vol. 40, No. 6, 1982, pp. 650-654.
- [7] Vary, A., Solid Mechanics Research for Quantitative Non-Destructive Evaluation (J. D. Achenbach and Y. Rajapakse, Eds.) Martinus Nijhoff Publishers, Dordrecht, The Netherlands, 1987, 134-152.
- [8] Tang, B. and Henneke, E. G., II, Materials Evaluation, Vol. 47, No. 8, 1989, pp. 928-934.
- [9] Egle, D. M., Journal of the Acoustical Society of America, Vol. 70, No. 2, 1981, pp. 476-480.
- [10] Karagulle, H., Williams, J. H., Jr., and Lee, S. S., Materials Evaluation, Vol. 43, No. 1, 1985, pp. 1446-1454.
- [11] Weaver, R. L., Solid Mechanics Research for Quantitative Non-Destructive Evaluation (J. D. Achenbach and Y. Rajapakse, Eds.) Martinus Nijhoff Publishers, Dordrecht, The Netherlands, 1987, pp. 426-434.
- [12] Bhatt, M. and Hogg, P. J., NDT International, Vol. 21, No. 1, 1988, pp. 3-10.
- [13] Russell-Floyd, R. and Phillips, M. G., NDT International, Vol. 21, No. 4, 1988, pp. 247-257.
- [14] Kautz, H. E., Materials Evaluation, Vol. 45, No. 12, 1987, pp. 1404-1412.
- [15] Hinricks R. J. and Thuen J. M., "Control System for Processing Composite Materials," U.S. Patent 4,455,268, 1984.
- [16] dos Reis, H. L. M. and McFarland, D. M., Journal of Acoustic Emission, Vol. 28, 1986, pp. 67-70.
- [17] dos Reis, H. L. M. and McFarland, D. M., British Journal of Non-Destructive Testing, Vol. 28, May

- 1986, pp. 155-156.
- [18] Tanary, S., "Characterization of Adhesively Bonded Joints Using Acousto-Ultrasonics," Thesis, Mechanical Engineering, University of Ottawa, Canada, 1988.
- [19] Lorenzo, L. and Hahn, T., Composite Materials: Testing and Design - 8th Conference, STP 972, American Society for Testing and Materials, Philadelphia, PA, 1988, pp. 380-397.
- [20] Govada, A., Henneke, E. G., and Talreja, R., Advances in Aerospace Sciences and Engineering, (U. Yuceoglu and R. Hesser, Eds.), American Society for Mechanical Engineering, 1984, pp. 55-60.
- [21] Williams, J. H., Jr. and Lampert, N. R., Materials Evaluation, Vol. 38, No. 12, 1980, pp. 1502-1510.
- [22] Talreja, R., Acousto-Ultrasonics - Theory and Applications, J. C. Duke, Ed., Plenum Press, New York, 1988, pp. 177-190.
- [23] Srivastava, V. K. and Prakash, R., Composite Structures, Vol. 8, Elsevier Applied Science Publishers, England, 1987, pp. 311-321.
- [24] Fahr, A., Lee, S., Tanary, S., and Haddad, Y., Materials Evaluation, Vol. 47, No. 2, 1989, pp. 233-240.

Michael T. Kiernan and John C. Duke, Jr.

## THEORETICAL BASIS OF THE ACOUSTO-ULTRASONIC METHOD

---

REFERENCE: Kiernan, M. T. and Duke, J. C., Jr. "Theoretical Basis of the Acousto-Ultrasonic Method," Acoustic Emission: Current Practice and Future Directions, ASTM STP 1077, W. Sachse, J. Roget, and K. Yamaguchi, Eds., American Society for Testing and Materials, Philadelphia, 1991.

ABSTRACT: This paper provides a physical interpretation and theoretical basis for acousto-ultrasonic (AU) results, using through-thickness-transverse-resonance (TTTR), Lamb wave theory, and elasticity. Major emphasis is given to building a model of the AU method. The paper begins with a brief introduction to the AU method and experimental results, physical interpretations, associated theory, and comparisons between theory and AU results. Finally, conclusions are presented identifying the modes of wave propagation influencing the AU measurements.

KEYWORDS: acousto-ultrasonic, composites, Lamb waves

Composite materials develop complex damage states which demand practical nondestructive evaluation (NDE) techniques. The AU method is one of many NDE techniques under development for ascertaining the extent and mechanical effects of damage in composite materials.

The AU method involves introducing a mechanical excitation at one position on a material surface and sensing how the disturbance is transmitted through the material by using a second receiving transducer at another position on the same material surface. The original premise was that a section of material which transmitted the most energy from the sending transducer to the receiving transducer would transfer loading stress more efficiently, and hence be less prone to fracture. This was successfully used to predict strength of composite specimens [1]. Additionally, early research showed that AU energy measurement decreased as a function of fatigue cycles [2].

Dr. Kiernan, a recent graduate of Virginia Tech, is an engineer at GE Nuclear Fuels and Component Manufacturing, M/C K-51, PO Box 780, Wilmington, NC 28402; Dr. Duke is a professor of Engineering Mechanics, VPI&SU, Blacksburg, VA 24061-0219.

Beyond the proven experimental successes, the AU method offers certain practical advantages for implementation:

- i. Wave motion is directed in the plane of the plate, in order to interact with the material in the direction of loading.
- ii. Requires access to only one surface of the material.
- iii. Rapid measurements are possible.
- iv. The method may be implemented inexpensively.

Following early AU experimental successes, research on the AU method branched out in a number of different directions, including advance methods of signal analysis [3-5], new applications [6,7], relations to material condition [8,9], and some work on developing a physical understanding of AU results [10,11]. However, an understanding of AU results for composite plates is still incomplete and no models exist for composite plate characterization. Models of the AU method will help guide future AU research and development, as well as develop the means for material characterization. The purpose of this paper is to provide a physical understanding of the AU method and state the associated theory, for the purpose of developing a refined AU technique and developing a basic understanding of wave propagation in composite materials, which may be of use in other areas, such as acoustic emission.

## EXPERIMENTAL SET-UP

Understanding AU results requires giving attention to experimental set-up and procedure, since experimental results and the physical phenomena causing those results are different for different experimental arrangements. A diagram of the AU set-up used in this work is shown in Fig. 1. Each component in the diagram has an effect on the results [12].

A 1.25 cm diameter, 2.25 MHz center frequency, wide band, normal mode, piezoelectric transducer was used for the sending transducer. For the specimens utilized, this met Vary's original criterion of having the resonant frequency of the transducer relating to a wavelength on the order of the material thickness [1]. For the results described in this work, the same type of transducer was used for both the sending and the receiving transducer. The signals were acquired and analyzed using a personal computer incorporating an analog to digital converter board.

## AU RESULTS AND THEORETICAL RELATIONS

Figure 2 shows the voltage/time plot obtained by performing the AU method on a 1.59 mm thick aluminum plate with the sending transducer approximately 25 mm from the receiving transducer.

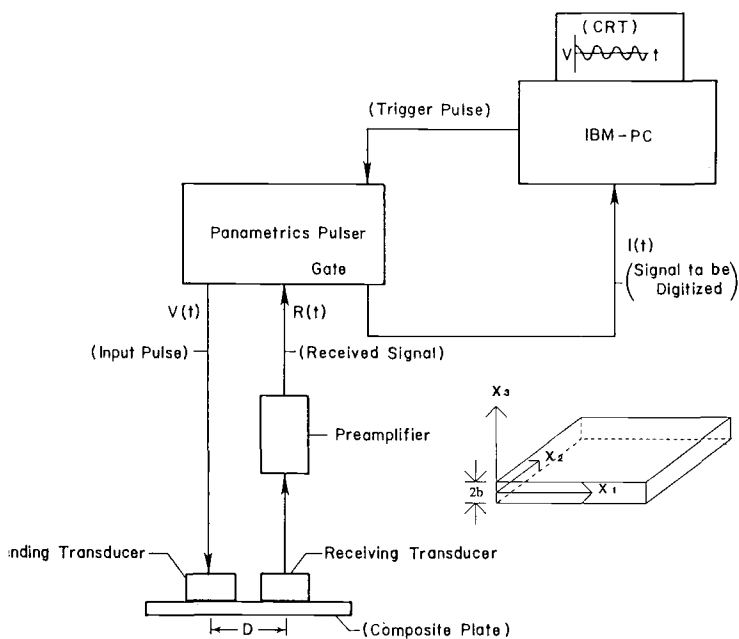


FIG. 1 -- Schematic diagram of the experimental set-up.

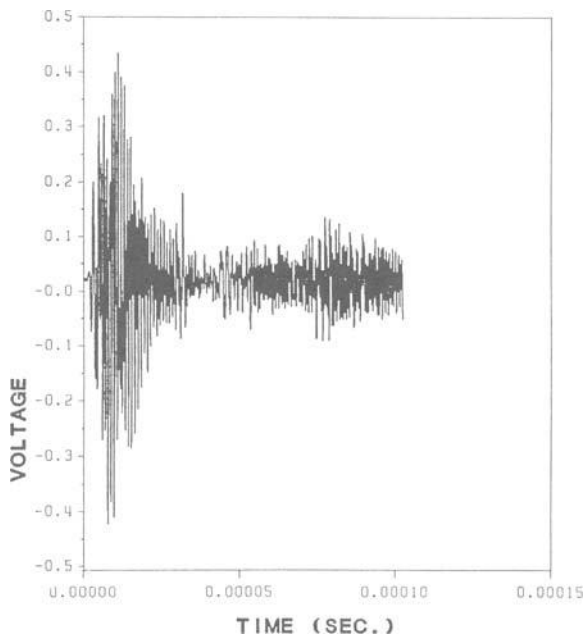


FIG. 2 -- Voltage versus time plot of an AU signal from a 1.59 mm thick plate of aluminum.



The wavetrain is quite long (>150 microseconds) compared to the short pulse length (5-10 microseconds). The long wavetrain would suggest that the AU signal is the result of some reflection pattern and not the result of a plane wave propagating between the sending and receiving transducer. Next, it should be noted that definite harmonic components exist in the wavetrain and that these components tend to be modulated.

In order to obtain more information, FFT data is provided in a plot of amplitude/frequency, Fig. 3. Peak amplitudes occur at 1 and 2 MHz, with a smaller peak at .7 MHz.

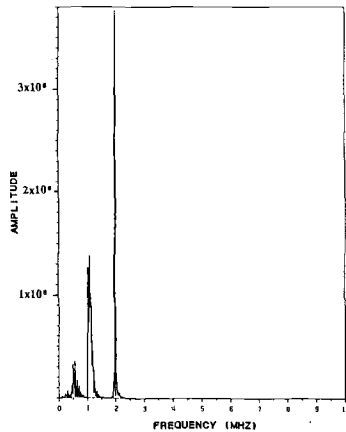


Fig. 3 -- Amplitude versus frequency plot of a signal from a 1.59 mm thick plate of aluminum.

Distinct peaks in the frequency response for physical systems, usually relate to resonant phenomena. By comparing the amplitude versus frequency plots for plates of different thicknesses, it was determined that the frequencies of resonant peaks were inversely dependent on plate thickness [12].

The theory of through-thickness-transverse-resonance (TTTR) predicts the frequencies associated with plane wave resonances between the top and bottom surfaces of a plate. TTTR is a limiting case of the more general modes of Lamb wave propagation for plates. The frequency and displacement equations for these modes are easy to calculate [13] and are given below:

#### Symmetric Modes

$$(a) \quad u_3 = B' \sin(m\pi x_3 / 2b) \quad u_1 = 0 \quad m=1,3, \dots$$

$$(b) \quad u_1 = C' \cos(n\pi x_3 / 2b) \quad u_3 = 0 \quad n=2,4, \dots$$

#### Antisymmetric Modes

$$(a) \quad u_1 = D' \sin(n\pi x_3 / 2b) \quad u_3 = 0 \quad n=1,3, \dots$$

$$(b) \quad u_3 = A' \cos(m\pi x_3 / 2b) \quad u_1 = 0 \quad m=2,4, \dots$$

## Frequencies and Velocities

$$f_p = Nv_p/2t \quad f_s = Nv_s/2t \quad v_p = (C_{33}/\rho)^{.5} \quad v_s = (C_{44}/\rho)^{.5} \text{ or } (C_{55}/\rho)^{.5}$$

$C_{33} = (1-\nu)[E/(1+\nu)(1-2\nu)]$   $C_{44} = C_{55} = [E/2(1+\nu)]$  for isotropic materials where  $t$  is the plate thickness,  $N=1,2,3,\dots$ ,  $C_{ij}$ 's are the stiffness matrix values, and  $E$  and  $\nu$  are the Young's modulus and Poisson's ratio, respectively. If  $C_{44}$  does not equal  $C_{55}$ , additional resonances would be expected. For materials where the  $x_3$ -axis is not in a plane of orthotropic symmetry, the shear wave velocities would be affected by the coupling terms in the stiffness matrix.

Table 1 shows the predicted TTTR frequencies for the aluminum plate discussed previously. Notice that the 1 MHz peak in Fig. 3 agrees with the predicted value for the first order antisymmetric resonance, as listed in Table 1. Similarly, the 2 MHz peak agrees with the predicted value for both the first and second order symmetric resonances. Basically, AU results tend to indicate that for a given plate, the value for the frequency at which peaks occur in the amplitude/frequency plot agrees with calculated TTTR values.

TABLE 1 -- Cutoff Frequencies for 1.59mm Al Plate

Number	Symmetric Mode Frequency (MHz)	Antisymmetric Mode Frequency (MHz)
0	0.0	0.0
1	1.9	1.0
2	2.0	3.8
3	5.7	3.0
4	4.0	7.6
5	9.5	5.0

Phase velocity measurements were made in order to gain more information on the modes of wave propagation. These measurements were made for each of the harmonic components noted in the spectrum; the resulting values are displayed in Table 2.

Table 2 -- Phase Velocity Measurements  
(1.59mm thick Al Plate)

Frequency (MHz)	Phase Velocity (km/sec)
.7	5.33
1.0	15.75
2.0	>25.4

It should be noted that the 1 and 2 MHz signal content showed phase velocities much higher than the values for plane waves in aluminum. Also, estimates of group velocities were made by noting the speed of the modulating components. The .7 MHz signal content showed a group velocity that was the same value as the phase velocity, while the 1 and 2 MHz signal content showed group velocities at roughly 1500 meters per second.

The theory which governs wave propagation in plates is well developed [11,13,14,21]. It can be used to derive dispersion curves, phase velocity versus frequency curves, and to estimate group velocities. In addition, this theory can be utilized to calculate

displacement and stress fields, and has been extended to calculate transient plate responses for an isotropic material [15].

Two basic approaches can be used to derive the equations for plate waves. The first is the more conventional Rayleigh/Lamb wave analysis. The other more recently developed approach is the method of partial waves or transverse resonance [14]. The Rayleigh/Lamb approach involves expressing the displacement vector as a scalar and vector potential and then solving for the potentials in the equations of motion by the separation of variables method. Next, the potentials are combined in an appropriate manner to satisfy the boundary conditions (stress free) at the top and bottom surfaces of the plate.

In the partial wave method, waves are assumed to reflect back and forth between the top and bottom surfaces of the plate. These combine to form traveling waves in the direction of wave propagation and standing waves in the thickness direction of the plate. These waves are found by establishing the condition for transverse resonance through the thickness of the plate. For anisotropic materials, the method of partial waves is more convenient method of solution than the classical approach. Also, as pointed out by Solie and Auld, [14], this method highlights certain physical features of plate wave propagation.

#### PLATE WAVES IN ISOTROPIC MATERIALS

Rayleigh-Lamb waves are produced by the introduction of a pressure wave (P-wave) and a vertically polarized shear wave (SV-wave) to the plate. These can be expressed by the scalar potential,  $\phi$ , for the pressure wave and one vector potential,  $H_2$ , for the SV-wave. Specifically, if consideration is given only to the propagation in the  $x_1$ -direction (see Fig. 1), then

$$\phi = \phi_0 e^{i(\xi x_1 \pm \alpha x_3 - \omega t)}, \omega^2 = v_p^2 (\alpha^2 + \xi^2) \quad H_2 = H_0 e^{i(\xi x_1 \pm \beta x_3 - \omega t)}, \omega^2 = v_s^2 (\beta^2 + \xi^2)$$

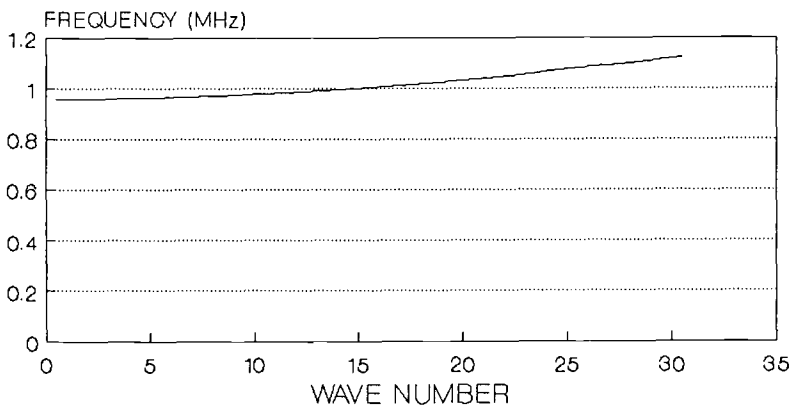


FIG. 4 -- Dispersion curve for the 1st order antisymmetric mode for Al.

The wave normal for the P-wave can be found to make an angle  $\theta_1 = \pm \tan^{-1}(\xi/\alpha)$  with the vertical axis and the SV-wave can be found to make an angle  $\theta_3 = \pm \tan^{-1}(\xi/\beta)$  with the vertical axis. By combining four of the SV-waves with four of the P-waves, each with the appropriate amplitude and phase, the motion can be shown to be harmonic in the  $x_1$ -direction; the amplitudes vary sinusoidally through the thickness, the phase velocity is  $v_p = \omega/\xi$  and the wavelength is  $2\pi/\xi$ . For a plate with traction free top and bottom surfaces, this can be described as a combination of motions which are symmetric and antisymmetric about the mid-plane of the plate. Using symmetry arguments with the traction free boundaries, equations for both the symmetric and antisymmetric motions can be found, including the displacements,  $u_1$  and  $u_3$ , the corresponding stresses that must exist, and the transcendental equations which describe the dispersion relations between the wave numbers. For the symmetric mode,

$$u_1 = i(B\xi \cos \alpha x_3 + C\beta \cos \beta x_3) e^{i(\xi x_1 - \omega t)} \quad u_3 = (-B\alpha \sin \alpha x_3 + C\xi \sin \beta x_3) e^{i(\xi x_1 - \omega t)}$$

$$F_1 = (\xi^2 - \beta^2)^2 \cos \alpha b \sin \beta b + 4\alpha\beta\xi^2 \sin \alpha b \cos \beta b = 0, \text{ for the antisymmetric mode,}$$

$$u_1 = i(A\xi \sin \alpha x_3 - D\beta \sin \beta x_3) e^{i(\xi x_1 - \omega t)} \quad u_3 = (A\alpha \cos \alpha x_3 + D\xi \cos \beta x_3) e^{i(\xi x_1 - \omega t)}$$

$$F_2 = (\xi^2 - \beta^2)^2 \sin \alpha b \cos \beta b + 4\alpha\beta\xi^2 \cos \alpha b \sin \beta b = 0, \text{ where the stresses can be calculated using the constitutive relations. The variables A, B, C, and D are defined by}$$

$$\phi = (A \sin \alpha x_3 + B \cos \alpha x_3) e^{i(\xi x_1 - \omega t)} \quad \text{and} \quad H_2 = i(C \sin \beta x_3 + D \cos \beta x_3) e^{i(\xi x_1 - \omega t)}$$

By examining the slowness surfaces for the SV and P waves in conjunction with the stress free boundary conditions,  $F_i$  it is possible to determine the nature of the Rayleigh-Lamb modes that will satisfy these conditions, where the stress components can easily be calculated using the constitutive relations.

Simple thickness modes occur when displacement components are only a function of the  $x_3$  coordinate and time. In this special case, the three types of plane waves each can propagate between the top and bottom surface, independent of the other waves, setting up separate plate waves which can be derived from the standard plate wave equations by setting  $\xi$  equal to zero. These modes correspond to where the higher order modes cross the ordinate ( $\omega$ -axis) on the dispersion curve (see Fig. 4). Since the phase velocity is defined as  $v = \omega/\xi$ , the phase velocity for a thickness mode is infinite.

The manner in which the phase velocities drop from infinity for the higher order modes, when  $\xi$  becomes nonzero, can be seen in Fig. 5. Also, note the slope of the dispersion curves for the higher order modes, near the TTTR condition, are relatively low, indicating that the group velocity or rate of energy flow is relatively low. Thus, these modes are characterized by rather high phase velocities and rather slow modulating (group) velocities. Moreover, the first order symmetric curve has a negative group velocity. However as a general trend, these curves start with very high phase velocities and rather low group velocities and move to higher group velocities (ie. the curves turn upwards at larger slopes) with lower associated phase velocities. Additionally, the higher the mode the flatter the curves tend to become (in general) and hence the less the group velocity. Generally, the

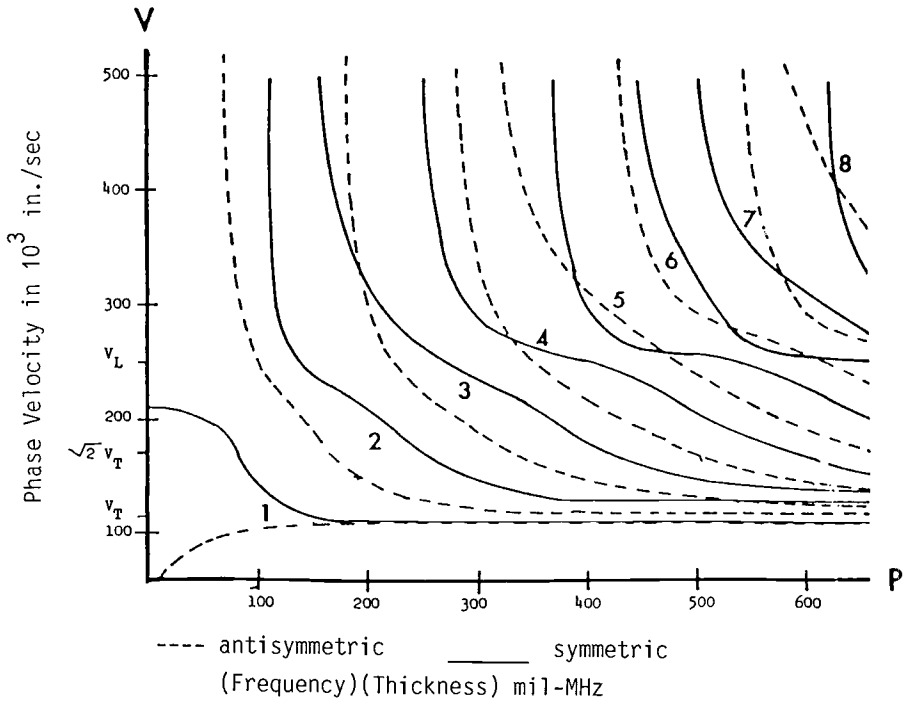


FIG. 5 -- Lamb wave spectrum in Aluminum (after [17]).

higher the mode; the higher the phase velocity and the slower the group velocity. Phase velocities and group velocities vary along each of these curves and vary from curve to curve, hence a great deal of dispersion is associated with these higher order modes for a small frequency range. It is again very important to note that for higher order modes the frequency of the resulting wave changes very little with  $\xi$ . Thus, many ray angles of input ( $\theta_1$ ) result in similar frequencies. Hence, a lot of energy may be created around these frequencies.

#### PLATE WAVES IN ANISOTROPIC MATERIAL

Several investigators have looked at the problem of plate waves in anisotropic materials. As might be expected, the anisotropic constitutive relation greatly complicates the analysis of the plate wave problem. A variety of extra plate wave modes are created due to the extra modes of plane waves which are possible. Also, the properties of the Lamb waves (ie. dispersion curves) depend on azimuthal angle. Further complications arise due to the fact that all modes are coupled into the same equations, hence vastly complicating numerical procedures. In fact, the full analysis of the anisotropic problem would be prohibitive without the use of the computer. However, Ekstein did formulate the full analytical solution to the problem for the case of orthotropic symmetry in 1945 [16]. Detailed analysis of the dispersion relations of anisotropic materials were not developed until Mindlin and

co-workers used a variational approach [13]. More recently the method of transverse resonance or partial waves has been forwarded as a solution technique [14].

In the method of partial waves, the particle displacement vectors of the partial waves are coupled to each other by reflections at the surface in accordance with Snell's Law.

$$u_j = \alpha_j e^{i(k_j x_1 + \omega t)} \text{ becomes } u_j = \alpha_j e^{ik(x_1 + l_2 x_2)} \quad k = \omega/v \quad l_2 = k_2/k$$

The displacement field may be taken as a linear combination of the six allowed partial waves. Mathematically this may be expressed as

$$u_j = \sum_{n=1}^6 C_n \alpha_j(n) e^{ik(x + l_z(n)z)}$$

Imposing the boundary conditions  $\tau_{12} = \tau_{32} = \sigma_{22} = 0$  leads to a system of six homogeneous linear equations where the coefficients of the  $C_n$  are now functions of  $\rho$ ,  $C_{ij}$ ,  $v$ , and  $h$ . Setting the determinant of the system of equations to zero results in the dispersion relations, which yields information on the dependence of velocity on frequency. These can be used to derive the commonly used dispersion curves with the infinite number of branches. Furthermore, the system can then be solved to find relative values of  $C_n$  indicating the relative displacements occurring in the plate.

## THEORETICAL RESULTS FOR THE ALUMINUM PLATE

Figure 5 shows the plot of velocity versus frequency thickness, derived from plate wave theory, for various possible Lamb waves in aluminum plates. Notice, that the only possible mode of propagation for the 1 MHz frequency content is the first order antisymmetric mode, at  $k$  values corresponding to very small input angles  $\theta_1$ . However, the 2 MHz signal content may correspond to either the first or second order symmetric mode at small values of  $\xi$ . Also, the small group velocities for AU signal contents agrees with plate wave theory. The .7 MHz signal content showed behavior which agrees with the fundamental symmetric mode. In particular, the .7 MHz signal content showed no dispersion and separated into the early portion of the wavetrain for greater transducer separation (due to greater group velocity); this portion of the wavetrain was on the order of the pulse width. Hence, the major portion of the wavetrain seems to be made up of higher order Lamb waves with small values of  $\xi$ , corresponding to small input angles  $\theta_1$ .

Elasticity solutions may be used to understand what disturbances may be created due to an applied force on a free surface, others have used this type of approach [9]. Calculated disturbances may then be used to determine exact magnitudes for the displacement fields calculated in the Lamb wave equations [11]. Figure 6 shows how  $u_z$  at the top surface, of the 1.59 mm thick aluminum plate, varies with frequency, if a point force elasticity solution [12,18] is used to provide the magnitude for the P-wave potential. It should be noted that this shows relatively similar behavior, at 1 MHz, compared to the 1 MHz peak in the experimentally obtained amplitude/frequency plot, Fig. 3.

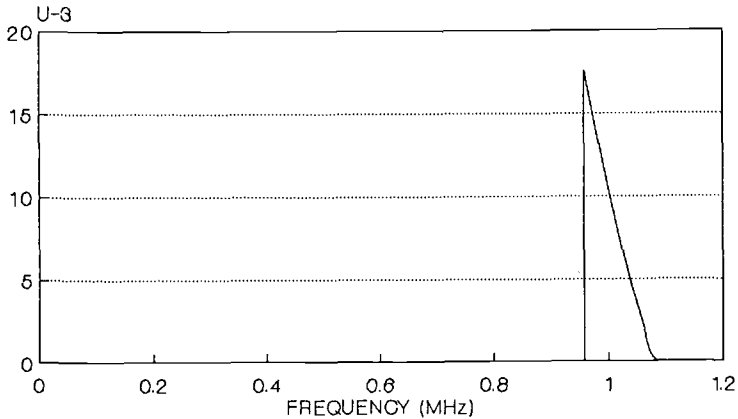


FIG. 6 --  $u_3$  displacement at the top surface as a function of frequency

The AU examination of composite plates is complicated by the issues of inhomogeneity and anisotropy. This paper will address the issue of anisotropy, but ignore the effects of inhomogeneity. The effects of inhomogeneity are minimized in this work by dealing with only unidirectional composites, the experimental effects of other lay-ups have been discussed previously [19]. Material anisotropy makes it necessary to perform AU measurements at different azimuthal angles relative to the fiber direction, in order to fully understand AU results. In this work, an azimuthal angle of zero denotes the fiber direction and an azimuthal angle of 90 corresponds to the cross fiber direction.

Figure 7 shows a voltage/time plot for a unidirectional gr/ep composite plate, for an azimuthal angle of zero. Notice, this plot shows the same general behavior as the plot for the aluminum plate. The major differences in the AU signatures for the composite plates are the shorter wavetrains and the existence of extra frequency components (see Table 3).

Table 3 displays theoretical values for TTTR frequencies for the plate used to obtain the voltage/time and amplitude/frequency plots in Figs. 7 and 8. The number of modes, bandwidth of peaks, and the nearness of their TTTR frequency values makes relating particular frequency peaks to particular Lamb modes more difficult, in fact some of the peaks in the amplitude/frequency plot are undoubtedly the result of combined modes (this may explain the double peak in the low frequency range in Fig. 8). However, all peaks in the amplitude/frequency plot are at predicted TTTR frequencies. Also, the values of peak frequencies for the composite plate showed the same inverse dependence on plate thickness seen in the aluminum plate, as predicted by TTTR theory.

An improved understanding of what modes are contributing most to certain frequency ranges may be obtained by noting how AU behavior varies with azimuthal angle and comparing this to theoretical predictions of how particular Lamb waves should vary with azimuthal angle for a normal input pulse on the top of the plate. This approach involves comparing how the energy measurements in certain frequency ranges varies with azimuthal angle to how displacement values should vary with azimuthal angle. Additionally, this involves comparing phase

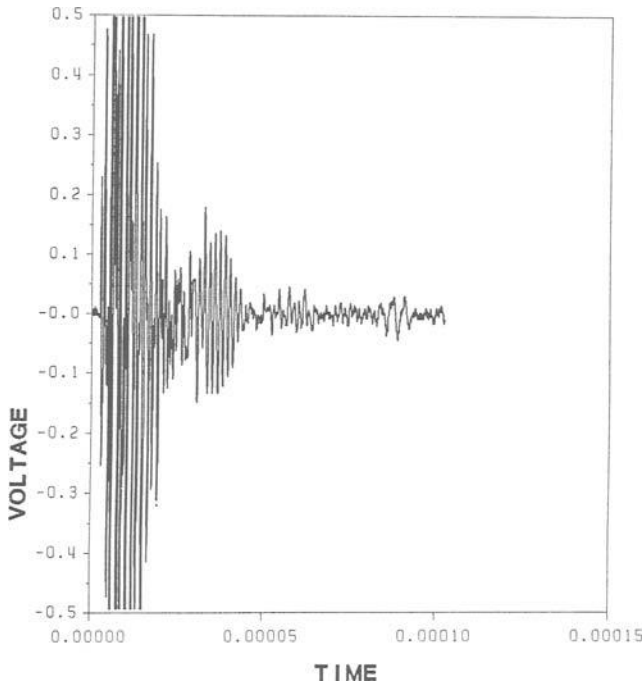


FIG. 7 -- Voltage versus time plot for 24 ply graphite/epoxy unidirectional plate

velocity and group velocity measurements. The full application of this approach involves comparing vast numbers of complicated measurements and difficult numerical calculations, however results to date seem to validate the approach in a qualitative way [12].

TABLE 3 -- TTTR Frequencies, (MHz).  
(24-ply Gr/Ep)

Mode	Symmetric	Antisymmetric
1	.36	.23 .31
2	.46 .62	.71
3	1.1	.69 .93
4	.92 1.2	1.4
5	1.8	1.2 1.6

As an example, Fig. 9 shows how the energy level for the frequency range between .15 and .32 MHz varies with azimuthal angle. This frequency range shows the greatest energy level in the 90 degree direction, unlike the general energy content, which is greatest in the fiber direction [19]. This seems to indicate that the mode of wave propagation for this frequency range is dominated by the first order antisymmetric mode, associated with the resonance of the shear wave polarized in the cross fiber direction, which would be expected to resonant in that frequency range. As an aside, the tendency for this shear mode to dominate the signal in the 90 degree direction may explain the correlation of AU energy, for measurements made in the cross fiber direction, with interlaminar shear strength of unidirectional composites



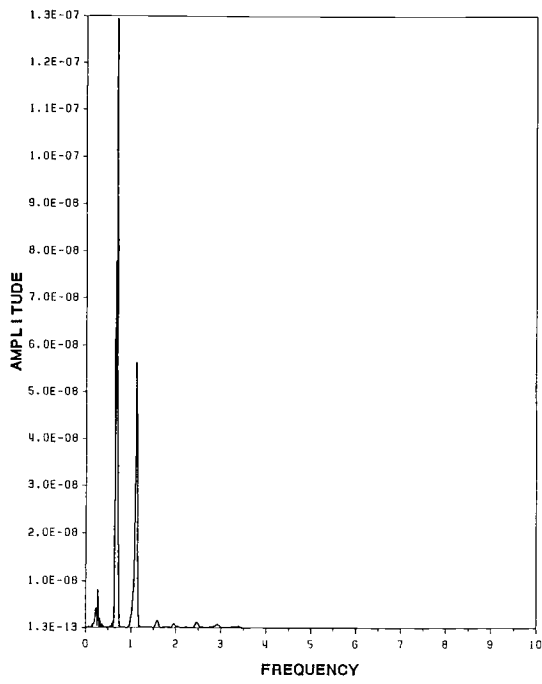


FIG. 8 -- Amplitude versus frequency for the signal shown in Fig. 7.

in the 90 degree direction [1]. Eventually, displacement values for this mode at various azimuthal angles should be computed and compared to the variation of the energy in the .15-.32 MHz energy range, in order to substantiate the heuristic argument that the Lamb wave caused by the shear wave polarized to the cross fiber direction should be biggest in the cross fiber direction. The complications of the pseudo waves that actually occur in the various directions are implicitly accounted for in the Lamb wave equations.

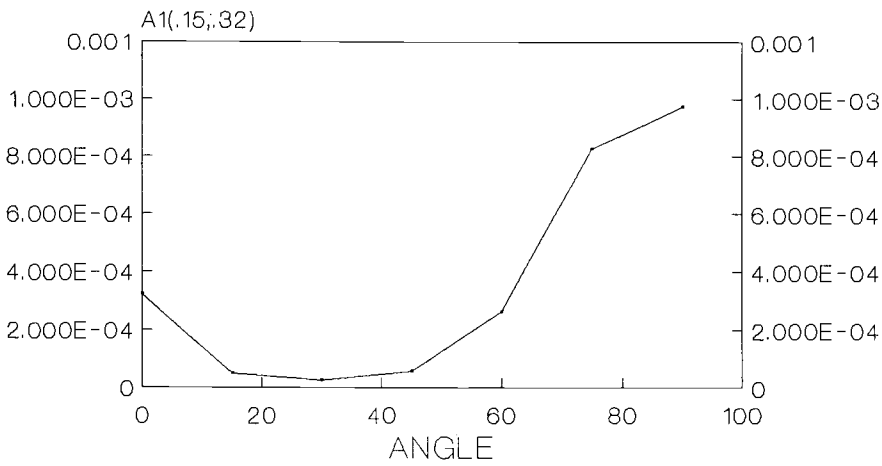


FIG. 9 -- Variation of energy in the .15-.32 Mhz range, 24-ply Gr/Ep.

Velocity measurements indicate that the bulk of the AU signal for composite plates is also made up of higher order Lamb waves, however in most cases measured phase velocities were not nearly as high for composite plates as for the aluminum plates. Some reasons for this behavior have been postulated [12].

Elasticity results, using Leknitskii's solution [20], predict that the most energy would be directed in the fiber direction and that it would show up early in the wavetrain, which agrees with experiment. Dispersion curve results [12], also predict that the energy level early in the signal should be high for the fiber direction, due to the high slope causing a high group velocity. Calculations of dispersion curves and elasticity results for the 0 and 90 degree direction showed the large effect azimuthal angle can have on Lamb wave behavior, which may help explain the vast differences in AU behavior with azimuthal angle.

In general, results indicate that the major energy content of the AU signal is higher order Lamb waves caused by plane wave interaction and reflection at various angles to the normal. This problem may be crudely modeled with Lamb wave theory and elasticity, but the computational details are extreme and other complications, such as the existence of both normal and shear disturbances resulting in the elasticity results. Additionally, the calculation of the dispersion curve for just one azimuthal angle is a sizeable computational task, usually requiring the use of coupled mode theory [14]. A further complication to interpreting experimental AU results is the effects of energy flux deviation [12] on waves propagating in an anisotropic material.

## CONCLUSIONS

AU results indicate that higher order Lamb waves are dominating AU results for flat plates, where the material thickness is on the order of a wavelength associated with the center frequency of the sending transducer. Lamb wave theory, TTTR, and elasticity show promise in helping to understand AU results; and hopefully eventually modelling them in composite materials. Specifically, elasticity solutions show that most of the input is for low angles  $\theta_1$ , resulting in the excitation of low wavenumber Lamb waves. The frequency range and low wavenumber associated with the input are both desirable for exciting higher order Lamb waves close to the TTTR frequencies. It is the nature of these modes to have quickly changing phase velocity and group velocity, hence causing a great deal of dispersion around the TTTR frequency and the associated modulating behavior. The potential for utilizing this theory to interpret slight variations in the signature are exciting. For instance, an indentation in a frequency peak may relate to a flaw blocking the input of energy for a certain angle  $\theta_1$ , hence blocking the rays emanating in that direction. In general, these results highlight the great dependence material geometry has on AU results and provides a means for accounting for these effects.

## REFERENCES

- [1] Vary, A. and Bowles, K. J., "Ultrasonic Evaluation of the Strength of Unidirectional Graphite/Polyimide Composites", NASA TM X-73646, Cleveland 1977.

- [2] Govada, A. K., Duke, J. C., Jr., Henneke, E. G., II, "A Study of the Stress Wave Factor Technique for the Characterization of Composite Materials," NASA CR 17480, Cleveland, 1985.
- [3] Talreja, R., Govada, A. and Henneke, E. G., II, "Quantitative Assessment of Damage Growth in Graphite/Epoxy Laminates by Acousto-Ultrasonic Measurements," in Review of Progress in Quantitative Nondestructive Evaluation, Vol. 3B, eds. D. O. Thompson and D. E. Chementi, Plenum Press, New York, 1984, pp. 1099-1106.
- [4] Kiernan, M. T. and Duke, J. C., Jr., "PC Analysis of an Acousto-Ultrasonic Signal" Materials Evaluation, Vol. 46, No. 10, Sept. 1988, pp. 1344-1352.
- [5] Karaguelle, H., Williams, J. H., and Lee, S. S., "Application of Homomorphic Signal Processing to Stress Wave Factor Analysis" Materials Evaluation, Vol. 43, Oct. 1985, pp 1446-1454.
- [6] Mittelman, A., Roman, I., Bivas, A., Leichter, I., Margulies, J. Y., and Weinreb, A., "Acousto-Ultrasonics Characterization of Physical Properties of Human Bones," in Acousto-Ultrasonics: Theory and Application, ed . J. C. Duke, Plenum Press, New York, 1988, pp. 305-309.
- [7] Patton-Mallory M. and Anderson, K. D. "An Acousto-Ultrasonic Method for Evaluating Wood Products," Acousto-Ultrasonics: Theory and Application ed . J. C. Duke, Plenum Press, New York, 1988, pp. 301-304.
- [8] Hemann, J. H., Cavano, P., Kautz, H., and Bowles, K., "Trans-Ply Crack Density Detection By Acousto-Ultrasonics," in Acousto-Ultrasonics: Theory and Application, ed . J. C. Duke, Plenum Press, New York, 1988, pp. 319-326.
- [9] Phani, K. K., and Rose, N. R., "Application of Acousto-Ultrasonics for Predicting Hygrothermal Degradation," in Acousto-Ultrasonics: Theory and Application, ed . J. C. Duke, Plenum Press, New York, 1988, pp. 327-336.
- [10] Kautz, H. E., "Ray Propagation Path Analysis of Acousto-Ultrasonic Signals in Composites," in Acousto-Ultrasonics: Theory and Application, ed . J. C. Duke, Plenum Press, New York, 1988.
- [11] Williams, J. H., Jr., Karaguelle, H., and Lee, S. S., "Ultrasonic Input-Output for Transmitting and Receiving Longitudinal Transducers Coupled to the Same Face of an Isotropic Elastic Plate," Materials Evaluation, Vol. 40, No. 6, May 1982, pp. 655-662.
- [12] Kiernan, M. T. "A Physical Model for the AU Method " Ph.D. Dissertation, Virginia Polytechnic Institute and State University, 1989, Blacksburg.
- [13] Pao, Y. and Kaul, R. K. "Waves and Vibrations in Isotropic and Anisotropic Plates," in R. D. Mindlin and Applied Mechanics, Pergamon Press Inc., New York, 1974, pp. 149-196.
- [14] Solie, P. and Auld, B. A. "Elastic Waves in Free Anisotropic Plates" Journal of the Acoustical Society of America, Vol. 54, No. 1, 1973.
- [15] Vasudevan, N. and Mal, A. K., "Response of an Elastic Plate to Surface Loads and Buried Dislocation and Sources," in Review of Progress in Quantitative Nondestructive Evaluation, Vol. 4A, eds. D. O. Thompson and D. E. Chementi, Plenum Press, New York, 1985, pp. 53-60
- [16] Ekstein, H., "High Frequency Vibrations of Thin Crystal Plates," in Physics Review, 68, 1945, pp. 11-23.

- [17] Wieczorek, A. and Schmitz, G., "Development of Nondestructive Testing Methods For The Evaluation of Thin and Ultrathin Sheet Materials" AFML-TR-65-320, Dec. 1965, Dayton.
- [18] Timoshenko, S. P. and Goodier, J. N., Theory of Elasticity, McGraw-Hill, New York, 1934.
- [19] Kiernan, M. T. and Duke, J. C., Jr., "Acousto-Ultrasonics as a Monitor of Material Anisotropy" Materials Evaluation, Vol. 46, No. 8, July 1988, pp. 1105-1113.
- [20] Lekhnitskii, S. G., Theory of Elasticity of an Anisotropic Body, Mir Publishers, Moscow, 1981.
- [21] Stiffler, R. C. and Henneke, E. G., II, "Low Frequency Plate Wave Modes" in Ultrasonic Stress Wave Characterization of Composite Materials, NASA CR-3976, edited by J. C. Duke, Jr., E. G. Henneke II, and W. W. Stinchcomb, May 1986, Cleveland.

# **Signal Processing Approaches**

ACOUSTIC EMISSION TECHNOLOGY USING MULTI-PARAMETER ANALYSIS OF  
WAVEFORM AND APPLICATION TO GFRP TENSILE TESTS

---

REFERENCE: Yamaguchi, K., Oyaizu, H., Johkaji, J., and Kobayashi, Y., "Acoustic Emission Technology using Multi-parameter Analysis of Waveform and Application to GFRP Tensile Tests," Acoustic Emission: Current Practice and Future Directions, ASTM STP 1077, W. Sachse, J. Roget, and K. Yamaguchi, Eds., American Society for Testing and Materials, Philadelphia, 1991.

ABSTRACT: Advanced acoustic emission instrumentation systems which can use multi-parameter data obtained by wave-envelope processing of all detected AE's have been developed. The systems were applied to different experiments such as fracture-monitoring of metal-structures and testing of materials. New parameters such as energy moments and zero crossing number were used together with conventional parameters and showed the usefulness for waveform analysis and source classification. In tensile tests of GFRP, the results indicated the high identification possibility on failure modes such as fiber-debundling, matrix-cracking and fiber-breakage. The performance of the advanced systems can be considered more powerful for material evaluation than that of usual systems depending on conventional AE parameters such as peak amplitude and event count, etc.

KEYWORDS: acoustic emission, signal processing, waveform parameters, fracture behaviors, FRP

## INTRODUCTION

For the analysis of fracture behaviors in materials, on-line measurement is very important. Correct characterization is desirable for material evaluation and improvement. Also, the needs of integrity monitoring of industrial structures are increasing rapidly. Acoustic

Dr. Yamaguchi, Mr. Oyaizu, Mr. Johkaji and Mr. Kobayashi are Professor, research assistant, former graduate students of the Department of Electrical Engineering and Electronics, the Institute of Industrial Science, University of Tokyo, 22-1, Roppongi-7, Minato-ku, Tokyo 106, JAPAN.

emission technology is being expected for such purposes as one of the most powerful tools [1,2].

For the actual development of the AE technology, accumulation of experience or database, improvement of analysis method and better information acquisition system are necessary. Basically, the AE technology has a limited performance because it is an indirect measurement method. As for information acquisition, it still can be advanced by utilizing more information from detected waves [3,4,5].

In general, the AE technology needs three kinds of information from detected waves as input, i.e. frequency, wave-features and location. As for wave-features, ordinary AE instrumentations, except off-line waveform analysis system, use comparatively simple parameters such as peak amplitude or energy, rise-time and duration-time for each event. Some systems can use integrated wave-energy of every event [6]. Most analyses on AE waves by the conventional instrumentations depend on peak amplitude or peak energy distributions [7] or wave-energy distributions [6]. In many cases, the performance of those methods using only amplitude or energy data of AE waves is not satisfactory because of insufficient information for the detail analysis. To improve this situation, pattern information of input waves should be employed. The advanced AE system which can use wave-pattern parameters and other new useful parameters is developed to improve the performance of the technology and to contribute to the practical applications [3,8,9].

The AE technology has evolved to utilize multi-parameter processing recently, and new systems use such parameters as rise-time  $T_r$ , duration-time  $T_d$ , total wave amplitude  $A_t$  and total wave energy  $E_t$  besides sorts of count and maximum amplitude  $a_p$  for analyses [6,10,11]. Some studies use wave frequency parameters [12,13]. However, the pattern parameters had not been available in usual instrumentations for a long time until 1988.

Regarding the AE applications to composites of high strength fiber, it was reported that the fiber breakage AE could be discriminated from the others very successfully by the amplitude distribution [14]. In the case of popular FRP such as GFRP and CFRP, the results of experimental analyses could not show very successful discrimination by the amplitude distribution [15,16,7]. Recently the applications of multi-parameter analyses to material tests and structural monitorings are being increased [13,17], but, in many cases, the results are not necessarily very successful.

Systems which extract waveform parameters including pattern parameters in real-time operation have been developed at the Institute of Industrial Science (IIS), University of Tokyo [5,18,19], and they have been applied successfully to the fatigue tests of metal-structures [8]. They are being applied to FRP material tests, etc. [9]. The multi-parameter signal processing method which employs pattern parameters seems powerful for analysis on fracture of composites which usually have complicated failure modes and behaviors. From the experimental results it seems that some failure modes, for example, fiber-debundling, matrix-cracking and fiber-breakage in GFRP could be presumed by waveform-parameters [9]. Also friction AE's at

cyclic loading tests could be discriminated at high probability by the specific features of waveform-parameters and loading phase information [9]. Comparison of these features with those of the tests on metal is to be discussed in this paper.

The supply of the instrumentations which employed the pattern parameters was started by a manufacturer in 1989 and the instrumentations are now being applied to the experiments of subsurface and civil engineering in Japan and Canada. Such new instrumentations will be available from some other manufacturers soon. Additional application results are expected to be published.

In this paper, the fundamental principles in design concepts for the advanced AE instrumentations are explained, and the typical processing architecture is stated. Then, the kinds of information which are available in the present AE technology are shown. Among the popular and new parameters in the AE information, kinds of wave moment as pattern parameters and some other parameters will be explained. Also, envelope detection method, multi-parameter processing and the instrumentation are explained and discussed. Finally, as an application of the system, some GFRP tensile tests and the results are shown and discussed.

#### CONCEPTS OF ADVANCED AE TECHNOLOGY

In general, AE techniques analyzing the detected waves are used for the identification and evaluation of AE sources and the cause of the sources [1,2,3,4]. There are variations of AE technology, from stochastic methods for macro-analyses to precise techniques for detailed analyses using micro-data of individual wave. However, in every AE instrumentation, the system performance firstly depends on the available input information. Therefore, the method and the capacity of the input processing stage essentially dominate the possible performance of the whole system. For high analysis performance the following two principles should be considered in the design of input processing [3,4,5,20].

- (1) All available waves or hits should be processed at the input stage as many as possible for the analysis of all possible AE sources at the later processing.
- (2) Every set of processed wave or hit data by the input stage should contain detailed information as much as possible to enable various and precise analysis by all possible ways at the later processing.

The above two principles should be considered at the input stage in real-time operation. Naturally the principles compete with each other in design engineering, and consequently increase of processor capacity and decrease of processing speed are brought on. In usual way the cost of the system has to be considered. Therefore, effective data-compression should be required for good compromise. Processing of envelope-detected waves can be the best solution in many cases.



In most cases the data processing in advanced AE instrumentations consists of the following four steps [4,5].

- (1) wave (hit)-data extraction, noise rejection and data recording
- (2) combination of hit-data for event-data composition, source-location, event-qualification, grouping
- (3) higher-level grouping, concentration and time-trend analysis, environment analysis
- (4) presumption of object status or behavior, characterization, estimation or evaluation, severity assessment, decision making

The steps (1) and (2) should be done by on-line processing. The step (3) can be done by on-line operation or by off-line analysis according to the purpose and the cost. Distributed processing system is a good and preferable structure for these three steps. Automatic processing of step (4) is necessary for on-line monitoring, but off-line processing or human decision on step (4) would probably be a good way for research and development.

#### INFORMATION AVAILABLE IN AE TECHNOLOGY AND WAVEFORM PARAMETERS

In the AE technology, very important problems are the selection of effective input informations and how to acquire and use them. Table 1 shows the sorts of information available or possibly available in the AE technology at present, except in the direct digitizing method. Waveform parameters of input AE waves can be classified into four categories, time, energy, pattern and frequency [3,4,5,10]. The data of waveform parameters from every input AE or hit are called wave or waveform microdata in contrast to macrodata such as counts and distributions. Such AE waveform information is effective for fracture behavior analysis when the propagation distance is short [4,5] and for the propagation route identification when the monitoring area is large [3,4,8].

Table 2 shows the content examples of wave microdata currently used in the actual advanced system recently developed at IIS. The consideration of the following characteristics are necessary for waveform parameters.

- (1) easy data-extraction of input waves in real-time operation
- (2) high data-compressibility from original waveform
- (3) good representation of the original waveform features
- (4) low sensitivity to noise and minor change of propagation conditions

The parameters in the pattern and the time categories is related to the AE waveform, but the pattern parameters such as moments are the better representations of the approximate shape of the waveform-envelope than the time parameters like rise-time  $T_r$  and duration time  $T_d$ . Thus, the pattern parameters can be general and it can fairly satisfy the above four requirements.

TABLE 1 -- Sorts of information available in AE technology.

Macro data	AE count (ring-down), Event count (Evc) Stochastic distributions (ap, ap <sup>2</sup> , etc.)
Location(Lc)	Arrival time difference Hit sequence Zone Propagated waveform (pattern analysis)
Waveform parameters	Energy (ap, ap <sup>2</sup> , At, Et, etc) Time (Tr, Td, ts, etc.) Pattern (Tam, Tem, Tam(2nd), Tem(2nd), etc.) Frequency (Nz, FFT, etc.)
Time trend	Location concentration Event activity (Number, Energy intensity) Waveform change
Loading condition	Load level and loading pattern Load sequence Load phase in cyclic loading (Ldph) Felicity ratio
Environmental condition	Atmosphere, Contents (vessel) Noise Process sequence or condition Plant operation

TABLE 2 -- Contents-examples of wave (hit) microdata including waveform parameters.

Parameter Categories		Contents	Symbol	Length (bits)
...	...	Channel number	ch	6
Waveform envelope	Time	Arrival time	ts	32
		Wave rise-time	Tr	12
		Wave duration time	Td	16
	Energy	Peak amplitude	ap	12
		Total wave energy	Et	32
	Pattern	Energy moment 1	Tem1	12
		Energy moment 2	Tem2	12
		2nd order energy moment	Tem(2nd)	16
Wave	Frequency	Number of zero-crossing	Nz	8
...	...	Auxiliary data	Aux	32
...		Total (24bytes)	...	190

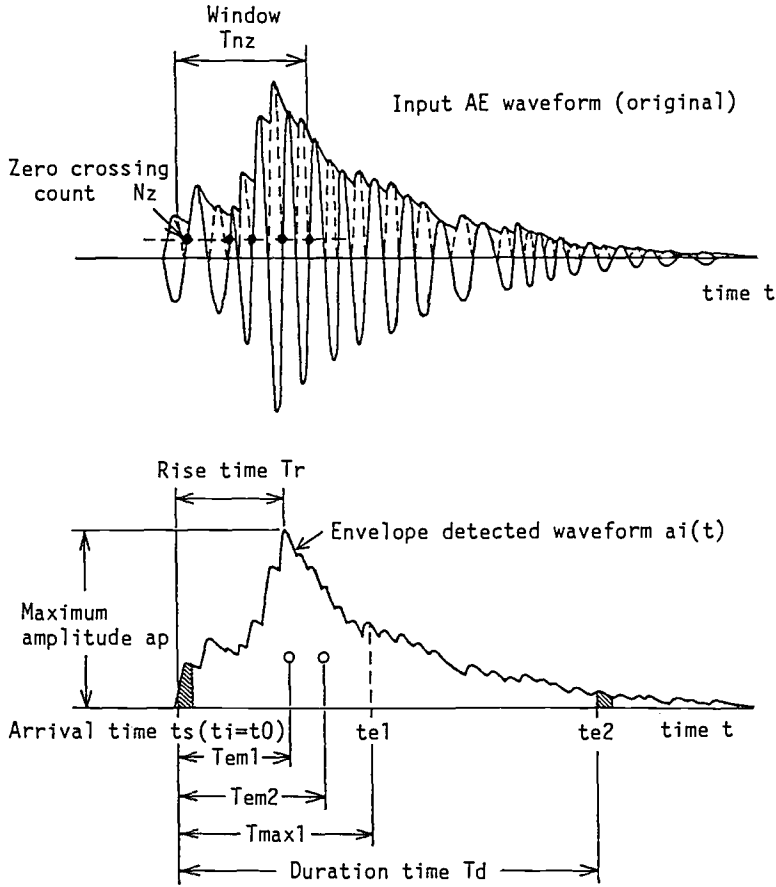


FIG. 1 -- Illustrations of waveform parameters.

$$\text{Total amplitude:} \quad A_t = \sum_{i=0}^n a_i \cdot dt \quad (1)$$

$$\text{Total energy:} \quad E_t = \sum_{i=0}^n a_i^2 \cdot dt \quad (2)$$

$$\text{1st order amplitude moment:} \quad T_{am} = \sum_{i=0}^n a_i \cdot t_i \cdot dt / A_t \quad (3)$$

$$\text{1st order energy moment:} \quad T_{em} = \sum_{i=0}^n a_i^2 \cdot t_i \cdot dt / E_t \quad (4)$$

$$\text{2nd order amplitude moment:} \quad T_{am}(2nd) = \sum_{i=0}^n a_i \cdot t_i^2 \cdot dt / A_t - (T_{am})^2 \quad (5)$$

$$\text{2nd order energy moment:} \quad T_{em}(2nd) = \sum_{i=0}^n a_i^2 \cdot t_i^2 \cdot dt / E_t - (T_{em})^2 \quad (6)$$

where  $dt$  is the sampling period of A/D conversion.

Fig.1 shows the illustrations of the waveform parameters in Table 2. Equations (1),(2),(3),(4),(5) and (6) are used for real-time calculations of the energy parameters, total wave amplitude  $A_t$  and total wave energy  $E_t$ , and the pattern parameters; the 1st and the 2nd order amplitude moment and energy moment  $T_{am}$ ,  $T_{am}(2nd)$ ,  $T_{em}$  and  $T_{em}(2nd)$ .

Pattern parameters had been used only by the systems developed at IIS during the time from 1980 to 1988. Processing of pattern parameters needs more complicated and higher speed hardware in input stage than processing of the other parameters in Table 2 [5]. This might have been the reason why pattern parameters had not been used in commercial systems until 1988. Wave rise-time  $T_r$  or duration time  $T_d$  has been used for pattern classification successfully in some cases [21,22]. Rise-time can be processed easily but it is less efficient than the moments in considering the point (3) waveform representation and in considering the point (4) insensitivity to noise. Zero crossing number  $N_z$  indicates approximately the main frequency of the first part of a waveform, if the window time is proper and fixed. Without a fixed window time  $T_{nz}$ , it is the same parameter as ringdown count. From another viewpoint, the zero crossing count is a very simple application of higher order crossing (HOC) method, i.e. zero crossings of the zeroth differentiation of the original time signal [23]. This simple frequency parameter  $N_z$  is not available in usual commercial AE systems.

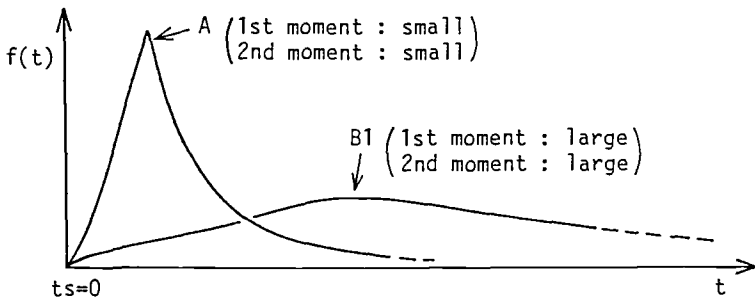
Through the calculations of equations (1) to (6) in real-time operation, high data compression from the sampled data of original wave to the parameters can be achieved.

The Moment-parameters in Table 1 can be used for waveform analysis. In general, the moments have the following two characteristics according to the orders.

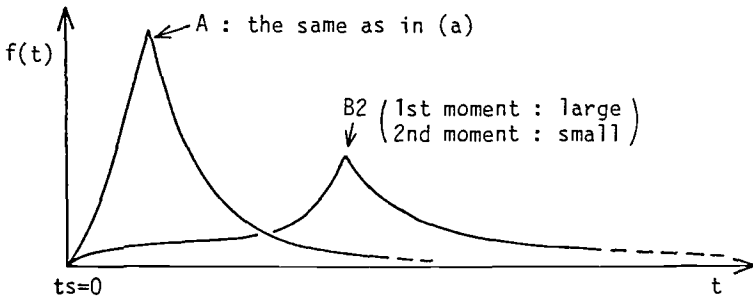
- (1) the 1st(or odd) order moment shows the asymmetry of the wave pattern
- (2) the 2nd(or even) order moment shows the peakedness or the concentration of the wave pattern

However, in the case of usual AE waveform as shown in Fig.2 (a), the 1st order moments calculated by eq.(3) and (4) as well as the 2nd moments show the peakedness and the concentration of the envelope patterns. Usually the 1st order energy moment  $T_{em}$  is most stable and insensitive to such disturbances as noise, threshold-shift, multi-path effect and waves-overlapping. Therefore, in usual AE applications, the 1st order energy moment can be the most effective and convenient pattern parameter. In some cases as B1 and B2 in Fig.2 (a)(b), the 2nd order energy moment  $T_{em}(2nd)$  or amplitude moment  $T_{am}(2nd)$  would be useful for wave discrimination between B1 and B2.

In the systems using the parameters illustrated in Fig.1, envelope detection is adopted for the input AE wave processing prior to A/D conversion except the processing for zero crossing number  $N_z$ . Advantages and disadvantages of the envelope detection are as follows.



(a) A usual case of AE waves of short distance A and long distance B1



(b) A special case of long distance (multi-path or overlapped wave) B2

FIG. 2 -- Relation between waveforms and the 1st and the 2nd order moments (energy and amplitude), where  $f(t)$ 's are envelopes of amplitude or energy waves.

TABLE 3 -- Change of AE waveform information according to propagation path.

propagation path	short, simple	long, complicated
Main information in AE waveform	source; (fracture mechanism source characters generation mechanism)	route; (plate wave effects overlapping reflections, multi-path)

Advantages;

- (1) bandwidth reduction to enable slow sampling and easy processing
- (2) good representation of approximate wave contour pattern

Disadvantages;

- (1) loss of frequency information of the original time signal
- (2) loss of precise shape and phase of the original wavefront

The advantages outweigh the disadvantages in many cases of actual application. Zero-crossing number  $N_z$  can be a good and simple compensation for frequency information of input AE waveform to some extent.

Information in a detected AE waveform changes from that of the source to the propagation distance and the medium structure as shown in Table 3. The degree of the change increases by the propagation path characters from left to right in the Table. Thus, by analyzing waveform parameters or wave microdata, grouping of events or identification of event-sources can be performed in the following two ways.

- (1) direct source-event grouping by source mechanism identification or presumption (at a short distance)
- (2) indirect source-event grouping by propagation route identification or classification (via long and complicated propagation route)

The methods of (1) can be used mainly for the fracture analysis or the evaluation of materials, while the methods of (2) would be useful for many structural integrity monitorings. The applicable variation of grouping methods is one of the flexible characters of the advanced system.

#### MULTI-PARAMETER PROCESSING

As stated in the previous section, an advanced AE instrumentation should perform real-time and multi-parameter processing in the input stage and high-speed processing for event qualification and grouping after the input stage. Also, except special purpose systems, it should be flexible for the various applications and objectives. Consequently, the advanced AE instrumentation should be based on a distributed high-speed processing architecture [4,5].

The advanced AE instrumentation system which is based on multi-level distributed structures is usually applicable to the wide range of versatile and precise use [8,9]. For example, the latest IIS system has two on-line processing levels (1) wave-data extraction and (2) combination of hit data and location which are explained in the section of CONCEPTS OF ADVANCED AE TECHNOLOGY. On-line processing can be extended to the higher processing level (3) which are now performed by off-line processing. The level (4) processing for characterization, evaluation or severity assessment would still needs human ability and knowledge.

Table 4 shows examples of selectable parameters, optional processing or analysis methods at the processing levels, (1),(2) and (3). Suitable processing methods can be selected in each level. Table 5 shows examples of effective parameter combination for the experiment examples to which the advanced systems including the prototype have been applied. In general, the methods-selection for the purposes is very important and it is one of the essential part of the AE technology which needs much experience and knowledge.

TABLE 4 -- Examples of multi-option processing or analysis method selection at each distributed processing level.

processing level	processing	processing option or selection
Level 1  input wave parameters extraction	waveform parameter extraction	energy (ap, ap <sup>2</sup> , At, Et,...) time (ts, Tr, Td,...) pattern (Tem, Tam, Tem(2nd),...) frequency (Nz)
	noise rejection	parameter value limit check abnormal waveform check
	auxiliary data processing	indexed data data pre-qualification
Level 2  event-qualification and grouping	qualification & combination	coincidence, master-slave (1-dimensional) waveform parameters (1,2-dimensional) location, arrival time difference
	location	4-, 3-, 2-sensors location hit sequence, zone
	event data filing	event data structure
Level 3  analysis	macro data processing	Evc, Evr parameter distributions (ap, Tem, Nz, Lc, etc.)
	grouping analysis	concentration of parameters Lc, Load, Ldph
	time trend analysis	parameter distributions number of groups, life of groups loading conditions, plant sequence Kaiser effect ratio Felicity ratio, etc.

Note: Evc: event count, Evr: event rate

Lc: location, Load: load level, Ldph: load phase

TABLE 5 -- Examples of effective parameter-combination out of waveform parameters and other information.

parameter combinations	application examples	objectives
Tem:Evc,Ldph ap:Evc,Ldph Evc:Lc, Ldph	fatigue tests of FRP piping components	grouping of friction AE sources
(Tem-ap):Evc,Lc (Tem-Nz):Evc,Lc	FRP tensile tests	classification of presumed failure modes in FRP (fiber breakage, debonding, matrix cracking, debundling, etc.)
Tem:Evc,Ldph ap:Evc,Ldph Evc:Lc, Ldph	FRP cyclic loading tests	grouping of friction AE sources
other effective combinations of: ap, At, Et, Tam, Tem, Tam(2nd), Tem(2nd), Nz, Evc, Lc, Ldph, Load, Environment		

## INSTRUMENTATION DEVELOPMENT AND APPLICATIONS

Several AE instrumentation systems have been developed at IIS, University of Tokyo, since 1972, and applied to experimental applications. The 1st-generation was a multi-channel AE source location system equipped with arrival time difference detectors [24]. This system had introduced the dead-time technique and was adopted since by most usual AE instrumentations. It was a fully digitized system specialized for arrival time-difference detection among input channels and it was used with an on-line mini-computer.

The 2nd system was the prototype of advanced AE instrumentation, and it is still in use after some of the improvement. The system have been showing the advantages of multi-parameter analysis in the experiments on metal structures [8] and FRP tests [9]. The 3rd system has been developed recently [5] and is used for current study. Besides the ability to perform multi-parameter processing, one of the noticeable features of the advanced systems is its very high input processing speed. The preparation-time after every input is about 40 microseconds and the ultimate input speed is 25,000 hits/second/input channel. In typical use, maximum input speed is 2,000-3,000 hits/second/channel according to the maximum signal duration of 300-500 microseconds [5].



## APPLICATION TO GFRP TESTS

Experimental Setup and Tests

Fig.3 shows the experimental instrumentation setup for tensile and cyclic loading tests. The envelope detected AE signals are processed at the AE waveform parameters extraction system which produces waveform microdata shown in Table 2. The waveform microdata are transferred to DEC 11/73 CPU which performs the processing of the level(2) and a part of the level(3) and records all the data sets in the disk for off-line analyses. In these experiments, the waveform parameters of energy moment, peak amplitude and zero-crossing number besides location data were mainly used for the analyses. A DC-servomotor driven test-machine of a lead-screw type was used for the experiments.

The improved 2nd system has an 8 bits (48dB) A/D converter (0-10V analog input) at each input channel. A wider dynamic range than 48 dB was preferable for the GFRP tests, therefore, the dynamic range extension method in Fig.4 (a) was applied to the tests. Two different gain channels were connected to one sensor output and extended the dynamic range up to 64dB. The 3rd system has 12 bits (72dB) converters. The dynamic range of 72dB is enough for usual tests but the range can be extended to 112dB as shown in Fig.4 (b) by the same way as in Fig.4 (a).

Fig.5 is the shapes and the specifications of specimens (G-1) and (G-2) used for tensile tests (Tt1 and Tt2) and cyclic loading tests (Tc1 and Tc2). Pre-cracking was made in the (G-2) specimen for the tests Tc1 and Tc2 by 288Kg pre-load which was 80% of the estimated maximum fracture load (360Kg). Loading ranges of 36-216Kg for Tc1 and 108-288Kg for Tc2 were applied to the specimens at each loading cycle [9]. Table 6 shows the types and the conditions of the loading for the tests.

The stepwise tensile loading during the tensile tests (Tt1 and Tt2) had the aims to slow the fracture progression and to make the AE measurement and the visual observation easy. The purpose of the cyclic loading is to observe friction AE and to analyze its features which are possibly different from those of the other types of AE.

Test Results

Fig.6 shows the stepwise loading and unloading process and the AE event rate at tensile test Tt1. At No.4 loading, whitening started at the tips of notches, and it spread out toward both of the longitudinal directions of the specimen. The whitening had reached at the locations of about 15mm from the center of the specimen at No.9 loading when the final breakage occurred. AE detection started at No.3 loading. Fig.7 (a) and (b) show the distributions of energy moment(Tem) and peak amplitude(ap) during No.1-7 (mostly at No.3-7) and No.9 loading. Most of the AE sources were located near the center of the specimen.

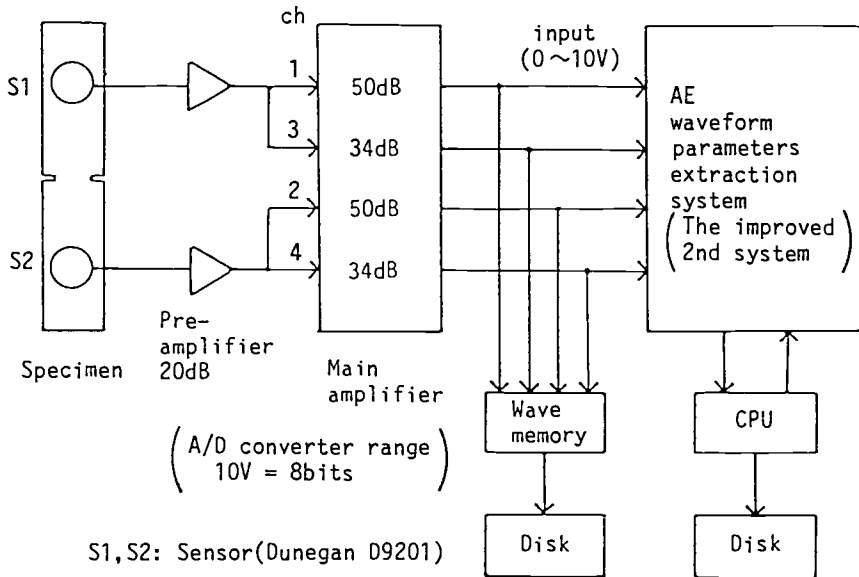


FIG. 3 -- Experimental instrumentation setup.

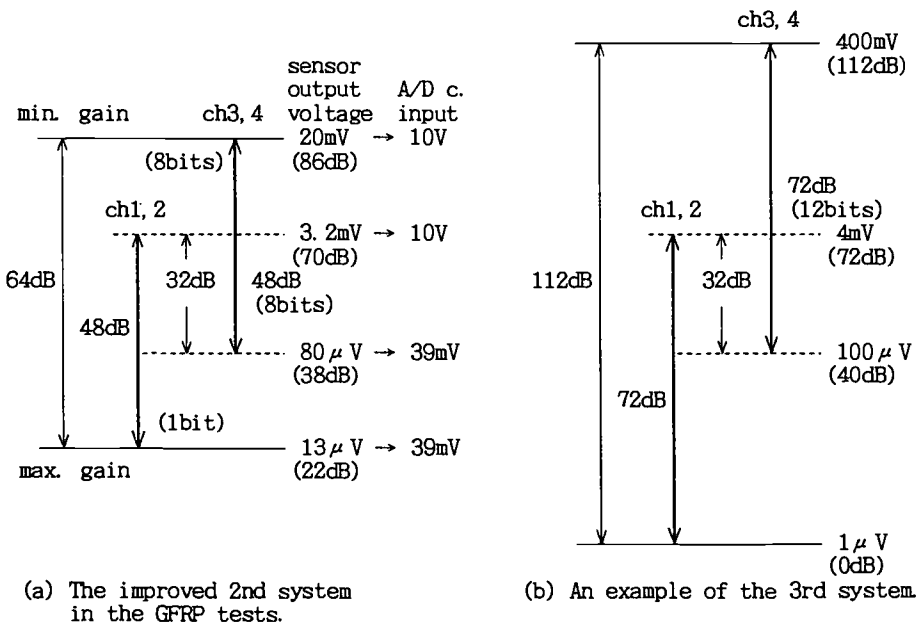


FIG. 4 -- Dynamic range extension method by overlapped connection of two different-gain channels.



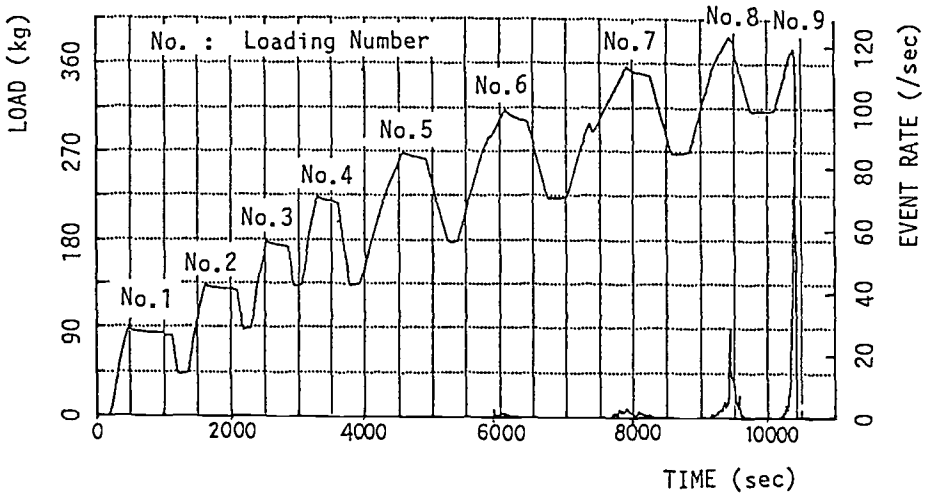


FIG. 6 -- Stepwise loading and unloading process and AE generation rate during tensile test Ttl.

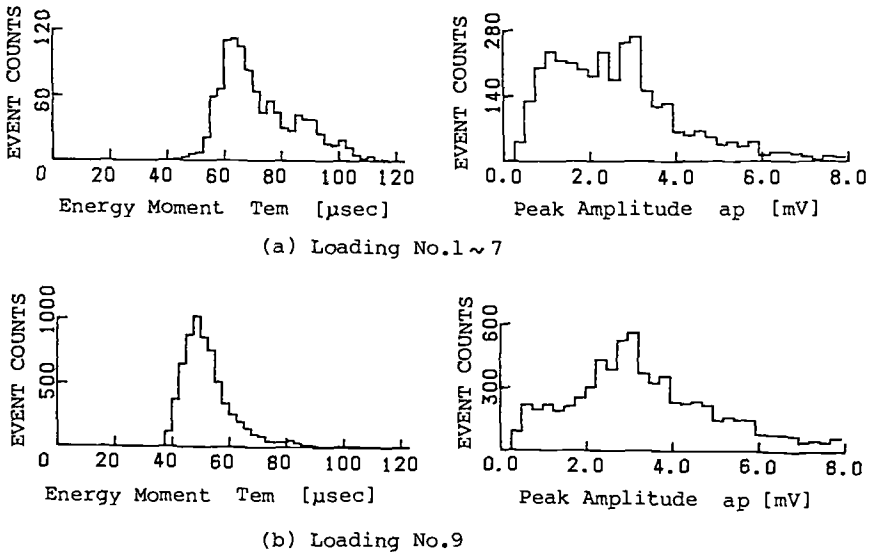


FIG. 7 -- Distributions of energy moment  $T_{em}$  and peak amplitude  $a_p$  at tensile test Ttl, (a) during No. 1-7 loading and (b) during No. 9.

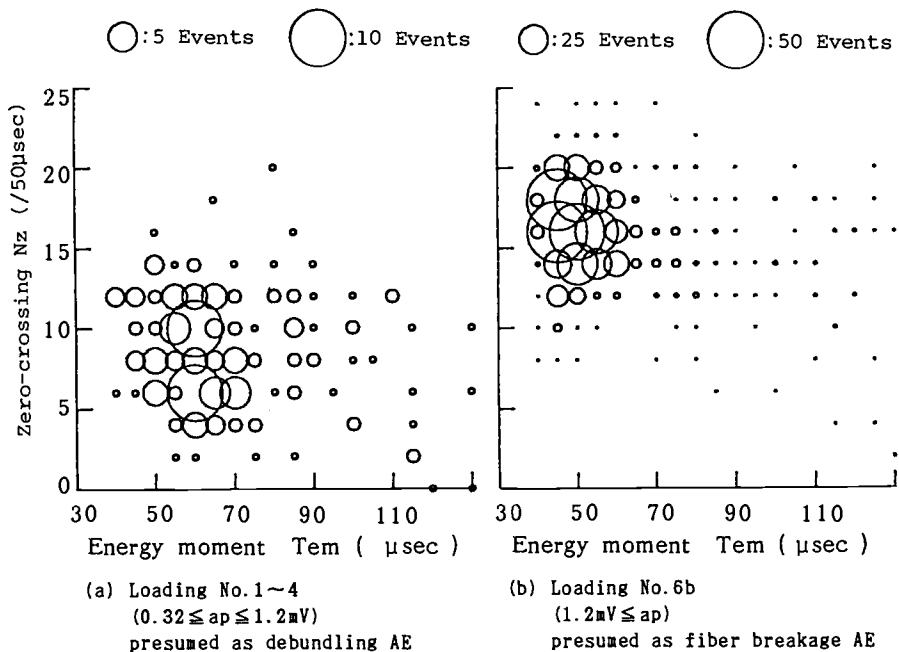


FIG. 8 -- Distributions of zero-crossing number Nz and energy moment Tem in tensile test Tt2 (specimen: G-2) by stepwise loading unloading (No.1-6), (a) during No.1-4 and (b) during No.6 (window time Tnz=50μsec.).

Fig.8 (a) and (b) show the distributions of zero-crossing number Nz and energy moment Tem during the tensile test Tt2 on the specimen G-2 by stepwise loading and unloading process similar to the test Tt2. Unlike Tt1, AE detection started from low load level of No.1 loading and continued at the following loading. The final fracture occurred at No.6 loading in the Tt2 tests. Fig.8 (a) is the results during the No.1-4 loading of Tt2, and (b) shows the results at the No.6 loading of Tt2 when the final fracture occurred. Three parameters, ap, Nz and Tem, were used for the AE analysis on Tt2. The AE sources were located at considerably wider range from the center than those of Tt1.

Fig.9 (a) and (b) are the AE generations in the cyclic loading tests Tc1 and Tc2 (G-2 specimens). Coordinate (0-100) of the vertical axis is the load increasing phase and (100-200) is the decreasing phase. In both tests, regularity of the AE generation at successive cycles such as Group A1 of Tc1 and Group A2 of Tc2 could be observed at the load increasing and decreasing periods. During the test Tc2, many AE's were detected near and at the peak load, while almost no AE was detected at the peak load of the test Tc1. Fig.10 shows the distributions of ap and Tem of the AE's in group A1 of Fig.9 (a). Fig.11 is the Tem and ap distributions in group A2 of Fig.9 (b). Fig.12 shows the two dimensional distributions of Tem by different ap values of the AE's in group B1 during the test Tc2 (1-200 cycles).

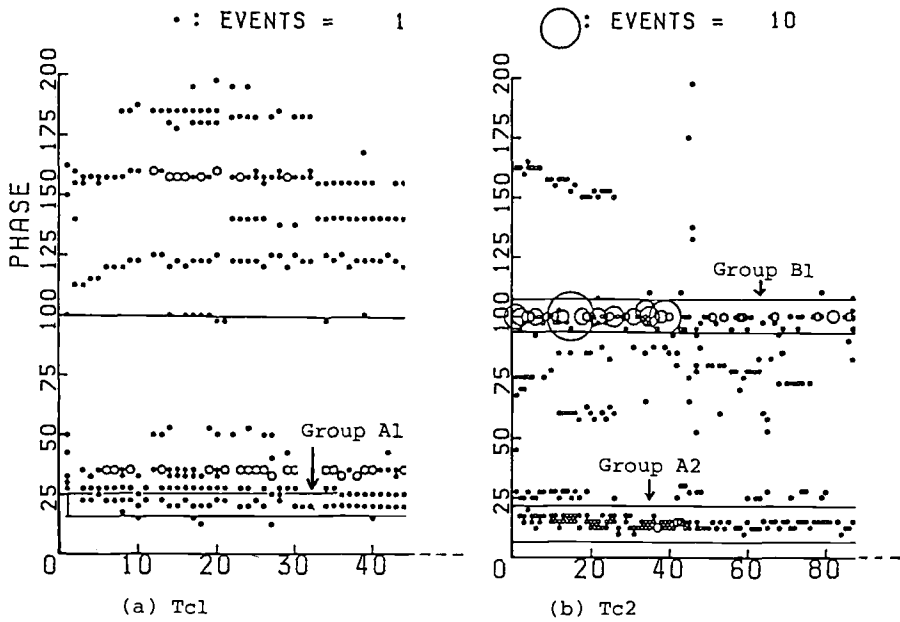


FIG. 9 -- AE generation related to load phase during cyclic loading test of (a) Tc1 (1-100 cycles) and (b) Tc2 (1-200 cycles). The first part of the results are shown.

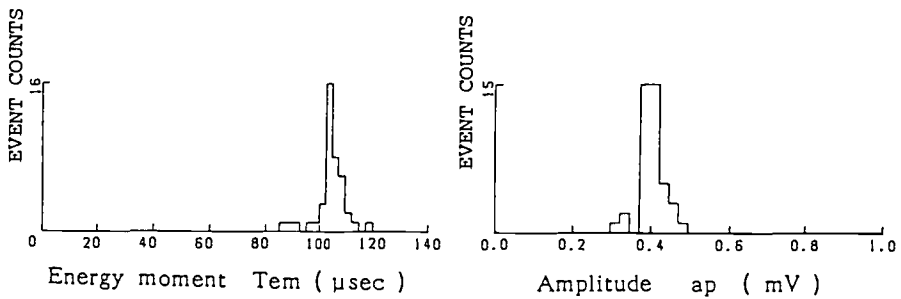


FIG. 10 -- Distributions of  $T_{em}$  and  $a_p$  in group A1 (1-53 cycles) at test Tc1.

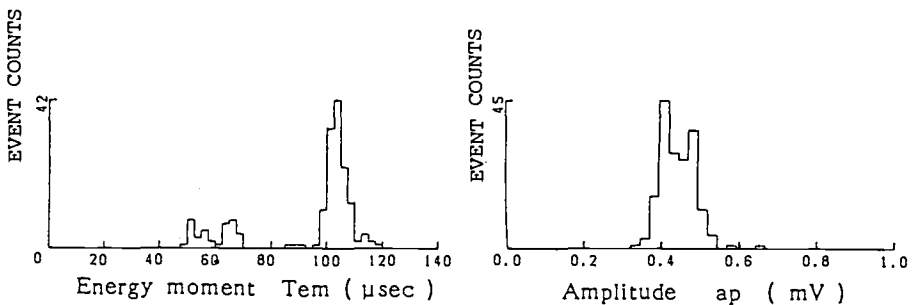


FIG. 11 -- Distributions of  $T_{em}$  and  $a_p$  in group A2 at test Tc2.

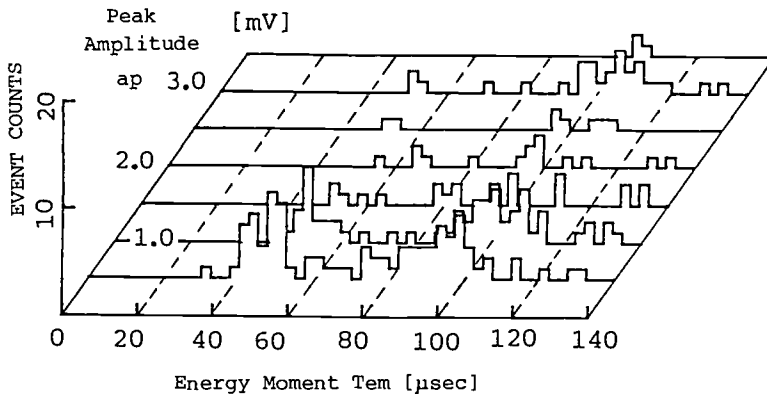


FIG. 12 -- Two dimensional distributions of energy moment  $T_{em}$  by different  $a_p$  values of AE's in group B1 during cyclic loading test Tc2 (specimen G-2).

## DISCUSSIONS

### Classification of Failure Modes

From the results of the loading-holding-unloading tensile test Tt1 on GFRP shown in Fig.7, two types of AE could be clearly sorted by the energy moment values. Supposedly the breakage of most fibers occurred at the final fracture of No.9 loading. The concentration of small  $T_{em}$  value in Fig.7 (b) seems to show a feature of the AE's generated from fiber breakage. Large amplitude AE's increased slightly at No.9 loading as shown in Fig.7 (b) but the change was not so clear. The similar feature is usually seen on the peak amplitude distributions in many test results by conventional AE systems [15,16,7]. Most of the AE's of large  $T_{em}$  during No.1-7 loading shown in Fig.7 (a) could be presumed as AE's from matrix cracking corresponding to the whitening by visual observation. In this case, the  $T_{em}$  threshold of about 57.5 microseconds can be applied for the discrimination of the two failure modes. Similar features of  $T_{em}$  distributions of final breakage AE and Other AE's were observed in the tests of unidirectional GFRP and silane treated cloth GFRP in the past [25].

In the case of tensile test Tt2 at which silane treated woven cloth was used in the specimen (G-2), small amplitude AE's could be observed at low load levels from No.1 loading. These AE's could be presumed as debundling AE's generated by cracking inside the transverse fiber-bundles, and the scatter of the source locations also supports the presumption. This type of AE can easily be discriminated from fiber breakage by zero-crossing number  $N_z$  and peak amplitude  $a_p$  as shown in Fig.8 (a)(b). From these results, multi-dimensional analysis using parameters,  $T_{em}$ ,  $N_z$ ,  $a_p$  or  $E_t$ , etc. is believed to be more reliable than analysis by using fewer parameters such as peak amplitude and wave-energy alone.

TABLE 7 -- An example of threshold list on waveform parameters for fracture mode presumption in GFRP by AE grouping.

fracture modes (presumed)	$T_m$ [ $\mu$ sec.]	$N_z$ [ $/50 \mu$ sec.]	$a_p$ [mV]	generation stage
fiber breakage	35~60	10~20	1.2~10	final breakage
debonding & matrix cracking	55~100	8~14	0.3~3	whitening
debundling	35~70	5~14	0.3~1.2	low load level

Table 7 shows examples of the threshold values for AE waveform parameters applicable to the classification of the failure modes in the above cases.

In the cyclic loading tests as shown in Fig.9 (a) and (b), the AE's which were observed at low or middle load level are presumed to be friction AE's. Many rows of AE generation, which correspond to the same load phase in successive cycles, were observed as shown in Fig.9. High uniformity of the AE generation during specific loading phase in successive cycles supports this presumption. Also the AE waveform parameters in a group such as A1 or A2 show concentrated distributions as Fig.10 or Fig.11.

Similar features have been observed on the AE's in metal and they were presumed to be generated from friction on crack surfaces [8]. The comparison will be discussed in the following section. In the case of GFRP, these friction AE's usually showed large  $T_m$  and small  $a_p$  as shown in Fig.10 and Fig.11. Two AE groups detected at close loading phases can be discriminated if they have different values of waveform parameters from each other.

The AE's of group B1 which were generated near the peak load of each cycle in the Tc2 cyclic loading test showed different features from those of group A1 and A2. The test Tc2 of which peak load was higher than that of Tc1 produced the AE's of B1 near the peak load, while almost no AE was generated near the peak load of the test Tc1. In the case of Tc2, probably the high peak load (about 80% of the estimated maximum fracture load of the specimen) caused some fractures near the peak load of many cycles.



The distributions of parameters (Tem, ap) in Fig.12 seem to show a few types of AE in group B1. For example, (1) small(Tem)-small(ap), (2) large(Tem)-small(ap), (3) small(Tem)-large(ap) and large(Tem)-large(ap). Some generation mechanisms can be supposed for these types of AE, e.g. matrix cracking, debonding, delamination and fiber breakage. The type of (3) small(Tem)-large(ap) showed approximately the same values of those parameters obtained at the final breakage of the tests Tt1 and Tt2, as shown in Fig.7 (b) and Fig.8 (b). Therefore, some fiber breakages are supposed to have been included in group B1, but the number is not so many. Further experiments and analysis using multi-parameter would probably make the characterization definitive.

#### Comparison of Friction AE's Between Metal and FRP

In the case of cyclic fatigue tests of FBR SUS 304 piping components, the following features on AE generation have been observed [8].

- (1) high regularity of repetitive AE generated at the same load phase in every successive cycle, i.e. groups of AE's in rows on successive cycles
- (2) almost identical waveform of AE's in a group of the same load phase
- (3) almost no detectable AE at peak load
- (4) major AE generations during load increasing phase
- (5) high correlation of generation phase drift to the AE peak amplitude generated in the same group
- (6) shifting trend of generation phase of the AE's in a row to lower load level
- (7) clear life span of a group or a row of repetitive AE generations

The AE's of group A1 and A2 in the cyclic loading tests of Tc1 and Tc2 showed the same features of the items (1) and (2) which are the most powerful reasons to presume the AE's as to be generated by friction. Now, they are supposed as the most noticeable characters of friction AE from metal. Also the other items are considered useful for discrimination of friction AE in metal.

The phenomenon of the item (3) has also been observed in the test Tc1. These coincidences of (1), (2) and (3) are considered very important and useful. The similar phenomena to (7) were observed during the Tc1 and Tc2 tests. The other items from (4) to (6) could not have been observed at these simple cyclic tests of GFRP. These characters (1), (2) and (3) seem to support the presumption of the friction AE in Tc1 and Tc2.

However, the difference of material characters between metal and GFRP is very large. For example, fracture surfaces which cause friction AE can be very complicated in composites. It would be important to make clear which characters would be proper to presume the behaviors in the case of FRP.

## SUMMARY AND CONCLUSION

On-line observation of material behaviors or structures integrity under load is a notable advantage of AE technology. On the other hand, it has a limited performance because it is an indirect method of observation. For the improvement, the AE technology should utilize more information of the detected waves.

In the advanced acoustic emission technology, the following methods can be considered important and advantageous for the design of instrumentation; (1) waveform multi-parameter analysis, (2) real-time processing of wave envelope, (3) wave-pattern classification by pattern parameters including moments, (4) zero-crossing count to compensate frequency information, (5) distributed high speed processing, (6) multi-option processings or analyses.

Multi-parameter analysis using waveform microdata could be a good way for relatively wide applications to material test and structure monitoring using AE technology. The technique would be a powerful tool especially for the fracture behavior observation and for the characterization of composites.

Some of the failure modes such as fiber breakage, matrix cracking and debundling can be identified by multi-parameter analyses. Also, friction AE in cyclic loading can be discriminated from the other types of AE. Interesting similarities between GFRP and metal under fatigue tests have been obtained. Further experiments and more detailed analyses using more parameters, e.g.  $a_p$ ,  $E_t$ ,  $T_r$ ,  $T_{em}$ ,  $T_{em}(2nd)$ ,  $N_z$ , etc., are being undertaken.

## ACKNOWLEDGMENTS

The authors are much thankful to Professor Teruo Kishi of Research Center for Advanced Science and Technology, University of Tokyo, and his staff for their kind help and advice on the experiments in their laboratory. The authors are also much thankful to Professor Isao Kimpara of Faculty of Engineering, University of Tokyo, and his staff for their suggestions on the tests and the specimens. The authors thank Mr. Katsushi Kobayashi, former member of their laboratory, for his cooperation on the tests and paper preparation. Finally, the authors are much thankful to Dr. Nelson N. Hsu of National Institute of Standards and Technology, United States Department of Commerce, for his helpful advice to complete this paper.

## REFERENCES

- [1] Scruby, C. B., "Acoustic Emission: Theory and Practice," Non-Destructive Testing (Proc. of the 16th EWGAE Conference, London, 1987), J.M. Farley and R.W. Nichols Eds., Pergamon Press, Vol.4, 1988, pp.2831-2838
- [2] Fowler, T. J., Blessing, J. A., Conlisk, P. J. and Swanson, T.L., "The MONPAC System," Journal of Acoustic Emission, Vol.8, No.3, 1989, pp.1-8
- [3] Fowler, T. J., Blessing, J. A. and Conlisk, P. J., "New Direction in Testing," Proc. of the 3rd International Symposium on Acoustic Emission from Composite Materials (AECM-3) (Paris), Published by American Society for Nondestructive Testing (ASNT), 1989, pp.16-27
- [4] Yamaguchi, K., "Instrumentation and Data Processing for Acoustic Emission Technology and Applications," Progress in Acoustic Emission IV (Proc. of the 9th International Acoustic Emission Symposium (IAES-9), Kobe), K.Yamaguchi, I.Kimpara and Y.Higo, Eds., Published by The Japanese Society for Non-Destructive Inspection (JSNDI), 1988, pp.1-10
- [5] Oyaizu, H. and Yamaguchi, K., "Advanced AE Instrumentation System for Versatile and Precise Use by Waveform-Microdata Processing," Proc. of AECM-3 (Paris), ASNT, 1989, pp.259-267
- [6] Vahaviolos, S.J., "AE Energy Signal Processing: An Overview," Proc. of AECM-3 (Paris), ASNT, 1989, pp.432-441
- [7] Li, L. and Zhao, J., "The Monitoring Damage Growth Processes in Glass Fiber Reinforced Composite by Amplitude Analysis," Proc. of the 2nd International Symposium on Acoustic Emission from Reinforced Composites (Montreal), The Society of the Plastics Industry (SPI), 1986, pp.90-95
- [8] Yamaguchi, K., Oyaizu, H., Matsuo, Y., Yamashita, A. and Sakakibara, Y., "Features of Acoustic Emission from Fatigue Crack in FBR Piping Component and its Generation Mechanism," Proc. of the 7th International Conference on Non-Destructive Evaluation in Nuclear Industry (Grenoble), COFREND and ASM, 1985, pp.367-370
- [9] Yamaguchi, K., Oyaizu, H., Johkaji, J. and Kobayashi, Y., "Recognition on Fracture Modes and Behavior in FRP by AE Waveform Microdata," Proc. of AECM-3 (Paris), ASNT, 1989, pp.268-277
- [10] Hoa, S.V., Smith, I.C., "Acoustic Emission Signal Classification of Graphite/Polyphenylene Sulfide Composite Subjected to Mode II Fracture," Proc. of AECM-3 (Paris), ASNT, 1989, pp.240-249
- [11] Shiwa, M., Kishi, T. and Ishida, T., "Acoustic Emission Evaluation of Aramid Reinforced Aluminum Laminates," Progress in AE IV (Proc. of IAES-9, Kobe), K.Yamaguchi, I.Kimpara and Y.Higo, Eds., JSNDI, 1988, pp.781-787
- [12] Suzuki, M., Imura, M., Iwamoto, M. and Jinen, E., "Fatigue Fracture Mechanisms of Short Fiber Reinforced PET Composites by Acoustic Emission Method," Progress in AE IV (Proc. of IAES-9, Kobe), K.Yamaguchi, I.Kimpara and Y.Higo, Eds., JSNDI, 1988, pp.695-701
- [13] Ohtsu, M. and Ono, K., "Pattern Recognition Analysis of Acoustic Emission from Unidirectional Carbon Fiber-Epoxy Composites by using Autoregressive Modeling," Journal of Acoustic Emission, Vol.6, No.1, 1987, pp.61-71

- [14] Madhukar, M. and Awerbuch, J., "Monitoring Damage Progression in Center-Notched Boron/Aluminum Laminates Through Acoustic Emission," Composite Materials: Testing and Design (Seventh Conference), ASTM STP 893, J.M.Whitney, Ed., ASTM, 1986, pp.337-367
- [15] Shiwa, M., Yuyama, S. and Kishi, T., "Acoustic Emission Signal Analysis during Fatigue Damage of GFRP," Progress in AE III (Proc. of IAES-8, Tokyo), K.Yamaguchi, K.Aoki and T.Kishi, Eds., JSNDI, 1986, pp.554-563
- [16] Shiwa, M., Enoki, M. and Kishi, T., "Acoustic Emission During Load-Holding and Unload-Reload in Fiberglass-Epoxy Composites," Journal of Acoustic Emission, Vol.4, No. 2/3, 1985, (Proc. of the 2nd International Conference on Acoustic Emission, Lake Tahoe), pp.s195-s198
- [17] Maslouhi, A. and Roy, C., "Analysis of AE Signals in Time and Frequency Domains Coupled to Pattern Recognition to Identify Fracture Mechanisms in CFRP," Journal of Acoustic Emission, Vol.8, No.1-2, 1989, (Proc. of the World Meeting on Acoustic Emission (WMAE), Charlotte), pp.s292-s296
- [18] Yamaguchi, K., Hamada, T. and Nakai, Y., "AE Source Location by Identification and Combination of Signals," Proc. of IAES-4 (Tokyo), High Pressure Institute of Japan (HPI), 1978, pp.24-49
- [19] Yamaguchi, K., Oyaizu, H. and Hamada, N., "Acoustic Emission Source Location by Identification and Combination of Signals," Advances in Acoustic Emission (Proc. of International Conference on Acoustic Emission, California, 1979), H.L. Dunegan and W.F. Hartman, Eds., Dunhart Publishers, 1981, pp.49-64
- [20] Fowler, T.J., "Recent Developments in Acoustic Emission Testing of Chemical Process Equipment," Progress in AE IV (Proc. of IAES-9, Kobe), K.Yamaguchi, I.Kimpara and Y.Higo, Eds., JSNDI, 1988, pp.391-404
- [21] McBride, S.L., Pollard, M.D., MacPhail, J.D., Bowman, P.S. and Peters, D.T., "Acoustic Emission Detection of Crack Presence and Crack Advance During Flight," Journal of Acoustic Emission, Vol.8, No.1-2, 1989, (Proc. of WMAE, Charlotte), pp.s4-s7
- [22] Tonolini, F., "AE Role in the Diagnosis and Prognosis of Defects in Industrial Plant Steel Components," Journal of Acoustic Emission, Vol.8, No.1-2, 1989, (Proc. of WMAE, Charlotte), pp.s62-s65
- [23] Hsu, N.N. and Eitzen, D.G., "Higher-Order Crossings - A New Acoustic Emission Signal Processing Method," Progress in AE IV (Proc. of IAES-9, Kobe), K.Yamaguchi, I.Kimpara and Y.Higo, Eds., JSNDI, 1988, pp.59-66
- [24] Yamaguchi, K., Onoe, M., Ichikawa, H., Shimada, T. and Shimoizuma, Y., "Multichannel Acoustic Emission Source Location System and its Application to Fatigue Test of Model Reactor Vessel," Proc. of IAES-2 (Tokyo), HPI, 1974, pp.82-102
- [25] Yamaguchi, K., Oyaizu, H., Hirai, J. and Johkaji, J., "Recognition of Fracture Modes in Fiber Reinforced Plastics by Acoustic Emission Waveform Parameters," Progress in AE IV (Proc. of IAES-9, Kobe), K.Yamaguchi, I.Kimpara and Y.Higo, Eds., JSNDI, 1988, pp.773-780

Stuart L. McBride, Michael D. Pollard, James D. MacPhail, Paul S. Bowman,  
David T. Peters

## ACOUSTIC EMISSION DETECTION OF CRACK PRESENCE AND CRACK ADVANCE DURING FLIGHT

---

REFERENCE: McBride, S. L., Pollard, M. D., MacPhail, J. D., Bowman, P. S., and Peters, D. T., "Acoustic Emission Detection of Crack Presence and Crack Advance During Flight", Acoustic Emission: Current Practice and Future Directions, ASTM STP 1077, W. Sachse, J. Roget, and K. Yamaguchi, Eds., American Society for Testing and Materials, Philadelphia, 1991.

ABSTRACT: Results are presented which show that it is possible to detect crack growth and crack presence in airframe components during flight. To accomplish this, a data acquisition system has been developed specifically for in-flight applications. It is shown that crack advance of less than 1 mm<sup>2</sup> was readily detected during flight and the fracture-related acoustic emission signals unambiguously identified.

KEYWORDS: acoustic emission, in-flight monitoring, crack growth, data acquisition

## INTRODUCTION

Since the mid-1970s, several studies have investigated the feasibility of using acoustic emission (AE) to monitor the integrity of aircraft structural components during flight. These studies are completely catalogued in an annotated bibliography of acoustic emission [1,2]. Of particular relevance is the work of Scott [3], Hutton and Lemon [4] and Scala et al [5]. AE has the advantage of being capable of monitoring large components with a single sensor, is truly a passive technique, and can be conveniently used in hard-to-reach locations. Successful development of this technique will offer tremendous savings by reducing the need for major disassembly in order to inspect critical load-bearing components.

The principal problem of acoustic emission monitoring is the unambiguous identification of signal sources (eg, crack growth, crack face rubbing, structural noises). This problem is addressed here, using a multiparameter criterion to identify signals originating at a crack in the presence of airframe noises. To accomplish this, we have developed a data acquisition system specifically for in-flight AE monitoring. This system is stand-alone, is battery-powered, and allows for dual-channel multiparameter processing of the data during flight. This multiple-criterion system greatly enhances the confidence level for the unambiguous separation of crack-related data from airframe noise.

Dr. McBride and Major Pollard (assisted by Mr. MacPhail, Mr. Bowman, and MCpl. Peters) are faculty members in the Department of Physics at The Royal Military College of Canada, Kingston, Ontario, Canada K7K 5L0.

This study also includes the use of an inertially-loaded specimen, containing a well-documented crack, which is attached to the support frame in the instrumentation bay of a Tornado aircraft. Aircraft manoeuvres produce crack advance in the specimen under known g-loading conditions and with superimposed airframe noise. This test apparatus, along with the prototype data acquisition system, has been flight tested in both the Canadian CF-5 and the British Tornado aircraft.

## EXPERIMENTAL

### The Data Acquisition System

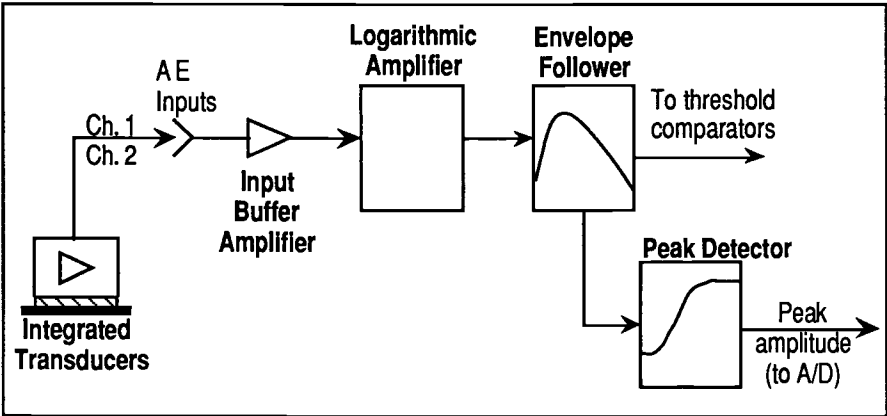
The dual-channel, digital data acquisition system used here was designed and constructed by us specifically for the recording and interpreting of acoustic emission data during flight. The design is based on criteria derived from the RMC work of almost a decade in the area of acoustic emission monitoring during flight [6,7,8]. These studies established the importance of the difference in arrival time of an event at different locations, signal risetime, and the magnitude and variation of the applied stress at the time of occurrence of the event. The efficacy of these parameters was also considered by Hutton and Lemon [4] and Scala et al [5]. All of these parameters are necessary to isolate crack related events from other noise sources during flight and are recorded by the data acquisition system used here. To provide maximum flexibility, the data acquisition system can be powered either by the aircraft electrical system or by batteries.

The outputs of the two 500 kHz piezoelectric sensor elements are each amplified by an integrated preamplifier (nominal gain 40 dB, bandwidth 300 kHz to 1 MHz) located inside the sensor casing. The type of integrated sensor used is Physical Acoustics Corporation, model R501. The resulting signal is buffered, logarithmically amplified, envelope followed and peak detected. The output of each envelope follower is separately fed into the digital data acquisition system where the times of preselected amplitude threshold crossings 6 dB apart are recorded. The lower of the two thresholds was selected to be -52 dB relative to 10 mV as measured at the preamplifier input. The output of the peak detectors and accelerometer are digitized by an A/D convertor and stored in memory (Fig. 1).

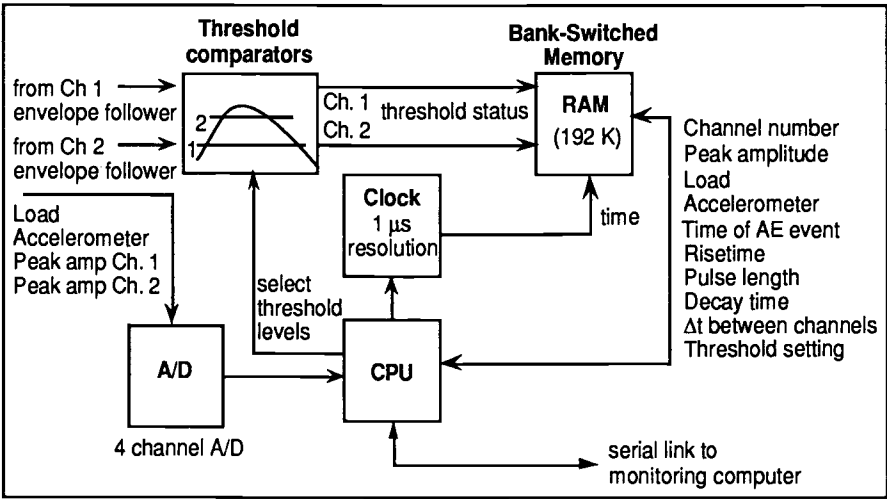
All of the above data are compressed into an event record which includes the time of occurrence of the event at each sensor, the difference in arrival times at two sensors ( $\Delta t$ ), event risetimes for 6 dB change in amplitude, event durations, event decay times and event peak amplitudes. The resulting data set is then extracted from the data acquisition system via an RS-232 interface and stored on disk on a portable personal computer. Extensive screening of data, field analysis and interpretation can be carried out immediately. Final analysis and interpretation are accomplished using spread sheet software. Table 1 lists the general specifications of the apparatus.

TABLE 1 -- General specifications for the RMC digital data acquisition system for in-flight acoustic emission monitoring applications.

2 Channels AE	60 dB dynamic range
2 Analog Channels	0-10 V full-scale deflection
Power	10 Watts maximum
Memory	internally battery-powered RAM
Dimensions	23 cm x 13.5 cm x 25 cm
Weight	2 kg
Mass Data Storage	transfer to laptop PC via RS232 interface



**Acoustic Emission Signal Conditioning**



**Data Acquisition Computer**

FIG. 1 -- Schematic diagram of the acoustic emission signal conditioning and data acquisition computer.

### The Inertially-Loaded Specimen

Figure 2 shows a schematic diagram of the inertially-loaded 7075-T651 aluminum fatigue specimen clamped in the inertial loading frame support block. The stress required to propagate the crack is applied to the specimen via the coupling pin. This is achieved as a result of the lever action of the 0.9 kg weight being subjected to the aircraft acceleration directed through the base of the inertial loading apparatus. Silicone fluid provides proper acoustic coupling of the fatigue specimen to the loading frame to ensure that airframe noises are transmitted to the fatigue specimen for detection by the acoustic emission sensors. Prior to mounting in the loading frame, the test specimen was precracked to a crack length which would cause crack propagation when the 0.9 kg inertial load was subjected to an acceleration in excess of 3.5 g perpendicular to the plane of the aircraft. The aircraft acceleration is sensed by an accelerometer (Entran Devices, Inc., model EGD-240) mounted in the loading frame support block. The inertially-loaded specimen was acoustically coupled to the aircraft support frame in the instrumentation bay.

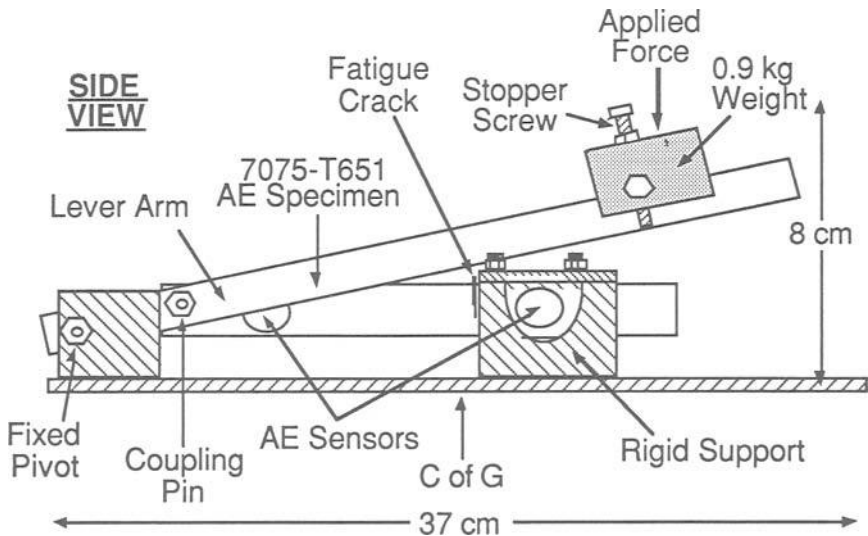


FIG. 2 -- Schematic diagram of the inertial loading apparatus and precracked 7075-T651 aluminum test specimen.



System Calibration

A detailed calibration of the acoustic emission system (inertial loading frame, fatigue specimen, sensors and data acquisition apparatus) was carried out for source signals injected at various locations. The source signals used are the helium gas jet, pencil lead fracture, pulsed YAG laser and fracture-related events generated during fatigue crack growth and overload in the laboratory. The measured arrival time differences ( $\Delta t$ ) and risetimes are listed in Table 2 for various locations. These two parameters were extremely efficient at isolating crack-related events from incoming airframe noise, as indicated in Table 2 and shown in Figure 3. Figure 3 shows the measured results obtained using 0.5 mm diameter pencil fracture as a simulation source. Data recorded during fatigue precracking of the specimen resulted in  $\Delta t=24 \pm 6$   $\mu$ sec and risetime of  $3 \pm 2$   $\mu$ sec for crack advance events occurring at maximum load. The wide range of values of  $\Delta t$  and risetime for signals originating in the base of the loading frame is due to multiple reflections within the structure.

TABLE 2 -- Measured mean values of  $\Delta t$  and signal risetime for various locations.

Position of Source	$\Delta t$ ( $\mu$ sec)	risetime ( $\mu$ sec)
Crack location	$24 \pm 2$	$3 \pm 2$
On specimen, outside sensor array	$41 \pm 4$	$2.5 \pm 2$
Base of inertial-loading frame	$65 \pm 15$	$16 \pm 15$

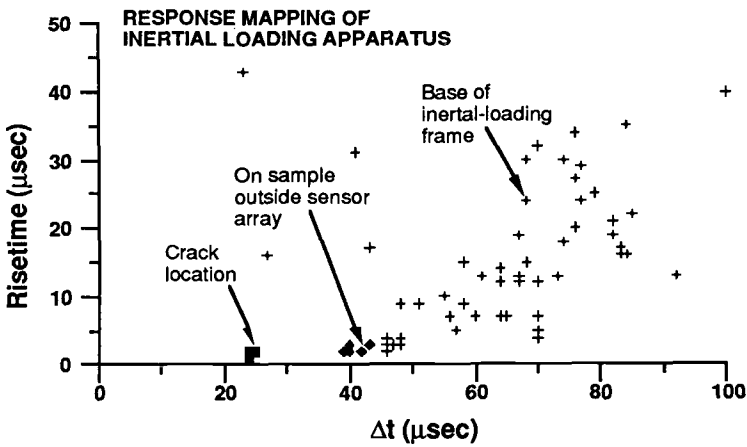


FIG. 3 -- Measured values of  $\Delta t$  and signal risetime for various locations.

### The Test Flight Results

Figure 4 shows the test flight profile as measured by the data acquisition system. Each recorded data point corresponds to the detection of an event. These events result from crack advance, crack face rubbing and airframe noises. Included in the flight profile are three aircraft manoeuvres at 15 min 12 sec, 67 min 38 sec and 68 min 30 sec, respectively, relative to takeoff. These manoeuvres resulted in successively increasing maximum  $g$  values of 2.7  $g$ , 4.3  $g$  and 5.2  $g$ , respectively, and applied a sequence of increasingly large stresses to the fatigue crack via inertial loading. The maximum load used to precrack the specimen corresponds to that applied by the inertially loaded specimen for an aircraft acceleration of 3.5  $g$ . Hence, the first overload occurring in the specimen during flight is identified with the first manoeuvre which exceeded 3.5  $g$ . This is the 4.3  $g_{\max}$  manoeuvre. Optical and electron microscopic examination of the fracture surface revealed an increase in crack face area of 0.63 mm<sup>2</sup> resulted from the first overload crack advance (4.3  $g_{\max}$  manoeuvre). Fracture of the specimen occurred during the 5.2  $g_{\max}$  manoeuvre.

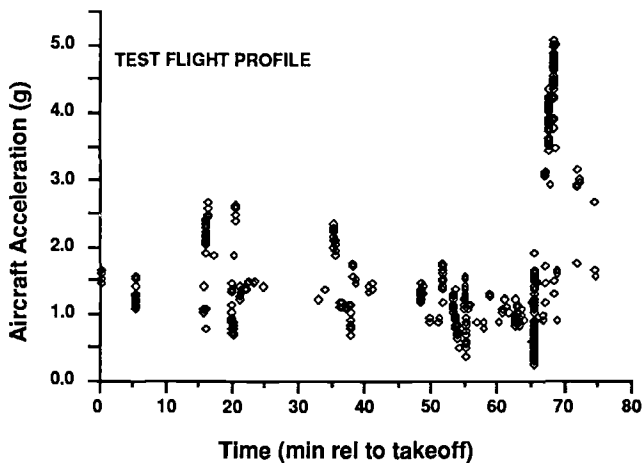


FIG. 4 -- Aircraft acceleration as function of time for all of the events detected during flight. These include all sources (crack advance, crack face rubbing and superimposed airframe structural noises).

Figure 5 shows the scatter plot of signal risetime and difference in arrival time of each acoustic emission event and noise signal detected during the test flight (Fig. 4) for comparison with the calibration data (Fig. 3). Comparison of Figures 3 and 5 show that the majority of detected signals arrive at the sensors via the base of the inertial-loading frame. Based on this comparison, only those events with  $\Delta t = 24 \pm 6 \mu\text{sec}$  and risetimes of  $3 \pm 2 \mu\text{sec}$  were accepted as crack-related events.

Figure 6 shows the effect of applying these conditions to the data of Figure 4. Note that all but the final two high- $g$  manoeuvres are removed from the data set by the dual-parameter filter.

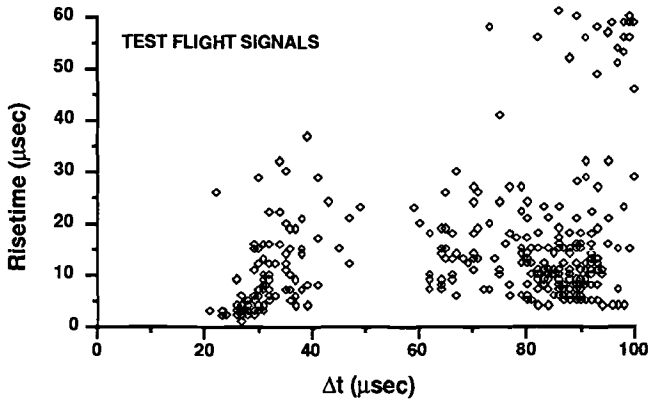


FIG. 5 -- Signal risetime as a function of difference in arrival time.

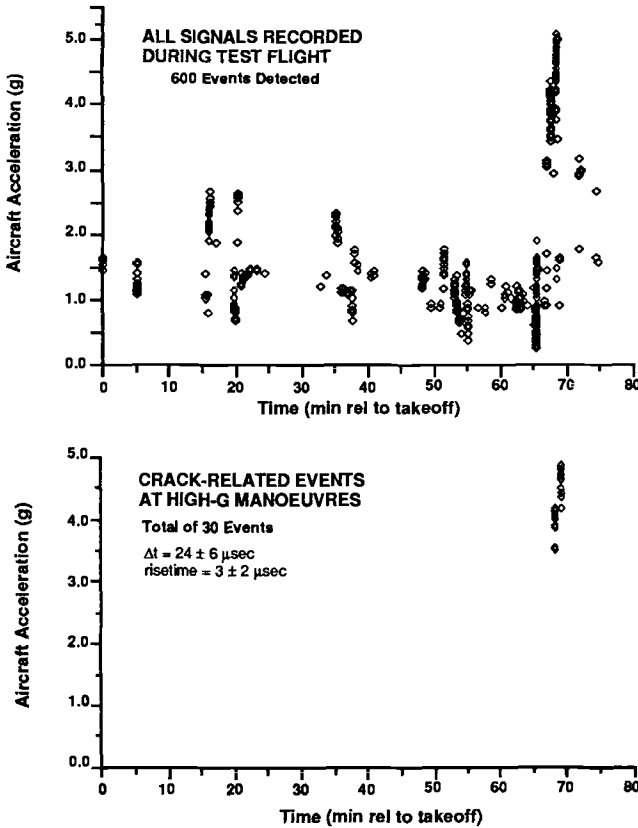


FIG. 6 -- Comparison of the occurrence of all events detected during the test flight (upper graph) with the occurrence of events unambiguously identified as crack-related ( $\Delta t = 24 \pm 6 \mu\text{sec}$  and risetime of  $3 \pm 2 \mu\text{sec}$ ). Note that these latter events occur only during progressively high-g manoeuvres which provide the stresses required for crack advance.

Figure 7 shows an expanded view of the data which occurred during the 4.3  $g_{\max}$  manoeuvre which resulted in crack advance. In the lower graph, only the crack-related events ( $\Delta t = 24 \pm 6 \mu\text{sec}$ ,  $\text{risetime} = 3 \pm 2 \mu\text{sec}$ ) are shown. By requiring crack advance events to be restricted to those which occur at loads which had not been achieved previously (Kaiser effect), each of the events occurring in this manoeuvre is identified separately as crack advance or other crack-related events.

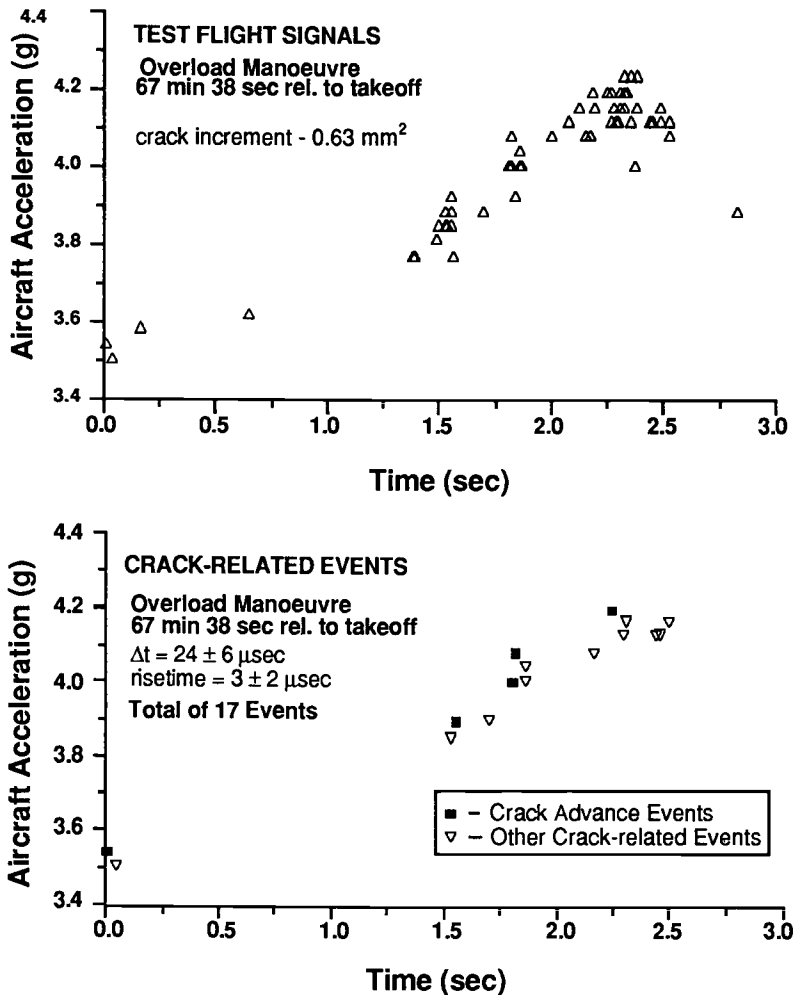


FIG. 7 -- Crack-related signals detected during the 4.3  $g_{\max}$  manoeuvres. The upper graph includes all detected events, while the lower graph includes only those events which are crack-related. The distinction of crack advance events from other crack-related events can be accomplished using the Kaiser Effect criterion as described in the text.

## SUMMARY AND CONCLUSIONS

A precracked 7075-T651 aluminum specimen mounted in an inertial loading apparatus was subjected to stresses large enough to propagate the crack during flight. These crack propagating stresses occurred during specific test flight manoeuvres of a British Tornado aircraft. The specimen and loading apparatus were part of a secondary structure bolted directly to the support frame in the instrumentation bay of the aircraft. Acoustic emission data and aircraft acceleration were recorded using a data acquisition system designed at RMC specifically for in-flight monitoring applications. The crack-related events were isolated immediately following the test flight. More detailed analysis was later carried out to confirm the results and to separate crack advance events from other crack-related events.

The selection of events which are unambiguously caused by crack-related sources was carried out using a very restrictive dual criterion ( $\Delta t = 24 \pm 6 \mu\text{sec}$  and risetime of  $3 \pm 2 \mu\text{sec}$ ) derived from specimen calibration and comparison of the test flight data with laboratory crack growth results obtained for 7075-T651 specimens with geometry and sensor configurations similar to that of the specimen used for the test flight. The 30 crack-related events selected in this manner from 600 events detected during the test flight occurred as the result of high-g manoeuvres during which crack advance would be expected. Eleven of the 30 crack-related events are attributed to crack advance by application of a temporary Kaiser Effect criterion. Thus, we confirm the feasibility of the unambiguous detection of crack growth and presence in 7075-T651 during flight, provided that detailed calibration of the structure is carried out.

Continuing work in this area includes application of the RMC data acquisition and analysis system to the monitoring of airframe fatigue tests, the monitoring of a slowly growing fatigue crack in a secondary structure during flight, and the in-service monitoring of failure-prone airframe structural components during flight.

## ACKNOWLEDGEMENTS

Supporting funds were provided by the Department of National Defence, Canada (ARP 3610-208, CRAD 144688RMC01 and DAS Eng 84778ACCA01). The project was monitored by Mr. W.R. Sturrock of the Materials Section, Defence Research Establishment - Pacific, Victoria, British Columbia, and Major W.J. Miller, National Defence Headquarters, Ottawa, Ontario. The Tornado test flight reported here was provided by British Aerospace, Warton, England, under contract to Dr. D.E.W. Stone of the Royal Aerospace Establishment, Farnborough.

## REFERENCES

- [1] Drouillard, T. F., Acoustic Emission. A Bibliography with Abstracts, Plenum Data Company, New York, N. Y., 1979.
- [2] Drouillard, T. F., "Bibliography Update", Journal of Acoustic Emission, 1982-87.
- [3] Scott, I.G., Proc. 13th Symposium on Nondestructive Evaluation, ed. B.E. Leonard, NTIAC, San Antonio, pp. 210-219.
- [4] Hutton, P.H. and Lemon, D.K., "Development of Acoustic Emission Methods For In-Flight Monitoring of Aircraft Structures", Review of Progress in Quantitative Nondestructive Evaluation, Vol. 2A, pp. 459-470, 1983.
- [5] Scala, C.M., Coyle, R.A. and Bowles, S.J., "An Analysis of Acoustic Emission Detected During Fatigue Testing of an Aircraft", Review of Progress in Quantitative Nondestructive Evaluation, Vol. 4B, pp. 709-718, 1985.
- [6] McBride, S. L. and MacLachlan, J. W., "In-Flight Acoustic Emission Monitoring of a Wing Attachment Component", Journal of Acoustic Emission, Vol. 1, pp. 223-228, October 1982.
- [7] McBride, S. L. and MacLachlan, J. W., "Effect of Crack Presence on In-Flight Airframe Noises in a Wing Attachment Component", Journal of Acoustic Emission, Vol. 1, pp. 229-235, October 1982.
- [8] McBride, S. L. and MacLachlan, J. W., "Acoustic Emission Due to Crack Growth, Crack Face Rubbing and Structural Noise in the CC-130 Hercules Aircraft", Journal of Acoustic Emission, Vol. 3, pp. 1-10, January 1984.

Brian R. A. Wood and Robert W. Harris

## STRUCTURAL INTEGRITY EVALUATION USING AE TECHNIQUES

---

**REFERENCE:** Wood, B. R. A. and Harris, R. W., "Structural Integrity Evaluation Using AE Techniques," Acoustic Emission: Current Practice and Future Directions, ASTM STP 1077, W. Sachse, J. Roget, and K. Yamaguchi, Eds., American Society for Testing and Materials, Philadelphia, 1991.

**ABSTRACT:** Acoustic Emission structural integrity evaluation tests rely on the validity of the detected acoustic emission data and the ability of the practitioner to both analyze and interpret the data to make a correct decision on the future use of the structure tested. Unfortunately with acoustic emission surveillance testing, it is not possible to know that all the available data has been assessed properly. The equipment sensitivity, threshold settings, and event capture capacity, when combined with the operator's decision making ability in real time, make it very difficult to achieve reliable integrity evaluation. The main problem is to interpret the data and so any monitoring programs should involve Expert Systems in conjunction with both acoustic emission and other operational monitoring data to maximise the utilization of the large amounts of information now available from operating plants and structures.

**KEYWORDS:** acoustic emission, expert systems, plant monitoring, integrity evaluation, remnant life prediction

### INTRODUCTION.

The determination of the structural integrity of a plant or

B. Wood and R. Harris are both scientists in the Commonwealth Scientific and Industrial Research Organization, Division of Geomechanics, PMB 7, Menai, N.S.W., 2234, Australia.

structure and the location of any defects are of prime concern for both statutory authorities and plant operators particularly as the current trend is towards more cost effective operations and quick returns on investments. A factor in many situations is that while some maintenance programs may be restricted; higher production rates are being expected from some older plants; higher loads are being applied to some older structures; and newer techniques are being introduced into plants and structures not originally designed for changing loads or process applications. One obvious example is the effect of increases in axle loadings of both road and rail freight vehicles on bridges which can be in excess of fifty years old. The advent of new alloys and materials used in the construction of plants enables designers to use these materials closer to the upper limits of their physical properties. The result of all the previously mentioned approaches to plant operation is that without correct and accurate surveillance the community can expect an increase in failures of critical plant components. Thus there is a need to utilize acoustic emission (AE) technology to monitor many structures as part of a package of monitoring techniques, but any monitoring scheme will not provide sufficient information unless there is satisfactory interpretation of any acquired data.

#### BASIC THEORY.

When a material or object is placed under stress then any defect which is activated by that stress will release energy and so act as a source of elastic waves. The elastic wave will initially radiate as a bulk wave with the wavefront determined by the nature of the source and the elastic properties of the material (especially the extent of any anisotropy). When the wave reaches an interface then some of the incident energy will be transmitted into the adjoining medium; some will be reflected; and some will be converted into a surface wave which will propagate along the boundary. The surface wave then can be detected by an appropriate transducer placed on or very close to the material surface. The transducer produces an electrical pulse which can be analyzed to provide information about the original acoustic emission source and hence facts about the structure.

The main analytical techniques employed are event counting, event location and pulse parameter measurements [1]. The detected pulse will be different from that generated by a source as a consequence of the microstructure of the material; the details of the elastic wave propagation between source and transducer; and the characteristics of the transducer and monitoring equipment. Simple analysis of the detected pulses may not always give results with a high degree of credibility for both source location and identification, so the interpretative procedures must take into account as many factors as possible. Some of the important factors that can affect any propagating elastic wave are the source attributes, wave propagation in the material; wave propagation along boundaries; structure geometry; transducer characteristics; electronic instrumentation.

Temperature and stress changes are usually considered



insignificant factors compared with the above under normal operating conditions.

An electrical signal may be viewed in either the time or more familiar frequency domain to provide a framework to determine much of the information contained in a signal. The power spectral density (PSD) of a source can be estimated if some knowledge about the transfer functions operating in the chain of events between source and transducer is available. Simple pattern recognition applied to the experimentally measured PSD's can provide further information about source attributes, however this does require a wideband response and also critical spatial positioning of the transducers, so that the approach is impractical for large transducer separations.

The results of the various analysis techniques applied to the detected acoustic emission signals form a knowledge base which is used to extract information about the nature of these signals. The operator must have some understanding about the processes involved in the generation, propagation, and detection of the signals, otherwise incorrect deductions may be made. The disciplines of electronic engineering and electronics cannot be simply used without regard to materials science and the nature of elastic wave propagation. A simple demonstration of the need for intelligent interpretation of acoustic emission data, is to consider the situation where an operator depends solely on the results obtained with equipment that measures only peak amplitude and rise and arrival times. A simple ray tracing approach will show that for a given geometry there will be many paths that allow wave propagation from source to transducer to occur so that as a result of the many reflections that can occur at interfaces, a situation can arise where components of the detected waveform will arrive after several reflections. Then if these waves reinforce with other waves arriving at the transducer site by different paths, some of the peak amplitudes in the resultant wave can have larger values than the peak associated with the first arrival. Typical waveforms obtained from an FRP structure are a simple pulse (figure 1) and one where reflections and other inhomogeneities in the propagation path have considerably modified the pulse (figure 2). The effects of dispersion (velocity of propagation is a function of frequency) together with the material and surface attenuation which are also functions of frequency will alter the propagating pulse. These effects should be measured prior to each monitoring program as the geometric and structural conditions will vary. Welds in the propagation path will result in interesting forms of waveform modification.

A desirable end-point for all of the processing is to present the data in ways which will readily provide a real time indication of structural integrity. Some parameters of use in the analysis procedures can be derived from the peak amplitude distributions of the detected pulses and for want of a better name these have been designated as indicative energies [2], since they do not give a true energy value, but only an indication of the energy released by the source. The fact that the transfer functions relating the

observed waveform to that generated by the source, are not all known or capable of measurement, means that a true energy cannot be obtained. However, provided all the equipment and the transducer locations remain the same, then valid comparisons both within a test and between tests are possible on the same structure. A graphical indication of structural integrity can be gained by viewing these indicative energy values plotted as a function of an appropriate activity/stimulus factor producing what has been termed a localised energy graph. These indicative energy values can be plotted as a function of time to predict maintenance requirements and estimate the remnant life of the structure. Alternatively the data can be plotted and continuously updated during a monitoring period so that areas of probable significant activity can be readily identified.

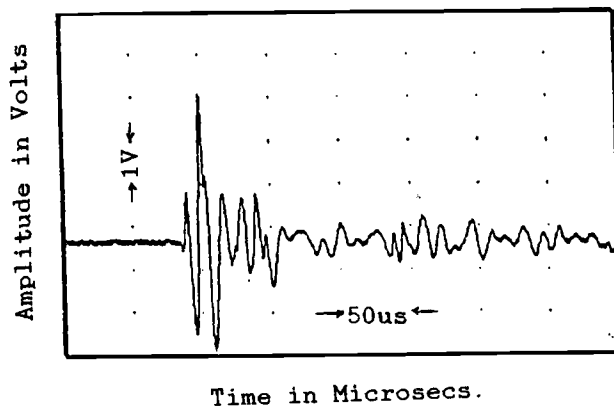


Figure 1. Simple AE waveform

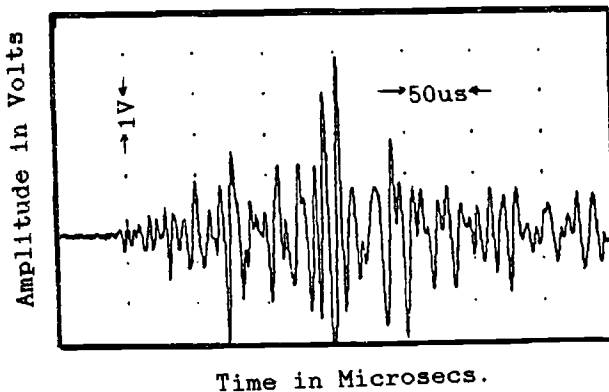


Figure 2. Modified AE waveform

Eventually some of the extensive knowledge required by an operator will be encapsulated within the framework of an expert system, which will allow the externalization of the interpretive procedures into a computer based system to carry out the logical steps needed to make a valid assessment. The knowledge base for such an expert system in a controlled stimulus situation, will take as input pertinent parameters such as count rate; the largest peak amplitude and/or weighted average (or possibly some of the indicative energy values); together with information obtained during laboratory evaluation of the material of which the structure is made and plant measurements (temperature, pressure etc); and use this information to provide some estimate of the integrity of the structure. An example of the type of decision tree that may be followed is given in figure 3 where the situation is considered for constant AE during a stimulus hold period. The simple decision tree of figure 3 has only "high" and "low" for the amplitude of the AE; "many" and "few" for the count rate; and "quiet" or "noisy" for the material characteristics. Quantification of these arbitrary values is very dependant on the realistic measurement of the AE source activity characteristics of the material concerned. A "clean" steel may generate less than 50 events before failure, while a fibre reinforced plastic would generate many thousands of events under the same load conditions. The estimate of mechanical integrity has been expressed as an integrity failure index (IFI) which has a value of 100 for completely suspect and 0 for not suspect. The values of this index are to a certain extent arbitrary and consensus needs to be reached on the choice of the values and their interpretation. An extended knowledge base would have many more options for the values and relate them to actual experimental data.

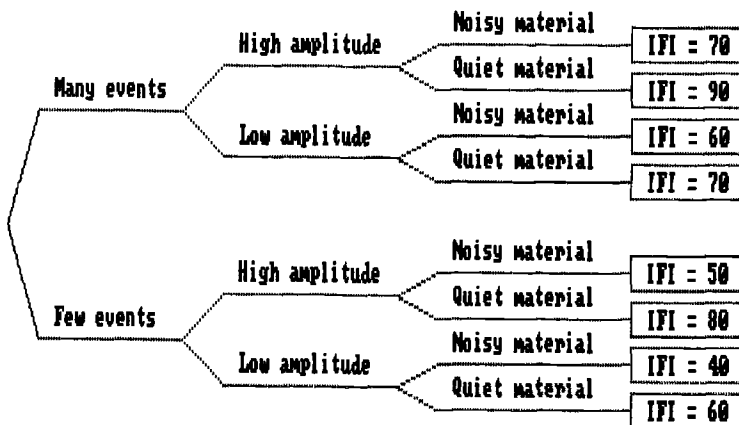


Figure 3. Decision tree for integrity assessment.

## PHILOSOPHY REGARDING AE MONITORING.

The most common use of AE is for structural integrity evaluation since the technique can locate active sources and provides some information about them. Short term tests may be conducted with little prior notice and minor disruption to plant operation, however for the testing to have a high level of confidence it is necessary for the structure to be subjected to a new peak stress level in the surveillance to overcome the AE load hysteresis phenomenon known as the "Kaiser Effect".

The use of AE techniques to monitor structures often employs a 10 hour monitoring program which is about 0.02% of the life of a vessel in operation for 5 years. The results of such a program have been used to provide a current evaluation of structural integrity and so gain certification for future operation. If the monitoring becomes an annual occurrence then the testing time rises to around 0.1% of the operating period. The use of continuous or periodic AE monitoring using the techniques described previously and taking into account the plant material characteristics together with test procedures which recognise the Kaiser Effect, makes it now feasible to use AE assessment as the basis for continuous plant operation (no statutory shut downs) when coupled with other NDT techniques, if there are realistic plant operating conditions.

Prior to start-up, any plant or structure should be in a new condition. On start-up the plant or structure is placed under considerable stress both localised and overall (particularly if it is a high temperature high pressure vessel). This traumatic experience often results in significant damage being done to the plant or structure, and it is possible that up to 60% of the operational degradation may be initiated by transient operating conditions specifically in the first 48 to 72 hours of operation, although other mechanisms such as fatigue and creep will both initiate and produce defect growth during plant operation. The growth of any defect or AE source will be dependant on the material properties and the plant operating conditions. Under "normal" plant operation the source/defect activity which may be connected with mechanisms such as fatigue, creep, stress corrosion etc, is usually associated with sustained long term deformation. Since any defect/source activity will vary depending on the surrounding stress it is not possible to get a definite measure of the damage/degradation of the structure. A number of plant monitoring programs and separate tests where vessels and samples have been stressed to failure indicate that there is a relationship between indicative energy 1 and indicative energy 2 which produces a local and/or overall indication of relative damage [3]. A typical form of the relative damage versus log time graph is given in figure 4. The exact nature of the regions of inflection and the approximately linear sections of the graph will vary for different situations.

After a prescribed period (typically 3 to 10 years depending on the structure and its operating conditions) there will be a statutory shut-down and maintenance program to restore the plant or structure to a near new or defect free condition. The next start-up will again cause degradation and so the cycle continues. AE monitoring during start-up and preferably also during operation, will highlight and assess the severity of any source activity so that operational conditions detrimental to structural integrity will be determined. Historical AE data will allow the determination of a cumulative indication of remnant life which can be graphed. This analysis can be applied to data obtained during a test program and may be related to both the whole structure or specific areas of interest for that test program providing a short term evaluation of integrity, stability and failure. It may also use data from a number of tests on the same structure using the same transducer locations over an extended period of time to provide a long term estimate of the operation, integrity and remnant life for both specific areas of interest or the entire structure. The values of the indicative energies will show no discernable trends for a defect free structure, however when significant defect activity occurs, then there will be trends similar to those depicted in figure 5 where parameters related to two of the indicative energies (the scaling will be material dependant) are plotted as a function of time where the stimulus is precisely controlled (e.g. hold period) and other parameters are still monitored such as the strain in FRP structures, or some function of the applied stress [3]. An indication of the structural integrity and the remnant life appears to be related to the separation of the two curves with the cross-over point having a special significance. This interpretative approach has been supported in a number of extended investigations on different FRP booms; a laboratory investigation of a structural steel; and a vessel constructed from the same steel [3]. As this approach is further investigated and validated it should be possible to estimate -

- the present structural integrity;
- abnormal changes in structural integrity;
- effects of changes in operating conditions on the integrity;
- effects of operational excursions on the integrity;
- timing of routine and preventative maintenance scheduling;
- remnant life of the structure.

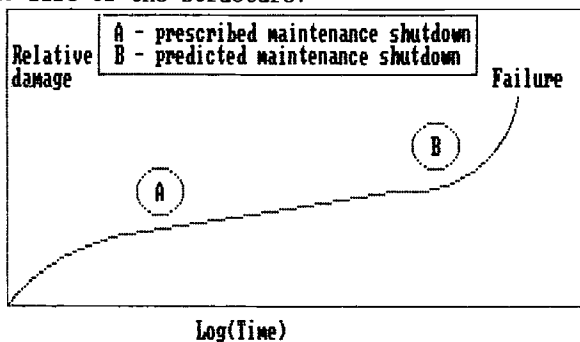


Figure 4. Relative damage curve.

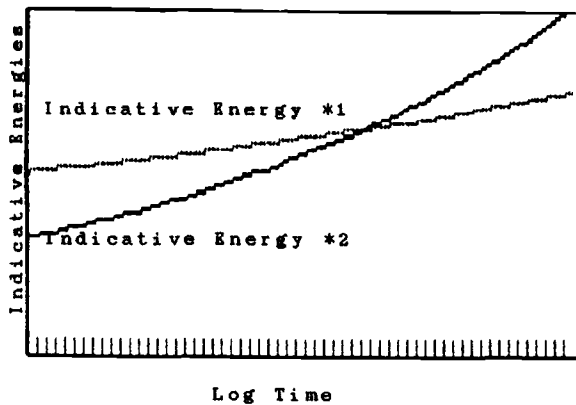


Figure 5. Structural Integrity Evaluation Graph.

#### FUTURE DEVELOPMENTS.

The future development of AE techniques is most likely to be in long term monitoring or permanent monitoring of structures such as pipelines, pressure vessels, storage tanks, critical areas in an industrial plant, process control, civil structure monitoring, and geotechnical applications. The equipment would tend to be less expensive and dedicated to a specific use but capable of some diversification in its application. Although it is possible to monitor entire plants and/or structures at regular intervals over long periods of time, it is preferable that continuous monitoring be employed. Otherwise important data can be missed since it is not always possible to intentionally over-stress the structure to stimulate defect activity and hence important data will arise at unpredictable times.

Data from permanent monitoring systems would give advance warning of areas requiring inspection; potential problem areas could be located; and in some cases the source may be identified. The results of permanent monitoring should be used to plan both the requirements and needs of maintenance and shut down programs. The analysis and interpretation of the indicative energies and remanent life evaluation will only be a viable tool after the correct relationship between material properties and AE activity is better defined and wave propagation factors are included in any AE analysis techniques.

The extraction of meaningful conclusions from all the gathered data subsequent to the application of the various analysis procedures requires a distillation of the methods used by a skilled practitioner in the field of acoustic emission. Since many of the steps used in the interpretation of the data involve

some form of decision tree, there will be an increasing use of expert systems to provide, in a computer literate form, the thought processes used by the skilled operator. The extraction of parameters that can be used to provide useful descriptors of the complex waveforms that are observed is still a fruitful field for research, and computer based pattern recognition will play an important part in this work. If a sufficiently large amount of data about actual waveforms and the associated conclusions becomes available, then it may be possible to use a learning algorithm such as that associated with neural networks to provide a workable computer based interpretative procedure.

#### ACKNOWLEDGEMENTS.

The authors wish to express their appreciation to the other members of the C.S.I.R.O. Acoustic Emission team who participated in both the laboratory and field test work associated with this report.

#### REFERENCES

- [1] Harris, R. W. and Wood, B. R. A., "The Detection, Transmission, and Interpretation of Acoustic Emission Signals," Metals Forum (Australia), Vol. 5, No. 4, 1982, pp. 210-215.
- [2] Wood, B. R. A. and Harris, R. W., "Acoustic Emission Applied to Railways," Progress in Acoustic Emission III, The Japanese Society of NDI, 1986, pp. 125-135.
- [3] Wood, B. R. A., Noyes, L. M., and Harris, R. W., "Comparison of Laboratory and Field Tests During Acoustic Emission Monitoring of Pressure Vessels," Progress in Acoustic Emission IV, The Japanese Society for NDI, 1988, pp. 373-381.

## SOLVING AE PROBLEMS BY A NEURAL NETWORK

---

REFERENCE: Grabec, I., Sachse, W., and Govekar, E., "Solving AE Problems by a Neural Network", *Acoustic Emission: Current Practice and Future Directions*, ASTM STP 1077, W. Sachse, J. Roget and K. Yamaguchi, Eds. American Society for Testing and Materials, Philadelphia, 1991.

ABSTRACT: This paper summarizes recent work utilizing an adaptive learning system to the characterization of acoustic emission phenomena. The processing system resembles a neural network including an associative memory. Data is input into the system as a vector composed of either AE signals or their spectra and encoded information about the source. The mapping of AE signals from the sensors to the descriptors of the source and vice versa is accomplished by learning in the system. This is performed by presenting experimental signals to the system and adaptively forming a memory whose output is an autoregression projection of the input. Discrepancies between the input and output are applied in a *delta learning rule*. Experiments are described which utilize a system running on a minicomputer to process signals from a localized, simulated source of discrete acoustic emission events in a block of material and to process the AE signals generated during a metal drilling operation. It is shown that the characteristics of the source can be estimated from the AE signals or vice versa by the auto-associative recall from the correlation memory.

KEYWORDS: Neural signal processing, neural networks, quantitative AE, inverse problems, adaptive systems, learning, source characterization, process monitoring

## INTRODUCTION

The use of acoustic emission (AE) measurements as a powerful, non-destructive testing tool is becoming well established, c.f. [1]. Essential to its success in many

Igor Grabec and Edvard Govekar are respectively, professor on the Faculty and graduate student of Mechanical Engineering, E. K. University of Ljubljana, Ljubljana, Yugoslavia and Wolfgang Sachse is a professor in the Department of Theoretical and Applied Mechanics at Cornell University in Ithaca, New York, 14853 - U S A.



applications is a signal processing procedure by which information about the source of emission can be extracted from the signals detected at one or more sensors on the surface of a structure. The source information includes its location and characteristics where the latter are directly related either to failure processes occurring in the material comprising the monitored structure or to changes in a process which is being monitored. The last thirty years have seen the increasingly rapid development of various systems for sensing and processing of AE signals by which various AE source phenomena can be detected and characterized.

In order to establish a direct connection between the parameters describing a source and the AE signals detected by a sensor, a major emphasis of recent research has been towards the development of quantitative signal analysis techniques by which the detected ultrasonic signals can be processed to recover the detailed characteristics of the source or the properties of the medium [2,3]. The success of this approach depends critically on the micro-mechanical modeling of AE sources, the determination of the response characteristics of the specimen using elastodynamic theory and a well-characterized, broadband signal detection system. In this approach, the source characteristics are recovered from the detected AE signals using an inversion procedure, called a *deconvolution*, of the detected signals [3]. This generally represents a so-called *ill-posed problem* requiring some sort of regularization in order to permit a stable processing of the experimental data [4]. One example is the minimization of the mean noise energy which leads to a so-called *optimal deconvolution* [5]. But even when a suitable mathematical method of regularization is found, the multi-component nature of many important AE sources and elastodynamic phenomena present serious obstacles for the practical implementation of quantitative AE procedures in most non-destructive testing applications. It would therefore be of advantage to find a quantitative method of analysis by which a rigorous elastodynamic treatment of the inverse problem could be avoided.

Many manufacturing processes, as for example the cutting of metal, are efficient generators of sound. Therefore, an analysis of the generated AE can be expected to provide important information related to the process [6]. In most cases, the sound generating process is continuous and it is therefore convenient to use a spectral distribution of the emitted signals for the description of the process. Various studies of the cutting process have shown that the spectra of the emitted acoustic signals have very complex structures [6]. Even for the simplest case of orthogonal cutting, the chaotic dynamics associated with the process is too complicated to be easily analyzed to obtain a theoretical basis of the emitted acoustic signals and their relation to details of the processing operation [7]. One is thus usually forced to rely on an empirical description of the process. The ultimate goal of such an approach however is to make a reasonable estimation of the parameters related to the manufacturing operation from the AE signals. This is of practical importance for an automatic identification and control of the process.

In order to preserve the preciseness that is inherent in a quantitative description of AE phenomena, yet at the same time avoid the difficulties related with an exact

elastodynamic modeling, an *adaptive system*, resembling the structure of a *neural network* has recently been proposed for obtaining approximate solutions of direct and inverse AE problems [8]-[12]. The same adaptive system as that used for the analysis of discrete AE events has recently been applied to the characterization of drilling and laser-based processes [13,14]. The purpose of this article is to review the structure of such a processing system and, using examples, to demonstrate its applicability to the analysis of AE signals.

Before proceeding to describe the formulation of the system, it is useful to review some of the characteristic properties of biological neural networks. The ability of an animal to recognize events in its environment from the sounds it has sensed was developed during evolution. For this task an animal needs no theory of sound generation and propagation or the corresponding physical models, but rather, only experience gained by learning. During this learning, a series of various acoustic, visual, touch and other signals from the corresponding sensors is presented to the neural network which, in its most complex form, represents a brain. By a self-organizing process, caused by the interaction between neurons, the brain then forms an internal representation of images of the environment [15,16]. Although it is still not known exactly how the brain operates, one of its most characteristic features can be illustrated by an example. If in certain situations the sensory signals provide only partial information about the environment, the brain is capable of supplying the missing information from the image in its memory by an associative recall from the previously formed representation. For example, when hearing a sound, an intelligent being is usually able to imagine where the sound is coming from and what its source is. Since this corresponds to the main task of AE analysis, one can therefore argue that in many NDT applications, an *adaptive* AE analyzer must be capable of storing in an internal memory, information about various possible AE events. This information is presented to the system during learning and it is subsequently able to utilize this stored information for completion of partial data so as to obtain a good estimate of the features by which an AE event is characterized [8,11].

In technical terms, the sensor signals can be treated as a multi-component input to a neural network, while the internal image can be interpreted as the output from the network [15,16]. One of the fundamental tasks of learning is then to adapt the response characteristics of the neural network so that when it is used, it can generate an appropriate output from only a partial input, provided that the environment has not changed. Here "appropriate" has to be understood in terms of some measure of statistical error which is determined during an analysis of the system's performance. The system operating in this way is said to be capable of performing an *auto-associative recall* [15].

Systems of this type have been already extensively studied in relation to research of pattern recognition, adaptive systems and artificial neural networks [15]-[19]. The main goal of the previous work has been to find an appropriate learning procedure and a structure of the information processing system which facilitates this. Much research has also been completed related to the various representations

of signals needed to obtain an amplitude, time and spatially invariant operation of the system [15,20,21]. The required data transformations can be performed in the pre-processing portion of the system or included with the neural network processor [21]. In the field of pattern recognition, the pre-processing is most frequently applied in order to present empirical data in a form most appropriate for the classification of clusters [20]. For this purpose, the representation of empirical data by a set of quite arbitrarily selected statistical parameters is often used. A typical example is the representation of an AE event by its risetime, energy, decay time, kurtosis, pulse duration etc., which all describe a point in a multi-dimensional feature space [22]. However, the results obtained by such processing of AE data often have no physical basis nor can they be compared with the detailed results obtained from a quantitative analysis of the AE phenomenon. In order to achieve the latter, the signals input into an information processing system or obtained from it should be interpretable in terms of directly measurable physical quantities, such as displacement, position or force or from quantities which have been derived from these, as for example, the spectral density of the sensor signal. Because there may be many transducers simultaneously used in an experiment, it follows that all the information about the phenomenon can be best represented by a multi-dimensional, time-dependent variable.

In view of all the aforementioned requirements, we wish to describe now in more detail an adaptive, auto-associative processing system which resembles a neural network having multi-component inputs and outputs whose application is the processing of AE signals [8,11]. In order to facilitate a simple physical explanation of the results of such processing, we first describe how an exact physical description of the AE phenomena can be approximated by a discrete system.

## FORMULATION OF THE SYSTEM

We consider an AE system to be a linear, elastodynamic system. In this system, the time-dependent displacement signal  $u(r, t)$  detected at the sensor position  $r (= x, y, z)$  results from the time-dependent force density field  $f(r', t)$  located at the source position  $r'$ . The source characteristics and the corresponding detected signals are related by the *Green's tensor* and a convolution in space and time. This is written in simplified form as,

$$u = G * f \quad (1)$$

The inverse of this expression permits a determination of the source function, including its temporal as well as its spatial characteristics. That is,

$$f = G^{-1} * u \quad (2)$$

This last equation corresponds to the elastodynamic equation together with the applied boundary conditions. Both of the previous equations can be written at once in the form

$$[u, f] - [G * f, G^{-1} * u] = 0 \quad (3)$$

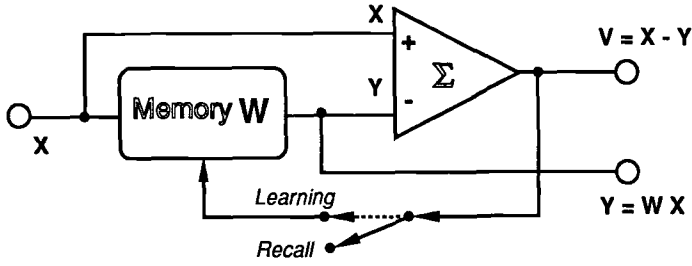


Figure 1: Schematic of an adaptive system.

If instead one uses the concatenated vector, sometimes called the *pattern vector*  $X(r, t) \equiv [u, f]$ , Eq. (3) becomes

$$X - W * X = 0 \quad (4)$$

where the tensor  $W$  is equivalent to the generalized matrix expression

$$W = \begin{bmatrix} 0 & G \\ G^{-1} & 0 \end{bmatrix} \quad (5)$$

It is seen from the above that the concatenated vector quantity  $X$  is mapped back onto itself by the tensor  $W$ . It is therefore sometimes called the *memory tensor*. According to the given definition, the vector  $X$  represents the measurable source quantities and the detected AE signals while the tensor  $W$  represents the response or dynamical characteristics of the material or structure.

In an empirical treatment, complete information about an ultrasonic phenomenon is supplied by the measured quantities. The problem is then how to determine the unknown tensor  $W$ . For this purpose the adaptive system shown in Fig. 1 is utilized. The system consists of two essential parts: the *memory* and the *subtractor*. The memory is represented by the tensor  $W$  which has the structure described by Eq.(5). The input to the system is the vector  $X$  and the corresponding output of the memory is the vector  $Y = W * X$ . The output  $Y$  is an *estimator* of the input vector. The *discrepancy*  $V$  is the difference between the input and the estimator and it is given by

$$V = X - Y = X - W * X \quad (6)$$

For an arbitrarily chosen memory tensor,  $W$ , the discrepancy generally differs from zero. However, by an adaptive modification of the memory tensor, the discrepancy, on average, reduces to zero. That estimator which is obtained after adaptation to all training input vectors is called the *ultimate estimator*. The corresponding memory tensor then appropriately models the unknown response characteristics of the material, at least for those input vectors which have previously been presented to the system during learning. From past research of adaptive

systems, various rules of adaption have already been discovered [15]-[21], with the simplest one given by the *delta learning rule* which is expressed as

$$\Delta \mathbf{W} = C (\mathbf{V} \otimes \mathbf{X}^T) \quad (7)$$

Here,  $C$  is a constant and  $\mathbf{X}^T$  is the transposed input vector while the operator  $\otimes$  denotes the outer product. By adjusting the value of the constant  $C$ , the rate of adaptation can be controlled.

Generally, only one sample of the vector  $\mathbf{X}$  does not contain sufficient information about the total response characteristics of the material and the measurement system. We therefore assume that there is available a series of  $N$  experimental samples  $(\mathbf{X}^{(1)}, \mathbf{X}^{(2)}, \dots, \mathbf{X}^{(N)})$  to which the memory can be simultaneously adapted. A statistically equivalent treatment of all samples is achieved if the complete series of experimental sample data is presented many times to the system. For this purpose it is reasonable to choose the adaptation constant appearing in Eq. (7) by  $C \leq 1/(N \cdot \|\mathbf{X}\|^2)$ , where  $\|\mathbf{X}\|$  denotes the average  $\mathcal{L}_2$ -norm of all the input samples. Such iterative formation of the memory matrix is generally called *learning*.

In actual experimental situations the input data is never detected simultaneously everywhere in space nor at all frequencies for all time. In addition, there exist no computers possessing a continuous, distributed memory by which the memory tensor  $\mathbf{W}$  could be calculated. We therefore must assume that the measured data is mapped onto a finite number of digitized experimental data from the displacement signals and the corresponding source data. If there are  $k$  signal components and  $l$  source components, the input pattern vector is mapped into a reduced input vector,  $\mathbf{X}$ , where

$$\mathbf{X}(\mathbf{r}, t) = [\mathbf{u}, \mathbf{f}] \mapsto \mathbf{X} = (u_1, u_2, \dots, u_k; f_1, f_2, \dots, f_l) \quad (8)$$

Furthermore, with this assumption the memory tensor is also mapped into the reduced memory matrix,  $\mathbf{W}$ . That is,

$$\mathbf{W} \mapsto \mathbf{W} \quad (9)$$

With these finite-dimensional quantities, the convolution operation appearing in the previous equations becomes a matrix multiplication. However, the fundamental scheme of the adaptive system's operation remains essentially unchanged. Because of such an arbitrarily truncated description of the signals and because of possible non-linearities in the ultrasonic phenomenon itself, the structure of memory matrix as described by Eq. (5) cannot be strictly realized in practice. Instead, the system memory is described by a more general matrix which, in contrast to that of Eq. (5), has non-zero elements also on its diagonal elements. At the start of learning, we choose  $\mathbf{W} = \mathbf{0}$ . During learning, the matrix  $\mathbf{W}$  converges to the solution of the equation

$$\mathbf{R}_{xx} - \mathbf{W} \mathbf{R}_{xx} = \mathbf{0} \quad (10)$$

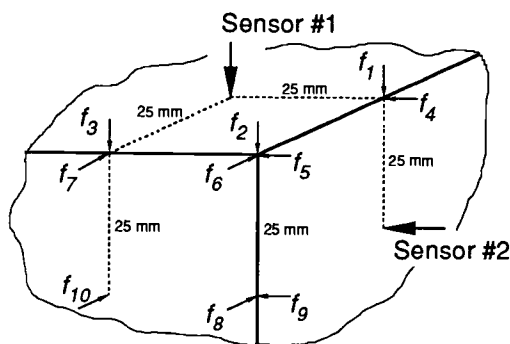


Figure 2: Sources and transducers on the corner of an aluminum block.

in which  $R_{xx}$  is the correlation matrix of the input vector  $X$ . The solution of this equation is a projector to the eigenvector of the correlation matrix corresponding to the largest eigenvalue. The estimator  $Y = W \cdot X$  therefore represents a linear autoregression in the multi-dimensional space of the input vector variable  $X$ .

After learning is complete, the system can be used as a trained analyzer. In this mode, the feedback to the memory is turned off. Then, an input vector which is only partially filled with experimental data, generates the estimator  $Y$  which, in turn, will include also an estimation of the missing data. Such an operation corresponds to the auto-associative recall of missing information [15,16]. The structure of the adaptive system described here is analogous to a simple neural network in which the synaptic joints between neurons represent memory elements.

## EXPERIMENTS

In order to demonstrate the applicability of adaptive system we present here the results of analysis performed during experimentation with two acoustic emission phenomena. In one of these, the AE signals were of discrete type, while in the other, they were continuous. The experiments were performed using a setup consisting of a specimen, sensors, amplifiers, waveform recorders or a spectrum analyzer and a computer with appropriate data acquisition software and processing software implementing the processing operations described in the previous section.

### Characterization of Discrete AE Events

In the first type of experiment, the processing system was applied to solve a forward and an inverse AE problem. The example studied was the ability of the proposed system to learn and to analyze AE signals excited at several fixed locations by forces acting in various directions. The test specimen was an aluminum block of dimensions  $450 \times 180 \times 350 \text{ mm}^3$ . In one corner of the specimen were mounted two miniature, broadband piezoelectric transducers as shown in Fig. 2. The diameter of the sensors' active area was 1.3 mm. The sources were activated by breaking a pencil lead of diameter 0.3 mm and of length 2.5 mm acting in various directions at each of the source locations. These are indicated by

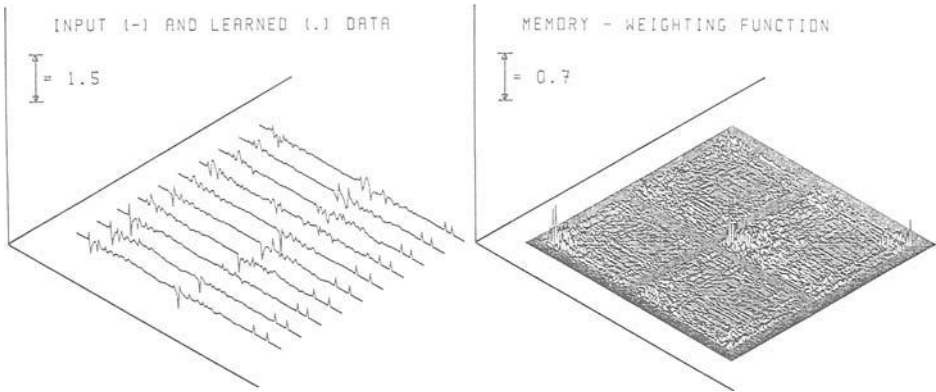


Figure 3: (a) The set of concatenated training signals and the corresponding output signals (superimposed). Coincidence of both data sets indicates a good adaptation of the system; (b) The *memory matrix* corresponding to the synaptic weights of the neural network.

$f_1, f_2, \dots, f_{10}$  in the figure. The signals from the transducers were amplified by 40 dB and recorded by a two-channel waveform digitizing system. The digitization rate was 10 MHz. The sample pattern vectors were composed of digitized data from both sensors and data about the orientation of the released force and the location of the source point which was entered via the keyboard. The AE signal from each sensor was represented by 64 components, evenly extracted from 1024 point-long time records, while 22 components were appended for encoding the source data by two descriptors. The complete experimental data for each AE event was thus represented by a pattern vector comprised of 150 components. The source position and the direction of the force were encoded by assigning to each a constant corresponding to an appropriate component out of eleven available while the others were set equal to zero.

The training set of pattern vector samples is shown in Fig. 3(a). The initial portions (left side) of each record correspond to the signals from both transducers while in the latter portions (on the right side) are the encoded source descriptors. These sample vectors were then presented to the processing system in twenty iterations. During the adaptation, the norm of the discrepancy  $V$  fell below  $10^{-4}$ . This indicates that a very accurate reproduction of the input signals was attained. This is represented by the dotted lines in Fig. 3(a) which practically coincide with the lines representing the input signals, making it nearly impossible to delineate between the training and learned signals.

The components of the memory matrix  $W$  can be treated as a data record so that the entire matrix can then be graphically represented as shown in Fig. 3(b). The displayed data consists of sixteen characteristic regions corresponding to four auto- and twelve cross-correlation fields of the segments comprising a sample vec-

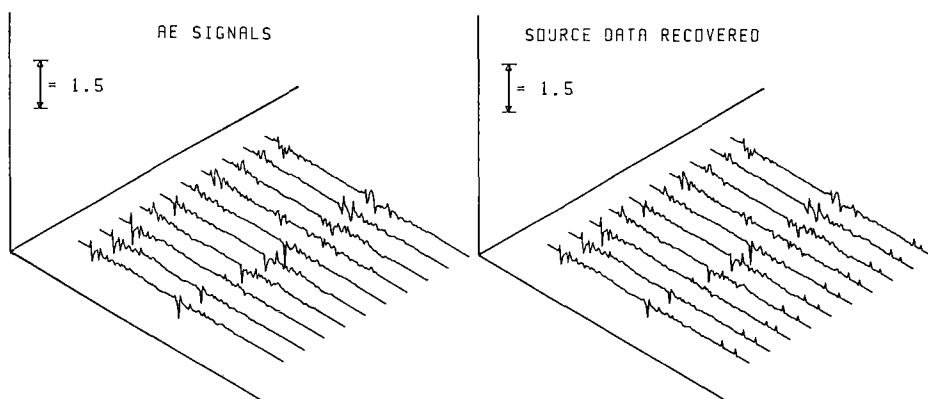


Figure 4: (a) The set of concatenated input signals, representing the partial information supplied to the adapted system; (b) The set of output signals including the recovered source descriptors of position and force orientation obtained from the data set (a).

tor. For the solution of the forward or inverse problems, the off-diagonal or cross-correlation elements of the matrix, corresponding to those formed from the products of the signals and the source coordinates, are essential.

After the learning has been completed, the system can be used as an adapted analyzer. To show this, we present here the results of two types of outputs excited by artificially truncated input pattern vectors. The first type of input vectors included only the signals from the transducers while the second type was formed using only the source descriptors. These input signals are shown in Figs. 4(a) and 5(a) while the corresponding output signals are presented in Figs. 4(b) and 5(b), respectively. The results of Fig. 4(b) demonstrate that the source descriptors of source position and orientation are correctly recovered in the processor's output signals. This example demonstrates the use of the processing to obtain a solution of the AE *inverse* problem. The recovery of the source descriptors is a consequence of the cross-correlation portions present in the memory of the system.

In the second type of processing, the missing AE signal portions in the input vectors were recalled by the source descriptors as shown in Fig. 5(b). This recovery corresponds to an approximate solution of the *forward* elastodynamic problem in which AE signals are determined for specified characteristics of the source and the dynamic response of the sample. We note that the recovered AE signals do not correspond exactly to the learned signals. The apparent corruption by noise is a consequence of the similarity between the training data which are not fully orthogonal to each other. However, the output represents an optimal mixture of those vectors of the training data whose source descriptors are similar to those in the presented input vector of the test data. It is also characteristic that in the elements of the vector containing the encoded source data, disturbances appear in



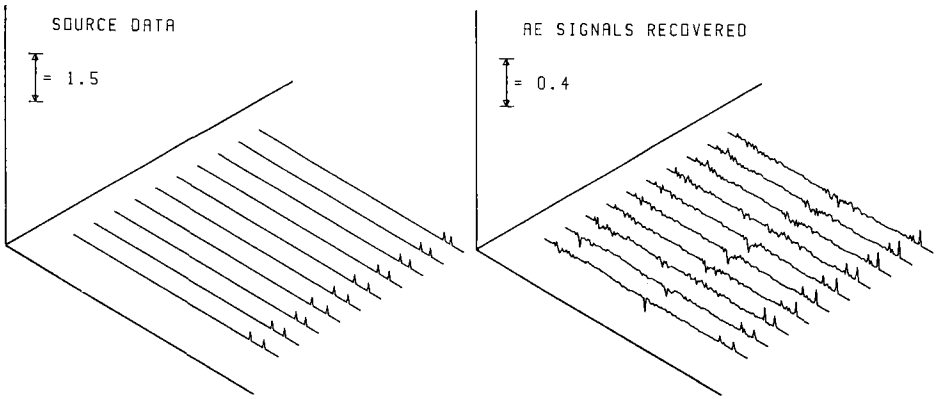


Figure 5: (a) The set of input signals, comprised of the source descriptors. The right peak represents the force direction and the left peak, its location; (b) The set of output signals generated by the source descriptors in (a). The AE signals are approximately recovered.

the output signals indicating the similarity between patterns and their cooperative formation of the output data.

In the above example the time-dependance of the AE sources was neglected because the encoded source descriptors were specified only in terms of the source's orientation and its location. Hence, it is only these parameters of the source that can be recalled from the memory. A further limitation of the example above is that the processing was not time-invariant and so the described procedure is only applicable to process those signals in which a proper triggering of the waveform recorder is possible when recording the AE signals. A time-invariant operation of the system will be demonstrated in the following example. Alternatively, one can optimally translate the signals in time [12] or assume that the memory has a multi-dimensional structure [21]. Both of these approaches are still under investigation. Unfortunately, it appears that an exact treatment of this problem leads back to a rigorous description of the AE phenomena by elastodynamic models, which, as stated earlier, because of their complexity, we are trying to avoid. A compromise between an exact description and the heuristic empirical method presented here leads to an optimal multi-component deconvolution, similar to the one-component version [5]. Its development for the analysis of AE signals remains a topic of future research.

#### Characterization of Continuous AE

A second type of experiment was performed to demonstrate the applicability of the proposed learning system to the analysis of acoustic signals emitted during a manufacturing process. The drilling of a mild steel plate was selected as a representative processing operation.

The acoustic emission signals from a cutting process can be treated as a sta-

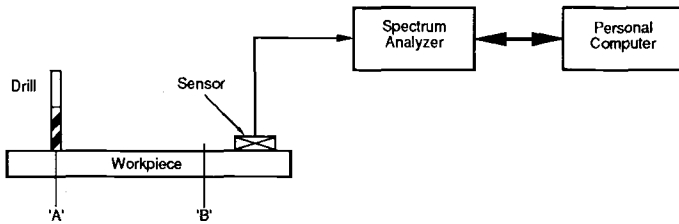


Figure 6: Experimental setup used to investigate the drilling process.

tionary random process over short time intervals. The representative signals from such a process are conveniently described in terms of their spectral density which is easily determined using a standard spectrum analyzer. The experimental setup that was used for this set of experiments is shown in Fig. 6. The experiments were carried out on a steel workpiece of dimensions  $145 \times 60 \times 15 \text{ mm}^3$  using a 3 mm diameter drill. The cutting speed was 55 m/min at the feed rate of  $4 \mu\text{m}/\text{revolution}$ .

The AE signals from the transducer were transformed in the spectrum analyzer into their corresponding spectral densities. The normalized records were represented by 20 components, which were approximately logarithmically distributed over the spectral interval between 100 Hz and 5 kHz. To these were added an additional 10 components to encode the logarithmic scale factor of the signal amplitudes. The input vector was then completed from the keyboard by appending a descriptor related to the drilling process. The features which were encoded included the drilling position, the drill condition, etc. This encoding required an additional ten components of the pattern vector. For each feature, one of the vector components was set equal to 1, while the remaining were left equal to 0. The complete pattern vector thus consisted of 40 components. This was applied as the input for the development of the auto-associative memory of the processor. For the learning, the same delta rule as used in the previous example was applied.

Training samples were recorded at free run and while drilling at two different sites on the plate, at A and B. The drilling at site A was repeated with a worn drill. The corresponding typical spectral density records are shown in Fig. 7. The signals were normalized and then transformed into thirty components corresponding to the signal portion of the input vector. However, because of the chaotic nature of the drilling process, the spectral density records measured over short time intervals of a few seconds, were statistically changing. Therefore three repeat samples were taken to represent each operation. Typical examples of pattern vectors from the training set are shown in Fig. 8.

After learning, the system could be used as an adapted analyzer to which the AE signals were input and the missing descriptors of the process were estimated by the auto-associative recall. Not surprisingly, when the input vector is similar to more than one training vector, then the recall is comprised of a mixture of the corresponding descriptors. In this case the amplitude distribution in that segment of the pattern vector representing the descriptor of the cutting process does not

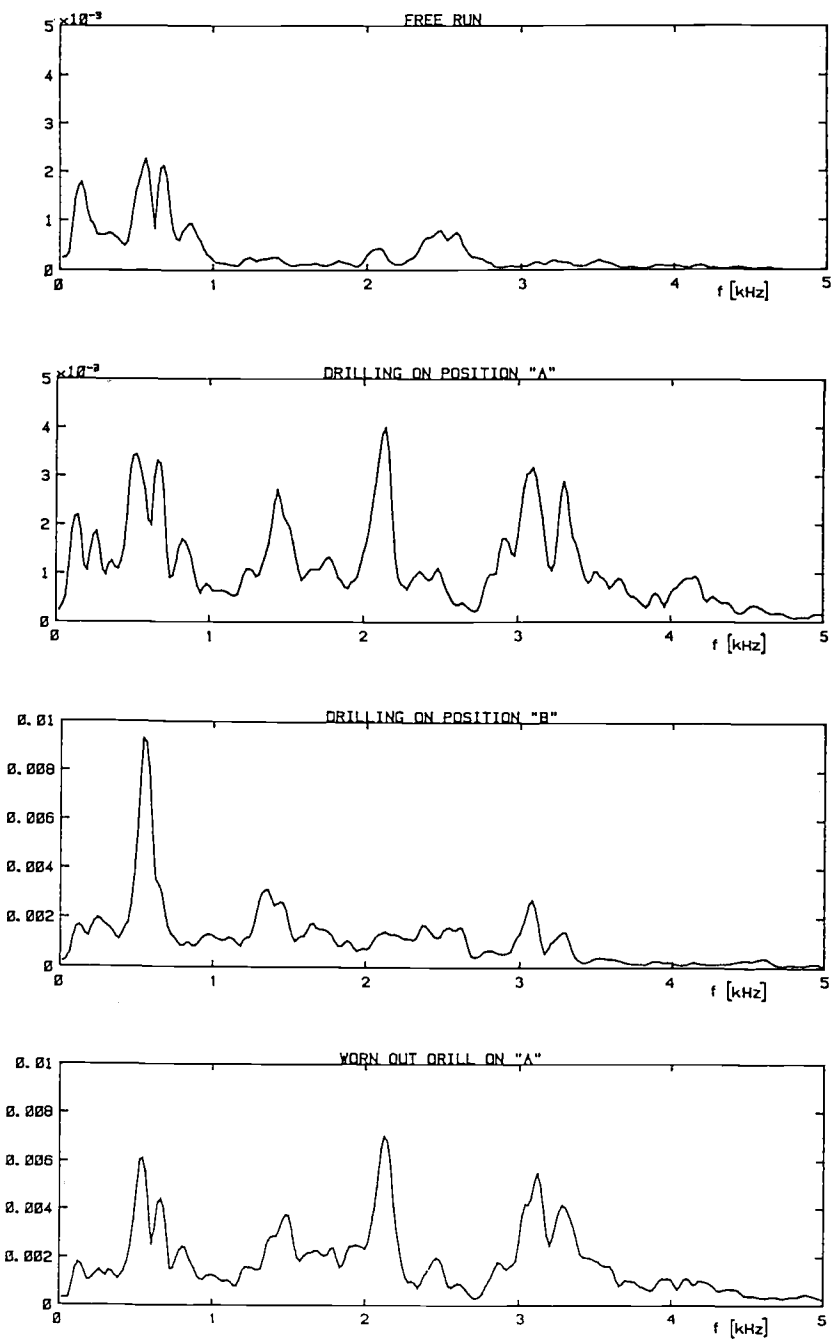


Figure 7: The set of typical AE spectral densities recorded during various phases of the drilling operation. The vertical, linear amplitude scale is the spectral density in volts.

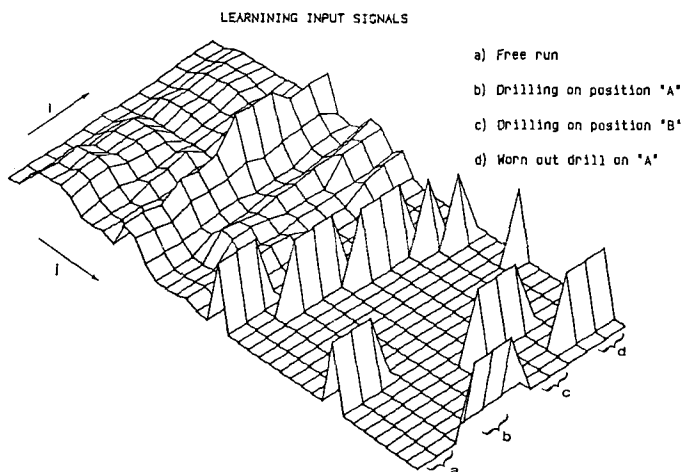


Figure 8: The set of completed training signals corresponding to the drilling operation.

exhibit a sharp peak and hence, the correct value of the descriptor cannot be easily determined. In order to circumvent this decision problem and to permit an automated identification of the manufacturing process, a second layer was introduced into the network. With this, the maximum of the amplitude distribution in the descriptor portion of the output pattern vector was determined and the corresponding descriptor index was supplied as a representative one for the process. The second layer was composed of laterally interconnected neurons, which interact by mutual inhibition [19]. A signal from the previous layer, corresponding to the descriptor amplitude, was input to each neuron. Because of lateral inhibition, only that neuron which was most strongly excited by the input signal attained a high excitation state, while the others were inhibited to remain in a low excitation state. The excitation signals from this layer could be applied for the automatic control of the manufacturing process or for displaying the optimal descriptor. The effect of the second layer is equivalent to searching for the maximum of a set of digitized data, which can be performed sequentially by standard maximum searching algorithms but this is not elaborated here.

In order to test the ability of the system to identify features of the drilling process, the input vectors consisting of only pre-processed AE signals were supplied as input to the system. Fig. 9 shows the records of the input signals together with the corresponding, recovered outputs in which the process descriptors were estimated by the auto-associative recall. In the majority of cases the proper descriptor of the process is already revealed from a visual examination of the vectors. An estimate of the system's performance with this example shows that it produced an approximately 90% correct estimation of the process descriptors. Errors cannot be completely avoided because of the inherently chaotic nature of the machining process and the dependence of the spectral distribution on the properties of the environment which are not very reproducible. A typical example is the strength

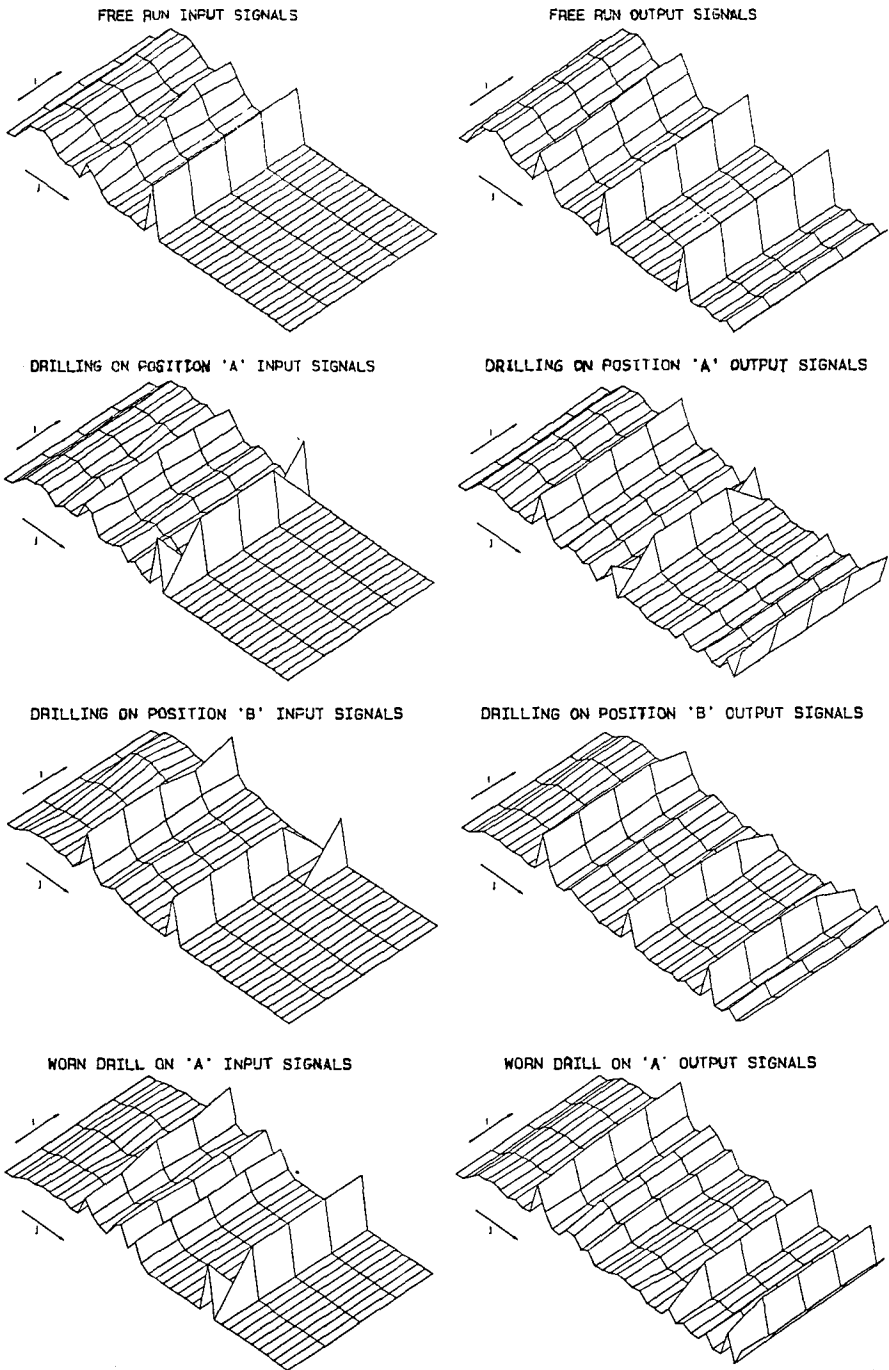


Figure 9: The set of input and corresponding output signals from the auto-associative memory. The descriptors are correctly recovered by the auto-associative recall.

of the clamping of the specimen and the cutting tool.

## CONCLUSIONS

We have summarized in this paper recent work utilizing an adaptive learning system to the characterization of acoustic emission phenomena. The processing system is comprised of an associative memory which resembles a neural network. Two examples were described which illustrated the operation of such a system. The example in which discrete AE signals were analyzed, demonstrated that a trained auto-associative system is capable of solving simple inverse or forward problems related to the determination of AE sources from the detected signals and vice versa. For this purpose no elastodynamic theory was needed since the method is completely empirical. The structure of the processing procedure was obtained from consideration of an exact description of the elastodynamic phenomena and it resembles a simple neural network.

It is recognized that one of the obstacles for the further application of the method presented here is the lack of typical AE sources needed for the training of the system in real applications. Simulated signals obtained by breaking a pencil lead are somewhat artificial and possibly not possessing equivalent source characteristics as those to be detected in the actual application. This problem corresponds to the reliable calibration of an AE system, which, up to now, is also only possible in special cases. As a consequence, the neural network cannot be properly trained and for this reason it cannot yet be applied to many structural integrity monitoring applications.

The applicability of the proposed auto-associative system to the analysis of continuous AE signals was demonstrated, provided that a spectrum analyzer is included as a pre-processor in the measurement system. By employing the spectral density data in the formation of the pattern vectors, a time-invariant presentation of the AE signal characteristics was obtained. In a sense, such an AE system resembles the auditory system of an intelligent being. When a manufacturing process in its various phases generates acoustic emissions of significantly different spectral distributions then the proposed adaptive analyzer is capable of correctly recalling the descriptors of the process from the detected AE signals. However, in those instances when the characteristics of the signals emitted during different phases of a process are very similar, then the characterization of the process from these signals becomes less reliable. In the example presented here, it was convenient to include in the processing network a second layer by which the optimal descriptor of the process was determined. A further step would be the connection of both or even more layers and the application of back-propagation algorithms for a complete adaptation of the network [16]-[19].

One important concluding remark can be made. The derivation presented here corresponds to a quasi-linear system in which the learning was achieved by a non-linear delta rule, but whose operation during the processing phase is linear. However, a linear system is inherently limited in its ability to identify features of machining processes which are characteristically non-linear chaotic. The prob-

lem remains how best to develop a general, non-linear, adaptive system by which manufacturing processes could be identified on the basis of acoustic emission signal analysis. There are two main problems. One is related to the non-linear formation of the memory during learning and the second involves the non-linear recall during analysis. The first problem appears to be solvable by a self-organization of information processing units [23], while for the second problem, an *optimal statistical estimation*, based on a conditional average, may be applicable [24]. It should be possible to implement both solutions in adaptive systems comprising a new generation of adaptive analyzers which can be realized as soon as low cost, parallel computers, capable of simulating the operation of neural networks in real time, become available.

#### ACKNOWLEDGEMENTS

This work has been supported by a contract to the Faculty of Mechanical Engineering of EK University by the Research Community of the Republic of Slovenia. Partial support has also been derived from grant MSM-8904384 from the National Science Foundation. Use of the facilities of the Materials Science Center at Cornell University is also acknowledged.

#### REFERENCES

- [1] Miller, R. K. and McIntire, P., Eds., *Acoustic Emission Handbook*, Vol. 5 of *Non-destructive Testing Handbook*, ASNT, Columbus, OH, 1988.
- [2] Scruby, C. B., "Quantitative Acoustic Emission Techniques", Chapt. 4, in *Research Techniques in Nondestructive Testing*, Vol. VIII, R. S. Sharpe, Ed., Academic Press, London, 1985, pp. 141-210.
- [3] Sachse, W., "Applications of Quantitative AE Methods: Dynamic Fracture, Materials and Transducer Characterization", in *Solid Mechanics Research for Quantitative Non-destructive Evaluation*, J. D. Achenbach and Y. Rajapakse, Eds., Martinus Nijhoff Publ., Dordrecht 1987, pp. 41-64.
- [4] Tarantola, A., *Inverse Problem Theory*, Elsevier, Amsterdam, 1987.
- [5] Grabec, I., "Optimal Filtering of Transient AE Signals", in *Ultrasonics International '85: Conference Proceedings*, Butterworth Scientific, Ltd., Surrey, UK, 1985, pp. 219 - 224.
- [6] Miller, R. K., Dornfeld, D., Hamilton, A., Mitchell, J., and Yee, K., "Process Monitoring with Acoustic Emission", Sect. 14, in *Acoustic Emission Handbook*, Vol. 5 of *Non-destructive Testing Handbook*, ASNT, Columbus, OH, 1988, pp. 467-511.
- [7] Grabec, I., "Chaotic Dynamics of the Cutting Process", *International Journal Machine Tools Manufacturers*, Vol. 28, 1988, pp. 19-32.

- [8] Grabec, I. and Sachse, W., "The Application of an Intelligent Signal Processing System to AE Analysis", *Journal of the Acoustical Society of America*, Vol. 85, 1989, pp. 1226-1235.
- [9] Grabec, I. and Sachse, W., "Experimental Characterization of Ultrasonic Phenomena by a Neural-like Learning System", in *Review of Progress in Quantitative Nondestructive Evaluation*, Vol. 8A, D. O. Thompson and D. E. Chimenti, Eds., Plenum Press, New York, 1988, pp. 649-656.
- [10] Grabec, I. and Sachse, W., "Application of an Intelligent Signal Processing System to Acoustic Emission Analysis", in: *Progress in Acoustic Emission IV*, I. Kimpara, Ed., Japanese Society of NDI, Tokyo, 1988, pp. 75-80.
- [11] Grabec, I. and Sachse, W., "Experimental Characterization of Ultrasonic Phenomena by a Learning System", *Journal of Applied Physics*, Vol. 66, 1989, pp. 3993-4000.
- [12] Grabec, I., Zgonc, K. and Sachse, W., "Application of a Neural Network to Analysis of Ultrasonic Signals", in *UI'89: Conference Proceedings*, Butterworth Scientific, Ltd., Surrey, UK, 1989, pp. 796-801.
- [13] Govekar, E., Grabec, I. and Peklenik, J., "Monitoring of a Drilling Process by a Neural Network", *CIRP Symposium on Manufacturing*, Stockholm (1989). In Press.
- [14] Šribar, R., Možina, J. and Grabec, I., "Optoacoustic Monitoring of Laser Manufacturing Process by a Neural Network", in *UI'89: Conference Proceedings*, Butterworth Scientific, Ltd., Surrey, UK, 1989, pp. 211-218.
- [15] Kohonen, T., *Self-organization and Associative Memory*, Springer Verlag, New York, 1984.
- [16] Rumelhart, D., McClelland, J. L., *Parallel Distributed Processing*, Vols. I and II, The MIT Press, Cambridge, MA, 1984.
- [17] Grossberg, S., Ed., *The Adaptive Brain*, North-Holland, Amsterdam, 1987.
- [18] Arbib, M. A., *Brains, Machines and Mathematics*, Springer Verlag, New York, 1987.
- [19] Kohonen, T., "An Introduction to Neural Computing", *Neural Networks*, Vol. 1, 1988, pp. 3-16.
- [20] Duda, R. O. and Hart, P. E., *Pattern Classification and Scene Analysis*, John Wiley and Sons, New York, 1973.
- [21] Widrow, B. and Winter, R., "Neural Nets for Adaptive Filtering and Adaptive Pattern Recognition", *Computer*, Vol. 21, 1988, pp. 25-39.



- [22] Spanner, J. C., Brown, A., Hay, D. R., Mustafa, V., Notvest, K. and Pollock, A., "Fundamentals of Acoustic Emission Testing", Section 1 in *Acoustic Emission Handbook*, R. K. Miller and P. McIntire, Eds., Vol. 5 of *Non-destructive Testing Handbook*, ASNT, Columbus, OH, 1988, pp. 27-33.
- [23] Grabec, I., "Self-organization Based on the Second Maximum-entropy Principle", *Artificial Neural Networks*, Conference Publication No. 313, Institute for Electrical Engineers, London, 1989, pp. 12-16.
- [24] Grabec, I. and Sachse, W., "Automatic Modeling of Physical Phenomena: Application to Ultrasonic Data", Materials Science Center Report #6771, Cornell University, Ithaca, NY, 1989. Submitted for publication.

# **Structural Monitoring Applications**

Hervé M. Barthélémy

PERIODIC INSPECTION OF COMPRESSED GAS CYLINDERS AND TRANSPORT  
VESSELS BY USING ACOUSTIC EMISSION TESTING

---

REFERENCE : Barthélémy, H.M., "Periodic Inspection of Compressed Gas Cylinders and Transport Vessels by Using Acoustic Emission Testing", Acoustic Emission : Current Practice and Future Directions, ASTM STP 1077, W.Sachse, J. Roget, and K. Yamaguchi, Eds., American Society for Testing and Materials, Philadelphia, 1991.

ABSTRACT : Gas cylinders and large transport vessels used for industrial compressed gases are subjected to hydrostatic retests. In this paper are presented results of an investigation concerning how to apply acoustic emission tests during such periodic inspections to detect flaws, i.e. internal corrosion and cracks. In conclusion a method for the periodic inspection (hydrostatic test with an acoustic emission testing) of such vessels is proposed. This method allows safe extension of the interval between re-tests.

KEYWORDS : periodic inspection, gas cylinders, pressure vessels, acoustic emission, flaws detection.

Containers for compressed gases used by industrial gas companies, whether single gas cylinders or big transport vessels, more than 1 m in water capacities (Fig. 1) are subjected every 5 to 10 yr to an official test. This test consists of an external and internal visual examination of the vessel, followed by a hydrostatic test at 1.5 times (in Europe) or 5/3 times (in North America) the service pressure. The cylinder or transport vessel should not have any leak at the test pressure. In North America, this hydrostatic testing is performed in a water jacket. The vessel fails the hydrostatic test by leaking or bursting, or also if the permanent expansion exceeds 10 percent of the measured total expansion.

Application of acoustic emission testing to periodic inspection of tubes in compressed gas service [1] has allowed some industrial gas companies (since early 1983), to use acoustic

Dr Barthélémy is Materials Manager at L'Air Liquide, 75, quai d'Orsay, Paris, 75321, France

emission testing in lieu of hydrostatic testing [2], [3]. We have, at this time, carried out investigations to check by ourselves the actual possibility of detecting flaws affecting compressed gas vessel [4]. Additional tests [5], [6] more recently allowed us to propose a re-testing method of compressed gas vessels making use of Acoustic Emission.

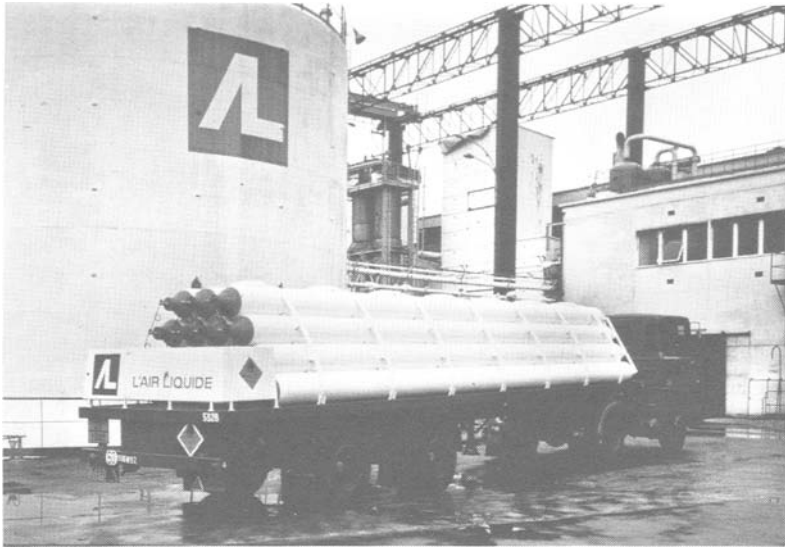


FIG. 1 - Tube trailer for transport of gaseous hydrogen

#### VARIOUS TYPE OF FLAWS

Previous investigations [6] showed us that in the case of compressed gas vessels two types of flaws are likely to occur :

- . corrosion or oxidation located inside or outside the cylinder
- . cracking located on the cylinder or tube wall.

To check the reliability of the AE method proposed, tests were carried out :

- . on internally corroded cylinders
- . on cylinders with artificially produced flaws.

These artificially produced flaws were mainly fatigue cracks. The method consists of creating, on the external surface of a cylinder, a geometrical flaw i.e. flat and notch with a rectangular bottom (see Fig. 2) on which a crack is initiated by hydraulic cycling from atmospheric pressure to the maximum service pressure of the cylinder. The crack initiation and propagation are monitored using an extensometer (Fig. 3). The maximum spread (ms) of the notch during the pressure cycles is recorded. When the crack is initiated, this spread

increases and continues increasing during propagation. It is therefore possible by monitoring this parameter (ms), to make cracks of different depths. In addition, these cracks being initiated on the external surface, it is possible to confirm their presence using magnetoscopy before acoustic emission testing. Other types of artificial flaws, flaws involving a notch, or arc burns, were also made.

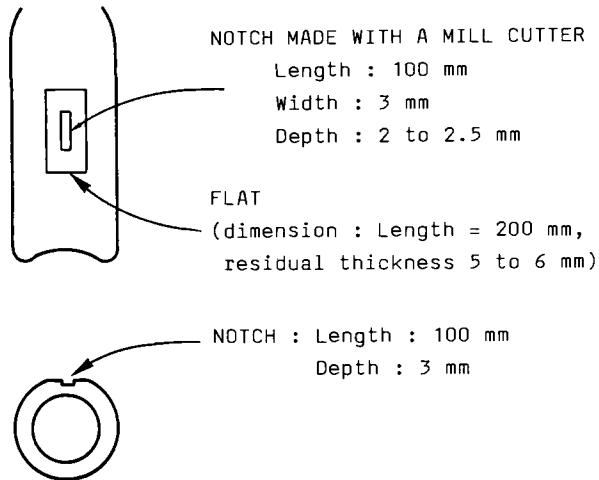


FIG. 2 - Shape of the notches machined on the gas cylinders

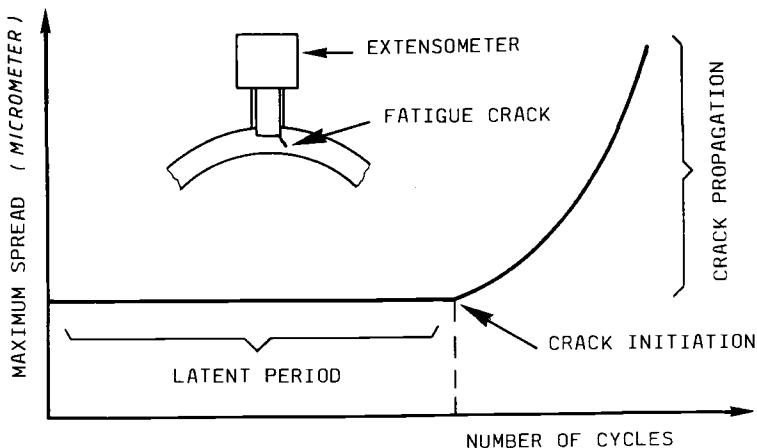


FIG.3 - Principle of the method for fatigue cracks production and detection using an extensometer

Such tests were mainly carried out on Cr-Mo quenched and tempered steels (see Table 1) gas cylinders with a water capacity of 0.05 m<sup>3</sup> (50 l) but more than 15 tests were carried out on flawed big transport vessels (sometimes more than 1 m<sup>3</sup> in water capacity, the largest ones being 0.558 m in diameter and 10.5 m in length).

TABLE 1 -- Chemistry, heat treatment and mechanical properties of cylinders tested

Chemistry (percent by weight)

C	Mn	P (max)	S (max)	Si	Cr	Mo
0.30/0.38	0.70/1.00	0.035	0.035	0.20/0.40	0.20/1.20	0.15/0.40

Heat treatment

Quenched in oil or other suitable medium and tempered at 640°C

Mechanical properties

Yield strength (MPa)	Ultimate tensile strength (MPa)	Elongation (percent)
750/850	880/1050	16/18

METHOD AND TEST CRITERIA

Tests were carried out on vessels equipped with two acoustic emission sensors, one located close to each end. They were performed during the hydrostatic pressurization, from atmospheric pressure up to a pressure which could at least detect the flaw, and in most cases even up to the failure of the vessels, in order to evaluate the difference ( $\Delta P$ ) between detection pressure and burst pressure. AE equipment used was previously described [6]. The flaw was considered to be effectively detected as soon as a pronounced increase in emission occurred, and when that emission corresponded to the flaws artificially produced (Fig. 4). The emission were recorded also as a count rate i.e., the total count per unit of time (Fig. 5) ; this makes it is possible to easily define the threshold rate above which the defect being detected can actually be considered dangerous. In our case this threshold count rate was 10<sup>3</sup>/10 sec).

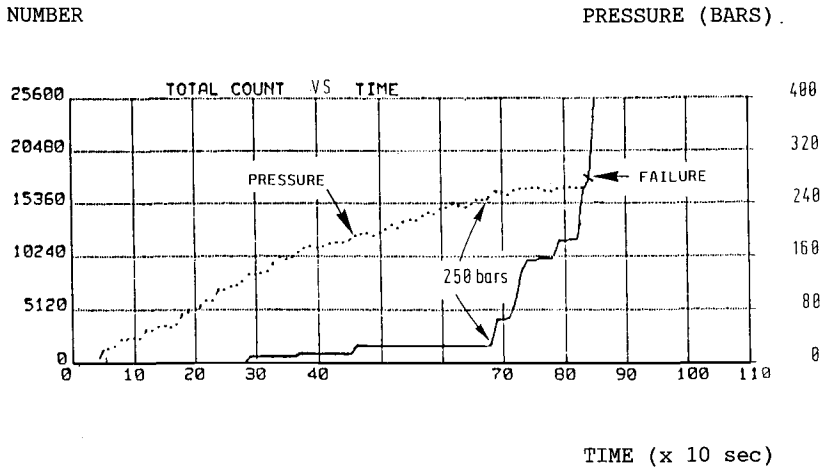


FIG. 4 - Example of crack detection -  
AE recorded as total count versus time + pressure

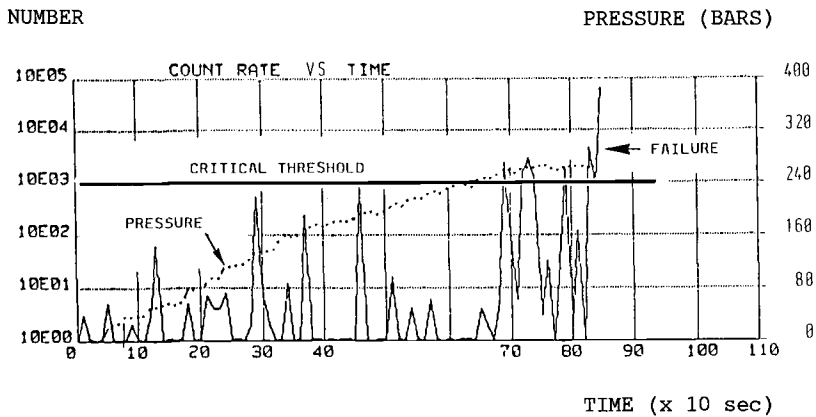


FIG. 5 - Example of crack detection - AE recorded  
as total count rate versus time + pressure

#### AE TEST RESULTS

Some results concerning fatigue cracks, notch-type flaws and arc burns on gas cylinders are compiled in Table 2. It was found that DP is equal to the minimum pressure which corresponds to a threshold count rate of  $10^3/10$  s. Peak amplitudes of acoustic emission recorded when testing cylinders with fatigue cracks were in the range of 50 to 70 dB for pressure greater than or equal to DP.

TABLE 2 - Crack, notch and arc burn types of flaws -  
summary of AE results on gas cylinders

Type flaw	SP (1) (bars)	BP (2) (bars)	$\frac{BP}{SP}$	DP (3) (bars)	$\frac{DP}{SP}$	$\Delta P = BP - DP$ (bars)
Crack	200	297	1.485	276	1.38	21
Crack	200	331	1.655	304	1.52	27
Crack	200	362	1.81	304	1.52	58
Crack	200	219	1.09	219	1.09	0
Crack	200	269	1.34	250	1.25	19
Crack	200	280	1.4	258	1.29	22

Type of flaw	SP (psi)	BP (psi)	$\frac{BP}{SP}$	DP (psi)	$\frac{DP}{SP}$	$\Delta P = BP - DP$ (psi)
Notch	2015	2437	1.21	2437	1.21	0
Notch	2015	5077	2.52	4677	2.32	400 (28 bar)
Notch	2015	5207	2.58	4007	1.99	1200 (82 bar)
Notch	2015	5021	2.49	5021	2.49	0
Notch	1800	3020	1.68	2400	1.33	620 (43 bar)
Arc	2015	5993	2.97	5700	2.83	293 (20 bar)
Burns	2015	5020	2.49	4585	2.27	435 (30 bar)

SP = Service pressure and/or cycling pressure to obtain fatigue crack.

BP = Burst pressure

DP = Acoustic emission detection pressure

1000 psi = 69 bars

AE results are also reported on the graph (Fig.6) giving

$\Delta P = BP - DP$  versus DP, with BP : burst pressure and DP : flaw detection pressure using acoustic emission. On the graph DP is expressed in terms of SP. It can be seen from this graph that :

- $\Delta P$  is at an optimum when burst pressure occurs between 1.5 SP and 2.5 SP
- $\Delta P$  is almost nil when the flaw is very serious ( $BP \leq 1.2 SP$ ) and when the flaw is extremely small ( $BP \geq 2.5 SP$ ).

Recent tests carried out on flawed tubes with notches (large transport vessels) confirmed results initially found on cylinders.



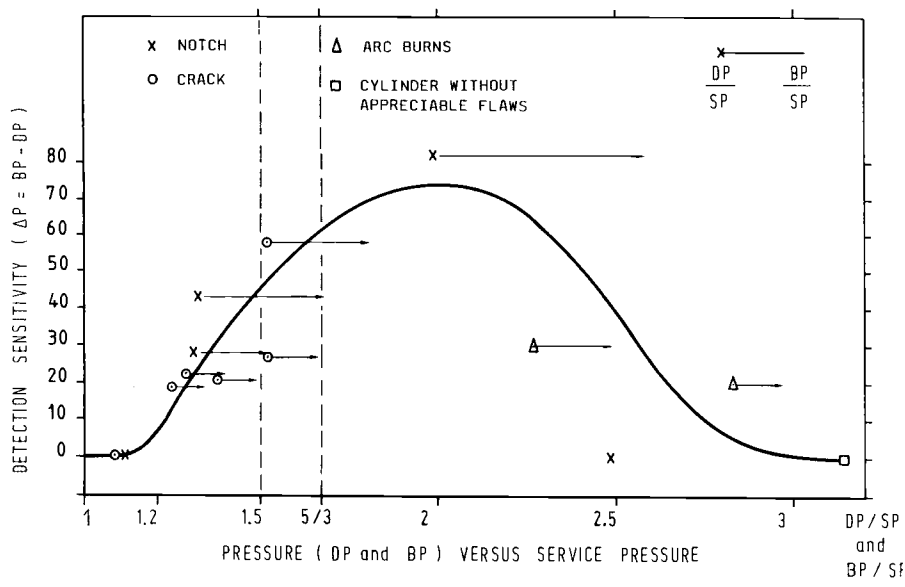


FIG. 6 - Sensitivity of AE detection versus flaws depth

Typical examples of notch locations on large transport vessels are given (Fig. 7 and 8) as well as detection graphs (Fig. 9 and 10). For such tests, pressure was increased up to the rupture pressure (Fig. 11a and 11b). Some results also are compiled in Table 3 where it is shown that it was possible when using only two sensors per vessel (one at each end) to detect flaw located either in the middle of the tube or at one end.

TABLE 3 -- Typical examples of notch detection on large transport vessels

Location of the notch	SP	BP	$\frac{BP}{SP}$	DP (bar)	$\frac{DP}{SP}$	P = BP-DP
MIDDLE	150	310	2.07	285	1.9	25
END	150	310	2.07	295	1.96	15
MIDDLE	180	338	1.88	268	1.48	70

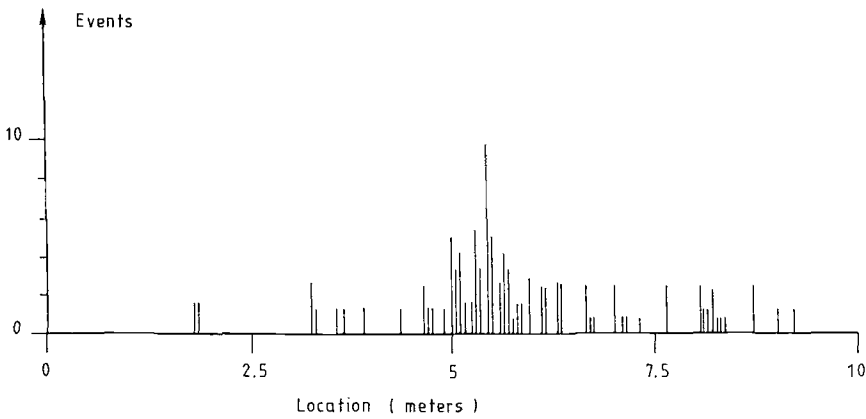


FIG. 7 - Large transport vessel N° 1 - Example of notch location by AE

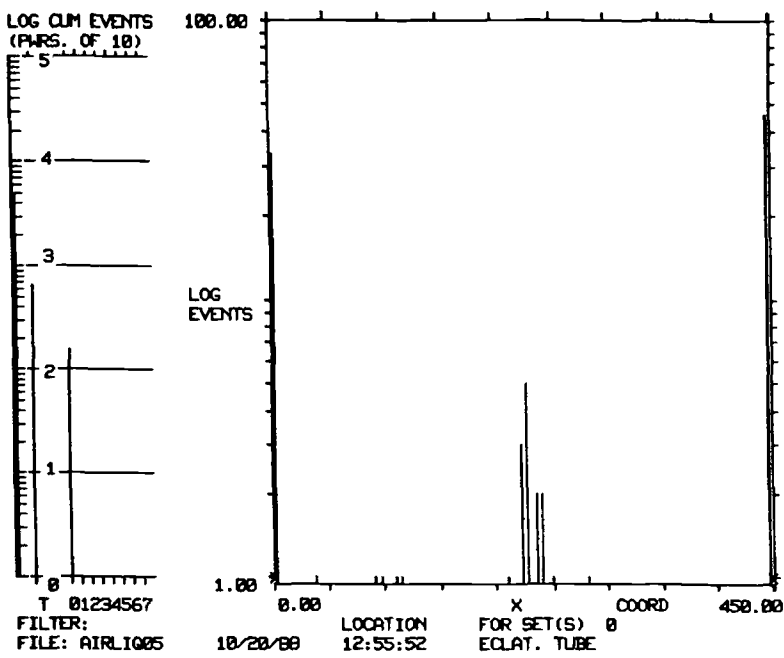


FIG. 8 - Large transport vessel N° 2 - Example of notch location by AE

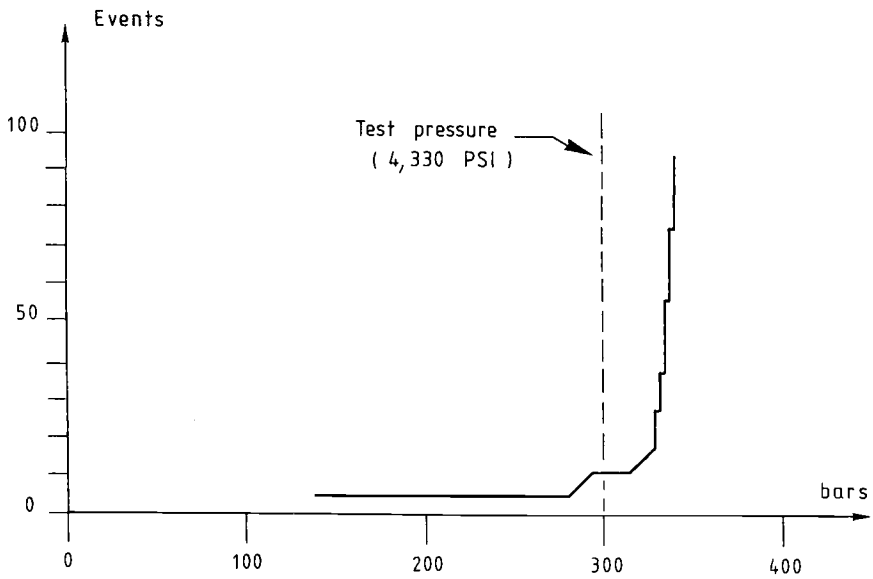


FIG. 9 - Large transport vessel N° 1 - AE versus time

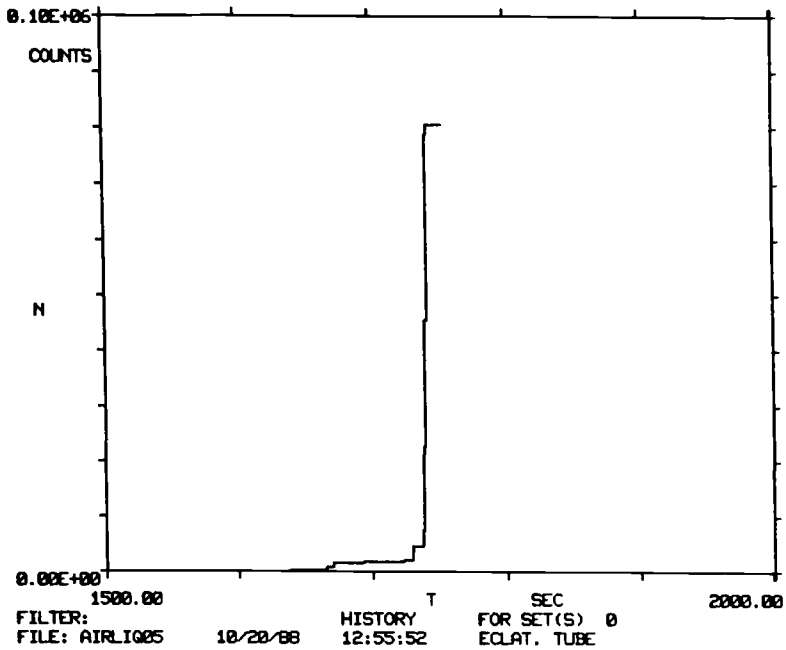


FIG. 10 - Large transport vessel N° 2 - AE versus time

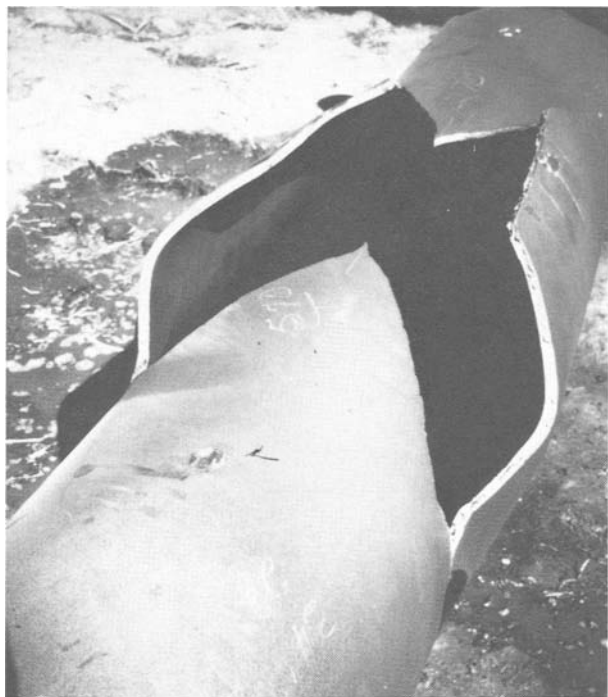


FIG. 11a - Large transport vessel N° 1 - Type of rupture



FIG. 11b - Large transport vessel N° 2 - Type of rupture

Additional tests were also performed on internally corroded cylinders [6]. It was confirmed that in these cases high emissions mainly occur when pressure is less than service pressure (Fig. 12 and 13). The AE events recorded during the beginning of the pressurization are due to the fracture of oxide layers.

It was also shown that hydrostatic tests (without permanent expansion test) performed at the same time as acoustic emission tests on vessels, are more accurate than hydrostatic tests performed in a water jacket for determination of expansion of the cylinders, as currently required in North America [6].

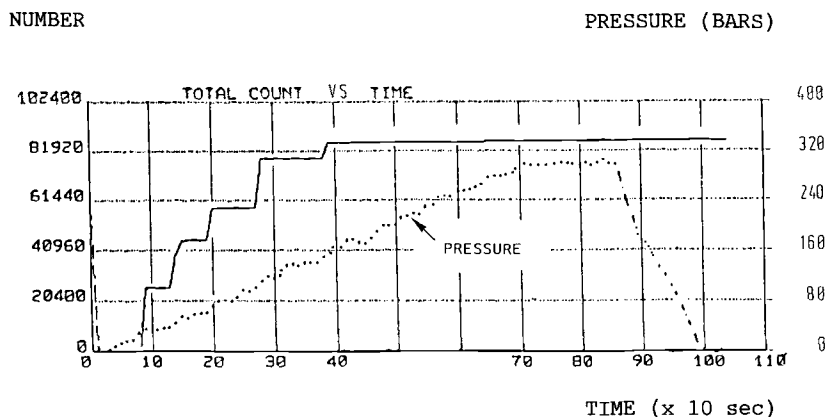


FIG. 12 - Example of corrosion detection - AE recorded as total count versus time + pressure

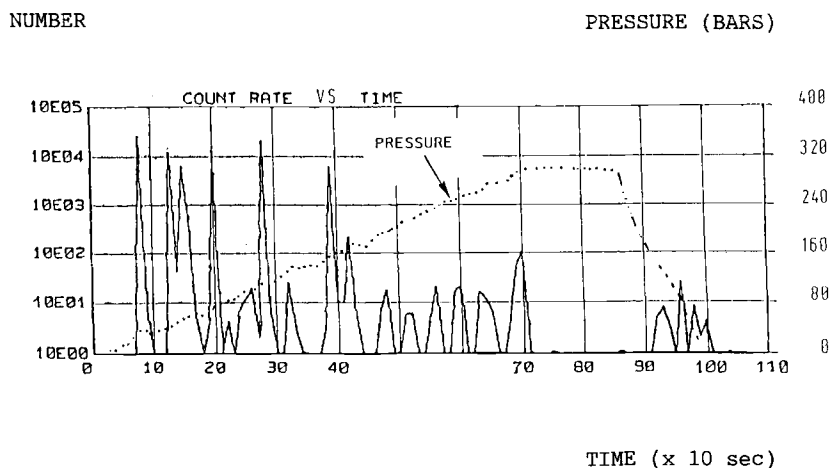


FIG. 13 - Example of corrosion detection - AE recorded as count rate versus time + pressure

## APPLICATION TO PERIODIC INSPECTION OF CYLINDERS AND TUBES

From our results, it follows that in order to best detect cracking, it is desirable to perform acoustic emission up to test pressure (tp). Therefore, we recommend to carry out hydrostatic pressurization from atmospheric pressure to tp. At the same time acoustic emission will be monitored, using two sensors located at each end of the vessel, and with appropriate measuring equipment. These will be performed without permanent expansion testing making it possible to inspect several vessels in a single operation while using multi-channel testing equipment.

If extensive emissions are noted at pressures below service pressure, the vessel probably has internal oxidation. Vessels should be examined through visual inspection and verification of thickness of the identified areas.

If extensive emissions are noted for pressures greater than service pressure, the vessel probably has a crack. Vessels should be examined through visual inspection and ultrasonic examination of the located emitting areas.

The critical level of emission above which signals are considered as "extensive emissions" will depend on the AE equipment used. For one of this equipment used, it was already mentioned that the critical count rate is equal to 10 /10 s.

## INTERVAL BETWEEN TWO PERIODIC INSPECTIONS

If acoustic emission testing is performed during hydrostatic testing, we have shown that it will also detect crack propagation. In addition, if there is no crack propagation, plastic deformation caused by the overload will occur at the tip of the crack. Such a plastic deformation results in blocking crack propagation, called crack retardation, during the subsequent pressure cycles, caused by the various fillings. This well known phenomenon has been extensively investigated for aluminium alloys [7]. Nevertheless, we decided to check this, using the system which has been used for testing the performance of artificial flaws of the fatigue crack type, a system which allows the detection and monitoring of crack growth (Fig. 2 and 3).

In Fig. 14, the result is given for one of these tests.

It was shown [6] that the "retardation effect" caused by the overload does block the crack (the propagation is stopped) for 1,500 to 3,000 cycles.

When considering that compressed gas cylinders and tubes are filled between 5 to 50 times a year, it can be noted that in extreme cases (50 times a year) and when using the minimum delaying effect (1,500 cycles), it would take 30 yr to trigger a new crack propagation process, following the blockage caused by the hydrostatic overloading.

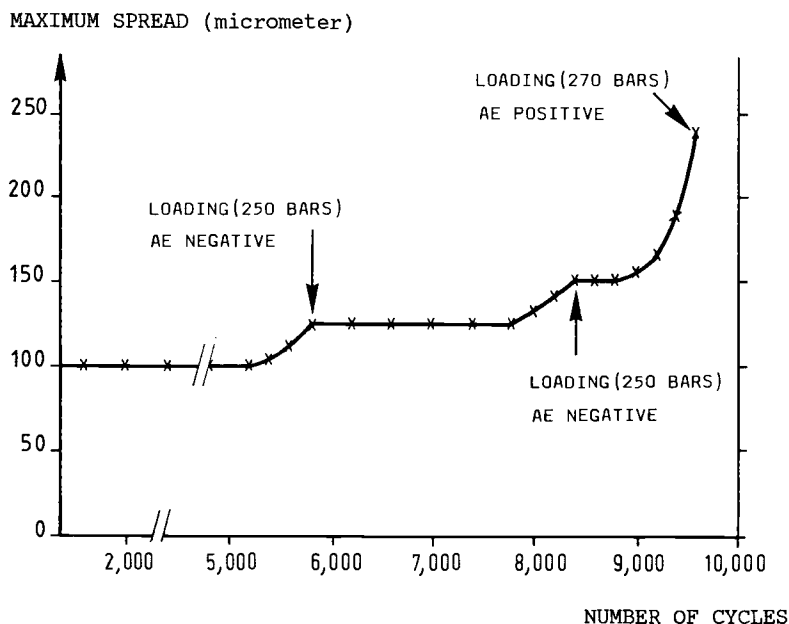


FIG. 14 - Delaying effect in crack propagation by overloading

Consequently, it is completely reasonable and safe to recommend a periodic inspection every 10 yr, since there will be then a safety factor greater than 3 on the life of the container.

Another safety factor that one could consider as well is the number of cycles for crack propagation. It was checked that if, for a gas cylinder, the pressurization is stopped as soon as the crack is detected by AE, it normally takes another 1,500 cycles for crack propagation up to the leak. This gives an additional safety margin which shows that it is possible to safely extend the retesting period when AE is performed during the hydro-test.

#### CONCLUSIONS

Acoustic emission of compressed gas cylinders and tubes will detect : internal oxidation and corrosion very easily ; fatigue cracks with greater difficulty than oxidations.

Our investigations showed that, to be sure of detecting cracks, it is best to perform this test during pressurization up to the test pressure (1.5 times service pressure in Europe, and 1.67 times service pressure in North America).

Consequently, we have recommended a method for the periodic inspection (hydrostatic test with an acoustic emission testing) of compressed gas containers, and we have shown that these tests can be performed every 10 yr, while still maintaining a very satisfactory safety margin.

Apart from the numerous technical advantages in comparison to the periodic inspection as presently performed, it appears to be of a high economical interest, to apply this method of periodic testing to trailer tube (which are normally re-tested every 5 yr).

#### REFERENCES

- [1] Blackburn, P.R., and Rana, M.D., "Acoustic Emission Testing and Structural Evaluation of Seamless, Steel Tubes in Compressed Gas Service", ASME Journal of Pressure Vessel Technology, Vol. 108, May 1986, pp 234-240.
- [2] US Department of Transportation - Research and Special Programs Administration, DOT-E8944, Mar. 1983.
- [3] US Department of Transportation - Research And Special Programs Administration, DOT -E 8944 (First revision), Dec. 1985.
- [4] Barthelemy H., "Acoustic Emission Test : An Alternative to Hydro-Retest for Compressed Gas Cylinders" Symposium AFIAP, Paris, France, Oct. 1986.
- [5] Barthélémy H. "How to Detect Flaws in Compressed Gas Cylinders and Tubes by Acoustic Emission" IOMA 1987 Annual Meeting Speech and IOMA Broadcaster, March-April 1988, pp 10-15.
- [6] Barthélémy H. "Periodic Inspection of Compressed Gas cylinders and Tubes - Flaw Detection Using Acoustic Emission Testing" ASME Journal of Pressure Vessel Technology, Vol. 110, May 1986, pp. 161 - 167.
- [7] Lankford, J., and Davidson, D.L., "The Effect of Overloads Upon Fatigue Crack Tip Opening Displacement and Crack Tip Opening/Closing Lads in Aluminium Alloys, "5th Int. Conf. on Fracture, Cannes, March 29-April 3, 1981.



DETECTABILITY OF DEFECTS IN REACTOR PRESSURE COMPONENTS  
BY LOCATION AND INTERPRETATION OF AE-SOURCES

---

REFERENCE: Sklarczyk C., and Waschkies, E., "Detectability of Defects in Reactor Pressure Components by Location and Interpretation of AE-Sources", Acoustic Emission: Current Practice and Future Directions, ASTM STP 1077, W. Sachse, J. Roget, and K. Yamaguchi, Eds., American Society for Testing and Materials, Philadelphia, 1991.

ABSTRACT: In the last years many hydrotests, cyclic fatigue tests and thermal shock tests have been carried out on reactor pressure vessels, which exhibited crack-like defects, with the aim to determine the conditions of detectability of growing and nongrowing cracks by acoustic emission (AE). The AE generated during these experiments has been recorded and analysed. Techniques for evaluation of AE-data have been developed which allowed the separation of AE-events from crack growth and crack surface friction by using the distributions of AE signal parameters, especially the rise time. Crack growth can be detected with high sensitivity at thermal shock and fatigue tests whereas detectability of crack surface friction increases with the amount of compressive stresses between the crack surfaces. At hydrotest only a low level AE is produced by nongrowing cracks due to the lack of compressive stresses.

KEYWORDS: acoustic emission, cracks, pressure vessel, signal analysis, localization, residual stress

In the frame of the German reactor safety research programme more than 20 experimental pressure hydrotests have been performed in the last seven years. All of them were surveyed by acoustic emission (AE). Three pressure vessels were available for these trials (fig. 1). All of these had artificial defects representing all types of defects which can occur. With regard to AE the goal of these experiments was the validation and further development of AE during hydrotest. Several commercial multichannel AE-systems were used and moreover more capable systems were developed.

Drs. C. Sklarczyk and E. Waschkies are research scientists at Izfp (Institut für zerstörungsfreie Prüfverfahren), University, Building 36, D-6600 Saarbrücken, FRG

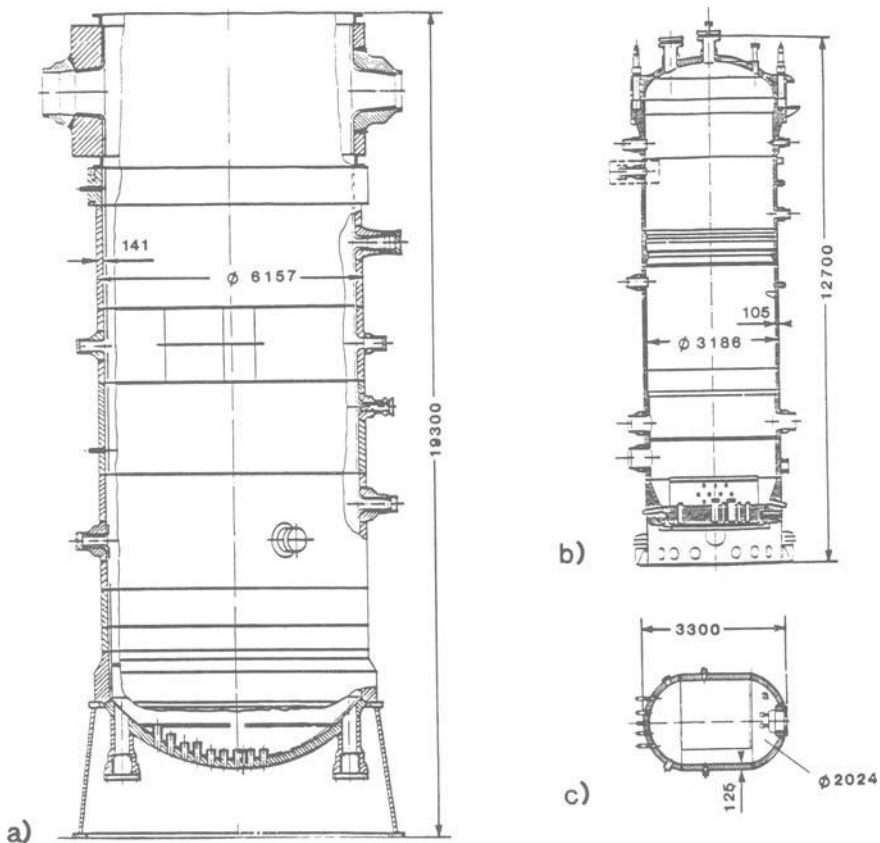


FIG. 1 Pressure vessels tested by AE-method  
 a) large vessel at MPA Stuttgart  
 b) HDR vessel  
 c) intermediate scale vessel ZB2

The experience leading to this very expensive series of experiments was that application of AE as available on the market on hydrotests of commercial vessels did not lead to conclusive results. The main reason for this was that crack growth of defects during hydrotest did not occur. As far as AE caused by friction did not occur or only on a very low level, AE could not be measured and evaluated reliably.

In this paper we give a brief summary of the improvements which were developed and approved during these experiments. This paper deals mainly with localization and signal processing for interpretation of different AE-source mechanisms like crack growth and crack surface friction.

## LOCALIZATION AND CHARACTERIZATION OF AE-SIGNALS

Localization of AE-Sources

Localization of AE-sources is not only important for determination of defect location but also to eliminate spurious noise. Commonly three probes are used for planar localization. In this case the sound velocity has to be inserted as a known constant value to calculate the source location. In many practical cases the real sound velocity is not constant and not known, especially when these signals propagate by dispersive guided waves. If triggering is done by constant amplitude threshold level, the real signal propagation velocity depends on amplitude of the signal. We have developed a four probe localization algorithm which considers the propagation velocity as unknown. In the four probe case the velocity is assumed to be the same for all passes from the source to the four probes. The details of this algorithm and the approval of it will be published elsewhere.

The efficiency of this algorithm is demonstrated in fig. 2 on an experimental vessel with flaws (indicated in fig. 2) and defected weldments (ZB2, vessel c in fig. 1). A hydrotest was performed and surveyed by AE. Along the corner of a patch which was inserted in the vessel and contained the three flaws F8 - F11 at the inner side of the vessel wall six AE-probes were installed. Localization was performed both with the planar three-probes-method with pre-given constant sound velocity and by the above mentioned four-probe-method where no value for the signal propagation velocity was inserted. The obtained results are shown in fig. 2; on the left side the three-probe-results are displayed. In the area of the flaws F8 and F11 and the middle weld seam much more signals were extracted by the four-probe-localization algorithm (right side of fig. 2). The achieved improvement is obvious. The localization method with 3 sensors handles the propagation velocities  $c_i$  from the AE-source to the sensors  $i$  as known values which are equal for all sensors  $i$  and fixed:

$$\begin{aligned} c_i &= c = \text{fixed} & r_i \times r_j & \text{path of flight difference} \\ c_i (r_i - r_j) &= \Delta t_{ij} & \Delta t_{ij} & \text{time of flight difference} \\ & & (r_i: & \text{distance between sensor and source}) \end{aligned}$$

In this case only that part of AE-signals is located correctly, which is propagating with this velocity. These are in our case only the signals around the nozzle. The inserted velocity was  $c = 3.5$  m/ms.

In the case of localization with 4 sensors the sound velocities  $c_i$  are also regarded as equal but not as a known fixed value but as unknown.

$$c_i = c, \quad 0 < c < c_1 \quad (c_1: \text{longitudinal wave velocity})$$

In this case, much more signals are located. Beside the signals from the nozzle also AE-signals from the flaws F8 and F10 are distinctly located.

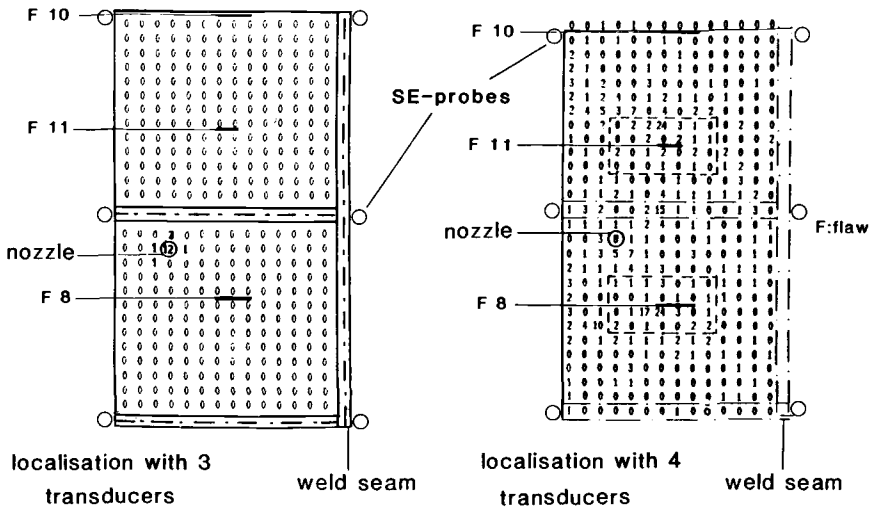


FIG. 2 Locations and numbers of AE-events of a hydrotest at the ZB2-vessel (comparison between two localizations algorithms)

#### Interpretation and Classification of AE-Events

Apart from the already mentioned hydrotests many trials have been carried out with different loading conditions in order to simulate the different possible types of real crack growth during the lifetime of a reactor pressure vessel. Following loading conditions have been applied:

- some thousand thermal shock tests at the edge of a nozzle and at the cylindrical part of a reactor pressure vessel (HDR, vessel b in fig. 1, see also [1-3]) which resulted in a macroscopic crack growth by fatigue and corrosion. Each thermal shock at the nozzle consisted in a cooling phase of 120 s and a reheating phase of 240 s. Cooling down was performed by injecting cold water at the location to be shocked. The interior of the vessel was filled with hot pressurized water (593 K, 11 MPa). The cracks opened at cooling down and closed at reheating [1-3].
- many thousand fatigue cycles by water pressurisation on a pressure vessel to produce real cracks and in service-crack growth (ZB2, vessel c in fig. 1)
- tensile tests in laboratory on fracture mechanical specimens made from reactor steels

In the frame of these investigations it has been found that the AE-signal parameters rise time (= time from the start to the absolute maximum of the signal), energy and duration exhibit characteristical distributions which can be used for classification and interpretation of AE-events from different sources like crack growth and crack surface friction whereby the signal rise time plays the most important role. This can be demonstrated by following examples: Fig. 3 shows that there exist two distinct maxima in the rise time distribution of located AE

recorded during some hundred thermal shocks on the nozzle of a pressure vessel (HDR). (The signal dead time used was 819  $\mu\text{s}$ , i.e. signals, whose time difference between end of the first signal and beginning of the second signal amounted to less than 819  $\mu\text{s}$ , were not separated but were concentrated to one single signal.) In fig. 4 it can be seen that most AE-events detected during a hydrotest on the same vessel possess long rise times similar to the right distribution in fig. 3. During this hydrotest no growth of the existing cracks occurred. The only possible AE-source during this hydrotest was crack surface friction. Therefore it can be concluded that friction events exhibit long rise times under the given experimental conditions. The AE-events with short rise time in fig. 3 can thus be assigned to crack growth.

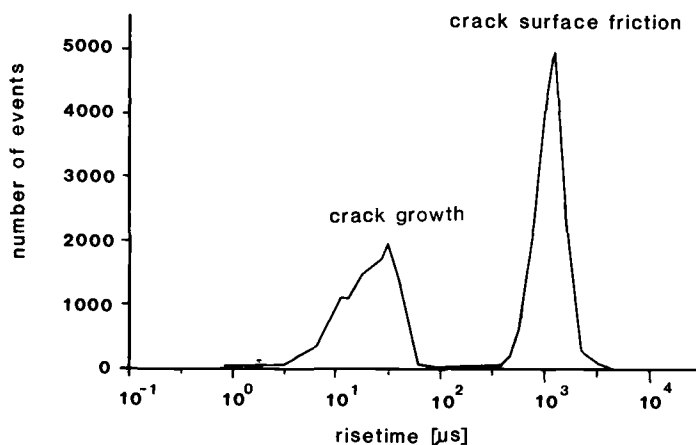


FIG. 3 Rise time distribution of AE-events during thermal shock test at the HDR-vessel (sum over 400 cycles)

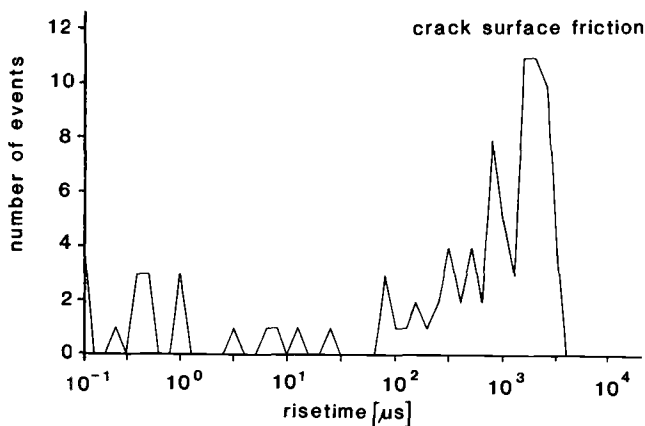


FIG. 4 Rise time distribution of AE-events during a hydrotest at the HDR-vessel

These results are verified by fracture mechanical tests on CT-specimens (thickness 50 mm). Fig. 5 displays two distinct rise time distributions of these tests: AE-events of the left distribution (solid curve) have been recorded during crack propagation. The right distribution (dashed curve) has been recorded during cyclic loading of pre-cracked specimens at low loads where no crack growth occurred. Then this AE is due to crack surface friction. As a result it can be concluded that small rise times are related to crack growth and longer rise times are related to crack surface friction. This agrees to the results gathered during the hydrotests and thermal shock experiments at the HDR-vessel.

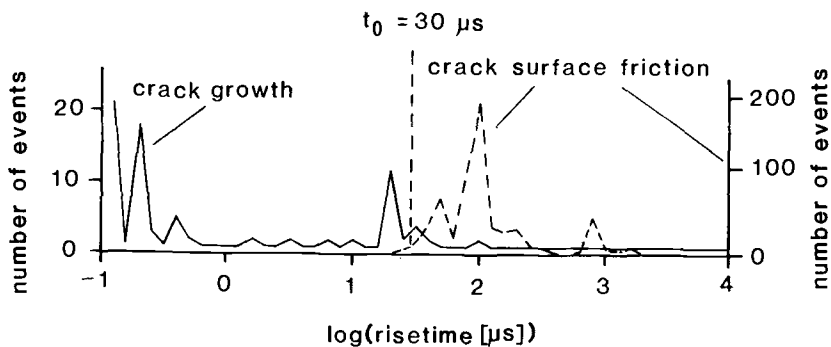


FIG. 5 Rise time distribution of crack propagation (solid) and crack surface friction (dashed) for CT-specimens

The limiting value  $t_0$  between these two groups depends on the experimental conditions.  $t_0$  is determined by the measured rise time resulting from broadening of an infinitely short ultrasonic test pulse (simulated crack growth signal) by sound propagation from the source to the transducer. It is given in our examples by  $t_0 = 50 - 100 \mu s$  for the HDR-nozzle (thermal shock) and  $t_0 = 30 \mu s$  for the CT-specimens. The value of  $t_0$  has to be estimated theoretically or experimentally for each test-setup.

The preference of the rise time compared to the other signal parameters is due to the fact that rise time is approximately independent from signal amplitude. This is not valid for e.g. the signal duration which obviously depends on amplitude. Thus rise time reflects the source lifetime if the signals are recorded in the nearfield. (The nearfield of a sound source extends to about five plate thicknesses [6].) Very short life times in the range of  $1 \mu s$  or less for microscopic crack growth events have been found by Wadley and Scruby and other researchers [5]. This coincides with the above given interpretation that short rise times are due to crack growth events. Correspondingly the distinctly longer rise times of AE-events from crack surface friction are obviously due to longer source lifetimes or to groups of events from different touching points which interfere and cannot be separated.

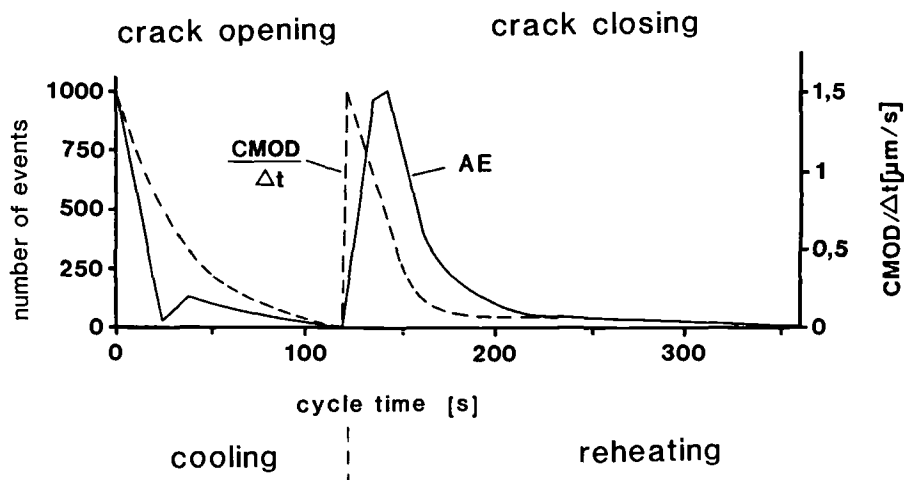


FIG. 6 AE-event rate (crack surface friction) and CMOD vs. cycle-time during thermal shock test at the HDR-vessel

This interpretation is also supported by fracture mechanical calculations: The solid curve in fig. 6 shows that the maxima of velocity of crack mouth opening displacement (CMOD) are found at the beginning of the cooling (0 s) and reheating (120 s) phase during thermal shock at the HDR-vessel. It can be seen that these maxima approximately coincide with maxima of those AE-signals (dashed curve) which exhibit long rise times [2]. In fig. 6 all signals with short rise times have been eliminated. Other calculations have shown that test phases with high rates of frictional AE are connected with large compressive stresses (up to 300 N/mm<sup>2</sup>) in the austenitic cladding material [4]: Fig. 7 shows the stress distribution in the vessel-wall of the HDR for several points of time during one thermal shock cycle. It can be seen that at the very beginning of the cooling phase at 0 s (this is equivalent to 360 s, see fig. 7 in the lower right corner) and at the beginning of reheating phase ( $t = 125$  s) there exist compressive stresses near the inner surface of the wall. Thus these time intervals where compressive stresses arise coincide with the maximum AE (fig. 6). These calculations show that the conditions which are necessary for a copious AE due to crack surface friction are fulfilled during thermal shock: a) relative movement of the rough crack surfaces (fig. 6) and b) compressive normal stresses between the crack surfaces (fig. 7).

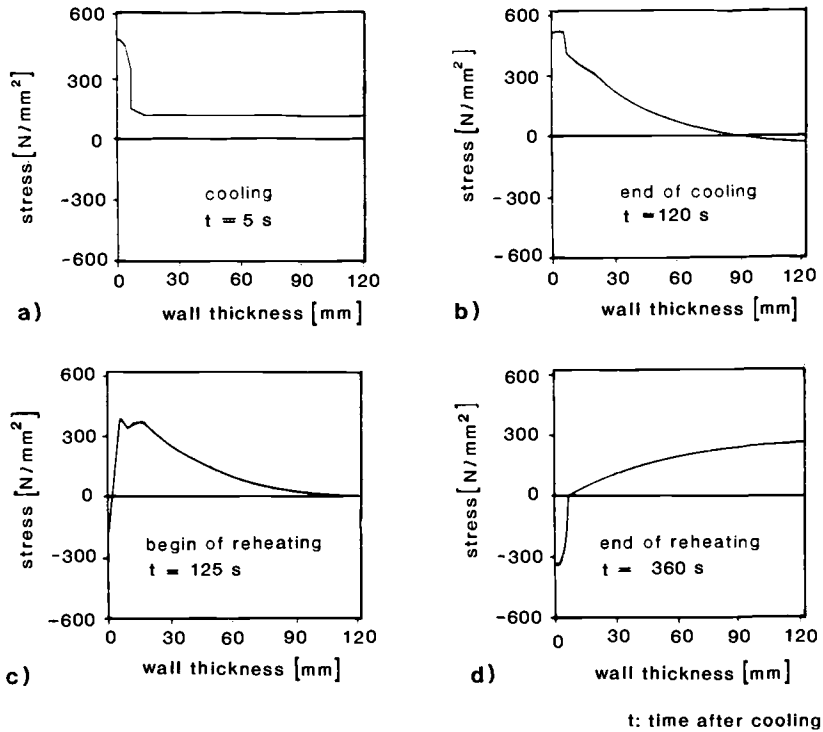


FIG. 7 Stress in the wall of the HDR-vessel during thermal shock test. The inner surface of the vessel lies at 0 mm; negative signs at the y-axis mean compressive stresses.

#### Transfer Functions of AE-Events

If the distance between transducer and source is greater than about five plate thicknesses it is necessary for interpretation of AE-events to perform a transfer correction of the signal parameters because sound waves are changed strongly by propagation in the component or specimen. The transfer functions are given elsewhere [6]. For dispersive lamb waves the rise time is proportional to the distance. At the above described experiments a transfer correction was not necessary because the transducers lay in the nearfield of the sources.

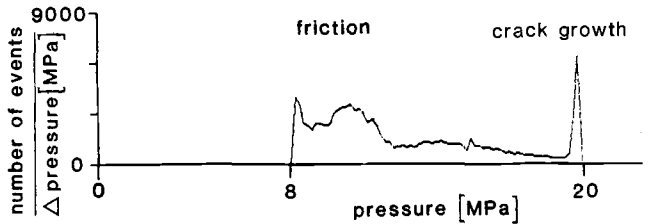
#### DETECTABILITY OF CRACKS

In the frame of the above mentioned tests it has been shown that the detection limit of spontaneously occurring stable crack growth by using AE-method lies in the range of a few  $\text{mm}^2$  [7]. This has been investigated for various types of crack growth: fatigue crack growth, crack propagation under monotonic increasing load and corrosion cracks. Fig. 8 gives an example of AE detected during fatigue crack growth (500 cyc-

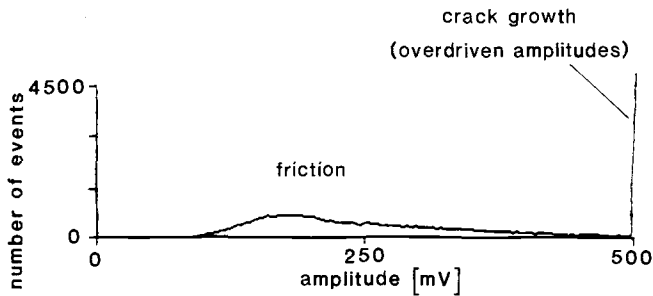


les,  $T = 513 \text{ K}$ ) of defects situated on the inner side of the wall of the pressure vessel ZB2 (fig. 1 and 2).

The AE-peak at pressure maximum can be assigned to crack growth because of the maximum stress intensity factor at the cracks whereas AE at lower pressure is likely to be due to crack surface friction (fig. 8 a). Most amplitudes of crack growth are higher than those of friction noise (fig. 8 b) and are overdriven, i.e. these amplitudes are beyond the measuring range of the AE-equipment.



a) AE-distribution versus pressure



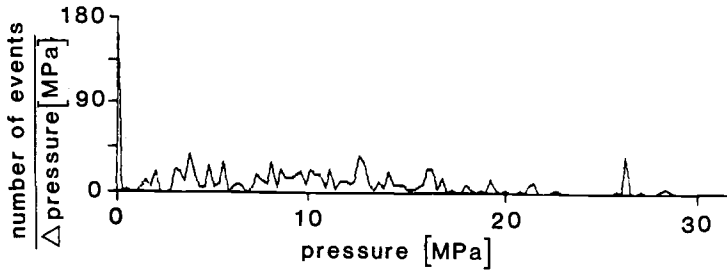
b) amplitude distribution

FIG. 8 Distributions of AE-events from 500 fatigue cycles at the ZB2-vessel

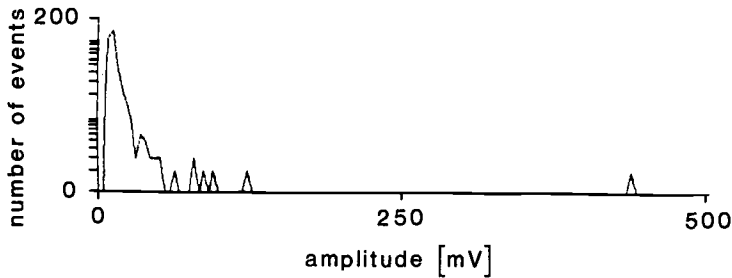
The detection limit of crack growth depends on the experimental conditions like stress state, steel type and structure. An important criterion is the crack velocity. A fatigue crack growth in the range of  $0.01 \text{ mm}^2/\text{s}$  was detectable [8].

One further aim of these tests was to examine whether AE-monitoring is a proper method to find non-growing defects during hydrotests. The results show that the detectability of nongrowing cracks during a hydrotest cannot be quantified up to now and depends on the special conditions of stress state and crack morphology. The AE-events recorded during hydrotests on pressure vessels (e.g. ZB2) exhibited only low maximum amplitudes, close to the threshold, even if macroscopic cracks exist in the vessel wall, but these cracks did not grow. Fig. 9 gives an example: fig. 9a shows that AE-events located during a hydrotest (ZB2) by using the four-transducer-algorithm are distributed over the whole pressure range and are low in quantity. In fig. 9b it can be seen

that these signals exhibit low amplitudes which are in contrast to the high amplitudes recorded during crack growth (fig. 8 b). The increasing of the pressure rate  $\Delta p/\Delta t$  (p:pressure, t:time) from 0.1 MPa/min. to about 20 MPa/min. yielded no better detectability.



a) AE-distribution versus pressure



b) amplitude distribution

FIG. 9 Distributions of AE-events from a hydrotest at the ZB2-vessel

The absence of an high amplitude-AE from crack surface friction can be explained by the lack of compressive stresses in the vessel wall [4]. This is displayed in fig. 10 which shows that there are only small compressive stresses in the vessel wall at the beginning of the hydrotest (curve a). During hydrotest this curve is shifted towards higher tensile stresses (curve b). In normal cases the conditions to generate frictional AE are not present during hydrotests of pressure vessels.

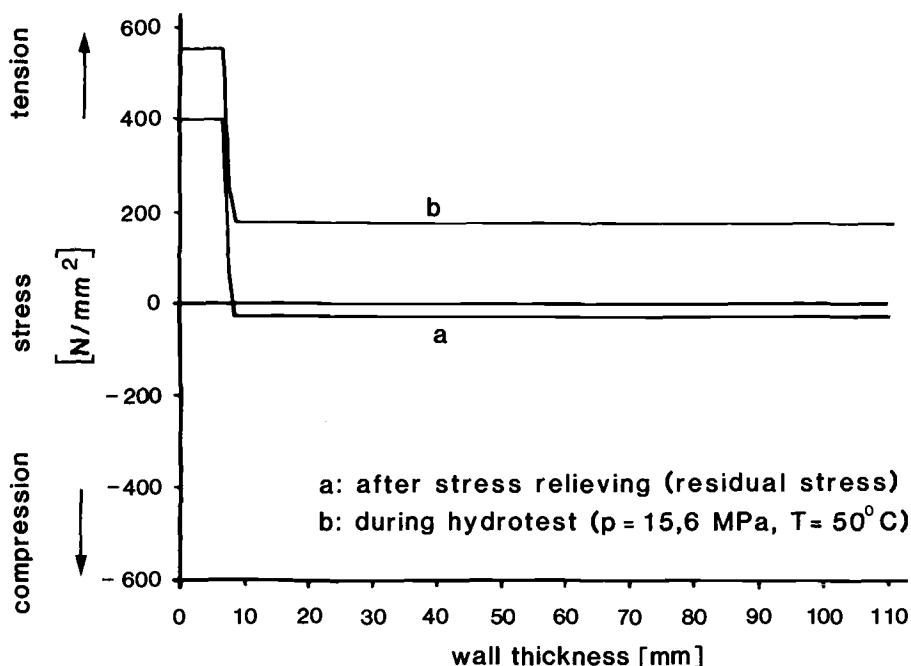


FIG. 10 Stress in the wall of the HDR-vessel

#### REFERENCES

- [1] Waschkies, E., Hepp, K., and Höller, P., NDT International, Vol. 19, 1986, 197 - 202
- [2] Deuster, G., Walte, F., Waschkies, E., and Neubrech, G. E., Proceedings of the 8th International Conference on NDE in the Nuclear Industry, Kissimmee, Florida, 17-20 Nov. 1986, 351 - 371
- [3] Neubrech, G. E., Walte, F., Waschkies, E., and Klein, M., Nuclear Engineering and Design, Vol. 112, 1989, 139 - 154
- [4] Gries, H., and Waschkies, E., Nuclear Engineering and Design, Vol. 106, 1988, 399 - 403
- [5] Wadley, H. N. G., Scruby, C. B., and Shrimpton, G., Acta Metallurgica, Vol. 29, 1981, 399 - 414
- [6] Waschkies, E., and Höller, P., International Journal for Pressure Vessels & Piping, Vol. 15, 1984, 151 - 157
- [7] Deuster, G., Waschkies, E., Maier, H.J., and Knoch, P., Conference Proceedings of the 13th MPA-Seminar, Stuttgart, FRG, 8 - 9 Oct. 1987
- [8] Final report of the research project RS 150675 of the GRS (Gesellschaft für Reaktorsicherheit, Cologne, FRG), 1989, in preparation

# **Deformation Studies**

Felix Zeides and Itzhak Roman

EFFECT OF PRE-EXPOSURE TO WATER ON THE ACOUSTIC EMISSION  
BEHAVIOR OF 2091-T3 Al-Li ALLOY

REFERENCE: Zeides F. and Roman I., "Effect of Pre-Exposure to Water on the Acoustic Emission Behavior of 2091-T3 Al-Li Alloy", Acoustic Emission: Current Practice and Future Directions, ASTM STP 1077, W. Sachse, J. Roget and K. Yamaguchi, Eds., American Society for Testing and Materials, Philadelphia, 1991.

ABSTRACT: The effect of pre-exposure to water with imposed weak ultrasonic field on the acoustic emission (AE) behavior of 2091-T3 Al-Li alloy was studied. AE characteristics were evaluated during tensile deformation utilizing a micro-computer based system and an rms voltmeter. Two types of AE were observed, initially, AE was of a continuous nature with a maximum at the yield, followed by a change to burst type AE coinciding with the onset of PLC serrations. A significant difference in AE behavior between as-received and pre-exposed material has been observed, especially in the yield region. The pre-exposed specimens gave rise to more intense AE activity manifested in higher peak amplitude AE events. Although the precise mechanism of the observed effect is not known, it is believed to stem from hydrogen charging that took place during pre-exposure, and which also caused reduction of the tensile elongation of the material.

KEYWORDS: acoustic emission, aluminium-lithium alloys, hydrogen charging, hydrogen embrittlement, ultrasonic field.

The growing interest in Al-Li alloys for advanced structural application is due to the decrease in density and increase in the elastic modulus with the addition of lithium (up to 3.5 w/o) [1]. As a result these alloys are good candidates

Dr. Zeides, researcher, and Professor Roman, Chairman of the division of Applied Physics and Materials Science, School of Applied Science and Technology, The Hebrew Univ. Jerusalem 91904, Israel.

for replacing the existing high strength aluminium alloys, primarily in aerospace applications. However, before this materializes, better understanding of fracture, isotropy and corrosion behavior of these alloys is desired [2]. In the present study, the effect of pre-exposure to water on the acoustic emission (AE) behavior of 2091-T3 Al-Li alloy was examined. Possible origins of the observed changes in AE behavior (as compared with that of reference, non exposed, samples) are discussed.

## EXPERIMENTAL

Longitudinal flat tensile samples employed in this study, were machined from a 2.5mm thick sheet of 2091 Al-Li alloy in the T3 conditions. The samples which were of the sheet thickness (2.5 mm) and had a 32mm gage, and were tested in a J.J. Loyd machine with a strain rate of  $10^{-4}$ /s in the as-received condition or after immersion in distilled water in an ultrasonic bath for three months. All samples were polished prior to testing. Acoustic emission characteristics were evaluated during tensile deformation utilizing a micro-computer based system (Model 5000, AET corp.) comprized of 175 kHz resonant transducer (MAC 175, AET), preamplifier (160, AET) with 125 to 250 kHz band pass filter and a rms voltmeter (201, AET).

## Results and Discussion

Typical load-displacement and the accompanying acoustic emission intensity - displacement curves for both the as-received and the pre-exposed samples are shown in Fig. 1, and in both cases, the AE behavior is qualitatively similar.

Continuous type AE was observed almost from the beginning of elastic deformation. The rms voltage level increased with load and exhibited a prominent peak close to the yield load. The decrease in rms voltage level during yielding was followed by numerous large AE bursts during work hardening which parallel stress level serrations (indicative of dynamic strain aging). Similar AE behavior was observed in another study on a 2.5 w/o Cu, 2 w/o Li, 1 w/o Mg Al-Li alloy with different heat treatment conditions [3]. There, it was suggested that the continuous peak associated with yielding is due to repeated shearing of the coherent  $\delta'$  precipitates, whereas the behavior of dynamic strain aging stems from the localized nature of slip brought about by the interaction of dislocations with mobile solute atoms in these alloys.

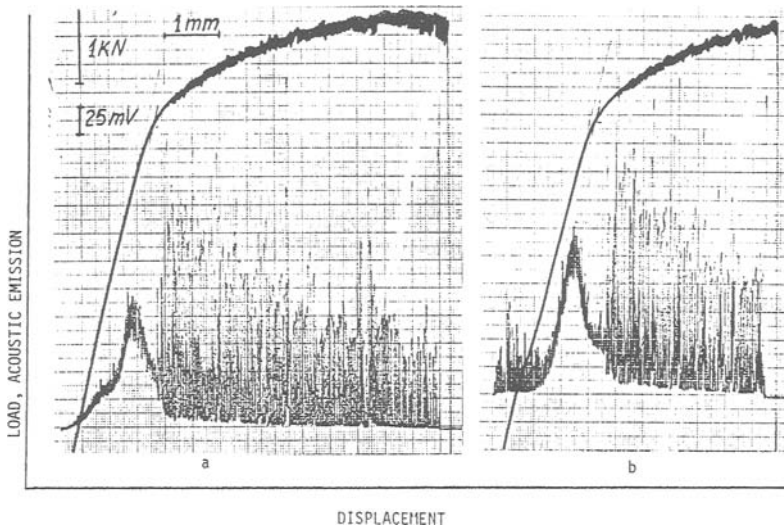


Figure 1: Load and AE intensity vs. displacement curves for unexposed (a) and pre-exposed (b) tensile samples.

In spite of the similar general behavior as demonstrated in Fig 1, of both the as-received material and the material exposed to water, a significant difference is noticeable. The dissimilarity is two fold, first it can be noted that the pre-exposure markedly reduced the tensile elongation of the material. Second, the pre-yield acoustic emission activity was more pronounced for the material pre-exposed to water, for which the peak of continuous emission close to the yield load was of higher intensity. The more intense AE activity after pre-exposure is also manifested in higher peak amplitudes of the AE signals as shown in Fig. 2, which shows the peak amplitude distribution of AE data in Fig. 1.

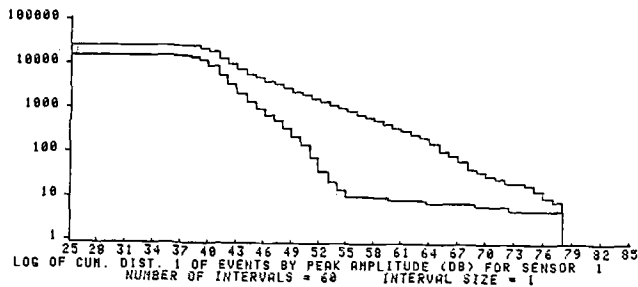


Figure 2: Cumulative distribution of events by peak amplitude for the unexposed (lower chart) and pre-exposed specimens. Data were accumulated for the entire tensile test.

While the distribution for the as-received material extends to about 55 dB, that of the pre-exposed material extends to 78 dB, indicating AE activities of higher amplitude as a result of pre-exposure. The evolution of the distributions shown in Fig. 2 which are accumulated over the entire test are shown in Figs. 3 and 4, and it can be seen that most of the higher amplitude AE activity originates in the pre-yield regime.

The origin of the observed higher AE activity in the pre-exposed samples is not clear. Careful examination of the samples prior to and during tensile testing revealed the existence of surface pits and formation of corner micro-cracks (during testing) only in the pre-exposed samples. These cracks did not appear when the corners were rounded before the test. However, the pre-exposure effect both on total elongation and on AE behavior still persisted. In addition similar behavior was found in the specimens pre-exposed to 0.1N NaOH water solution not subjected to the ultrasonic field.

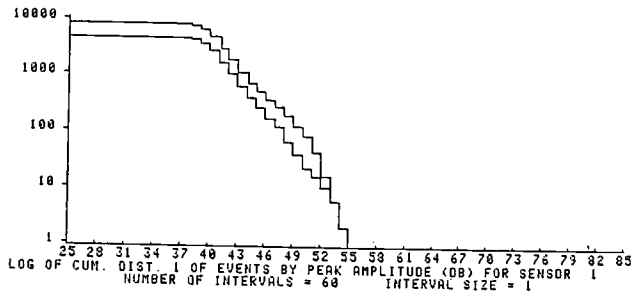


Figure 3: Cumulative distribution of events by peak amplitude for the unexposed specimen. The upper curve corresponds to the burst type AE and the lower one to the continuous type AE.

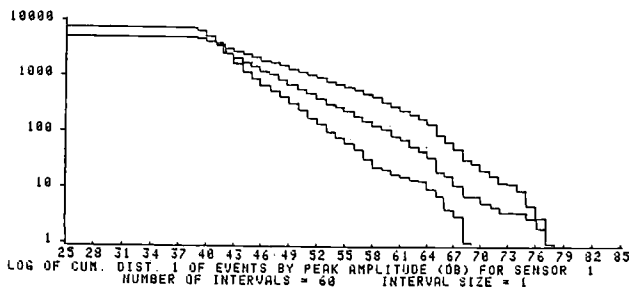


Figure 4: Cumulative distribution of events by peak amplitude for the different stages of deformation of the pre-exposed sample. The upper curve represents AE prior to AE continuous peak, the middle curve relates to the AE continuous peak and the lower curve is for the burst type AE.



Thus, the observed effects can not be related to a specific environment. In both cases, it has been found that large amount of hydrogen was introduced into the pre-exposed samples [4]. It is not yet clear which mechanism is responsible for the higher AE activity of the pre-exposed tensile samples, however, it certainly relates to the hydrogen charging that took place during the pre-exposure. In another study, comparison between AE during uniform tension and uniform compression has been employed and the conclusion, that the major source of AE in the studied Al-Li alloys was plastic deformation has been reached [5]. No pre-exposure effects were found in the compression test. The possible sources for the hydrogen induced modification of AE in tensile test are hydrogen induced modification of plastic deformation in tension, cracking of hydrides that possibly formed or hydrogen induced internal microcracking. In addition, it should be realized, that AE can be used as a very sensitive tool for evaluating environmental effects in Al-Li alloys.

#### ACKNOWLEDGMENTS

Discussions with Prof. Kanji Ono in the course of this study are gratefully acknowledged. We are grateful for the support of portions of this research by grant No. 85/00103 from the U.S.-Israel Binational Science Foundation (BSF), Jerusalem, Israel.

#### REFERENCES

- [1] Divecha, A. P. and Karmarkar, S. D., Advanced Materials & Process Vol. 130, No. 4, October 1986, pp 74-79.
- [2] Lavernia, E. J. and Grant, N. J., J. of Material Science, Vol. 22, 1987, pp 1521-1529.
- [3] Roman, I., Ono K. and Johnson C. H., J. of Acoustic Emission Vol. 4, No. 2/3, 1987, pp 111-115.
- [4] Zeides, F. and Roman, I., to be published.
- [5] Zeides, F., Roman, I., J. of Acoustic Emission, Vol. 8, No. 3, September 1989, pp 47-49.

**B. Raj and T. Jayakumar**

## ACOUSTIC EMISSION DURING TENSILE DEFORMATION AND FRACTURE IN AUSTENITIC ALLOYS

---

REFERENCE: Raj, B., Jayakumar T., "Acoustic Emission during Tensile Deformation and Fracture in Austenitic Alloys," Acoustic Emission: Current Practice and Future Directions, ASTM STP 1077, W.Sachse, J.Roget and K.Yamaguchi, Eds., American Society for Testing and Materials, Philadelphia, 1991.

ABSTRACT: The nature of the Acoustic Emission (AE) generated during tensile deformation and fracture of two austenitic alloys i.e., AISI type 316 Stainless Steel (SS) and Nimonic alloy PE-16 are presented and discussed. Effects of second phases on the AE are considered. For 316 SS, the second phases are carbides and inclusions. For PE-16, the second phases are carbides and coherent precipitates i.e.,  $\text{Ni}_3(\text{Al}, \text{Ti})$ . Time and frequency domain analyses have been used

to characterise the dislocation behaviour. Correlations of dynamic strain ageing in 316 SS with AE signal are presented. A method to amplify the weak AE signals in 316 SS is highlighted. The studies in PE-16 have shown that AE can be correlated with the type of interactions i.e., whether Orowan looping and/or particle shearing is operating.

KEYWORDS: acoustic emission, stainless steel, deformation, fracture, alloy PE-16

Acoustic Emission (AE) from metals has been studied for about forty years starting with the pioneering work of Kaiser in 1950 to evaluate the dynamic behaviour of materials [1]. However, serious interest in the potential of this technique for materials research began only in the 1970s. AE technique has shown an ability to explain the micromechanisms of dynamic changes in materials and to solve problems related to structural monitoring.

Examples of dynamic changes where AE technique promises to generate

Baldev Raj is Head, Division for PIE and NDT Development, and T.Jayakumar is research scientist in the same Division, Indira Gandhi Centre for Atomic Research, Kalpakkam, 603 102, India.

new information are kinetics of dislocations, behaviour of microcracks and ductility of coatings/hard layers. The present studies have been specifically undertaken in order to establish correlations of mechanisms (deformation and fracture) with AE signals.

The paper discusses the characteristics of AE generated during tensile plastic deformation and fracture of two austenitic alloys i.e., AISI type 316 stainless steel and Nimonic alloy PE-16. Steels of AISI type 316 and similar to this are major structural materials for chemical and nuclear plants. PE-16 is a nickel base alloy suitable for high temperature operations and finds applications in aerospace and nuclear industry.

The studies of AE in these alloys are significant for the following reasons: AE investigations for materials research or structural integrity monitoring have been very limited for steels similar to AISI type 316 SS. It is known that this steel emits weak AE making it difficult to obtain good correlations with microstructures and dynamic changes.

As regards PE-16, there has not been any systematic study on the characterisation of AE generated during plastic deformation and fracture of this alloy. PE-16 can have several combinations of microstructural constituents that may help obtain useful correlations with AE signals.

The paper is divided into two main parts. The first part is related to studies on 316 SS and the second to PE-16. Both the parts are based on work carried out at the authors' laboratory.

## PART A

### STUDIES ON AUSTENITIC STAINLESS STEELS

Present studies on austenitic stainless steels describe the nature of AE signals and their correlations with sources operational during tensile plastic deformation and fracture in the following microstructures; (a) single phase solution annealed, (b) austenitic matrix with inter and intragranular carbide precipitates, (c) carburised case and (d) austenite matrix with inclusions. Influence of temperature (298-873 K) during deformation on AE signals for solution annealed nuclear grade austenitic stainless steel material is also reported.

### Materials and Test Arrangements

The chemical compositions of the stainless steels used in the present investigations are given in Table 1. Table 2 gives the inclusion ratings for the commercial grade 316 SS used in this study. There were only a few inclusions in the nuclear grade 316 SS. The sizes of these inclusions were in the range 0.5 to 1.0  $\mu\text{m}$ . Three types of tensile specimens and four types of mounting arrangements were used in the investigations. Four types of arrangements are designated as

TABLE 1 -- Chemical compositions of stainless steels used in present investigations

Material	Chemical Composition ( Wt % )
Nuclear grade type 316 (VIRGO 14 SB)	Ni-12.43, Cr-16.46, Mo-2.28, C-0.054, Mn-1.69, Si-0.64, S-0.006, P-0.02, B-0.0013, Ti-0.01, Nb- 0.01, Cu-0.132
Commercial 316	Ni-12.5, Cr-16.5, Mo-2.3, C-0.06

TABLE 2 -- Inclusion ratings in AISI type 316 commercial grade austenitic stainless steel (average of 60 fields, carried out as per ASTM: E45-85)

A <sub>T</sub>	A <sub>H</sub>	B <sub>T</sub>	B <sub>H</sub>	C <sub>T</sub>	C <sub>H</sub>	D <sub>T</sub>	D <sub>H</sub>
1.33	1.0	2.0	0.0	4.5	0.0	2.06	1.12
( A-Sulphide type, B-Alumina type, C-Silicate type, D-Globular type, T-Thin series, H-Heavy series							

A, B, C and D types. Figures 1(a-d) shows the arrangements. Table 3 gives details of experimental conditions for microstructural variables, high temperature testing and transfer function and acoustic amplification studies. For studying the influence of single phase matrix and inter and intragranular carbide precipitates on time domain AE signal, type A arrangement has been used. B type arrangement has been used for 32 x 6.35 x 3 mm gauge length specimens designated as B1 and 50 x 20 x 3 mm gauge length specimens designated as B2. For studying the influence of progressive plastic deformation on frequency spectrum of AE signal generated, B type arrangement (B1) was used. For finding the influence of inclusions, B type arrangement (B2) was used. For high temperature deformation, type C arrangement was used. For transfer function and acoustic amplification studies, type D arrangement was used. Tensile tests were performed in an Instron 1195 machine. AET 5000 system and Iwatsu 2100 B signal analyzer were used for recording and analysing the AE signals.

Solution annealing of tensile specimens was carried out in a vacuum better than  $10^{-5}$  Torr at  $1323 \pm 2$  K for 1/2 h in a three zone furnace. Inter and intragranular precipitates  $M_{23}C_6$  were introduced by thermal ageing in vacuum better than  $10^{-5}$  Torr in the temperature range 773-1073 K for a maximum duration of 2000 hrs. Time-Temperature conditions employed are indicated in Fig.2 [2]. Specimens Nos. 1 to 11 in this figure indicate time-temperature thermal ageing treatments with respect to sensitisation curve of this material.

Carburisation of tensile specimens made from nuclear grade steel

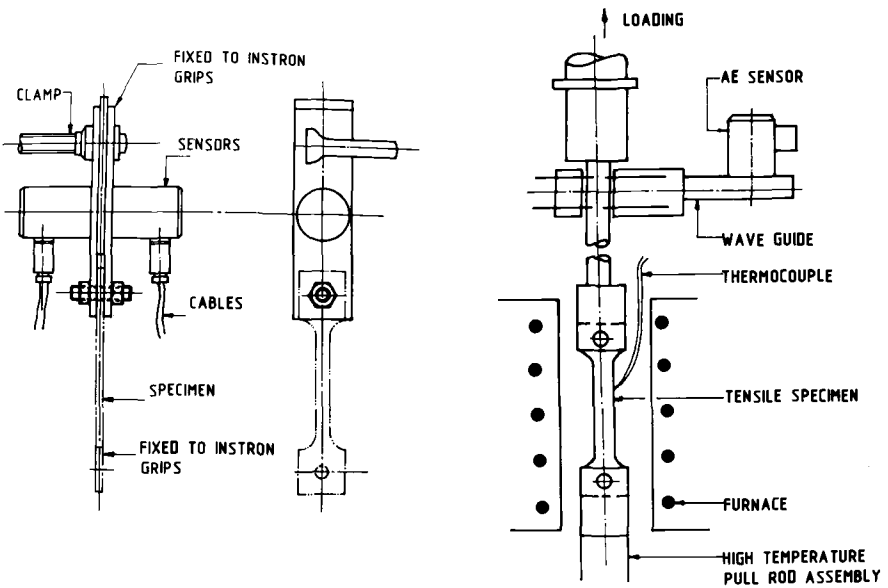


TABLE 3 -- Experimental conditions for investigations on AISI type 316 stainless steel

S.No.	Microstructural / Test Variable	Frequency of AE Sensor (kHz)	Threshold (V)	Total Gain (dB)	Strain Rate ( $10^{-4} s^{-1}$ )	Specimen Gauge Dimensions (mm)	Type of Mounting Arrangement
1.	Solution annealed	375	0.75	99	5.2	32 x 6.35 x 3	A
		100-2100 (Broadband)	--	84	2.6	32 x 6.35 x 3	B1
2.	Transfer function	100-2100 (Broadband)	--	99	2.8	60 x 50 x 3	D
3.	Amplification	100-2100 (Broadband)	--	99	2.8	60 x 50 x 3	D
4.	Temperature (298-873 K)	375	0.75	99	5.2	32 x 6.35 x 3	C
5.	Carbide precipitation	375	0.75	99	5.2	32 x 6.35 x 3	A
6.	Inclusions	375	0.20	96	3.3	50 x 20.0 x 3	B2

was carried out in oil contaminated sodium at  $873 \pm 2$  K for a period of 1000 hours to represent the carburisation phenomenon that takes place in this steel when used as construction material for sodium loops of fast breeder reactors, under off-normal conditions of oil leakage.

The studies on transfer function and amplification required injection of ultrasonic waves in the frequency range 100 kHz to 600

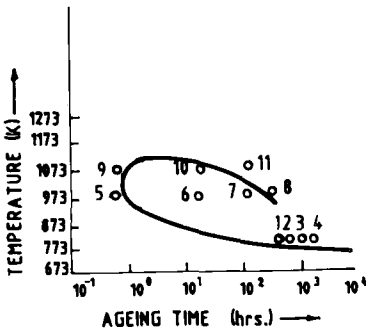


FIG.2 -- Time -temperature thermal ageing conditions for test specimens of AISI type 316 Nuclear Grade Material.

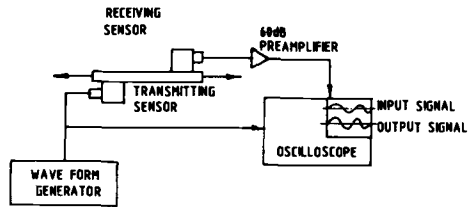


FIG.3 -- Block diagram of the experimental set-up for transfer function and acoustic amplification studies.

kHz. The specimen mounting arrangement is shown in Fig.1(d) and the experimental set-up in Fig.3. For the transfer function studies, acoustic wave with suitable amplitude and frequency was injected using a broadband AE sensor placed at one end of the specimen. The frequency of the signal was varied from 100 kHz to 550 kHz. The acoustic signal transmitted through the specimen was picked up by another broadband AE sensor. The frequency selected for the injected signal for acoustic amplification studies was 156 kHz, which is the frequency corresponding to the first transmittance peak [3].

For acoustic amplification, simultaneous injection of acoustic signal and recording of AE data was used. Injection of waves has been done only for certain strain ranges enabling comparison of data obtained during this strain range with that obtained at the other strain levels where injection was not done. The location of AE sensors and methods of injecting acoustic wave were similar to that used for transfer function studies. A fixed frequency acoustic signal (156 kHz) with varying amplitude in the range 0.2 to 0.7 V peak-to-peak was applied. The specimen was plastically deformed at a strain

rate of  $2.8 \times 10^{-4} \text{ s}^{-1}$  and the AE signals generated during deformation were picked up by the receiving sensor. The signals received were

digitised at a sampling rate of  $10^7$  samples per second or a data length of 2K bytes, before processing and analysis.

### Ensuring Worthiness of Captured Signal

The threshold and gain for various series of experiments were so selected that no external noise was picked up. The response from a pencil lead breakage with a fixed gain and threshold conditions, was observed to be repeatable. When the transducer was fixed onto an extended grip assembly, there was no necessity for removal and refixing of transducer when the specimen was changed. This eliminated the possible variation in the acoustic coupling between the transducer and the specimen.

The background noise spectrum generated from a broad band sensor was used to compare the system response for various experiments. The response of the system for certain simulated frequencies was also found to be consistent. In order to ensure that no external noise was associated with extended grips and other components, preloading using a dummy specimen to more than 1.5 times the maximum expected load for any of the specimens tested was carried out. This was repeated for a number of cycles. It was found that an ideal Kaiser effect operated in the austenitic materials tested in the study. Theoretical analysis, discussed below, coupled with consistent observations in various specimens with different microstructures give credence to the use of extended grip assemblies for acquiring weak AE signals.

In order to make sure that the natural frequency response for different types of specimen geometries, and gripping assemblies would not interfere with the AE signals, natural frequency response of various types of assemblies was determined. This has been carried out using a computer code, Programme for Automatic Finite Element Computation (PAFEC) [3]. Natural frequencies for 32 x 6.35 x 3 mm gauge length specimens for the third mode in the initial and final (prior to necking) stages of plastic deformation were found to be 7.122 and 5.737 kHz respectively. Displacement response for 180 x 50 x 3 mm specimen at 150 kHz, with no material damping, were calculated. The values are much less ( $10^{-15}$  m) than the sensitivity of the piezoelectric transducer ( $10^{-14}$  m) at 1 microbar. This ensured that acoustic amplification values are not influenced by displacement response of the specimen due to injection of acoustic energy.

### Solution Annealed AISI 316 Nuclear Grade Austenitic Stainless Steel

Solution annealed nuclear grade AISI type 316 stainless steel is a weak emitter as evidenced by low peak amplitude (9 to 15 dB) emissions during uniform plastic deformation (Fig.4 (a)). The material does not show significant variations in AE 'rms' signal (averaged for 4 seconds) during the complete tensile test. Ringdown counts (RDC) vs. strain plot (Fig.5(a)) shows a number of bursts. There is a burst at very low strains (during the initial plastic strain range upto 2%), a few occasional bursts at intermediate strains and a final strongest burst at final fracture.

The burst in RDC during initial 2% plastic strain range (Fig. 5(a)) is attributed mainly to dislocation multiplication by Frank-Read (FR) and grain boundary (GB) source operations and motion of dislocations. Though these sources are operating throughout the plastic strain region, the activity is mostly below the threshold



level beyond yielding except a few occasional burst emissions. Reasons for occasional burst emissions are explained later in the text. Phase transformation during tensile deformation is ruled out as the source of AE because it is known that formation of martensite does not occur in type 316 stainless steel during deformation at 300 K [4,5]. The absence of martensite in AISI type 316 stainless steel after deformation was confirmed by examining the tensile tested specimens by ferritescope, eddy current testing and X-ray diffraction analysis. The observed burst in RDC during initial plastic strain range upto 2% in this material is in agreement with the reported observation in metals and alloys having a single phase FCC structure [6]. These

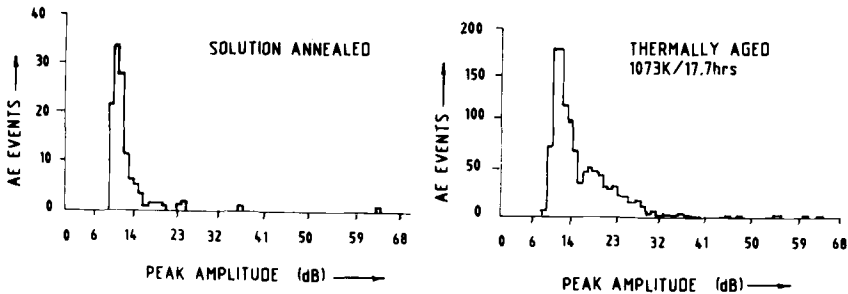


FIG.4 -- Peak amplitude distribution plots for the AE events obtained from (a) solution annealed and (b) thermally aged specimens.

materials are known to have a single burst in AE near the plastic strain of 2% of the material. In many materials, the burst is a smooth curve in either count rate or  $V_{rms}$ .

The burst is usually narrow and falls off rapidly with increasing strain. Similar feature was also observed in this study for RDC vs. strain plot (Fig.5(a)). However, no burst in  $V_{rms}$  was

observed. This is attributed to the measurement mode of 'rms' value using AET 5000 system. We attribute the burst in RDC at fracture to final linkage of microvoids and microcracks formed during early stages of deformation including necking. The fracture surface was indicative of ductile failure by microvoid formation and coalescence.

The occasional bursts in RDC beyond 2% plastic strain and before necking are possibly due to the following reasons: (i) Decohesion and fracture of inclusions, (ii) Microcracking of matrix and (iii) Statistical probability of strong acoustic activity from dislocations during deformation [3]. It is difficult to establish specific correlation of mechanisms with bursts. However, one or a combination of the three possibilities discussed above appears logical.

Frequency spectrum analysis of AE signal: In order to find out the influence of progressive plastic deformation (strain) on AE generated, frequency analysis of AE signal has been carried out. The predominant frequency present in the frequency spectrum should be inversely proportional to the duration of the dynamic event. Thus the measurements can provide information on the time scale of the AE process and can thus be used to evaluate dynamics of source events [7]

Two main observations are as follows :

a) Beyond 2% plastic strain and upto the onset of necking, the predominant frequency increases from 0.475 MHz to 0.66 MHz varying linearly with total strain (Fig. 6).

b) In the necking region, the predominant frequency has a low value of 0.14 MHz which is about 1/3 to 1/4 of those found in the uniform deformation region of the stress - strain curve. The value of predominant frequency in the necking region is arrived at by averaging ten AE signals in each of the three specimens.

The lower value of predominant frequency in the necking region could be associated with microvoid coalescence and / or crack growth, whose life times are reported [8] to be higher than dislocation related AE phenomena. The shift in predominant frequency during

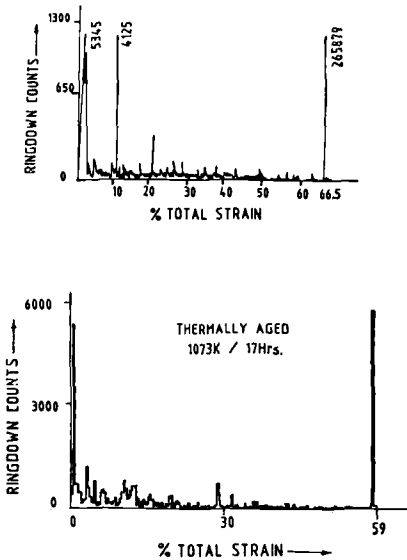


FIG.5 -- Variation of ringdown counts with strain for (a) solution annealed and (b) thermally aged specimen.

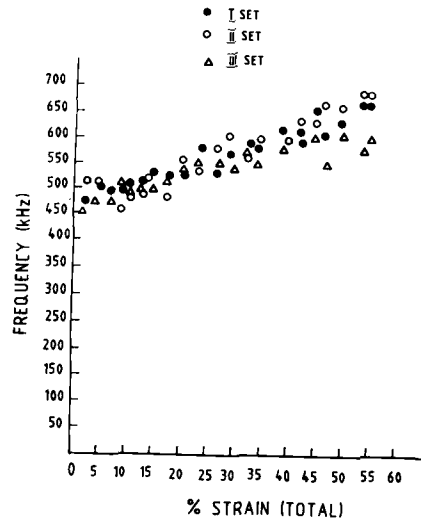


FIG.6 -- Variation in predominant frequency of AE signal with strain.

uniform plastic deformation is explained on the basis of dynamic events related to waiting time of dislocations at obstacles [7]. Attempts to correlate time-of-flight with predominant frequencies resulted in unreasonable calculated values of mean free path (a few millimetres). AE source related to waiting time of dislocation at obstacles resulted in reasonable values of mobile dislocation density ( $10^3 - 10^4 / \text{cm}^2$ ) [7].

Acoustic amplification: AE generated during tensile deformation in AISI type 316 nuclear grade austenitic stainless steel are weak (Fig.4(a)). An innovative technique has been developed to amplify such signals [9].

It has been reported that spontaneous stress (elastic) waves emitted by various nucleation (microfracture) events interact with other potential nucleation sites, and tend to promote fracturing of these sites [10]. It has also been reported from damping studies that plastic deformation can be produced by injecting waves of very large strain amplitude [11]. It is thus plausible that externally injected acoustic signals of a certain frequency can interact with subcritical (energetically) AE sources and give rise to enhanced acoustic emission signals which otherwise would not have been released at those stress levels. Further, similar possibility of stimulating subcritical sources in the case of continuous AE appears to be more favourable considering the energetics involved, although no such suggestion has been made in the literature.

The AE signals emitted under either injection or otherwise were acquired at various strain levels. Figure 7 shows typical time domain signals and the corresponding auto-power spectra of continuous type AE signals for the non-injected and the injected conditions. The values of Y-axis (Fig. 7) are in arbitrary units. The spectrum of the signals recorded with the injected condition contains a strong peak at the injected frequency in addition to new frequencies. The data for the injected case at a strain level where the new frequencies are dominantly seen is given in Fig. 7. It must be emphasised that the amplitude level of the frequencies without injected acoustic wave are more than one order of magnitude less dominant than that with the frequency components with the injected acoustic wave as may be noted from Fig. 7. It should also be emphasised that the emission of frequencies in the neighbourhood of the injected frequency is typical for all values of the injected voltages.

Figure 8 depicts net acoustic energy (total energy minus the energy due to the injected component) of various continuous AE signals recorded as a function of the strain levels for both injected and non-injected conditions. It was not necessary to eliminate any other energy components as no harmonics corresponding to the injected signal frequency were observed.

The possible explanation of amplification is that the injected

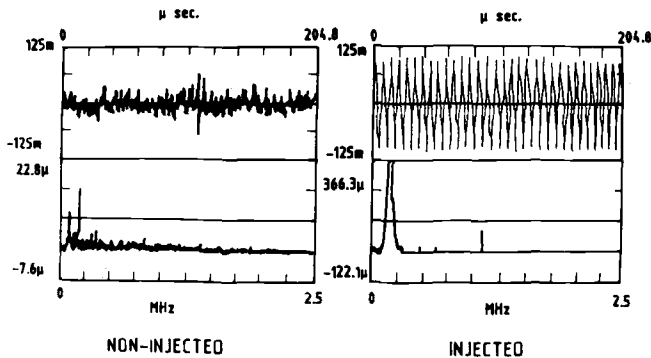


FIG.7 -- Time signal and its auto-power spectrum for a typical continuous type AE signal.

acoustic wave would trigger the groups of dislocations arrested at obstacles to overcome energy barrier stimulating the subcritical sources to contribute additional sources of AE. These would then result in the enhancement of integrated power. Further, it is expected that there would be a distribution of energy barriers which can only be overcome by increasing the amplitude of the injected acoustic wave. Associated with the distribution of barriers, there would be a distribution of relaxation time scales implying that, in general, there will be a distribution of frequencies around the injected frequencies with the maximum amplitude corresponding to the injected frequency (due to the resonant type of interaction). Further, since the relaxation time scales are expected to depend on the local

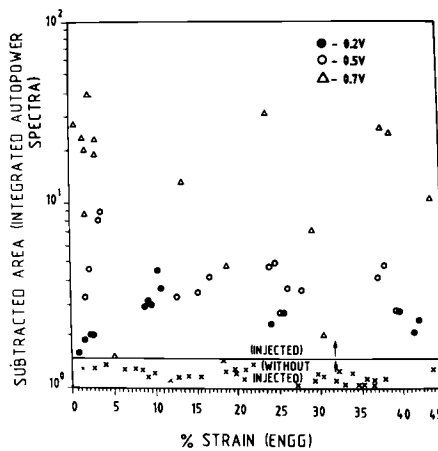


FIG.8 -- Acoustic amplification for various injected voltages.

environment of the activated energy releases, there is a possibility of the release of acoustic energy at other frequency bands when new subcritical sources are stimulated under the influence of injected acoustic waves. There is, however no compelling reason that new frequencies should be found in every situation. The proposed mechanism explains both the amplification of the total AE power and the frequency response under the influence of injected signals.

Influence of temperature: Various investigators have studied AE generated during serrated flow from various materials like Al alloys, brass etc. and correlated them with the types of serrations [12,13]. However, there is no reported literature on the AE behaviour from the serrated plastic flow occurring in AISI type 316 stainless steel. Since, there is systematic changeover from irregular to A to B to C type serrations with a change in the testing conditions [14], this material is ideal for correlating the AE behaviour with various types of serrations.

The acoustic activity increased with increase in temperature of deformation upto 773 K. There was reduction in acoustic activity when

temperature of deformation was further increased to 873 K. There is one to one correspondence between serrations and AE generated. In general, burst type AE occurred during serrations. They occurred either during load drop or during rise or during both for different serrations. The serration changed over from irregular (548 K) to type A (588 K) to type A+B (773 K) to type B (lower strains at 873 K) and type C (higher strains at 873 K). At 548 and at 773 K, AE occurred during load drops for all serrations and during load rise for a few serrations. At 588 and at 873 K, AE occurred during load drops. Figure 9 shows the portions of load and AE rms voltage vs. elongation for a few representative serrations. Continuous type AE was also observed

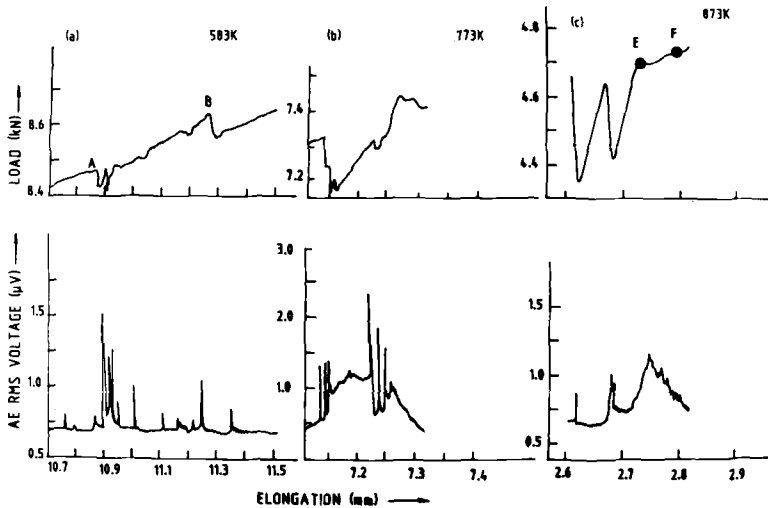


FIG.9 -- AE rms voltage peaks in correlation with change in load during serrated flow in austenitic stainless steel at various temperatures (a) 583 K (b) 773 K (c) 873 K.

when the serrations occurred over a longer period (as shown in Fig. 9(b)) or during small load fluctuations (points E, F in Fig. 9(c)) taking place immediately after C type serration. Rate of load drop rather than the magnitude of load drop or load rise decides the energetics of AE signals. Even though the amount of load drop at point A was smaller compared to that at point B in Fig. 9(a), the former generated higher rms voltage since the load drop occurred at a faster rate. Caceres et al. [13] reported generation of AE during load rise or drop in different materials and correlated them with the processes related to dislocation phenomena. The results of our work indicate that a definite conclusion is not always possible because (i) the relative contribution of change and rate of change in mobile dislocation density, average velocity or both, which cause different types of serrations and which also strongly affect AE, are not known and (ii) the time scale involved for dislocation phenomenon associated with serrations is orders of magnitude lower than that of load measuring system, AE recording system and strip chart recorder [3,15].

### Effect of Second Phase : Inter and Intragranular Carbides in Nuclear Grade AISI 316 Stainless Steel

Predominant precipitates formed after the thermal ageing treatments are inter and intragranular  $M_{23}C_6$  precipitates. In a

solution annealed and thermally aged material, the expected sequence of precipitation as a function of time at a given temperature would be grain boundaries, twin boundaries and dislocations [16]. Figure 5(b) gives typical RDC vs. total strain for thermally aged specimen. Figure 4 (b) shows typical amplitude plots for AE events generated in thermally aged (1073 K, 17.7 hours) specimen cumulated till uniform elongation. It can be seen that there is higher AE activity in thermally aged specimen (RDCs). Thermally aged specimens show an additional broad peak in the amplitude range, 15 - 40 dB. This broad peak was observed in all the thermally aged specimens where grain boundary cracking occurred.

Figure 10 shows representative plots indicating variations of AE data obtained during tensile testing of thermally aged specimens. Figure 11 shows variation of the maximum values of various AE parameters with thermal ageing. The maximum amplitude values corresponding to second broad peak (for example 40 dB in Fig. 4 (b))

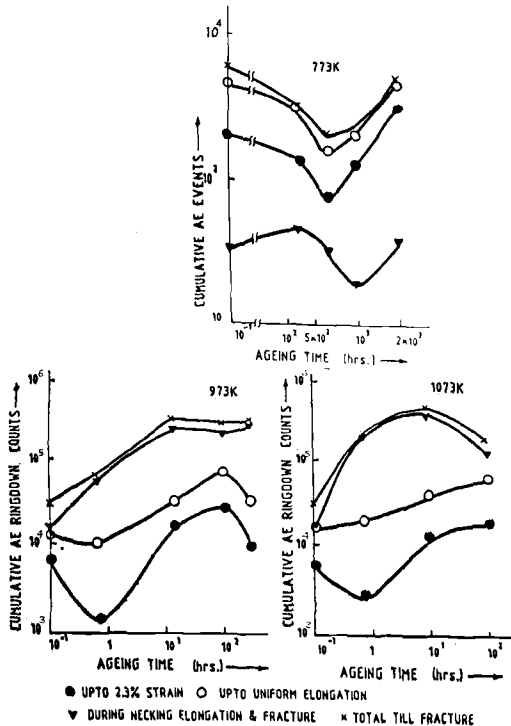


FIG.10 -- Typical plots showing variation of cumulative ringdown counts / events from specimens aged at various temperatures and time durations.

for various thermally aged specimens were used for making this plot. It was observed that there is a progressive change in fracture mode from fully ductile type by microvoid formations and coalescence to mixed mode type containing ductile microvoids (dimples) on grain facets and intergranular cracking with the increase in duration of thermal ageing at each of three temperatures. As the ageing time increased, there was a gradual change even within the mixed mode type, in the sense that the dimples on grain facets were reduced and the intergranular cracking was increased [17].

In Fig. 10, it can be seen that similar trends in the variations of events/ringdown counts with duration of ageing are observed for deformation upto 2.3 % strain level. There is however a change in the points on the time scale at which the particular variations have taken place.

The decrease in AE activity upto 2.3 % strain during initial time periods of thermal ageing can possibly be due to:

(i) Diffusion of chromium or substitutional elements to dislocations thereby reducing their mobility and detectability,

(ii) Reduced dislocation mean free path resulting from the finely dispersed intragranular carbide precipitation thus reducing the statistical probability of detection of weak AE phenomena as reported by Agarwal et al. [18] and

(iii) Size and morphology of grain boundary  $M_{23}C_6$  precipitation at lower times of ageing treatments is such that it strengthens the boundary and reduces the dislocation activity and detectability.

The arguments though attractive are not amenable to be isolated or confirmed in this present analysis. Increased AE activity at all temperatures at higher thermal ageing times is attributed to increased grain boundary cracking due to favourable size and morphology of precipitates. The cracking propensity was observed by SEM studies to increase as the ageing time increased. The decrease in AE activity at 973 K and 300 hours is attributed to desensitisation (point 8, Figure 2) and decrease in grain boundary cracking.

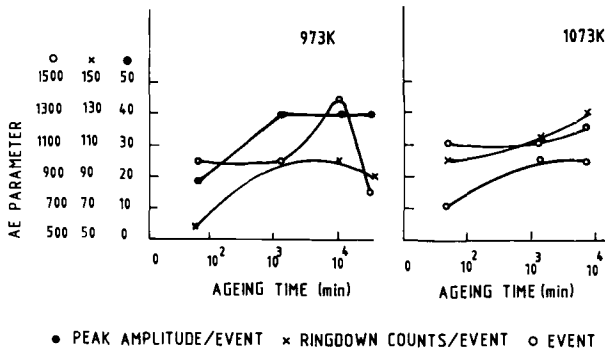


FIG.11 -- Maximum values of various parameters of AE events below which most of the events generated are present.

The initial drop in AE activity between 2.3 % strain and start of necking at 773 K and 973 K can be explained by the same arguments as (i),(ii) and (iii) as suggested for dynamic phenomena upto 2.3 % strain. The initial decrease is not observed for 1073 K. This is due to the possibility that the size and morphology of grain boundary precipitates at this temperature are favourable for cracking at lower thermal ageing times too. This is also confirmed from the observation that higher peak amplitude events corresponding to grain boundary cracking have been generated after lower thermal ageing times at 1073 K (Fig. 11). The second reduction in AE activity during uniform elongation for specimens aged at 973 K for 300 hours is attributed to the occurrence of less intergranular cracking due to desensitisation (point 8, Fig. 2). The reduced intergranular cracking is also reflected in the increase in uniform elongation value from 43 to 46 % and total elongation from 50 to 57 % for thermally aged specimen at 973 K, 300 hours as compared to thermally aged specimen at 973 K, 106 hours. The ductility effects are less pronounced for 1073 K, 113.5 hours specimen as compared to 1073 K, 17.7 hours specimen. (Uniform elongation shows an increase from 50 to 52 % and total elongation increases from 59 to 62 % in the former specimen.) This increase in ductility value does not decrease AE activity.

The reduction in ringdown counts during necking elongation and fracture in a specimen aged for 108 hours at 973 K and for 113.5 hours at 1073 K is attributed to the decrease in the net available cross-sectional area for fracture by progressive intergranular cracking during uniform elongation. The increase in ringdown counts for a specimen aged for 300 hours at 973 K is due to the availability of higher cross-sectional area for fracture. This is due to reduced intergranular carbide precipitation and hence reduced grain boundary cracking (confirmed by SEM) during uniform elongation. The reduction or increase in AE events or ringdown counts generated during necking elongation corresponding to increase or reduction in propensity for intergranular cracking during uniform elongation observed in specimens thermally aged at 973 K and 1073 K could not be seen in a specimen thermally aged at 773 K. The increase in values of such parameters as ringdown counts per event, time duration per event, peak amplitude per event (Fig. 11) are due to contributions from more and more intergranular cracking. Reduction in ringdown counts per event and

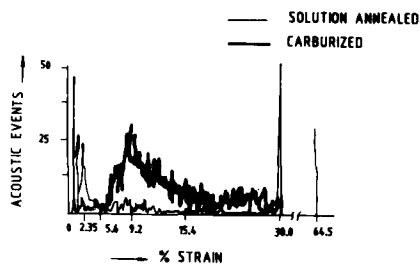


FIG.12 -- Effect of carburisation on acoustic emission during tensile testing.



time duration per event at 973 K beyond 108 hours of ageing is attributed to the reduction in cracking tendency. It agrees with the observation; i.e., trends in AE activity for 2.3 % strain and from 2.3 % strain to the end of uniform plastic deformation for 973 K and 1073 K thermally aged specimens.

Influence of carburised case: Figure 12 shows plots of AE events vs. time for both solution annealed specimen and specimen carburised in oil contaminated sodium. There is four to five times increase in the total AE events in the carburised specimen compared to solution annealed specimen. In the solution annealed material, 40 % of the total events occurred during yielding and upto 2.3 % plastic deformation. The material is silent almost during the entire plastic deformation stage. On the other hand, in carburised specimens, AE was observed throughout the tensile test. In addition to normal peaks at yielding and fracture, an additional broad peak was seen extending over a strain range 5 to 15 % with a maximum at 9 % strain. Also, a large number of events in the carburised specimen were of higher peak amplitudes.

Optical metallography showed extensive inter and intragranular carbide precipitation in carburised specimen upto a case depth of 6 % resulting due to carbon pick-up from oil contaminated sodium and beyond this depth precipitation was observed to a less extent (due mainly to thermal ageing). SEM revealed mixed mode type fracture in the core and intergranular cracks in the carburised case. The study brings out the potential of AE technique for characterising mechanical properties of case hardened layers.

#### Effect of Inclusions in Nuclear and Commercial Grades of AISI type 316 Austenitic Stainless Steels

Comparison of nuclear and commercial grades of a material is logical for identifying AE generated by fracture and debonding of inclusions. The significant difference between the two grades is their inclusion content. The type, size, composition and other features of inclusions have been characterised in numerous AE investigations [19-21]. It has been inferred from AE studies that inclusions that fracture at high stresses and with higher crack velocity produced stronger AE events. Thus, there exists a possibility (indirectly) to characterise inclusions and their behaviour in a particular material by observing AE activity.

The present study compares AE release from commercial and nuclear grade AISI type 316 stainless steels. AE ringdown counts with total strain plot for nuclear grade material is representative of different specimens as the variations from specimen to specimen are minimal (Fig.5(a)). In case of commercial grade steel, the RDC vs. strain plots show considerable variations in AE obtained from different specimens of the same batch of materials. Figure 13 shows typical variations of AE ringdown counts with total strain in commercial grade stainless steel. This variation in acoustic activity (but similar burst emission in the range 2 to 25 %) is attributed to variations in size, shape and distributions of inclusions in different specimens. The ratio of ringdown counts upto 2% strain to the total ringdown

counts generated upto necking reduced drastically in commercial grade material (typically 1.2% in one particular case) compared to nuclear grade material (typically 57%). This is attributed to the presence of inclusions in the former causing a reduction in the dislocation mean free path which in turn reduced the AE activity generated before 2% total strain. In one typical commercial steel specimen, 96% of total ringdown counts generated before fracture were generated during 2 to

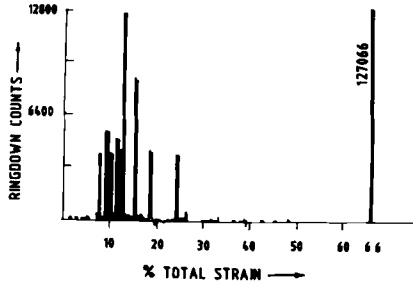


FIG.13 -- Typical plot of RDC vs. total strain for commercial grade AISI type 316 stainless steel.

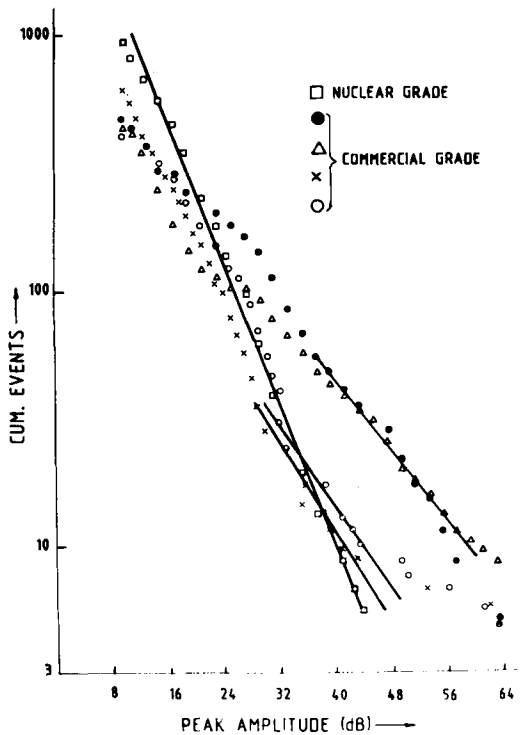


FIG.14 -- Logarithmic cumulative peak amplitude distribution of events generated in nuclear and commercial grade AISI type 316 stainless steel specimens.

25% of the strain in comparison to 33% in the nuclear grade material. This is attributed to the large number of ringdown counts generated during decohesion and cracking of matrix and inclusions.

It has been found by SEM observations using stop tests at various strain levels that fracture/decohesion took place before 25 % strain levels in all specimens tested. This agrees well with higher AE levels in all the specimens tested. This agrees well with higher AE activity before 25 % total strain level in commercial grade steel. The total ringdown counts observed before fracture are almost doubled in commercial grade steels as compared to nuclear grade material. The ringdown counts at fracture in commercial grade material are reduced considerably compared to nuclear grade material. The RDC at fracture are found to be consistently higher (for different specimens tested) in nuclear grade material compared to those generated in commercial grade material. As most of the separations of cross-section of the fractured region in commercial grade steel occurred during earlier stages of plastic deformation (by inclusion decohesion and cracking), the net cross - sectional area separated at fracture is reduced resulting in lower amount of ringdown counts at fracture.

Figure 14 shows logarithmic cumulative peak amplitude distribution plot for events generated in nuclear grade and commercial grade steel specimens. The representative data for one nuclear grade and data from four different lots of commercial grade specimens are included in Fig. 14. The figure shows generation of more number of events with higher peak amplitudes in commercial grade specimens compared to those in nuclear grade specimens. Stop tests had revealed that AE activity due to inclusion decohesion and fracture is in the peak amplitude range of 24 dB to 48 dB. Even though the number of events generated in different specimens have varied at higher amplitude levels, the commercial grade specimens show similar slope ( b - parameter from 24 dB to 48 dB) indicating that the events generated in commercial grade specimens result in a characteristic b - parameter. Also, the figure indicates that there are large number of events with lower peak amplitude (PA) in nuclear grade steel. Lower PA events are attributed to dislocation generation and motion at the early stage of deformation. More number of AE events with lower PA are detected possibly due to larger mean free path in nuclear material as compared to commercial grade material.

## PART B

### STUDIES ON NIMONIC ALLOY PE-16

Studies have been carried out on the influence of the following three types of second phases in a  $\gamma$ -austenite matrix : (a) MC type carbides, (b)  $\gamma'$  and (c) conjoint presence of  $\gamma'$  and MC.

#### Materials and Test Arrangement

The nominal chemical composition (wt %) of Nimonic alloy PE-16 used for investigations is as follows:  
C/0.07, Si/0.26, Mn/0.4, Fe/33.8, Cr/16.5, Al/1.24, Ti/1.2, Mo/3.3,

Co/0.27, Cu/0.06, S/0.004, B/0.0015, Zr/0.03 and Ni/balance. PE-16 tensile specimens, having gauge dimensions 32 x 6.35 x 3 mm were

tested at 298 K at a nominal strain rate of  $5.2 \times 10^{-4} \text{ s}^{-1}$ . AE was recorded with 375 kHz resonant sensor (250-500 kHz filter). Total system gain was 99 dB. Threshold voltage was 0.75 V. Solution annealing was carried out at 1313 K for 4 hours for all specimens to obtain single phase austenite (type N-1). Thermal ageing was carried out on type N-1 specimens at 973 K for 24 hours, to obtain  $\gamma'$  with 9 nm average size (type N-3), 1023 K for 24 hours to obtain  $\gamma'$  with 20 nm average size (type N-4) and 1173 K for 1/2 hour to obtain MC (M = Ti, Mo) (type N-2). Double thermal ageing was carried out on type N-1 specimens at 1173 K for 2 hours and 973 K for 24 hours to obtain  $\gamma + \gamma' + \text{MC}$  microstructure (type N-5). Type A (Fig. 1 (a)) arrangement was used for all the investigations. Approach for ensuring worthiness of captured signal was the same as mentioned for austenitic stainless steels.

TABLE 4 -- Microstructural details, operating deformation processes and various time domain AE parameters for different specimens

Specimen type	Micro-structure	Deformation process	AE parameters during pre-yield				
			Total events	Total RDC	Max. values		
					PA(dB)	ED(us)	RT
N-1	$\gamma$	*	63	780	27	650	225
N-2	$\gamma + \text{MC}$	****	400	19500	45	2500	175
N-3	$\gamma + \gamma'$	**	3550	32000	40	2000	500
N-4	$\gamma + \gamma'$	***	875	32750	32	1000	325
N-5	$\gamma + \gamma' + \text{MC}$	*****	3825	44000	40	2000	500

\* Dislocation multiplication with Frank-Read and grain boundary sources and dislocation motion

\*\* Size of  $\gamma' = 9 \text{ nm}$ , particle shearing process

\*\*\* Size of  $\gamma' = 20 \text{ nm}$ , Orowan looping processes

\*\*\*\* i) Dislocation activity at  $\gamma$ /carbide interface and  
ii) Decohesion and Fracture of MC

\*\*\*\*\* All the above deformation processes, low volume fraction of  $\gamma'$  (10 nm)

#### Deformation Mechanisms, AE Results and their Correlations

Microstructural details, operating deformation processes and various time domain AE parameters for different specimens are given in Table 4. In all the specimens tested, plots showing 'rms' voltage variation with strain were made with the X-axis scale being selected to be ten times more (expanded) upto around 2 % total strain as compared to that used beyond 2 % total strain. This was done in order to highlight the AE data during micro and macro yielding.

Influence of MC type carbides: Figures 15(a-b) show 'rms' voltage of AE signal vs. strain plots for solution annealed condition

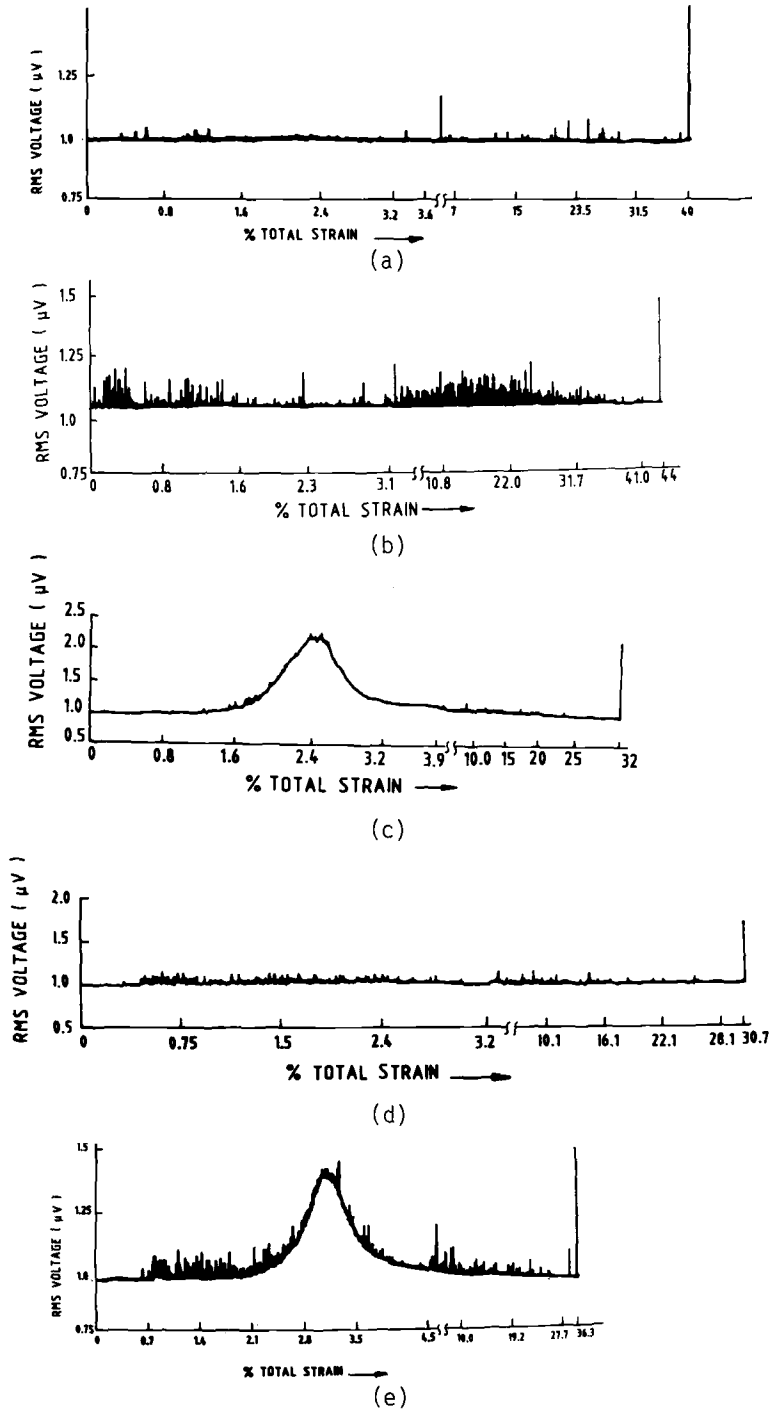


FIG.15 -- Variation in AE rms voltage with % total strain (a) Type N-1 (b) Type N-2 (c) Type N-3 (d) Type N-4 and (e) Type N-5.

and microstructure with MC type carbides. The plots show occurrence of burst type AE in thermally aged specimens throughout the tensile test. Only occasional bursts were generated in solution annealed specimen. Burst emissions represented by high ringdown counts and 'rms' voltage peaks observed in specimens with MC type carbides during the early part of sample loading can be attributed to decohesion of bigger size and favourably oriented carbides (with respect to the tensile axis). This agrees with the results of Gladman et al [22]. Gladman et al. have indicated that depending on the type, size and distribution of the second phases, decohesion and/or fracture can start at small strain levels well below yield point. Very high acoustic activity generated during plastic deformation strain range 8-38 % (Fig. 15(b)), number of burst emission peaks seen in 'rms' voltage vs. strain plot and also high energetic acoustic events indicated by peak amplitude (PA) in thermally aged specimens compared to solution annealed specimen are attributed to the events generated by decohesion and fracture of MC type carbides [23,24]. AE during fracture in thermally aged specimens are of lower energy. This is attributed to reduced ligament length for incremental joining of the microcracks (formed by decohesion and fracture of MC carbides during plastic deformation) during final fracture.

Influence of coherent  $\gamma'$ : The large scale increase in acoustic activity indicated by large number of AE events (Table 4) and very high 'rms' voltage peaks in the yield region in specimen of type N-3 (Fig. 15(c)) is attributed to deformation taking place by particle shearing process [23,24]. However when the process of deformation changes from particle shearing to predominantly Orowan looping (confirmed by TEM studies) as in the case of type N-4 specimens there is considerable reduction in the number of AE events (Table 4) and complete absence of AE 'rms' peak in the yield region (Fig. 15(d)). However, ringdown counts generated in specimens of type N-4 are comparable to these in type N-3 specimen [23,24].

The above observations are in agreement with those found in precipitate hardenable stainless steel and some aluminium alloys wherein the influence of shearable precipitates under different ageing treatments have been studied [25,26]. The broadness of the 'rms' voltage peak during yielding stage in type N-3 specimens is attributed to progressive yielding taking place in the complete volume of the specimen. The yielding starts on a microscopic scale initially at favourable regions and progresses throughout the gauge volume as the load increases. The favourable regions for early yielding are grains favourably oriented with respect to tensile axis and microscopic regions with finer size of  $\gamma'$ . As  $\gamma'$  size approaches the optimum size of 10 nm, AE events with relatively higher PA are generated. This also results in increase in 'rms' value of the signal.

Generation of AE events with higher event duration and rise time during yielding stage in types N-3 and N-4 specimen as compared to those generated in solution annealed specimens (type N-1) indicates that events associated with particle shearing and Orowan looping processes are characterised by slow build-up and longer duration compared to the dislocation processes in solution annealed specimens. Generation of higher ringdown counts during post-yield and pre-necking region of strain in specimens of N-4 type was observed. This was

attributed to higher work hardening rate that is associated with Orowan looping process.

Influence of conjoint presence of  $\gamma'$  and MC: Generation of higher events and ringdown counts in N-5 type specimens compared to those in N-3 type specimens is due to contribution from decohesion and fracture of MC present in specimens of N-5 type. It was observed that characteristic AE signatures observed in specimens containing  $\gamma'$  (type N-3) and MC (type N-2) individually have been maintained even when the two phases are present conjointly in the microstructure (Fig. 15 (e)).

The energy of events generated with this microstructural condition is lower as compared to N-2 type specimens. These is attributed to possible reasons such as: (i) the reduction in interfacial energy between matrix and MC and (ii) higher attenuation of AE signal in the presence of  $\gamma'$  in the matrix.

## CONCLUSIONS

Frequency spectrum analysis and acoustic amplification provides means to characterise weak AE sources due to dislocation movements in solution annealed austenitic stainless steel. Influence of carbide precipitates and inclusions can be characterised by conventional time domain AE parameters in AISI type 316 stainless steels.

The strength of AE signals in PE-16 material decreases in the following order (i) Decohesion and fracture of MC type carbides (ii) Particle shearing process (iii) Orowan looping process (iv) Dislocation generation and multiplication by operation of Frank-Read and grain boundary sources and motion of dislocations. The AE events associated with the above mentioned deformation processes can be distinguished since the AE parameters i.e., the maximum value of peak amplitude, energy, event duration and rise time for the events generated are distinctly different. The characteristic signatures during plastic deformation are unique. Even conjoint presence of phases like  $\gamma'$  and carbide precipitates do not alter the unique signatures due to  $\gamma'$  and MC type carbides when they operate independently.

## ACKNOWLEDGEMENTS

Authors are thankful to Mr.C.V.Sundaram, Director, Indira Gandhi Centre for Atomic Research and Dr.Placid Rodriguez, Head, Metallurgy and Materials Programme, Indira Gandhi Centre for Atomic Research, for their encouragement and support. Sincere thanks are due to Prof.A.K.Rao, Prof.S.Ranganathan of Indian Institute of Science, Bangalore and Prof.O.Prabhakar of Indian Institute of Technology Madras, for many useful discussions during the course of the studies. Authors are also thankful to Mr.D.K.Bhattacharya, Mr.P.Kalyanasundaram, Mr.B.B.Jha and Mr.C.Rajagopalan, Division for Post-

Irradiation Examination and NDT Development, Indira Gandhi Centre for Atomic Research, Kalpakkam, for many useful discussions during the preparation of the manuscript.

## REFERENCES

- [1] Kaiser, Joseph, "Untersuchungen über das auftreten Geräuschen beim Zugversuch", Ph.D. Thesis, Technische Hochschule, Munich, 1950.
- [2] Mannan, S.K., Dayal, R.K., Vijayalaxmi, M., and Parvathavardhini, N., "Influence of Deformation on Sensitisation kinetics and its Microstructure Correlation in a Nuclear Grade 316 Stainless Steel", Journal of Nuclear Material, Vol. 126, No. 1, September 1984, pp.1-8.
- [3] Raj, Baldev, "Acoustic Emission for Characterising Deformation and Fracture during Tensile Testing in Austenitic Stainless Steels", Ph.D. Thesis, Indian Institute of Science, Bangalore, 1989.
- [4] Mannan, S.L., Samuel, K.G. and Rodriguez, P., "Stress-Strain Relation for 316 Stainless Steel", Scripta Metallurgica, Vol.16, No.3, March 1982, pp.255-257.
- [5] Seetharaman, V. and Krishnan, R., "Influence of the Martensitic Transformation on the Deformation Behaviour of an AISI 316 Stainless Steel at Low Temperatures", Journal of Material Science, Vol.16, No.2, February 1981, pp.523-530.
- [6] Imeda, H., Kuganagi, H., Kimura, H. and Nakasa, H., "Acoustic Emission Characteristics during Tensile Tests of various Metals with several Types of Crystal Structures", presented at the Third Acoustic Emission Symposium, Tokyo, 1976.
- [7] Raj, Baldev, Jha, B.B. and Rodriguez, P., "Frequency Spectrum Analysis of Acoustic Emission Signal during Tensile Deformation in an AISI 316 Type Austenitic Stainless Steel", Acta Metallurgica, Vol.37, No.8, August 1989, pp.2211-2215.
- [8] Curtis, G., "Spectral Analysis of Acoustic Emission", Non destructive Testing, Vol.7, No.2, April 1974, pp.82-91.
- [9] Raj, Baldev, Ananthakrishna, G., Kalyanasundaram, P., Barat, P. and Jayakumar, T., "Stimulated Amplification of Acoustic Emission Signals during Deformation", Scripta Metallurgica, (In Press).
- [10] Smith, C.W., "Observations on Prediction of Non-self-similar Sub-critical Crack Growth and Stress Intensity Distributions", in Advances in Fracture Research Vol. 1, Pergamon Press, Oxford, 1982, pp.3-10.
- [11] Swift, I.H. and Richardson, J.E., "Internal Friction of Zinc Crystals", Journal of Applied Physics, Vol.18, No.4, April 1947, pp.417-425.
- [12] Heiple, C.R. and Carpenter, S.H., "Acoustic Emission produced by Deformation of Metals and Alloys", Report No. RFP-4046, Rockwell International, Colorado, U.S.A., 1987.
- [13] Caceres, C.H. and Rodriguez, A.H., "Acoustic Emission and Deformation Bands in Al-2.5%Mg and Cu-30%Zn", Acta Metallurgica, Vol.35, No.12, December 1987, pp.2851-2864.
- [14] Mannan, S.L., Samuel, K.G. and Rodriguez, P., "Dynamic Strain Ageing in Type 316 Stainless Steel", Transactions of Indian



- Institute of Metals, Vol.36, No.4 & 5, August/October 1983, pp.313-320.
- [15] Raj,Baldev, Jayakumar,T., Kalyanasundaram,P., Barat,P., Jha,B.B., Bhattacharya,D.K. and Rodriguez,P., "Comparative Studies on AE Generated during Luder's Deformation in Mild Steel and Portevin-Le Chatelier Effect in Austenitic Stainless Steel", Journal of Acoustic Emission, Vol.8, No.1-2, January-June 1989, pp.S149-S152.
- [16] Lai,J.K.L. and Wickens,A., "Microstructural changes and variations in Creep Ductility of Three Casts of Type 316 Stainless Steel", Acta Metallurgica, Vol.27, No.1, January 1979, pp.217-230.
- [17] Raj,Baldev and Jayakumar,T., "Acoustic Emission during Tensile Plastic Deformation and Fracture in Austenitic Stainless Steel,"Journal of Acoustic Emission, Vol.7, No.3, July 1988, pp.S1-S12.
- [18] Agarwal,A.B.L., Fredrick,J.R. and Felback,D.K., "Detection of Plastic Microstrain in Aluminium by Acoustic Emission", Metallurgical Transactions, Vol.1A, No.4, April 1970, pp.1069-1071.
- [19] Heiple,C.R. and Carpenter,S.H., "Acoustic Emission produced by Deformation of Metals and Alloys", Journal of Acoustic Emission, Vol.6, No.3, July-September 1987, pp.177-204.
- [20] Shibata,M. and Ono,K., "Stress Concentration due to an Oblate Spheroidal Inclusion", Materials Science and Engineering, Vol.34, No.1, January 1978, pp.131-137.
- [21] Shibata,M. and Ono,K., "Internal Stresses due to an Oblate Spheroidal Inclusion: Misfit, Inhomogeneity and Plastic Deformation Effects", Acta Metallurgica, Vol.26, No.6, June 1978, pp.921-932.
- [22] Gladman,T., Holmes,B. and Mcirror,I.D., "Effects of Second Phase Particles on Toughness and Ductility", in Proceedings Conference on Effects of Second Phase Particles on the Mechanical Properties of Steel, The Iron and Steel Institute, Scarborough, Cox and Wymon Limited, London, 1971, pp.68-73.
- [23] Jayakumar,T., Raj,Baldev, Bhattacharya,D.K., Rodriguez,P. and Prabhakar,O., "Effect of Heat Treatment on Acoustic Emission in Nimonic Alloy PE-16 during Tensile Deformation", Transactions of Indian Institute of Metals, Vol.40, No.2, April 1987, pp.147-150.
- [24] Jayakumar,T., Raj,Baldev, Bhattacharya,D.K., Rodriguez,P. and Prabhakar,O., "Studies on Acoustic Emission in Nimonic Alloy PE-16 during Tensile Deformation and Fracture", presented at Twelfth World Conference on Non-destructive Testing, Amsterdam, The Netherlands, 1989.
- [25] Scruby,C.B., Wadley,H.N.G., Rushbridge,K.L. and Stockholm-Jones,D., "Influence of Microstructure on Acoustic Emission during Deformation of Aluminium Alloys", Metal Science, Vol.15, No.11 & 12, November-December 1981, pp.599-608.
- [26] Rushbridge,K.L., Scruby,C.B. and Wadley,H.N.G., "Origin of Acoustic Emission in Aged Al-Zn-Mg alloys I: The Base Ternary Alloy", Materials Science and Engineering, Vol.59, No.2, June 1983, pp.151-168.

RELATIONSHIP BETWEEN ACOUSTIC EMISSION AND FLAW SIZE IN  $\text{Si}_3\text{N}_4$  CERAMICS

---

REFERENCE: Mori, Y. and Kishi, T., "Relationship between Acoustic Emission and Flaw Size in  $\text{Si}_3\text{N}_4$  Ceramics," Acoustic Emission: Current Practice and Future Directions, ASTM STP 1077, W. Sachse, J. Roget and K. Yamaguchi, Eds., American Society for Testing and Materials, Philadelphia, 1991.

ABSTRACT: Acoustic emission behavior was investigated in the  $\text{Si}_3\text{N}_4$  ceramics in order to study the effect of flaw size on fracture strength. A close relation between the generation of acoustic emission and flaw size was found. It was found that acoustic emission signals can be detected only just before specimen failure with flaw size of  $15\text{ }\mu\text{m}$ , a critical flaw size estimated for the materials, or larger. Whereas flaws smaller than  $15\text{ }\mu\text{m}$  began to generate emissions at the stress level, approximately 50 % of the strength of the specimens failed. In the latter case, it was concluded that emissions were due to microscopic fracture events around inherent flaws.

KEYWORDS: acoustic emission, silicon nitride, artificial flaw, flaw size, nondestructive test, fracture

Ceramics have been used for structural materials because of their intrinsic properties, such as high strength or high heat resistivity. However, the brittle fracture occurs easily in ceramics, therefore more work is being devoted to enhancing the fracture toughness of ceramics [1-3]. In the fracture of ceramics the critical crack size is very small, and it is generally accepted that cracks can often originate from microscopic inherent flaws and coalesce [4,5]. It is, therefore, important to understand the dynamic microscopic fracture process in details.

On the other hand, nondestructive testing (NDT) technique for

Dr. Y. Mori is associate professor at College of Industrial Technology, Nihon University, 2-1 Izumi-cho-1, Narashino, Chiba 275, Japan; Professor Dr. T. Kishi is at Research Center for Advanced Science and Technology, The University of Tokyo, 6-1 Komaba-4, Meguro-ku, Tokyo 153, Japan.

quantitative assessment of ceramics reliability is also important. Some innovative techniques have been studied and investigated for their applicability to ceramics, such as micro-focused x-ray, scanning acoustic microscope (SAM), scanning laser acoustic microscope (SLAM) and so on [6,7]. Acoustic emission (AE) is one of the most expedient techniques both to improve fundamental understanding of fracture dynamics and to evaluate structural integrity. Many researchers have made remarkable advances [5,8-11].

Japan Fine Ceramics Center (JFCC, Nagoya Japan) has promoted R & D project on the development of NDT techniques for the fine ceramics, contracted with Government, since 1987. The present study was carried out as one of the part of the JFCC's project.

In the present paper, acoustic emission during the four-point bend test both in hot-pressed and in pressure-less sintered  $\text{Si}_3\text{N}_4$  specimens with artificial defects has been analyzed. The purpose of this study is to investigate the influence of flaw size both on acoustic emission and on strength of the material. This paper also describes an attempt to seek an explanation for the generation of acoustic emission observed in the present material, by comparing with the results obtained by the fracture surface topography analysis (FRASTA) technique.

## EXPERIMENTAL PROCEDURE

### Specimens and Four-point Bend Test

Hot-pressed  $\text{Si}_3\text{N}_4$  (HPSN) and pressure-less sintered  $\text{Si}_3\text{N}_4$  (PLSSN) were used as the test materials for this experiment because of their potential importance as a structural ceramics. Material properties are listed in Table 1.

The specimens for the four-point bending test were machined from the disks fabricated by a hot press or by a sintering, and machining damage was removed mechanically by polishing to produce an optical finish. The specimen was the rectangular bar with dimensions of 3 by

TABLE 1 -- Properties of materials used.

	HPSN	PLSSN
Mean grain size, $\mu\text{m}$	$\phi 1 \times 10$	$\phi 1 \times 10$
Density	3.35	3.27
Strength(4-point bend test), MPa	863	1050
Young's modulus, GPa	306	260
Poisson's ratio	0.26	0.27
Fracture toughness, $\text{MPa}/\sqrt{\text{m}}$	5.3 <sup>a</sup>	6.3 <sup>b</sup>
Sound velocity; P-wave, km/s	10.3	10.0
S-wave, km/s	6.0	5.5

<sup>a</sup> by indentation microfracture (IM) method [12].

<sup>b</sup> by IM method and indentation strength-in-bending (ISB) method [13].

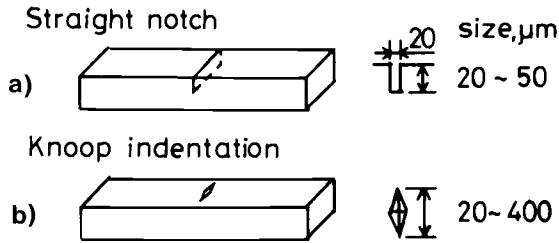


FIG. 1 -- Schematic illustration of artificial flaws introduced into specimens.

4 by 40 mm (Fig. 1).

In order to examine the effect of defects both on the strength of the specimen and on acoustic emission, artificial defects were introduced into the specimens. Straight-through notches which had a depth varying from 20 to 50  $\mu\text{m}$  were made at the center of the test piece by a 20  $\mu\text{m}$  thick diamond cutter (Fig. 1a). Knoop indentations were placed on the bend surface of the specimen using a routine microhardness tester at load levels of 0.1 to 150 N, taking care to accurately align the indentation diagonal perpendicular to the longitudinal axis of the specimens (Fig. 1b). The resulting dimensions of the indentations were 20 to 400  $\mu\text{m}$ . In general for indentation flaws, residual stresses are induced by the indentation required to create the flaw [14,15]. Such residual stresses would aid the applied tensile stress in producing fracture, thus leading to a lower measured  $K_{Ic}$  value. In this experiment, neither annealing nor removal of material from the surface was treated on the Knoop specimens to eliminate the residual stresses near the flaw.

Four-point bend tests were performed using a universal testing machine at a constant crosshead speed of 0.1 mm/min and/or 0.5 mm/min. A bend test jig with inner span of 10 mm and outer span of 30 mm was used. All testing was performed in air at room temperature.

#### AE Measurement

Two 400 kHz resonant type AE sensors were employed to detect and locate emission events. Detected signals were amplified 60 dB by a preamplifier and analyzed by a commercial AE analyzer. Total amplifier gain of 90 dB and threshold level of 100  $\mu\text{V}$  at sensor output were chosen.

#### NDT Examination

Flaw detectability of nondestructive testing (NDT) methods which are expected to be techniques for the inspection of ceramics were also examined.

TABLE 2 -- Results of NDT examinations.

NDT Methods	Flaws and sizes, $\mu\text{m}$					
	Notch		Knoop			
	20	50	20	50	100	400
Fluorescent penetrant	0	0	X	X	X	...
Micro-focused X-ray (10 $\mu\text{m}$ )	0	0	X	X	X	...
Ultrasonic (15 MHz)	0	0	X	X	X	...
SAM (50 MHz)	0	0	0	0	0	...
SLAM (100 MHz)	0	0	X	X	X	...

0: detected, X: not detected

Prior to the bend test, all specimens were examined by micro-focused (10  $\mu\text{m}$ ) X-ray technique, ultrasonic inspection (15 MHz), scanning acoustic microscope (SAM, 50 MHz), scanning laser acoustic microscope (SLAM, 100 MHz), and fluorescent penetrant inspection. The test results are shown in Table 2. Notch flaws were detected by all of the methods employed in this study, however, Knoop flaws, which were the resulting indentation cracks, were detected only by SAM. Details of the examination have been reported elsewhere [16].

## RESULTS AND DISCUSSION

### Test Results

All specimens were loaded in the four-point bending test until the specimens were fractured, and the acoustic emissions were measured throughout the test. Figure 2 shows two examples of bending load,  $P$ , applied vs. elapsed time,  $t$ , curve for Knoop specimens. For all specimens tested, unstable fractures occurred at a critical applied stress level without an obvious precursor compliance change.

Acoustic emission total event counts,  $N$ , are also plotted in

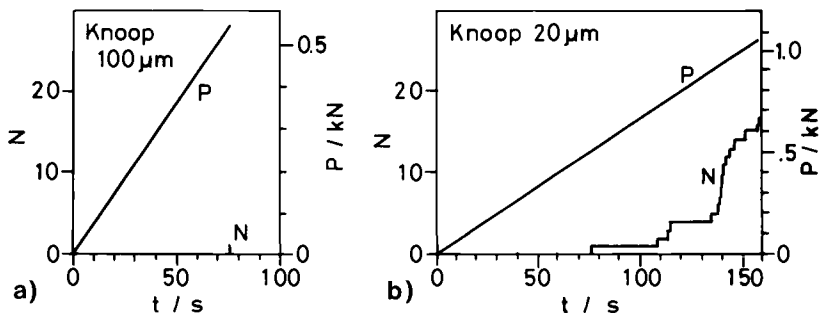


FIG. 2 -- Two examples of the four-point bend test results.  
a) Knoop 100  $\mu\text{m}$  and b) Knoop 20  $\mu\text{m}$  specimens (PLSSN).

Fig. 2. In this study, emission events located on the part of the specimen within inner loading points of bend test jig were analyzed as effective acoustic emission signals generated by fracture events in the specimen. Here the sound velocity of 6000 m/s was used.

AE event counts measured were few in all specimens, and there was no difference in acoustic emission behavior between HPSN and PLSSN specimens. The AE test results showed that there were two types of emission behaviors during the bend test, i.e., (A) emissions were observed only when the specimen failure occurred, as seen in Fig. 2a, and (B) the occurrence of emissions began at load levels about or below 50 % of the fracture strength of the specimen, Fig. 2b. Therefore, the stress level at which high emission activity was firstly observed during the bend test was evaluated. This stress level is referred hereinafter to as  $\sigma_{AE}$  and  $\sigma_B$  for the bending strength of each specimen.

#### Relation Between Acoustic Emission And Flaw Size

Figure 3 shows the relationships between flaw size, stress  $\sigma_{AE}$  (open symbols) and  $\sigma_B$  (solid symbols) for HPSN and PLSSN specimens. In Fig. 3, the flaw size of a notch or a Knoop is expressed by the equivalent crack length,  $a_{eq}$ , in terms of through-the-thickness crack in an infinite plate. For a Knoop flaw, the resulting indentation crack could not be observed for all of the specimens, though scanning electron microscope (SEM) observation on the fracture surface was made, therefore, the equivalent crack length was deduced by assuming a semicircular flaw shape with a radius of Knoop diagonal measured. The data for the specimens whose failure did not occur from the flaw site are plotted in the hatched region at left of plot. Here, the strength data for Knoop specimens involves the effect of residual

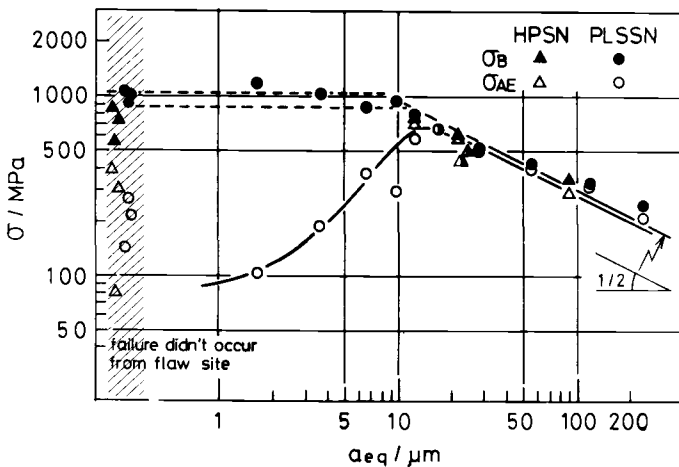


FIG. 3 -- Relationships between equivalent crack length  $a_{eq}$ , stress  $\sigma_{AE}$  and  $\sigma_B$ .

indentation stresses.

Regarding the fracture strength, it is concluded from Fig. 3 that the value of about  $10\text{ }\mu\text{m}$  is estimated as the minimum flaw size which affected the fracture strength of the present materials. In addition, the strength of specimens having a flaw larger than  $10\text{ }\mu\text{m}$  can be expressed by a straight line of slope  $-1/2$ , that is the linear fit in accordance with the relation for stress intensity factor of  $K = \sigma/\sqrt{\pi a_{\text{eq}}}$ . The resultant value of fracture toughness  $K_{\text{Ic}} = 5.5\text{ MPa}/\sqrt{\text{m}}$  from the fit line corresponds very closely with the  $K_{\text{Ic}}$  values of  $5.3\text{ MPa}/\sqrt{\text{m}}$  for HPSN and  $6.3\text{ MPa}/\sqrt{\text{m}}$  for PLSSN obtained using fracture test procedure (see Table 1).

On the other hand, the relationship between acoustic emission and flaw size, that is applicable both to HPSN and to PLSSN, is found as shown in Fig. 3. In the region of  $a_{\text{eq}}$  smaller than about  $10\text{ }\mu\text{m}$ , the level of  $\sigma_{\text{AE}}$  increases with the increase of  $a_{\text{eq}}$ , though the corresponding fracture strength for each specimen remains constant. The plots of  $\sigma_{\text{AE}}$  of the specimens with a flaw larger than  $15\text{ }\mu\text{m}$  lie more or less on a line parallel to the  $K_{\text{Ic}}$  corresponding lines drawn on plots of  $\sigma_{\text{B}}$ . By using notation,  $K_{\text{AE}}$ , the resulting value,  $K_{\text{AE}} = 5\text{ MPa}/\sqrt{\text{m}}$ , gives a good coincidence to  $K_{\text{Ic}}$  values of the materials. In addition, a critical crack length is estimated by acoustic emission to be about  $15\text{ }\mu\text{m}$ . It is of interest that this flaw size of  $15\text{ }\mu\text{m}$  is comparable to the critical flaw size which affected the fracture strength of the materials.

#### Microfracture Process Leading To Acoustic Emission

Figure 4 shows the examples of the macroscopic fracture surfaces of PLSSN notch specimens, illustrating three different fracture

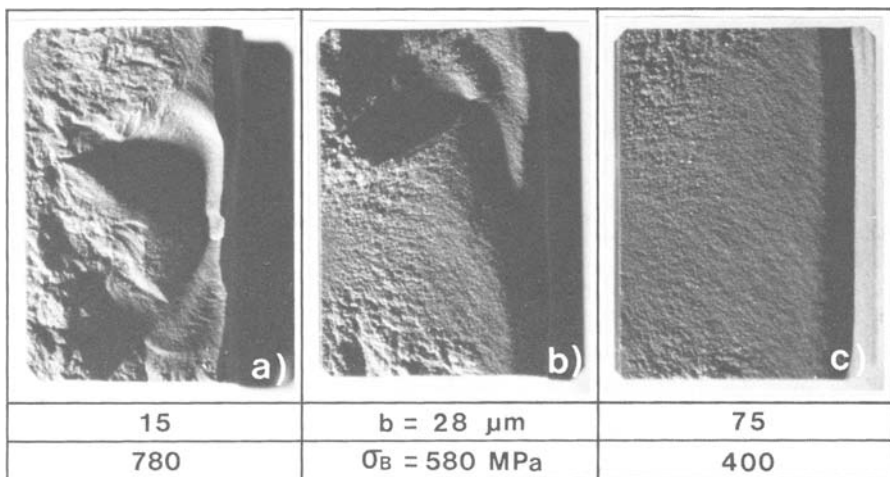


FIG. 4 -- Macroscopic fracture surfaces of PLSSN notch specimens, illustrating three different fracture surface profiles.

surface profiles. The crack propagation direction is from left (notch root) to right in each photograph. With increasing  $\sigma_B$ , that is, with decreasing notch depth, b, a fracture surface profile reveals a much rougher surface from a flat surface. It is interesting to compare the fracture surface profile with the acoustic emission behavior and the fracture strength of the specimen. The rough fracture surface profile such as a) in Fig. 4 was observed only in the specimens with a flaw smaller than about  $10\text{ }\mu\text{m}$  (Fig. 3), and its acoustic emission behavior fell under the Category B, mentioned above. On the other hand, the specimens showed Category A's emission behavior had a profile of c) or b) on rare occasions. It was estimated that the surface profile of b) which lay between profiles a) and c) corresponded to the change in the level of  $\sigma_{AE}$  near an  $a_{eq}$  of  $15\text{ }\mu\text{m}$  in Fig. 3.

The fracture surfaces shown in Fig. 4 and the fact that the specimens showed the fracture surface profile of Fig. 4a) broke in small pieces at the fracture site suggests that the crack branching took place in the specimens with higher strength. In general, the crack branching occurs after crack grew to a certain length. Therefore, acoustic emission data shown in Fig. 3 can be interpreted as follows. In the high strength specimens that not did fail from artificial flaw site, acoustic emission began at stresses as low as 100 MPa. This emission is associated with the microscopic fracture events initiated at the natural flaws that existed on or beneath the tensile surface of a bend specimen where the high tensile stress is achieved during stressing. On the other hand, in specimens with larger artificial flaws, because of the stress concentration at the flaw tip, the contributions of natural flaws to the emission are few here. This explanation will be supported by the following discussion.

In order to seek an explanation for the acoustic emission observed in the present material, fracture surface topography analysis (FRASTA) technique developed by T. Kobayashi was employed. FRASTA technique under development at SRI is a procedure for reconstructing the fracture process by computer matching of conjugate fracture surface topographs [17]. The failure process produces irregularities on the fracture surface, and hence the sequence of microfracturing is recorded in the topography of the fracture surface. The topography of the surfaces is extracted by photographing the surfaces in stereo with a SEM, and by using aerial cartographic technique. In preparation for reconstructing the fracture process, using a computer, the topographic map of one fracture surface is inverted and superimposed on the map of the conjugate surface. The two maps then are adjusted so that identifiable corresponding points on the two surfaces are in alignment and overlap everywhere. The fracture process is reconstructed by increasing the distance between the conjugate maps in small increments. The results can be displayed as fractured-area projection plots.

FRASTA was carried out by Kobayashi on a specimen of PLSSN used in this study [18]. The specimen was a smooth rod specimen with gauge length of  $\phi 6 \times 20\text{ mm}$ . The specimen was fractured in tensile test at room temperature, and FRASTA was then carried out on the fracture surfaces. In the tensile test, acoustic emission located at the fracture site of the specimen began at a stress level of 340 MPa, and the specimen failed, with initiation site at the specimen surface, at a stress level of 486 MPa. The mean tensile strength of the material



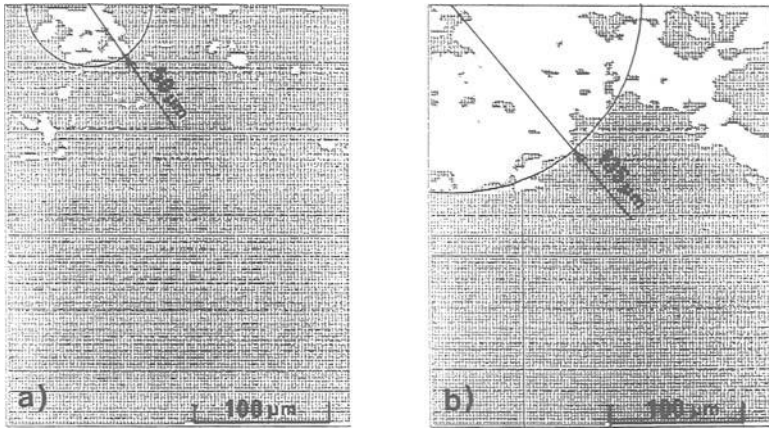


FIG. 5 -- Fractured-area projection plots obtained by separating the conjugate topographic maps (FRASTA technique). a)  $1.617 \mu\text{m}$  separation and b)  $2.861 \mu\text{m}$  separation (after Kobayashi [18]).

was 516 MPa with shape parameter of Weibull distribution of 12.

Figure 5 shows the result of FRASTA, showing the fractured-area projection plots obtained by matching and separating the conjugate topographic maps. In these plots the dark areas indicate continuous material, and white areas are the fractured areas. The crack propagation direction is from top (specimen surface) to bottom. Figure 5a) illustrates the specimen state at the onset of loading, and also shows microcracks or cavities, which are enclosed with a semicircle with radius about  $50 \mu\text{m}$  ( $a_{eq} = 22 \mu\text{m}$ ) below the specimen surface, possibly formed during the sintering process of the material. An examination of Figs. 5a) and 5b) reveals that despite a separation increment of  $1.244 \mu\text{m}$  the existing crack increased rapidly in size up to about  $135 \mu\text{m}$  [Fig. 5b)], though the crack extension toward the right is also found. On following sequence in which the maps were separated up to  $5 \mu\text{m}$ , it was revealed that after the crack was arrested for a while the crack started to grow, and the accelerated specimen failure took place. It is, therefore, expected that the final failure of the specimen occurred from the crack which is approximated with a semicircle with a radius of about  $135 \mu\text{m}$  ( $a_{eq} = 59 \mu\text{m}$ ) in Fig. 5b). This value was used to compute the fracture strength of the specimen using the stress intensity factor  $K_{Ic}$  of  $6.3 \text{ MPa}\sqrt{\text{m}}$  (see Table 1). The resulting value of 462 MPa agrees well with the measured value of 486 MPa.

From the above discussions, it is concluded that the occurrence of acoustic emissions generated before the specimen failure were due to the pop-in fracture in the specimen such as that shown in Fig. 5. It is also expected that the microscopic fracture events, such as the growth and coalescence of microscopic inherent flaws and the nucleation of new microcracks [Fig. 5a)], resulted in the sources of emissions observed at an early stage of the stressing. For the microscopic fracture process in ceramics, Okada and Sines reported

that microscopic cracks, which may not be detectable by nondestructive testing, could propagate more readily than macroscopic cracks and that cracks can coalesce in a very short time [4]. Wakayama et al. also reported that by quantitative acoustic emission analysis, nucleation of microcracks with a diameter of 15 to 30  $\mu\text{m}$  could be detected at an early stage of stressing [5]. The result of FRASTA presented here was obtained from SEM fracture surface photographs taken at low magnification. Thus, it was not possible to estimate such microscopic fracture process. FRASTA with higher-magnification SEM photographs may be able to give informations about these problems.

The subject of using the acoustic emission technique as an NDT for ceramics remains questionable as the acoustic emission could not predict the failure of a specimen with a flaw larger than 15  $\mu\text{m}$  (Fig. 3), which must be successfully detected by NDT for the practical use of ceramics. However, it is of interest that acoustic emission is sensitive to such fracture event which can not be detected by NDT. The relationship between acoustic emission and crack length obtained in Fig. 3 shows that acoustic emission can detect the nucleation of crack, from which as further stressing is applied the onset of final crack growth in the specimen occurs.

#### SUMMARY

A relationship between acoustic emission and flaw size, applicable both to the hot-pressed and the pressure-less sintered  $\text{Si}_3\text{N}_4$ , was found. Flaws of which sizes were larger than 15  $\mu\text{m}$ , which was almost the same as a critical flaw size estimated by a conventional materials testing, generated emissions only just before specimen failure, whereas flaws smaller than 15  $\mu\text{m}$  began to generate emissions at the stress level, below 50 % of the fracture strength of each specimen. It was known that emissions were due to microscopic fracture events around inherent flaws, suggesting that, by using acoustic emission measurement, a critical size of the flaw from which a crack initiates and extends under loading may be estimated. FRASTA technique gave an objectivity to the explanation of acoustic emission source in the materials.

#### ACKNOWLEDGMENTS

This work is related to that carried out in Japan Fine Ceramics Center (JFCC) for Research on the Development of NDT Techniques for the Fine Ceramics. The authors would like to thank Mr. Kenichiro Kitadate and Makoto Ueda of JFCC for providing the specimens and performing NDT examinations on the specimens. The authors express their indebtedness to Dr. T. Kobayashi of SRI International, formerly professor of Nagoya Institute of Technology, for the use of his FRASTA data.

## REFERENCES

- [1] N. Claussen, J. Steeb and R. F. Pabst, Journal of the American Ceramic Society, Vol. 56, No.6, 1977, p. 559.
- [2] R. Knehans and R. Steinbrech, Journal of Materials Science Letter, No. 1, 1982, p. 327.
- [3] A. G. Evans and K. T. Faber, Journal of the American Ceramic Society, Vol. 67, No.4, 1984, pp. 255-260.
- [4] T. Okada and G. Sines, Journal of the American Ceramic Society, Vol. 66, No. 10, 1983, pp. 719-725.
- [5] S. Wakayama, T. Kishi and S. Kohara, Progress in Acoustic Emission III, The Jap. Soc. Non-destructive Inspection, 1986, pp. 653-660.
- [6] D. Munz, K. Goebbels and H. Reiter, Proceedings of the 4th International Symposium on Fracture Mechanics of Ceramics, Blacksburg, U.S.A., 1985.
- [7] M. Ando, T. Matsuda and K. Kitadate, Journal of JSNDI, The Jap. Soc. Non-destructive Inspection, Vol. 36, No. 9A, 1987, p. 722.
- [8] A. S. Tetelman and A. G. Evans, Fracture Mechanics of Ceramics, Vol.1, Plenum Press, New York, 1975, pp. 895-924.
- [9] K. Ohta, H. Hashimoto and H. Iwasaki, Proceedings of National Conference on AE, The Jap. Soc. Non-destructive Inspection, Tokyo, 1983, p. 98.
- [10] T. Kishi, Progress in Acoustic Emission II, The Jap. Soc. Non-destructive Inspection, 1984, pp. 302-309.
- [11] M. Nishino, Y. Mori, T. Kishi, M. Ando, T. Matsuda and K. Kitadate, Journal of JSNDI, The Jap. Soc. Non-destructive Inspection, Vo. 37, No. 2A, 1988, p. 194.
- [12] G. R. Antis, P. Chantikul, B. R. Lawn and D. B. Marshall, Journal of the American Ceramic Society, Vol. 64, 1981, p. 533.
- [13] P. Chantikul, G. R. Antis, B. R. Lawn and D. B. Marshall, Journal of the American Ceramic Society, Vol. 64, 1981, p. 539.
- [14] J. J. Petrovic, L. A. Jacobson, P. K. Talty, and A. K. Vasudevan, Journal of the American Ceramic Society, Vol. 58, No. 3-4, 1975, p. 113.
- [15] T. Fett, Journal of Material Science, Vol. 19, 1984, p. 672.
- [16] JFCC Report No.61-R-3, Japan Fine Ceramics Center, June 1987, p. 92.
- [17] T. Kobayashi and D. A. Shockey, Metallurgical Transactions A, Vol. 18A, November 1987, pp. 1941-1948.
- [18] JFCC Report No.61-R-3, Japan Fine Ceramics Center, June 1987, p. 160.

Steve H. Carpenter and Zuming Zhu

## A COMPARISON OF THE ACOUSTIC EMISSION GENERATED FROM THE FRACTURE AND DECOHESION OF GRAPHITE NODULES WITH THEORETICAL PREDICTIONS

---

REFERENCE: Carpenter, S.H. and Zhu, Zuming, "A Comparison of the Acoustic Emission Generated From the Fracture and Decohesion of Graphite Nodules with Theoretical Predictions," Acoustic Emission: Current Practice and Future Directions, ASTM STP 1077, W. Sachse, J. Roget and K. Yamaguchi, Eds., American Society for Testing and Materials, Philadelphia, 1991.

ABSTRACT: It has been known for many years that the fracture and/or debonding of inclusions or second phase particles during deformation can act as a source of acoustic emission. A number of experimental studies of this phenomena have been reported. Excellent theoretical investigations of the fracture of an elastic spherical particle in a plastic matrix have been carried out and expressions have been derived for the energy released during fracture. However, there is little work where a direct comparison between experimental data and theoretical predictions can be carried out. The purpose of this paper is to report on the acoustic emission generated from the fracture and/or decohesion of spherical graphite nodules during the compressive deformation of nodular cast iron. The correlations of the experimental acoustic emission data with theoretical predictions will be reported.

KEYWORDS: acoustic emission, inclusion fracture, second phase particles, nodular cast iron

The fracture and/or debonding of inclusions and second phase particles during deformation have been recognized as possible sources of acoustic emission for many years [1]. A recent review [2] has provided a discussion of the current understanding of acoustic emission from the fracture and decohesion of inclusions and second phase particles. To date there has been a great deal of experimental work reported and some excellent theoretical work as well, however there is little work where a direct comparison of theory and experiment can be carried out. The theoretical work has concentrated on the fracture of an elastic spherical particle in a plastic matrix. Expressions have been derived for the energy

Dr. Carpenter is a Professor of Physics at the University of Denver, Denver, CO 80208. Dr. Zhu, formerly a visiting scholar at the University of Denver, is a distinguished scientist at Institute of Metals Research, Shenyang, CHINA

released during the fracture of the spherical particle. The primary difficulty in evaluating the validity of these expressions by experimental data is obtaining suitable test samples from which to obtain the data. The requirement for samples with well characterized spherical second phase particles with small variations in diameter is difficult to satisfy. Carefully prepared nodular cast iron is a material in which it is possible to obtain uniform spherical particles, i.e. the spherical graphite nodules. Data will be presented in this paper on the acoustic emission generated from the fracture and decohesion of graphite nodules during the compressive deformation of ductile cast iron. Samples have been carefully prepared with a constant carbon concentration and a uniform distribution of spherical graphite nodules of near the same diameter. A series of samples with different diameter nodules have been tested. The change in average nodule diameter varies over a factor of four. Correlations between the experimental acoustic emission data and theoretical predictions as a function of average nodule diameter will be presented and discussed.

#### EXPERIMENTAL PROCEDURE

A series of well characterized ductile cast iron samples having uniform chemistry but different graphite nodule diameters were supplied by Dr. Richard Salzbrenner, Sandia National Laboratories, Albuquerque, N.M., for this investigation. Samples with five different graphite nodules diameters were supplied and tested. Measurements of the average nodule diameter were performed by Salzbrenner [3]. Figure 1 is a micrograph showing typical microstructure for group 5 samples (see Table 1 below). The average nodule diameter varied from 0.136 mm to 0.031mm. Compression samples 7mm x 10 mm x 20 mm were deformed at a constant crosshead speed of 0.0064 cm/min. The acoustic emission measurements were carried out using standard commercial equipment. The transducer used was a resonant piezoelectric (PZT-5) type, with a resonant frequency of approximately 140 kHz. Measurements were made at a gain of 105 dB with a frequency bandpass of 100 - 300 kHz. The RMS voltage generated by the acoustic emission was measured by a Hewlett-Packard 3400A voltmeter. The RMS data presented in this paper have been corrected for noise and are referenced to the transducer. Care was exercised to eliminate any and all sources of extraneous noise during testing.

#### RESULTS

The acoustic emission generated during the compressive deformation of nodular cast iron has been investigated and reported previously [4,5]. The measurements reported on in this paper are in general agreement with the earlier results. Typical acoustic emission reported in terms of the RMS voltage and the applied stress for the compressive loading of a nodular cast iron sample are shown as a function of the crosshead displacement in Figure 2. The data shown in Figure 2 are for a group 4 sample. The RMS data are characterized by a peak near yield and a much broader peak well past yield. The peak at yield is believed due to avalanche motion of

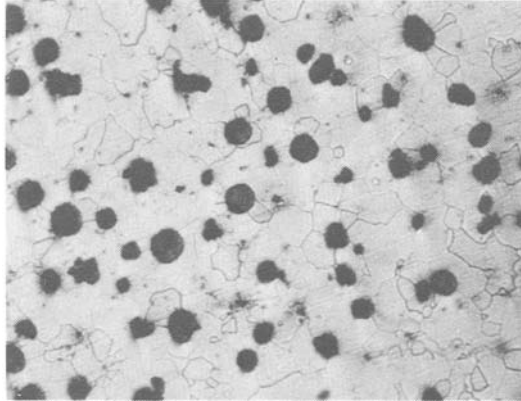


Figure 1.- Typical microstructure of a group 5 sample, average nodule diameter = 0.031 mm. ( $\times 183$ )

dislocations and will not be discussed further in this paper. The broad RMS peak past yield has been attributed to the fracture and/or decohesion of the graphite nodules [4,5]. The strain at the onset or beginning of the second RMS peak, the maximum value of the second RMS peak and the applied stress at the maximum of the second RMS peak, as expected, were found to be dependent on the graphite nodule diameter. Table I provides a listing of the averages of experimental data from at least three compressive tests of samples from each sample group. The column RMS [Peak(2) - Bg] is the maximum value of the RMS bursts at the second peak less the value of the background or continuous emission at that point.

TABLE I

Sample Group No.	Nodule Diameter mm	RMS Peak(1) $\mu\text{V}$	RMS Peak(2) $\mu\text{V}$	RMS [Peak(2) - Bg] $\mu\text{V}$	Strain at Onset %	Yield Stress $\text{MPa}$	Stress Peak(2) $\text{MPa}$
1	0.136	0.48	1.46	1.03	1.78	214	450
2	0.123	0.47	1.16	0.76	1.88	177	460
3	0.078	0.62	0.80	0.36	2.88	199	500
4	0.088	0.83	0.77	0.40	3.00	295	525
5	0.031	0.20	0.31	0.04	3.20	300	780

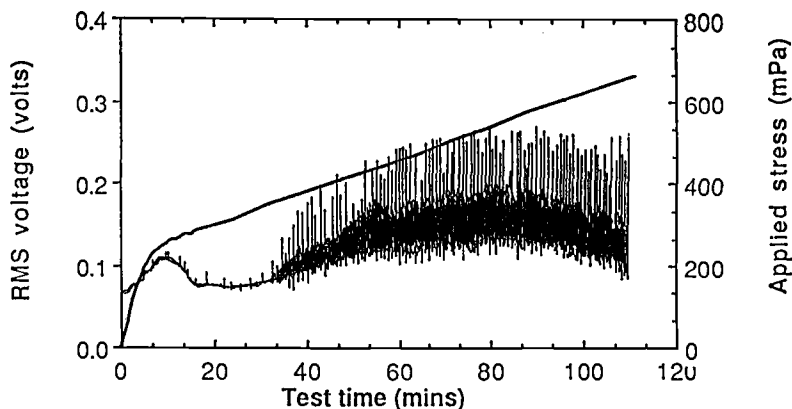


Figure 2.- Acoustic emission in terms of the RMS voltage and applied stress for the compressive loading of a group 4 nodular cast iron sample.

## DISCUSSION

An examination of the experimental data in Table I indicates that there are definite correlations between a number of the experimental measurements and the average nodule diameter. Only the the RMS Peak(1) and the yield stress fail to show a distinct correlation with the average nodule diameter. Earlier work has shown that the yield properties are not dependent upon the nodule size in ductile cast iron [6]. The other experimental data show an ordering in magnitude in accordance with the average nodule diameter.

Scruby [7] and Kant [8] have estimated the energy released from the fracture of an elastic spherical inclusion in a infinite plastic matrix where the matrix and the inclusion have different elastic properties. Both found that the energy released should be given approximately by

$$E_n = (4/3)(1 - \nu)(\sigma^2 r^3/E) \quad (1)$$

where  $\nu$  is Poisson's ratio,  $\sigma$  is the applied stress,  $r$  is the radius of the crack and  $E$  is the Young's modulus of the inclusion. Gerberich and Jatavallabhula [9] have derived the following expression for the RMS voltage generated during the fracture of a spherical particle of radius  $r$ :

$$V_{RMS} = [2K''(f)/uD][\sigma Ar] \quad (2)$$

where  $K''(f)$  is a function of frequency,  $u$  is the shear modulus,  $D$  is the distance the crack is located below the surface and  $A$  is the area swept out by the crack. Clearly if the particle cracks

completely across its diameter then equation (2) predicts that the RMS voltage generated during fracture of the spherical particle will be proportional to  $[\sigma r^3]$ . Recently published work [10] has shown that the RMS voltage generated by an acoustic emission event is proportional to the energy in the acoustic emission waveform. It should then be possible to also use equation (1) to predict the value of RMS voltage generated. Equation (1) predicts that the RMS voltage generated will be proportional to  $[\sigma^2 r^3]$ . Hence, both treatments predict an  $[r^3]$  dependence but disagree on the stress dependence.

Assuming that the values of RMS voltage and applied stress at the second peak maximum are the best choices to correlate with the average nodule diameters it is possible to evaluate the validity of equations (1) and (2). Figure 3 shows a plot of the maximum value of the second RMS peak versus the applied stress squared times the average radius cubed, i.e. equation (1). Figure 4 shows a similar plot of the maximum value of the second RMS peak versus the applied stress times the average radius cubed, i.e. equation (2). In both cases good straight lines are obtained.

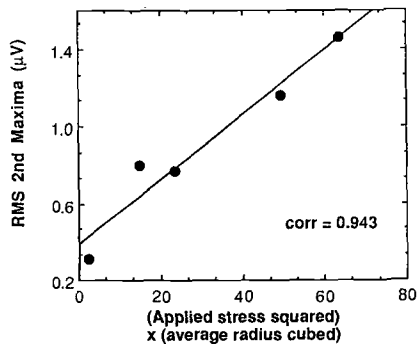


Figure 3.- Maximum value of the second RMS peak versus the applied stress squared times the average radius cubed. Check on equation (1).

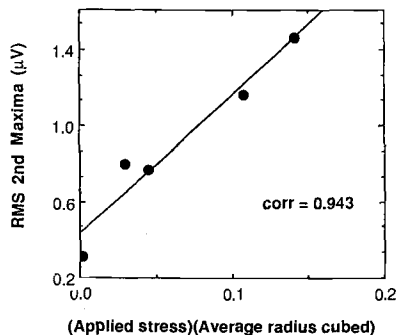


Figure 4.- Maximum value of the second RMS peak versus the applied stress times the average radius cubed. Check on equation (2).



A paper [10] contained in this STP reports on the acoustic emission from the fracture of boron particles in a 2219 aluminum matrix. In that investigation a small countable number of boron particles were used. The authors of that investigation report that there were many more small bursts of emission than could be accounted for by the number of particle fractures. They postulate that the additional smaller bursts of acoustic emission were caused by the partial decohesion of the boron particles from the aluminum matrix. With this background information, similar reasoning can be used to analyze the nodular cast iron data, i.e., the individual RMS voltage bursts rising from the background in Figure 2 are due to the fracture of the graphite nodules and that the background emission is most likely due to the decohesion of the graphite nodules from the ferrite matrix. If this explanation of the data is correct, then the height of an RMS burst less the background, should be the appropriate measure of the RMS voltage (or energy since the two are proportional) generated from fracture of a graphite nodule. It is possible to estimate the validity of equations (1) and (2) by using the values of  $\text{RMS}(2)[\text{Peak} - \text{Bg}]$ , the value of stress at the second maximum and the average nodule size. Plotting  $\text{RMS}(2)[\text{Peak} - \text{Bg}]$  against  $[\sigma^2 r^3]$  and  $[\sigma r^3]$  should give a straight line fit for equations (1) and (2) respectively. The results are shown in Figures 5 and 6. As can be seen, a good straight line fit is obtained in both cases. Clearly the  $[r^3]$  dependence dominates.

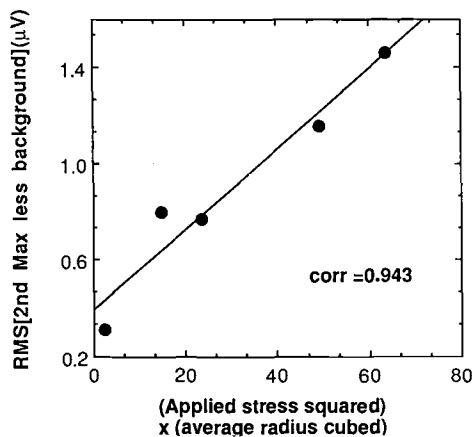


Figure 5.-  $\text{RMS}(2)[\text{Peak} - \text{Bg}]$  versus applied stress squared times the average radius cubed. Check on equation (1).

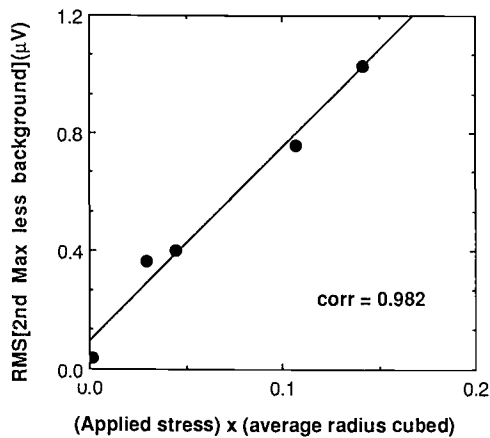


Figure 6.- RMS(2)[Peak - Bg] versus applied stress times the average radius cubed. Check on equation (2).

Gerberich and Jatavallabhula [7] have also derived an expression for the tensile stress applied to the matrix which is necessary to fracture a spherical inclusion of radius  $r$ . Their result is the following:

$$\sigma = q(e)^{-1} [6E^* \gamma_c / 2r]^{1/2} \quad (3)$$

where  $q(e)$  is a complicated strain concentration factor which increases slowly with strain,  $\gamma_c$  is the specific work of fracture and  $E^*$  is Young's modulus for the particle. If one assumes that there is little change in  $q(e)$  then  $\sigma$  is proportional to  $[r^{-1/2}]$ . Using this result in equations (1) and (2) leads to a prediction that the RMS voltage generated during the fracture of a spherical particle should be proportional to  $[r^2]$  for equation (1) and proportional to  $[r^{2.5}]$  for equation (2). Log-log plots of the maximum value of the second RMS peak and RMS(2)[Peak - Bg] against the average nodule radius are shown in Figures 7 and 8. Both plots show good straight lines. However, the data for the RMS second maxima give a slope of 1 while the data for RMS(2)[Peak - Bg] gives a slope of 2.17 which is between the two predicted values.

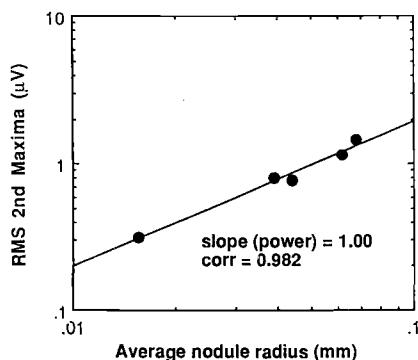


Figure 7.- Log-log plot of the maximum value of the second RMS peak versus the average nodule radius.

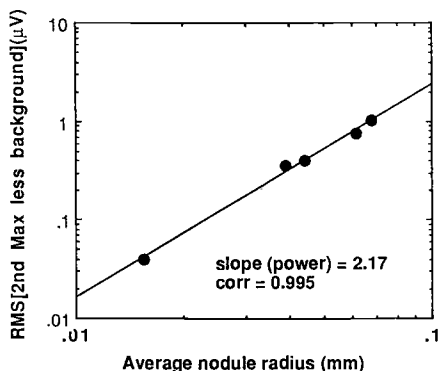


Figure 8.- Log-log plot of RMS(2)[Peak - Bg] versus the average nodule radius.

## CONCLUSIONS

The acoustic emission generated from the fracture and/or decohesion of spherical graphite nodules during compressive deformation has been analyzed in terms of theoretical predictions. The dependence of the applied stress, the average nodule diameter and the RMS voltage produced by the fracture and/or decohesion of spherical graphite nodules has been investigated. The nodule diameter was found to be the predominant factor in determining the resulting acoustic emission. Using the predicted dependence of the applied stress on the average nodule diameter, it was shown that the value of the RMS voltage bursts less the background voltage agrees very well with the theoretical predictions for the fracture of an elastic particle in a plastic matrix.

## ACKNOWLEDGEMENTS

The authors appreciate helpful discussions with Dr. C.R. Heiple of Rockwell International Corp., Rocky flats Plant. Portions of this work were supported by the U.S. Department of Energy through Grant No. DE-FG02-85ER45182. This support is gratefully acknowledged. Thanks are also extended to Dr. Richard Salzbrenner, Sandia National Labs, for the sample materials used in this investigation.

## REFERENCES

- [1] Ono, K., Proceedings of the Second Acoustic Emission Symposium, Japan Industrial Planning Association, Tokyo, Japan, Sec. 4, 1974, pp 1-63.
- [2] Heiple, C.R. and Carpenter, S.H., Journal of Acoustic Emission, Vol.6, 1987, pp 177-204 and 215-237.
- [3] Salzbrenner, R.J., Journal of Material Science, Vol. 22, 1987, pp 2135-2147.
- [4] Carpenter, S.H. and Higgins, F.P., Proceedings of the Third Acoustic Emission Symposium, Japan Industrial Planning Association, Tokyo, Japan, 1976, pp 288-304.
- [5] Egle, D.M., Tatro, C.A. and Brown, A.E., Materials Evaluation, Vol. 39, pp 1037-1044.
- [6] Salzbrenner, R.J., Sandia Report, SAND86 - 0470, Sandia National Laboratories, Albuquerque, New Mexico 87185, 1986.
- [7] Scruby, C.B., Quantitative Acoustic Emission Techniques, AERE-R 11262, AERE Harwell, Oxfordshire, U.K., July, 1984
- [8] Kant, R., The Elastostatic Axisymmetric Problem of a Cracked Sphere Embedded in a Dissimilar Matrix, Doctoral Thesis, University of California, Berkeley, CA., 1979.
- [9] Gerberich, W.W. and Jatavallabhula, K., Nondestructive Evaluation: Microstructural Characterization and Reliability Strategies, ed. O.Buck and S.M.Wolf, TMS-AIME, Warrendale, PA., 1981, pp 319-348.
- [10] Heiple, C.R., Carpenter, S.H. and Christiansen, S.S., World Meeting on Acoustic Emission, AEWG, Charlotte, N.C. (extended abstract in Journal of Acoustic Emission, Vol. 8, 1989, pp S184-S187) also in this volume ASTM STP 1077.

Yoshihiko Obata, Hirokazu Kobayashi, Ken-ichiro Aoki,  
Takuro Yamaguchi and Kimihiro Shibata

EVALUATION OF FATIGUE CRACK GROWTH RATE OF CARBURIZED GEAR  
BY ACOUSTIC EMISSION TECHNIQUE

---

REFERENCE: Obata, Y., Kobayashi, H., Aoki, K., Yamaguchi, T., and Shibata, K., "Evaluation of Fatigue Crack Growth Rate of Carburized Gear by Acoustic Emission Technique", Acoustic Emission: Current Practice and Future Directions, ASTM STP 1077, W. Sachse, J. Roget and K. Yamaguchi, Eds., American Society for Testing and Materials, Philadelphia, 1991.

ABSTRACT: Acoustic emission measurements of carburized steel were carried out in room-temperature fatigue tests at the constant load-amplitude condition, in order to evaluate the crack growth behavior. An extremely large number of acoustic emission events were recorded near the maximum load in a flexural fatigue cycle. The increasing behavior of acoustic emission event counts was associated with the distribution of fractured intergranular facets in the fracture surface. Many emissions were also recorded in the spur gear tests. The crack growth rate of the gears can be estimated using the relation between the acoustic emission event counts and the intergranular fracture area on the crack surface. It can be concluded that the acoustic emission technique was powerful and quantitative method to evaluate the fatigue crack behavior of carburized mechanical parts.

KEYWORDS: carburized steel, spur gear, acoustic emission, fatigue crack growth, crack detection, intergranular fracture

A carburized treatment is one of the surface hardening process of the steel, and has been applied to power driving mechanical parts such as shafts and gears, where high fatigue strength and wear properties are required. However, the fatigue crack growth behavior

Dr. Obata, Mr. Kobayashi and Dr. Aoki are research assistant, graduate student and professor, respectively, College of Industrial Technology, Nihon University, Narashino, Chiba 275, Japan; Mr. Yamaguchi and Dr. Shibata are researcher and senior researcher, respectively, Central Engineering Laboratories, Nissan Motor Co., Ltd., Yokohama, Kanagawa 237, Japan.

in carburized steel is not well understood partly due to lack of crack detection methods. A few reports on the fatigue crack initiation life and propagation rate in carburized layers have been presented not only for the gear specimen but also for small-sized specimen [1-2]. But few reports for acoustic emission(AE) in carburized steel have been presented [3].

The present paper describes the acoustic emission behavior in notched flexural-fatigue specimens of carburized steel and the spur gears in order to discuss applicability of the acoustic emission technique for the evaluation of the fatigue crack growth rate.

EXPERIMENTAL METHOD

Materials and Specimen

Materials used are Ni-Cr-Mo steel(JIS SNCM420H) for flexural specimen and Cr steel(JIS SCr420H) for spur gear. The shape and the size for both specimens are shown in Fig. 1. Four types of flexural specimens were prepared by the heat treatment and the shot-peening process as shown in Table 1. On the other hand, the spur gear was prepared using only one carburized condition without shot-peening. Its effective case depth was about 0.7 mm.

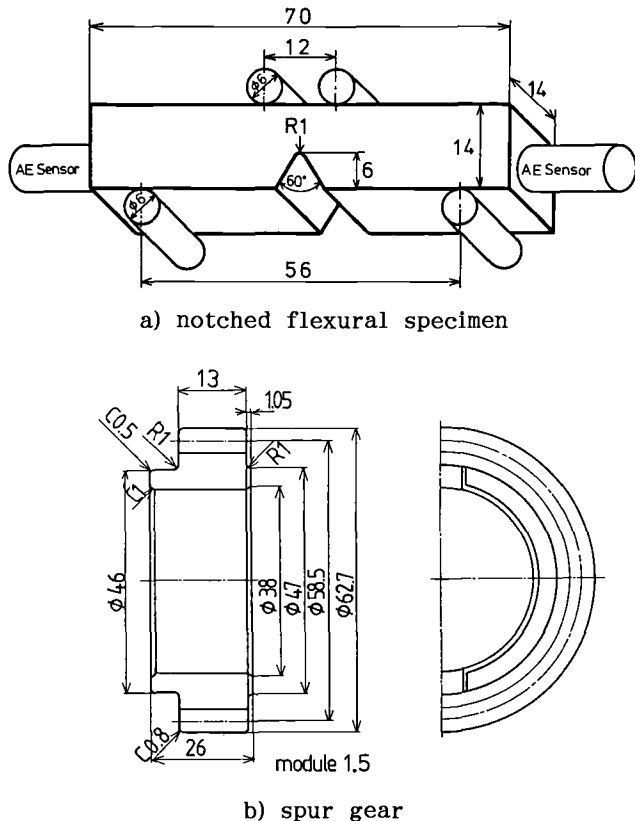


FIG. 1 -- Specimen shape and size.

TABLE 1 -- Variety and its symbol for flexural specimen.

BN	: non-carburized (normalized heat treatment only)
BS	: carburized (effective case depth is 0.5mm)
BD	: carburized (effective case depth is 0.7mm)
BP	: carburized (effective case depth is 0.7mm) and shot-peening

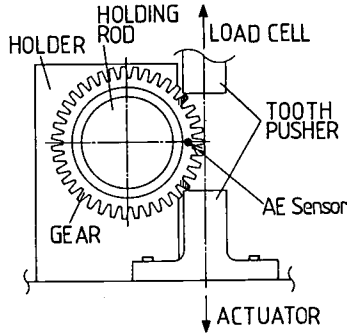


FIG. 2 -- Schematic diagram of spur gear test machine.

#### Fatigue and Acoustic Emission Test

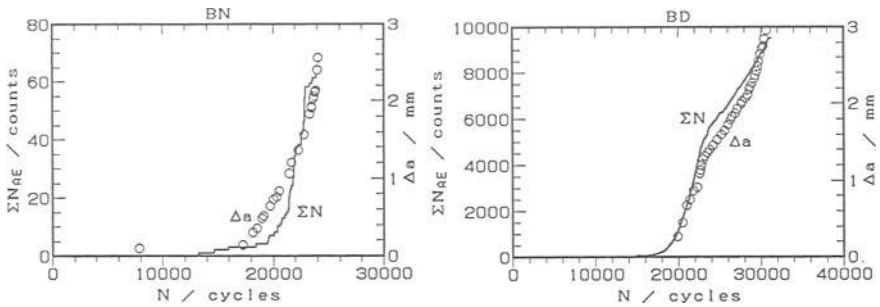
A closed-loop electro-hydraulic test machine was used in the fatigue test. Schematic diagram for the gear test machine is shown in Fig. 2. Both notched flexural and gear specimens were loaded in air at room temperature with a constant amplitude as a function of sine wave. The stress ratio was 0.1, Test frequency was 4 Hz in most tests.

Two AE sensors were mounted to the both ends of the bending specimen as shown in Fig. 1. They are 8 mm diameter and 15 mm height sensor with a resonant frequency of 200 kHz. Recorded signal parameters each event are the number of fatigue cycle, the load level in a cycle, the difference of arrival time ( $\Delta t$ ) and the event amplitude. In the gear test, a 150 kHz resonant sensor was mounted at the place as shown in Fig. 2. This is a small (3 mm diameter, 3 mm height) caseless sensor, and is used non-reproducible such as the strain gage. The  $\Delta t$  was not recorded in the gear test.

#### RESULT FOR FLEXURAL SPECIMENS

##### Effect of Carburizing Treatment on Emission Activity

Figure 3 shows the cumulative event counts, recorded near the maximum load range in a fatigue cycle (peak-load AE), and the crack growth length from the notch root measured by mobile optical microscope as a function of the number of fatigue cycles. Good correlation between event counts and crack lengths was obtained for each specimen. The emission activity of carburized specimens is 100 times larger than that of non-carburized specimens. Intergranular fracture mode was observed in the region of effective case depth at the notch root and at the specimen side in each carburized specimen, as shown in Fig. 4. On the other hand, the intergranular fracture was not observed in the non-carburized specimens. Therefore, a large number of emissions for carburized specimens caused by the intergranular fracture. It can be suggested that non-carburized steel gives us few emissions even for high-strength materials such as BN specimen of which tensile strength is about 1000 MPa.



a) non-carburized(BN) specimen      b) carburized(BD) specimen  
 FIG. 3 -- Difference of AE cumulative event counts between non-carburized specimen and carburized specimen.

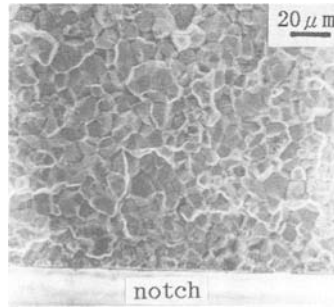


FIG. 4 -- Fractograph of intergranular fracture at notch root of BD carburized specimen

#### Evaluation of Fatigue Crack Growth Rate

The AE event rate and crack growth length obtained by the microscope are shown in Fig. 5 for both sides of the specimen. This example of the BS specimen was recorded at 0.1 Hz. The high emission rate was observed up to 15000 cycles even though crack growth rate was not high while a crack propagated in a carburized layer. When a crack passed through the carburized layer in front of the notch root, first the emission rate became low, and then gradually increased with increasing crack growth rate. This interesting AE characteristics are associated with the distribution of the intergranular fracture on the cracked surface. Therefore two relations must be used in the crack growth length estimation by the emission event count. The boundary between two relations was associated with the effective carburized depth. The crack growth rate obtained by the optical microscope and AE method is shown in Fig. 6. Both data represent the same behavior. In this specimen, unhomogenized crack growth behavior through the thickness was observed as shown in the microscope data. However emission data represent more homogeneous crack growth behavior than that of the microscope. It can be concluded that emission data faithfully represent the crack growth behavior through the thickness.



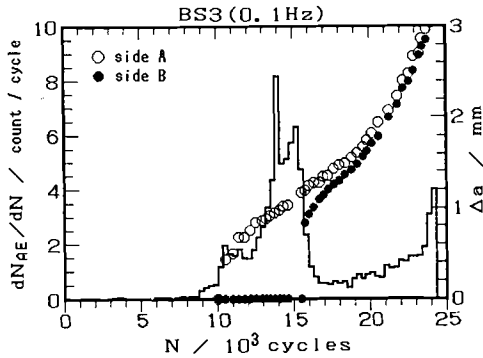


FIG. 5 -- AE event rate and crack growth length behavior as a function of number of fatigue cycle.

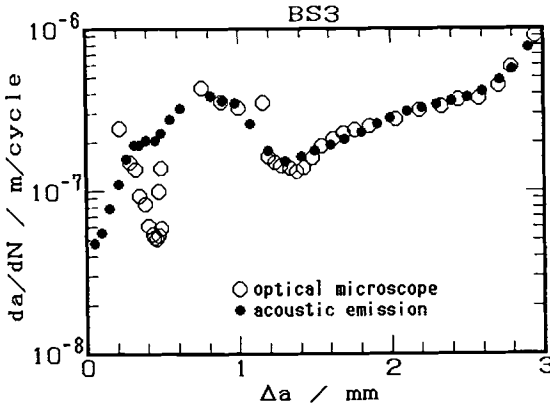


FIG. 6 -- Comparison of crack growth rate with AE method and optical microscope observation.

## RESULTS FOR SPUR GEARS

### Fatigue and AE Behavior

Figure 7 shows a relation between the maximum stress and the number of failure fatigue cycles. An estimated fatigue strength at  $10^7$  cycles is 650 MPa. Two teeth were simultaneously fractured in a gear which was tested at 2 Hz. On the other hand, one tooth was fractured in the other three gears.

Figure 8 shows load level distributions of AE as a function of the number of fatigue cycles. We can clearly discriminate the peak-load AE due to crack propagation and AE at the lower load level due to friction of crack surfaces and mechanical noises. The peak-load AE initiates at about a half stage of the fatigue life, and increases with increasing fatigue cycles. This AE pattern is observed in all four gears tested. On the other hand, the opening and closure AE shows quite low activity except a specimen tested at 10 Hz. A very interesting result was obtained in the case of fractured in both teeth at 2 Hz as shown in Fig. 8-b. That is, AE due to crack propagation is observed at two load levels as at the peak-load and in the unloading range.

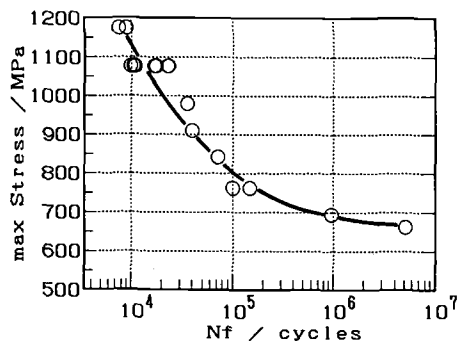


FIG. 7 -- Relation between maximum stress and number of failure fatigue cycle in spur gear.

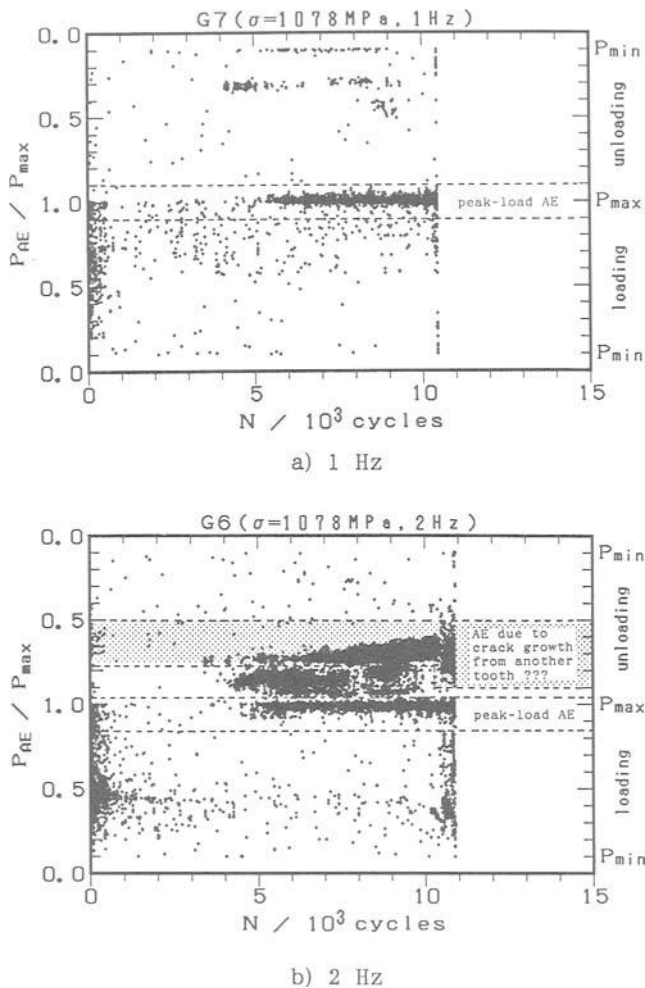


FIG. 8 -- AE load level distribution at different test frequencies in spur gear tests.

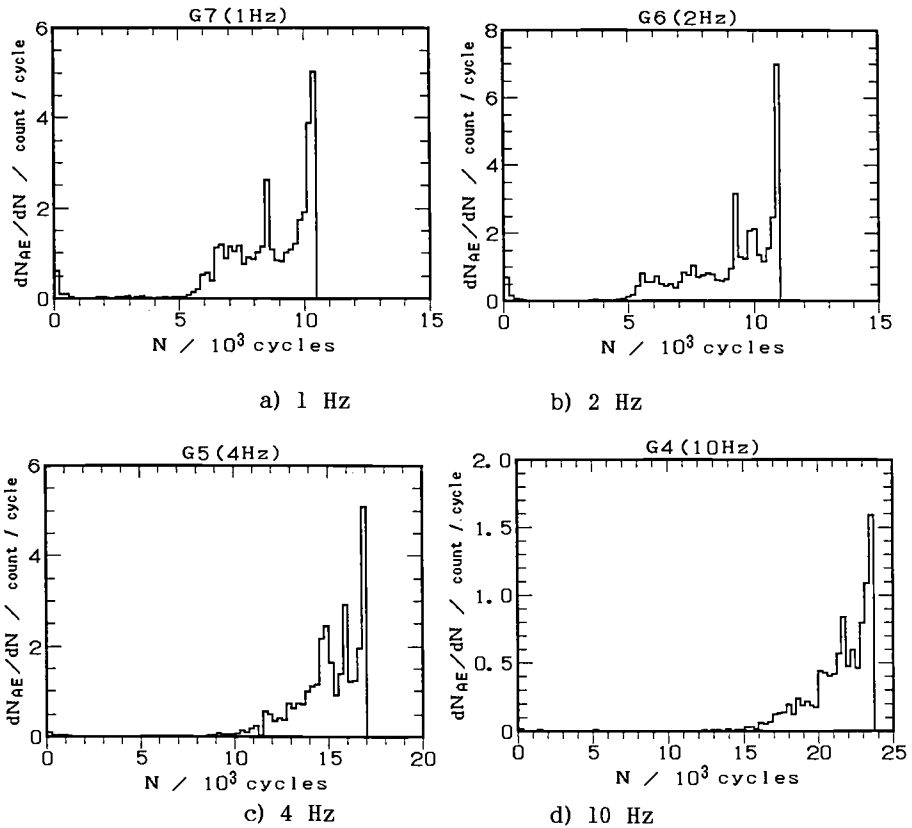


FIG. 9 -- Peak-load AE event rate behavior in spur gear tests.

Figure 9 shows the rate of the peak-load AE as a function of the number of fatigue cycles. The increasing pattern of AE did not depend on test frequency and also the absolute value of the rate did not change at different frequencies from 1 Hz to 4 Hz.

#### Estimation of Fatigue Crack Growth Rate

There is no doubt that it is easy to evaluate the fatigue crack initiation life from the onset of the peak-load AE as shown in Fig. 9. The AE behavior obtained from carburized gears is almost the same as that of the flexural specimen test. Therefore it is considered that AE signals of these gear tests were emitted due to the intergranular fracture. The schematic diagram of the relation between the distribution of the intergranular fractures on crack surface and the cumulative event counts of the peak-load AE is shown in Fig. 10. That is, the crack length can be estimated using two linear relations. At the Stage I, the crack propagates in the carburized layer through the tooth width, giving us an extremely large number of AE events. At the stage II, on the other hand, the crack propagates the region where the carburized layer exists at only side surfaces, giving us fewer AE events. The boundary between two stages is estimated as the effective case depth at the tooth root.

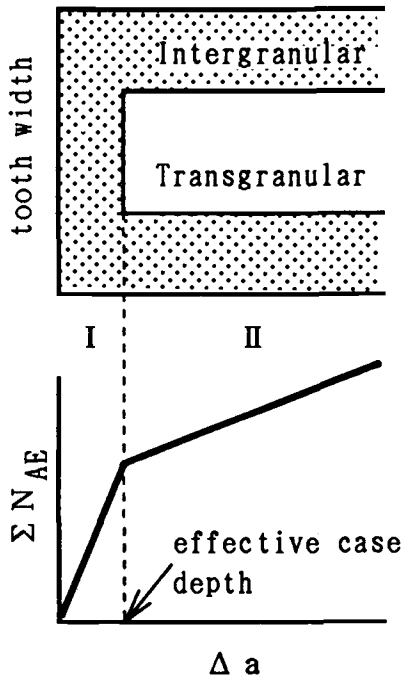


FIG. 10 -- Schematic diagram between distribution of intergranular on crack surface and AE cumulative event counts.

The final crack length at the unstable fracture of the tooth has not yet been measured. However the final crack length was estimated as about the effective case depth at the tooth root, because of AE rate behavior. That is, there is no evidence of decreasing behavior of AE rate up to the tooth failure. Therefore we tried to estimate the crack length using the following assumptions and conditions.

- 1) crack initiation is onset of the peak-load AE
- 2) unstable fracture occurs at 0.7 mm crack length at stage I
- 3) the peak-load AE cumulative event count( $\Delta N_{AE}$ ) is proportional to the intergranular fractured area( $A_{IG}$ ) represented by Eq.(1)

$$A_{IG} = K \times \Sigma N_{AE} \quad (1)$$

Thus, crack growth length( $\Delta a$ ) is obtained by Eq.(2),

$$\Delta a = K/W \times \Sigma N_{AE} \quad (2)$$

where  $W$  is width of the tooth and  $K$  is a constant. Constant  $K/W$  values used are  $1.0 \times 10^{-4}$  mm/count tested at 1 Hz to 4 Hz and  $2.6 \times 10^{-4}$  mm/count tested at 10 Hz. Figure 11 shows the fatigue crack growth rate of the carburized gears obtained by the peak-load AE event counts. It can be considered that the AE technique is very useful to evaluate fatigue crack growth behavior for carburized gears.

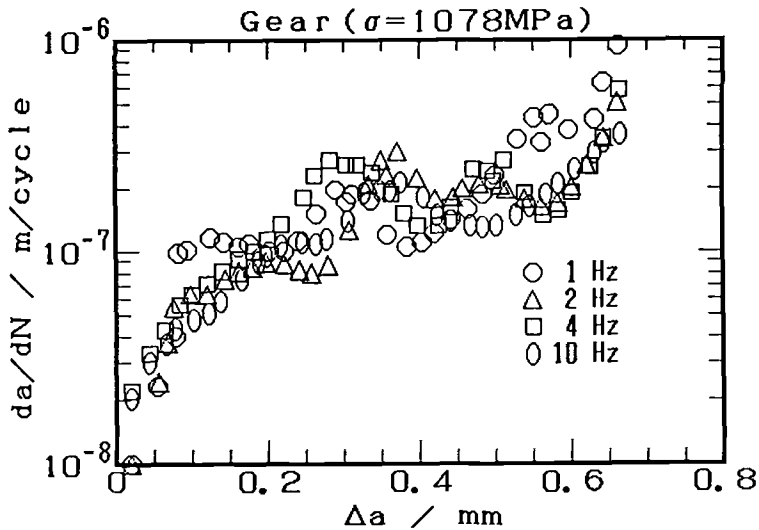


FIG. 11 -- Fatigue crack growth rate of spur gear teeth estimated by AE method

#### Possibility of 1-channel AE Measurement to Evaluate Fatigue Crack

An automatic and simple measurement is required in the AE application such as crack monitoring of practical mechanical elements. Figure 12 shows test frequency dependence on cumulative AE event counts at different load levels. There is not a big difference between overall AE and the peak-load AE up to 4 Hz. Relatively many events of the overall AE at 2 Hz resulted from the fact that cracks propagated at both teeth. It is suggested that a simple and traditional measurement with one sensor could be applied to evaluate the crack propagation behavior for carburized gear fatigue tests. For example, the overall AE behavior as shown in Fig. 13 exhibits the same as the peak-load AE behavior as shown in Fig. 9-c. However relatively high threshold must be selected in the noisy test at high test frequency, although relatively few emission are expected.

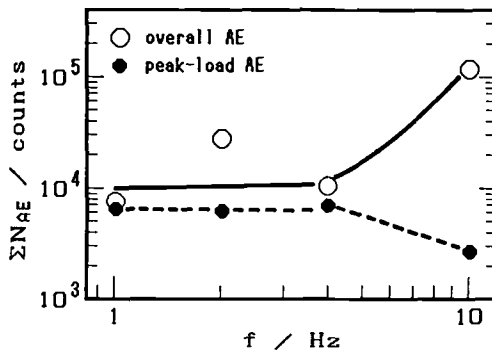


FIG. 12 -- Test frequency dependence on AE cumulative event counts in spur gear tests.

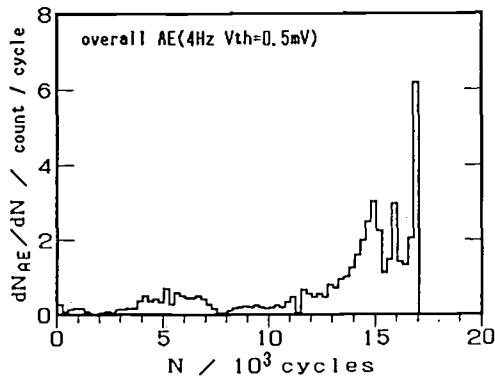


FIG. 13 -- Behavior of overall-AE event rate in spur gear tested at 4 Hz.

#### CONCLUSION

In order to evaluate the fatigue crack growth rate of carburized spur gears in pulsator gear tests, AE test were carried out using flexural specimens and spur gears. Our main results are as follows:

1. A carburized heat treatment for steel gives us an extremely large number of AE events during the fatigue crack growth. These events are recorded in the peak-load range in a fatigue cycle, and associated with intergranular fracture in the region of the carburized layer.
2. Fatigue crack growth rate can be estimated using the relation between AE event counts and distribution of intergranular fractures on the crack surface.
3. A simple and traditional AE measurement can be applied as a crack evaluation method of the pulsator spur gear test, which have a high signal to noise ratio.

#### REFERENCES

- [1] Furukawa, T., Konuma, S. and Sakaniwa, H., "Effect of Chemical Composition and Heat Treatment on Mechanical Properties of Carburized Steels", Journal of The Iron and Steel Institute of Japan, vol. 65, No. 8, 1979, pp 596-605
- [2] Asami, K., "Effect of Compressive Residual Stress on Fatigue Strength of Tufftrided Steel", Journal of the Society of Materials Science, Japan, vol. 31, No. 346, 1982, pp 638-643
- [3] Obata, Y., Nishi, K., Aoki, K., Matsumoto, T., Shibata, K., Kawabe, K., "Many Acoustic Emission Events from Propagating Fatigue Crack on Carburized Layer", Progress in Acoustic Emission IV, (1988), Kobe, pp 499-505

## **Novel Applications**

David J. Buttle and Christopher B. Scruby

CHARACTERISATION OF DUST IMPACT PROCESS AT LOW VELOCITY BY  
ACOUSTIC EMISSION

---

REFERENCE: Buttle, D.J. and Scruby, C.B. "Characterisation of Dust Impact Process at Low Velocity by Acoustic Emission", Acoustic Emission: Current Practice and Future Directions, ASTM STP 1077, W. Sachse, J. Roget, and K. Yamaguchi, Eds., American Society for Testing and Materials, Philadelphia, 1991.

ABSTRACT: An acoustic emission (AE) technique is developed for monitoring hard particle impact for eventual use as an on-line erosion rate sensor. In a preliminary study the elastic impact of bronze and glass particles (size range 50 - 100  $\mu\text{m}$ , velocities 2.5 - 7.1 m/s) on a aluminium target was investigated. The plate Green's function and system response were deconvolved from AE signals due to impact at epicentre. The velocity and time dependence and the absolute values of the peak impact force and impact time thus obtained compared well with predicted theoretical values. The quantitative technique developed was also used to size the particles, giving the correct mean particle size to within 4%. This fundamental approach provides a framework for later extension to plastic particle impact.

KEYWORDS: Erosion, particle, Green's functions, elastic and plastic impact, deconvolution.

## INTRODUCTION

The wear of important components in industrial plant caused by dust entrained in gas streams can often cause problems. For example heat exchangers, ducts and especially gas-turbines associated with coal-fuelled combustors can become irrevocably damaged if unchecked [1]. The particles responsible can be of a wide range of sizes from just a few to several hundred micrometres in diameter. The largest particles inevitably cause the greatest damage, but where erosion is known to be a problem these are usually removed by filtration of the gas stream. The erosion rate depends strongly upon the particle velocity, this usually being in the range 2 to 200 m/s. The incident angle of the eroding particle is also important. Erosion rate is a maximum at normal incidence for 'brittle' materials whilst for 'ductile' materials the erosion process is more rapid for larger angles

Drs. Buttle and Scruby are research scientists at AEA Technology, Harwell Laboratory, Didcot, Oxon OX11 0RA, U.K.



of incidence. Other factors which influence erosion are the shape of the particles, and the roughness, composition and state of both the target and erodant [1-3].

There is a need for a robust probe for the in-situ monitoring of erosion, either directly or indirectly, which should be capable of operating in the often harsh environments of high temperature and pressure. The Laser Doppler Anemometry technique has been used to measure gas flow in rigs [4,5], but does not address the erosion process itself. Thin Layer Activation is an established technique for monitoring erosion and wear in internal combustion and gas turbine engines [6,7], but the cost is relatively high and the component to be monitored must be portable, making it unlikely to be used for routine plant monitoring. Thus an acoustic emission (AE) technique, which offers the potential for on-line monitoring and should be inexpensive, is proposed as a method which fulfils the requirements of a robust probe for in-situ monitoring.

Although, to the best of the authors' knowledge, an AE technique has not yet been employed industrially in erosion monitoring, the theoretical aspects of elastic wave generation from simple transient force impact upon relatively thick sections has already been solved numerically [8]. Waveform analysis of the observed AE signals could therefore yield information relating to such parameters as the particle size, velocity, angle of impact and degree of elasticity or plasticity of the impact itself. If this last parameter could be deduced, it would be most useful for characterising the erosion process provided that plasticity of impact could be correlated with removal of material from the target.

The work presented here is a first stage for development of an AE technique for erosion rate monitoring. After laying a theoretical framework for determination of the characteristics of AE waveforms from elastic and plastic impact, measurements from individual elastic particle impacts upon plates are made. Parameters relating to the particle and impact dynamics are then deconvolved using a Green's function formalism and the results are compared with theoretical predictions.

## THEORY

### Acoustic Emission Signal Analysis

When hard projectiles make an impact with a massive plate their kinetic energy is redistributed into a combination of plastic deformation in the target surface, elastic waves propagating away from the impact site and kinetic energy in the rebounding projectile. The fraction of energy dissipated as elastic waves is typically only a few percent [9], of which approximately 2/3 is in the form of Rayleigh waves, 5-10% in the form of compression waves, and the rest in shear waves. These acoustic waves will propagate through the target according to the elastic properties of that medium before being detected by a suitable acoustic sensor. The resulting signal,  $V(t)$ , will therefore be dependent, not only upon the projectile and dynamics of the impact itself, but also upon the propagation of the sound in the target medium and the functional response of the acoustic sensor. This

can be represented by:

$$V(t) = S(t) * G(t) * D(t) \quad (1)$$

where,  $S(t)$  is the acoustic source function,  $G(t)$  the propagation function,  $D(t)$  the detector function and '\*' represents convolution in time.

Hence, in order to extract the information concerning the erosion process, which is contained in  $S(t)$ , it is necessary to determine and deconvolve the propagation and detector functions from the observed AE signal. We shall consider each of these functions in turn.

#### Particle Impact Source Function

Particle impact will create an impulsive force at the surface of the target with a duration equal to the impact time. The spatial form of the function will depend upon the nature of the impact. In our work the size of the acoustic source was small compared to the propagation distance and so the source could conveniently be modelled as a point. If then, it is assumed that all parts of the source radiate with the same time dependence, the source can be represented by a cluster of orthogonal forces. For example, a perfectly elastic normal impact will generate a force normal to the surface. A highly plastic impact would however result in forces parallel to the surface in addition to a normal force. For normal impact plastic deformation can be assumed to produce pairs of equal and opposite forces, i.e. force dipoles. Figure 1(a,c) summarise these forces for normal impact. If the impact is at some oblique angle there will be an additional horizontal component to the monopolar force for both elastic and plastic collisions (figure 1(b,d)).

Thus the determination of the impact source function should yield the impact time and the magnitude of the force, both of which depend upon the particle size and velocity. The determination of the spatial dependence of the function should indicate the degree of plasticity of the impact and should also therefore relate to the rate of erosion.

#### Propagation Function for a Plate

The elastic waves generated by the impact will propagate through the target medium according to the transfer function of the plate before being detected. This can be calculated from the appropriate wave equation which describes the dynamic displacements in time and space according to the elastic constants of the material. The solution for a delta function source in time and space is known as the Green's function,  $G_{ij}$ . This describes the  $i$ th component of displacement at the observation position due to a point force acting at the source location in the  $j$ th direction as a function of time. Thus the displacements are given by the convolution integral:

$$U_i(t) = \sum_{j=1}^3 G_{ij}(t) * f_j(t) \quad (2)$$

where  $f_j(t)$  = point force component acting in  $j$ th direction.

If the plate normal is defined as the  $z$  direction (i.e.  $j=3$ ), then

the vertical displacements at the detector,  $U_3$ , for each of the examples of figure 1 are given by:

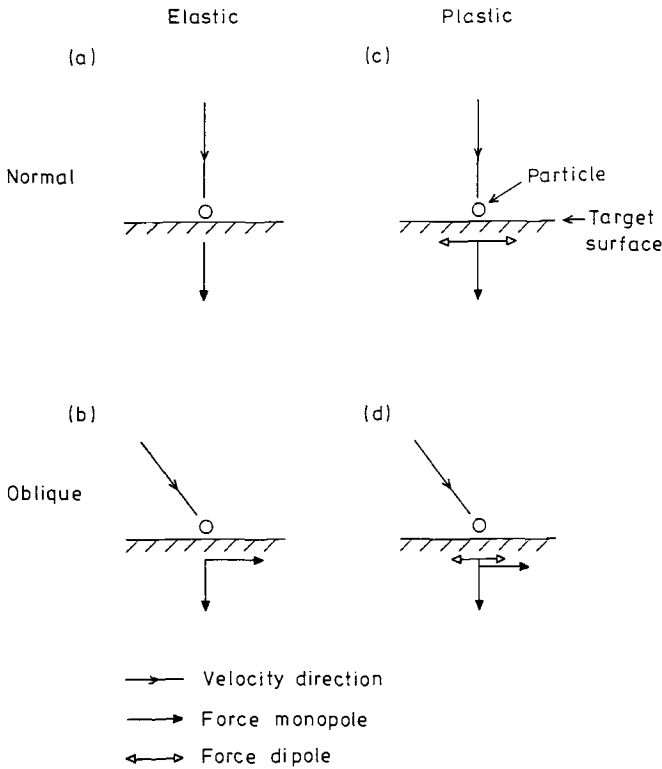


Figure 1 Schematic of forces during (a) normal and (b) oblique elastic particle impact and (c) normal and (d) oblique plastic particle impact.

$$U_3 = G_{33} * f_3 \quad \text{for normal elastic impact} \quad (3)$$

$$U_3 = \sum_{i=1}^3 G_{3i} * f_i \quad \text{for oblique elastic impact} \quad (4)$$

$$U_3 = G_{33} * f_3 + \sum_{i=1}^3 G_{3i,i} * D_{ii} \quad \text{for normal plastic impact} \quad (5)$$

and

$$U_3 = \sum_{i=1}^3 G_{3i} * f_i + G_{3i,i} * D_{ii} \quad \text{for oblique plastic impact} \quad (6)$$

where  $D_{ii}$  = the force dipole components.

The third index of the Green's function represents differentiation with respect to that index. For plastic impact the component  $G_{3,3,3}$  is included for the case where the plasticity may extend to depths greater than the acoustic wavelength thus incurring an additional vertical dipole moment. One of the force monopole terms can

always be set to zero by choice of axes. The two Green's functions  $G_{3,2}$  and  $G_{3,1}$  are equal, and  $G_{3,1,1} = G_{3,2,2} = -\alpha G_{3,3,3}$  ( $\alpha$  constant) when measurements are made at epicentre [10].

### Detector Function

In order to minimise the distortion of the AE signal voltage due to an imperfect detector, a high fidelity piezo-electric transducer was used. This was a point-contact transducer (contact area  $0.9 \text{ mm}^2$ ) with an omni-directional sensitivity and a frequency response which falls only slowly at high frequencies ( $-12 \text{ dB}$  at  $10 \text{ MHz}$ ). Details of this transducer design and sensitivity can be found in [11]. The sensitivity was calibrated absolutely in terms of output signal level per unit surface displacement by comparison with a capacitance transducer on a standard test block. A Nd-YAG pulsed laser was used as a standard acoustic source. The overall signal fidelity was good, but there was some loss of low frequency content and small reverberation following the early wave arrivals [11,12].

The ideal response of a transducer to a short impulse would be a Gaussian with a small risetime. Figure 2 shows the observed epicentral response of the transducer together with its charge amplifier for (a) a sharply focussed  $10 \text{ ns}$  laser pulse (ablation mode) and (b) a partially focussed pulse (thermoelastic mode). For comparison, the Green's functions  $G_{3,3}$  and  $G_{3,1,1}$ , at epicentre, convolved with a Gaussian of width (at half peak)  $120 \text{ ns}$  are also shown. Note that the Green's function of figure 2(a) corresponds to an elastic impact of a particle at normal incidence (equation 3). The agreement is good, there being some loss of low frequency after  $6 \mu\text{s}$  in both signals and a strong reflection of the compression waves in the first example delayed approximately  $0.5 \mu\text{s}$ . This reflection was believed to occur from the back face of the piezoelectric element. The agreement between the Green's functions and the transducer response was sufficient to indicate that, (a) the ablative laser source can be represented by the single function  $G_{3,3}$ , and (b) the thermoelastic laser source can likewise be represented simply by the waveform  $G_{3,1,1}$  (as the three spatial derivatives of the green's function dipoles are proportional).

The detector function was obtained explicitly by deconvolving the Green's function (unsmoothed) from the experimental signals of figure 2. Details of the deconvolution method used are given elsewhere (12).

The transducer and charge amplifier response, thus obtained, is given in figure 3. The decay time is longer than the risetime and the reflection from within the transducer element is clearly seen to occur almost  $0.5 \mu\text{s}$  following the initial peak. The smaller bipolar signal occurring  $1.0 \mu\text{s}$  after the peak corresponds to the shear wave arrival and was thought to be due to a small error in the shear wave velocity used for the Green's function calculation.

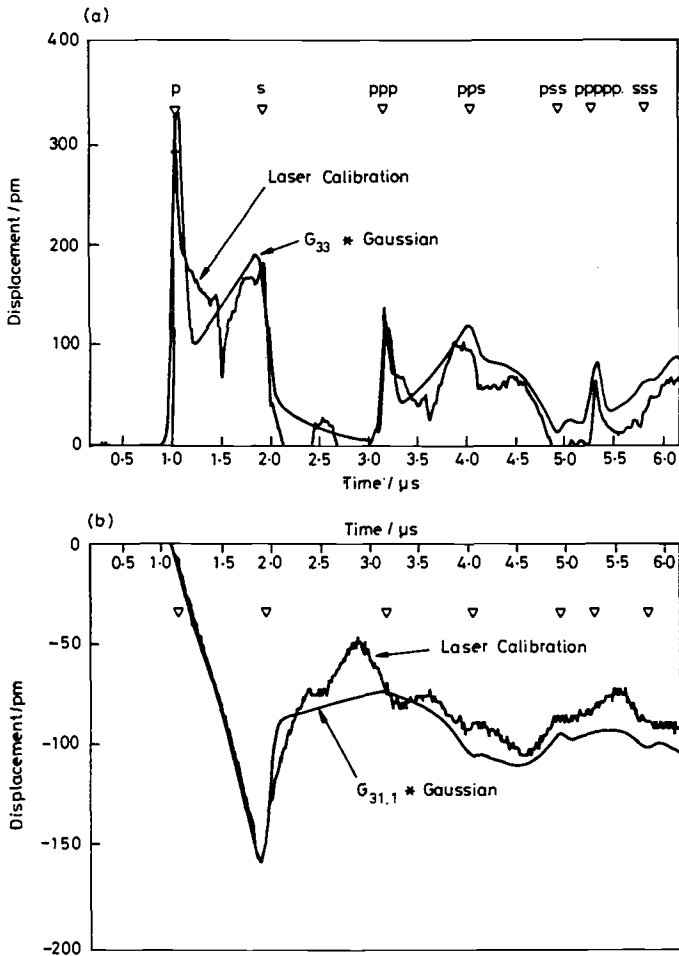


Figure 2 Comparison of transducer/charge amplifier response to (a)  $G_{33}$  and (b)  $G_{31,1}$  both convolved with 0.12 μs width Gaussian. Wave arrivals also shown.

## EXPERIMENTAL

### The Free-fall Impact System

A long vacuum tube arrangement was used [12] whereby particles were allowed to fall freely under gravity before impact onto the target. A vibrator 'shakes' particles out of a dispenser positioned at the top of the evacuated tube. The number of particles falling was controllable. The particle drop length was adjustable enabling the impact velocity to be selectable in the range 2.5 to 7.1 m/s. The target consisted of a 5.8 mm thick aluminium plate with a transducer located on the underside such that the particles strike the target close to the epicentre. This was further ensured by positioning a mask plate above the target which contained a hole of diameter 1.5 mm. The vacuum

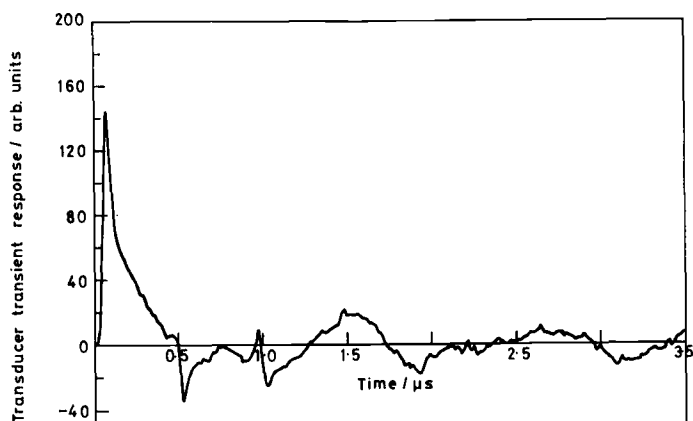


Figure 3 Deconvolved transducer/charge amplifier response to impulsive force generated by pulsed laser.

was maintained between  $10^{-4}$  and  $10^{-5}$  torr which was considered low enough to prevent significant 'drag'.

#### Acoustic Emission System and Measurements

The AE signals detected at the transducer were amplified, filtered with a bandwidth of 30 kHz to 7 MHz (3 dB points) and stored digitally (10 ns sampling time) onto the hard disk of a personal computer. Spherical bronze particles with a diameter between 53 and 75  $\mu\text{m}$  or glass particles with a diameter between 80 and 100  $\mu\text{m}$  were used. The glass particle size distribution was measured under an optical microscope.

Two experiments were carried out: (a) Bronze particles impinging obliquely at 0, 10 and 20 degrees to the target normal at a single velocity and (b) glass particles impinging normally at a selected range of velocities. The glass particles were almost perfectly spherical and data from these impacts was used for an absolute comparison with theoretical predictions.

#### RESULTS AND DISCUSSION

AE waveforms from particle impact (figure 4(a)) were similar to the AE system response to an ablative laser pulse. The experimental signals differed primarily in having longer risetimes and lower bandwidth than in figure 2(a), indicating that, although still of short duration, the particle impact force function must be longer than the laser pulse.

The sensitivity of the AE signal to impact angle between 0 and 20 degrees for bronze particles was small (data not shown) and this was confirmed by comparison with theoretical waveforms calculated from  $D(t) * G(t)$ , where  $G(t)$  is the appropriate propagation function, i.e. containing both normal and horizontal components to the impact force.

The clearest effect of small angle oblique impact upon the AE signals was to reduce the amplitude of the first compression wave arrival and increase that of the first shear wave arrival. For example at 10 and 20 degrees impact the first compression wave arrival was reduced in amplitude by a factor 0.98 and 0.94 respectively, whilst theoretically it should be 0.985 and 0.940 in excellent agreement. This insensitivity to impact angle for small angles from the target plane normal can be considered to be beneficial to the technique, since a high sensitivity would tend to hide the effects of plastic deformation in later studies.

The impact force function,  $S(t)$ , was derived by deconvolution of the propagation and system response functions, i.e. figure 2(a). The AE signal of figure 4(a) is shown deconvolved in figure 4(b). The relatively high noise level following the initial impact force is due to errors in the deconvolution process, particularly in the

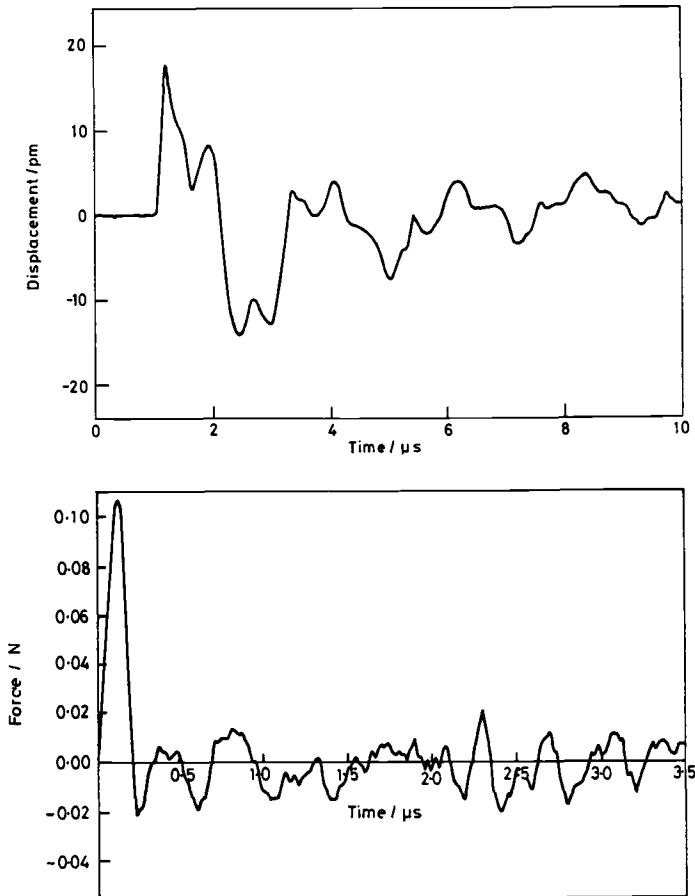


Figure 4 (a) Typical AE signal from bronze particle impact at 7.0 m/s and (b) deconvolved force impact signal. Note different time scales.

determination of the inverse function, and to noise in the original AE signal itself. Two useful parameters which can be extracted from this signal are the impact time and the peak impact force.

Glass particle impacts on the aluminium target plate were observed for the whole available range of impact velocities from 2.49 to 7.09 m/s. The shape of the AE signal did not change appreciably with increasing velocity (data not shown) although the amplitude increased as would be expected. This implies that the impact velocity was never high enough to result in significant plastic deformation. The impact force function was deconvolved (assuming no plasticity during impact) for a total of 81 AE signals. Figure 5 shows an example for

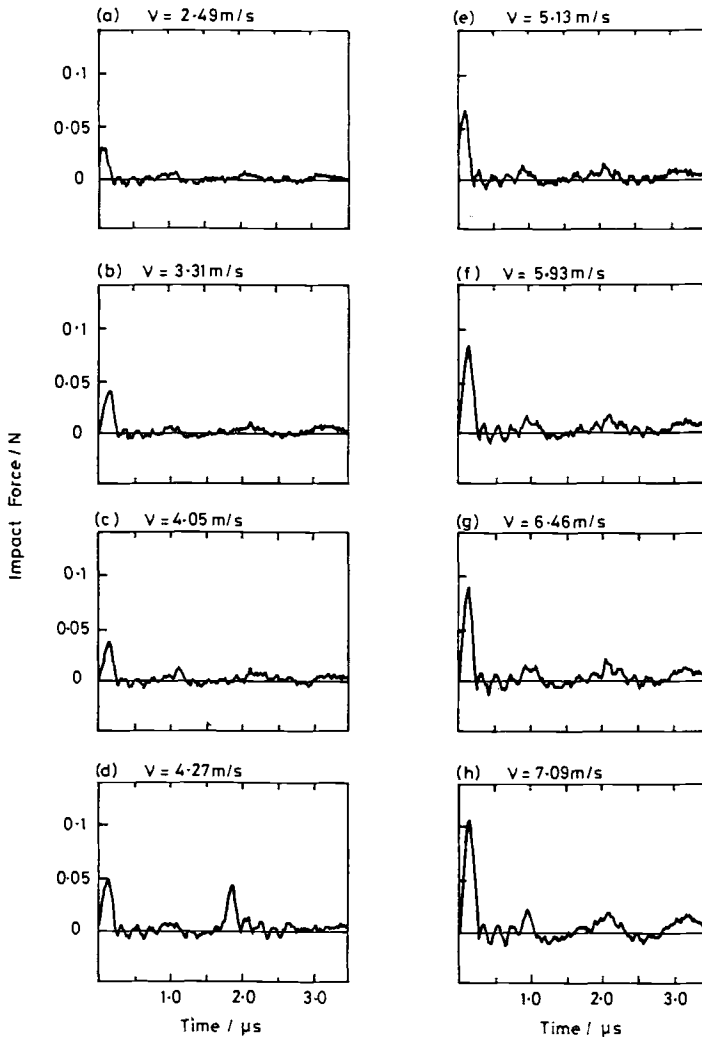


Figure 5 Deconvolved force impact signals from AE signals for several impact velocities.



each impact velocity. We observe: (i) The peak impact force increases consistently with increasing impact velocity and (ii) the impact time is not strongly dependent upon the impact velocity. Note that figure 5(d) shows a double impact (observed also in the original AE waveform).

The deduced peak impact force and impact time data were directly compared with semi-empirical calculations for normal elastic particle impact on an elastically deforming plane. Thus the impact time,  $t_{el}$ , is given by Hutchings [13] as:

$$t_{el} = 2.94 \times \left(\frac{5\pi}{4}\right)^{2/5} \rho^{2/5} \frac{r}{v^{1/5}} \left[ \frac{(1-v_1^2)}{E_1} + \frac{(1-v_2^2)}{E_2} \right]^{2/5} \quad (7)$$

where  $\rho$  is the density of particle material of radius,  $r$ , and  $v$  the impact velocity.  $v$  and  $E$  are Poisson's ratio and Young's modulus respectively for the target and particle materials.

Similarly, the peak impact force developed is given a (12,13):

$$F_{el} = [8.23 \pi^3 \rho^3 v^6]^{1/5} \left[ \frac{(1-v_1^2)}{E_1} + \frac{(1-v_2^2)}{E_2} \right]^{2/5} r^2 \quad (8)$$

where the coefficient of restitution is assumed to be unity. In the extreme limit where the particles stick to the surface of the target the maximum force will only be half as great.

Using the formula above the theoretical impact time and peak force were calculated for glass particles of diameter 80, 89.2 and 100  $\mu\text{m}$  impinging on an aluminium target. These sizes were chosen because they were the minimum, mean and maximum particle sizes used. The results are shown together with the experimental values measured from the deconvolved signals in figures 6 and 7 for impact force and time respectively. The results indicate that:

(a) Nearly all the peak impact force and impact time data measured from the deconvolved acoustic waveforms, fell between the minimum and maximum bounds of the theory.

(b) At any given impact velocity the scatter in the peak force or impact time was similar to the scatter expected due to the particle size range. However, the mean experimental peak impact force data were generally less than the mean theoretical values.

Observation (a) indicates that the acoustic technique was capable of giving realistic peak impact force values whilst observation (b) implies the coefficient of restitution was less than unity. The data of figure 6 suggests a value of 0.7. This was subsequently measured using the Laser Doppler Anemometry technique to be 0.5 for 100 $\mu\text{m}$  particles [14], which is in reasonable agreement. The impact force depends upon the impact velocity raised to the power 1.2 (equation 8) whilst the acoustic data suggested a power of 1.15. These results show a remarkable agreement considering that the theory is based on semi-empirical calculation.

An alternative approach is to use the acoustic data together with the theory (equation 8) to calculate the particle size. This was done and the resulting particle size distribution for the 81 AE signals is

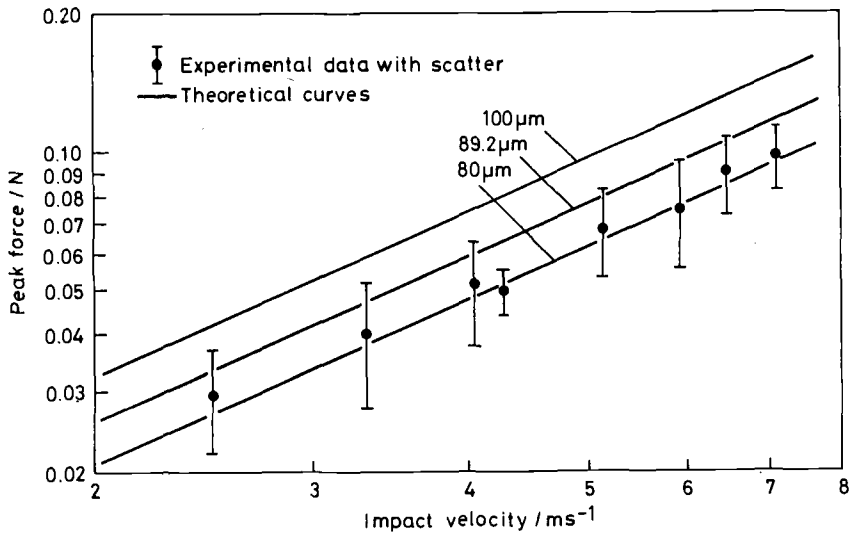


Figure 6 Experimental measurements of impact force together with scatter as a function of impact velocity for glass particles. Also shown are theoretical curves for minimum, mean and maximum particle diameters.

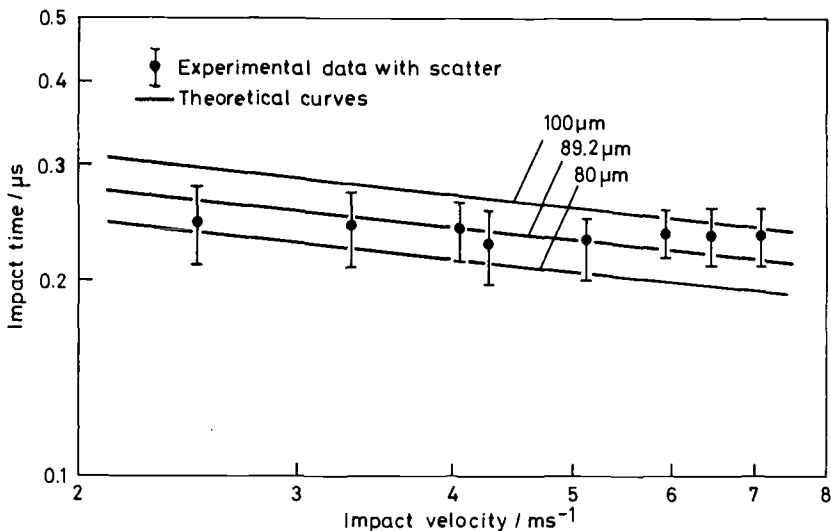


Figure 7 Experimental measurements of impact time together with scatter as a function of impact velocity for glass particles. Also shown are theoretical curves for minimum, mean and maximum particle diameters.

given in figure 8(a) (coefficient of restitution of 0.5 assumed). For comparison figure 8(b) gives the size distribution determined from optical microscopy measurements taken of particles from the same stock. The two distributions compare well, the mean particle size differing by just 4%. A different coefficient of restitution would give a different result but the particle radius depends only on the square root of the impact force (equation 8). For example, assuming a coefficient of unity only results in a 10% error in the mean particle size. The distribution determined from the acoustic data is broader due to a combination of factors such as (i) variations in the coefficient of restitution from one impact to the next caused by variations in surface conditions, (ii) errors in determination of the peak impact force, and (iii) lack of sphericity in the particles.

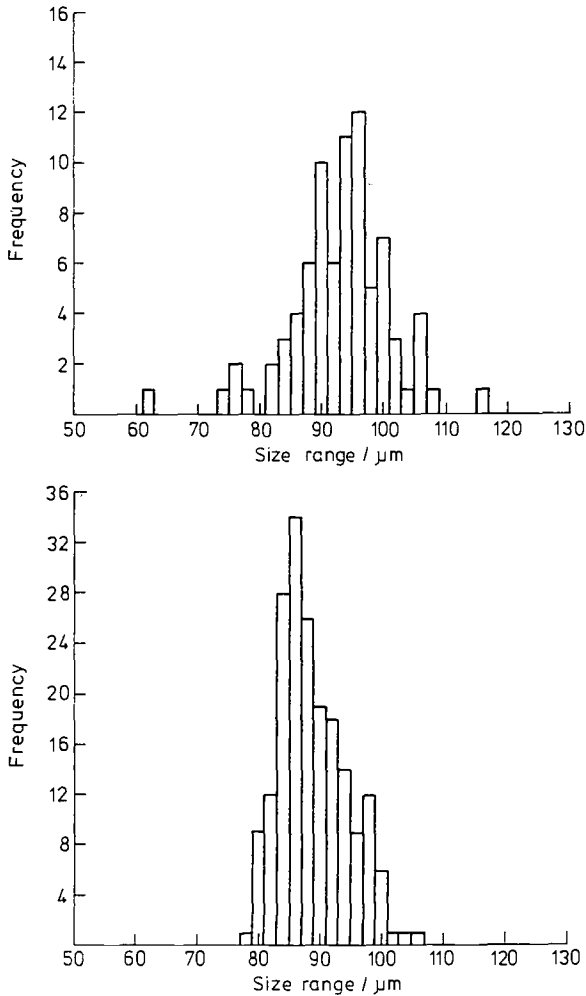


Figure 8 Size distribution of glass particles (a) calculated from deconvolved AE impact signals and (b) measured using an optical microscope.

As a final consideration, the minimum particle size detectable was estimated. The diameter of a bronze particle necessary in order to give a peak displacement larger than the sensitivity limit of the transducer (1.5 nm) for an impact at 10 m/s was determined as  $\sim 1.4 \mu\text{m}$ . A higher impact velocity would reduce this still further, if the current noise level were maintained.

## CONCLUSIONS

A broadband high-fidelity acoustic technique has been developed for characterising particle impact on plates. This work has included: (a) Derivation from first principles of the elastic waveforms from normal and oblique, elastic and plastic impacts. This has provided a framework for future experiments on plastic particle impact, where it is hoped to relate acoustic parameters to the effects of plastic deformation. (b) Measurement and analysis of acoustic signals from bronze and glass particle impact in the size range 50 - 100  $\mu\text{m}$  over the velocity range 2.5 - 7.1 m/s. The impact force function was deconvolved from these signals, and both the peak impact force and impact time deduced. The results compared well with semi-empirical theoretical models. Particle diameters were also determined from the AE particle impact signals and the resulting size distribution was consistent with that measured optically.

## ACKNOWLEDGMENTS

This work has been carried out as part of the UKAEA Underlying Research (Non-nuclear Energy) Programme. N Hsu of the US Department of Commerce, National Bureau of Standards, Gaithersburg is gratefully acknowledged for supplying the computer code for Green's function calculations. The authors also would like to thank Dr D H Saunderson for many helpful discussions, S Martin and T Pinfold for LDA measurements and C Duffil for construction of the particle free-fall vacuum system.

## REFERENCES

- [1] Buttle, D. J., Hemsley, D. J., Martin, S. and Saunderson, D. H., "Erosion in the Power-Generation and Utilisation Industries," Harwell Report AERE-R12663, Harwell Laboratory, U.K., Feb., 1988.
- [2] Preece, C. M., (ed.) Erosion: Treatise on Materials Science and Technology, Vol. 16, Academic Press, New York, 1979.
- [3] A.S.M.E., Wear of Materials, American Society of Mechanical Engineers, New York, 1981.
- [4] Drain, L. E., The Laser Doppler Technique, Wiley Publications, London, 1980.
- [5] Yeoman, M. L., Hemsley, D. J., Hadded, O. and Bates, C. J., "A Single Particle Optical Counting Instrument for On-Line Simultaneous Measurement of Drop Size, Velocity and Concentration in Sprays and Spray Systems", International Conference on Liquid Atomisation and Spray Systems, Imperial College, London, 1985.
- [6] Duncan, D., Bellanca, C. P., Blatchley, C., Sioshansi, P. and Scheibel, J. R. Joint ASME-IEEE Power Generation Conference Milwaukee, Wisconsin, JPGC-Pwr-57, Oct. 1985.

- [7] Sioshani, P., American Society of Mechanical Engineers, New York, ASME 83-JPGC-24, 1983.
- [8] Ceranoglu, A. N. and Pao, Y., "Propagation of Elastic Pulses and Acoustic Emission in a Plate, Part 1: Theory, Part 2: Epicentral Responses, Part 3: General Responses", Trans ASME, Journal of Applied Mechanics, Vol. 48, pp. 125-147, Mar. 1981.
- [9] Hutchings, I. M., "Energy Absorbed by Elastic Waves During Plastic Impact", Journal Physics D: Applied Physics Vol. 12, pp. 1819-1824, 1979.
- [10] Wadley, H. N. G., Simmons, J. A. and Stockton, C. K., "Dynamic Elastic Displacements due to Pulsed Laser Absorption at the Surface of an Infinite Plate", Harwell Report AERE-R10401, AEA Technology, Harwell Laboratory, Didcot, U.K. 1982.
- [11] Scruby, C. B., "Acoustic Emission Measurements Using Point-Contact Transducers", Journal of Acoustic Emission, 4(1), pp. 9-18, 1985.
- [12] Buttle, D. J. and Scruby, C. B., "Characterisation of Particle Impact by Quantitative Acoustic Emission", Accepted for publication in Wear (1989) and Harwell Report AERE-R13028, AEA Technology, Harwell Laboratory, Didcot, U.K. Sept. 1988.
- [13] Hutchings, I. M., "Strain Rate Effects in Microparticle Impact", Journal Physics D: Applied Physics Vol. 10, pp. L179-L184, 1977.
- [14] Martin, S. R., Pinfold, T. M. and Wallace-Sims, G. R., "Impact and Rebound Velocity Measurements on Small Particles", Harwell Report AERE-R13439, AEA Technology, Harwell Laboratory, Didcot, U.K. Apr. 1989.

Ichiya Sato, Takao Yoneyama, Kouichi Sato, Toshiyuki Tanaka,  
Minoru Yanagibashi, and Kazuo Takikawa

## APPLICATIONS OF ACOUSTIC EMISSION TECHNIQUES FOR DIAGNOSIS OF LARGE ROTATING MACHINERY AND MASS PRODUCTION PRODUCTS

---

**REFERENCE:** Sato, I., Yoneyama, T., Sato, K., Tanaka, T., Yanagibashi, M., and Takikawa, K., "Applications of Acoustic Emission Techniques for Diagnosis of Large Rotating Machinery and Mass Production Products," Acoustic Emission: Current Practice and Future Directions, ASTM STP 1077, W. Sachse, J. Roget, and K. Yamaguchi, Eds., American Society for Testing and Materials, Philadelphia, 1991.

**ABSTRACT:** In order to maintain efficient plant operability, better reliability and preventive maintenance are required. When a machine experiences some problem during use, operators must find the cause of trouble, then take measures to prevent serious damage. Acoustic emission (AE) is a useful means of machine condition diagnosis. The AE technique can detect incipient failure and locate the source.

This paper describes applications of AE techniques for large rotating machinery diagnosis, development of diagnosis systems using algorithms obtained from AE characteristics analyses, and applications for the diagnosis of rotary compressors in air conditioners.

**KEYWORDS:** acoustic emission, machine condition diagnosis, rotating machinery, mass production products

## INTRODUCTION

In large plants such as power plants, steel plants, and chemical plants, machinery is used under severe conditions. For instance,

I. Sato and Yoneyama are researchers at Energy Research Laboratory, Hitachi Ltd., 1168, Moriyama-cho, Hitachi-shi, Ibaraki-ken, 316, Japan; K. Sato and Tanaka are engineers at Tochigi Works, Hitachi Ltd., 800, Ohira-cho, Shimotsuga-gun, Tochigi-ken, 329-44, Japan; Yanagibashi and Takikawa are engineers at Hitachi Engineering Service Company, 2-9-1, Ohse-cho, Hitachi-shi, Ibaraki-ken, 317, Japan.

the machinery in thermal power plants are being operated by daily start stop, or weekly start stop schedules. Therefore, in order to maintain efficient plant operability, better reliability and preventive maintenance are required. So, development of high accuracy diagnostic techniques is very necessary. On the other hand, automation of mass production factories which manufacture consumer products or automobile appliances is rapidly progressing. In the inspection of mass products, automatic inspection and high accuracy diagnosis are required.

In order to perform high accuracy diagnosis in large plants and mass production factories, the following conditions are necessary.

- (a) Detection of primary abnormal phenomenon.
- (b) Early detection of abnormal condition.
- (c) Location of abnormal sources.
- (d) On line inspection of these above conditions.

The acoustic emission technique can satisfy all these conditions. This paper describes applications of acoustic emission techniques for diagnosis of large rotating machinery and mass production products.

Figure 1 shows the machine condition diagnosis systems. First, we have developed individual diagnosis systems with analog processing techniques. The rubbing diagnosis system can detect a slight rubbing phenomenon and locate the source in a rotating machine which is giving rise to abnormal vibration [1]. The bearing diagnosis system was developed in order to detect bearing damage at a early stage in journal bearings for steam turbines, generators [1] and rolling mills [2]. AE wireless monitor was developed in order to detect and transmit directly AE signals from an operating rotor [1].

In these applications, the relationship between various abnormal conditions and the AE characteristics were investigated systematically. Next, we developed a total diagnosis system with digital processing techniques using the algorithm obtained from the analyses [3].

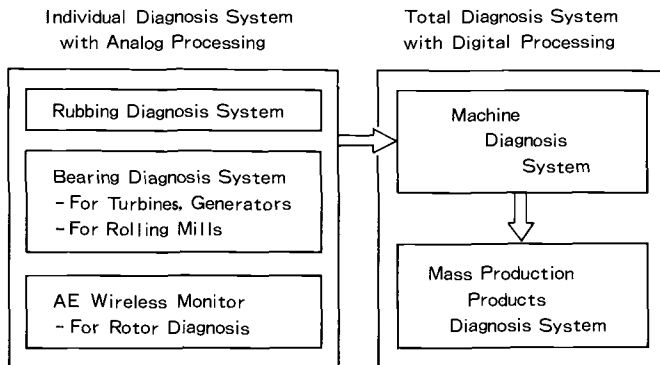


FIG.1 -- The machine condition diagnosis system.

For application to mass production products, we developed a diagnosis technique with the digital system for rotary compressors of air conditioners [4].

RUBBING DIAGNOSIS

Large scale rotating machines have a potential for metal to metal contact between rotors and stators. Figure 2 shows a view of a rubbing diagnostic test. The test rotor is a turbine rotor for a 350 MW high-intermediate pressure steam turbine. Each rubbing test piece is composed of a steel rod with an aluminum oil splatter guard fixed to one end. AE sensors were mounted on the bearings.

Figure 3 shows envelope detection waveforms and frequency spectra in the rubbing test. As can be seen from upper waveforms, it is difficult to distinguish rubbing phenomena from background noise.

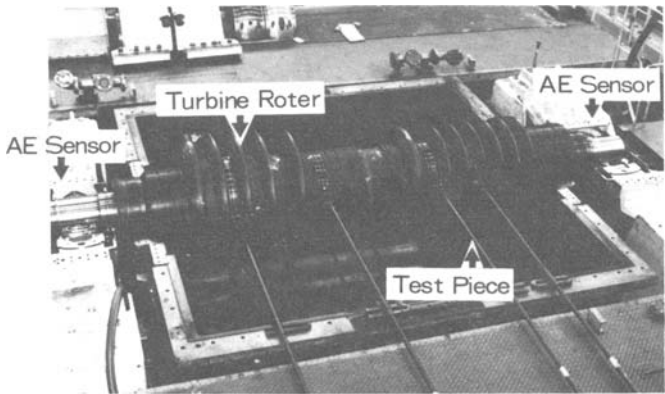


FIG.2 -- A view of the rubbing diagnosis test.

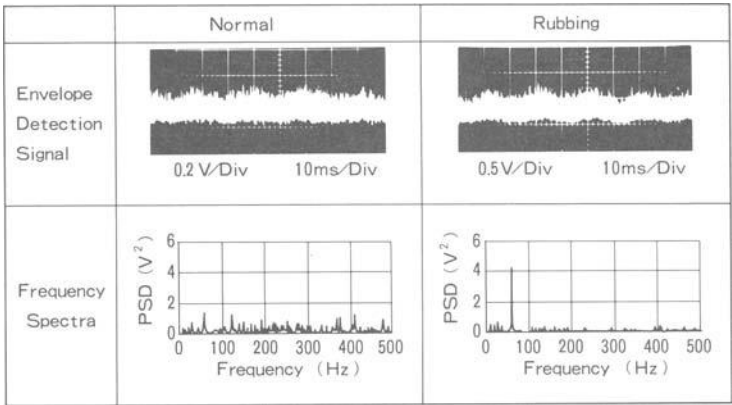


FIG.3 -- Envelope detection waveforms and frequency spectra in the rubbing test.



In order to extract rubbing signals from the noise, a frequency analysis of the signal was performed after envelope detection. Such analyses have shown that the main frequency component of signals caused by rubbing is equal to the frequency of the rotation signal.

Figure 4 shows a schematic diagram of the rubbing diagnostic technique. This technique separates rubbing signals from background noise using a variable bandpass filter which has a center frequency identical to that of the rotation signal. A rubbing source can be located by correlating the rubbing signals detected by the two sensors. Then, source location is obtained from the time difference  $\Delta T$ .

Figure 5 shows examples of rubbing signals observed in a actual steam turbine. The upper waveforms are amplifier output signals from two sensors. It is difficult to distinguish the difference between normal condition and rubbing.

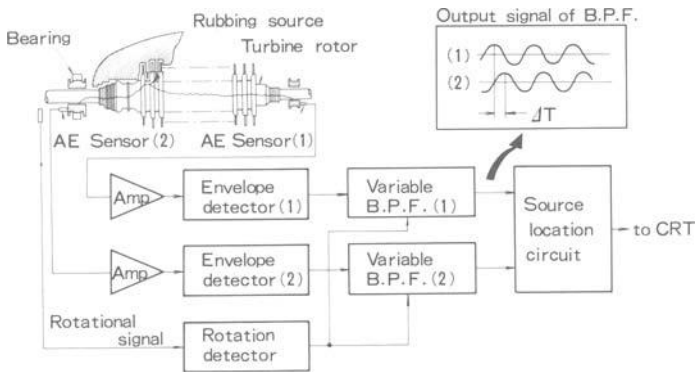


FIG.4 -- Schematic diagram of rubbing diagnostic technique.

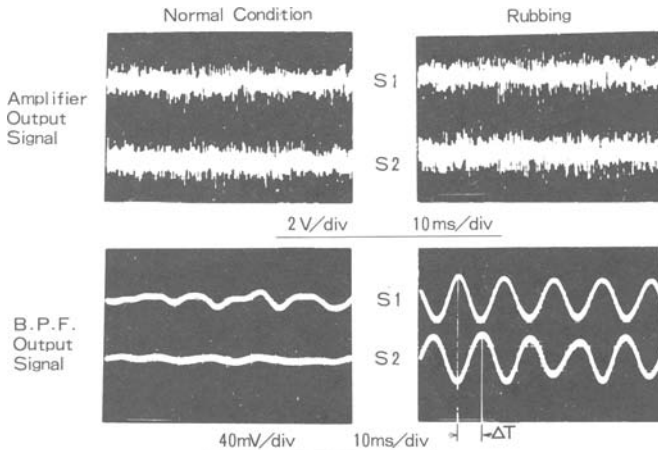


FIG.5 -- Rubbing signal in rubbing diagnosis test.

The lower waveforms are corresponding signals that have been processed with the rubbing diagnostic technique. Rubbing phenomena can easily be detected. In this case, it was found that a rubbing source was at a vicinity of the sensor S1.

BEARING DIAGNOSIS

We applied the acoustic emission technique to diagnose backup roll journal bearings for a rolling mill. Up to now, monitoring of the journal bearings were performed by temperature measurement of lubricating oil. This method lacks accuracy. Therefore, some bearings have been damaged due to an increase in oil temperature or excessive load on the bearing.

The main factors contributing to journal bearing damage are radial plane damage and thrust batting as shown in Figure 6. In radial plane damage, an excessive load on a bearing causes an increase in the temperature of the lubricating oil. This causes the oil to thin, which results in the bushing face of the bearing being worn off. The thrust batting is a metallic contact between the sleeve side and the bushing side.

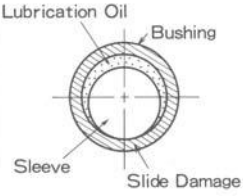
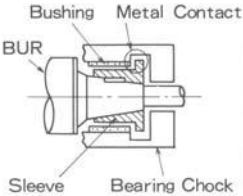
	Radial Plane Damage	Thrust Batting
Cause of Damage	<ul style="list-style-type: none"><li>•Excessive Load on Bearing</li><li>•Increase in Oil Temperature</li></ul>	<ul style="list-style-type: none"><li>•Mechanical Missetting</li></ul>
Bearing Damage Phenomena		
	<ul style="list-style-type: none"><li>•Wearing of Bushing Phenomena</li></ul>	<ul style="list-style-type: none"><li>•Metallic Contact Between Sleeve Side and Bushing Side</li></ul>

FIG.6 -- Classification of slide bearing damage.

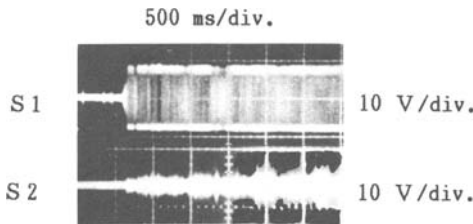


FIG.7 -- AE waveforms produced by thrust butting.

In order to observe acoustic emission behavior during damage of journal bearings, artificial damage tests were conducted with an actual mill. Figure 7 shows AE waveforms produced by thrust butting. The AE waveforms have a long duration time.

Figure 8 shows an example AE waveform and the frequency spectrum of an envelope detection signal caused by radial plane damage. As seen in this figure, the waveform characteristics are burst type, and the frequency spectrum has a wide band. The AE signals were analyzed for waveform and frequency characteristics. From these results, it was found that the frequency spectra of signals after envelope detection are useful for diagnosis of journal bearing damages.

Figure 9 shows a rolling mill with a bearing diagnosis system which was developed through the artificial damage test and signal analysis. This system can be monitored by scanning several bearings during the milling process. The system is being used successfully in an actual mill.

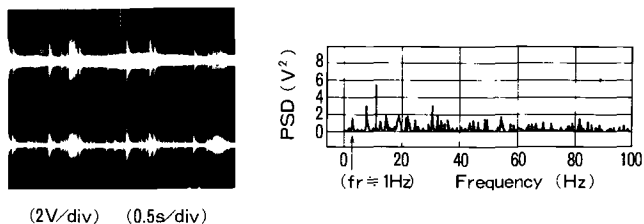


FIG.8 -- AE waveform and its frequency spectrum of envelope detection caused by the radial plane damage.  
(Object: Journal bearing for backup roll of rolling mill)

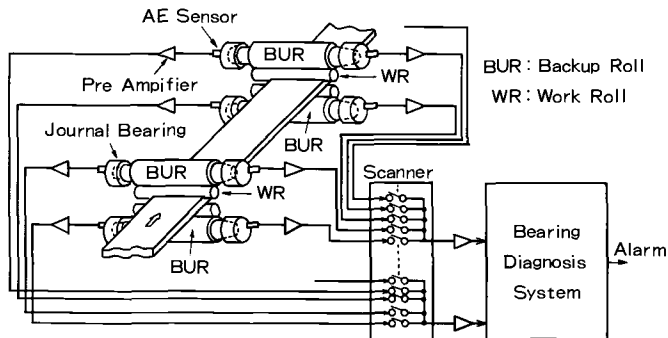


FIG.9 -- A diagram of a monitored rolling mill using the bearing diagnosis system.

## DIAGNOSIS SYSTEM

Basic Diagnosis Algorithm

A machine condition diagnosis system was developed using an algorithm obtained from the AE characteristics analyses. As shown in Table 1, the basic algorithm of the system discriminates between various abnormal conditions in machinery using AE waveform characteristics and frequency characteristics of envelope detection signals.

Using waveform characteristics, AE signals are classified as either a continuous type or a burst type signal. Then, using the frequency characteristics, the AE signal is identified as either a narrow band type or a wide band type. The narrow band type is further identified as either a rotation tuned type or an untuned type. The AE signal is categorized by six types of abnormal conditions. Typical phenomena are shown in parentheses in this table.

Figure 10 shows a block diagram of the diagnosis system. The AE and external signals are converted in to digital signals, and are memorized in a digital memory. Waveform and frequency analyses are done by a personal computer, as well as evaluation of the analyses' results.

TABLE 1 -- Basic algorithm of the diagnosis system.

Frequency Characteristics of Detection Signal		Waveform Characteristics	
		Continuous Type	Burst Type
Narrow Band Type	Rotation Tuned Type	A 1 (Rubbing)	A 2 (Rotor Crack)
	Untuned Type	B 1 (Metal Wipe)	B 2 (Fatigue Crack)
Wide Band Type	Untuned Type	C 1 (Bearing Tilt)	C 2 (Radial Plane Damage)

Note : ( ) is An Example of Abnormal Condition

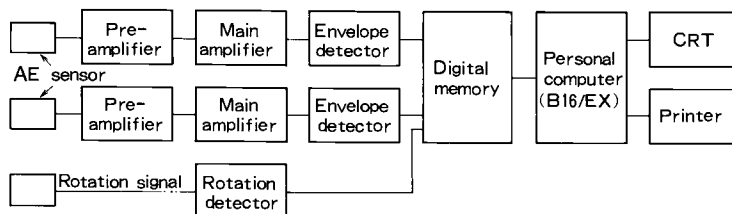


FIG.10 -- A block diagram of the diagnosis system.

Figure 11 shows a flow diagram of the diagnosis system software. In order to analyze the waveform and frequency characteristics, such parameters are calculated by a personal computer. This includes mean value, AE event, duration time, peak value, rise time, AE energy and FFT.

Figure 12 shows one approach for waveform analysis. Table 2 describes the calculation method of the waveform parameters. The frequency analysis is performed by the FFT calculation. Figure 13 shows the algorithm of the basic diagnosis software. It consists of three judgment functions: frequency band judgment, tune/untune judgment, and continuity judgment. The frequency band judgment is decided by employing a frequency band judgment constant  $K_{fw}$  as shown in the following equation:

$$A_p / A_m \geq K_{fw} \tag{1}$$

where

$A_p$  = highest peak value of power spectrum (PSD) in the frequency spectrum,

$A_m$  = mean value of PSD in the frequency spectrum,

$K_{fw}$  = frequency band judgment constant.

If equation (1) is satisfied, the AE signal is determined as a narrow band type, otherwise it is a wide band type.

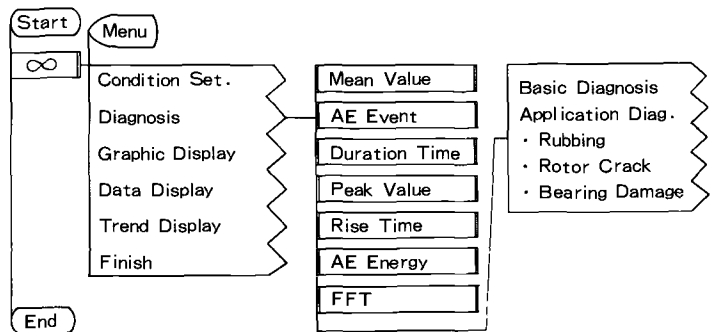


FIG.11 -- Flow diagram of the diagnosis system software.

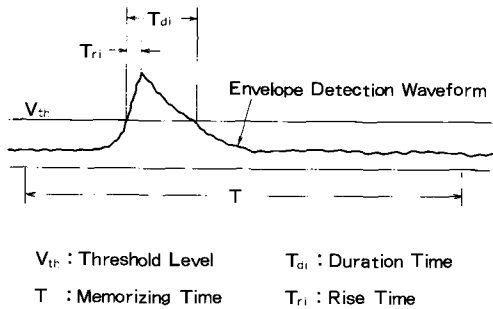


FIG.12 -- Illustration of waveform parameters.

The algorithm for tune/untune judgment classifies as a rotation tuned type or untuned type using the following equation.

$$|1 - F_p / F_r| \leq S_e \quad (2)$$

where

$F_p$  = frequency at the highest peak in the frequency spectrum,

$F_r$  = main frequency of the rotation signal,

$S_e$  = permitted error for the tune/untune judgment.

If the equation is satisfied, the AE signal is judged as the rotation tuned type, otherwise as untuned.

TABLE 2 -- Calculating method of waveform parameters.

Waveform parameters	Calculating method
Mean value ( $V_{mean}$ )	$V_{mean} = \frac{1}{n} \sum_{i=1}^n V_i$
AE event (N)	N is total counts over the threshold level $V_{th}$ .
Duration time ( $T_{durat}$ )	$T_{durat} = \frac{1}{N} \sum_{i=1}^N T_{di}$
Peak value ( $V_{peak}$ )	$V_{peak} = \frac{1}{N} \sum_{i=1}^N V_{pi}$
Rise time ( $T_{rise}$ )	$T_{rise} = \frac{1}{N} \sum_{i=1}^N T_{ri}$
AE energy ( $V_{ener}$ )	$V_{ener} = \frac{1}{N} \sum_{i=1}^n V_i^2$

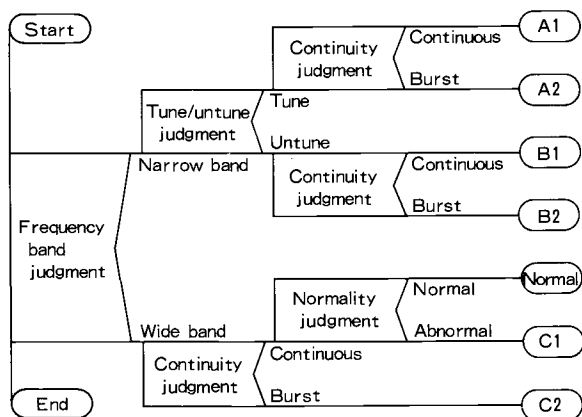


FIG.13 -- Algorithm of the basic diagnosis software.

Figure 14 indicates the algorithm for the continuity judgment, which classifies the signal into continuous type or burst type. The judgments of waveform analysis are performed with the following waveform parameters: AE event (N), maximum duration time ( $T_{dmax}$ ), mean value of peak amplitude ( $V_{peak}$ ), mean value ( $V_{mean}$ ), mean duration time ( $T_{durat}$ ). The continuity judgment of the AE signal is processed as follows;

- (1) If there is no AE event, the signal is the continuous type.
- (2) If  $T_{dmax}$  is larger than  $T_{cont}$  (continuous judgment time), the signal is the continuous type.
- (3) If conditions (1) or (2) are not met, and  $V_{peak}/V_{mean}$  is larger than  $K_{pw}$  (waveform judgment constant), the signal is the burst type.
- (4) If conditions (1), (2) or (3) are not met, and  $T_{durat}$  is larger than  $T_{burst}$  (burst type judgment time), the signal is the burst type. Otherwise it is the continuous type.

Using the algorithms for the three judgment functions as described above, the AE signal is categorized into six types of abnormal conditions which are denoted as A1, A2, B1, B2, C1 and C2 type. Generally, normal conditions have to be determined by a normality judgment algorithm.

The system has basic diagnosis and application diagnosis software. Suitable application software is provided for rubbing diagnosis, rotor crack diagnosis and bearing diagnosis. Thus, abnormal conditions and source locations can be monitored in detail.

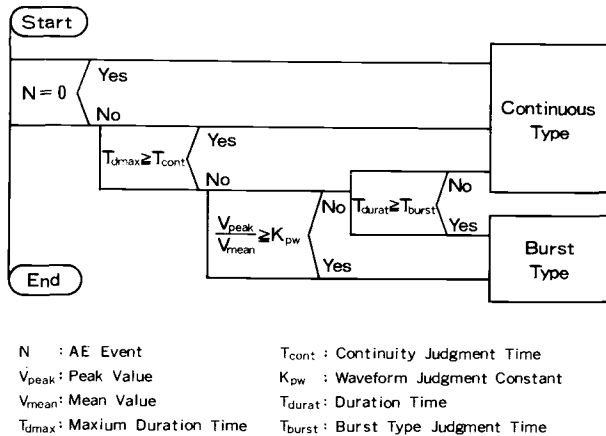


FIG.14 -- An algorithm for continuity judgment.

Evaluation Test on Rubbing Diagnosis

The system evaluation test was done with the data of rubbing diagnosis tests of steam turbine. Table 3 shows an example of "data display" obtained with the basic diagnosis software. From the experimental results, it is found that the abnormal condition belongs to the A1 type. This means that the rubbing signal is judged as a continuous type signal and its frequency characteristics are rotation tuned type belonging to the narrow band type. Figure 15 shows an example of "graphic display" obtained with the rubbing diagnosis software. From the experimental results, it is seen that the source location of the continuous signals is determined accurately.

TABLE 3 -- An example of "data display" obtained with the basic diagnosis software (object:steam turbine).

DATA	1986/06/26	TIME	13:31:07	DATA #	17
		SENSOR #1		SENSOR #2	
1. $V_{mean}$	(Volt) :	0.36		0.39	
2. $V_{peak}$	(Volt) :	0.52		0.65	
3. $V_{ener}$	(Volt <sup>2</sup> ) :	0.15		0.17	
4. N	(Count/sec) :	126.00		96.00	
5. $T_{durat}$	(msec) :	0.70		0.62	
6. $T_{rise}$	(msec) :	0.16		0.10	
7. Spectrum					
7.1 F1 (Hz, Volt.%) :	50.29	0.22 (4.2%)	50.29	0.20 (3.8%)	
7.2 F2 (Hz, Volt.%) :	26.84	0.03 (0.6%)	27.65	0.03 (0.6%)	
7.3 F3 (Hz, Volt.%) :	274.41	0.01 (0.2%)	2.93	0.01 (0.2%)	
7.4 TOTAL (Volt) :		5.17		5.26	
8. EXT					
CH1	(Volt) :	1.11			
CH1-Fr	(Hz) :	50.51			
CH2	(Volt) :	0.03			
9. SIGNAL TYPE :		A 1		A 1	
10. LOCATION (m) :		-3.30			

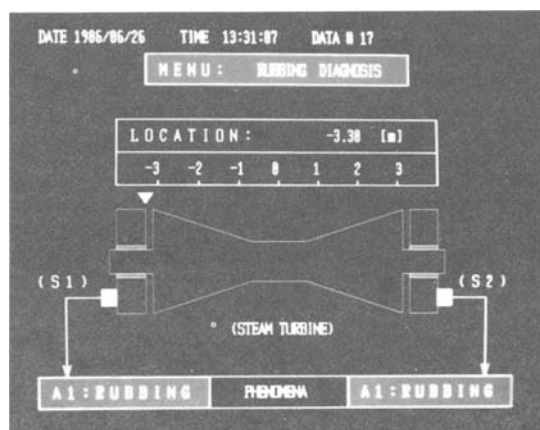


FIG.15 -- An example of "graphic display" obtained with the rubbing diagnosis software.



## DIAGNOSIS OF MASS PRODUCTION PRODUCTS

Mass production product diagnosis techniques were developed so that the rotating slides of compressors can be monitored nondestructively. The reliability of rotary compressors in production has been evaluated through visual inspection of disassembled parts after long-term testing. If techniques become available and allow evaluation without disassembly, the inspection efficiency improves and the development of new products would be promoted. This will also enable 100% inspection of compressors in production.

Structure of a Compressors and Diagnostic Objectives

Figure 16 shows the structure of a rotary compressor used in room air conditioners. The key part of the rotary compressor consists of a crank shaft, a roller, and a vane. The crank shaft is supported by an upper bearing, and a lower bearing, and it is driven by a motor mounted on top. The crank shaft and the roller move in a rolling piston motion. The vane slides on the rotating roller, and moves in and out of a slit in a cylinder that forms the compression and suction spaces, as illustrated in the lower drawing of Fig. 16.

The objectives of diagnosis are to detect damages in the following portions of the sliding surfaces.

- (1) Slide surfaces between the crank shaft and bearings.
- (2) Slide surfaces between the roller and the faces of the bearings.
- (3) Slide surfaces between the outside of the roller and vane.
- (4) Slide surfaces between the inside of the roller and crank shaft.

When any of these sliding surfaces of a compressor is damaged as described above, the operating efficiency of the compressor decreases and an abnormal stoppage during operation may result. This means the premature failure of the air conditioner that uses such a compressor. Hence early detection of the damage in sliding surfaces is important for improved operating efficiency and reliability.

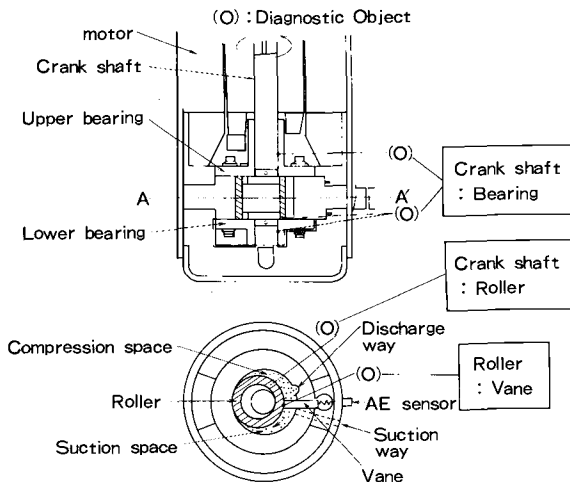


FIG.16 -- Structure of rotary compressor.

### AE Behavior under Normal Conditions and Compressors with Defects

Acoustic emission behavior under normal conditions was observed with an AE sensor which was mounted on the compressor chamber as shown in Fig. 16. This AE sensor was a broad band type, with a maximum sensitivity of  $-70\text{dB}$  (ref.  $1\text{V}/\mu\text{bar}$ ) at  $160\text{kHz}$ . Figure 17(a) shows a typical AE waveform under normal operation ("normal AE"). This indicates burst type AE signals generated in synchronization with a rotation signal which is obtained from a motor control signal. AE signal of excepting the burst type signal is low level.

In order to evaluate the AE phenomenon under normal operating conditions further, experiments were performed using test compressors on which several sensors were mounted. From these, we conclude that the generating mechanism for the normal AE signal is the butting phenomenon of the vane at the top dead center of the roller, as shown in Fig. 18. In Fig. 18(a), the vane is pushed to the suction-side wall

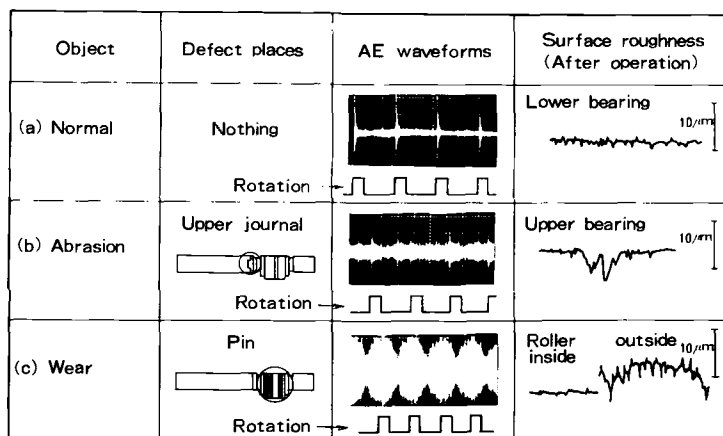


FIG.17 -- Examples of compressors with artificial defects and their AE waveforms.

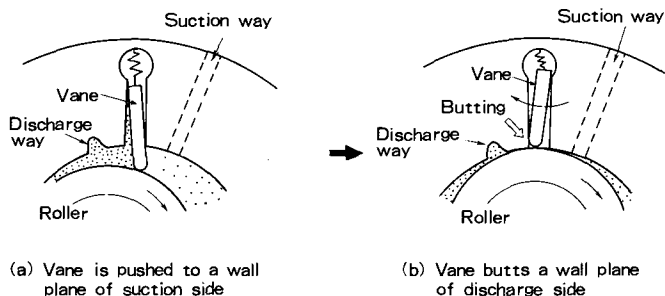


FIG.18 -- The generating mechanism of normal AE.

by the roller. In Fig. 18(b), the normal AE is generated when the vane butts the discharge-side wall as the roller reaches the top dead center position.

In order to investigate AE patterns of rotary compressors with defects, experiments were conducted using compressors with artificial defects. Figure 17(b) and (c) show examples of compressors with artificial defects and their AE waveforms. It also includes measurements of surface profiles after operation. The artificial defects to simulate abrasion damages were made by a punch on the upper and lower journals of crank shafts. Wear damages were simulated using a sandpaper on the pin surface of crank shafts and on the nose of a vane. AE patterns of the compressors with defects have the following characteristics.

- (1) AE characteristics of compressors with artificial abrasion damages include a number of burst type signals. These are generated between normal burst type AE signals from vane butting.
- (2) AE characteristics of compressors with artificial wear damages are exemplified as the continuous type signal. These may mask normal burst type AE signals as in the case of wear.

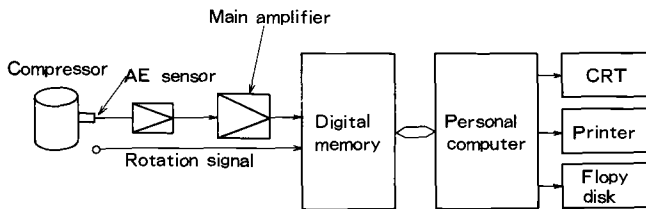


FIG.19 -- A block diagram of the diagnosis system.

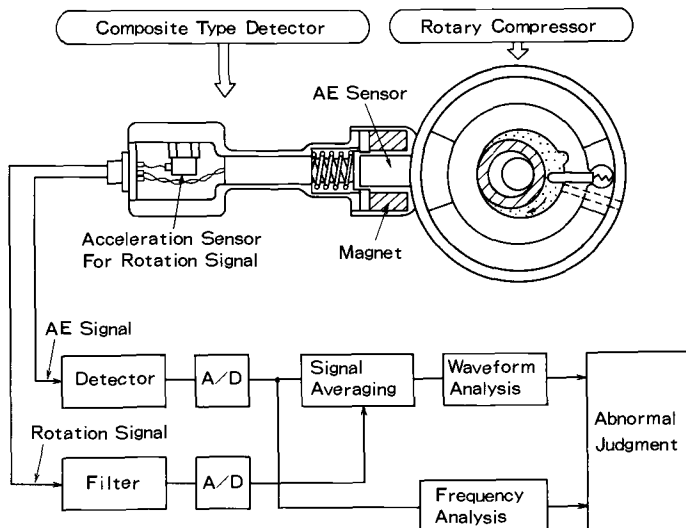


FIG.20 -- An AE detection and signal processing diagram for diagnosis of rotary compressors.

Signal Analysis Method

Signal analysis of the acoustic emission signals was conducted with the machine condition diagnosis system, described previously. Figure 19 shows its block diagram. The AE and external sensor signals are converted into digital forms, and are stored in a digital memory. Waveform and frequency analyses are performed by a personal computer, which also evaluate the results of these analyses. Signal analyses are performed by waveform analysis and frequency analysis using envelope detection signals, as shown in Fig. 20. In order to analyze the waveform characteristics, the following waveform parameters are calculated with averaging of the processed signals: AE events, mean, peak, and minimum values.

Figure 21 shows typical data of frequency and waveform analyses. As can be seen from the figure, the results of frequency analysis are useful to discriminate slides with wear damage from normal products. The results of AE events are useful to discriminate abrasion damaged slides from normal products.

In order to develop the diagnosis algorithm for rotary compressors, the following parameters were extracted to evaluate the results of the signal analyses. From the frequency analysis, a rotating tune factor,  $K_{rf}$ , is obtained by the following equation.

$$K_{rf} = A_{fr}/A_{ft} \tag{3}$$

where

- $K_{rf}$  = rotating tune factor,
- $A_{fr}$  = PSD of the fundamental rotation frequency in the frequency spectrum,
- $A_{ft}$  = total PSD of the whole frequency band in the frequency spectrum.

From the results of waveform analysis, the mean-to-peak ratio,  $K_{mp}$ , is obtained with the following equation:

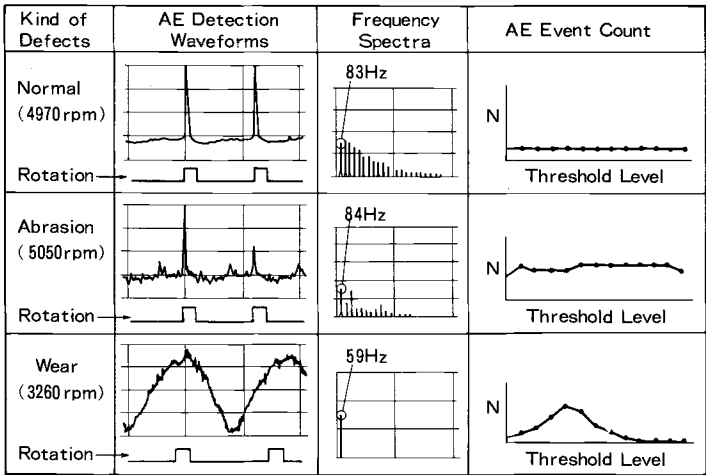


FIG.21 -- Typical signal analyses data of AE detection signals.

$$K_{mp} = V_{mean}/V_{peak} \quad (4)$$

where

$K_{mp}$  = mean-to-peak ratio,  
 $V_{mean}$  = mean value,  
 $V_{peak}$  = highest peak value.

Diagnosis System and its Application to Factory Inspection

Diagnostic tests were conducted with numerous compressors of various types. After the tests, these were disassembled and inspected visually. Table 4 shows examples of results which were obtained in the diagnostic tests. The results obtained were correlated either to the AE events counts and the rotating tune factor, or to the mean-to-peak ratio and the rotating tune factor. A diagnosis algorithm for rotating slides of rotary compressors was developed using the resultant correlation, as shown in Fig. 22. It consists mainly of three judgment functions:

TABLE 4 -- Examples of results which were obtained in the diagnostic tests.

Samples	Revolution (rpm)	AE parameters			Results of diagnosis	Results of Disassemble
		$K_{rf}$	N	$K_{mp}$		
No 1	2,376	0.29	1.3	0.22	Normal	Without Damage
No 2	3,394	0.12	1.0	0.18	Normal	Without Damage
No 3	5,124	0.37	2.3	0.79	Abnormal (Wear)	Wear of Vane Nose
No 4	5,213	0.12	2.7	0.46	Abnormal (Abrasion)	Abrasion at Bearing

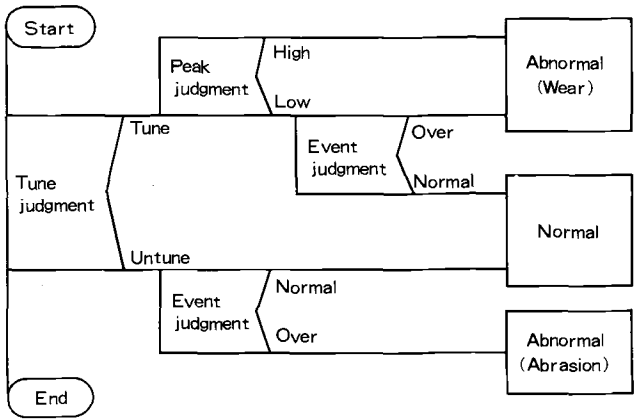


FIG.22 -- Basic diagnosis algorithm for rotary compressors.

- Tune judgment using the rotating tune factor,
- Peak judgment using the mean-to-peak ratio, and
- Event judgment using the AE event count.

Using the algorithm, the AE signal is categorized as normal or as one of two types of abnormality; wear or abrasion. This diagnostic algorithm can be applied to all types of rotary compressors for air conditioners.

The detector used in the system is a composite type consisting of an AE sensor and a rotation signal sensor. The structure of the composite type detector developed for on-line inspection, as shown in Fig. 20. The rotation signal sensor is an accelerometer which detects vibration signal tuning to determine the rotational frequency. The detector with a magnetic holder can be easily mounted on the compressor under test.



FIG.23 -- The on-line test in an air conditioner factory.

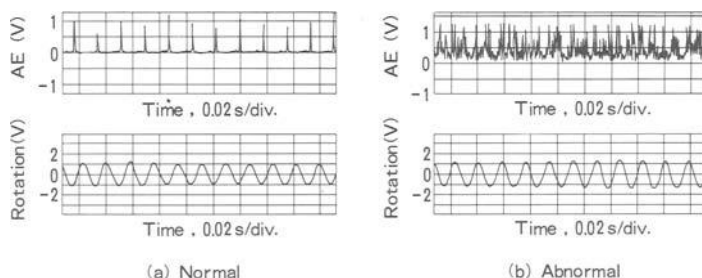


FIG.24 -- An example of data which were obtained in factory tests.

Results of AE tests correlated well with the visual inspection of disassembled rotary compressors following life-time tests. The developed AE system was applied to on-line inspection of air conditioners on factory floor with satisfactory results. Figure 23 shows a photograph of the on-line inspection in an air conditioner factory. Many products more than several hundred thousand have already tested until July 1989. Some products with such defects were discovered by the tests. Figure 24 shows an example of data which were obtained in factory tests. The developed diagnostic techniques should also be applicable to other mass produced goods.

## CONCLUSIONS

In order to perform high accuracy diagnosis in large plants and mass production facilities, we have developed machine condition diagnosis system with acoustic emission techniques.

- (1) Each individual diagnosis system with analog processing techniques, rubbing diagnosis, bearing diagnosis and rotor diagnosis system, were developed and are in use in actual plants.
- (2) The machine condition diagnosis system which uses a digital processing technique was developed for the diagnosis of various abnormal conditions of rotating machinery.
- (3) For application to mass production products, the digital system for rotary compressors of air conditioners was developed, and is applicable in on-line inspection of these products.

## REFERENCES

- [1] Sato, I., Yoneyama, T., Sasaki, S., Suzuki, T., Inoue, T., Koga, T., and Watanabe, T., "Rotating Machinery Diagnosis with Acoustic Emission Techniques", Journal of Acoustic Emission, Vol. 2, No. 1/2, 1983, pp. 1-10.
- [2] Inoue, N., Ozaki, K., Sato, I., Yoneyama, T., Kakehuda, M., and Hiruoka, S., "Diagnosis of Backup Roll Journals for Rolling Mill by Acoustic Emission", Kawasaki Steel Giho, Vol. 17, No. 4, April 1985, pp. 52-58.
- [3] Sato, I., Yoneyama, T., Sasaki, S., and Suzuki, T., Proceedings of the 8th International Acoustic Emission Symposium, Tokyo, 1986, pp. 65-72.
- [4] Sato, I., Yoneyama, T., Sato, K., Tanaka, T., and Hata, H., "Diagnosis of Rotating Slides in Rotary Compressors using Acoustic Emission Technique", Journal of Acoustic Emission, Vol. 7, No. 4, 1988, pp. 173-178.

## CAVITATION MONITORING OF HYDROTURBINES WITH RMS ACOUSTIC EMISSION MEASUREMENT

---

REFERENCE: Derakhshan, O., Houghton, J. R., Jones, R. K., and March, P. A., "Cavitation Monitoring of Hydroturbines with RMS Acoustic Emission Measurement," Acoustic Emission: Current Practice and Future Directions, ASTM STP 1077, W. Sachse, J. Roget, and K. Yamaguchi, Eds., American Society for Testing and Materials, Philadelphia, 1991.

ABSTRACT: Acoustic Emission measurements are shown to be a reliable indicator of cavitation pressure pulses. The method of display is the root mean square, RMS, of the AE signal integrated over 1 second that is proportional to the average cavitation energy. An inexpensive AE transducer, amplifier, filter, and RMS circuit is described with a gain of 22 dB and a frequency range of 10 kHz to 1.25 MHz. Data from two laboratory controlled cavitation experiments is presented. The system is tested on two TVA hydroturbines. Kaplan-type and Francis-type turbines had a similar shaped increased RMS AE curve with wicket gate opening but the numerical maximum values are different in each hydroturbine installation. A real-time continuous RMS AE monitor is recommended on each hydroturbine for the evaluation and control of cavitation erosion.

KEYWORDS: Cavitation, Acoustic Emission (AE), Energy, Root Mean Square (RMS).

Cavitation in hydromachinery has been known to the scientists and engineers since the early part of this century [1]. It is considered as one of the important damage mechanisms that must be dealt with. Cavitation is defined as the process of generation (inception) and collapse of vapor and/or gas bubbles in liquids. Inception occurs when the pressure of the liquid is reduced rapidly to or below that of its vapor pressure, and then the bubble collapses once it has moved to a region of higher pressure. The bubble collapse is accompanied by a high amplitude pressure pulse, which at times reaches damaging shock wave proportions. This high amplitude pressure pulse is the cause of cavitation damage (pitting of the boundary surface).

The cavitation damage to the hydroturbines (i.e. damage to the turbine blades and also to the surrounding surfaces) costs the hydropower industry enormous amounts of revenue for repairs and replacement of hydroturbine systems annually. Although the designers try to rectify cavitation inception in their designs, it is not possible to do so efficiently for all operating and environmental conditions. Thus it often happens that the hydroturbines are operated in cavitating range. Consequently the hydropower industry for years has been interested in some type of real-time, low cost, monitoring system to inform the operators of the cavitation status of their systems.

---

Mr. Derakhshan and Prof. Houghton are affiliated with Dept. of Mechanical Engineering, Tennessee Technological University, Cookeville, TN 38505; Mr. Jones and Mr. March are engineers at Engineering Laboratory, Tennessee Valley Authority, Norris, TN 37828.



This paper reports on a low cost solution to cavitation monitoring of hydroturbines. The monitoring system employs a transducer which is positioned on the exposed metal liner of the draft tube, whose signal is then amplified and converted to its root mean square (RMS) value. This RMS value can then be displayed in variety of forms. The cost of this system is about \$180.00 plus 20 hours of labor for assembly and testing.

To investigate the cavitation bubble collapse as a viable source for Acoustic Emission (AE) purposes, a number of single spark generated bubble collapse tests were performed. In these tests such issues as the attenuation of the pressure pulse in water with distance and its transmissibility through a second medium (i.e. steel pipes) are addressed.

The Cavitating Jet Erosion Test Facility [2] (see Fig. 1) at the Tennessee Valley Authority (TVA) Engineering Laboratory in Norris, Tennessee, was used to determine the effect of cavitation bubble cloud on the propagation of the pressure pulses. For this tests the AE signal is from two transducers: (1) located on the test specimen, and (2) placed on the outside wall of the tank.

## INSTRUMENTATION

The preliminary plan for the monitoring system was to verify that the cavitation bubble collapse has the characteristics of an AE signal source and then to design the monitoring system.

The energy level of the cavitation was the parameter that was selected to be monitored. To reduce cost and amount of electronic components, it was decided to use the RMS voltage of the AE event as the indication of the AE intensity level. In Acoustic Emission (AE) an energy release is transmitted through the medium in a displacement form and is sensed by a transducer. The transducer in turn converts this displacement into a voltage signal. The energy of a voltage signal, as measured using a thermocouple power meter, is

$$E = \frac{1}{R} \int_0^T V^2(t) dt, \quad (1)$$

and since root mean squared voltage  $V_{rms}$ , of the signal is

$$V_{rms}^2 = \frac{1}{T} \int_0^T V^2(t) dt, \quad (2)$$

then substitution of Eq. 2 in Eq. 1 yields

$$E = \frac{T}{R} V_{rms}^2 \quad (3)$$

where  $R$  represents the balancing resistance used in the power meter, and  $T$  is the time duration of the whole digitized waveform over which the voltage signal is averaged. If the exact value of the energy is of no interest, but rather its relative value, then comparing the  $V_{rms}$  is sufficient. That is to say, the system only needed to distinguish between no cavitation, cavitation, and intense cavitation.

The transducer, used for detecting the pressure pulses transmitted through the metal liner, is a Valpey-Fisher VP1093 Pinducer; a broadband transducer with a good frequency response up to 1.25 MHz.

The signal from the transducer is amplified by an amplifier built around the AD5539JN ultra-high frequency Op-Amp. It has a constant gain of about 22 dB from 100 Hz to 3 MHz and a maximum signal to noise ratio of 62 dB. A 10 kHz highpass, double pole filter was found to be necessary to reduce the extraneous background signals. Also for the purpose of matching the impedances between the transducer and the amplifier, a 1 M $\Omega$  input impedance buffer was added between the transducer and the amplifier.

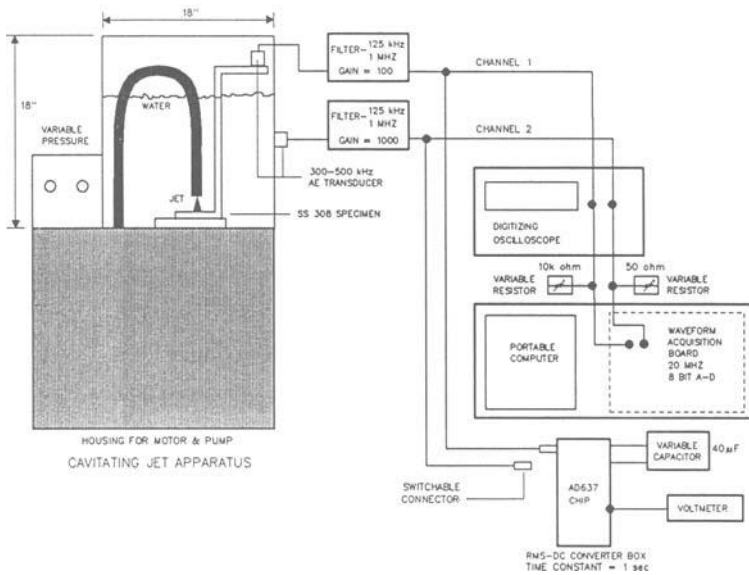


FIG. 1 - TVA Engineering Laboratory Cavitation Jet Erosion Test Setup.

The output signal of the amplifier is then fed to a RMS circuitry built around the AD637JD TRMS converter chip whose averaging time duration  $T$  (as shown in Eq. 2), can be changed by changing the averaging capacitor. Presently the averaging time is switchable for either  $64 \times 10^{-3}$  or 1 second.

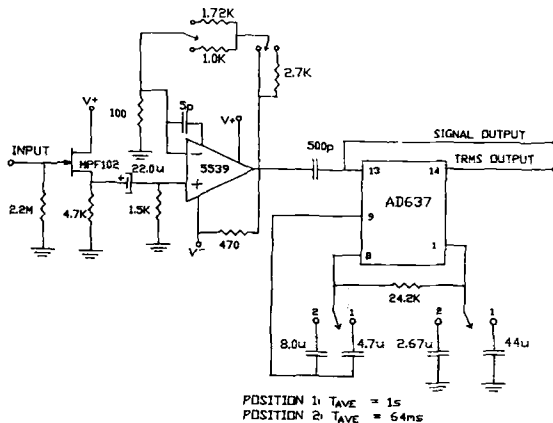


FIG. 2 - Schematic of the monitoring system circuitry.

Figure 2 shows a schematic of the monitoring system circuitry. The circuit is placed within a metal box which shields the sensitive circuitry from electromagnetic and high frequency radio disturbances. The DC output of the system can be displayed in many ways, and presently a DC panel voltmeter is being used. Beeswax is used as couplant between the draft tube liner and the transducer.

EXPERIMENTAL STUDIES

Experiments were performed to evaluate the nature of the pressure pulse amplitude of a bubble collapse, using single bubbles generated in water by single sparks. Such issues as the change in amplitude and frequency content with distance and with passing through steel pipes are addressed. Also investigated is the transmission of the pressure pulse in a cloud of cavitation bubbles. However the usefulness of the transducer as an Acoustic Emission sensor had to be verified first.

Pinducer

The pinducer was compared using the Seismic Surface Pulse method [3] against a NBS Standard Reference Material(SRM) AE displacement transducer. Figure 3 shows a typical response of the SRM and the pinducer to the same capillary glass break input, and Fig. 4 shows the frequency spectrum of the pinducer. Suitability of the pinducer as an AE transducer is self evident from Figs. 3 and 4.

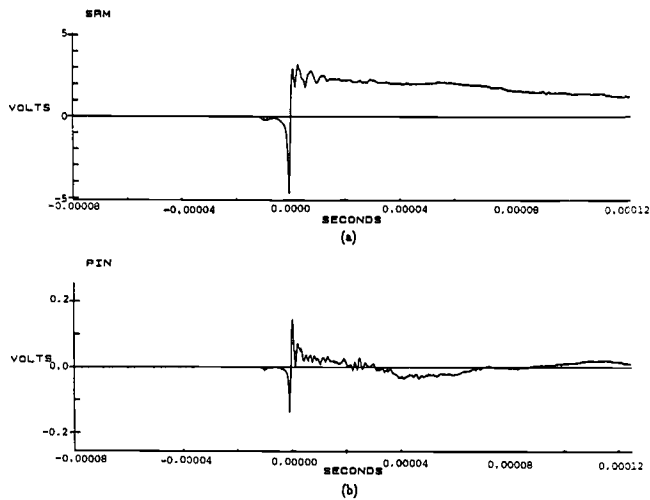


FIG. 3 – Response of the NBS Standard Reference Material displacement transducer and the pinducer to a seismic surface pulse.

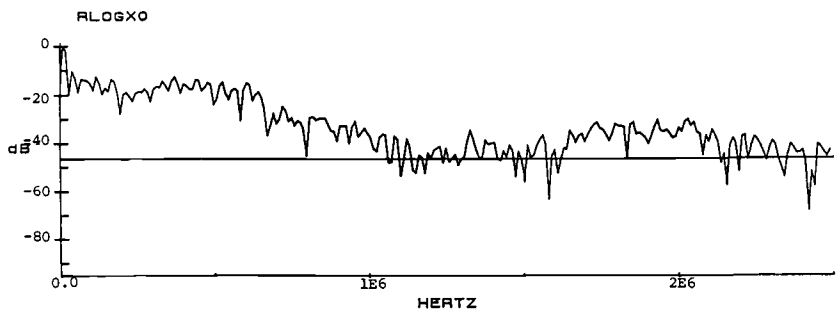


FIG. 4 – Frequency spectrum of the pinducer.

### Pressure Pulse In Water

A spark generating system was used. The spark is produced by first charging a 4000-V, 4  $\mu$ F capacitor to about 2500 volts using a DC power supply. The capacitor is then discharged through the gap (approximately 0.5 to 1 mm) between two tungsten electrodes using a solenoid relay switch. The discharge causes a spark across the gap, which consequently produces a vapor bubble due to point vaporization of the water between the electrodes. This technique has been previously used by references [4-6].

To verify the presence of the bubble and that the second pulse is due to the bubble collapse, see Fig. 5, high speed filming (3000 frames/sec) was used. In Fig. 5 the rectangular pulse and the pulse immediately following it are the signature of the spark jump across the gap. The reason for such a displayed form was not investigated since the spark signature was not of any immediate concern. The next two pulses are initial and rebound bubble collapse, respectively.

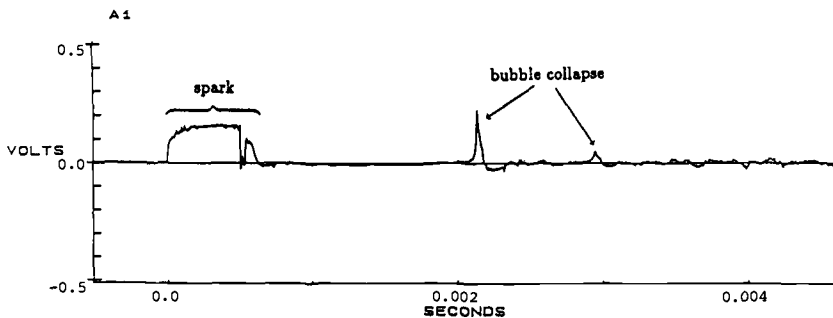


FIG. 5 - A typical pressure waveform from a spark generated bubble collapse.

The electrodes were lowered into a plastic tank approximately  $1 \times 0.75 \times 1$  meter to a depth of about 152.4 mm and the pinducer, covered with petroleum jelly, was placed at different distances from the electrode gap. At each location the pressure pulse signature was captured using a Data Precision Data 6000 digital data acquisition and analyzing system at a sampling rate of 300 ns. The relative energy of each captured signature was then found by first squaring and then integrating it (Eq. 1). Figure 6 shows a sample pressure pulse and its energy waveform as calculated using the above procedure.

Figure 7 is the log-log plot of the relative energy of the pressure pulses against the distance from the electrode gap. After a radius of 19 mm the energy is seen to decrease at a rate of 3.5. There is also the indication that the rate of energy decrease to be even higher for radii larger than 60 mm. The lower energy level for radii less than 19.0 mm is believed to be due to the disturbance of the bubble growth by the transducer, and/or the pressure front may not yet be fully developed.

From the above mentioned experiment it was found that the pressure pulse of a bubble collapse did not follow the acoustic laws for a spherical point source. The acoustic law states that energy attenuates inversely with square of distance from the source. However more experimental data are needed (larger range of distances) to be able to show a governing law for cavitation energy attenuation.

### Through Steel Pipe Transmission

A number of different thickness, 6.35, 9.53, 12.70, and 22.23 mm ( $1/4$ ,  $3/8$ ,  $1/2$ , and  $7/8$  in.) steel pipes with 101.60 mm (4 in.) inside diameter were placed in the tank filled with water. The pinducer was placed against the outside wall while the electrodes were positioned, opposite to the pinducer inside the pipe.

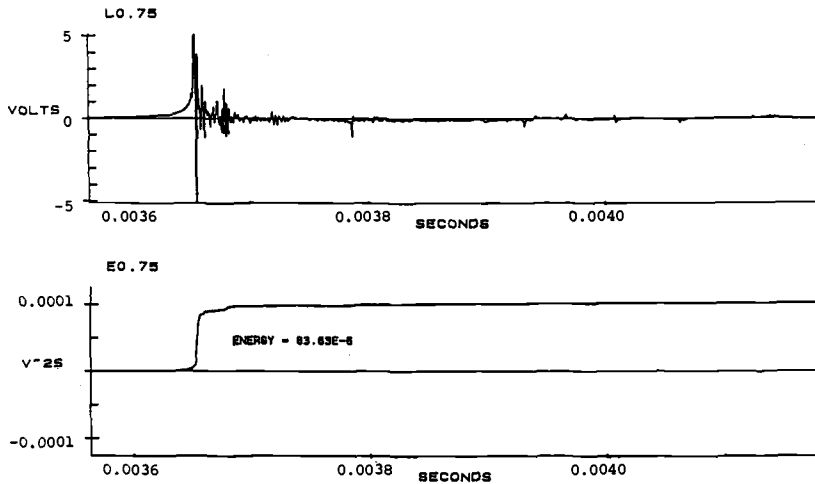


FIG. 6 - A sample pressure pulse and its calculated energy.

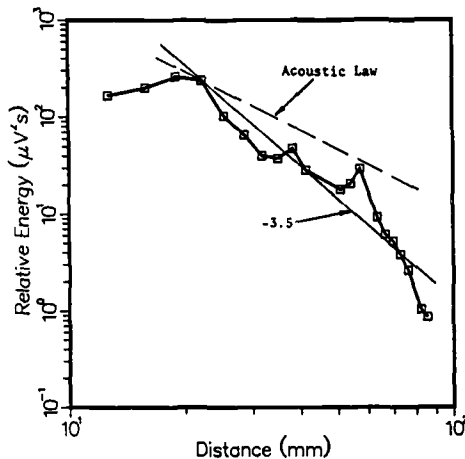


FIG. 7 - Plot of energy vs. Distance on log axes (through water transmission).

For each pipe two sets of data were captured, one set with the electrode gap at about 3.18 mm (1/8 in.) from the inside wall and a second set with the gap at about 50.80 mm (2 in.) from the inside wall. Figure 8 shows a sample waveform, for the 9.53 mm thick pipe, as sensed by the pinducer with the electrode gap at center of the pipe and its frequency content. The 279.95 kHz peak is very close to the longitudinal natural frequency across the wall thickness.

#### Cavitating Jet Erosion

Laboratory tests were conducted at Tennessee Valley Authority (TVA) Cavitating Jet Erosion Test Facility to provide a comparison of the AE signals from a test specimen

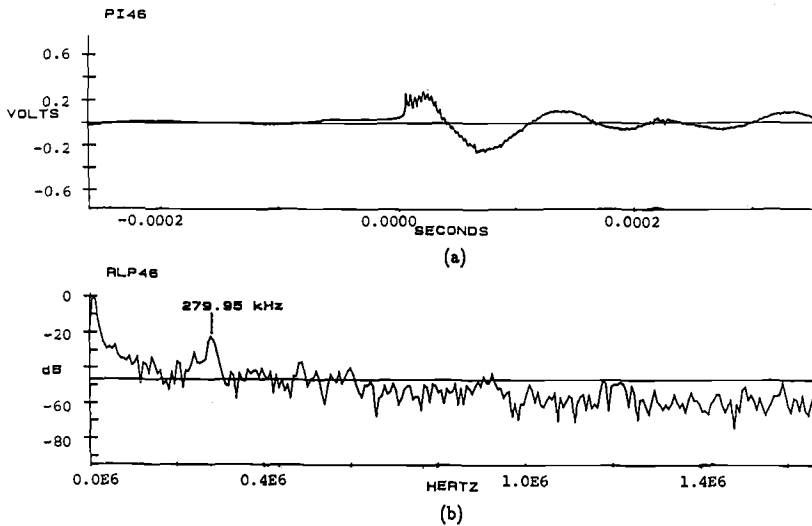


FIG. 8 - Through steel pipe sample waveform and its frequency content.

with a transducer located directly on the test specimen and another transducer located on the outside wall of the test chamber, see Fig. 1.

The setup included two 300-500 kHz AET AE transducers whose signals were amplified, filtered and displayed on a digital oscilloscope. The signals were then recorded using a personal computer equipped with an 8 bit A/D board. Also a RMS circuitry with a 1 second averaging time was used to measure the related energy of the cavitation. The tests were conducted with an initial jet pressure of 51.8 MPa (7500 psi) in decrements of 3.5 MPa (500 psi) down to 3.5 MPa (500 psi). At each pressure, after allowing for stabilization, the signal from each transducer was recorded at a sampling frequency of 10 MHz and their RMS value was noted.

## DISCUSSION OF RESULTS

It was verified that the cavitation bubble collapse can be used as an AE source. The pressure pulse is short in duration and strong enough to pass through such materials as steel. It has not been possible to draw any reliable conclusion on the change in the frequency content of the pressure pulse as it moves through water. Although there are some differences in the frequency contents, no relation with distance has yet been established [7].

There is the indication that the wall thickness can be measured from the frequency content of the pulse as sensed by the pinducer on the outside wall of the pipes. There are frequency peaks coinciding with the longitudinal natural frequency of the walls as calculated using theory. This frequency for the 9.53 mm (3/8 in.) thick pipe is noted on Fig. 8b. Theoretically this frequency is calculated to be approximately 270 kHz as compared to the 279.95 kHz found experimentally. This is a striking agreement. The percentage difference in the calculated and measured frequencies ranged from 0.14% to 6.63% for the four different thickness pipes [7].

In the case of the jet erosion tests, the RMS output from the tank wall mounted transducer decreased (almost linearly), Fig. 9, with increasing pressure and cavitation.

There was a visible bubble cloud that increased with pressure. This bubble cloud appears to attenuate the signal before it reaches the transducer. On the other hand the RMS output from the specimen mounted transducer, Fig. 10, increased with pressure and cavitation. This result supports the feasibility of using the TRMS chip to provide an indication of cavitation level when the transducer is mounted on the cavitating piece.

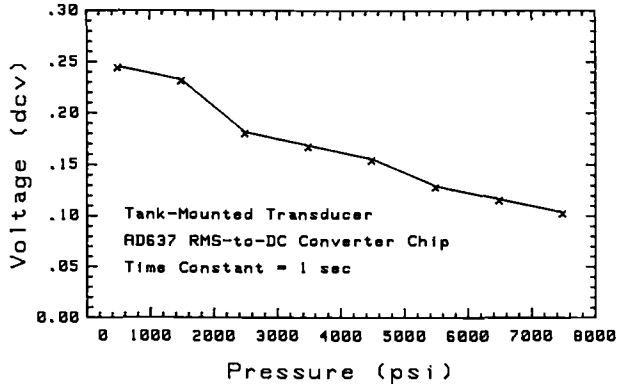


FIG. 9 – RMS output of the wall mounted transducer vs. pressure.

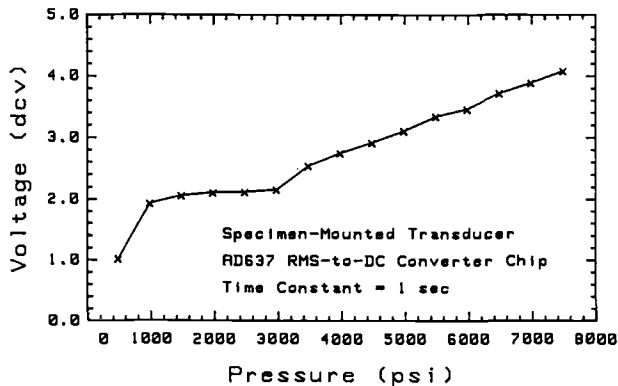


FIG. 10 – RMS output of the specimen mounted transducer vs. pressure.

Furthermore, a sharp 1.2 MHz frequency peak was present in the frequency spectrum of the tank wall mounted transducer at all pressure levels. This frequency corresponds to the calculated wall resonance frequency of 1.14 MHz [8]. This result again shows that cavitation signals can be used in measuring wall thickness.

## TESTING AND APPLICATION OF THE MONITORING SYSTEM

Since the monitoring system is to operate in real-time mode, it was tested for longevity, and reliability of the circuitry. These tests met with success and since a DC power supply is included in the circuitry, there is only a need for a 110-V AC power source.

The frequency response of the amplifier-filter combination was verified as can be seen in Figs. 11 and 12. The system -3 dB points fall around 9 kHz and 7 MHz, with no

significant phase shift from 100 kHz to 3 MHz. Also the  $V_{rms}$  output of the system was checked against known value sinusoidal, triangular, and square waveforms, and the rate of the deviation to the exact value was within plus or minus 0.002.

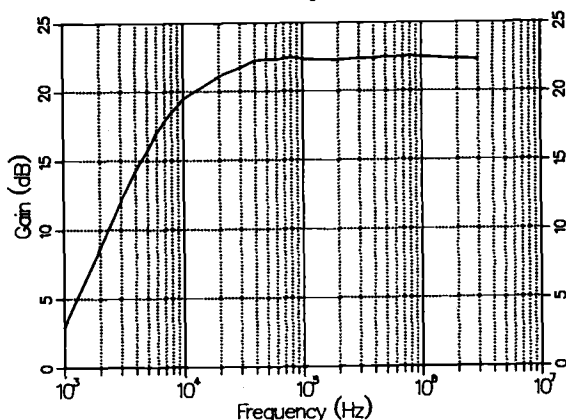


FIG. 11 – Frequency response of the amplifier-filter combination.

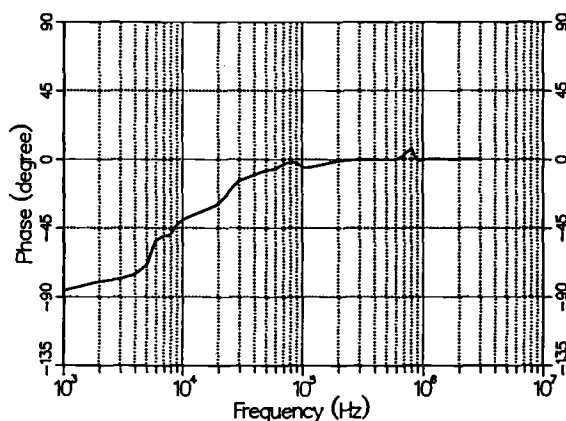


FIG. 12 – Phase response of the amplifier-filter combination.

After the above tests were performed, the system was then applied to the hydrosystem. Tests have been conducted at Douglas and Chickamauga hydroplants, operated by Tennessee Valley Authority, with Francis and Kaplan turbines respectively. It was found that each system has different cavitation intensity characteristic and thus the amplifier gain must be adjusted from one hydroturbine to another. Figure 13 is a sample cavitation signal acquired by the monitoring system. Figure 14 shows the RMS output of the cavitation monitoring system against the percentage wicket gate opening for unit #3 of Douglas and that of unit #1 of Chickamauga hydroplants. Since each unit had a different cavitation intensity level the ordinate has been normalized as a percentage of the maximum RMS value for each curve. In case of Douglas Hydroplant two sets of data are presented, one is for decreasing gate opening from 100% to 10% and the other for increasing gate opening from 30% to 100%. In this case the head and tail water levels had increased by about 1.0 m and a period of two hours had elapsed when the increasing gate opening data were taken. From the two different RMS voltage sets (notice the maximum RMS values), it can be seen that there can be differences from hour to hour at any particular hydroturbine. It would require long term statistical study of the cavitation of each hydroturbine in order to be able to draw a cavitation performance function with



five or more variables. Thus a real-time cavitation monitor is advocated for the system operator or a computer to record cavitation. It would then be possible to change turbine load condition in a rational way and reduce cavitation erosion.

It must be mentioned that signals such as bearing noises, flow noises (mostly random in nature), machine vibrations, etc. affect these AE measurements. The scope of this project did not facilitate a more in-depth investigation of these other effects. However, their effects on the AE measurements were reduced by introducing the 10 kHz highpass, double pole filter in the amplifier circuitry.

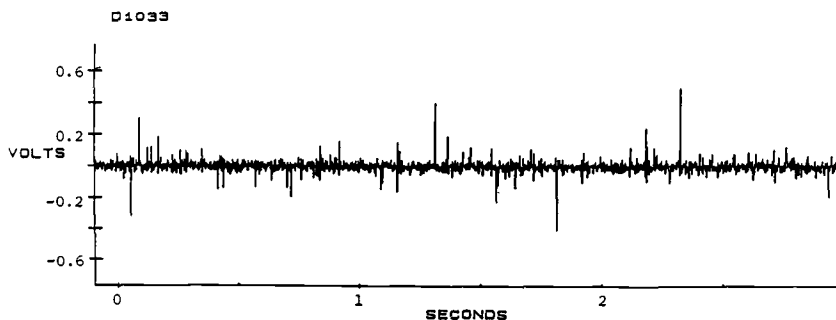


FIG. 13 - A sample waveform of cavitation signals (Douglas hydropplant, unit #-3).

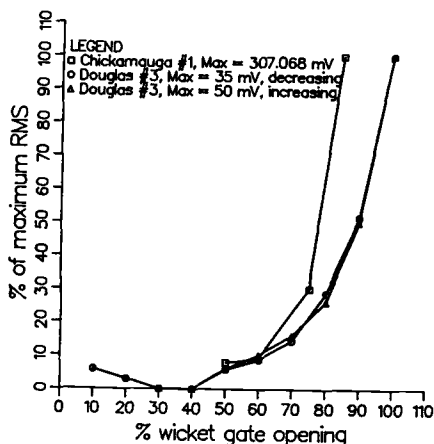


FIG. 14 - RMS output of the cavitation monitoring system vs. % wicket gate opening.

## CONCLUSIONS

Experiments have shown that consideration of cavitation as an AE source is feasible. Also it has been shown that cavitation intensity can be monitored using the RMS representation of an AE signal, as long as there are no attenuation effects caused by the form of the cavitation itself which could defeat this approach to monitoring. This possibility is suggested by the results of the cavitation jet erosion tests where the bubble

cloud that was increasing with cavitation level attenuated the signals considerably. It is clear that if the signal is detected directly from the cavitating surface then the RMS representation is an effective way of monitoring cavitation intensity.

A real-time cavitation monitoring system has been designed, built and tested. The system is inexpensive, versatile, and has shown reliability for long term operation. The system measures the  $V_{rms}$  value of an AE signal detected by the transducer and in the case of cavitation in hydroturbines it is shown to be proportional to the cavitation intensity [7]. However there is some caution in our conclusion because of the differences in cavitation location of different hydroturbine designs. Cavitation in a Kaplan-type hydroturbine is at the discharge ring (blade tip cavitation), which is directly related to the blade cavitation. This location is almost in contact with the draft tube liner where the AE transducer was located. Whereas in the case of a Francis-type hydroturbine, cavitation occurs within the vanes. This requires the cavitation signal to be transmitted through water and the cavitation bubble cloud to the draft tube liner (about 1.2 m in case of the Douglas hydroplant unit #3). This suggests that there could be a significant attenuation of cavitation signals, however the field tests have not confirmed this, see Fig. 14. One suggestion is that the field test results may have been provided with a clear signal transmission path because the attenuating bubble clouds were drawn toward the low pressure vortex in the center of the draft tube.

The results from this research have been successful, however they also suggest further study of cavitation levels using a RMS AE monitoring system in hydromachinery.

#### ACKNOWLEDGEMENT

This research was supported principally by Research and Development, Generation Projects Department of Tennessee Valley Authority, and in part by Center for Manufacturing Research and Technology Utilization of Tennessee Technological University.

#### REFERENCES

- [1] Lord Rayleigh, "On the Pressure Developed in a Liquid During the Collapse of a Spherical Cavity," Philosophical Magazine, Vol. 34, August 1917, pp. 94-98.
- [2] March, P. A., "A Cavitating Jet Facility for Cavitation Erosion Research," Proceedings of the International Symposium on Cavitation Test Facilities and Techniques, ASME Winter Annual Meeting, Boston, Massachusetts, December 1987.
- [3] Breckenridge, F. R., "Acoustic Emission Transducer Calibration by Means of the Seismic Surface Pulse," Journal of Acoustic Emission, Vol. 1, No. 2, April 1982, pp. 87-94.
- [4] Mellen, R. H., "Ultrasonic Spectrum of Cavitation Noise in Water," Journal of Acoustical Society of America, Vol. 26, May 1954, pp. 356-360.
- [5] Kling, C. L. and Hammitt, F. G., "A Photographic Study of Spark-Induced Cavitation Bubble Collapse," ASME Journal of Basic Engineering, Vol. 94, No. 4, December 1972, pp. 825-833.
- [6] Hirose, T., Tsuda, Y., and Kimoto, H., "An Experimental Study of the Model Microjet," Bulletin of Japanese Society of Mechanical Engineering, Vol. 26, No. 218, 1983, pp. 1340-1347.
- [7] Derakhshan, O., "Acoustic Emission Monitoring of Cavitation in Hydroturbines," M.Sc. thesis, Department of Mechanical Engineering, Tennessee Technological University, June 1989.
- [8] Jones, R. K., and March, P. A., "Application of Acoustic Emission for Real-Time Monitoring of Cavitation," Report No. WR28-4-900-234, Tennessee Valley Authority Engineering Laboratory, Norris, Tennessee, March 1989.

James Roget, Pascal Souquet, Marc Deschamps, Nayeb Gsib

## TOOL MONITORING BY ACOUSTIC EMISSION

---

REFERENCE : Roget, J., Souquet, P., Deschamps, M., and Gsib, N., "Tool Monitoring by Acoustic Emission", Acoustic Emission: Current Practice and Future Directions ASTM STP 1077, W. Sachse, J. Roget and K. Yamaguchi, Eds, American Society for Testing and Materials, Philadelphia, 1991.

ABSTRACT: Monitoring cutting tools is a strong need in automated un-manned production systems. However tool breakage detection should be separated from tool wear monitoring. The works presented in this paper show that Acoustic Emission (AE) can be used for detecting tool breakage in most conditions and an industrial system is available. Tool wear monitoring is much more complex. As demonstrated by some results in turning and milling, there are a great number of influencing parameters. It appears that AE has also capabilities for tool wear monitoring but no industrial system is presently available. Expert system or intelligent system such as Neural Networks using multiparameter appear to be the best solution for the future.

KEYWORDS: Acoustic emission, tool monitoring, tool breakage, tool wear, turning, milling.

In all industries, automation is developing very quickly aiming at improving production efficiency and quality. In modern workshops, an operator looks after several production units, therefore he should be replaced by monitoring systems able to detect any abnormal change in the process. In that way a particular attention should be paid to the state of the tool in cutting operations.

J. Roget directs the Test and Physical Measurements group of the CETIM, B.P. 67, 60304 SENLIS Cedex, France, P. Souquet and M. Deschamps are technicians in this group. N. Gsib is a graduate student preparing a doctorate.

Considering industrial requirements for tool monitoring CETIM initiated in 1983 a large study aiming at assisting engineering staff in the design, selection and implementation of automatic monitoring systems for machining operations. The various usable physical parameters were critically analyzed. [1]. In the same time, Acoustic emission (AE), because of the large experience of CETIM in this technique, has been extensively studied up to now.

In this paper, general consideration on tool monitoring will be presented. Then results of tool breakage detection and tool wear monitoring will be summarized and discussed under practical point of views. Future directions of developments will be pointed out.

#### GENERAL CONSIDERATIONS ON TOOL MONITORING

The aim of tool monitoring is to evaluate continuously the tool state, and various methods have been proposed in the literature. They can be separated in 2 groups [2]:

- direct techniques give a direct measurement of the cutting edge (crater depth, flank wear) such as optical techniques or contact measurement.
- indirect techniques measure any physical parameter changing when tool damages. Cutting forces, electrical power, acoustic emission are indirect techniques.

Direct techniques cannot normally be used for in-process monitoring while indirect techniques allow continuous on-line monitoring.

Concerning tool damage, 2 cases should be distinguished :

- *tool fracture* is a full destruction of the cutting edge. Typical causes of tool fracture are unsuitable cutting conditions, hard areas in workpiece, excessive wear ...

In any case, tool breakage is unexpected and of short duration. It can induce large damage in workpiece or in the machine itself, especially in roughing conditions when high powers are used. Consequently tool breakage must be detected instantaneously to allow safety actions to be taken. Only continuous and real time monitoring is suited.

- *tool wear* is a change in the cutting edge geometry. Several damaging processes are observed according to cutting conditions (figure 1). For well chosen conditions, tool wear is a slow phenomenon. Therefore direct and off-line measurements are acceptable and commonly used but they require time and do not consider cases of bad conditions resulting in incidental high wear rates. A continuous monitoring is preferable. It will be noted that a tool wear monitor can have a longer response time allowing more complex signal processing and decision algorithm than a tool breakage detector.

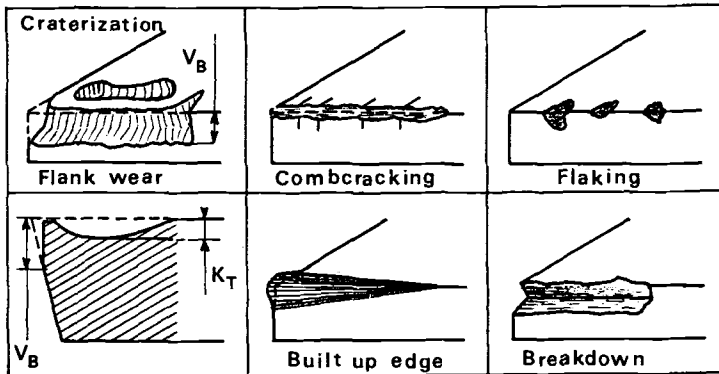


FIG. 1 -- Some typical damage of cutting tools

#### TOOL BREAKAGE DETECTION

##### Experimental Procedure

After preliminary tests aiming at optimizing sensor location and sensor type (frequency, bandwidth) systematic tests were performed in turning and in milling to analyze the AE behaviour associated with tool breakage and to identify the most efficient AE parameters. Analyses of all results allowed the design of a tool breakage monitor which was tested in very different conditions during laboratory tests (CETIM) and in workshops of various machine-tool manufacturers. Then an industrial system was developed in cooperation with an AE manufacturer.

##### Results of Preliminary Tests

Various sensor locations were tested [3]. In turning, sensors should be fixed on the tool holder or on the turret in preference to every other locations, even on the tool itself where low frequency noise and vibrations are very high.

In milling, spindle does not usually transmit AE waves., so sensors were systematically placed on the workpiece.

Resonance frequency will be preferably chosen higher than 300 KHz to ensure a good signal over noise ratio.

The best suited signal processing technique is RMS measurement (or equivalent measurement as average), with a medium integration time (200 ms). This parameter was systematically used during later tests.

##### Results of systematic Fracture Tests

In turning, shocks on carbide inserts allowed to produce reproducible tool fractures. Such a breakage creates high energy transient signals, easy to detect and to identify over the RMS time evolution curve as shown in figure 2.

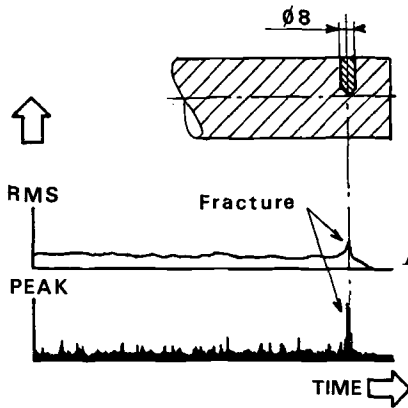


FIG 2 -- tool breakage on a hardpoint. - AE behaviour

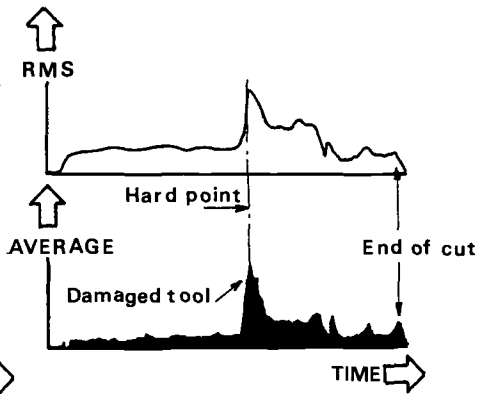


FIG 3 - - Milling of a hardened zone AE behaviour

The same result was obtained in milling (surfacing operation) with 1-tooth and 8-teeth milling cutters. Various cutting conditions from semi-finishing to gross roughing were tested and all breakages were detected in turning and in milling.

In a second phase, a tempered area instead of a carbide insert was used to cause tool fracture. As an example during a surfacing operation (figure 3), cutting the hardened area causes a high and sudden increase of AE. At the output of the hardened area, the tool is not broken but highly worn. The corresponding AE level is clearly higher than previously.

Unexpected breakages were also obtained during wear tests. They were due to an excessive wear (slump of the cutting edge) or to an overload of the machine tool in gross roughing. They were all detected.

Finally, AE appeared to be very sensitive to edge flaking or chipping. That could be a disadvantage, particularly in roughing, where small flakings affecting a very small part of the cutting edge are not considered detrimental. This detection could then be considered as a false indication.

These positive results allowed the design of a tool breakage detector.

#### Tool Breakage Detector

Such a detector ought to be applicable in the flexible environment as well as in mass-production. So it was decided to design a self-adapting system usable for finishing and roughing. No setting-up by the operator and no prior learning phase are needed. This system performs the functions of tool breakage detection (electronic response time is about a few milliseconds) and of tool touch detection. (usable by numerical control to define the initial conditions of the parts).

Connections with various numerical controls are easy to perform but the system is also usable on a manual or an automatic machine.

### Industrial Validation

In turning, many tests were carried out in industrial workshops on carbon steels, low-alloyed steels, cast iron, and very hard alloys (inconel). Cutting conditions ranged from finishing (chip cross section  $.15 \times 1 \text{ mm}^2$ ) to gross roughing (chip  $8 \times 1.25 \text{ mm}^2$ ).

Concerning sensor installation several cases were easily solved: vertical lathe with automatic tool-changer, horizontal lathe with a turret of 12 tools.

In drilling, the system was tested with drills ranging from .9 mm to 8 mm diameters. Figure 4 shows that it would have been possible to stop the machine 5 holes before breakage with a drill of 4 mm diameter, which is practically very important, for the workpiece is not scrapped.

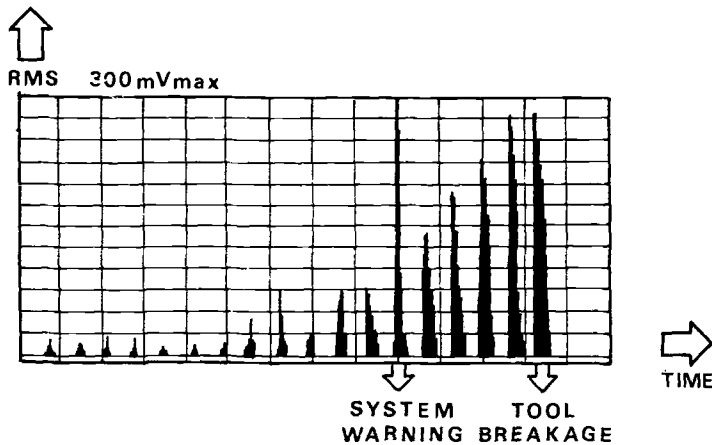


FIG. 4 -- Wear test in drilling - Detection of incipient tool breakage

Other tests were also performed in tapping and grooving. Table 1 summarizes the results.

Clearly the system is not of interest in tapping because the breakage is brittle and cannot be predicted. In case of breakage, the workpiece is no longer usable.

On grooving, spurious detections were very numerous and would not allow an industrial use of the system.

Very hard materials are another difficult case [4] because chip breakages can be confused with tool breakage.

TABLE 1 -- Summary of the results of the tool breakage monitor validation.

Diameter mm	Nr of Test	Nr of Rupture	Nr of Detection Before Fracture	Nr of detection at Fracture	Nr of No Detection	Nr of Spurious Detection	Tool nature
D R I L L I N G							
6	269	4	2	2	0	1	HSS *
4	305	3	3	0	0	0	HSS
2	458	3	0	3	0	0	HSS
0,9	14	2	0	2	0	0	HSS
T A P P I N G							
M 14	122	2	0	2	0	3	HSS
G R O O V I N G							
2 T	51	2	0	2	0	1	HSS
3 T	2	1	1	1	0	2	HSS
T U R N I N G							
0,5x0,15	1	1	0	1	0	0	** Carbide
0,25x0,15	2	2	0	2	0	0	ISO -7NMM
0,15x0,10	3	3	0	3	0	0	120 408
9 x 1,5 à 4 x 0,2	21	18	0	18	0	2	SNMM 250 405 415 P15

\* HSS : High Speed Steel

\*\* Tool reference according to ISO 3365/1

## TOOL WEAR MONITORING

### General Problem of Tool Wear Monitoring

Whereas the objectives of a tool breakage detection are very clear - To stop the operation to protect the machine and/or the workpiece - the objectives for tool wear monitoring are not well defined. Several questions can be asked:

- in practice, what are the criteria used by an operator to change the tool ?
- how to quantify tool wear ?

In fact, several criteria and several measurements are commonly used. According to the nature of the workpiece, its costs, and the habits of the operator, one of the following will be used:

- flank wear,
- dimensional margin of the workpiece,
- state of surface,

None of these criteria can be used in all cases.

Another problem is that the use limit of a tool will be very different in roughing (just before breakdown) and in finishing (roughness modified or dimension not good), which complicates the quest for a correlation between Acoustic Emission and tool wear limit.



### Experimental Procedures

Tests were carried out in turning and in milling (surfacing) on carbon steel (.48% C) and on an alloyed steel (34 CND 7 AFNOR). Finishing, semifinishing and roughing operations were investigated.

In roughing conditions, tool state was evaluated by means of Kt (crater depth), Vb (flank wear) and Ra (workpiece roughness). In finishing conditions, tool state was measured by Ra values.

AE equipment consisted of a damped piezoelectric transducer (center frequency 400 Khz) and of a system which delivered:

- cumulated number of hits  $\Sigma N_r$
- cumulated number of counts  $\Sigma N_c$
- maximum peak amplitude during a basic period of time Vc
- RMS value
- Average value
- Damped envelope

These parameters were plotted on a graphic recorder and digitized for storage and post-processing by a microcomputer. Post analysis consisted of an analysis of sliding statistical characteristics: mean value, 2nd order moment, 3rd order moment and 4th order moment, in the way described by Dornfeld [5].

Seven wear tests were carried out in turning, four in roughing conditions and 3 in finishing conditions.

Table 2 summarizes the tests performed in milling.

### Results in Turning

#### AE Behaviour in Roughing

During a wear test, AE goes through a maximum then decreases up to very low level values through other local and less high maxima. Simultaneously, fluctuations around the mean level show also a maximum and deeply decrease as shown on figure 5 by the evolution of the 1st order and 2nd Order moment of RMS.

The 1st higher maximum corresponds to the excessive wear as indicated by the operator :

Qualitatively, this behaviour was observed during all the roughing tests in turning. After a certain amount of wear, AE decreases in level and becomes more stable.

#### AE Behaviour in Finishing

State of roughness Ra was used for deciding to remove the tool. AE level does not show large evolution but fluctuations around mean level increases when the tool wears.

TABLE 2 -- Wear tests performed in milling

test NR	material	depth of cut mm	feed per tooth	cutting speed m/mn	number of teeth	type of operation	tool state parameter	number of cuts
1	XC 38	4	.3	250	8	rough.	VB	27
2	34CND7	4	.3	250	8	"	VB	8
3	34CND7	4	.3	250	8	"	VB	11
4	"	4	.3	250	8	"	VB	10
5	"	4	.3	250	8	"	VB	10
6	XC38	4	.3	250	8	"	VB	29
7	34CND7	.5	.2	250	6	finish	Ra	12
8	"	.5	.2	250	1	"	Ra	2
9	"	.5	.2	250	1	"	Ra	3

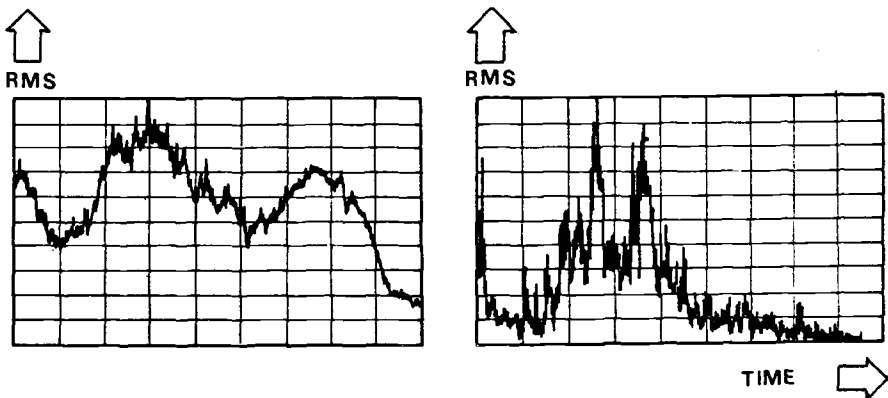


FIG. 5 -- Evolution of AE mean value and deviation during a test in turning with roughing conditions.

#### Discussion of Results in Turning

Results in turning were only preliminary results used for optimizing the choice and setting up of AE equipment before performing milling tests, which were more difficult to control.

With the cutting conditions chosen, the 2nd order moment of RMS value give a good qualitative indication of the tool state. This needs to be confirmed by modifying cutting conditions, materials and tools, which was not completed in this work as milling was the main objective.

Results in Milling (Surfacing Operation)Influence of Cutting Conditions

By analyzing the results of the performed tests it was possible to get an idea of the influence of some cutting parameters.

In that way,  $V_{rms}$  was found to be linearly correlated with the squared cutting velocity (figure 6) with the number of teeth and with the squared depth of penetration. Feed had no clear influence on AE level.

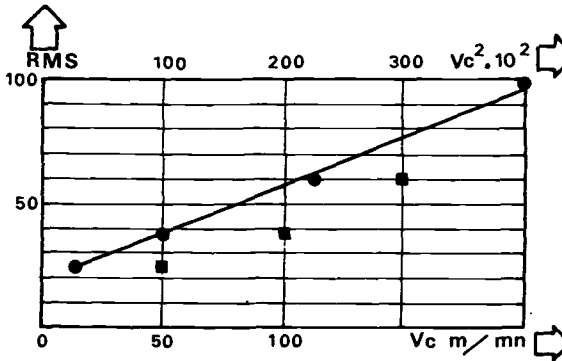


FIG.6 -- Influence of the cutting speed on the RMS value of acoustic emission in surfacing

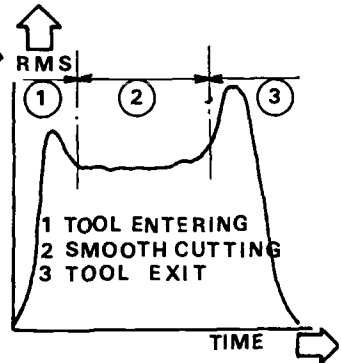


FIG.7--Typical AE behaviour during a cut in milling.

Wear Tests in Roughing Conditions

Each cut carried out in normal conditions can be divided in 3 stages (figure 7).

- the entering of the milling cutter in the workpiece.
- a smooth cutting phase.
- the going out of the tool from the workpiece.

Usually the first cuts are disturbed and these 3 stages are not well defined, but after one or two cuts, this behaviour becomes very clear. When the tool becomes worn AE fluctuates (local maximum) or increases during the phase 2 as shown in figure 8. It can be seen that the change in AE behaviour is clearly correlated with a jump in the flank wear (cut 9). A jump in electrical power was observed during cut 10.

This behaviour was reproducible in roughing. In later experiments, a special force transducer was interposed between table and workpiece specially designed with a high stiffness. This transducer gives the 2 force components (parallel and orthogonal to

feeding direction). A finer correlation can have been studied between tool state and AE behaviour and confirmed the previous results.

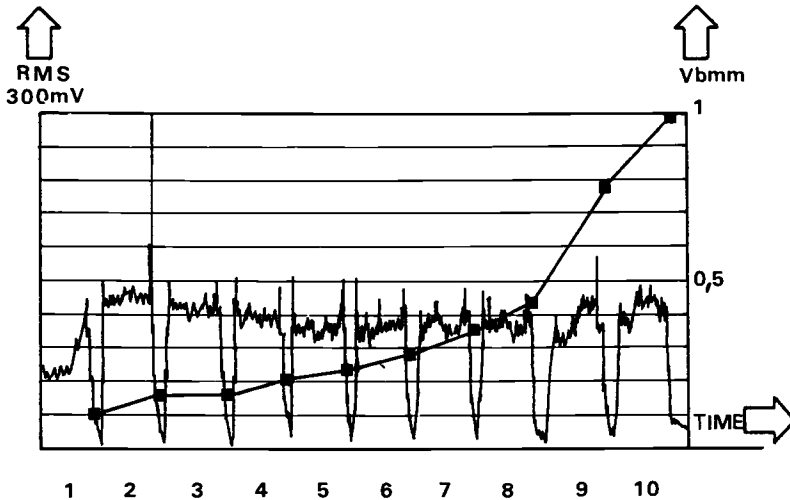


FIG.8 -- Evolution of AE RMS and Vb during successive cuts in surfacing (roughing conditions)

#### Wear Tests in Finishing Conditions

In the studied conditions, a continuous increase of AE RMS was observed, clearly correlated with the workpiece roughness ( $R_a$ ) ( $R_a$  is measured over 4mm in the feed direction) (see figure 9). In this case, the electrical power is non significant as only a small fraction of the machine power is used.

During a test, a scratch was created and clearly detected (figure 10) but AE showed that a previous phenomenon took place resulting in the scratch.

#### CONCLUDING DISCUSSION

Our works, as others previously published, clearly separate tool breakage detection and tool wear monitoring.

Tool breakage detection is possible in most of current conditions. Industrial systems such as that one we developed are available. They can differ by their easiness to be integrated and also their need for a preliminary learning phase. In our case we looked for an automated system requiring very few adjustments from the operator and no learning phase. This objective has been reached. However some problems can be met with very hard materials (inconel) where false detections are encountered due to chip breakage. Some investigations are in-progress on this point.

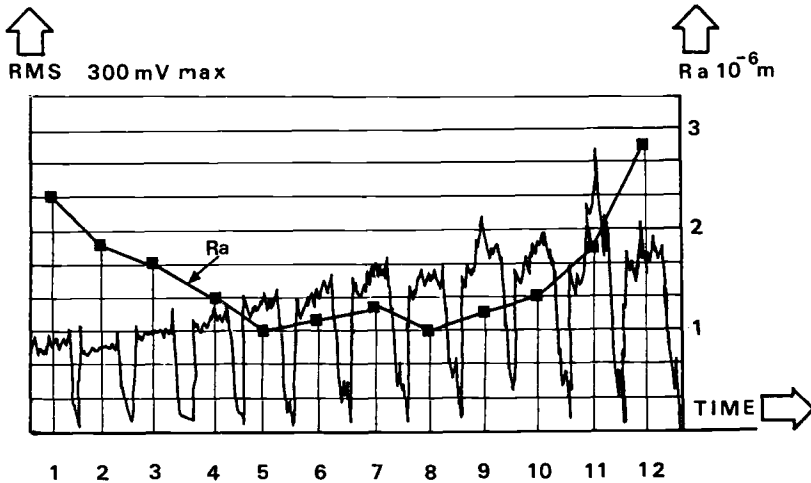


FIG 9 -- Evolution of AE RMS and Ra during successive cuts in surfacing (finishing condition)

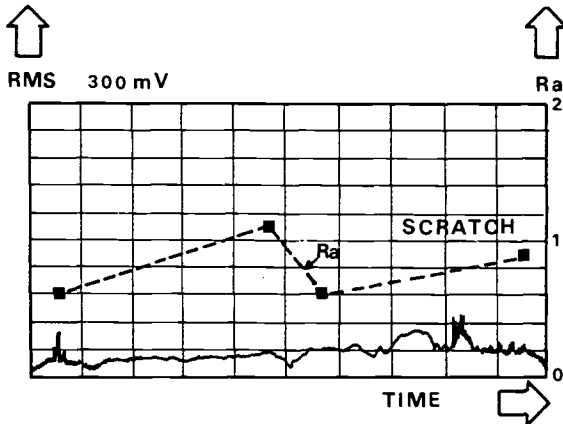


FIG 10.-- Detection of a scratch by A.E.

The main problem for installing an AE monitor remains the location of the transducer. In turning, typical cases such as horizontal lathe or vertical lathe can have been solved.

But presently for milling and centers of machining, no general solution can be given. Very often spindle does not transmit AE waves so the transducer should be placed on the workpiece or a special transducer with a rotating coupling as described by Blum et al. [6] has to be used.

Concerning tool wear monitoring, all the investigators found that AE gives information on tool wear progress. However no general relationships between an AE parameter and a significant wear measurement is presently available. At this time, only experimental

or partial relationship have been proposed and it remains difficult to correlate results coming from different investigators when cutting conditions are modified. A lot of parameters are needed for characterizing a cutting operations:

- cutting conditions (depth of cut, feed, cutting speed)
- workpiece and tool materials
- cutting and characteristics
- workpiece geometry
- lubrication ...

The problem of tool wear monitoring is then very complex, which explains that existing monitors, using force or power, need training phases for adjusting parameters. They are well-suited for mass-production but very heavy to use in flexible cells.

Moreover we think, as others, that it is not possible to monitor all the operations with only one parameter. For us, future systems will simultaneously combine several parameters such as force, power, temperature, acoustic emission ... and will choose criteria and their decision strategy according to cutting conditions. Expert systems or intelligent system such as neural networks could be a suitable solution for this sensor fusion [7].

Our present investigations go into 2 directions:

- accumulating experimental data in various cutting conditions
- developing an expert system analyzing several parameters.

This project is supported by the Commission of the European Communities (Brite Program) and associate 8 european partners.

#### REFERENCES

- [1] Tanguy, J.C., "Les Moniteurs de Surveillance de l'Usinage à l'Epreuve des Ateliers de Production", in Surveillance automatique de l'usinage, solutions et applications industrielles, CETIM, France, 1987.
- [2] Sampath, A., and Vajpayee, S., "Tool Health Monitoring Using Acoustic Emission", International Journal of Production Research, Vol 25, N°5, 1987, pp. 703-719.
- [3] Roget, J. Souquet, P., and Gsib N., "Use of Acoustic Emission for In-Process Monitoring of Tool During Turning and Milling", Progress in A.E. III, The Japanese Society of NDI, 1986, pp. 94-101.
- [4] Jarnet, J.P., and Pontier, J.M., "Système de Détection de Bris d'Outil interprétant l'Emission Acoustique", Le décolletage Nr. 86, April 1989, pp. 59-60.
- [5] Dornfeld, D.A., and Kannatey-Asibu, E., "A Study of Tool Wear Using Statistical Analysis of Metal Cutting Acoustic Emission", Wear, Nr. 76, 1982, pp. 247-261.
- [6] Blum, T., Suzuki, I., Inasaki, I., "AE Monitoring Systems for the Detection of Single Point and Multipoint Cutting Tool Failures", Journal of Acoustic Emission, Vol 7, Nr.4, 1988, pp. 179-184.
- [7] Agogino, A., M., Scrinivas, S., and Schneider, K., M., "Multiple Sensor Expert System for Diagnostic Reasoning, Monitoring and Control of Mechanical Systems", Mechanical systems and signal processing, Vol 2, Nr2, 1988, 2, pp. 165-185.

David A. Dornfeld

## MONITORING OF THE MACHINING PROCESS BY MEANS OF ACOUSTIC EMISSION SENSORS

---

REFERENCE: Dornfeld, D. A., "Monitoring the Machining Process by Means of Acoustic Emission Sensors," *Acoustic Emission: Current Practice and Future Directions*, ASTM STP 1077, W. Sachse, J. Roget, and K. Yamaguchi, Eds., American Society for Testing and Materials, Philadelphia, 1991.

ABSTRACT: Research over the last several years has established the effectiveness of acoustic emission (AE) based sensing methodologies for machine condition analysis and process monitoring. Acoustic emission has been proposed and evaluated for a variety of sensing tasks as well as for use as a technique for quantitative studies of manufacturing processes. This paper discusses some of the motivations and requirements for sensing in automated or untended machining processes as well as reviews the research on acoustic emission (AE) sensing of tool condition (wear and fracture) in machining. The background for AE generation in metal cutting and its relationship to the condition of the cutting tool for single and multiple point tools (turning and milling) is presented. Research results will be summarized relating to the sensitivity of AE signals to process changes, AE signal sensitivity to tool condition in turning and milling for wear and fracture, AE signal processing methodologies for feature extraction including time series modeling to remove influences of machining conditions on wear tracking and AE sensor fusion using neural networks for process monitoring with several sensors.

KEYWORDS: machining, sensors, tool wear, fracture, acoustic emission

### INTRODUCTION

The requirements for advanced sensing systems for monitoring manufacturing processes are driven by the changes in manufacturing systems, Goldhar and Burnham [1], including:

- consistent high quality is a required output of a productive, cost-effective system, and

Dr. Dornfeld is Professor of Mechanical Engineering and Director, Engineering Systems Research Center in the College of Engineering at the University of California, Berkeley, CA 94720.

- increasing complexity and technical sophistication of many products requires comparable increases in capabilities of manufacturing techniques and complexity of manufacturing systems.

In general these systems are comprised of three basic components determined, in part, from the mapping of the actions and capabilities of the human worker into the automated system, Okada [2]. These components are, first, information collection done by the human with the physical senses and performed in the automated system by sensors; second, experience and knowledge of the human gained from years of work at the task represented in the automated system by controllers, process models, data bases, etc. or, more recently, expert systems; and third, manipulation by the worker of the machinery and work to accomplish the task required by the worker's understanding of what is required as observed by his or her senses. This last component is represented in the automated system by actuators controlled by the machine controller or, perhaps, new processes altogether. It is clear that in some instances the human worker possesses much greater abilities to recognize the state of the process from the sensed data and suggest any appropriate action needed. However, it is also clear that the human worker has many limitations that can be overcome by appropriate hardware and software. The focus of this paper is on the sensor functions in the manufacturing systems, and, specifically, the use of acoustic emission (AE) sensors for monitoring the machining process.

Achieving untended manufacturing has been described as perhaps "the biggest obstacle" to the development of computer integrated manufacturing or, on the smaller scale, flexible manufacturing systems [3]. Sensors function to collect information for the evaluation of the performance for the system and its consistency with analytical predictions. Further, sensors also play an important role in the diagnostic capabilities of systems and methodologies for predictive maintenance. The Machine Tool Task Force Study [4] identified the lack of reliable, rugged sensors as a main stumbling block to the real time control and monitoring of manufacturing systems. Sensors must operate in often hostile environments and existing sensors are either limited in accuracy, reliability, range or response or are inappropriate for some of the phenomena under observation. An excellent review of sensors for untended machining operations can be found in [5,6]. A recent survey by Iwata [7] reviews the needs identified by machine tool builders for improving the machine performance.

It is important to insure that sensing methodologies that are applied to process monitoring yield data that can be quantitatively related to the process being investigated or monitored. This is often not the case and the result is limitedly reliable sensor data. Here the word reliable is used in the sense of the *dependency* of the data on the basic process parameters as well as the *repeatability* of performance of the sensor in real environments. A sensing technique which has application in data collection for process modeling and analysis as well as real time monitoring is most desirable.

The interest in developing the capability for untended manufacturing systems is growing along with the implementation of advanced flexible manufacturing systems. To remove the need for observation of the manufacturing processes and minimize the time lost due to repair or correction of unexpected failures in the system new sensing methodologies and sensor-based control schemes are being proposed and evaluated. Clearly, one of the major roadblocks to implementation of true untended manufacturing is the lack of suitable sensors for process monitoring. In spite of many sensing technologies in existence today, few, if any, totally untended operations exist.

The sensing tasks for untended manufacturing operations are substantial. In addition to being economical, sensors must be nonintrusive, rugged and resistive to the hazardous environment in which they operate, accurate, exhibit a high sensitivity



to the feature or phenomena being monitored, have an output that is linear (or linearizable) with respect to the sensed feature if possible, and highly repeatable and reliable. It is also desirable to have sensors that have diagnostic capabilities as well as are self-calibrating. Few sensors can meet all of these specifications.

It seems most reasonable that, to be effective in untended manufacturing, combinations of sensors will be needed to provide corroborative information on the state of the manufacturing operation. This often includes integration with other sensors and the co-processing of data from several basic different sources since one sensor alone may be unable to adequately determine the process state. This will require efficient methodologies for integration of sensor information. Easily available information on the operation of the process (such as speeds, feeds, etc. in machining) will need to be considered as well. Some early efforts by Matsushima and Sata [7] have demonstrated the potential of combining information from several sources in process monitoring. Others are mentioned here.

### ACOUSTIC EMISSION FROM METAL CUTTING

Research over the past several years has established the effectiveness of AE based sensing methodologies for machine tool condition monitoring and process analysis. The problems of detecting tool wear and fracture of single point turning tools motivated much of this early work. In addition, the sensitivity of the AE signal to the various contact areas and deformation regions in the cutting and chip formation process has led to the analysis of AE signals as a basic tool for analysis of the cut ting process.

Investigations of AE from the metal cutting process have often been limited to two-dimensional or orthogonal machining because of the simplicity of the geometry and chip flow. In the orthogonal machining configuration the cutting edge of the tool is normal to the direction of the tool motion, chip flow is up the rake face of the tool with no side flow and the uncut chip thickness ahead of the tool corresponds to the feed increment. In this configuration we can define three primary areas of interest with respect to the generation of the AE signal. These are in the primary deformation zone ahead of the tool where the initial shearing occurs during chip formation, the secondary deformation zone along the chip-tool rake face interface where sliding and bulk deformation occurs, and the tertiary zone along the tool flank-work surface interface, Figure 1. In addition, there is a fourth area of interest, that associated with the fracture of chips during formation of discontinuous chips. If we are studying the milling process (or other processes with interrupted cutting) an additional source of AE is the impact of the tools on the workpiece and the noise due to swarf motion on the work. A summary of acoustic emission sources, transmission characteristics and signal processing is shown in Figure 2, after Moriawaki [27].

A basic model for the generation of AE during machining (in this case primary and secondary shear generated AE in orthogonal machining) was proposed and evaluated by Dornfeld and Kannatey-Asibu [9-11]. The formulation of the model is based on the simplified Ernst and Merchant model of orthogonal machining and builds a dependency of AE energy on material properties such as flow stress, volume of material undergoing deformation and the strain rate. The generation of AE was derived from the portion of the applied energy that results in plastic deformation. Hence, a strong dependency on cutting speed (influences strain rate), depth of cut and feed rate (both influencing volume of material undergoing deformation) was seen. This model was reasonably successful in predicting the energy (RMS) of the AE signal during orthogonal machining due to speed variations but did not accurately predict the influence of feed and depth of cut variations. Tests by Pan and Dornfeld [12] of diamond machining of a variety of materials indicated better correlation between the model predicted values and experimental results. This is due in some sense to the reduced contact area at the tool flank, the more sharply defined cutting edge, and reduced friction on the rake face with diamond machining. Lan

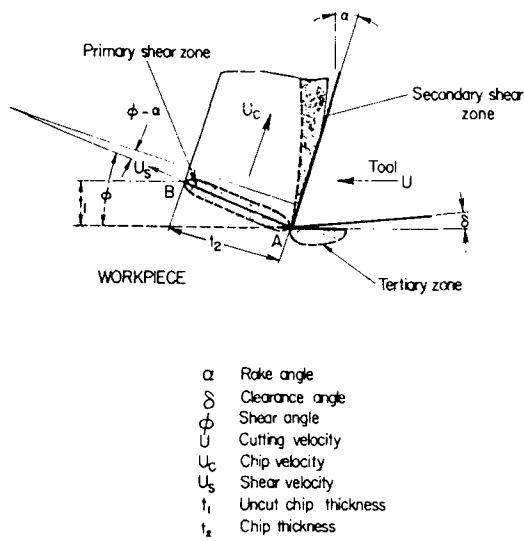


Figure 1. Zones of AE generation in machining.

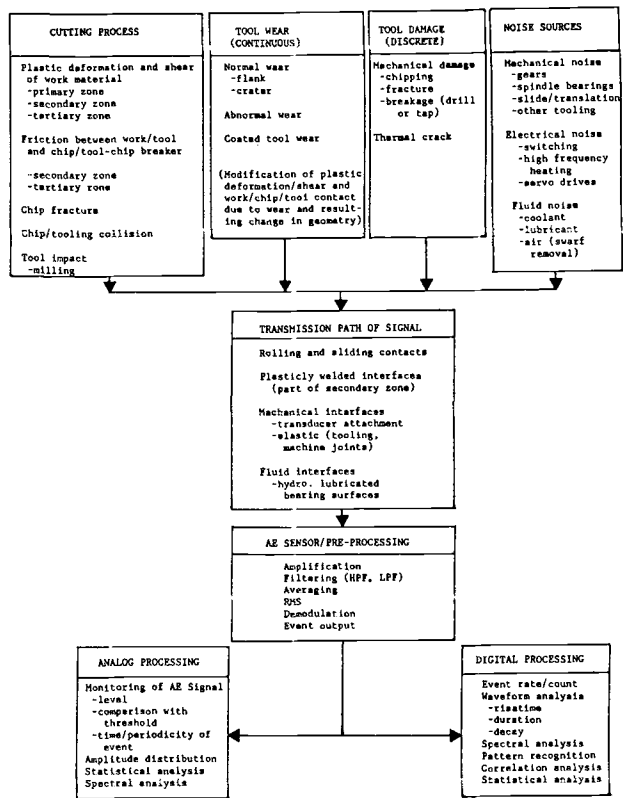


Figure 2. Sources, transmission, and processing of acoustic emission signals in machining, after Moriwaki [29].

and Dornfeld [13] modified the basic model to include the contribution due to flank contact and to include relative attenuation of the signal from the sources in the process.

Additional studies have focussed on AE generated during machining based on experimental observations. Lan and Naerheim [14-15] have investigated the effect on the AE generated of changes in machining conditions and the influence of lubrication with differing materials. Schmenk [16] suggested the use of metal removal rate to normalize the AE energy measured during machining to reduce sensitivity to process parameters. Diei and Dornfeld studied the AE generated during face milling operations with form and insert tooling [17]. Teti and Dornfeld [18] reviewed the past research on AE from metal cutting based on both signal energy and current/count rate techniques.

### TOOL CONDITION MONITORING

Acoustic information has been associated with the state of the cutting tool for many years. Experienced machinists can detect a change in the cutting condition or tool state from the sound of the machining process. This was reported as early as 1969 by Weller, et al [19] related to tool wear. Acoustic emission, typically defined to be in the frequency range above that described by Weller, was first associated with machine tool applications in the 1970's. The utilization of AE signals for monitoring the machining process has been most extensively researched for tool fracture detection and tool wear monitoring.

Iwata and Moriwaki [20-21] studied the sensitivity of the AE RMS energy to progressive tool flank wear and observed a dramatic increase in energy as the wear land increased, Figure 3, as well as an increase in the AE event counts per cut with wear. Investigations of tool fracture in single point tooling were conducted by Kakino [22-23] (who also studied milling), Kaneeda and Tsuwa [24], Iwata and Moriwaki [25], Miwa, Inasaki and Yonetsu [26-27], and Moriwaki [28-29]. The effectiveness of detecting tool fracture and, in some cases, chipping [30] was demonstrated in these investigations.

Kannatey-Asibu and Dornfeld [31] applied statistical analysis techniques to the AE RMS energy recorded during progressive tool wear to attempt to minimize the sensitivity of the signal on process parameters (speed, initially, and then the influence of chip formation and crater wear) for flank wear tracking. Lan and Dornfeld [32] studied the flank and crater wear influence on AE measured during machining with insert single point tooling. Blum, Suzuki and Inasaki [33] use the amplitude distribution of the enveloped AE signal at low frequencies to detect tool wear for insert tooling. The fracture of single point insert tooling and the influence of the fracture area on the insert on the spike in AE RMS energy detected was documented by Lan and Dornfeld [34] and Kakino, et al [30]. This work, together with the studies on the wear and fracture of inserts during machining with multi-insert milling cutters by Diei and Dornfeld [35, 36] lead to development of a model for tool fracture generated AE dependent upon the surface area of the fracture, the stress on the tool at fracture and tool material properties. This model was verified by data from turning (data from Lan and Dornfeld [34] and Moriwaki [28] for interrupted cutting) and milling, Figure 4. The offset seen in Figure 4 between the data of Moriwaki and the Berkeley data is most likely due to differences in detection sensitivity.

More recently, attention has been directed at improved transducers and coupling techniques for in-process sensing. Ramalingam, et al, have developed and evaluated a thin film AE-sensitive deposited layer directly on an insert for AE and tool vibration monitoring during turning and milling [37, 38]. Inasaki, et al, [39] have developed a mounting technique for AE monitoring of multipoint tools and Yu and Hutton [40] evaluated a liquid coupling technique for transmitting the AE signal from a rotating spindle of a milling machine.

The sections that follow describe the results of research at the University of California at Berkeley on tool condition monitoring using acoustic emission (fracture

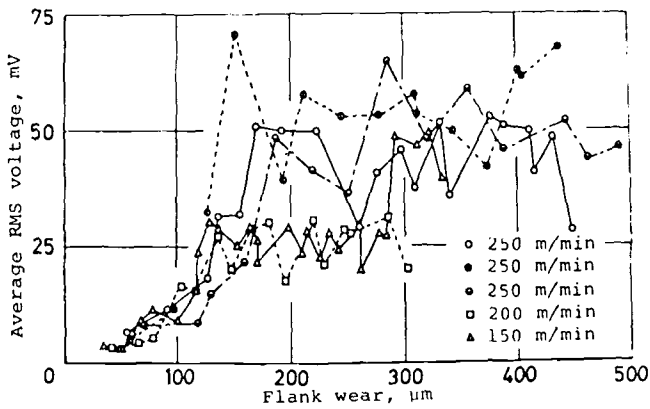


Figure 3. Average AE RMS voltage vs. flank wear, from Iwata and Moriwaki [20].

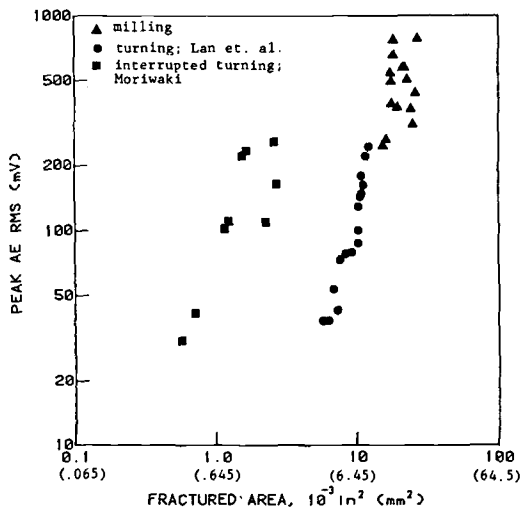


Figure 4. Peak AE RMS voltage as a function of area of the fractured surface of the insert, from Diei and Dornfeld [36].

detection for milling cutters), signal processing methodologies for minimization of the influences of machining conditions and sensor fusion for AE and force data using neural networks.

## INSERT FRACTURE DETECTION DURING MILLING

### Acoustic Emission from Milling

In milling (rotating multiple toothed cutters) the cutting process is discontinuous with varying chip load and relative rubbing generated noise. Thus the basic AE signal due to the material deformation inherent in chip formation and chip/tool contact is complicated by these other sources of noise and the periodic interruptions of the cutting process. This is in contrast to the relatively "stationary" single point turning generated AE. In both cases tool work velocity and metal removal rate are significant parameters affecting the energy of the AE signal.

Because of the geometry of tool-work interaction, there are additional variations in the AE generated, mainly resulting from chip thickness and tool velocity changes as the tool rotates through the work material. If tool deterioration (wear) or catastrophic failure (fracture) occurs the AE signal during cutting is either modified, or, in the case of fracture, exhibits a dramatic spike from the energy released at fracture.

Tests were conducted over a range of conditions on a vertical milling machine using a Kennametal KISR-3-CP4-0 milling cutter, with grade K420 inserts machining AISI 1018 steel. Figure 5 illustrates the geometry of the test setup and Figure 6 shows a schematic of the instrumentation. A signal processing technique based on time difference averaging (TDA) was developed to overcome the difficulties of analyzing the AE signal from milling due to strong periodic components and noise [35].

A typical AE root mean square energy (RMS) signal from a flycutting operation is shown in Figure 7. The TDA methodology decomposes a compound repetitive signal into a periodic component that is time locked to the basic signal period and a residual. The output of a TDA analysis of AE during fly cutting, including mean and residual, is shown in Fig. 8. Here the magnitude of the AE RMS is plotted as a function of rotation of the milling cutter. The initial AE peak due to tool contact, and final peak due to tool exit and chip breakoff is clearly seen. The chip formation related acoustic emission is seen at the center of the active region. The residuals from the sampled data indicate the degree of "randomness" in the signal due to variations in entry and exit as well as noise due to chip conjection.

### Fracture Detection

A primary objective was to evaluate the sensitivity of the AE signal to insert fracture and chipping during single and multi-toothed face milling. A theoretical analysis of the AE spike generated at fracture had indicated that the AE was dependent primarily on the area of fractured surface, as well as material geometry constants [36]. This was also observed by Kakino [30] and Moriwaki [29].

To assess the sensitivity of AE to insert fracture during realistic machining operations a series of tests were conducted. These tests included both single and multiple insert milling operations on hardened steel (AISI 4340, 40 R<sub>c</sub>) for a "natural" fracture of AISI 1018 with notched inserts for "artificially induced" fracture as in [34]. Figure 9 shows the response of feed force and RMS AE signal to the fracture of the insert in fly cutting under the following conditions: velocity, 262 sfm (1.33 m/s), feed = 0.105 ipr (2.67 mm/rev) and axial depth of cut = 0.08 in. (2.03 mm). The dramatic change in the level of both force and acoustic emission RMS at fracture is evident.

Although the presence of additional cutting inserts complicates the process, as seen in Fig. 10, the fracture event is clearly distinguished above the background level of cutting generated AE. A similar response is seen in the force data.

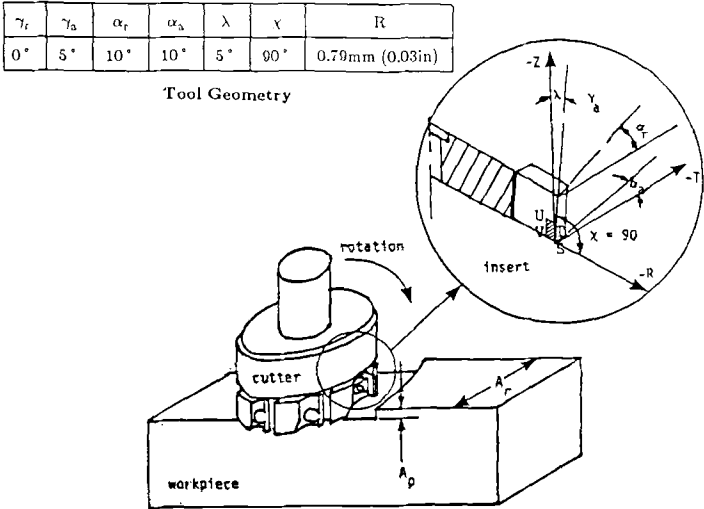


Figure 5. Flycutting with a single tooth of a multi-tooth cutter.

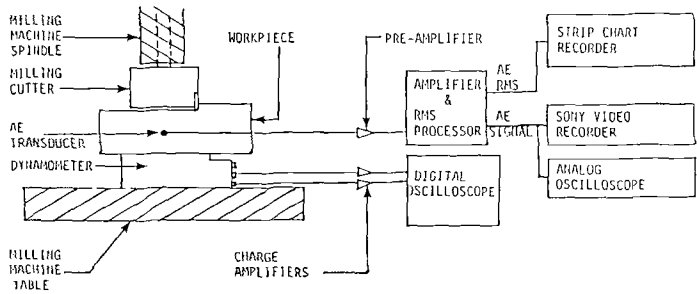


Figure 6. AE/force data acquisition setup.

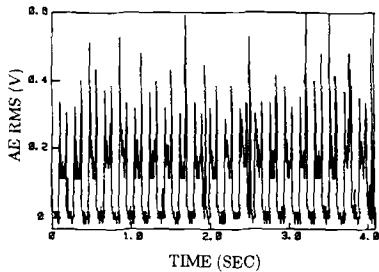


Figure 7. Typical AE RMS signals from flycutting, from [35].

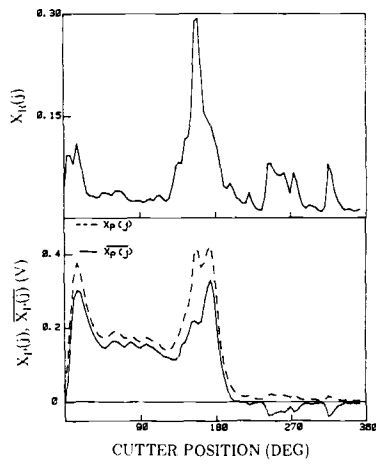


Figure 8. Outputs of TDA and variance analysis routine of the AE RMS signal for flycutting showing a sample signal  $X_p(j)$ , mean  $X_p(j)$ , and residual analysis  $X_R(j)$ , from [35].

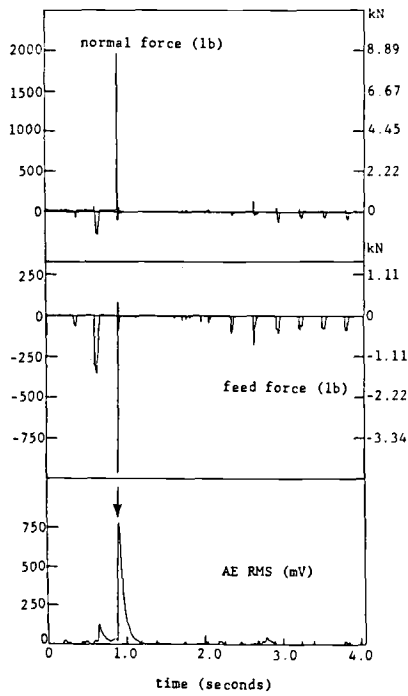


Figure 9. The response of cutting forces and RMS AE signal to large fracture of insert tool, arrow indicates location of fracture, from [36].

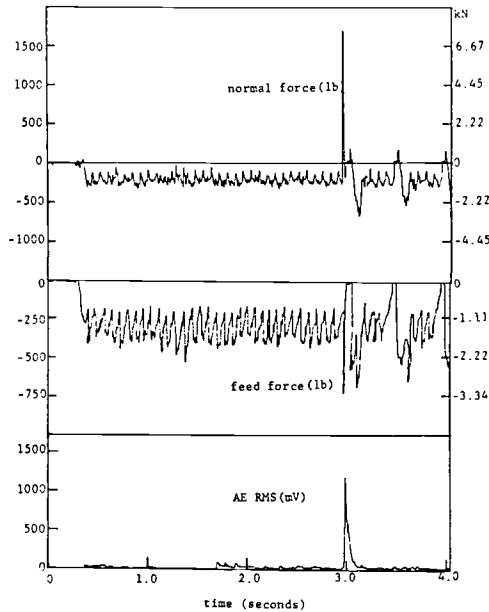


Figure 10. Typical response of cutting forces and RMS AE signal to tool fracture in multi-tooth cutting with 6 inserts, from [36].

Conditions for this test were: 97 sfm (.493 m/s), feed = 0.027 ipr/tooth (0.686 mm/rev/tooth), and axial depth of cut = 0.040 in. (1.016 mm).

The AE signal analysis was based on the peak value of the AE RMS voltage produced at fracture. The fractured area was measured from an SEM photograph of the insert using a planimeter. This fracture generated AE data was seen previously as Figure 4. As expected, the higher the fracture energy, reflected in the force at fracture, the more AE energy observed.

#### ADAPTIVE TIME SERIES MODELS OF AE SIGNALS FOR WEAR DETECTION

The success of many attempts at tracking progressive tool wear using AE RMS have been limited by the strong dependency of the average RMS on the cutting conditions or changes in material deformation and tool/work contact due to advanced crater wear. Kannatey-Asibu and Dornfeld proposed statistical analysis (skew and kurtosis) of the AE RMS to obtain additional indicators of the tool condition [31]. With the objective of removing the sensitivity of the AE signal to process parameters (feed, speed, and depth of cut) so that the tool wear-related signal components can be reliably determined, a time series analysis technique was also used to characterize the AE root mean square (RMS) energy signal from single point turning with an autoregressive model [41]. The model parameters are constantly updated according to the RMS signal dynamics which are strongly dependent upon the AE source mechanism. The stochastic gradient algorithm approach is utilized here for modeling thus no prior knowledge of the signal's statistical properties are needed. The modeling algorithm is adaptive in the sense that the parameters are updated every time step. These features make the approach well suited to real-time applications.



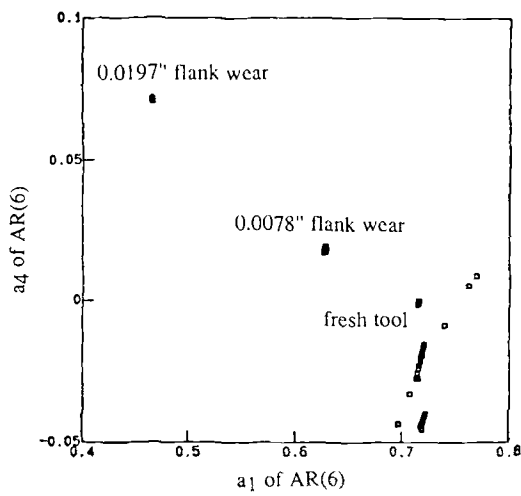


Figure 11. Parameter plane of the first and fourth parameters of AR(6) model of AE RMS, from [41].

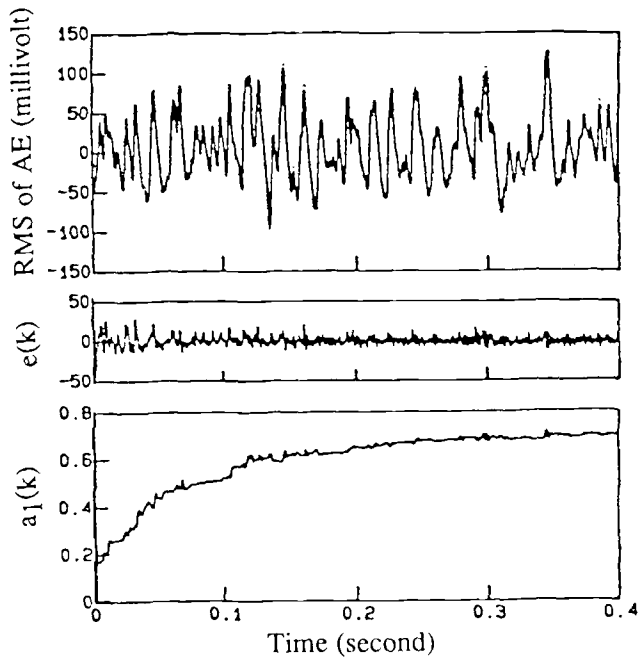


Figure 12. RMS AE signal; top, solid line is measured signal and dots are model predicted values; middle, error signal between measured and predicted; bottom, adaptation of first model parameter of AR(6) model, from [41].

A series of experiments were conducted to evaluate the feasibility of the modeling technique to real-time tracking of tool flank wear during the machining of medium carbon steel with carbide insert tooling. Machining conditions covered the following ranges: speed 2.12-2.66 m/s; feed rate 0.127-0.203 mm/rev; depth of cut 0.508-0.762 mm. The success of the approach is illustrated in Figure 11. For a sixth order autoregressive model, the separation of the various states of tool wear, from the fresh tool to heavy flank wear, is clearly seen when plotting the magnitude of the fourth model parameter as a function of the size and separation of wear effects.

The model adapts to the AE RMS signal rapidly (time constant < 150 ms for the first model parameter) at the start of each cut. Figure 12 illustrates, for one test, a comparison between the measured RMS and model-predicted signal, top, the error (measured-predicted), middle, and the adaptation of the first model parameter showing the successful tracking of the model parameter, bottom.

## INTEGRATION OF SENSORS VIA NEURAL NETWORKS FOR WEAR DETECTION

It is unlikely that any one sensing methodology will be able to adequately monitor all the necessary aspects of a process. Further, it may be advantageous to use several sensors so that the reliability or performance of the sensor system can be guaranteed at a high level. Thus, it is necessary to develop methods that can efficiently integrate information from several sensors at a fast enough rate to be used in real time control. This is often referred to as sensor fusion and one of the most promising architectures for this integration is a neural network.

In the artificial intelligence context, a neural network is a parallel processing architecture in which a large number of processors are interconnected and the knowledge is represented by the strength of the interconnections between the processors. The connection strengths are achieved through a learning process. The knowledge is usually distributed over a large number of connections so that the operation of these networks degrades gracefully if part of the connections are destroyed due to malfunction. Neural network structures are able to make decisions based upon incomplete or noisy information, a characteristic which is advantageous in performance of the diagnostic function in a manufacturing environment. Finally, since the knowledge is stored in the connection strengths of the network it can be brought to bear almost instantaneously, making such systems attractive from a real time implementation point of view. The typical structure of a feedforward neural net, such as that used in this research, is shown in Figure 13.

As used here, neural nets perform recognition tasks through a process of pattern association. That is, they are able to associate input patterns (in this case, patterns of sensor signals) with output patterns (decisions on the tool wear level). Neural nets develop knowledge based on the training samples presented to them. The knowledge is stored in the connection strengths of the network and is used directly in the pattern recognition task. This obviates the requirement for searching for patterns in a separate knowledge base and results in pattern recognition systems that are practical in a real time environment.

The difficulty of extracting tool wear state information from the AE signal, as discussed in the previous section, was motivation for the application of neural networks [42]. In addition, as documented by many researchers, the tool force information is helpful in determining the state of tool wear but, very often, suffers from the same limitations as the AE information - the difficulty of determining wear related characteristics of the signal from those due to variation in machining conditions, work material properties or work geometry. It may be advantageous to integrate information from several sensors in such a way that the best features of all the sensors are utilized. Multisensor schemes would also be more robust against sensor drift and failure in the harsh manufacturing environment.

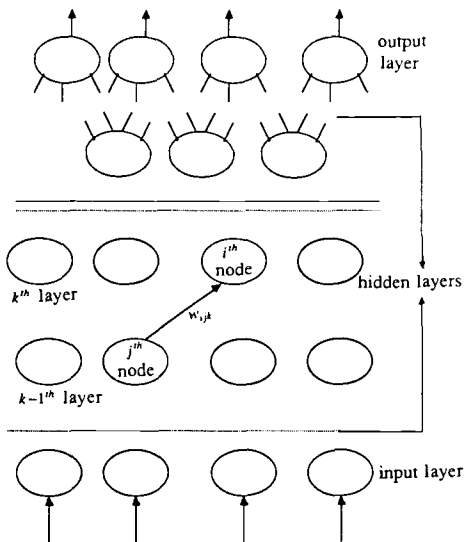


Figure 13. Typical structure of a feedforward neural network, from [42].

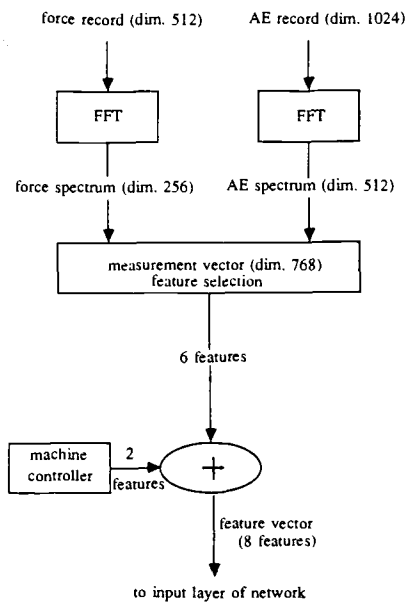


Figure 14. Signal processing flow diagram, from [42].

The research work reviewed here demonstrates how tool force and metal cutting acoustic emission information along with process information can be used successfully to make decisions about the state of tool wear in a turning operation. The different information sources (selected frequency bands in the AE and cutting force signals, along with process conditions) are integrated via a neural net structure. Figure 14 illustrates the signal processing flow diagram feeding the network.

The results of the research indicated that pattern classifying systems which utilize information from several sources show superior performance by combining the best features from these sources. Successful classification rates as high as 95% were obtained and, depending upon the training patterns used, the network was able to correctly classify the actual tool wear levels for all samples which could be correctly classified as being either worn or fresh. Some confusion in the AE signal was caused by chip breaking. However, since the force signal is not very sensitive to chip breaking, inclusion of the force features in the input vector to the net tends to reduce the misclassification of the fresh tool state (for which the influence of chip breaking on AE is most noticeable.) Present research is aimed at extending the range of performance of these networks. Recently, coefficients of the AR models, such as those described in Section 5 above, of AE and tool force signals have been used as input to the neural network. Techniques for monitoring sensor degradation and damage and information retrieval in the case of sensor failure are also being developed.

## SUMMARY

This objective of this paper was to review research on AE sensing of metal cutting and to provide some detail on the research activities ongoing at the University of California at Berkeley. The research to date has shown the tremendous potential for utilization of acoustic emission information for both process monitoring as well as process investigation. Challenges to be met include developing a better understanding of the basic AE generation mechanisms in metal cutting, advanced signal processing methodologies to further extract significant process-related information from the AE while maintaining high insensitivity to system noise and process environmental changes, and methodologies to incorporate the AE information with other sensor outputs to better characterize the state of the manufacturing process. All of the challenges can be met and, at the same time, make the goal of untended manufacturing processes realizable.

## ACKNOWLEDGMENTS

Research on acoustic emission sensing of manufacturing processes at the University of California at Berkeley has been supported by grants from the National Science Foundation, National Institute of Standards and Technology, IBM, Omron Tateisi, Inc., and a consortium of industries supporting the Laboratory for Manufacturing Automation in the Mechanical Engineering Department at Berkeley. Kennametal, Inc. has donated tooling for use with this research.

## REFERENCES

- [1] Goldhar, J.D. and Burnham, D. C., "Changing Concepts of the Manufacturing System," *Proceedings of the U.S. Leadership in Manufacturing Symposium*, National Academy of Engineers, National Academy Press, Washington, D.C., 1983, pp. 99-103.
- [2] Okada, A., "Automation in Arc Welding-State of the Art and Problems," *Journal of the Japan Society of Mechanical Engineers*, March, 1979 (in Japanese).
- [3] Schaffer, G., "Sensors: the Ears and Eyes of CIM," *American Machinist*, Special Report #765, July, 1983.

- [4] *Machine Tool Task Force Study - Technology of Machine Tools*, G. Sutton, ed., UCRL-52960, Lawrence Livermore National Laboratory, Livermore, CA, October, 1980.
- [5] Birla, S. K., "Sensors for Adaptive Control and Machine Diagnostics," *Machine Tool Task Force Study-Machine Tool Controls*, Vol. 4, ed. G. Sutton, SME, Dearborn, MI, October, 1980, pp. 7.12.1-7.12.70.
- [6] Tlustý, J. and Andrews, G. C., "A Critical Review of Sensors for Unmanned Machining," *Annals of CIRP*, Vol. 32, No. 2, 1983, pp. 563-572.
- [7] Iwata, K., "Sensing Technologies for Improving the Machine Tool Functions," *Proceedings of the 3rd International Machine Tool Engineers Conference*, JMTBA, Tokyo, Japan, October 1988, pp. 87-109.
- [8] Matsushima, K. and Sata, T., "Development of the Intelligent Machine Tool," *Journal of the Faculty of Engineering University of Tokyo*, Vol. 35, No. 3, 1980.
- [9] Dornfeld, D. A., "An Investigation of Orthogonal Cutting via Acoustic Emission Signal Analysis," *Proceedings of the 7th North American Metalworking Research Conference*, Univ. of Michigan, Ann Arbor, May, 1979.
- [10] Dornfeld, D. A. and Kannatey-Asibu, Jr., E., "Acoustic Emission During Orthogonal Metal Cutting," *International Journal of Mechanical Sciences*, Vol. 22, 1980, pp. 285-296.
- [11] Kannatey-Asibu Jr., E. and Dornfeld, D., "Quantitative Relationships for Acoustic Emission from Orthogonal Metal Cutting," *Transactions of ASME, Journal of Engineering for Industry*, Vol. 103, No. 3, 1981, pp. 330-340.
- [12] Pan, C. S. and Dornfeld, D. A., "Modeling the Diamond Turning Process with Acoustic Emission for Monitoring Applications," *Proceedings of the 14th North American Manufacturing Research Conference*, SME, University of Minnesota, Minneapolis, May, 1986.
- [13] Lan, M. S. and Dornfeld, D. A., "Acoustic Emission and Machining- Process Analysis and Control," *Journal of Advanced Manufacturing Processes*, Vol. 1, No. 1, 1986 pp. 1-21.
- [14] Lan, M. S. and Naerheim, Y., "Application of Acoustic Emission Monitoring in Machining," *Proceedings of the 13th North American Manufacturing Research Conference*, Berkeley, 1985, pp. 310-313.
- [15] Naerheim, Y. and Lan, M. S., "Acoustic Emission Reveals Information About the Metal Cutting Process and Tool Wear," *Proceedings of the 16th North American Manufacturing Research Conference*, SME, Univ. of Illinois, Champaign, May, 1988, pp. 240-244.
- [16] Schmenk, M., "Acoustic Emission and the Mechanics of Metal Cutting," *Acoustic Emission Monitoring and Analysis in Manufacturing*, D. Dornfeld, ed., ASME, New York, 1984.
- [17] Diei, E. N. and Dornfeld, D. A., "Acoustic Emission from the Face Milling Process- The Effects of Process Variables," *Transactions of the ASME, Journal of Engineering for Industry*, Vol. 109, No. 2, 1987, pp. 92-99.
- [18] Teti, R., and Dornfeld, D. A., "Modeling and Experimental Analysis of Acoustic Emission from Metal Cutting," *Transactions of the ASME, Journal of Engineering for Industry*, Vol. 111, No. 3, 1989, pp. 229-237.
- [19] Weller, E. J., Schrier, H. M., and Weichbrodt, B., "What Sound Can be Expected from a Worn Tool?," ASME Paper No. 68- WA/Prod-4, 1969, p.10.
- [20] Iwata, K. and Moriwaki, T., "An Application of Acoustic Emission to In-Process Sensing of Tool Wear," 26, *Annals of CIRP*, Vol. 26, No. 1, 1977, pp. 21-26.
- [21] Iwata, K. and Moriwaki, T., "Cutting State Identification and In-Process Tool Wear Sensing by Acoustic Emission Analysis," *Bulletin of the Japan Society of Precision Engineering*, Vol. 12, 1978, pp. 213-215.

- [22] Kakino, Y., "In-Process Detection of Tool Breakage by Monitoring Acoustic Emission," *Proceedings of the International Conference on Cutting Tool Materials*, Fort Mitchell, Kentucky, September, 1980, pp. 29-43.
- [23] Kakino, Y., "Detection of Cutting Tool Failure by AE," *Machinery and Tooling*, June, 1980, pp. 140-144 (in Japanese).
- [24] Kaneeda, T. and Tsuwa, H., "Detecting Fracture Phenomena in Separation Process at Tool Tip in Metal Cutting by Acoustic Emission Technique," *Journal of the Japan Society of Precision Engineering*, Vol. 13, No. 3, 1979, pp 159-160.
- [25] Iwata, K., Moriwaki, T., Hasimoto, H. and Shibasaka, T., "Detection of Cutting Tool Damage by Acoustic Emission Signal," *Precision Machinery*, Vol. 48, No. 7, 1982, pp. 95-100 (in Japanese).
- [26] Inasaki, I. and Yonetsu, S., "In-Process Detection of Cutting Tool Damage by Acoustic Emission Measurement," *Proceedings of the 22nd Machine Tool Design and Research Conference*, Manchester University, UK, 1981, pp. 261-268.
- [27] Miwa, Y., Inasaki, I., and Yonetsu, S., "In-Process Detection of Cutting Tool Damage by Acoustic Emission," *Transactions of the Japan Society of Mechanical Engineers*, Ser. C, 1981, pp. 1680-1689.
- [28] Moriwaki, T., "Detection for Cutting Tool Fracture by Acoustic Emission Measurement," *Annals of CIRP*, Vol. 29, No. 1, 1980, pp. 35-40.
- [29] Moriwaki, T., "Application of Acoustic Emission Measurement to Sensing of Wear and Breakage of Cutting Tool," *Bulletin of the Japan Society of Precision Engineering*, Vol. 17, 1983, pp. 154-160.
- [30] Kakino, Y., Suizu, H., Hashitani, M., Yamada, T., Yoshioka, H. and Fujiwara, A., "In-Process Detection of Thermal Crack of Cutting Tool by Making Use of Acoustic Emission," *Bulletin of the Japan Society of Precision Engineering*, Vol. 17, 1983, pp. 241-246.
- [31] Kannatey-Asibu, Jr, E. and Dornfeld, D. A. "A Study of Tool Wear Using Statistical Analysis of Metal Cutting Acoustic Emission," *Wear*, Vol. 76, No. 2, 1982, pp. 247-261.
- [32] Lan, M. S. and Dornfeld, D. A., "Experimental Studies of Tool Wear via Acoustic Emission Analysis," *Proceedings of the 10th North American Manufacturing Research Conference*, SME, McMaster University, Hamilton, Ont., Canada, 1982, pp. 305-311.
- [33] Blum, T., Suzuki, J. and Inasaki, I., "AE-Monitoring Systems for the Detection for Single Point and Multi-Point Cutting Tool Failures," *Journal of Acoustic Emission*, Vol. 7, No. 4, 1988, pp. 179-184.
- [34] Lan, M.S. and Dornfeld, D. A., "In Process Tool Fracture Detection," *Transactions of the ASME, Journal of Engineering for Industry*, Vol. 106, No. 2, 1984, pp. 111-118.
- [35] Diei, E. and Dornfeld, D., "Acoustic Emission Sensing of Tool Wear in Peripheral Milling," *Transactions of the ASME, Journal of Engineering for Industry*, Vol. 109, No. 3, 1987, pp. 234-240.
- [36] Diei, E. N. and Dornfeld, D. A., "A Model of Tool Fracture Generated Acoustic Emission During Machining," *Transactions of the ASME, Journal of Engineering for Industry*, Vol. 109, No. 3, 1987, pp 227-234.
- [37] Ramalingam, S. and Frohrib, D. A., "Real Time Tool Condition Sensing with a New Class of Sensor-Transducer System," *Interdisciplinary Issues in Materials Processing and Manufacturing*, ASME, New York, 1987, pp. 277-284.

- [38] Ramalingam, S., Shi, T., Frohrib, D. A. and Moser, T., "Acoustic Emission Sensing with an Intelligent Insert and Tool Fracture Detection in Multi-Tooth Milling," *Proceedings of the 16th North American Manufacturing Research Conference*, SME, Univ. of Illinois, Champaign, May, 1988, pp. 245-255.
- [39] Inasaki, I., Blum, T., Suzuki, I., Itagaki, H. and Sato, M., "A Practical Mounting Device for an Acoustic Emission Sensor for the Failure Detection of Multipoint Cutting Tools," *Proceedings of the USA-Japan Symposium on Flexible Automation*, ASME, Minneapolis, MN, July, 1988.
- [40] Yu, Q. H. and Hutton, D. V., "Liquid-Coupled Acoustic Emission Measurement for Milling Operations," *Proceedings of the 16th North American Manufacturing Research Conference*, SME, University of Illinois, Champaign, IL, May, 1988, pp. 403- 407.
- [41] Liang, S. Y. and Dornfeld, D. A., "Detection of Cutting Tool Wear Using Adaptive Time Series Modeling of Acoustic Emission Signals," *Transactions of the ASME, Journal of Engineering for Industry*, Vol. 111, No. 3, 1989, 199-205.
- [42] Rangwala, S. and Dornfeld, D. A., "Integration of Sensors via Neural Networks for Detection of Tool Wear States," *Intelligent and Integrated Manufacturing Analysis and Synthesis*, C. R. Liu, et al, eds., ASME, New York, 1987, pp. 109-120.

# **Geotechnical Applications**



## MICROSEISMICS AND GEOTECHNICAL APPLICATIONS

---

**REFERENCE:** Ohtsu, M., "Microseismics and Geotechnical Applications," Acoustic Emission: Current Practice and Future Directions, ASTM STP 1077, W. Sachse, J. Roget, and K. Yamaguchi, Eds., American Society for Testing and Materials, Philadelphia, 1991.

**ABSTRACT:** AE events in the low frequency range ( $<1$  kHz) are sometimes referred to as microseismic activity. In microseismics and geotechnical applications, higher frequency components are preferentially attenuated. The detection of low frequency components can minimize the effect of material inhomogeneity. So far, quantitative treatment of AE in geotechnical fields is limited to the source location analysis. In the present paper, a source inversion procedure in geologic materials is discussed. The procedure consists of the SIGMA (simplified Green's function for a moment tensor analysis) inversion to determine moment tensor components and the unified decomposition of the eigenvalues to characterize crack types and crack orientations. AE sources are classified into tensile cracks and shear cracks, and crack orientations are determined from the directions of the eigenvectors. As an application, AE events observed in a hydrofracturing test are analyzed. Results show a great promise of AE for clarifying failure mechanisms in geotechnical fields.

**KEYWORDS:** acoustic emission, geotechnical applications moment tensor analysis, source inversion, crack kinematics

AE techniques have been extensively employed in the field of microseismics and geotechnology [1]. The original observation of AE activity in geological media dates back to the late 1930's, when Obert and Duvall were surprised to find that stressed rock-pillars emitted microlevel sounds [2]. Since then, AE in geotechnical fields has been investigated in laboratory tests and in situ applications. One of main subjects in rock-sample tests is the estimation of geo-stress by means of Kaiser effect [3], while in-situ AE measurements play

Dr. Masayasu Ohtsu is an associate professor at Department of Civil and Environmental Engineering, Kumamoto University, Kumamoto 860, Japan

important roles for the prediction of impending failure in geologic structures, such as tunnels, slopes, reservoirs, and mines.

One inherent aspect in the geotechnical applications is the use of low frequency range for AE detection, because the attenuation in the high frequency range is known in geological materials. In the case of microseismics, the frequency range lower than 1 kHz is normally employed. In a variety of applications, the frequency range could be extended up to several 100 kHz, depending on material properties and monitoring areas. The stiffer the materials become and the smaller the monitoring areas are restricted, the higher frequency range can be employed. Generally speaking, the range is still lower than that of AE in metallic materials.

AE detection of low frequency components correspond to the observation of long-wavelength waves. Since the scattering of elastic waves due to material inhomogeneity is observed in the case of the wavelengths shorter than the sizes of inclusions, the detection of low frequency components in geologic materials insures that the effect of material inhomogeneity can be minimized.

In many applications reported, a source location analysis provides the only quantitative information on failure mechanisms of microseismic or AE activity [1]. Because the effect of inhomogeneity is minimal, theoretical treatment on AE wave motions can be introduced, based on the integral representation of elastodynamics and the elastic dislocation theory in homogeneous materials. The treatment is closely associated with the theory of seismology [4]. So far, the theory on seismic sources is applied in a limited fashion to AE [5]. This is because the focal mechanisms are mainly referred to as fault motions due to shear motion, whereas both tensile and shear cracks are possible AE sources in geotechnical applications.

The theoretical treatment on AE source characterization is investigated and is summarized as a generalized theory of AE [6]. Although the treatment was originally utilized for a simulation analysis [7], it leads to the concept of a moment tensor [8] and can be eventually extended to a source inversion analysis of AE [9].

In the present paper, an application of the source inversion procedure to geological field is discussed. AE waveforms detected during a hydraulic fracturing test are analyzed. Since the hydraulic fracturing is known for augmenting the production of tight oil-gas bearing rocks and for the development of geothermal reservoirs, results provide a promise for quantitative in-situ AE observation.

## THEORY OF AE SOURCE INVERSION

### SiGMA Procedure

On the basis of a moment tensor representation [4], displacement vector  $u_i(\mathbf{x}, t)$  of AE wave motion is formulated in the following

equation,

$$u_i(\mathbf{x}, t) = G_{ip,q}(\mathbf{x}, \mathbf{y}, t) m_{pq} * S(t), \quad (1)$$

where  $*$  denotes a convolution integral in respect to time.  $G_{ip,q}$  means spatial derivatives of Green's function  $G_{ip}$ .  $m_{pq}$  is the moment tensor, which contains kinematic information on AE source.  $S(t)$  is the source-time function, associated with the time dependence of crack nucleation.

Taking into account only the P wave portion in Eq. 1 in an infinite space, a simplified Green's function for a moment tensor analysis (SiGMA) can be introduced [10]. Thus, a relationship between the amplitude of first motion,  $u_i$ , and moment tensor components,  $m_{pq}$ , is obtained, as follows;

$$u_i(\mathbf{x}) = r_i r_p r_q m_{pq} / (4 \rho \pi R v_p^3). \quad (2)$$

Where  $\rho$  is the mass density and  $v_p$  is the velocity of P wave.  $R$  is the distance from AE source to the observation point and  $r_i$  is its direction cosine. Because only the amplitude of the first motion (P wave) is taken into account, the time dependency is omitted from Eq. 1.

When elastic waves due to one AE event are detected at more than five locations, AE source coordinates are determined by the source location analysis [11]. The amplitudes of the first motions correspond to displacement  $u_i$  and the results of the source location analysis provides information on distance  $R$  and direction cosines  $r_i$  in Eq. 2. Eventually, a set of linear algebraic equations with unknown  $m_{pq}$  is obtained. The moment tensor,  $m_{pq}$ , is the second-rank symmetric tensor. It implies that the number of independent components is six. Therefore, the detection of the first AE amplitudes at more than six locations can provide complete solutions of components,  $m_{pq}$ .

In conventional AE devices, it is not precise AE amplitudes but relative AE amplitudes which can be measured. According to Eq. 2, ratios of moment tensor components can be recovered from the relative amplitudes at sensor locations. In this case, the minimum requirement for the measurement is the equal sensitivity of each sensor. Except for coupling nonuniformities, this condition is attainable in the AE measurement, because the conventional standards for commercial AE devices demand a sensitivity variation less than 3 dB.

### Eigenvalue Analysis and Unified Decomposition

Because the moment tensor is a second-rank symmetric tensor, the determination of the principal components results in the eigenvalue analysis. As well known in seismology [4], in the case of a pure tensile source (crack), the eigenvalues of one maximum value and double roots are obtained. These are decomposed into the compensated linear vector dipole (CLVD) and isotropic mean vales [12]. The CLVD consists of the maximum value and two values of half magnitude and opposite sign of the maximum. Consequently, basic ratios of the CLVD components are 1 : -0.5 : -0.5. Thus, the isotropic components are 1 : 1 : 1. For

the case of a pure shear source (crack), the eigenvalues consist of the null value and two values of the same magnitude and the opposite sign. As a result, the ratios of the shear components become  $1 : 0 : -1$ .

On the basis of the above results, it is assumed that AE sources of mixed mode are classified into either a tensile crack or a shear crack [9]. Setting the maximum value of the shear component as  $X$ , the shear crack contains three eigenvalues of  $X$ ,  $0$ , and  $-X$ . In the case that the maximum value of the CLVD is set as  $Y$ , the eigenvalues of the CLVD model become  $Y$ ,  $-Y/2$ , and  $-Y/2$ . The isotropic components are denoted as  $Z$ ,  $Z$ , and  $Z$ . Provided that the principal directions of the shear crack are in agreement with those of the tensile crack, these decomposition is represented as shown in FIG. 1.

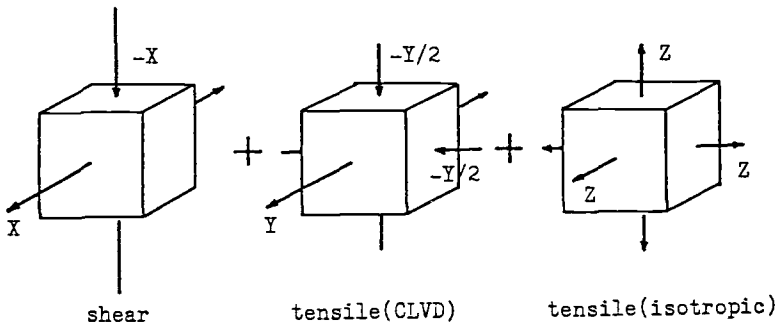


FIG. 1 -- Decomposition of eigenvalues into the shear-crack component, the CLVD component, and the isotropic component.

In this case, the decomposition is unique and the normalized ratios of the eigenvalues are expressed, as follows;

$$1.0 = X + Y + Z$$

the intermediate eigenvalue/the maximum eigenvalue =  $0 + -Y/2 + Z$  (3)

the minimum eigenvalue/the maximum eigenvalue =  $-X + -Y/2 + Z$ .

After determining the eigenvalues of the moment tensor, ratios of  $X$ ,  $Y$ , and  $Z$  are easily obtained by solving a simple algebraic equation of Eq. 3. From the results of this decomposition, a simple criterion for the classification of AE sources was proposed and the validity was confirmed by numerical experiments [8]. When the ratio,  $X$ , is greater than 50 %, AE source is referred to as a shear crack. In the reverse case, AE source is classified into a tensile crack.

The directions of crack motions are derived from eigenvectors [8]. It is known that the eigenvector corresponding to the maximum (first) eigenvalue of a tensile crack directs the opening motion. Crack orientations, of which AE source are classified into tensile cracks, are readily determined from the direction of the first eigenvector. For a shear crack, either the direction of crack motion

or that of unit normal to a crack surface is derived from the sum of the first and the third eigenvectors. In the case of the shear crack, the direction of crack motion is known to be vertical to the unit normal vector. Therefore, either information on the direction of crack motion or the direction of crack normal is sufficient to determine the shear-crack orientation.

#### AE DATA IN A HYDROFRACTURING TEST

Small scale hydraulic fracturing tests were carried out at a working tunnel in Imaichi underground power plant. According to results of the geological survey, the tested site was composed of siliceous sandstone. Hydrofracturing tests were conducted by

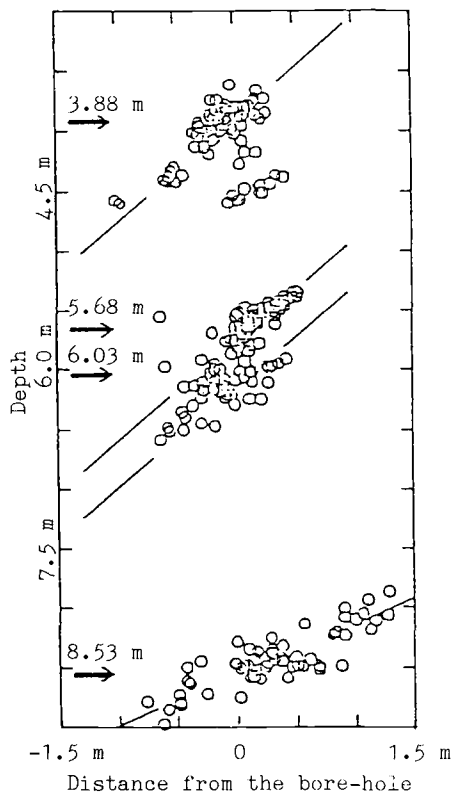


FIG. 2 -- Located AE sources in the elevation view for fluid injections at four depths.

injecting pressurized water into an inflatable packer located in a bore-hole of 66 mm diameter. The injection was performed at four depths : 3.88 m, 5.68 m, 6.03m, and 8.53m. During fluid injection, AE events were observed to characterize AE activity associated with

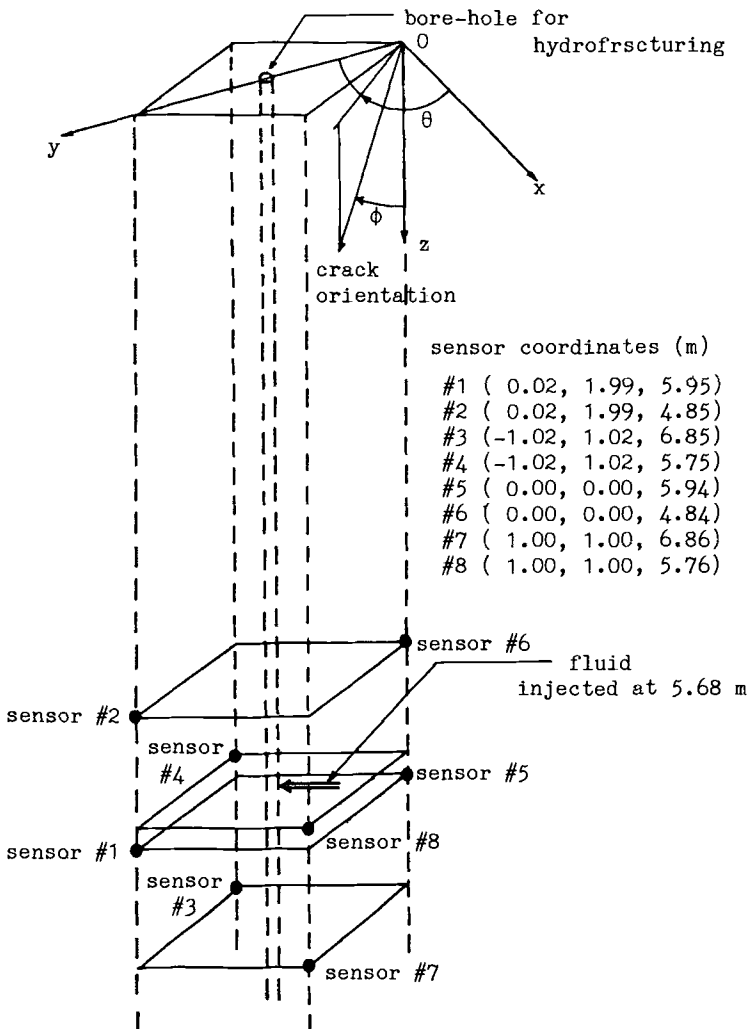


FIG. 3 -- Configuration of hydrofracturing site and sensor locations for the 5.68 m-depth injection.

hydraulic fracturing process. A total of thirty-four AE sensors were mounted in four other bore-holes, which were 1 m apart from the injected bore-hole. The sensor employed were accelerometers of 25 kHz resonance and piezoelectric AE sensors of 65 kHz resonance. All sensors were embedded in the four bore-holes and oriented horizontally to the treatment bore-hole. Total amplification of AE signals was 60 dB to 100 dB and the frequency range recorded was 1 kHz to 100 kHz.

In the first phase of the tests, the source location analysis of AE events was performed from the arrival time differences of the first motions. P wave velocity was determined as 5300 m/s from a field test

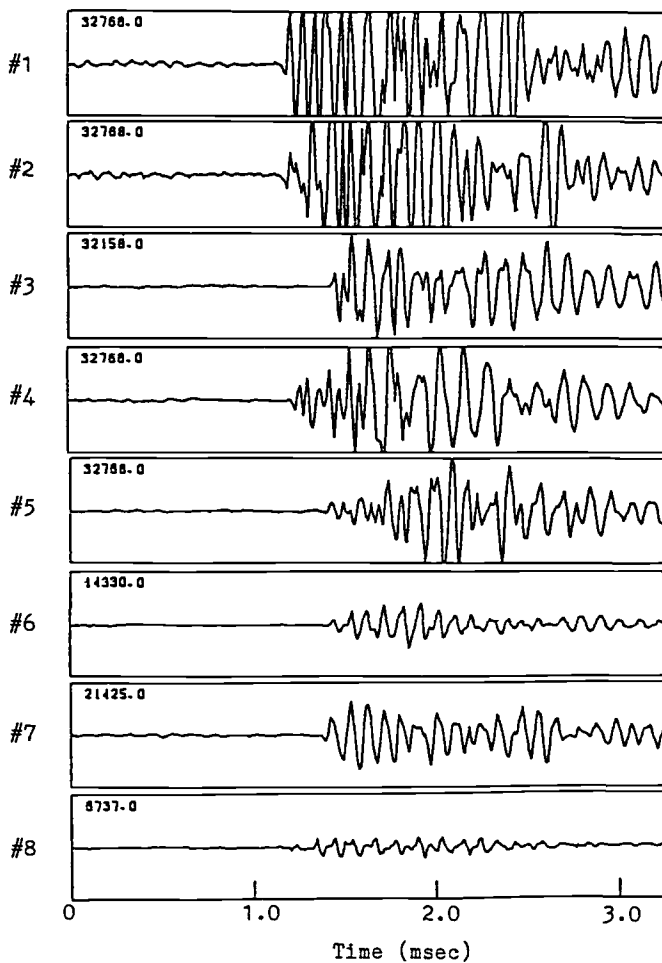


FIG. 4 — AE waveforms recorded for event No. 14.

of the site. An elevation view of all sources located by four-depth injections is shown in FIG. 2. Approximately two hundreds sources are plotted. Detailed discussion was reported elsewhere [13]. In the figure, solid lines denote failure planes predicted from AE swarms. According to a bore-hole TV observation prior to the tests, dip angles of existing natural joints were varied from  $40^{\circ}$  to  $60^{\circ}$  from the horizontal direction in FIG. 2. The figure shows reasonable agreement between existing joints and AE clusters.

In the second phase of the analysis, AE data to be analyzed by the source inversion procedure are AE waveforms due to the hydraulic fracturing test at 5.68 m depth. Ten AE waveforms were detected at eight sensors of accelerometer type. The coordinate system and all

TABLE 1 -- Located sources and moment tensor solutions for AE events due to a hydrofracturing test.

event number	source location(m)	moment tensor components		
2	x = 0.854 y = 0.595 z = 5.979	-0.018 sym.	-0.127 0.801	-0.135 0.658 1.000
14	x = -0.181 y = 1.708 z = 5.439	-0.251 sym.	0.784 -0.127	1.000 -0.214 -0.074
18	x = 0.618 y = 0.863 z = 5.910	-0.508 sym.	0.225 -0.976	0.034 -0.622 1.000
19	x = 0.254 y = 0.940 z = 5.997	0.190 sym.	0.143 -0.479	0.111 -0.748 1.000
20	x = 0.563 y = 1.023 z = 5.777	-0.049 sym.	0.098 0.195	-0.207 -0.061 1.000
117	x = 0.666 y = 0.905 z = 5.795	-0.298 sym.	-0.195 1.000	-0.503 0.136 -0.226
147	x = -0.048 y = 2.015 z = 5.002	-0.089 sym.	0.088 0.036	0.114 0.535 1.000
163	x = 0.616 y = 1.280 z = 5.551	0.266 sym.	0.377 -0.938	0.574 -0.473 1.000



AE sensor locations for the 5.68 m-depth injection are shown in FIG. 3. The sensors were installed in four bore-holes, which are approximately 1 m apart horizontally from the injected bore-hole.

The AE waveforms detected for the event No. 14 are shown in FIG. 4. Each waveform consists of 1024 discrete points at 320 kHz sampling frequency. The maximum amplitude of each waveform is indicated at the upper left corner as the reference number. Consequently, relative amplitudes of the first motions are readily determined. The arrival time and the relative amplitude of the first motion in each waveform was read. The SiGMA procedure was applied to the amplitude for determining moment tensor components, following the source location analysis based on the arrival time differences.

#### APPLICATION OF SOURCE INVERSION TO AE

Crack locations were obtained by the source location analysis and moment tensor components were determined by the SiGMA procedure. Results are indicated in TABLE 1. For two events out of ten,

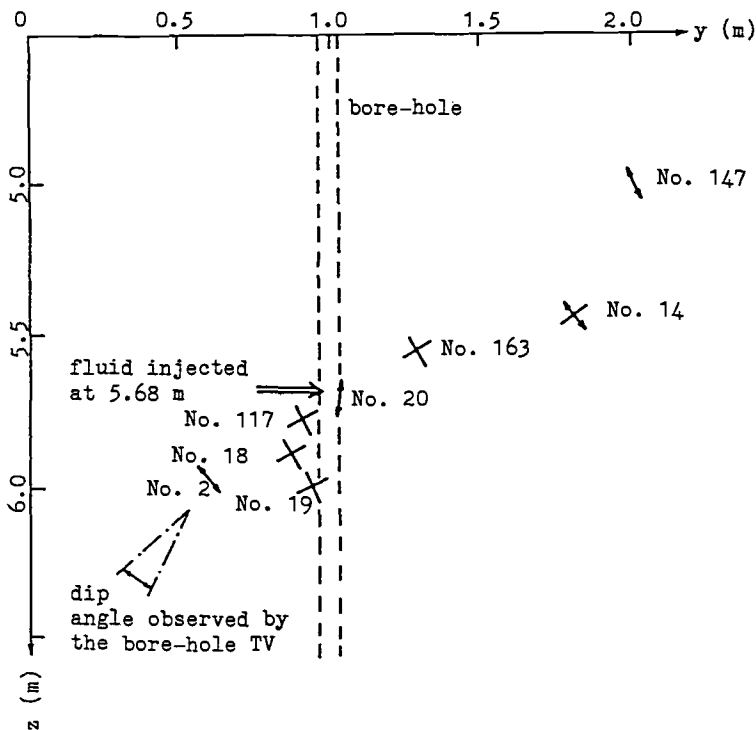


FIG. 5 -- An elevation view of crack locations and orientations.

converged solutions in the iteration procedure of the source location analysis were not obtained. Therefore, results of eight events : No. 2, No. 14, No. 18, No. 19, No. 20, No. 117, No. 147, and No. 163 are shown. These numbers of the events were labelled in the first phase analysis according to the order of occurrence. Results of AE location show that AE sources are scattered near the injected bore-hole, whose coordinates were (0.01 m, 1.01 m, 5.68 m). The moment tensor components are normalized by the maximum value observed. An inversion procedure to determine only diagonal components was proposed previously [14]. The table, however, obviously shows the presence of off-diagonal components. It implies that the full components of the moment tensor need be determined to fully characterize AE sources.

After the eigenvalue analysis and the unified decomposition were performed, all AE events were classified into either tensile cracks or shear cracks on the basis of the criterion mentioned above. X ratio of event No. 14, however, was estimated as 58 %. Due to the accuracy of the SiGMA procedure [9], it is considered to be reasonable not to classify event No. 14 into a shear crack, but to take into account both cases of a tensile crack and a shear crack. An elevation view of these results is shown in FIG. 5. The dip angle observed by the bore-hole TV is indicated by chain lines. As the same as the location analysis in FIG. 2, sources are located reasonably between the dip angles. Furthermore, crack-opening directions of tensile cracks are clearly vertical to the joint plane predicted from AE swarms. It implies that tensile cracks were nucleated as opening motions on the joint plane. On the other hand, crack orientations of shear cracks are obtained approximately along the joint plane. It implies that shear motions are generated parallel to the joint plane. For event No. 14, both directions of tensile and shear motions are shown. It is interesting that the direction of tensile motion is almost vertical to that of shear motion. All crack orientations drawn in the figure suggest us that failure mechanisms occurred on the joint plane.

## CONCLUSION

The source inversion procedure consisting of the SiGMA inversion and the unified decomposition of the eigenvalues was developed for determining crack kinematics in microsesismics. To demonstrate the applicability of the procedure, AE waveforms detected during a hydraulic fracturing test were analyzed. Crack kinematics determined procedure were in good agreement with the experimental findings. These results show a great promise in geotechnical applications for identifying failure mechanisms by means of AE.

## ACKNOWLEDGEMENT

The author wishes to thank Messers S. Sasaki, T. Ishida, T. Kanagawa in the Central Research Institute of Electric Power Industry

Kanagawa in the Central Research Institute of Electric Power Industry for their valuable data. AE waveforms analyzed in this report were kindly offered by them. The collaboration of Mr. M. Shigeishi was also extremely valuable in the analysis of the data.

## REFERENCES

- [1] Hardy, Jr., H. R. and Leighton, F. W. Leighton, Eds., Acoustic Emission, 1975; Acoustic Emission II, 1978, Acoustic Emission III, 1981, Trans Tech Publications.
- [2] Obert, L., "Measurement of Pressures on Rock Pillars in Underground Mines, Part I," U. S. Bureau of Mines, RI 3444, 1939.
- [3] Kanagawa, T., Hayashi, M. and Nakasa, H., "Estimation of Spatial Geo-stress Components in Rock Samples Using Kaiser Effect of Acoustic Emission," Proc. Third Acoustic Emission Symposium, Tokyo, JSNDI, 1976, pp. 229-248.
- [4] Aki, K. and Richards, P. G., Quantitative Seismology Theory and Methods Vol. I and Vol. II, W. H. Freeman and Company, San Francisco, 1980.
- [5] Niwa, Y., Kobayashi, S., and Ohtsu, M., "Source Mechanisms and Wave Motions of Acoustic Emission in Rock-like Materials," Acoustic Emission III, Trans Tech Publications, 1981, pp. 101-115.
- [6] Ohtsu, M. and Ono, K., "A Generalized Theory of Acoustic Emission and Green's Functions in A Half Space," J. of Acoustic Emission, Vol. 3, No. 1, 1984, pp. 27-40.
- [7] Ohtsu, M. and Ono, K., "The Generalized Theory and Source Representations of Acoustic Emission," J. of Acoustic Emission, Vol. 5, No. 4, 1986, pp. 124-133.
- [8] Ohtsu, M., "Determination of Crack Orientation by Acoustic Emission," Materials Evaluation, Vol. 45, No. 9, 1987, pp. 1070-1075.
- [9] Ohtsu, M., "Source Inversion of Acoustic Emission Waveform," Structural Eng./Earthquake Eng.(Proc. of JSCE), JSCE, Vol. 5, No. 2, 1988, pp. 275s-283s.
- [10] Ohtsu, M., "Source Kinematics of Acoustic Emission Based on A Moment Tensor," NDT International, Vol. 22, No. 1, 1989, pp. 14-20.
- [11] Ohtsu, M. and Ono, K., "AE Source Location and Orientation Determination of Tensile Cracks from Surface Observation," NDT International, Vol. 21, No. 3, 1988, pp. 143-150.
- [12] Knopoff, L. and Randall, M. J., "The Compensated Linear-Vector Dipole : A Possible Mechanism for Deep Earthquakes," Journal of Geophysical Research, Vol. 75, No. 26, 1970, pp. 4957-4963.
- [13] Sasaki, S., Ishida, T. and Kanagawa, T., "Source Location and Focal Mechanisms of AE Events during the Hydraulic Fracturing," CRIEPI Report U86032, the Central Research Institute of Electric Power Industry, 1987.
- [14] Kim, K. Y. and Sachse, W., "Characteristics of Acoustic Emission Signals from Indentation Cracks in Glass," Progress in Acoustic Emission II, JSNDI, 1984, pp. 163-172.

## ACOUSTIC EMISSION/MICROSEISMIC ACTIVITY AT VERY LOW STRAIN LEVELS

---

REFERENCE: Armstrong, B. H. and Valdes, C. M., "Acoustic Emission/Microseismic Activity at Very Low Strain Levels," Acoustic Emission: Current Practice and Future Directions, ASTM STP 1077, W. Sachse, J. Roget, and K. Yamaguchi, Eds., American Society for Testing and Materials, Philadelphia, 1991.

ABSTRACT: Laboratory experiments have shown that strain levels as low as one microstrain in competent rock samples produce detectable acoustic emissions (AE) in the frequency range from 100 to 300 kHz. Naturally occurring strain and strain rates have similar levels to those at which laboratory AE was detected. In the buildup of a strain field over the "preparation zone" of an impending earthquake, strain in collapsing pores, grain boundary slippage, and other microscopic ruptures may cause high frequency AE. However, this AE due to tectonic strain must be distinguished from AE from other sources such as air pressure changes, thermal expansion/contraction, earth tides, and cultural activities. Sufficient AE at very low strain levels, and detectable above noise backgrounds, might provide a useful precursor to earthquakes.

KEYWORDS: acoustic emission, secondary acoustic emission, microseismic activity, low strain, earthquake preparation zone

## INTRODUCTION

Recently, there have been independent suggestions of very low strain level acoustic emission (AE) in geophysical/geotechnical contexts as well as indications of practical implications. Armstrong (1) suggested such emission on purely theoretical grounds, and introduced the terminology "secondary AE" in an attempt to distinguish between AE from an identified or deliberate excitation of AE, and the production of AE under hitherto unexpected low-strain circumstances by a primary strain field of uncontrolled, natural, and/or incidental circumstances. Repsher and Sheblay (2) inferred the existence of high-frequency (36-144kHz) AE resulting from a distant, low-level strain source in the course of field studies in a mine. More recently, Hardy, *et al* (3) have obtained laboratory confirmation that high-frequency (100 - 300 kHz) AE is produced in competent rock samples at strain-level amplitude increments down to one microstrain, and Ersoy (4) has effectively reproduced the Repsher-Sheblay field experiment results. Hardy's (3) results, furthermore, strongly suggest that AE will be produced at still lower strain level increments in porous, fractured or weakened materials.

## RELEVANCE TO SEISMOLOGY

Very low-level AE has not been investigated extensively in the seismological environment, and merits further study. In the buildup of a strain field over the "preparation zone" of an impending earthquake, one would expect production of high-frequency AE from the action of strain in

---

Dr. Armstrong is manager of Numerically Intensive Computing Applications, and Mr. Valdes is a Visiting Scientist at the IBM Scientific Center 1530 Page Mill Rd., Palo Alto, CA 94304

producing microscopic effects, e. g., collapsing pores, grain boundary slippage, and opening and closing of microscopic cracks. Sources from a few cm to a few mm in size can produce vibrations from a few kHz to a few MHz. We include this size regime in the present definition of "microscopic", because source sizes smaller than a tenth of a mm or so can produce frequencies sufficiently high so as to be academic in the seismological context, and due to the difficulties of measurement and interpretation. Furthermore, if a strain buildup is caused by relatively sudden, discontinuous, creep movements, "loading waves" with frequencies in the normal short-period seismic regime should be produced. This follows from the standard elastic theory of mechanical excitation and response applicable to geological structures encompassed within an earthquake preparation zone. Such sudden movements may also result, e. g., in opening and closing of pre-existing macroscopic cracks, movement along fissures, or squeezing of unconsolidated material. The friction and impacts involved in such macroscopic effects can, in principle, produce vibrations in the range of a few hundred to a few thousand Hz. (Physical sizes of vibrating structures of the order of one to tens of meters.) These vibrations may not be clearly or usefully distinguishable from microearthquakes or nanoeearthquakes, which would include ruptures on the physical size scale stated above, in addition to the sources mentioned. Thus, sources and excitations exist in an earthquake preparation zone that can, in principle, produce elastic vibrations which we can (perhaps arbitrarily) refer to as AE over the entire frequency range above conventional seismic frequencies. Microearthquakes, for example, are thus included in this definition of AE. Toward the lower end of the frequency spectrum, we could even class an earthquake itself as a giant AE event, thus further generalizing the notion of AE. However, in both the high and low frequency regimes (omitting now the earthquake itself as an AE event), such AE must be expected to be near to or within the ambient noise level, so discrimination may be required. This follows because the power released in the mechanisms cited above is small compared to that released in most measured earthquakes, as well as compared to some sources of cultural noise and natural microseisms. In the case of high-frequency AE, potential sources of ambient noise are air pressure changes, thermal expansion/contraction, and earth tides, as well as cultural activities. Except for the earth tides, which are readily identifiable, these sources can generally be avoided by locating detecting sensors a few meters below the surface.

The "normal", or expected behavior of unconfined samples of porous, heterogeneous rock (5) is suggestive of copious production of AE at very low strain levels. Certainly, strong AE generation is exhibited at the initial strain amplitude increment levels of some conventional experiments (6), typically about  $\Delta\epsilon = 10^{-3}$ , where  $\epsilon$  is the strain amplitude. This initial high level of AE falls off rapidly as strain increases because closing of cracks, collapsing of pores, etc., as enumerated above, comprise source mechanisms that die out as they occur. Therefore, a minimum appears in the magnitude of AE generation as a strain level is reached where sources which are self-stimulating begin to exceed those which are self-destructive. The former are the microfracture and deformation events that lead to failure. As the strain increases beyond this point, the rate of AE increases rapidly to failure. If one extrapolates this normal behavior toward lower strain increment levels than conventional experiments have dealt with, the rate of AE, of course, increases rapidly. The question then arises as to how low a strain increment level such an extrapolation continues to be meaningful (7). The strain rate  $\dot{\epsilon}$  is also important to the generation of AE; it has been noted that the AE pulse rate is proportional to the strain rate (8-9).

The frequency regime of interest to the present study is from a few tens of kHz and above. Sufficient low-strain-induced AE in this regime to be detectable above background noise might provide a useful precursor to earthquakes. The fact that such emissions have already been demonstrated to have predictive value in the mining environment (2, 4), lends support to this suggestion. The regime from a few Hz to a few kHz (the microearthquake and nanoeearthquake regimes) is being studied elsewhere (e. g., 10, 11), and such study may well prove profitable. However, the strain level excitations required to produce such AE events is likely to be higher than levels required to produce AE from microscopic events at several tens of kHz and above. Thus, a much larger source volume (the entire earthquake preparation zone) may be available to produce high-frequency AE than is available to produce events in the microearthquake regime. Also, the detection of high-frequency AE is simpler because these events can occur in the immediate neighborhood of the sensor (arbitrarily close). Because of this, the limitations of attenuation are of less importance. Such low-strain-level, high-frequency AE could, for example, provide an explanation for the well-known phenomenon of anomalous animal behavior before earthquakes.

## NATURALLY OCCURRING vs LABORATORY STRAIN/STRAIN RATE LEVELS

It is of interest to compare the regimes in  $\Delta\epsilon$  and  $\dot{\epsilon}$  occurring in nature with laboratory regimes in these parameters over which AE has been detected. The point is to note whether the laboratory experiments are indicative of natural occurrence of AE in circumstances of interest. Strain rate is important as mentioned above; unfortunately, it is also difficult to determine unambiguously in most situations. In the laboratory, stress is often applied in more-or-less discontinuous steps, or in uniform ramps with discontinuities at the beginning and end. In nature, the buildup of strain may be sporadic; it may also increase or decrease in relatively sudden jumps (12,13). Hence, in such instances, only an average value will be available. Table 1 shows the strain amplitude increment  $\Delta\epsilon$  and strain rate  $\dot{\epsilon}$  characteristics of three different naturally occurring situations. Column 2, "Preseismic Strainfield", gives the upper limit of the entries in Table 15-XIII of Rikitake (14), for  $\Delta\epsilon$ , and the strain rate figure is an observed average change on the San Andreas fault as described on p. 94 of the same reference. Because of the possibility of sporadic jumps in this rate, we take this as an approximate lower limit. Col. 3 gives the characteristics of a nuclear event at the Nevada test site as felt at Stone Canyon well, near Hollister, CA. These numbers were estimated from the equivalence of this event to an earthquake of Richter magnitude 6.2, a frequency of 2 Hz, and normal earthquake propagation characteristics. AE in the frequency range 20-35 Hz appeared to be triggered in Stone Canyon well by the passage of this seismic wave. Col. 4 gives estimates of the listed parameters for a foreshock as noted, which is roughly at the limit of human perception. Further details of these entries in Table 1 are given by Armstrong and Stierman (7). Table 2 lists strain increments and rates for nominal parametric values involved in thermal expansion and contraction, and in atmospheric pressure changes associated with weather variations. These are somewhat arbitrary because of the variability of weather, but represent the order of magnitude of effects which are not uncommonly observed.

For a volume coefficient of thermal expansion  $\alpha$  representative of earth materials, the value  $4 \times 10^{-5}$  per Kelvin given by Magnitskiy (15) was selected. This same author's value of modulus of compression  $K$  equal to  $1.2 \times 10^{12}$  dynes  $\text{cm}^{-2}$  was used. For thermal expansion, the strain increment shown in the table was computed from  $\Delta\epsilon = \alpha\Delta T$ , with a temperature increment  $\Delta T$  of 1 K. The thermal strain rate was computed on the basis of a change in temperature of about 1 K per hour. A pressure change of 10 millibars occurring in 3 hours was used to calculate a strain and strain rate according to  $\Delta\epsilon = \Delta p/K$  and this same equation differentiated with respect to time. Here  $\Delta p$  is the pressure change.

TABLE 1 -- Naturally occurring strain amplitude increment/strain rate combinations. The column headings are more fully explained in the text.  $\dot{\epsilon}$  is in  $\text{s}^{-1}$ .

Source	Preseismic Strainfield	300km, 2Hz	2km, 40Hz
		$M = 6.2$ Earthquake	$M = 1$ Foreshock
$\Delta\epsilon$	$\leq 3 \times 10^{-5}$	$10^{-7}$	$2 \times 10^{-7}$
$\dot{\epsilon}$	$\gtrsim 10^{-9}(\text{av})$	$10^{-6}$	$4 \times 10^{-5}$

On the one hand, atmospheric pressure changes are seen to have strain increment and strain rate, on this order-of-magnitude basis, a little less than those due to earth tides, so can probably be neglected. (Particularly in calm weather.) On the other hand, thermal expansion strain characteristics are essentially the same as those estimated for the preseismic strainfield in Table 1. As will be seen later (Table 3), the magnitude of the thermal expansion strain increment and rate are about those that have been observed in the laboratory by Lockner and Byerlee (16). Although any thermal expansion AE would vary considerably around our estimate, it will in general be universally present at the earth's surface. Thus, for strain field AE detected at the surface to be important, one would conclude that abrupt changes in strain level would be required, so that the strain rate is much higher than the figure  $10^{-9}$  given in Table 1, or that a gross difference in frequency/amplitude characteristics of thermal-expansion-induced and earthquake strain-field-induced AE exists. We are unaware of any measurements of AE from rock subjected only to thermal expansion. If such

measurements have not been made, it would be interesting to perform them in order to explore the characteristics of such AE pulses.

TABLE 2 -- Naturally occurring strain amplitude increment/strain rate combinations of potential AE noise sources. The column headings are more fully explained in the text.  $\dot{\epsilon}$  is in  $s^{-1}$ .

Source	Thermal Expansion	Atmospheric Pressure	Earth Tides
$\Delta\epsilon$	$4 \times 10^{-5}$	$10^{-8}$	$10^{-7}$
$\dot{\epsilon}$	$10^{-8}$	$10^{-12}$	$2 \times 10^{-12}$

Because temperature changes damp rapidly beneath the earth's surface due to the thermal skin effect, at most several meters below the surface will be thermally active. Thus, the effect can be avoided by placement below the surface at modest depths (3 m.) It may also be possible to avoid thermal expansion AE by taking measurements only during the diurnal cycle when the ambient temperature is changing from the warming to the cooling phase or vice versa. There should be a few minutes to a few hours on most days when the rate of temperature change is very low.

TABLE 3 -- Strain amplitude increments and rates of laboratory observations of AE.  $\dot{\epsilon}$  is in  $s^{-1}$ .

Source	Lockner & Byerlee, 1980	Sondergeld & Estey, 1981
$\Delta\epsilon$	$\approx 10^{-4}$	$\approx 10^{-4}$
$\dot{\epsilon}$	$2 \times 10^{-9}(av)$	$10^{-7}$

Tables 3 and 4 list strain increments and rates for laboratory experiments as given in the references at the top of the columns. Lockner and Byerlee (16) (column 2, Table 3), and Sondergeld and Estey (17) (column 3, Table 3), have both observed AE from rock samples at strain levels of about  $10^{-4}$ , although at different strain rates as noted. Lockner and Byerlee used piezoelectric transducers with peak response at 600 kHz for AE detection, while Sondergeld and Estey's piezoelectric transducer resonant frequency was at two MHz. Cols. 2 and 3 of Table 4 refer to two different sets of measurements due to Hardy, *et al* (3). These are (a), Final Test Series 2, and (b), Series 3, in the cited reference.

TABLE 4 -- Strain amplitude increments and rates of laboratory observations of AE.  $\dot{\epsilon}$  is in  $s^{-1}$ .

Source	Hardy, <i>et al</i> (a) 1987	Hardy, <i>et al</i> (b) 1987
$\Delta\epsilon$	$10^{-6}$	$10^{-6}$
$\dot{\epsilon}$	$\approx 2 \times 10^{-6}$	1

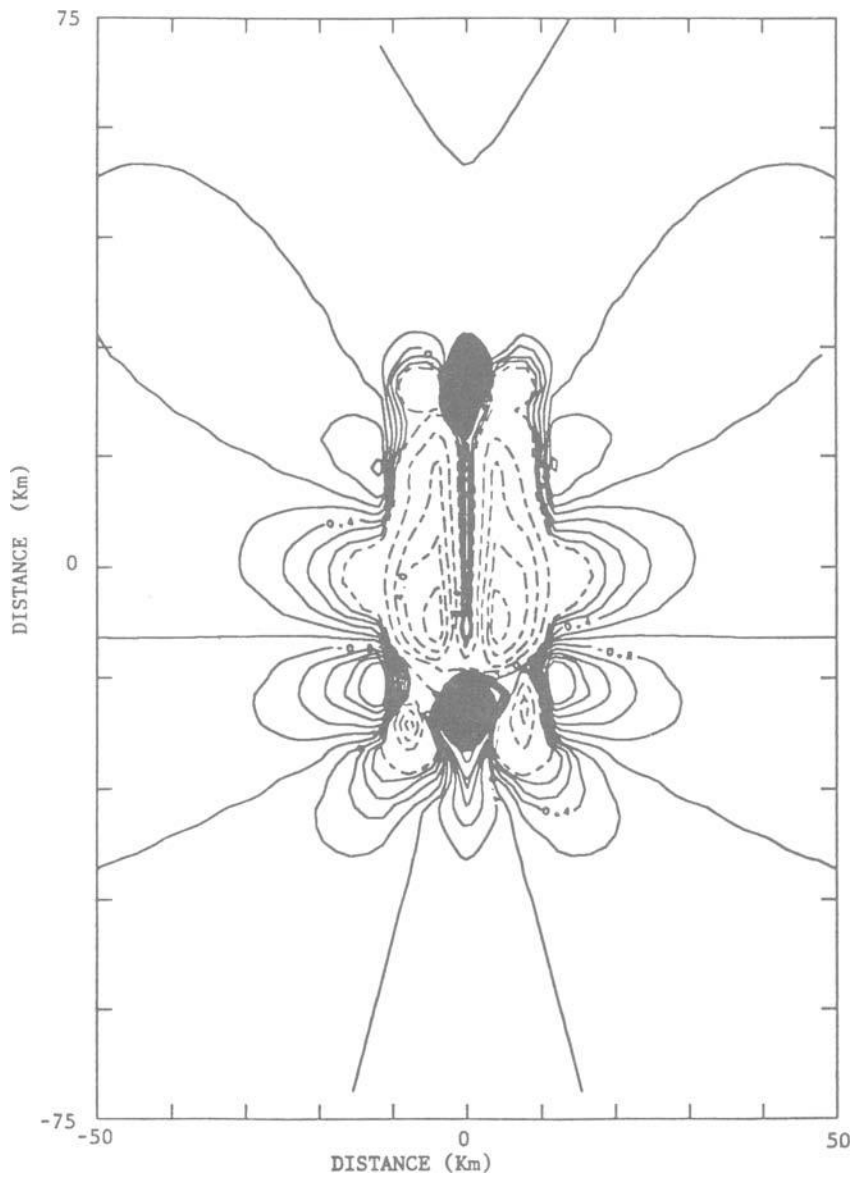


Figure 1. Shear strain at the surface, due to a vertical fault 40 km long, and 15 km depth. The displacement of the fault is taken from the preferred model of Segall and Harris (16, Figure 9c), that simulates the yearly slip in the Parkfield, California area. Dashed contour lines represent positive microstrain levels. The shaded area represents negative microstrain levels, and the solid contour levels represent strains in the order of  $10^{-7}$ . The irregular strain distribution suggest careful selection of sites to monitor acoustic emissions in earthquakes preparation zones.



The strain rate in Col. 2 of Table 4 (Test Series 2 of Hardy's experiment) is shown as approximate because of the presence of the discontinuity in the ramp function of pressure vs time. Cyclic loading was used in Series 3, so Col. 3 of Table 4 is not subject to this problem. Col. 3 of Table 1 supplements Tables 3 and 4, since it is believed that AE was observed for these conditions. By comparison of the results in the tables, we see that Hardy's (3) measurements have produced AE at  $\Delta\epsilon$  levels below those observed in preseismic strain fields. If this were the only variable involved, we should expect to observe AE in the earthquake preparation zone. However, Hardy's strain rate is considerably higher than the preseismic field average. If this average contains sporadic high-rate periods, then Hardy's results may imply the generation of measurable AE in the earthquake preparation zone. However, we cannot, of course, be sure of this. And the further possibility exists that Hardy's effective strain rate is actually higher because of the above-mentioned discontinuity in the loading function. Thus, measurements of AE at still lower strain rates at or below the microstrain level are desirable, as are direct measurements of AE in a developing earthquake strainfield.

### AE AND THE STRAIN FIELD IN AN EARTHQUAKE PREPARATION ZONE

Small strain changes due to large earthquakes have been detected at teleseismic distances. The magnitude 8.4 Alaska earthquake of 1964, produced a  $10^{-8}$  strain change at Oahu, Hawaii (18). Many observations of strain changes in the range of  $10^{-4}$  to  $10^{-7}$  have been reported before earthquakes with magnitudes of 5 or greater (14, Table 15-XIII). The epicentral distance for these observations ranged between 3 and 320 km. There is not sufficient information in these reports to relate the different shape and size of faults, and magnitude of earthquakes with the strain field. In order to study the pattern and amplitude of the strain field due to the increase of stress in an earthquake preparation zone, we have modeled a segment of the San Andreas fault in the area of Parkfield in central California. This area breaks out about once every 22 years in a moderate earthquake of approximately magnitude 6.0 (19). The last earthquake in that area occurred in 1966, and many studies (20) have provided information about the rupture dynamics, and the deformation cycle for this earthquake. Segall and Harris (20), inferred the interseismic, coseismic and postseismic slip for the 1966 earthquake by modeling the geodetic information obtained before and after the earthquake. We multiplied their preferred yearly interseismic slip model (20, Fig. 9c) by 22 to represent the time elapsed since the 1966 Parkfield earthquake. This model was used with a three dimensional dislocation computer program (21) to obtain the static strain field at the surface. Fig. 1 shows the shear strain contour levels. The dashed levels correspond to positive microstrain levels, the filled areas represent negative microstrain levels, and the solid contours represent the  $10^{-1}$  microstrain level. From Fig. 1, we observe deformation at the microstrain level, which according to Hardy (3), can produce acoustic emission (in the 100 to 300 kHz band). It is also clear from this figure that the strain field at the surface is not uniform. We can see that areas within 1-2 km from the trace of the fault have strains only in the order of  $10^{-7}$ , while the maxima (negative) are located at the ends of the fault trace. The strain field depends on the slip distribution, and dip of the fault. Thus an earthquake preparation zone is capable of producing strain amplitudes in the range where acoustic emission has been detected in laboratory experiments (3). However, careful attention should be paid in selecting sites to monitor acoustic emission, in order to avoid monitoring areas of low strain amplitudes. Model calculations as described above, and as illustrated in Fig. 1, provide a useful tool in this selection process.

### REFERENCES

- (1) Armstrong, B. H., *EOS* Vol. 64, 1983.
- (2) Repsher, R. C. and B. J. Steblay, "Structural Stability Monitoring Using High-Frequency Microseismics", *Proceedings 26th U. S. Symposium on Rock Mechanics* (Rapid City, SD, June, 1985), Vol. 2, A. A. Balkema, Rotterdam/Boston, pp. 707-713, 1985.
- (3) Hardy, H. R., M. Mrugala, and R. M. Belesky, "Generation and Propagation of Acoustic Emissions at Low Strain Levels in Earth Materials", Pennsylvania State Univ. Dept. of Mineral Engineering Final Report, IBM Corp. Contract, Dec. 31, 1987.

- (4) Ersavci, M. N., "Laboratory and Field Evaluation of a High Frequency Acoustic Emission/Microseismic Monitoring System", Pennsylvania State Univ., Dept. of Mineral Engineering, MS Thesis, August, 1988.
- (5) Lord, A. E., Jr. (1975), Acoustic Emission, in Physical Acoustics, Vol. XI, ed. by W. P. Mason and R. N. Thurston, Academic Press, NY., pp. 289-353, 1975.
- (6) Scholz, C. H., "Microfracturing and the inelastic deformation of rock in compression", J. Geophys. Res. Vol. 73, pp. 1417-1432, 1968.
- (7) Armstrong, B. H. and D. J. Stierman, "Acoustic Emission from Foreshocks and Secular Strain Changes Prior to Earthquakes", Proceedings of Fourth Conf. on AE/MS in Geologic Structures and Materials, Pennsylvania State University, Oct. 1985, ed. by H. R. Hardy, Jr., 1989.
- (8) Fisher, R. M. and J. S. Lally, Can. J. Phys., Vol. 45, pp. 1147-1159, 1967.
- (9) Dunegan, H. L., and A. T. Green, "Factors Affecting Acoustic Emission Response from Materials", in Acoustic Emission, ASTM, Special Publ. 505, Philadelphia, PA 19103, 1972.
- (10) Foxall, W. and T. V. McEvilly, "The Parkfield Downhole Seismic Array: Preliminary Analyses of MicroEarthquakes", EOS, Vol. 68, No. 44, Nov. 1987, p. 1346.
- (11) Teng, T., and T. L. Henyey, "The Detection of Nanoearthquakes", in Earthquake Prediction An International Review, ed. by D. W. Simpson and P. G. Richards, American Geophys. Union, Washington, D. C., 1981.
- (12) Thatcher, W., "Nonlinear Strain Buildup and the Earthquake Cycle on the San Andreas Fault", J. Geophys. Res., Vol. 88, pp. 5893-5902, 1983.
- (13) Li, V. C. and J. R. Rice, "Crustal Deformation in Great California Earthquake Cycles", J. Geophys. Res., Vol. 92 pp. 11,533-11,551, 1987.
- (14) Rikitake, T., Earthquake Prediction, Elsevier, Amsterdam, 1976.
- (15) Magnitskiy, V. A., The Internal Structure and Physics of the Earth, NASA Technical Translation NASA TT F-395, National Aeronautics and Space Administration, Washington, D. C., April, 1967.
- (16) Lockner, D. and J. D. Byerlee, "Development of Fracture Planes During Creep in Granite", in Proceedings Sec. Conf. on AE/MS, ed. by H. R. Hardy, Jr. and F. W. Leighton, Trans Tech Publications, Clausthal-Zellerfeld, W. Germany, 1980.
- (17) Sondergeld, C. H. and L. H. Estey, J. Geophys. Res., No. 86, pp. 2915-2924, 1981.
- (18) Press, F., "Displacements, Strains, and Tilts at Teleseismic Distances", J. Geophys. Res., No. 70, pp. 2395-2412, 1965.
- (19) Bakun, W. H. and A. G. Lindh, "The Parkfield, California earthquake prediction experiment", Science, No. 229, 619-624, 1985.
- (20) Segall, C. H. and R. Harris, "Earthquake Deformation Cycle on the San Andreas Fault Near Parkfield, California", J. Geophys. Res., No. 92, pp. 10511-10525, 1987.
- (21) Erickson, L., L., "A Three Dimensional Dislocation Program with Applications to Faulting in the Earth", Stanford Univ., Dept. of Applied Earth Science, MS Thesis, November, 1986.

Xiaoqing Sun, H. Reginald Hardy, Jr., and M. V. M. S. Rao

## ACOUSTIC EMISSION MONITORING AND ANALYSIS PROCEDURES UTILIZED DURING DEFORMATION STUDIES ON GEOLOGIC MATERIALS

---

**REFERENCE:** Sun, X., Hardy, Jr., H. R., and Rao, M. V. M. S., "Acoustic Emission Monitoring and Analysis Procedures Utilized during Deformation Studies on Geologic Materials", Acoustic Emission: Current Practice and Future Directions, ASTM STP 1077, W. Sachse, J. Roget, and K. Yamaguchi, Eds., American Society for Testing and Materials, Philadelphia, 1991.

**ABSTRACT:** During a recent detailed study, AE signals generated from rock specimens stressed to failure during uniaxial compressive tests were monitored and recorded on a SONY (AV-3650) videocorder. Various AE parameters, including: amplitude, pulse width, ringdown count, rms level, etc..., were then extracted during videocorder playback. The data acquisition and processing techniques used are discussed in this paper. Amplitude distribution analysis was carried out by dividing the AE events into four categories according to their maximum amplitude. This analysis provides a better appreciation of the overall deformation process.

**KEYWORDS:** AE quiescence, amplitude distribution, b-value, dilatancy point, elliptical crack model, event increment rate, geologic materials, inelastic deformation, microfracturing, precursor of failure, rock, stress concentration, total stress-strain curve

## INTRODUCTION

Inelastic deformation due to microfracturing in rock has been extensively studied in recent years. Such studies have been undertaken, in order to understand, analyze and model the basic mechanisms underlying the development of micro-fracturing processes in rock under various loading conditions. The development of such a physically based model is a critical step in the extrapolation of laboratory results to the long-time scales associated with geophysical phenomena, such as earthquakes and their recurrence intervals, as well as in the engineering analysis of the stability of mine openings and support pillars [1, 2].

Mr. Xiaoqing Sun is a graduate assistant and Professor H. R. Hardy, Jr. is chairman of the Geomechanics Section, Department of Mineral Engineering, The Pennsylvania State University, University Park, Pennsylvania 16802, USA; Dr. M. V. M. S. Rao is assistant director of the National Geophysical Research Institute, Hyderabad, India.

It has been found, through direct observations using the SEM, that microcracks originate from local stress concentrations that occur due to mismatches in elastic properties either at grain boundaries or at natural flaws and pores [3]. With increase in stress, these microcracks begin to nucleate and when the stress concentration becomes critical they propagate in a direction parallel to the greatest compressive stress [4]. Although the rate of crack growth is a strong function of the crack-tip stress intensity factor, it has been observed in recent years that cracks may undergo slow and stable growth (subcritical crack growth) at stresses that are far below those required for fracture initiation, either in the presence of a chemically active environment due to stress corrosion cracking [5] or under cyclic fatigue [6, 7]. Such environmental features are normally encountered in seismically active areas and also in the working panels of underground mines. Therefore more detailed laboratory experiments are necessary to study the development of microfracturing processes in rock, and also to estimate and evaluate microcrack damage in rocks under such conditions.

## EXPERIMENTAL FACILITIES AND PROCEDURES

### Specimens

Specimens of five different rock types were used in the study, namely: Barre Granite and Berea Sandstone from the U. S. and micaquartz schist, dolerite and epidiorite from the Kolar Gold Field, India. Some of the petrographical characteristics of these rocks are listed in table 1.

TABLE 1 -- Petrographical characteristics of the test specimens.

Specimen #	Rock	Location	Texture	Mineral composition
S-11	Berea Sandstone	USA	Sandy	Quartz, Quarzite, Chert, Mica Feldspars, Matrix, Cement and Miscellaneous
G-11	Barre Granite	USA	inequi-granular	Quartz, Potash-feldspar, and Biotite
C-10B-3	Micaquartz Schist	India†	Schistose	no information
N-2A-1	Dolerite	India†	Ophitic	Plagioclase, Augite
M-7B-1	Epidiorite	India†	Randomly arranged flakes of actinolite	Actinolite, Hornblend (relict) and biotite

†Kolar Gold Field region

All specimens were drilled using diamond core barrels, and then cut to proper length by a diamond saw. The Berea Sandstone and Barre Granite cores were of NX size, while the schist, dolerite and epidiorite cores were of AX size. Finally, the ends of each specimen were ground on a surface grinder. The geometry and basic mechanical properties of each rock type are listed in table 2.

### Loading Facilities and Data Acquisition

The MTS loading facility used in the current studies incorporated an electrically programmable, closed loop electro-hydraulic loading system [8] capable of carrying out mechanical tests over a wide range of conditions. The facility also included equipment for monitoring and recording stress, strain, and AE data during testing. An important feature of the MTS loading facility was the ability to program functions such as load, strain, and stroke. In the current study, load control was utilized. A block diagram of the loading and data acquisition system is shown in figure 1.

TABLE 2 -- Geometry and mechanical properties  
of the specimens used in the AE study.

Specimen #	Length cm	Diameter cm	L/D	$\rho$ gm/cc	$\sigma_f$ MPa	Young's Modulus GPa	Poisson's Ratio
S-11	11.30	5.39	2.10	2.175	78.73	11.06	0.19
G-11	11.11	5.39	2.06	2.621	186.39	43.44	0.18
C-10B-3	6.18	3.00	2.06	2.750	100.46	49.94	0.23
N-2A-1	6.18	3.00	2.06	3.075	142.44	105.73	0.28
M-7B-1	6.10	3.00	2.03	3.074	110.00	41.30	0.11

Strain information was obtained by SR-4 strain gages attached to the specimens. An associated Wheatstone bridge completion unit changed the gage resistance variation to an electrical analog voltage. This analog signal was then sent to the  $\mu$ Mac5000 A/D conversion system for digitization, and the digitized signal was then stored in the storage diskette of an IBM PC for further analysis or print out. The various analog voltages were also recorded on associated strip chart recorders (SCR).

The acoustic emission signals were obtained by a transducer attached to the upper loading platen. The transducer (Dunegan/Endevco Model D140-B) was a resonant-type AE transducer with a differential configuration. This transducer had a peak sensitivity value, at approximately 230 KHz, of -75 dB ref 1V/ $\mu$ bar. The transducer output was fed into a Dunegan/Endevco dual-channel AE signal processing system. The overall gain in the system, including the preamplifier, was 85 dB. The signal was then channeled to two different circuits. The first incorporated a threshold detector and related logic circuit, where parametric development of AE ringdown count and count rate was obtained. The analog voltages associated with the ringdown count and count rate were recorded on a dual-channel strip chart recorder, and also sent to the  $\mu$ Mac 5000 A/D conversion system for digitization and storage on diskette. The second circuit incorporated a 20 dB attenuator (for dynamic range matching) and a videocorder. The videocorder provided a 40 dB dynamic range, which could accommodate 0.01-1 V analog electric signals without any difficulty. Calibration showed that the actual dynamic range was still greater than 40 dB. The latter results also verified that this dynamic range was sufficient for the research. The sensitivity of the overall AE signal conditioning at the videocorder was calculated to be:  $-75 + 85 - 20 = -10$  dB ref 1V/ $\mu$ bar.

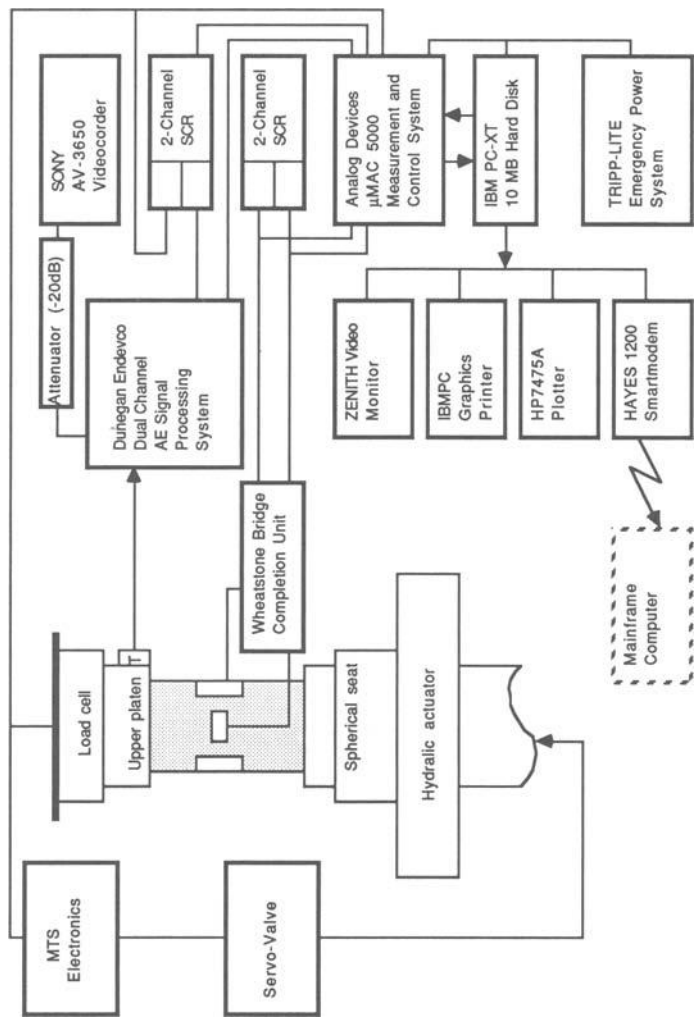


FIG. 1 -- Block diagram of MTS loading facility and the associated PSURML microcomputer-based digital data acquisition system.

The complete data acquisition system was operating throughout the experiments. This allowed the experimental data, including load, strains (longitudinal and transverse), AE ringdown counts, and count rates to be recorded by the computer in digital form; and the associated analog AE signal to be recorded on video tape.

### Outline of Test Procedure

During testing the specimen was loaded between an upper platen and a lower spherical loading seat, as shown in figure 1. The spherical seat was used to ensure automatic load alignment. During the set-up the ability of the spherical seat to rotate freely was checked. All the interfaces in the loading system were then cleaned, and a prepared test specimen was placed between the upper platen and spherical seat. Then the associated strain gages were connected to Wheatstone bridge completion unit, and the AE transducer was attached to the upper platen. A water based acoustic couplant was used to increase the efficiency of AE/MS energy transmission. After the necessary connections were made, the monitoring system was activated. The compressive load was then gradually applied to the specimen, and the stress increased from zero to failure continuously. The overall loading process required approximately 20 minutes, which resulted in a loading rate of about 4 ~ 8 MPa/min. for different specimens. This rate was a little slower than ASTM standards which specifies 5 ~ 15 min. to complete a standard compression test. The acoustic emission data collected during the compression test was then analyzed as discussed in the next section.

### Data Analysis

The various AE parameters, namely: amplitude distribution, AE event pulse width, rms value, etc., were extracted from the AE analog signal recorded on video tape. A block diagram of the playback system used is illustrated in figure 2. The output of the videocorder first passed through a signal gating unit (AET Model 502). This unit was used for selecting particular AE events of interest, and for eliminating undesired signals. The output of the gating unit was connected to an adjustable bandpass filter (Butterworth type) with a pass band from 100 KHz to 470 KHz, which eliminated most of the tape noise. This was followed by a Dunegan 302A signal conditioner, which was used to arise the AE signal level to that required by the distribution analyzer. In the current study a 10 dB gain was used. The AE signals were monitored by a dual-channel oscilloscope connected into the system at points before and after the signal conditioner. Since the amplitude distribution was of major concern in this paper, only the procedures for performing amplitude distribution analysis will be included here.

For amplitude distribution analysis the AE signals to be studied were applied to the input of the amplitude detector. The amplitude detector generates pulses proportional to the logarithm of the peak amplitude of the incoming AE events, and sends them to the distribution analyzer. The analyzer accepts and sorts pulses into 101 memory slots with assigned values of 0, 1, ..... 99, 100. It then updates its 101 segment memory with the numerical value of the measured parameter so that, at the conclusion of the test or at an appropriate test increment (as in the present study), the distribution of the events in the form of an amplitude distribution histogram can be obtained. The contents of the memory can be directly read on an oscilloscope, and permanent record of the output can be obtained by an associated X-Y plotter.

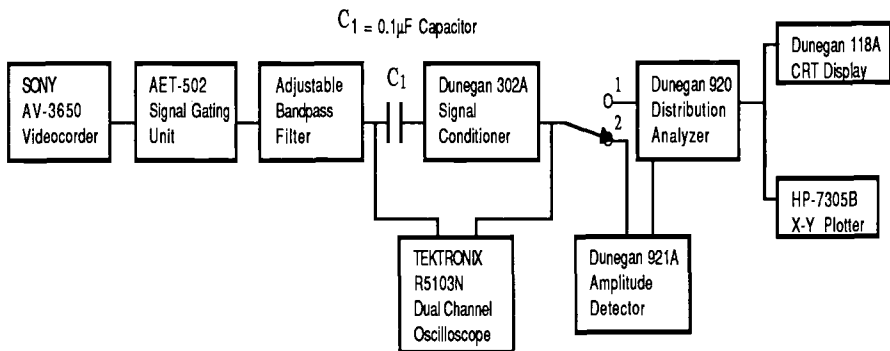


FIG. 2 -- Block diagram of the tape playback system for acoustic emission amplitude distribution analysis.

## EXPERIMENTAL RESULTS

It is interesting to note in the experiments that the general characteristics of the AE amplitude distribution are very similar for different rocks, although they exhibit a variety of different amplitude values. Therefore, in this paper only the AE amplitude distribution data for Berea sandstone is described in detail.

The histogram record of the amplitude distribution of AE events recorded for Berea Sandstone (specimen S-11) during the various stages of rock deformation is shown in figure 3. Histograms are displayed for various stages of increasing stress level. These indicate that pronounced AE activity begins at about 50% of the failure stress and increases gradually with increasing compressive stress. Further the histograms show that there are essentially two groups of events, namely: group I for which the amplitude levels range between 60~80 dB ref 100  $\mu$ V (peak at around 70 dB), and group II for which the range is 80~100 dB (peak at around 90 dB). Events of group I are larger in number at all levels up to 90% of the compressive stress at failure ( $\sigma_f$ ) where they become almost equal to those of group II. When the applied stress increases beyond this point, group I events are significantly reduced in number while a sharp rise in the number of group II events is noted. In general, group I events with lower amplitude (60~80 dB) dominated the early part of the experiment, and group II events with higher amplitude (80~100 dB) overwhelmed the later part. This may infer that the AE sources responsible for the two groups of events have completely different mechanisms. Group I events could be attributed to micro-crack closure and intergranular friction caused by material deformation, whereas the AE events of group II could be ascribed to the development of mini-fractures and the formation of major faults. These deductions will automatically lead to the establishment of the fact that the sudden increase in group II events can be used as a precursor of material failure. Further discussion, in the later part of the paper, will substantiate this point.

The amplitude distribution histograms also show that the total number of AE events decreases when the uniaxial stress is in the range 88.9~100% of the ultimate strength. This is due to an apparent quiescence in AE activity which occurs just prior to specimen failure. A better appreciation of this can be obtained by a closer look at the amplitude distribution record in the vicinity of the failure point as shown in figure 4. At a stress level of 96.3~98% of the failure strength the recorded number of AE events is drastically reduced, and at the 98~100% level there are basically few AE events. In contrast, the characteristics of the AE events in this stage are very different from others.



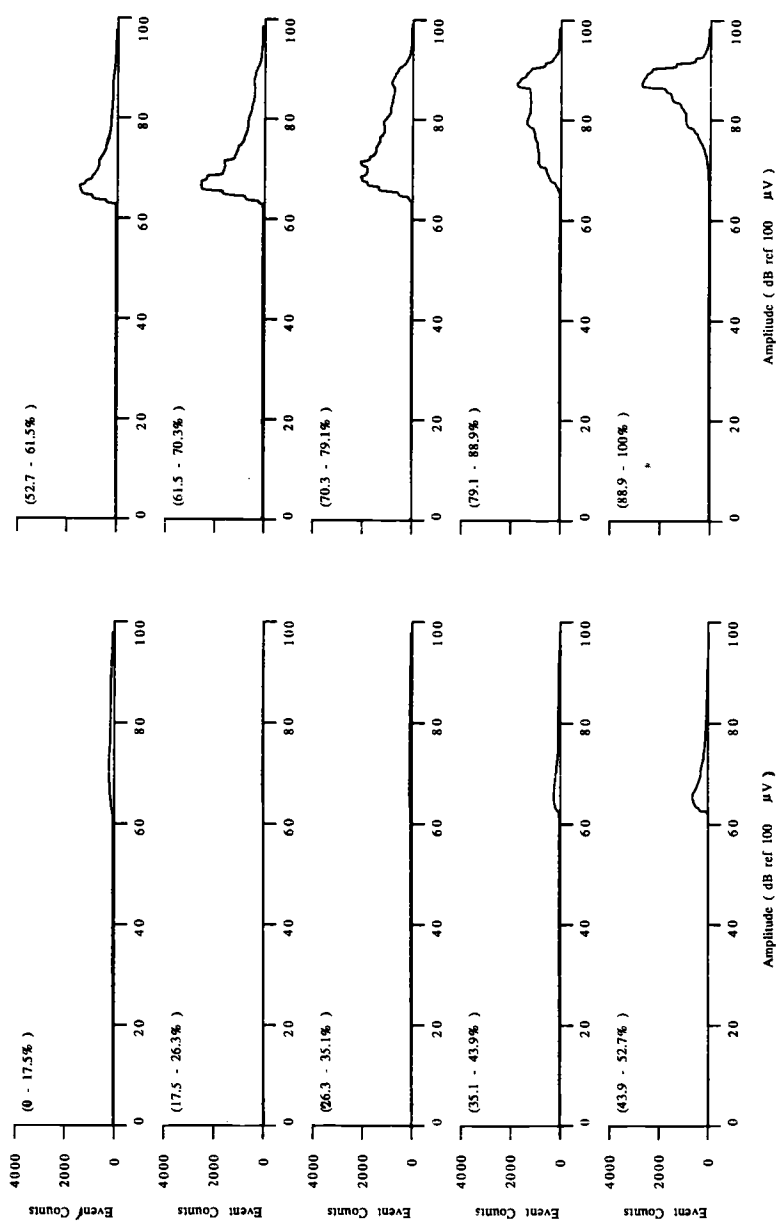


FIG. 3 -- Differential event amplitude distribution shown at increasing stress levels for Berea Sandstone specimen (S-11). [ Values in brackets beside the vertical axis indicate the associated range of applied stress in terms of percentage of failure stress ]

Figure 5 shows a comparison of AE events sampled at about 70% of failure strength (fig. 5a) and at a point just prior to the specimen failure (fig. 5b). Since the AE transducer used in the experiment is of resonant type (natural frequency is about 230 KHz), the difference in frequency cannot be seen clearly, although a difference in frequency content is expected. Direct observation shows that the amplitude of AE events just prior to failure is much higher, generally 2~3 times, than those at lower stress levels. This indicates that the maximum acoustic energy released for events near failure were 4~9 times larger than observed for events occurring at 70% of the failure stress. However, the total energy release in the form of AE just prior to failure was not necessarily greater than that of the previous stage since the rate of AE occurrence was considerably less. Analysis also indicated that the rise time and decay time of AE events increased just prior to failure.

The phenomenon of AE quiescence just prior to material failure has been observed by other researchers [9 - 11]. Brady [10] explained this phenomenon by his inclusion theory which states that an intense concentration of cracks, termed the primary inclusion zone, develops in rock near failure within a localized region in which major fractures are nucleated. One of the major effects of these crack concentrations is to cause an increase in the least principal stress, and this in turn creates a drop in the difference between the principal stresses. The formation of these crack concentrations induces an increase in acoustic emission, as can be seen in the early part of the current experiment. According to this theory, the increase would be followed by a decrease in AE activity which results from the decrease in the principal stress differences, or maximum shear stress, produced by the formation of crack concentrations. This quiescence of AE just prior to failure can be seen in the later part of the current experiment.

A two-dimensional elliptical crack model in an infinite medium [12] can be used to describe the stress drop caused by the inclusion zone. The relation between the stress drop and other parameters is:

$$\Delta\tau = 2U_m \mu / (3D) \quad \text{.....(1)}$$

where  $\Delta\tau$  is the stress drop caused by the inclusion zone,  $U_m$  is the maximum offset of the two points, which were originally at the ends of the shorter axis of the ellipse, along the length direction of the inclusion zone,  $\mu$  is the shear modulus of the material,  $D$  is the length of the inclusion zone.

B-values have also been used to describe the characteristics of the amplitude distribution in AE studies. A simple empirical relation between the number of seismic events and their magnitude was given by Gutenberg and Richter [13]:

$$\log_{10} N(A) = a - bM(A) \quad \text{.....(2)}$$

where  $N(A)$  is the number of events with maximum amplitude  $A$  and greater;  $a$  and  $b$  are constants; and  $M(A)$  is the magnitude of event with maximum amplitude  $A$ , which is defined as:

$$M(A) = \log_{10}(A/A_0) = \log_{10}A - \log_{10}A_0 \quad \text{.....(3)}$$

where  $A_0$  is a constant (i.e. a standard reference level);  $A$  is the maximum amplitude of a particular seismic event of interest. If equations (2) and (3) are combined, it can be seen that:

$$\log_{10} N(A) = a_0 - b \log_{10}A \quad \text{.....(4)}$$

where  $a_0 = a + b \log_{10}A_0$ .

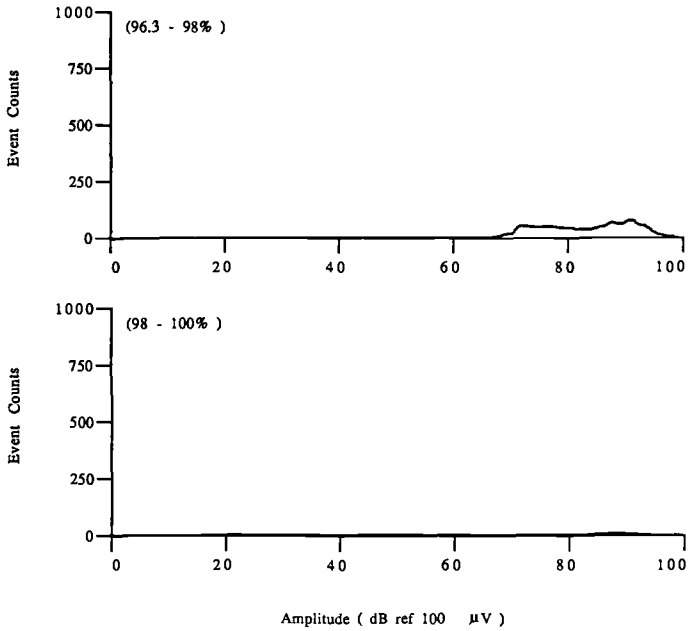


FIG. 4 -- Detailed record of amplitude distribution near failure point in Berea Sandstone (S-11).

(5a)



(5b)

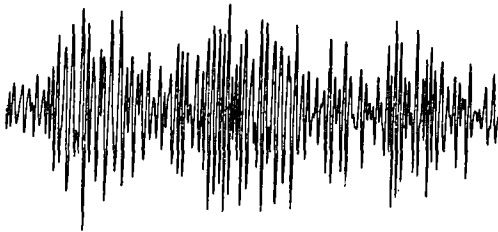


FIG. 5 -- Comparison of AE signals sampled at 70% of the failure stress (5a) with the AE signals sampled just before failure (5b). [Berea Sandstone (S-11)]

Since  $a_0$  is also a constant, which means that no matter what reference is used in magnitude evaluation, the slope of  $\log_{10} N(A)$  vs.  $M(A)$  plot will be invariant. The  $b$ -value is, therefore, a constant. It is essentially the slope of the  $\log_{10} N(A)$  vs.  $\log_{10} A$  curve. Based on the preceding discussion, the equation (2) is, in essence, a linear relation between the logarithm of the number of events as defined above and the logarithm of the maximum amplitude. This empirical relation has been used by Mogi [14], Scholz [15], Pollock [16], and others to describe laboratory scale AE data. The associated  $b$ -values were also found to correlate with the deformation properties of a variety of rock materials.

In the current study, 10000 AE events were taken from each of five stress intervals with initial stress levels of 0%, 20%, 40%, 60%, and 80% of the failure stress. Logarithms of both the maximum AE event amplitude ( $\log_{10} A$ ) and the number of events with amplitude  $A$  or greater ( $\log_{10} N$ ) were found. The  $b$ -value of each of these data groups was obtained by linear regression with respect to equation (4). The  $\log_{10} N(A)$  vs.  $\log_{10}(A/100\mu V)$  plots and the results are shown in figure 6. Note that, as discussed earlier, the use of a reference level  $100\mu V$  will not influence the resulting  $b$ -values. Finally, the  $b$ -values were plotted against the mid-values of respective stress intervals, as shown in figure 7. The observed variation tendency of the  $b$ -values is very similar to that obtained by Scholz [15] for Pottsville sandstone, although the Berea Sandstone has higher  $b$ -values at high stress levels.

By using the concept of mechanism of brittle rock failure proposed by Bieniawski [17], the observed variation of  $b$ -values can be clearly interpreted. For Berea Sandstone the initial crack closure stage extended to more than 20% of the failure stress. At the beginning of this stage, closure of many small cracks were occurring, each being accompanied by the generation of small AE events with very low amplitude. With increasing load, the behavior was dominated by larger cracks or pores being closed, since these required higher associated stresses. Correspondingly, AE events with higher amplitude would be generated, and as a result, the  $b$ -value should decrease. When the deformation proceeded into elastic stage (about 40% of  $\sigma_f$ ), the specimen was relatively "quiet" and the high  $b$ -values observed about this point indicated that most of the observed AE was of low amplitude. Above approximately 60% of the failure stress, with the associated development of stable and unstable fractures, the percentage of high amplitude AE events increased, causing the  $b$ -values to drop gradually in the later stages of the experiment.

The authors feel that it is unrealistic to develop a statistical model to describe the rock behavior, based on the  $b$ -values obtained from this purely empirical relation (equation 2). The decision is based on the following considerations: First of all, a rigid straight line cannot give a satisfactory fit to the complex distribution of  $\log_{10} N(A)$  vs.  $\log_{10} A$  data in many cases. Secondly, the error caused by the regression in a log-log plot will be enhanced exponentially in the linear scale. For example, if an arbitrary point is chosen from stress level  $a$  in figure 6 at  $\log_{10}(A/100\mu V) = 4$ , the real  $\log_{10} N(A)$  at this point is 2.9 which corresponds to 794 events, whereas on the regression line  $\log_{10} N(A) = 2.5$  which is 361 events on the linear scale. Needless to say the situation is even worse at other points. From this point of view, it is felt that the  $b$ -value is only a very rough estimate of the variation tendency of the amplitude distribution, and may well badly distort important aspects of the real distribution.

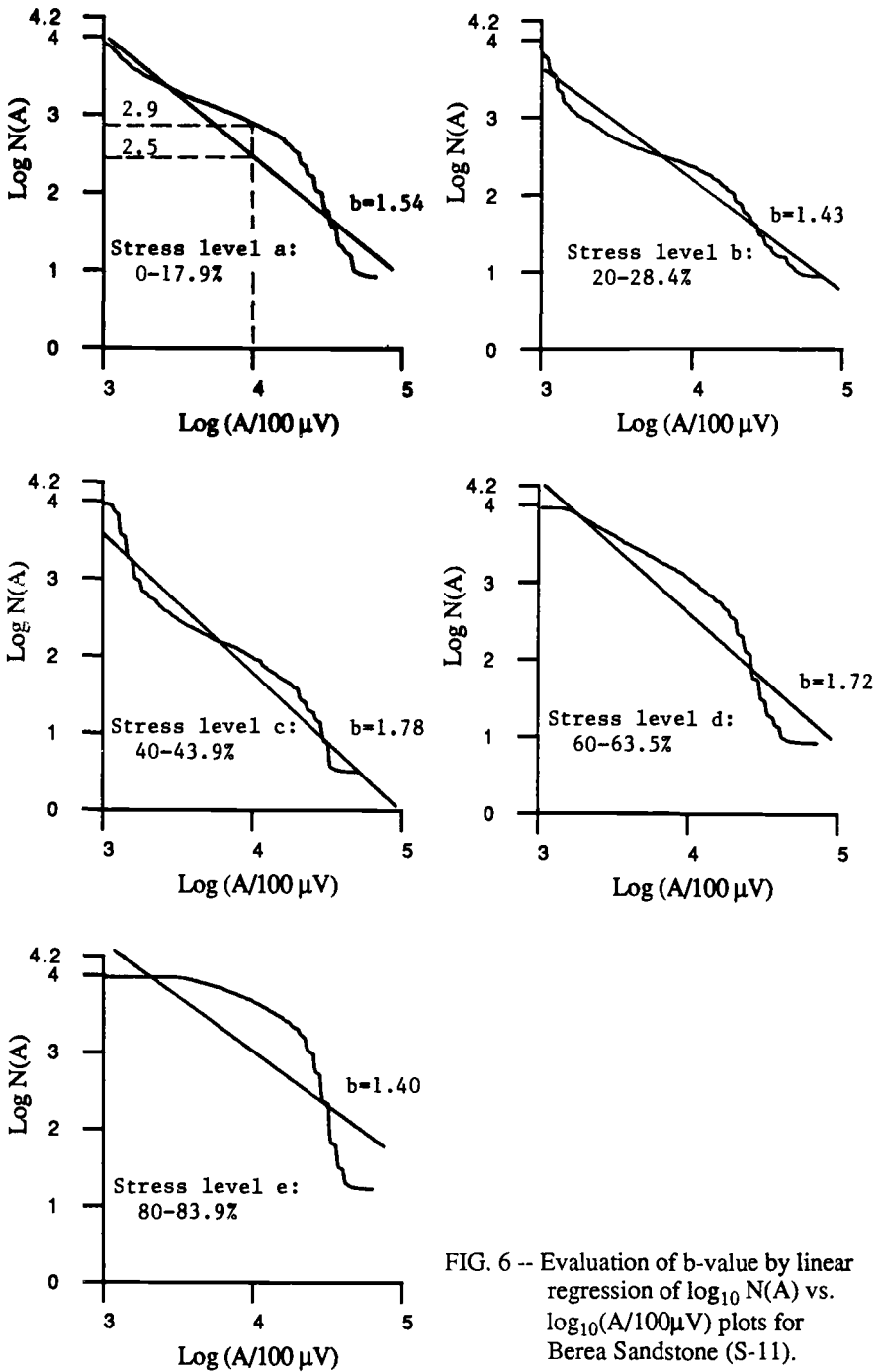


FIG. 6 -- Evaluation of  $b$ -value by linear regression of  $\log_{10} N(A)$  vs.  $\log_{10}(A/100 \mu V)$  plots for Berea Sandstone (S-11).

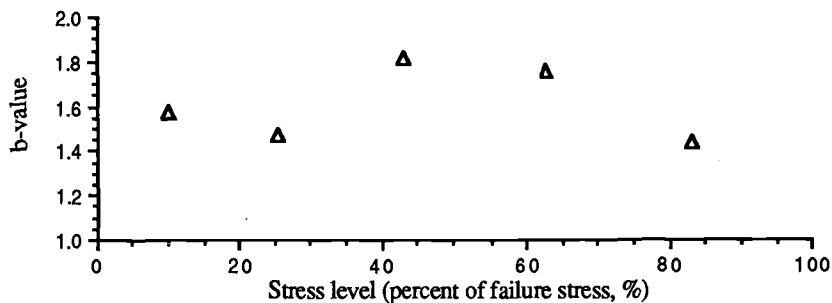


FIG. 7 -- b-value vs. stress level for Berea Sandstone (Specimen S-11).

For more detailed studies, the AE events were categorized on the basis of their amplitude data in four ranges, viz. 60~70 dB, 70~80 dB, 80~90 dB, and 90~100 dB all referred to 100  $\mu$ V. The AE event numbers of the respective segment under the histograms in figure 3 were summarized for the cumulative events. The results are plotted vs. stress level in figure 8. Since the events were recorded and sorted on the basis of amplitude data, it became possible to better characterize the AE activity and also to identify the stress levels at which distinct changes in the development of the micro-fracturing process take place. If careful observation is made relative to the increases of AE events for the four different ranges, one can see that sudden increases of AE event number in the four different ranges occur at different points. As noted acoustic emission event number with 60~70 dB amplitude begin to increase at about 60% of the failure stress,  $\sigma_f$ , events of 70~80 dB amplitude increase in a uniform manner until approximately 90% of  $\sigma_f$ . A sudden increase for 80~90 dB signals occurs at a level above 80% of  $\sigma_f$ , and for the 90~100 dB category at approximately 92% of

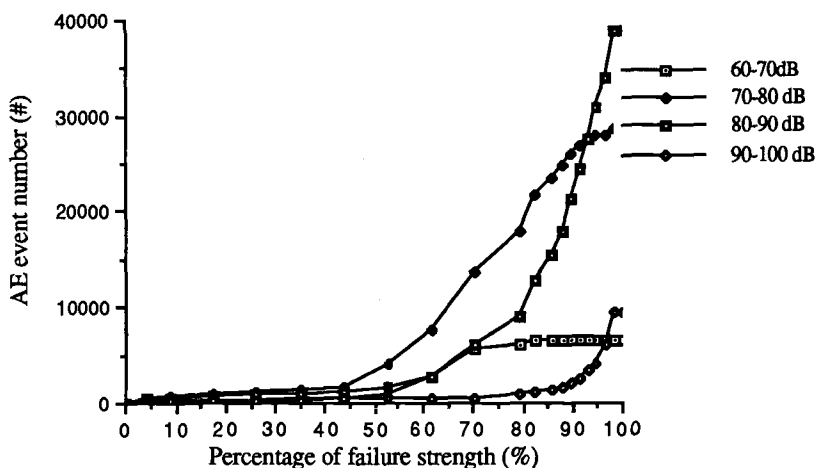


FIG. 8 -- Cumulative AE event number vs. stress levels for various amplitude values for Berea Sandstone (Specimen S-11).

$\sigma_f$ . These results indicate that the AE events with different amplitude ranges have specific characteristics, and could well be related to the different mechanisms active in the overall deformation process.

When the AE total count or AE event number is used in predicting structural failure, one of the major problems is to determine to which point the total number of AE events will indicate the occurrence of significant structure damage. Since in such analyses the AE events with different amplitudes are grouped together, a particular variation in a single amplitude range of AE events can be very easily overwhelmed by the large number of events of different amplitude. Figure 8 shows clearly, that AE events with a 90~100 dB ref 100  $\mu$ V amplitude (group II) exhibit a sudden increase just prior to material failure. This sudden increase of the high amplitude AE signals, at about 92% of  $\sigma_f$ , could well be attributed to the dramatic development of mini-fractures or major faults just prior to specimen failure, and this fact could be a valid precursor of material failure.

To investigate the data further the finite difference quotient ( $\Delta n/\Delta \sigma$ ) was taken for the four curves in figure 8 relative to the applied compressive stress. For individual categories of 60~70 dB, 70~80 dB, 80~90 dB and 90~100 dB events, the finite difference quotients, defined here as event increment rate, are denoted by  $\Delta n_1/\Delta \sigma$ ,  $\Delta n_2/\Delta \sigma$ ,  $\Delta n_3/\Delta \sigma$ , and  $\Delta n_4/\Delta \sigma$ , respectively. These data are plotted versus stress level in figure 9, and approximate the first order derivatives of the functions of cumulative AE event numbers with respect to stress levels shown in figure 8. These data represents the increment of AE event numbers when loading is increased by 1 MPa, illustrating how the AE activities change with a change in the applied stress at a stress level.

If figure 9 is compared with the total stress-strain curve, as shown in figure 10, a number of interesting observations concerning the material behavior can be obtained. Here the overall deformation process has been divided into four stages [17],

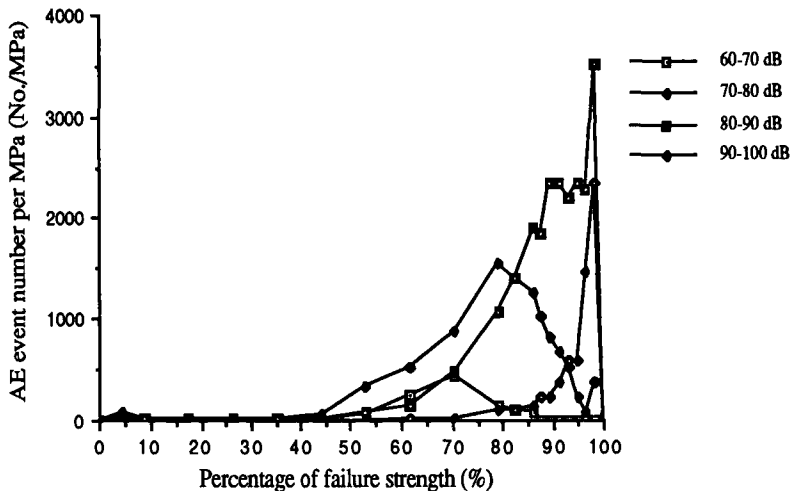


FIG. 9 -- Event increment rate of different amplitude categories vs. stress levels for Berea Sandstone (Specimen S-11).

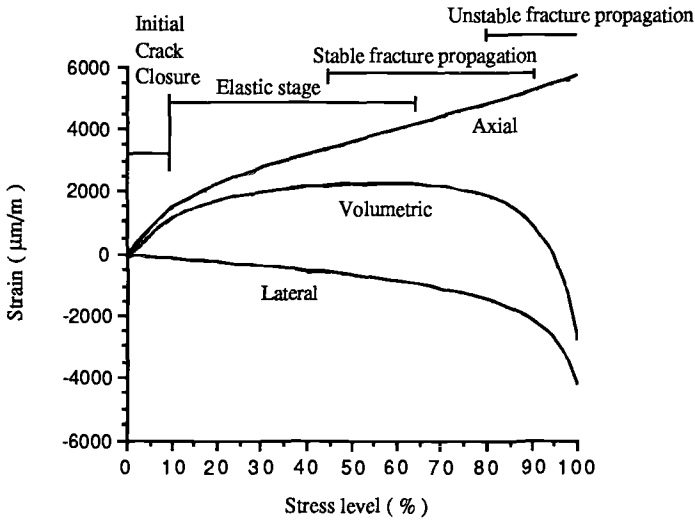


FIG. 10 -- Stress-strain curves for Berea sandstone specimen (S-11).

namely, micro-crack closure, elastic deformation, stable fracture propagation, and unstable fracture propagation. In figure 9, it can be seen that there is only a little change in  $\Delta n/\Delta\sigma$  for stresses in the range 0~10% of  $\sigma_f$  for all the four amplitude categories. This stress range is associated with micro-crack closure within the specimen [18]. For stresses in the range 10% to 50% of  $\sigma_f$ , only a few AE events occurred. On the total stress-strain curve very good linearity can be observed in this range, and since this is the elastic deformation region, little inter-granular sliding or mini-fracture development will occur. This may explain the absence of AE activity in the range of elastic deformation. In figure 10, the volumetric strain begins to drop at a stress level of 60% of  $\sigma_f$ . This is the so-called the dilatancy point, where the volume of the specimen begins to increase. However, figure 9 indicates that  $\Delta n/\Delta\sigma$  for the amplitude range 60~90 dB begins to increase over the range 45~55% of  $\sigma_f$ . This suggests that mini-fracture development starts earlier than 60% of  $\sigma_f$ , when the fractures were not prominent enough to cause dilatancy, but did in fact develop. Up to 80% of the failure stress, where unstable fracture propagation starts,  $\Delta n_1/\Delta\sigma$  starts to vanish,  $\Delta n_2/\Delta\sigma$  has a very sharp turn accompanied by a steep rise in  $\Delta n_3/\Delta\sigma$  and the initiation of a slow rise in 90~100 dB events ( $\Delta n_4/\Delta\sigma$ ). If these phenomena could be attributed to the possible nucleation and growth of mini-fractures, it may further be inferred that these mini-fractures begin to grow rapidly, coalesce and lead to the formation of microscopic faults. In other words, unstable fracture propagation dominates the deformation process around 95% of the failure stress, where  $\Delta n_2/\Delta\sigma$ ,  $\Delta n_3/\Delta\sigma$ , and  $\Delta n_4/\Delta\sigma$  exhibit a sudden increase. Finally AE quiescence occurs, which has been discussed in detail earlier in the paper, and this is followed by the macroscopic specimen failure.



## CONCLUSIONS

The experimental and analytical procedures utilized during the deformation studies on rocks described in this paper have proven to be suitable. Since a number of mechanisms may be active in a deformation process, such as inter- or intra-granular friction, shattering of mineral grains, stable or unstable fracture growth, and major fault development, the observed acoustic emission events may be very different from each other, where the differences could involve amplitude, frequency content, event duration, and so forth. The amplitude distribution analysis introduced in this paper provides a convenient and meaningful way of separating the data into several categories according to their amplitude values. Since the AE events in each category have similar amplitude values and may be associated with similar source mechanisms. Consequently, the analysis of data in terms of event amplitude should provide a better appreciation of the development of particular mechanisms in the overall deformation process. Studies in this area are continuing.

## ACKNOWLEDGEMENTS

The authors would like to acknowledge the Fulbright Foundation, whose fellowship made it possible for Dr. Rao to spend time at the Pennsylvania State University, making this cooperative study possible; Mr. Edward Kimble, Jr., Research Aide in the Penn. State Rock Mechanics Laboratory, provided valuable technical assistance during the experimental phase of the study; and the Department of Mineral Engineering, at the Pennsylvania State University, assisted in the support of the research project.

## REFERENCES

- [1] Costin, L. S., "Time Dependent Deformation and Failure," in Fracture Mechanics of Rock, ed. by Atkinson, B. K., Academic Press, 1987, London, pp.167-215.
- [2] Atkinson, B. K., "Introduction to Fracture Mechanics and Its Geophysical Applications," in Fracture Mechanics of Rock, ed. by Atkinson, B. K., Academic Press, 1987, London, pp.1-26.
- [3] Topponnier, P. and Brace, W. F., "Development of Stress Induced Microcracks in Westerly Granite," International Journal of Rock Mechanics and Mining Sciences, Vol. 13, No. 4, 1976, pp.103-112.
- [4] Kranz, R., "Microcracks in Rocks: a Review", Tectonophysics, Vol. 100, 1983, pp.449-480.
- [5] Waza, T., Kurita, K. and Mizutani, H., "The Effect of Water on Subcritical Crack Growth in Silicate Rocks," Tectonophysics, Vol. 67, 1980, pp.25-34.
- [6] Hardy, Jr., H. R. and Chugh, Y. P., "Failure of Geologic Materials under Low Cycle Fatigue," in Proceedings of the 6th Canadian Rock Mechanics Symposium, Department of Energy, Canada, 1970, pp.33-47.
- [7] Rao, M. V. M. S., "A Study of Acoustic Emission in Granites during Stress-cycling Experiments," Proceedings of National Seminar on Acoustic Emission, Kalpakkam, 1987, India.
- [8] Hardy, Jr., H. R., Stefanko, R., and Kimble, E., "An Automated Test Facility for Rock Mechanics Research," International Journal of Rock Mechanics and Mining Sciences, Vol. 8, No. 1, 1971, pp.17-28.
- [9] Lui, C., Zhang, B., Ma, Y., Jiang, N., and Han, F., "AE Activity and Its Kaiser Effect in Granite Specimens under Uniaxial Compression," Transactions of Stress and Earth Structure of Earth Crust, PRC Bureau of Seismology, 1987, (in Chinese).

- [10] Brady, B. T., "An Investigation of Scale Invariant Properties of Failure," International Journal of Rock Mechanics and Mining Sciences, Vol. 14, No. 3, 1977, pp.121-126.
- [11] Brady, B. T. and Leighton, F. W., "Seismicity Anomaly Prior to a Moderate Rock Burst: A Case Study," International Journal of Rock Mechanics and Mining Sciences, Vol. 14, No. 3, 1977, pp.127-132.
- [12] Starr, A. T., "Slip in a Crystal and Rupture in a Solid Due to Shear," Proceedings of Cambridge Philosophical Society, Vol. 24, 1928, pp. 489-500.
- [13] Richter, C. F., "Elementary Seismology," W. H. Freeman and Company, San Francisco, 1958, pp 338-345, 359-361.
- [14] Mogi, K., "Study of Elastic Shocks Caused by the Fracture of Heterogeneous Materials and Its Relations to Earthquake Phenomena," Bulletin of Earthquake Research Institute, Vol. 40, Tokyo, Japan, pp.125-173.
- [15] Scholz, C. H., "The Frequency-Magnitude Relation of Microfracturing in Rock and Its Relation to Earthquakes," Bulletin of the Seismological Society of America, Vol. 58, No. 1, 1968, pp.399-415.
- [16] Pollock, A. A., "Acoustic Emission Amplitude Distributions," International Advances in Nondestructive Testing, Vol. 7, 1981, pp.215-239.
- [17] Bieniawski, Z. T., "Mechanism of Brittle Fracture of Rock," International Journal of Rock Mechanics and Mining Sciences, Vol. 4, No. 4, 1967, pp.365-430.
- [18] Sun, X., "A Non-constant Parameter Rheological Model for Time-dependent Behavior of Geologic Materials," MS Thesis, Department of Mineral Engineering, The Pennsylvania State University, 1986, pp.142-145.

Stephen D. Falls, Tom Chow, R. Paul Young, and David A. Hutchins

## ACOUSTIC EMISSION ANALYSIS AND ULTRASONIC VELOCITY IMAGING IN THE STUDY OF ROCK FAILURE

---

**REFERENCE:** Falls, S. D., Chow, T., Young, R. P., and Hutchins, D. A., "Acoustic Emission Analysis and Ultrasonic Velocity Imaging in the Study of Rock Failure," Acoustic Emission: Current Practice and Future Directions, ASTM STP 1077, W. Sachse, J. Roget, and K. Yamaguchi, Eds., American Society for Testing and Materials, Philadelphia, 1991.

**ABSTRACT:** Two methods were used to examine the effects of stress changes and microfracture activity during Brazilian disk tests performed on Lac du Bonnet Granite. Acoustic emission analyses examining source locations and source mechanisms led to two main findings. Firstly, the sources were clustered in the regions with the greatest difference between the minimum and maximum principal stresses. Secondly many sources involved some degree of shear motion. This indicates that dilatancy in these rocks may be largely controlled by hybrid shear-tensile microfractures. Ultrasonic tomographic imaging of p-wave speed was the second technique used to study stress induced effects on the samples. The images created have successfully delineated areas of the rock with high stress concentrations.

**KEYWORDS:** ultrasonic imaging, difference tomography, acoustic emission, source location, source mechanism, Brazilian tests

## INTRODUCTION

According to Griffith crack theory, formation and opening of tensile microfractures throughout a rock precedes the failure. There is evidence to suggest that microfractures eventually cluster and coalesce to form failure surfaces [1]. Microfracture activity is generally associated with acoustic emissions. The changing state and concentration of microfractures causes changes in the elastic properties of the rocks, thus changing the velocity and attenuation of waves propagating through the rocks. Our study, has taken advantage

Mr. Falls and Professor Young are at the Rock Physics and Engineering Seismology Laboratory, Department of Geological Sciences, Queen's University, Kingston, Canada K7L-3N6. Mr. Chow and Professor Hutchins are with the Department of Physics at Queen's University.

of these relationships by using acoustic emission analyses and ultrasonic tomographic studies to examine microfracture processes occurring within intact rock. The results are interpreted with regard to theoretically determined stress conditions and the location of the eventual failure surface.

Using full waveform acoustic emission analyses with an array of sensors, some important parameters may be determined. From the polarities of p-wave first motion, the type of microfracture and its orientation can often be determined [2]. Knowing this, the principal stress directions can be estimated. Source locations can also be calculated. With this information, the spatial and temporal variation in microfracture activity can be monitored. These techniques have been used extensively in seismic and microseismic studies for many years [3]. The studies reported in this paper used an array of only four sensors. With these, acoustic sources were located in time and space, and the sources were characterized into three mechanism types.

Ultrasonic tomographic imaging is a technique used to map the wave speed fields and possibly wave attenuation fields on planes within rocks. Data for this technique are obtained by actively inducing seismic sources at various locations around a plane within the rock and recording waveforms at an array of sensors within the same plane. In these experiments the same transducers are used as both transmitters and receivers of ultrasonic waveforms. Travel time information between sources and receivers are picked from the recorded waveforms and used as path integrals. Tomographic inversion schemes such as the simultaneous iterative reconstruction technique (SIRT) are used to invert the path integral data to obtain a tomogram of the slowness ( the inverse of velocity ) within the plane [4]. Slowness tomograms can be converted to wave speed images. Because wave speed is sensitive to changes in stress concentration associated with the closure of microfractures in some directions, and formation of fractures in other directions, these images can be used to map stress induced changes in the character of the rocks.

By applying these ultrasonic techniques to the study of failures resulting from various types of applied loads, a great deal can be determined about the mechanisms by which such failures take place in rocks. These techniques may have practical applications in both attempts to prevent failures, and attempts to maximize the efficiency of rock breaking techniques.

#### EXPERIMENTAL SET-UP

A series of experiments using the above techniques have been undertaken on Brazilian disks 5 cm thick and 19.6 cm in diameter. The samples are Lac du Bonnet granite from the Atomic Energy of Canada Limited Underground Research Laboratory in Pinawa, Manitoba. One of the reasons for using Brazilian disk samples in the experiments is that we are limited to four channels of recording. It was felt that source locations could best be solved unambiguously for a two dimensional geometry. With a two dimensional geometry, three unknowns must be solved rather than four in the three dimensional case. This allows some tolerance for

experimental error. The tabular nature of the disk samples approximates a two dimensional geometry. A further reason for using the Brazilian disks is that they fail in a predictable location and their stress patterns can be calculated analytically. This allows for optimization of the positions of arrays of sensors for both acoustic emission and tomographic imaging data acquisition.

A schematic diagram of the experimental set-up for these preliminary tests is shown in Figure 1. The loading frame is omitted from this diagram. For acoustic emission recording, the waveforms are captured using Panametrics ultrasonic transducers. These give a virtually flat frequency response to 1 MHz. The output voltage is proportional to particle velocity. The signals go through Cooknell pre-amplifiers with a 10 kHz high pass filter, and are recorded on a Nicolet 4094 digital oscilloscope with 72 dB dynamic range and a 10 MHz sampling frequency. Between pre-amplification and recording, the signals are passed into a trigger box to trigger recording in the Nicolet if any of the four channels surpasses a threshold amplitude. Pre-trigger memory in the Nicolet allows full waveforms to be captured. Because of the time required to write captured events to the Nicolet disk drive, there is a considerable dead time, about one second per event. Acoustic emission events can occur at a much greater frequency than this, especially as failure approaches. To get more information about such parameters as the rate of events, a Physical Acoustics Corporation LOCAN acoustic emission analyzer is used to continuously monitor A.E. events. This instrument can monitor up to several hundred events per second on four channels.

At various stages throughout the test, acoustic emission monitoring is suspended and tomographic scans are conducted. For tomographic imaging, sixteen ultrasonic pin transducers are fixed to the sample. These are connected to a computer controlled multiplexer box which selects four of the channels to be amplified and then recorded on the Nicolet. Data recording is also controlled by the computer, an IBM PS/2 Model 30 microcomputer. A Panametrics ultrasonic pulser may also be connected to the multiplexer such that one pin transducer can be selected as an ultrasonic source. Using this set-up a scan of the sample with each transducer transmitting a signal to all of the other transducers can be rapidly and automatically conducted. Platen displacement and load are also monitored using the computer controlled autonomous data acquisition unit (ADU).

## DATA PROCESSING

Acoustic emission data are analyzed in several ways. Initial analyses include first arrival time picking and determinations of first motion polarity for each of the four waveforms recorded per event. Source location is done using the seven point approximation method (SPAM) [5]. This method is employed rather than a direct solution because the algorithm allows one to minimize the error independently on each channel. If there is obvious noise on any one channel, its error criteria may be relaxed. Furthermore, velocity fields can be entered into the program to give a more realistic model than a homogeneous velocity field.

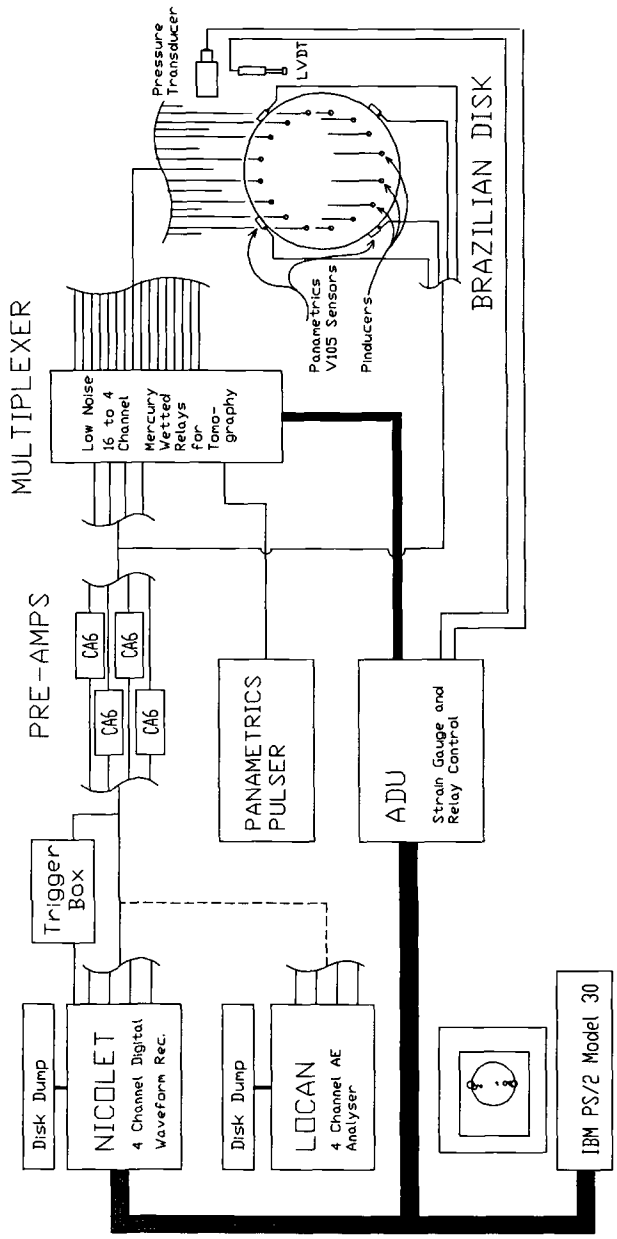


FIGURE 1 Schematic diagram of instrumentation for ultrasonic tomographic imaging and acoustic emission experiments.

The polarities of first longitudinal wave motions are used to differentiate between events caused by purely tensile mechanisms, closure mechanisms, and those with some component of shear motion. The sense of motion at the source is indicated by the polarities of first motion detected at the transducers. Different event mechanisms have distinctive directivity functions in terms of amplitude and polarity of the first longitudinal wave motion in different directions. With only four transducer locations, the events cannot be fully characterized other than to group them into these three types of mechanisms. These different types of sources can be compared with respect to spatial and temporal occurrence.

In this study, tomographic imaging is accomplished by determining the difference in travel time for each ray-path through the sample between different states of stress, and imaging these. Many studies have shown that there is generally some error involved in picking arrivals based on the first break in amplitude. Analysis of the errors associated with our initial first break picks indicated that the errors might overwhelm the changes in travel time that we were trying to detect. Total velocity images were created using first break arrival time data. The resulting models showed large velocity variations showing no coherent patterns. While there was considerable variation between images produced at different load levels, the variations appeared to be quite random, with no correlation to the patterns of applied stresses. Having determined that velocity models created using first break picks were not a reliable means of monitoring stress induced changes in the rock, a second approach was taken. Rather than using first break picks directly, we selected a window around the first pulse of each waveform from a scan and then used a cross correlation method to compare each waveform with its equivalent from a scan at higher stress. This gave us a time difference value for each receiver-transmitter pair between two stress states. With these data, images of the difference in wave speed between two stress states were created directly. This difference tomography method proved far superior to comparisons of tomograms from first break picks. The method has been used with longitudinal wave data. In the future, similar analyses will be done with shear wave travel time differences. Furthermore, attenuation of both shear and longitudinal waves will be analyzed and used as data in tomographic imaging algorithms.

The SIRT program models the image plane as a 15 by 15 pixel grid. Each square of the grid is modelled as having constant wave speed. The images created are a best fit to the data given the starting model. Results are often slightly smoothed and anomalies somewhat smeared out because of relatively low resolution.

In media with inhomogeneous velocity fields, ray bending occurs. Ray tracing schemes can be incorporated into the tomographic imaging routines to overcome these effects. However, our studies, and those of others [6], have shown that ray bending has a negligible effect on models produced using tomographic imaging unless the variation in velocity is greater than about 10 percent of the mean velocity. The changes that we encountered in this study were much less than this. Therefore, to simplify matters, longitudinal waves were assumed to travel in straight paths between sources and receivers in this study.

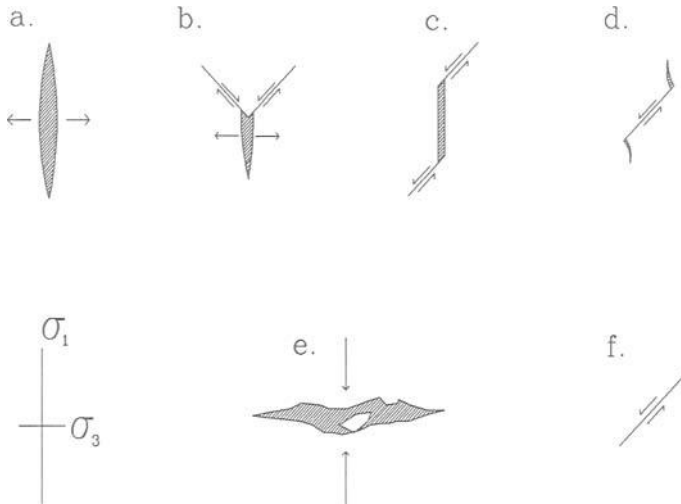


FIGURE 2 Mechanisms associated with acoustic emission signals. a. is a simple tensile microfracture mechanism. b., c. and d. are mixed shear tensile microfractures. e. is a crack closure involving the crushing of interstitial material in the microfracture. f. is a simple shear type event. Note that  $\sigma_1$  is taken as the maximum compressive stress.

## RESULTS

The samples failed in tension under an applied load of approximately 10,000 kg. Calculating the tensile strength of the samples gives a value of  $7 \text{ MN/m}^2$ . Longitudinal wave first motion analysis of the acoustic emission data revealed three types of acoustic sources. A variation in source type with both time and spatial distribution within the samples was observed. Closure mechanisms with first motion toward the source in all measured directions may be associated with crushing of grains or the closure of microfractures. Batzle et al. [7] report that there are often interstitial dislodged grains within microfractures which would inhibit closure until these grains crushed (Figure 2e.). This might be a more reasonable explanation for an event with first motion toward the source in all directions than a simple crack closure. Such a mechanism would involve a sudden release of strain energy, unlike the more gradual crack closure. Sources interpreted as tensile microfracture formation or opening (Figure 2a.) have first motions away from the source in all directions.

One of the most common types of events is characterized by motions away from the source in some directions and toward it in other directions. These events are interpreted as having some degree of shear motion. Because the Brazilian test leads to indirect tensile failure within the samples, it was anticipated that tensile microfracture



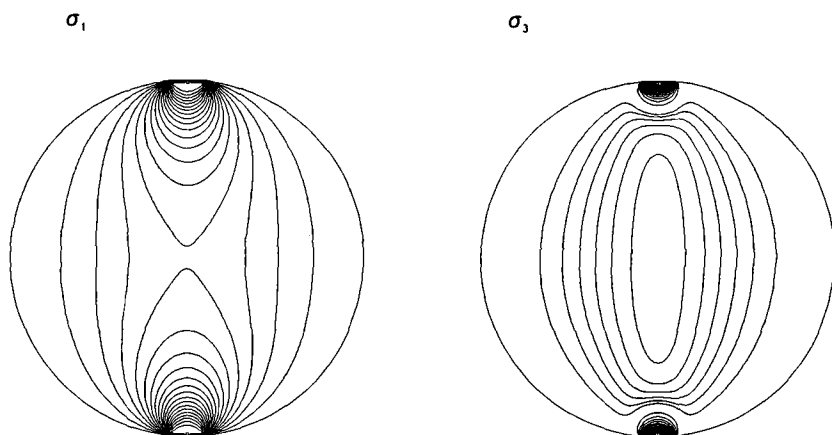


FIGURE 3 Normalized principal stress isovalues for the maximum compressive principal stress ( $\sigma_1$ ) on the left, and the minimum principal stress ( $\sigma_2$ ) on the right.  $\sigma_1$  is compressive everywhere with highest stresses concentrated at the sample-platen interfaces (top and bottom).  $\sigma_2$  is strongly compressive in the tightly contoured areas around the sample-platen interfaces, and tensional everywhere else. The strongest tensional  $\sigma_2$  stresses are at the centre of the disk. These patterns are based on an analytical solution [9].

deformation would dominate. We postulate that the shear type mechanisms we detect may not all be simple shear motion on a plane (Figure 2f.), but a part shear part tensile mechanisms such as those suggested by Brace et al. [8] (Figure 2b,c,d). The relative abundance of randomly-oriented pre-existing microfractures in these rocks might result in these mixed shear-tensile microfractures dominating pure tensile events. Because only four sensors are used in these tests, very little more detail can be directly determined about the sources other than grouping them into the three general classifications.

Before examining the source locations of these event types, it will be interesting to look at the analytically derived principal stress fields within the disk. Figure 3 shows the isovalue patterns as calculated based on the analytical solution of Hondros [9]. The maximum compressive principal stress ( $\sigma_1$ ) is most concentrated at the sample-platen contacts. It is interesting to note however, that the minimum principal stress ( $\sigma_2$ ) is also compressive in this region, almost equalling the maximum stress. This means that the sample is effectively experiencing a confining pressure near the platens. Such a stress regime is not conducive to tensile microfracturing. The  $\sigma_2$  stress becomes tensional moving toward the centre of the disk. In the region where  $\sigma_1$  is still fairly strong, and  $\sigma_2$  is tensional, shear type microfracture activity is more likely to occur. Such activity depends upon a high stress difference. Localized variation in stresses due to inhomogeneities will also affect the microfracture activity. Such variations cannot be predicted with the model solution used.

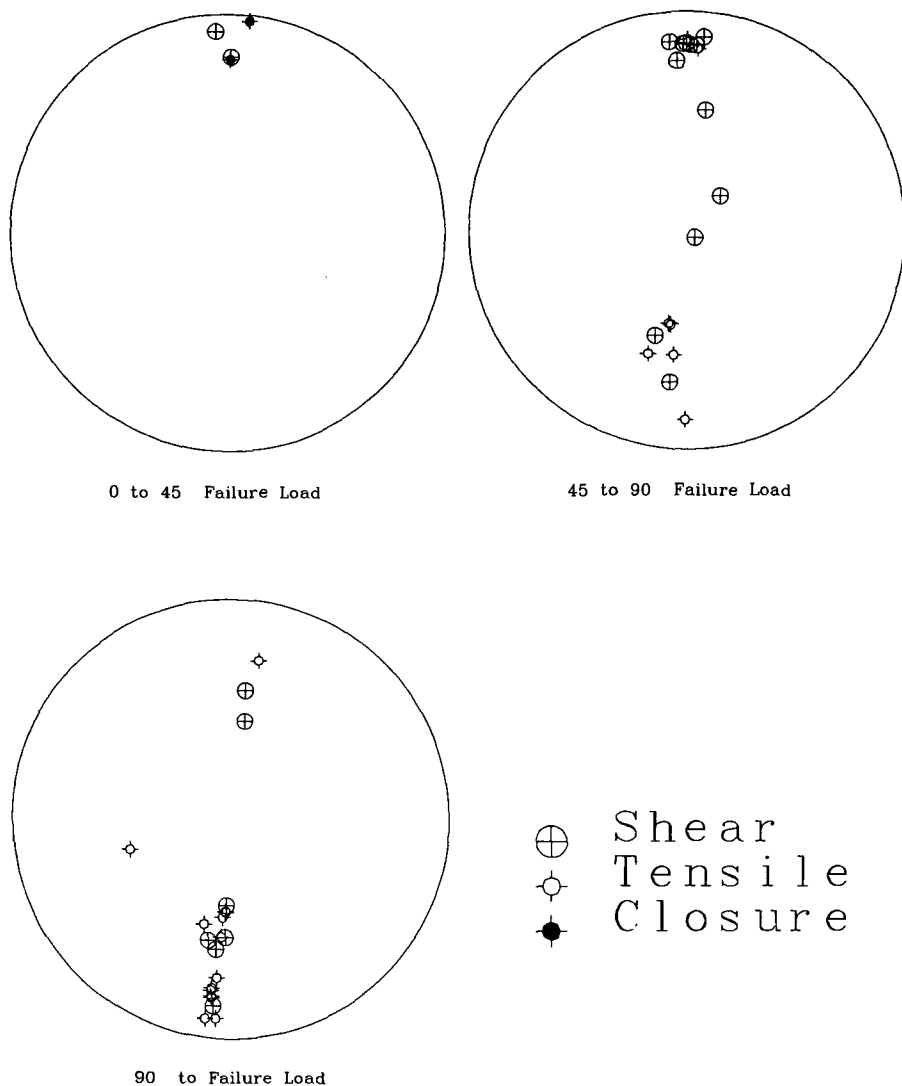


FIGURE 4 Acoustic emission source locations from different stages during the tests. The loading direction is top to bottom of the page in all figures. Note the predominance of shear type events.

Figure 4 shows the spatial variation of sources at various stages in the loading history of the sample. For each set of source locations, an updated velocity model, appropriate to the stress conditions while the AE events occurred, was used in the location program. Only events with calculated errors in source location of less than 0.5 cm are plotted. This error limit is based on travel time residuals between the true data

and the times calculated for modelled event locations and velocity field. It is possible that the true location error is greater than the quoted level. As we would expect from the stress patterns, there is very little acoustic activity from the region that is experiencing confining pressure at the sample-platen contacts. The samples were prepared with the contact points ground flat as suggested by Hondros [9], and a layer of teflon was placed between the sample and the platens. These precautions were taken to minimize frictional noise at the contacts.

Tensile and shear type source mechanisms occur in approximately equal abundance. There are very few crack closure events except early in the loading history of the sample, where stresses result in a confining pressure. Brace et al. [8] postulated that mixed tensile-shear mechanisms may dominate pure tensile events during dilatancy. Assuming that most of our mixed polarity events result from such a mechanism, our results seem to concur with their's. We suspect that this is the main shear type event being recorded. If this is true, it will have implications on the fracture process as a whole. Such an event type relies on a high difference between the maximum and minimum principal stresses more than a pure tensile microcrack event, which relies on a relatively high tensional stress. Ideally in a Brazilian disk test, failure should initiate at the centre of the disk. In this region the  $\sigma_1$  stresses are most tensional, but the compressive  $\sigma_3$  stress is relatively low. Our tests indicate a clustering of events just in from the sample-platen contacts, even just prior to failure. Unfortunately, our recording rate is not able to capture all the events in the critical final stages of the test because of the time required to write events to a storage device. However, the region where we see events clustering is the region with the greatest difference between  $\sigma_1$  and  $\sigma_3$ . This suggests that this is the region where failure is initiating in our tests because it is a favourable environment for the formation of mixed shear-tensile microfractures, which dominate the deformation.

It is important to make some distinction between the recorded A.E. activity, and the microfracture activity as a whole. Acoustic emissions result from sudden releases of strain energy. Some crack opening and closure mechanisms, including sub-critical fracture, may involve a gradual strain. Furthermore, crack closures may often be accompanied by frictional sliding, possibly resulting in a mixed polarity radiation pattern. The relative amplitudes of signals associated with different mechanisms may also vary. The amplitude threshold used to trigger recording could have caused a bias in the types of events recorded. Therefore, it might be erroneous to take our results as completely representative of the microfracture activity as a whole.

The tomographic images show the differences in longitudinal wave speed between an unstressed state, and different stages throughout the loading history of the samples (Figure 5). They were obtained at about 45 and 90 percent of the ultimate failure strength of the samples. They clearly show an increase in wave speed in the regions of the sample near the platens. There does not appear to be a strong difference in the pattern between the two loaded states. However, change is significantly magnified at the higher stress state. The mean longitudinal wave speed in the samples was about 4400 m/s prior to loading. The maximum

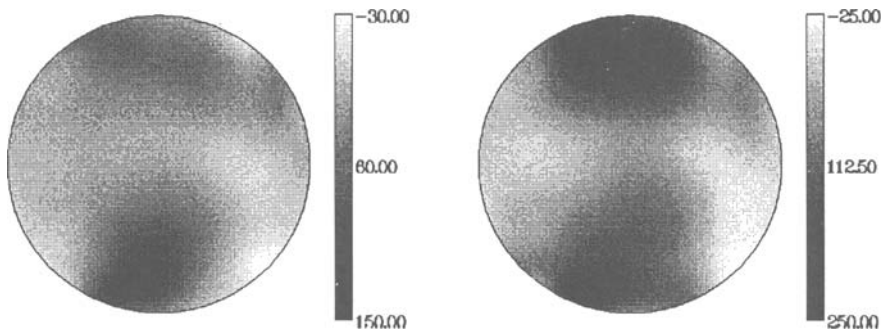


FIGURE 5 Wave speed difference images form showing the difference in wave speed (m/s) in a test sample between no load and 45% of the failure load on the left, and no load and 90% of the failure load on the right.

variation at the highest stress is about a 6 percent change. This is compared to a maximum 3.5 percent variation at the lower stress level. An expected wave speed decrease as failure approaches was not detected. This may be a result of running the final scan too soon before failure. Many indicators of failure, including accelerated rates of acoustic emissions do not occur until after about 90 percent of the ultimate failure strength of the samples in uniaxially loaded samples [10]. A similar phenomenon seems to occur in these tests.

## CONCLUSIONS

Both techniques have been successful in determining where stresses are acting and causing deformation. Acoustic emission analyses have been used to differentiate between three main types of source mechanisms: tensile; closure; and mechanisms involving shear. These shear mechanisms were observed in greater abundance than expected for Brazilian tests in which failure is thought to occur by tensile fracture. Shear type mechanisms were as abundant as simple tensile microfracturing. These shear mechanisms are thought to result mostly from hybrid shear-tensile microfractures. The relative abundance of randomly-oriented pre-existing microfractures may facilitate the formation of these mixed shear-tensile events rather than pure tensile Griffith type cracks. In these samples of Lac du Bonnet Granite, mixed mode microfractures appear to be the predominant means of dilatancy.

Clustering of acoustic sources occurred throughout the tests. This phenomenon appears to be directly related to the differential stress levels. The differential stress is highest just inward from the sample-platen contacts. At all stress levels, these were the areas where the events are most strongly concentrated. In some instances macroscopic failure has been seen to initiate in these regions. This may be the case in these tests, although more strain data would be required to verify this.

Ultrasonic difference tomography has shown a strong agreement with the theoretical stress fields expected in the rock. The cross correlation method of determining differences in travel times between stress states has yielded much more precise data for tomographic imaging than other methods of travel time estimation. The images have discerned very slight variations in longitudinal wave speed difference. The maximum speed change detected was under four percent of the mean velocity for the lower stress change. The images have also shown a trend of increasing wave speed with increasing stress.

#### ACKNOWLEDGEMENTS

The authors wish to extend their appreciation to their co-workers at Queen's University, especially Mr. Dion Jansen who wrote the tomography programs and was instrumental in initiating the idea of difference tomography. NSERC and Queen's University must be thanked for financial support. Thanks to A.E.C.L. for providing test samples.

#### REFERENCES

- [1] Scholz, C.H., "Experimental study of the fracturing process in brittle rock," J. Geophys. Res., Vol. 73, 1968, pp. 1447-1454.
- [2] Ohtsu, M., "Source Mechanism and Waveform Analysis of Acoustic Emission in Concrete," Journal of Acoustic Emission, Vol. 1, No. 2, pp. 103-112.
- [3] Gibowicz, S.J. "The Mechanism of Seismic Events Induced by Mining: A Review", Proceedings of the 2nd International Congress on Rockbursts and Seismicity in Mines, University of Minnesota, 1988.
- [4] Censor, Yair, "Finite Series-Expansion Reconstruction Methods," Proceedings of the IEEE, Vol. 71, No. 3, 1983, pp. 409-419.
- [5] Deckman, G. H., and Sun, M.-C., "Iterative Approximation Techniques for Microseismic Source Location," United States Bureau of Mines Report on Investigations 8254, 1977, 23p.
- [6] Peterson, J.E., Paulsson, B. N. P. and McEvilly, T.V., "Applications of algebraic reconstruction techniques to crosshole seismic data." Geophysics, Vol. 50, 1985, pp. 1566-1580.
- [7] Batzle, M. L., Simmons, G., and Seigfried, R. W., "Microcrack Closure in Rocks Under Stress: Direct Observation," Journal of Geophysics Research, Vol. 85, No. B12, 1980, pp. 7072-7090.
- [8] Brace, C. H., Paudling, B. W. Jr., and Scholz, C.H., "Dilatancy in the Fracture of Crystalline Rocks," Journal of Geophysical Research, Vol. 71, No. 16, 1966, pp. 3939-3953.
- [9] Hondros, G., "The Evaluation of Poisson's Ratio and the Modulus of Materials of a Low Tensile Resistance by the Brazilian (Indirect Tensile) Test With Particular Reference to Concrete," Australian Journal of Applied Science, Vol. 10, 1959, pp 243-268
- [10] Walsh, J.B., "Precursors to rock failure observed in laboratory experiments." Proceedings of the 1st International Congress on Rockbursts and Seismicity in Mines, Johannesburg, 1982, SAIMM, Johannesburg. pp. 269-275.

## **Applications to Composite Materials**

## FRACTURE MECHANISM STUDIES OF A CARBON FIBER-PEEK COMPOSITE BY ACOUSTIC EMISSION

---

REFERENCE: Ono, K., Jeng, J.S., and Yang, J. M. "Fracture Mechanism Studies of A Carbon Fiber-PEEK Composite by Acoustic Emission," Acoustic Emission: Current Practice and Future Directions, ASTM STP 1077, W. Sachse, J. Roget and K. Yamaguchi, Eds., American Society for Testing and Materials, Philadelphia, 1991.

ABSTRACT: Failure mechanisms of a thermoplastic matrix composite, a carbon fiber reinforced PEEK (Polyetheretherketone) matrix laminate, were studied. Three-point bending, ENF (end-notched flexure), and tensile tests were used. During each test, load and acoustic emission (AE) parameters were recorded. Several AE parameters of processed AE events were analyzed to distinguish different fracture modes, such as fiber breakage, delamination, matrix cracking, and splitting (longitudinal matrix cracking). The features such as peak amplitude, signal duration and energy distributions of AE events as well as a plot of peak amplitude vs. signal duration were used, but clear discrimination of different mechanisms by AE alone was difficult as the distributions overlapped. In conjunction with other findings, the first two mechanisms show certain features that may be useful in isolating the failure processes.

KEYWORDS: acoustic emission, thermoplastic, polyetheretherketone, fiber composites, carbon fibers, fracture

Thermoplastic polymers (such as PEEK and PPS) have been shown to offer several advantages over conventional thermoset polymers as matrix materials for advanced composites [1-3]. These advantages include lower manufacturing costs due to faster fabrication rates, infinite shelf life, reprocessing, improved repairability, better moisture resistance, as well as improved fracture and impact damage tolerance. However, the ability of thermoplastic structural composites to be tolerant to damage induced by service usage remains one of the primary concern in composite applications.

Several fracture mechanisms may occur in a fiber reinforced composite during its loading history. Four main modes of fracture have been found in structural composite materials. They are fiber breakage, matrix cracking, splitting (or matrix cracking along fibers), and delamination. Although the predominance of each fracture mode will be determined by specimen geometry and loading conditions, delamination is the most prevalent life-limiting failure mechanism in advanced composite materials. Thus, to ensure the structure reliability, it is necessary to understand the nature of the failure in the thermoplastic composites and to distinguish between unlike fracture types.

The authors are with Department of Materials Science and Engineering, University of California, Los Angeles, California 90024-1595 USA. Mr. Jeng is now at Johnson Matthey Electronics, San Diego, CA 92131.

A non-destructive inspection procedure is needed to assure that the damage monitoring can be achieved successfully. Acoustic emission (AE) has been verified to be one of a few acceptable techniques for detecting failures in laminated composites [4]. The main goal of the AE technique is to determine if a specific signal was due to delamination or other failure types. In this paper, both distributions of standard AE parameters and plots of peak amplitude vs. signal duration are obtained to assess the damage monitoring capability of AE on a thermoplastic composite.

## EXPERIMENTAL PROCEDURES

To isolate dominant failure modes, only unidirectional laminated samples were employed. A thermoplastic matrix composite, carbon fiber reinforced polyetheretherketone (C/PEEK) was used. 16-ply C/PEEK (AS4/APC2) composite sheets were obtained from ICI, Inc. and the thickness of these sheets was about 1.8 mm.

All of the specimens with nominal width of 13 mm were cut from the sheets using a diamond blade saw and the edges of the samples were polished by 240 grit sandpapers followed by 400 and 600 grit sandpapers. Tensile samples, 0-degree and 90-degree to the fiber direction, were 250 mm long and had 75 mm long PVC endtabs glued on to each end. Three-point bending samples were 75 mm long without any notch. ENF specimens were precracked by wedging to open one end of unnotched three-point bending samples to introduce 25 mm long precracks in the midplane.

The mechanical testing was performed on a floor model Instron machine. The screw-assisted wedge grips were used for tensile tests while a flexure testing fixture was employed for three-point bending and ENF tests. Crosshead speeds for tensile and flexure tests were fixed at 0.5 and 0.125 mm/min., respectively. The span-to-depth ratio of flexure tests was between 4 and 30. All tests were conducted at room temperature.

Acoustic emission tests were conducted during mechanical testing. An acoustic emission sensor (a resonant type, AET MAC175L, nominal resonance frequency of 175 kHz) was attached on the face of the sample using viscous resin and springs (at the center of the tensile samples and near the middle of bend and ENF samples). The sensor was connected to a 40 dB preamplifier (AET 140B) with a plug-in filter of 125 kHz to 2 MHz. The output from the preamplifier was fed to an AEA Phoenix system having a threshold set at 40 dB in reference to 1  $\mu$ V at the output of the sensor. The definition time for signal recognition was 100  $\mu$ s. Signals detected by Phoenix were processed and transferred to an IBM PC/AT and stored on an internal hard disk for off-line post processing. The root-mean-square (rms) voltage of AE signals and applied load were also recorded using a two-pen recorder. After the test, AE parameters stored on the hard disk were post-processed by the use of Asyst/Phoenix software to create graphs of the differential distribution for the standard AE parameters; peak amplitude, rise time, signal duration and energy, which is defined by the formula; energy = 100 x log (Peak Amplitude x 2 x AE Counts).

## RESULTS AND DISCUSSION

With a combination of results of mechanical tests and fractographic studies, four fracture mechanisms, fiber breakage, delamination, transverse matrix cracking and splitting, were observed in different types of tests. AE behavior associated with each fracture mechanism will be presented below. Results on C/PEEK composites will be discussed here. Further details of these tests and those on C/PPS samples that behaved similarly are given elsewhere [5].

(1) FIBER FRACTURE The 0-degree C/PEEK laminates tested in tension and three-point bending with a span-to-depth ratio of 30 failed by fiber fracture. The average ultimate flexure stress was 2.42 GPa while the tensile strength was 1.04 GPa. Figure 1



shows the load vs. time and AE count rate vs. time plots of a 0-degree three-point bending test, during which the fiber fracture dominated. AE event count rates gradually increased with increasing load above ~40% of the ultimate load and rapidly as the failure load was approached. Tensile test results were similar except AE started at lower loads (~25% of the ultimate load).

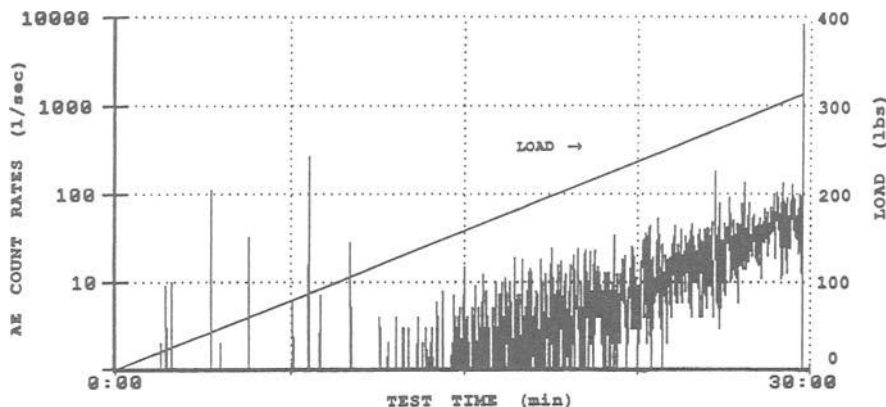


Fig. 1. Load and AE count rates vs. time curves for 0-degree C/PEEK specimen tested in three-point bending.

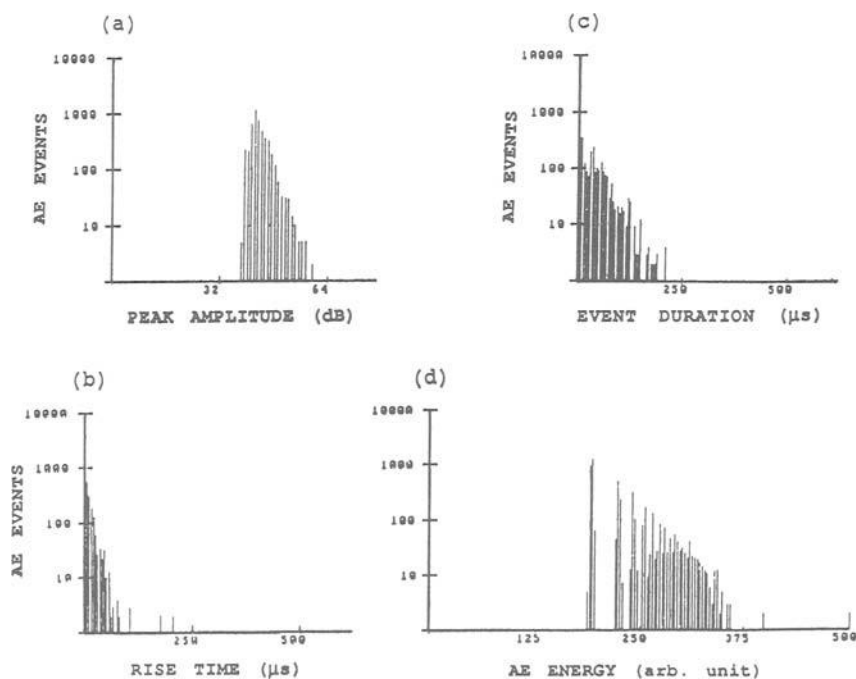


Fig. 2. Distributions of AE parameters for 0-degree C/PEEK specimen tested in three-point bending. a) peak amplitude distribution. b) rise time distribution. c) signal duration distribution. d) energy distribution.

Typical distributions of AE parameters are shown in Fig. 2. The peak amplitude distribution indicates the upper limit to be about 60 dB and a linear (in a log-log plot) decrease from 43 to 60 dB. This amplitude distribution features were also observed when narrower data analysis windows were used; i.e., the amplitude distribution was unchanged. The rise time and signal duration plots show the short character of the signals. Over 90% of the signals had  $< 40 \mu\text{s}$  rise time and  $< 120 \mu\text{s}$  duration. The energy plot has a large scatter below 250, but appears to have a peak at  $\sim 280$ . Few events exceed energy value of 350.

The amplitude distribution data was converted to a cumulative amplitude distribution. A power law distribution resulted, fitting

$$N_e = 5.06 \times 10^{11} V_p^{-3.76},$$

where  $N_e$  is the cumulative event count below peak amplitude of  $V_p$ . This amplitude distribution drops off much more sharply than the Gaussian distribution with  $V_p^{-2}$  dependence. A cross plot of peak amplitude and signal duration revealed that almost 90% of the AE events occurred with  $< 100 \mu\text{s}$  duration and  $< 50$  dB peak amplitude as shown in Fig. 3. The concentration of AE events near the origin of this plot is characteristic of fiber fracture and is similar to our previous results on AE from carbon fiber reinforced epoxy composites [6, 7]. As systematically studied by Wolters [8], small diameter fibers produce only low level AE signals. Long duration signals are apparently from frictional noise. It is important to note that acoustic emissions and the fracture of carbon fibers start at relatively low loads in carbon fiber composites. In glass-fiber composites, fiber-induced emissions are observed only above 90% of the composite fracture load, producing high-amplitude emissions.

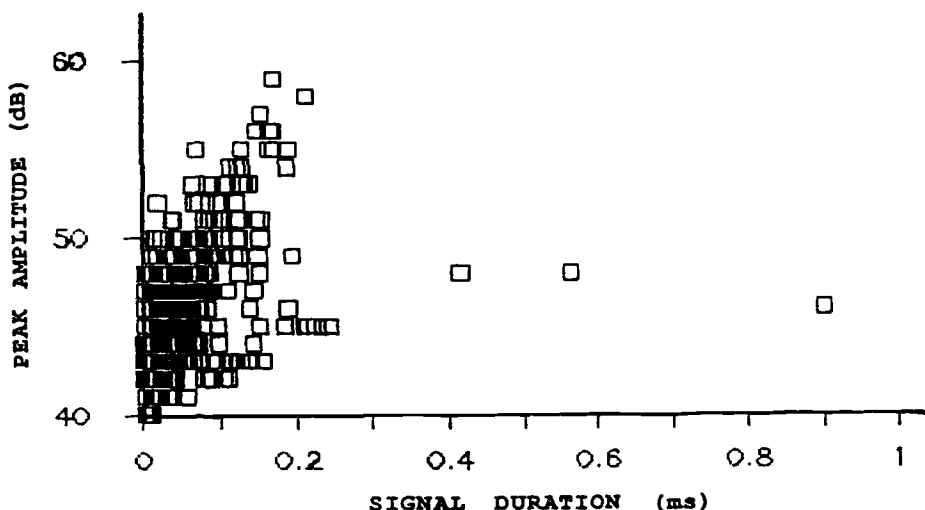


Fig. 3. A cross-plot of peak amplitude and signal duration for 0-degree C/PEEK specimen tested in three-point bending.

(2) **DELAMINATION** Delamination was produced by three-point loading of the end-notched flexure samples. The load vs. time curve of an ENF test is shown in Fig. 4 along with AE event rate vs. time plot. During the test, delamination initiated from the tip of the existing precrack. Starting at 23 min, observable delamination started to grow slowly accompanied by a continuous decrease in the load. Once the length of delamination reached the center loading pin, the delamination stopped (24.8 min). AE activities increased prior to the load drop and reached 80 - 100 events/sec levels during the load drop. These AE activities were dominated by delamination, although it is not possible to rule out completely other competing fracture mechanisms, notably crack face friction [9].

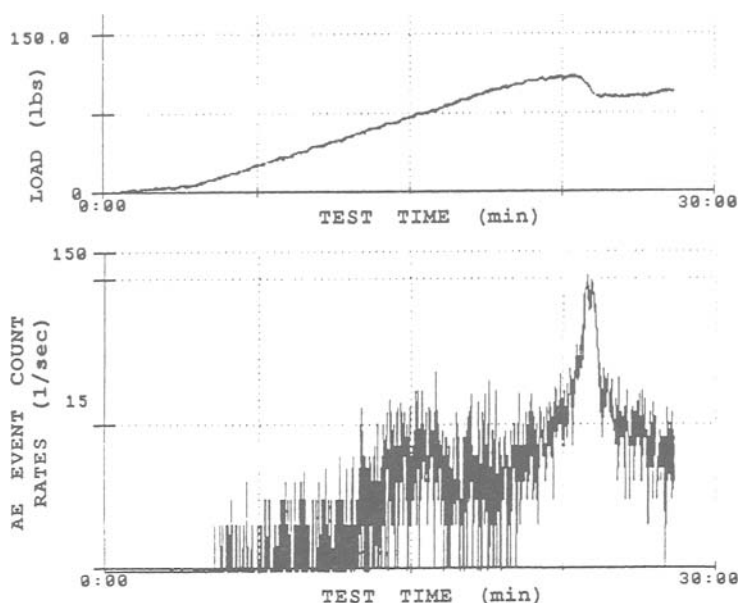


Fig. 4. Load (top) and AE event rates (bottom) vs. time curves for 0-degree C/PEEK ENF specimen.

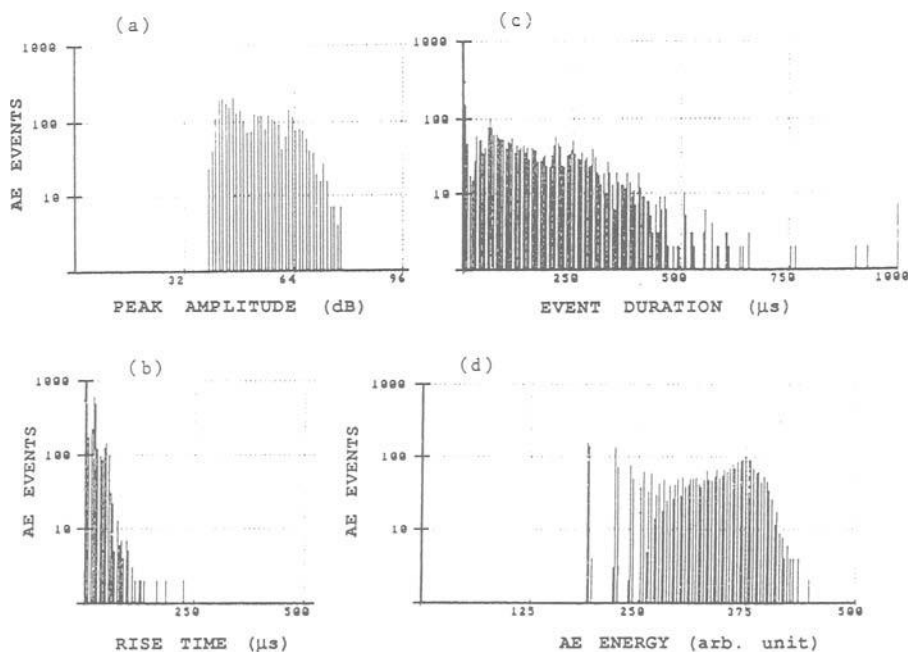


Fig. 5. Distributions of AE parameters for 0-degree C/PEEK ENF specimen for the segment of 23 to 24.5 min. a) peak amplitude distribution. b) rise time distribution. c) signal duration distribution. d) energy distribution.

Typical distributions of AE parameters are shown in Fig. 5. These were taken when delamination grew (23 - 24.5 min range). The peak amplitude distribution indicates the upper limit to be about 78 dB and a nearly flat distribution from 40 to 65 dB. Above this level, the amplitude distribution exhibited a sharp drop. The rise time and signal duration plots indicate longer signals. In contrast to the fiber fracture data discussed above, only about a half of the signals had  $< 40 \mu\text{s}$  rise time and less than 40% had  $< 120 \mu\text{s}$  duration. The energy plot again has a large scatter below 250, but clearly shows a peak at 375. Few events exceed energy value of 440. Both the peak amplitude and energy distributions had different shapes from those due to fiber only fracture, indicating the feasibility of discrimination between the two mechanisms. The cumulative peak amplitude distribution shows also distinct characteristics, quite unlike the single power law distribution observed above. The cumulative peak amplitude distribution for AE due to the delamination-dominated region is shown in Fig. 6. This data can be nominally represented by two separate power law distributions, as indicated in the figure. Physically, the observed distribution is likely to result from the superposition of multiple distributions due to delamination and other mechanisms. Regardless of the underlying reasons, the shape of the cumulative amplitude distribution is a useful means of discrimination of failure mechanisms.

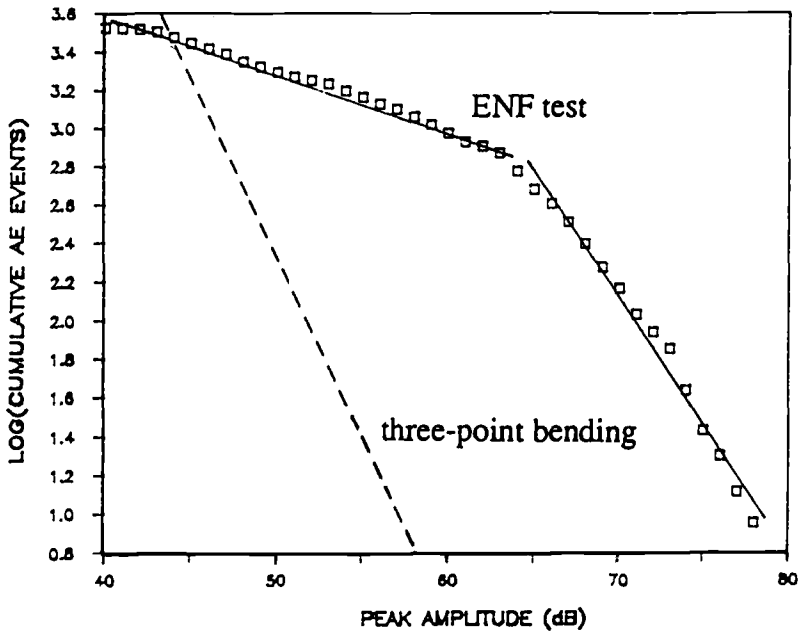


Fig. 6. The cumulative peak amplitude distribution of AE events for 0-deg C/PEEK ENF specimen for the segment of 23 to 24.5 min. The broken line is the data for the bend test discussed earlier.

A cross plot of peak amplitude and signal duration for the above data is given in Fig. 7. This plot reveals that the concentration of AE events extends from near the origin of this plot to the region of about 70 dB, 400  $\mu\text{s}$ . Since about 4000 AE events are represented here, the density distribution is not expressed adequately. Still over 90% of the AE events occurred with  $< 400 \mu\text{s}$  duration and  $< 70$  dB peak amplitude. As some fiber fracture is expected, the low amplitude, short duration region contains AE events due to fiber breakages. However, the difference between this plot and that in Fig. 3 is clear. A line connecting 42 dB, 0  $\mu\text{s}$  and 70 dB, 400  $\mu\text{s}$  on Fig. 7 passes through the most densely distributed region. This apparent straight line is related to the damped sinusoid represen-

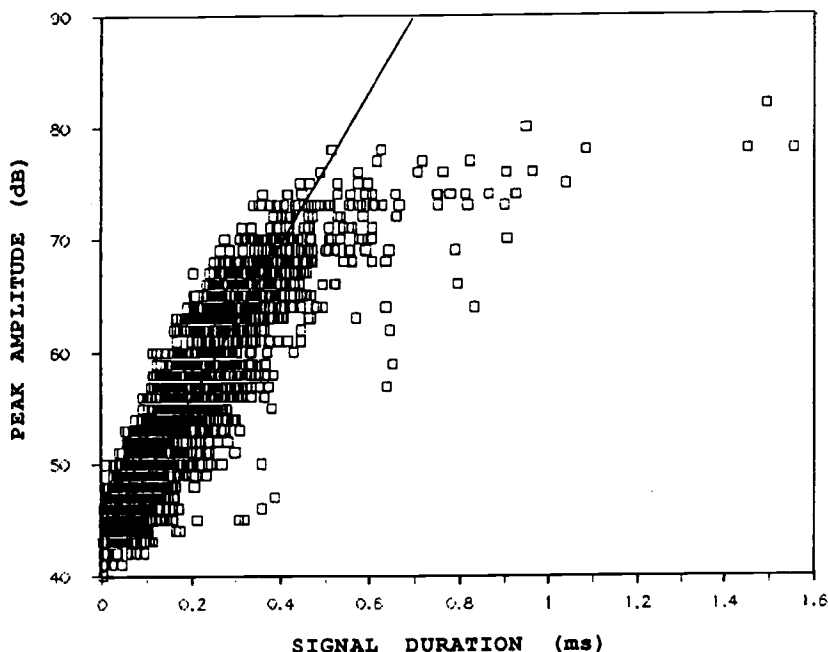


Fig. 7. A cross-plot of peak amplitude and signal duration for 0-degree C/PEEK ENF specimen for the segment of 23 to 24.5 min.

tation of an AE signal, which has been used for a long time. That is, taking 42 dB as the apparent threshold, the line corresponds to the exponential decay of AE signal as given by

$$V = V_p \exp(-t/t_0)$$

where  $V_p$  is the peak amplitude,  $t_0$  is the decay constant, or time over which the amplitude decreases to  $(1/e) = 0.368$ . In the present case,  $t_0$  is equal to 124  $\mu$ s. Most signals fall within  $\pm 8$  dB of this line. Some signals in Fig. 7 were found with high peak amplitude (60 - 82 dB) and long duration (400 - 1600  $\mu$ s). These can arise from rapid delamination as previously suggested [6], but also may be due to overlapping of several events. If these were to have a single decay constant, the decay time would be 200 to 400  $\mu$ s. The decay time in this range is expected to be caused by structural consideration, such as sample size and gripping. As the most of the signals have a lower decay constant (124  $\mu$ s), it is natural to expect the superposition of multiple signals to be the source of the long AE events.

(3). **MATRIX CRACKING** Matrix cracking was produced when 90-degree laminates were stressed in three-point bending or tested in tension. Both flexure and tensile samples failed suddenly. The average ultimate flexure stress and tensile stress were 21.9 and 11.1 ksi, respectively. In terms of rms voltage spikes and high amplitude (60 to 88 dB) events, more AE activities were found in 90-degree tension samples than in 0-degree samples. However, the total number of AE events was much lower (by a factor of 30). The distributions of AE parameters were not well defined due to the limited number of AE events, but these were not clearly different from the fiber fracture data. This may imply that even in the 90-degree samples, fiber fracture can not be ignored. Another point that must be reported is the fact that some matrix cracks produce very low amplitude signals that cannot be quantified. This is observable during a test on an oscilloscope screen barely above the background noise. Thus, matrix cracks can have a wide range of peak amplitude and more careful studies are required to identify their characteristic features.

(4) **SPLITTING** Splitting was a prominent failure mode when 0-degree coupons were stressed in tension. During a typical test, multiple longitudinal matrix cracks (splits) were initiated from the opposite sides of the tested coupon. These cracks then grew with the increasing load through the length of the specimen and became approximately parallel splits. Eventually, the splits were connected by the occurrence of a normal fracture between them. When splitting occurred, there was no large load drop because the rigidity of the specimen had not been reduced significantly.

These splits produce strong AE events, which are reflected in a significant number (~5% of the total) of high amplitude (>60 dB) signals and numerous spikes on the rms voltage-time curve. These were not found in 0-degree samples stressed in bending. Unfortunately, the splitting overlaps fiber fracture and AE characteristic solely due to splitting can not be separated.

Peak amplitude and energy distributions have been used to discriminate one failure mode against another in many thermosetting resin matrix composites [6, 8-14]. Two groups of resin systems, thermoplastic and thermoset, exhibited similar AE characteristics when the present results are compared to similarly performed experiment on thermoset-matrix composites. The present study also shows that various AE parameter distributions are useful in thermoplastic matrix composites for fracture mechanism studies. However, AE parameters by themselves cannot separate some of the mechanisms. That is, matrix cracking and splitting are still difficult to positively identify via these parameters. The rise time and signal duration distributions also have overlapping features among different fracture types. The shapes and the event density distribution on the amplitude-duration cross plot appear to provide a better means to discriminate one failure type from another.

## CONCLUSIONS

1. Mechanical and acoustic emission behavior of a carbon/PEEK composite was investigated.
2. Signals emitted from AE sources due to fiber breakage and delamination had different peak amplitude, signal duration and energy distributions. Other mechanisms were not clearly separated.

## ACKNOWLEDGEMENT

This study was supported by the Office of Naval Research, to which the authors are grateful. They also appreciate the assistance of ICI Inc. which supplied sample material.

## REFERENCES

- [1] Willats, D. J., "Advances in the Use of High Performance Continuous Fiber Reinforced Thermoplastics," SAMPE Journal, Vol. 20, No. 5, 1984, pp. 6-10.
- [2] Hartness, J. T., "An Evaluation of Polyetheretherketone Matrix Composites Fabricated from Unidirectional Prepreg Tape," SAMPE Journal, Vol. 20, No. 5, 1984, pp. 26-31.
- [3] Ma, C. C. Martin, O'Connor, James E., and Lou, Alex Y., "Polyphenylene Sulfide High Performance Composites," SAMPE Quarterly, Vol. 15, No. 1, 1984, pp. 12-24.
- [4] Fowler, T. J., "Experience with Acoustic Emission Monitoring of Chemical Process Industry Vessels," in Progress in Acoustic Emission III, eds. K. Yamaguchi et al, Japan Soc. Non-Destructive Inspection, Tokyo, 1986, pp. 150-162.
- [5] Jeng, J.S., MS Thesis, University of California, Los Angeles, 1988.

- [6] Ono, K., "Acoustic Emission Behavior of Flawed Unidirectional Carbon Fiber-Epoxy Composites," in Proceedings of Second International Symposium on Acoustic Emission from Reinforced Composites, Montreal, Canada, July 21-25, 1986.
- [7] Ohtsu, M., and Ono, K., "Pattern Recognition Analysis of AE from Unidirectional Carbon Fiber-Epoxy Composites by Using Autoregressive Modeling," Journal of Acoustic Emission, Vol. 6, No. 1, Jan.-March 1987, pp. 61-71.
- [8] Wölters, J., "Description of Compound Parameters of Particle-Filled Thermoplastic Materials by Acoustic Emission Techniques," Journal of Acoustic Emission, Vol. 3, No. 1, Jan.-March 1984, pp. 51-58.
- [9] Awerbuch, J., and Ghaffari, S., "Monitoring Progression of Matrix Splitting During Fatigue Loading Through Acoustic Emission in Notched Unidirectional Graphite/Epoxy Composite," in Proceedings of Second International Symposium on Acoustic Emission from Reinforced Composites, Montreal, Canada, July 21-25, 1986, Session 2, 3:15-3:50.
- [10] Davidovitz, M., Mittelman, A., Roman, I., and Marom, G., "Failure Modes and Fracture Mechanisms in Flexure of Kevlar-Epoxy Composites," Journal of Materials Science, Vol. 19, 1984, pp. 377-384.
- [11] Short, D., and Summerscales, J., "Amplitude Distribution Acoustic Emission Signatures of Unidirectional Fiber Composite Hybrid Materials," Composites, Vol. 15, 1984, 200-206.
- [12] Wu, Y. H., Yang, M. H., Kuo, J. Y. and Chang, S. P., "Acoustic Emission Analysis of Composite Failure Mechanisms with Special Reference to the Modeling of Amplitude Distributions," in Proceedings of Second International Symposium on Acoustic Emission from Reinforced Composites, Montreal, Canada, July 21-25, 1986.
- [13] Wevers, M., "Identification of Fatigue Failure Modes in Carbon Fiber Reinforced Composites," Ph.D. Thesis, Katholieke Universiteit Leuven, 1987.
- [14] Dharan, C.K.H., "Delamination Fracture and Acoustic Emission in Carbon Aramid and Glass/Epoxy Composites," ICCE & MCCE, Vol. 1, 1987, pp. 1.405-1.414.

## ON THE CORRELATION BETWEEN ACOUSTIC EMISSION AND PROGRESSION OF MATRIX SPLITTING IN A UNIDIRECTIONAL GRAPHITE/EPOXY COMPOSITE

---

REFERENCE: Ghaffari, S. and Awerbuch, J., "On the Correlation Between Acoustic Emission and Matrix Splitting in a Unidirectional Graphite/Epoxy Composite," Acoustic Emission: Current Practice and Future Directions, ASTM STP 1077, W. Sachse, J. Roget, and K. Yamaguchi, Eds., American Society for Testing and Materials, Philadelphia, 1991.

ABSTRACT: This paper presents results on monitoring initiation, accumulation, and progression of matrix splitting through acoustic emission in double-edge notched graphite/epoxy coupons. In this specimen geometry matrix splitting is the single dominant mode of damage. Detailed acoustic emission data analysis was performed by which most of the emission generated by the grating among the split fracture surfaces has been identified. Only the acoustic emission generated by the actual growth of matrix splitting has been accounted for. Based on the location distribution histograms of these events the progression of the matrix splits could be tracked. The acoustic emission results were compared with optical observations and excellent correlations were established for all cases studied.

KEYWORDS: acoustic emission, graphite/epoxy, matrix splitting, friction emission, failure mechanisms

Recent studies by the authors have shown that in addition to the acoustic emission (AE) generated by damage progression in graphite/epoxy composites, the grating among existing fracture surfaces is also a major source of emission [1,2,3,4]. In fact, it has been determined that the emission generated by such grating can exceed that caused by new damage. Consequently, in correlating AE with actual damage progression these two sources of emission must first be identified and separated.

The emission caused by friction has been identified in [1,2,3,4] based on the event intensities (duration, energy, and counts per event) of those AE events known to be generated by grating. This was achieved by analyzing the AE events generated within the low load range during cyclic loading, in fatigue [1] and in quasi-static loading [2]. It has been determined that these "friction events" are all of low intensities. Specifically, friction emission threshold (FRET) values were defined. Based on these FRET values, the emission caused by actual damage (i.e. "damage events") could then be separated from the total emission. In this paper, the results obtained in the previous studies are

Drs. Ghaffari and Awerbuch are Research Associate and Professor, respectively, in the Department of Mechanical Engineering and Mechanics, Drexel University, Philadelphia, Pennsylvania 19104.



employed to establish a quantitative correlation between acoustic emission and the actual initiation and growth of matrix splitting in double-edge notched unidirectional graphite/epoxy specimens.

## EXPERIMENTAL PROCEDURE

Unidirectional  $[0]_{16}$  double-edge notched (D.E.N.) graphite/epoxy (AS4/3501-6) specimens were subjected to uniaxial quasi-static loading in tension, by an Instron servo-hydraulic testing machine, under stroke controlled mode (0.05 mm/min). Parallel sided tensile coupons having notch length-to-width ratios of  $a/W = 0.1, 0.2,$  and  $0.3$  were tested. Two loading functions were applied, both in tension: 1. monotonically increasing the load up to failure; and 2. loading/unloading cycles, incrementally increasing the load up to failure. Failure is defined here as the load at which all four matrix splits reached the specimen's end tabs. Specimens were subjected to between 24 and 30 load cycles, depending upon the rate of split progression. Since matrix splitting progresses very rapidly, the maximum stress level applied at each load cycle was determined either by the sudden extension of the split (observed optically) or by an abrupt surge in the emission. The length of the four matrix splits was measured in real-time through optical observations using a closed-circuit television (CCTV) system with a high magnification microscope (150X). Acoustic emission was monitored using Physical Acoustics Corporation (PAC) 3000/3004 AE instrumentation system. Two resonance (150 KHz) sensors, type R-15, were placed 220 mm apart, equidistant from the notches. Only the events generated within 20% to 80% of this gage length were analyzed. Other details of the testing procedure and data analysis are reported in [1,2,3,4].

## RESULTS AND DISCUSSION

In unidirectional D.E.N. graphite/epoxy specimens a single dominant mode of failure occurs, namely, matrix splitting. Four macro cracks (i.e. matrix splits) emanate from the tips of the two notches. Therefore, it is expected that emission of distinct event intensities will be generated. However, results indicate that events of a wide range of intensities are generated, as discussed in more detail in [1,2] and shown, for example, in the amplitude distribution histograms (A.D.H.) of events of Fig. 1. These A.D.H. seem to indicate that matrix splitting generates AE events of a wide range of amplitude, primarily in the 40 dB to 85 dB range, and a significant number of even higher amplitude events. Clearly, no specific amplitude range could be associated with the particular failure mode of matrix splitting. The location distribution histograms (L.D.H.) of all the events generated, Fig. 2, indicate that emission was generated throughout the specimen length. These AE events are caused not only by the actual damage progression but also by the grating among the split fracture surfaces and by the large number of failures which occur along the edges of the specimen. Therefore, the site of the artificially induced notches (location "50") could not be located and the progression of the matrix splits could not be tracked.

From the results such as those shown in Figs. 1 and 2 it is clear that based on all the AE events generated a direct correspondence can not be established either between event intensities and mode of damage or between AE results and actual progression of the matrix splits. Thus, the interpretation of the AE results is inconclusive even for a relatively simple specimen geometry in which only four macro cracks occur, all progressing along the same direction, and all of the same failure mode. Therefore, it could be concluded that there are additional sources of emission which obscure the emission caused by the propagation of the four matrix splits.

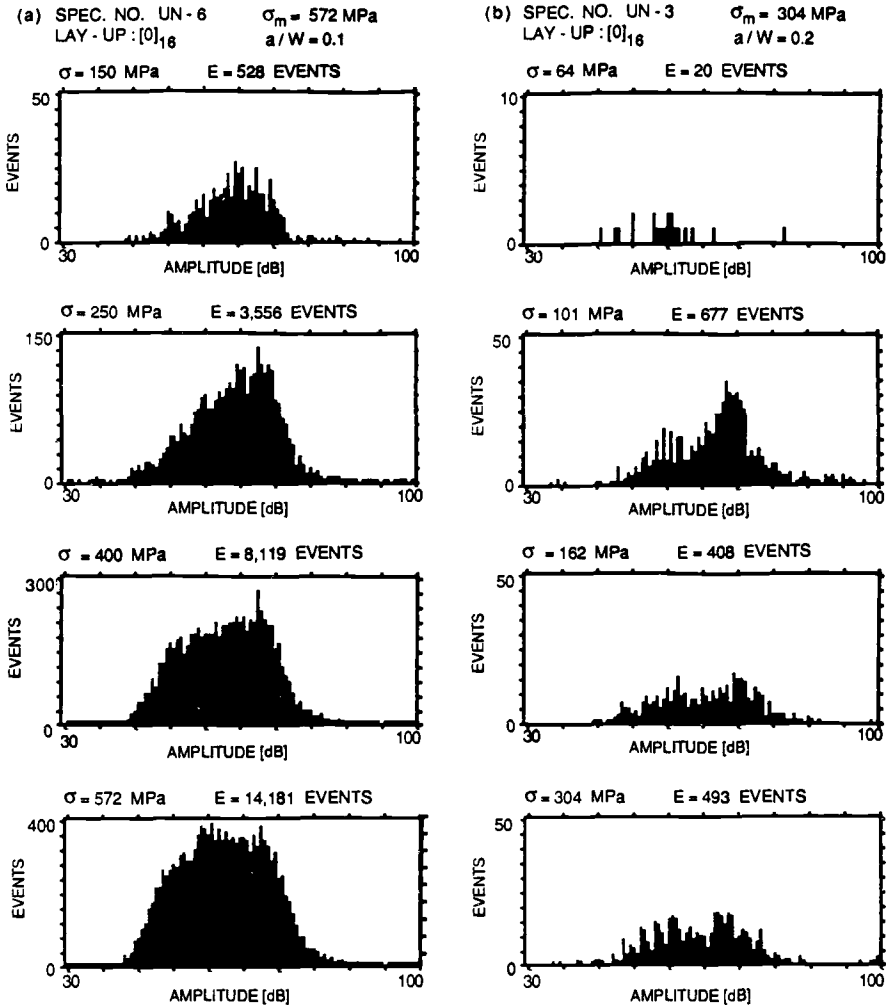


FIG. 1.— Amplitude distribution histograms of all the events generated during:  
a. monotonic loading to failure; b. four representative loading/unloading cycles.

Based on real-time optical observations it has been reported in [1,2] that the matrix splits initiate and progress asymmetrically and intermittently. Split branching, fiber bridging, and secondary splits also occur. Consequently, grating among the fracture surfaces occurs in this simple specimen geometry during both cyclic and monotonic loading, generating friction emission [2]. The primary source of this emission is the significant grating among the fracture surfaces and the large number of microfailures. The friction emission was investigated in detail in [1,2,3,4] and it was determined that its intensities are all below certain FRET values, namely, 250  $\mu\text{sec}$  in duration, 20 in energy counts and 40 in counts per event. The emission caused by the actual damage was shown to be separable from the total emission based on these FRET values. The "damage events" were defined there as those events for which all three intensities (energy counts, duration, and counts per event) are simultaneously above the FRET values. By imposing such a strict criterion most of the events generated by grating or microfailures

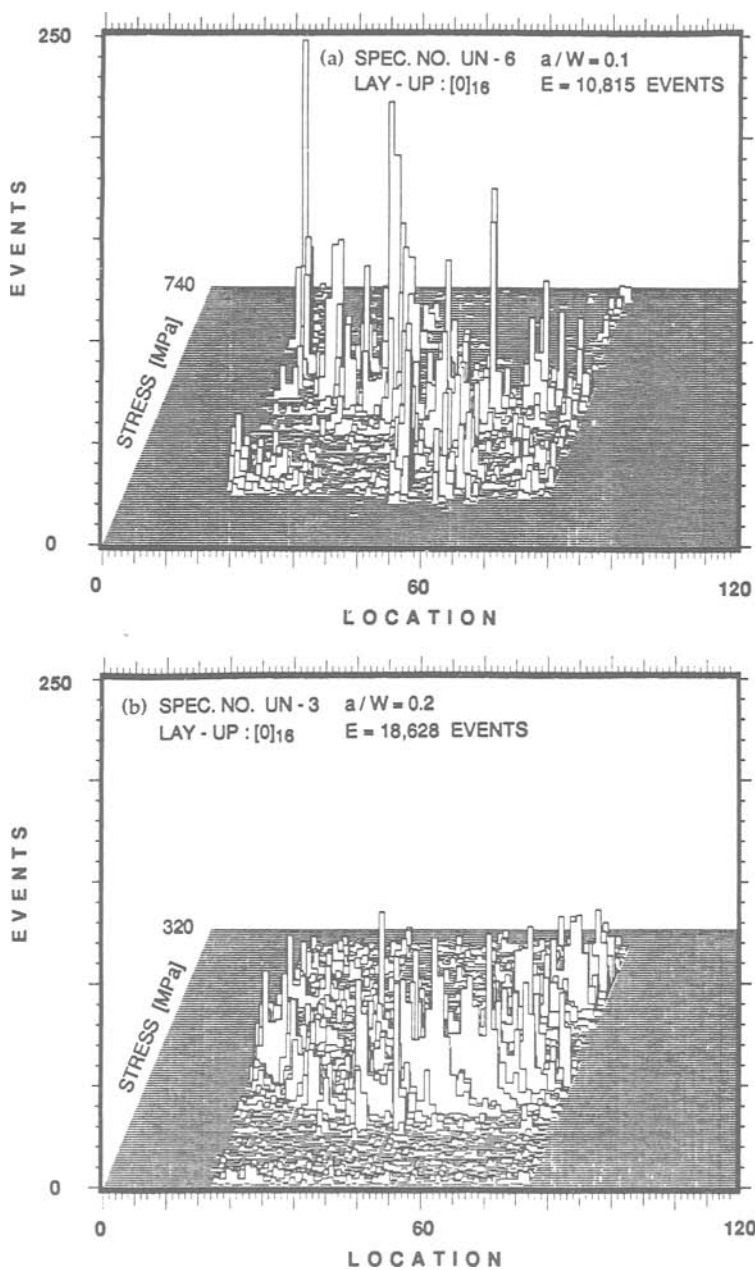


FIG. 2.— Location distribution histograms of all the events generated during:  
a. monotonic loading to failure; b. the entire loading/unloading cycle sequence.

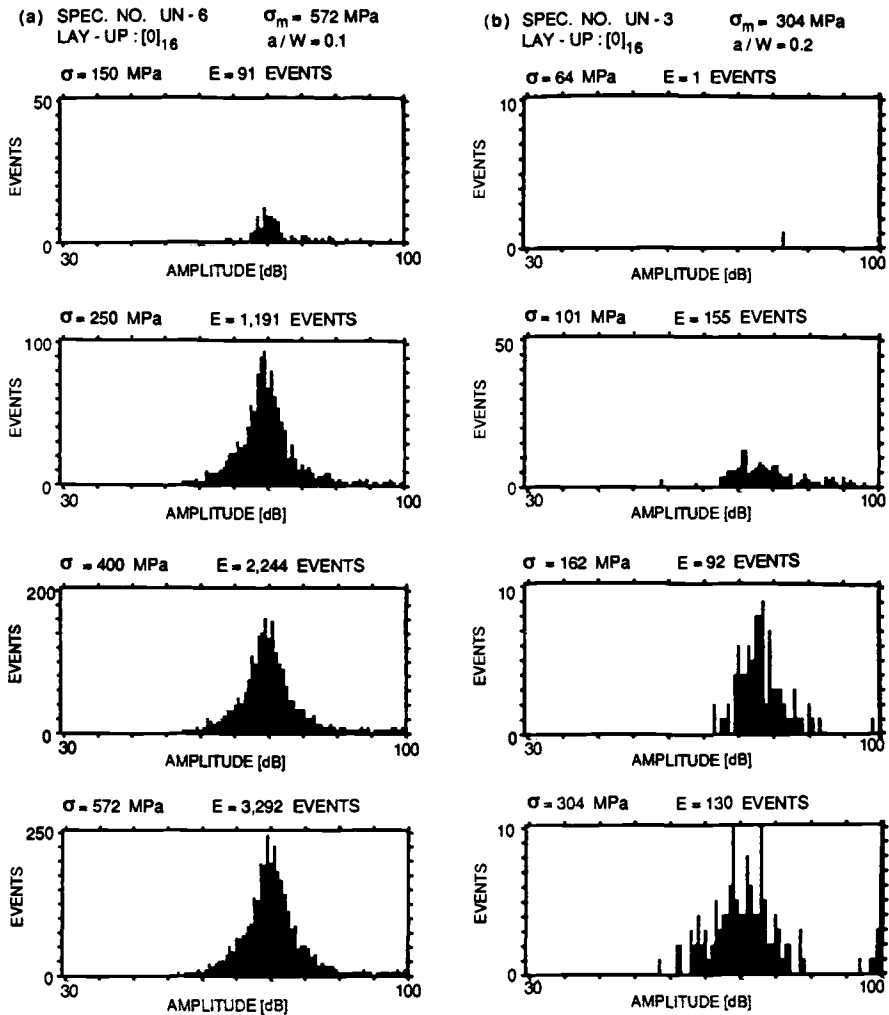


FIG. 3.— Amplitude distribution histograms of events having intensities above FRET values for the same specimens and load intervals shown in Fig. 1.

were eliminated from the data file. Thus, the remaining data contained only the "damage events". The intensities of the "damage events" should therefore be associated with the macrofailures, i.e. matrix splitting and or fiber breakage. The characteristics of the emission caused by the microfailures (e.g. matrix crazing, fiber/matrix interface debonding, matrix micro-cracking, edge damage along weak spots, etc.) are difficult to identify. These micro-failures can all occur simultaneously, in addition to the emission caused by the other different sources (i.e. grating and macrofailures). However, it is assumed that most of the AE events generated by the microfailures are of low intensities, that is below the FRET values.

Employing the same AE instrumentation variables as in [1,2], the above FRET values and criteria were used also in his study in order to separate the friction emission from that caused by macrocracks (matrix splits). When this is done, the A.D.H. of the

damage events, extracted from the A.D.H. of Fig. 1, have a distinctly narrower range of event amplitude of approximately 70 dB to 80 dB, as shown in Fig. 3. These results suggest a close correspondence between the above amplitude range and the specific damage mode of matrix splitting. The higher amplitude events (85 dB to 100 dB), which occur primarily at the higher load ranges, could be attributed to fiber breakage. Clearly, the number of damage events (Fig. 3) is significantly smaller than the total number of events generated (Fig. 1). It should be pointed out that the A.D.H. of the damage events (Fig. 3), all of which are of intensities above the FRET values, contain also low amplitude events (40 dB to 65 dB). These low amplitude events could be caused by 'trains' of events which occur when several events hit the AE sensors simultaneously. The AE instrumentation will record such trains of events as a single event of increased intensities, i.e. above the FRET values [5,6]. Trains of friction events could be caused when grating occurs simultaneously at several sites along the different fracture surfaces. The low amplitude events could also be generated by the different microfailures. Additional study is warranted to prove the latter issues more conclusively.

In order to determine the initiation, progression, and accumulation of the matrix splits, the events of intensities above the FRET values were first separated from the total events generated. Then, the file of damage events was further post-filtered for the events having the amplitude range of 70 dB to 80 dB (for the reasons explained above, Fig. 3). It is assumed that these events are primarily caused by matrix splitting. The L.D.H. of these events, extracted from the L.D.H. of Fig. 2, are shown in Fig. 4. The comparison between these L.D.H. and the actual progression of the four matrix splits (measured from optical observations), Fig. 5, shows an excellent qualitative correlation in terms of the initiation stress of the matrix splits and the rate of their progression. It should be recalled that from the L.D.H. of all the events generated (Fig. 2) no such correlation could be made.

A quantitative correlation between the results shown in Figs. 4 and 5 can be established by analyzing the L.D.H. of Fig. 4 in further detail. For this purpose, two-dimensional L.D.H. of the events accumulated during each loading/unloading cycles were plotted. Two representative examples are shown in Fig. 6 for events accumulated during the tenth and seventh loading/unloading cycles for two different specimens having notch length-to-width ratios of  $a/W = 0.2$  and  $0.3$ , respectively. Similar two-dimensional L.D.H. plots can be prepared for specimens subjected to monotonic loading to failure. In this case these plots are obtained by slicing (filtering) the three-dimensional L.D.H. (such as shown in Figs. 2 and 4) for different load intervals.

From the L.D.H. of all the events generated, Figs. 6a and 6b (see also Fig. 2), the extent of the splits can not be determined. The emission generated from throughout the specimen length by grating, microfailures, and edge effects overwhelms that generated by the actual progression of the matrix splits. However, when the friction events are eliminated, the resulting two-dimensional L.D.H. of the "damage events", Figs. 6c and 6d, clearly indicate those events which were generated in the vicinity of the high stress concentration regions, such as at the tips of the matrix splits. A clearer L.D.H. is obtained when only the "damage events" within the amplitude range of 70 dB to 80 dB are considered, Figs. 6e and 6f. The extent of the matrix splits can now be determined by measuring the distance between the outermost events, defined in Figs. 6e and 6f as the "damaged zone". The remaining events within the "damaged zone" itself could be 'trains' of events resulting from simultaneous grating at different sites. Such trains of events could not be identified by the data analysis employed here. Note, that the artificially induced notches (location "50") are not depicted in these plots. Most of the emission occurred at the tips of the splits which extended away from the notch regions during the two load cycles shown in Fig. 6.

The comparison between the split length (i.e. "damaged zone") based on the L.D.H. such as shown in Figs. 6e and 6f and the actual split extension, measured from optical observations (Fig. 5), is shown in Fig. 7 for three specimens having different

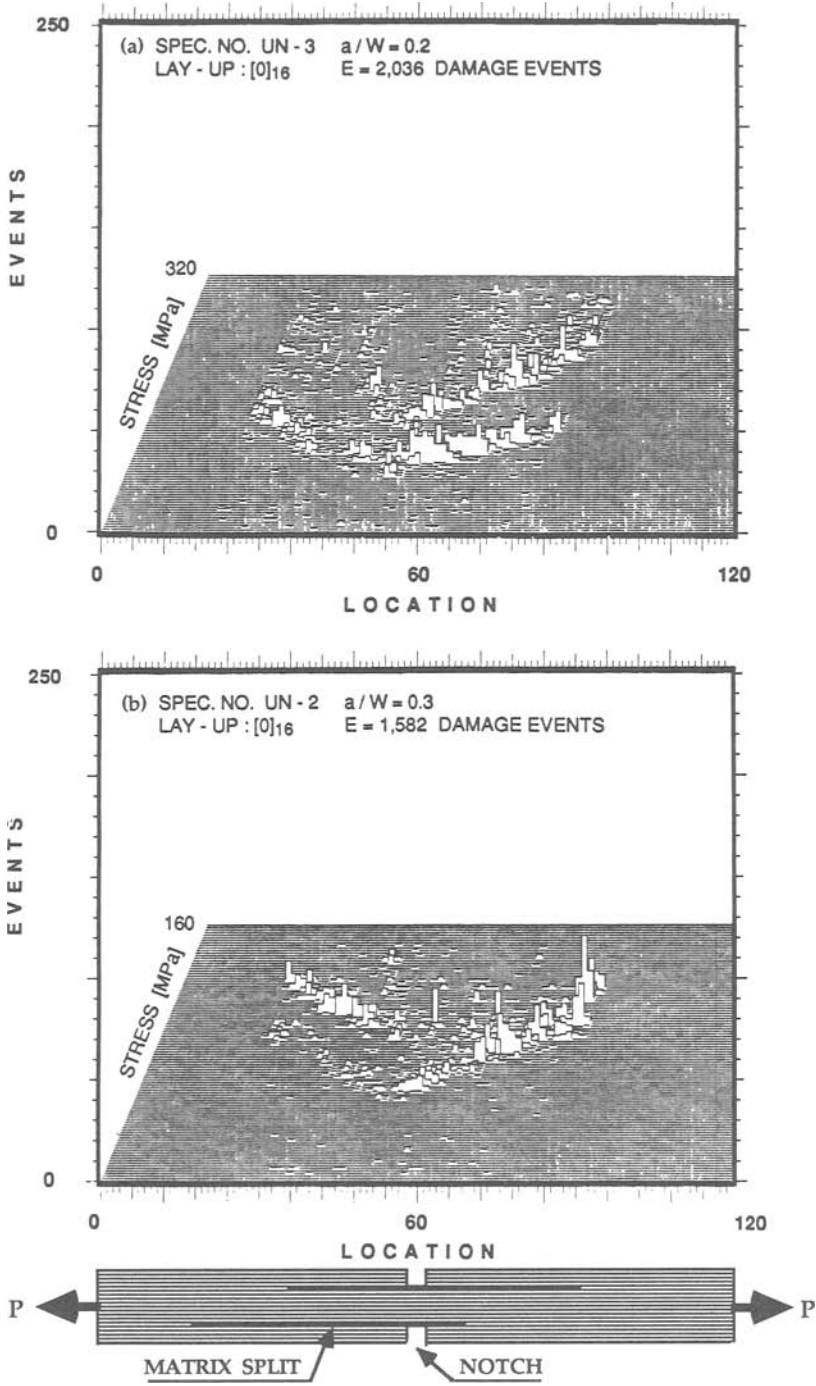


FIG. 4.— Location distribution histograms of "damage events" within the amplitude range of 70 dB to 80 dB for the same specimens shown in Fig. 2.

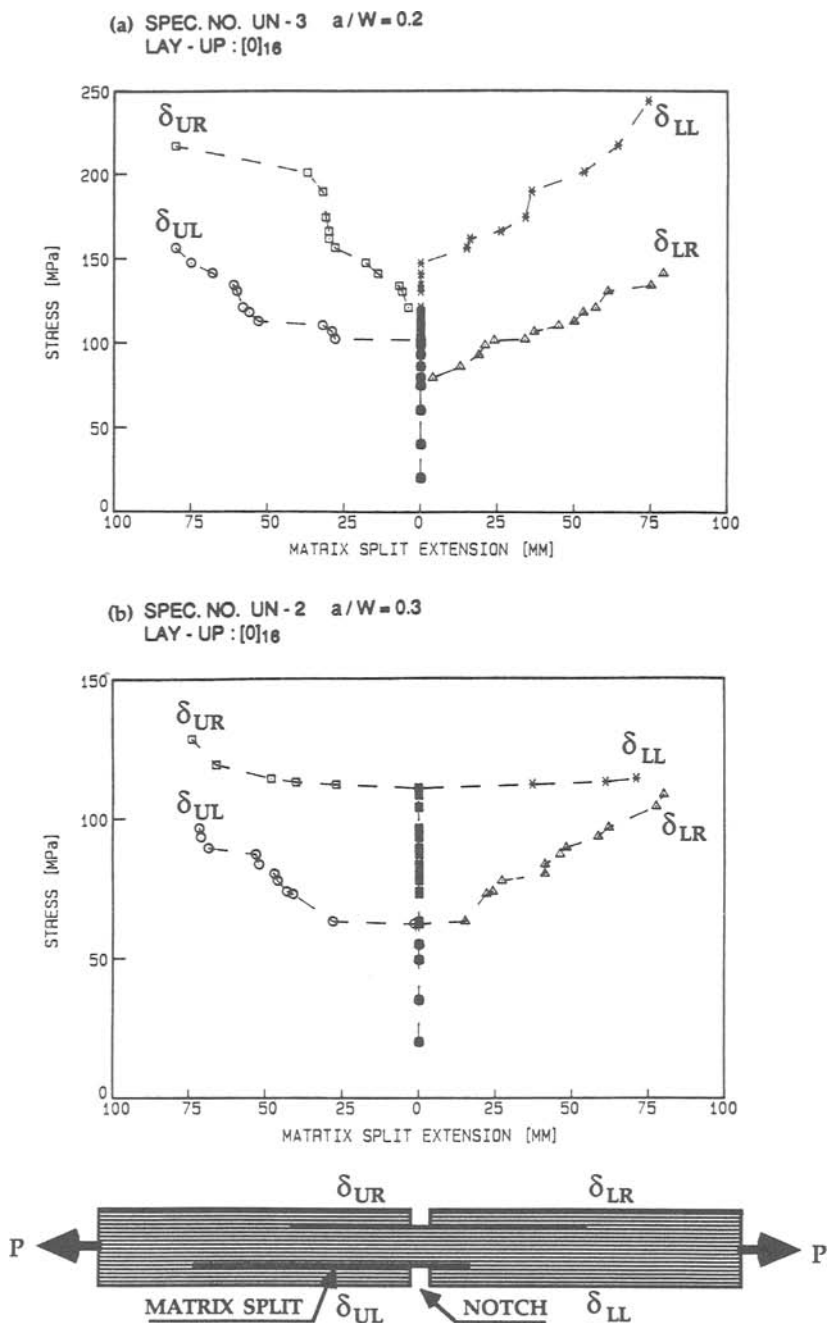


FIG. 5.— Initiation and progression of four matrix splits during loading/unloading cycles, measured through optical observations.

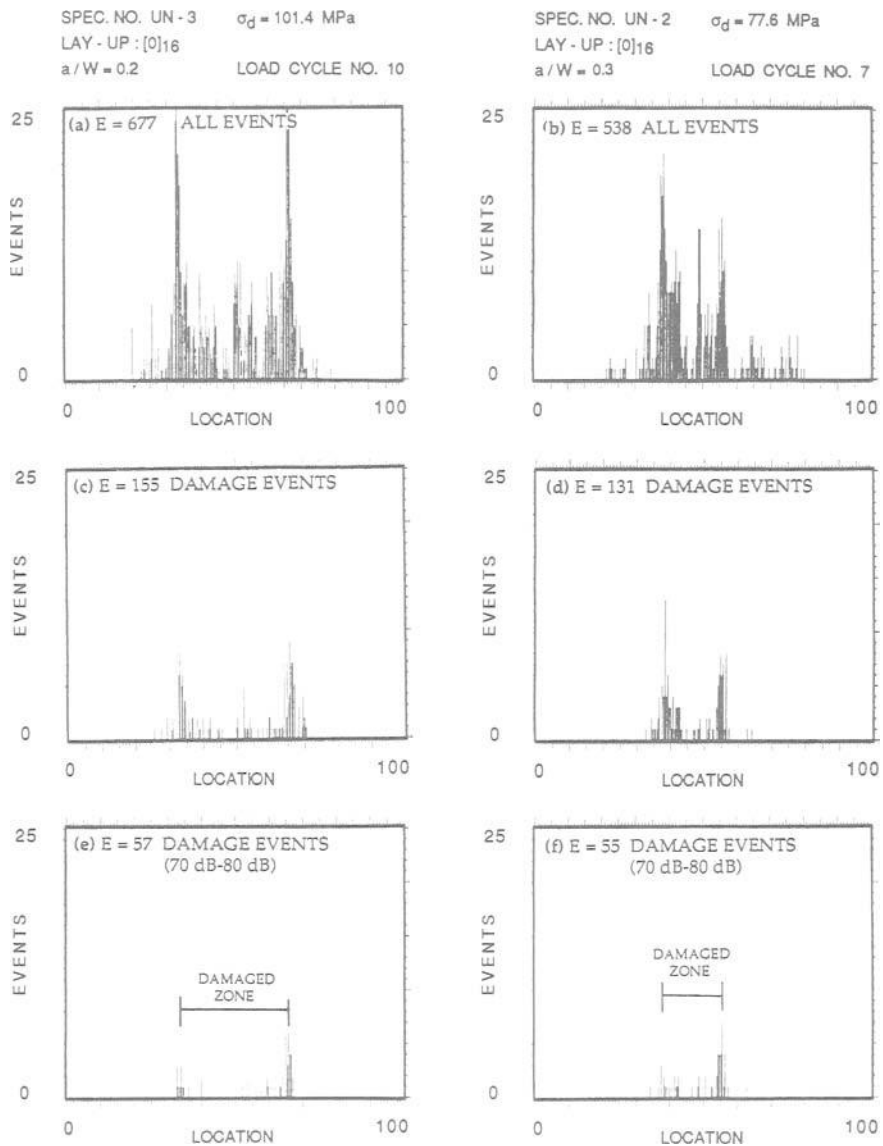


FIG. 6.— Location distribution histograms of events generated during a given load cycle for two specimens: a. and b. all the events; c. and d. "damage events"; e. and f. "damage events" within the amplitude range of 70 dB to 80 dB.

notch lengths. The comparison indicates that an excellent correlation can be established for each specimen in terms of locating the artificially induced notch, detecting split initiation stress, determining rate of split progression, and tracking the extent of the matrix splits. Moreover, the AE results agree very well with the asymmetric and intermittent nature of the initiation and progression of the four matrix splits. A comparison among the three cases shown in Fig. 7 indicates differences in the split



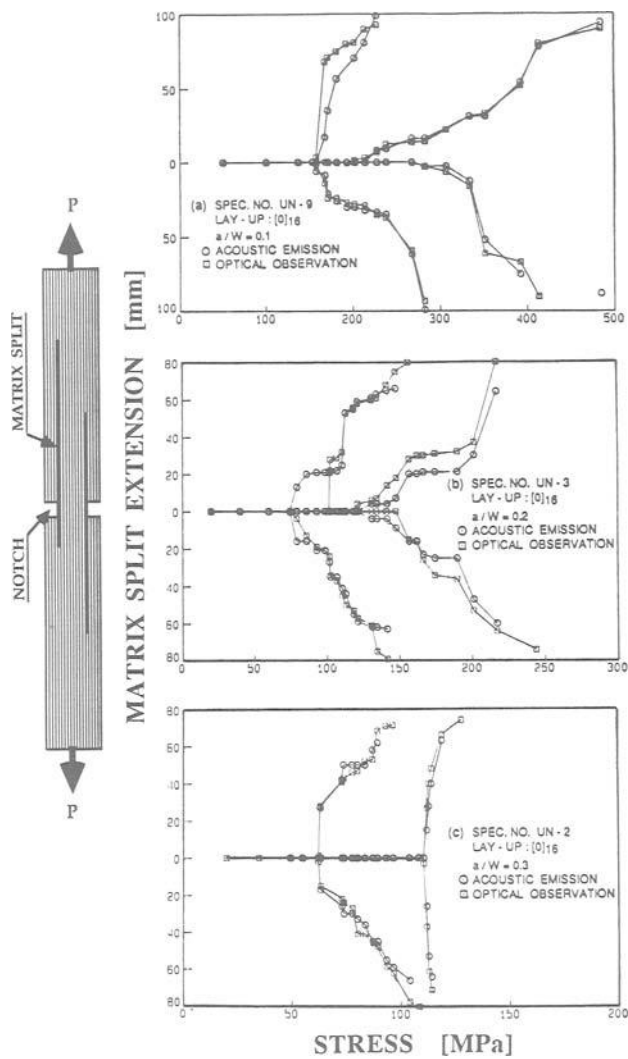


FIG. 7.— Comparison between location distribution histograms of "damage events" within the amplitude range of 70 dB to 80 dB (e.g. Figs. 6e and 6f) and optical observations (e.g. Fig. 5).

initiation stress and in the rate of progression of the matrix split for the different specimens. These differences are clearly confirmed by the AE results. It should be pointed out here that it is possible to track all four matrix splits separately only because the second pair of matrix splits initiates after the first pair has progressed to the specimen's ends (i.e. asymmetry in split initiation and progression). If all four splits progress simultaneously, then only the longer split on each side of the notch can be tracked.

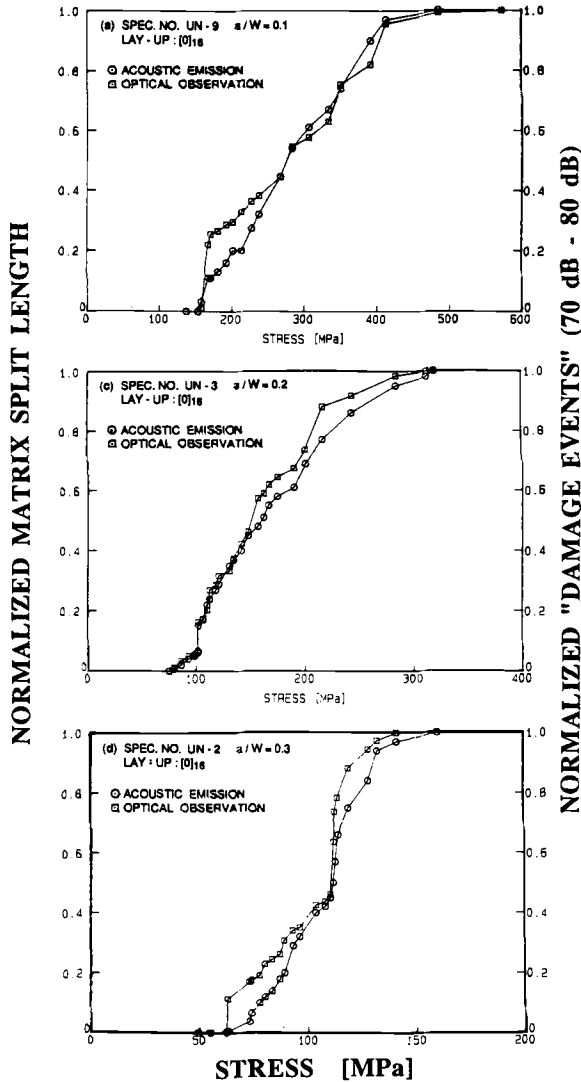


FIG. 8.— Comparison between the accumulation of the "damage events" within the amplitude range of 70 dB to 80 dB and the total extent of all four matrix splits.

Finally, the accumulation of damage events (within the amplitude range of 70 dB to 80 dB) has been compared with the accumulation of the actual damage (in terms of the total extension of the four matrix splits). The comparison, shown in Fig. 8, clearly indicates the similarity between the AE results and the total extension of all four splits, primarily in terms of split initiation stress and rate of accumulation. Each change in the rate of the split growth is accompanied by a change in the rate of accumulation of these events. In fact, an excellent correlation was established (coefficient of correlation = 0.98 to 0.99) for all three cases. Moreover, other test results (not shown here) indicate that the reproducibility of the AE data and the split extension data and the correlation between the two is also quite good.

## CONCLUSIONS

It has been demonstrated that based on the total acoustic emission generated during quasi-static loading no direct correspondence between matrix splitting and AE event intensities could be established. Also, locating damage initiation and tracking its progression is not possible. It is suggested that acoustic emission caused by grating (which is all of low intensity) be first identified and distinguished from the emission caused by actual damage. The screening procedure is based on the intensities of the friction emission, which are all below certain friction emission threshold values. Based on this data analysis, the amplitude distribution histograms of the remaining AE events, defined here as "damage events" can be correlated more confidently with the failure mode of matrix splitting. Based on the "damage events" which are within the amplitude range of 70 dB to 80 dB, the progression of the matrix splitting can be accurately tracked. The accumulation of these events correlates very well with the actual damage growth as measured through optical observations.

## ACKNOWLEDGEMENTS

This research has been sponsored by the Solid Mechanics Program, Office of Naval Research, under Contract No N00014-84-K-0460 and by the Naval Air Development Center, under Contract No. D.N. N6 2269/86/RC/0032. The program monitors were Dr. Y. Rajapakse of the ONR and Dr. W.R. Scott of the NADC.

## REFERENCES

- [1] Awerbuch, J. and Ghaffari, S., "Monitoring Progression of Matrix Splitting During Fatigue Loading Through Acoustic Emission in Notched Graphite/Epoxy Composite," Journal of Reinforced Plastics and Composites, Vol. 7, May 1988, pp. 245-264.
- [2] Awerbuch, J. and Ghaffari, S., "Tracking Progression of Matrix Splitting During Static Loading Through Acoustic Emission in Notched Unidirectional Graphite/Epoxy Composites," in Progress in Acoustic Emission III, The Japanese Society of NDI, 1986, pp. 575-585.
- [3] Eckles, W. F. and Awerbuch, J., "Monitoring Acoustic Emission in Cross-Ply Graphite/Epoxy Laminates During Fatigue Loading," Journal of Reinforced Plastics and Composites, Vol. 7, May 1988, pp. 265-283.
- [4] Awerbuch, J. and Ghaffari, S., "Effect of Friction Emission on Monitoring Damage in Composite Laminates through Acoustic Emission," in Progress in Acoustic Emission III, The Japanese Society of NDI, 1986, pp. 638-652.
- [5] Cohen, J. and Awerbuch, J., "Monitoring Delamination Progression in Graphite/Epoxy Composite Through Acoustic Emission During fatigue Loading," in Proceedings of the Fourth Japan-U.S. Conference on Composite Materials, Technomic Publishing Co. Inc., 1988, pp. 1035-1046.
- [6] Cohen, J. and Awerbuch, J., "Tracking Progression of Delamination in Model Composites Through Acoustic Emission During Quasi-Static Loading," (to be published).

M. Wevers, I. Verpoest, P. De Meester and E. Aernoudt

## **IDENTIFICATION OF FATIGUE FAILURE MODES IN CARBON FIBRE REINFORCED COMPOSITES WITH THE ENERGY DISCRIMINATING ACOUSTIC EMISSION METHOD**

---

REFERENCE: Wevers, M., Verpoest, I., De Meester, P., and Aernoudt, E., "Identification of Fatigue Failure Modes in Carbon Fibre Reinforced Composites with the Energy Discriminating Acoustic Emission Method", Acoustic Emission: Current Practice and Future Directions, ASTM STP 1077, W. Sachse, J. Roget, and K. Yamaguchi, Eds. American Society for Testing and Materials, Philadelphia, 1991.

ABSTRACT: Tension-tension fatigue of carbon fibre reinforced composite laminates is characterized by the initiation and growth of specific damage modes. A method was developed to study the AE-signals released from each individual damage source so that the growth of distinct fatigue damage modes could be monitored. The obtained results correlated well with the real damage extent of each individual damage mode. This is an improvement compared to the general information the total number of acoustic emission signals can give on the fatigue degradation of the specimens.

KEYWORDS: carbon fibre reinforced composite laminates, tension fatigue, damage modes, acoustic emission, energy discriminating acoustic emission method.

Dr. ir. M. Wevers is a Research Associate of the Belgian National Fund for Scientific Research (NFWO) and lector at the Department of Metallurgy and Materials Engineering at the Katholieke Universiteit Leuven, de Croylaan 2, 3030 Leuven, Belgium. Prof. Verpoest is a senior Research Associate of the NFWO and Associate Professor at the Department MTM. Prof. De Meester is head of the section Mechanical Metallurgy and Materials Engineering at the Department MTM and Prof. Aernoudt is dean of the Faculty of Applied Science of the Katholieke Universiteit Leuven and Prof. at the department MTM.

The fatigue behaviour of composites differs in many aspects from the fatigue behaviour of conventional materials such as metals. Fatigue of metals is characterized by the initiation and growth of cracks which grow in a self-similar fashion. Fatigue of composites however is characterized by the initiation and growth of distinct,

interacting damage modes: matrix cracking, delamination, debonding between the fibre and the matrix and fibre fracture. Fatigue damage in composites can lead to an early degradation of the stiffness of the composite while for metals this is only the case when 90% of the total lifetime has expired. Thus monitoring and controlling fatigue damage in composites with appropriate non-destructive testing (NDT) techniques is very important.

For the research on the fatigue behaviour of carbon fibre reinforced epoxy laminates described here, an "Energy Discriminating Acoustic Emission Method" (EDAEM) was developed which made it possible to monitor the growth of each individual damage mode and from which *quantitative* information on the extent of each damage mode could be obtained.

#### MATERIAL AND MECHANICAL TESTS.

Test specimens, angle plied  $(\pm 45^\circ)_2$ s, unidirectional  $(0^\circ)_8$  and cross plied  $(0^\circ_2, 90^\circ_2)_8$  laminates, having a fibre volume fraction of about 60%, were fabricated from the Fibredux 920C-TS-5-42 prepreg material (Ciba-Geigy Co.). The geometry of the test specimens is depicted in Fig. 1 and Aluminum end tabs were used. Fatigue tests were carried out on a servo hydraulic fatigue testing machine, Schenck Hydropuls 25 kN, in an air conditioned room at  $20 \pm 2^\circ\text{C}$  and  $45 \pm 5\%$  relative humidity. The grips of this machine were hydraulic. The tension-tension fatigue cycle was sinusoidal with a maximum fatigue load of a certain percentage of the ultimate tensile strength (UTS), the R-ratio was in all cases 0.03 unless specified differently and the frequency was 3 Hz.

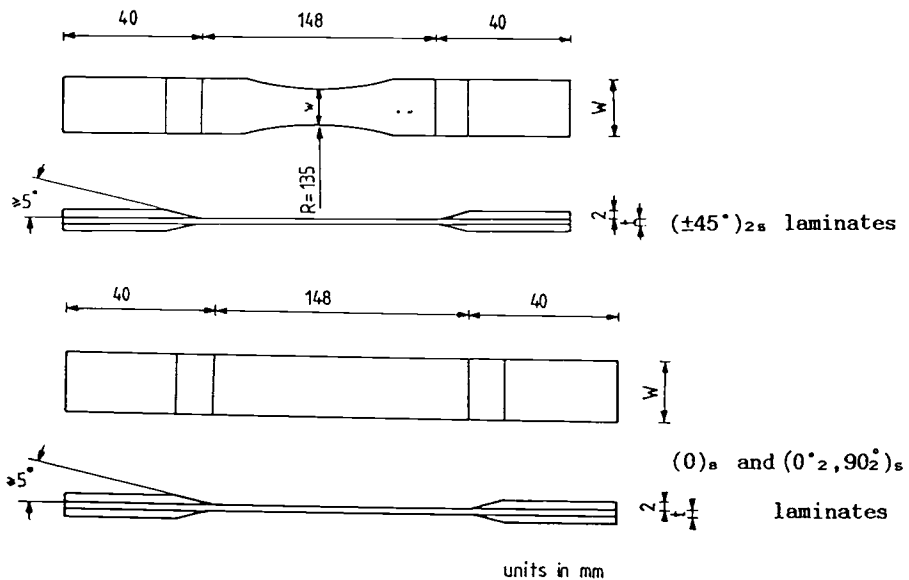


Fig. 1: Geometry of the test specimens.

## DAMAGE MONITORING TECHNIQUES.

Three different NDT-techniques have been used to monitor the damage initiation and development: X-ray radiography, edge replica technique and acoustic emission. The use of these techniques has been described elsewhere (ref. 1-3). Only the use of the acoustic emission technique will be outlined in the following.

The acoustic emission technique was chosen for continuous and passive, real time damage monitoring. The AET 5000A acoustic emission system (Acoustic Emission Technology Co.) was employed for the research and postprocessing of the data was done with a personal computer (the Northstar Advantage computer or a HP 9816 Hewlett Packard series 200 computer).

Two resonant AE transducers, Model AC 375L of AET Co., were mounted on the fatigue test specimen leaving a distance of 40 to 75 mm in between the transducers. This distance depended on the geometry of the test specimen and on the fact whether or not longitudinal stiffness degradation measurements were to be carried out. The AE-attenuation over a certain distance was dependent on the laminate type and was maximum for the angle plied laminates: 3.9 dB/cm. A couplant, type SC6 solvent soluble resin V2 resistant to 150°C, was used to obtain good signal transfer between the specimen and the transducers, which were fixed on the specimen with a flexible insulating tape.

The 60dB preamplifiers, model 160A of AET Co., were used and the signals were filtered using 200-500 kHz bandpass filters, type FL25 of AET Co.. The signal processing unit (SPU) added an additional amplification of 20 dB to the signal and compared the signals with a threshold of 0.2 Volt before further analysis. The dead time of the acoustic emission system was set to 128  $\mu$ sec and was correlated with the clock period of 500 nsec of the event duration module. So acoustic emission signals with an event duration up to 1919.50  $\mu$ sec could be measured with a small dead time of the AE-system.

All acoustic emission signals, measured during the course of each sinusoidal fatigue cycle whereby no distinction was made whether the AE-signal was measured during the lower or the upper part of the fatigue cycle, were localized using a linear location procedure. Only AE-signals generated in a central region (20-55 mm) between the two transducers, and caused by damage, were characterized by the AE-equipment. Using this linear location procedure the extraneous noise from the machine and grips was also eliminated during the fatigue test.

To make the correlation between the damage mode and it's characteristic AE-signal, the pseudo energy content of the AE-signal, a system dependent characteristic as it was calculated by the SPU using the following formula:  $\text{ENERGY} = \text{PEAK AMPLITUDE (dB)} + 10 \log \text{EVENT DURATION (\mu sec)}$ , was focussed on. This energy is just an approximation of the area underneed the envelope of the AE-signal. The (total) number of AE-events in each energy interval which gathered the AE-signals of a specific damage mode and the total number of acoustic emission events detected during each test were also measured during the fatigue tests.

## RESULTS

Tests on the angle plied  $(\pm 45^\circ)_2$  and unidirectional  $(0^\circ)_8$  carbon fibre reinforced epoxy laminates.

The edge replica study of the fatigued angle plied laminates clearly indicated (Fig. 2) that at first matrix cracks developed due to fatigue loading in tension and secondly delaminations, while both damage modes extended during the whole fatigue process.

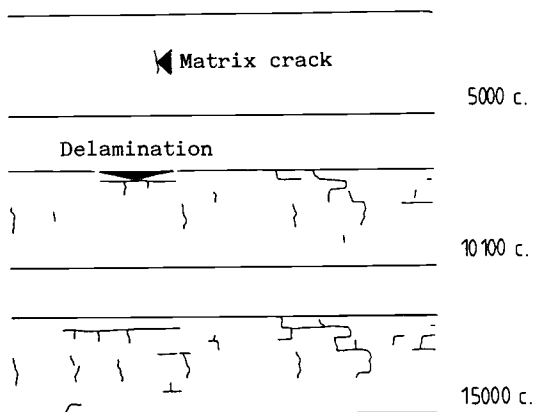


Fig. 2: Damage on the edge replicas of the  $(\pm 45^\circ)_2$  laminate fatigued at 34% of the UTS.

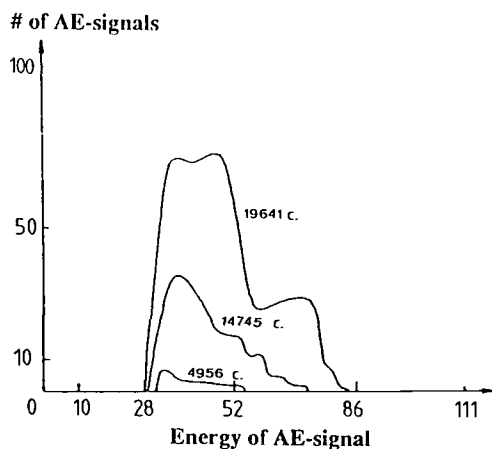


Fig. 3: Distribution graph of the energy content of the AE-signals generated during fatigue of the  $(\pm 45^\circ)_2$  laminate at 34% of the UTS.

Studying the distribution graphs of the energy content of the acoustic signals (Fig. 3) it was clear that the first AE-signals detected had low energy values: 28 to 52 energy units, and when the fatigue test progressed towards a higher number of fatigue cycles

AE-signals with a higher energy content were measured: 53 to 86 energy units.

From the correlation that exists between the damage state of the fatigued angle plied laminates and the corresponding AE-data, one can conclude that the energy interval [28,52] collects the AE-signals caused by matrix cracks and that delamination growth emits signals of the [53,86] energy interval.

For the unidirectional laminates two supplementary energy intervals could be distinguished on the energy distribution graph namely the intervals of [78,98] and [99,111] energy units. (Fig. 4)

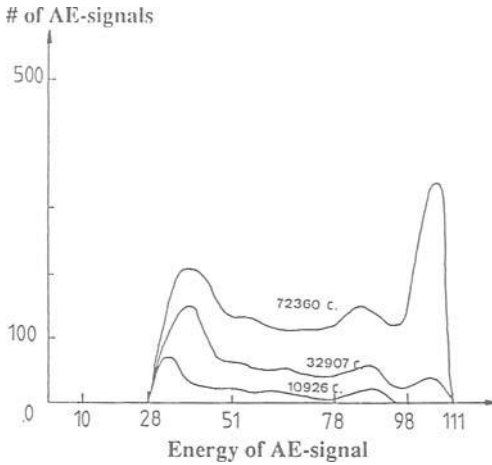


Fig. 4: Distribution graph of the energy content of the AE-signals generated during fatigue of the  $(0^\circ)_8$  laminate at 56% of the UTS.

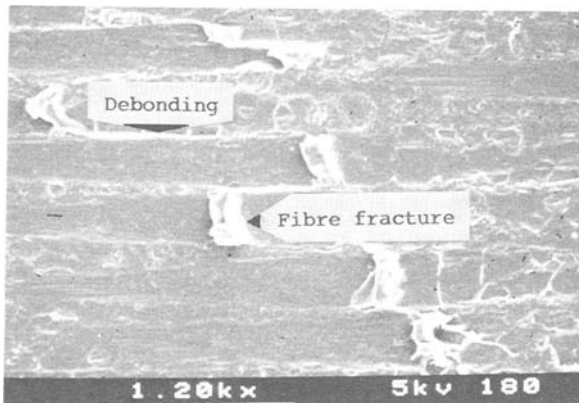


Fig. 5: SEM photograph of an edge replica of a  $(0^\circ)_8$  laminate taken after 961300 fatigue cycles at 70% of the UTS.



The unidirectional laminate contains two more fatigue damage types: debonding between the fibre and the matrix and fibre fracture. These two damage modes can be revealed by studying the edge replicas of the specimens. (Fig. 5)

As the fatigue damage process in the unidirectional laminates proceeded, one could notice a strong increase in the AE-signals of the highest energy interval [99,111]. This, combined with the fact that the specimens finally had to fail by multiple fibre fractures, led to the conclusion that the last energy interval contains signals of fibre fractures and so the energy interval [78,98] can gather the AE-signals generated by debonding.

Note: The experience gathered during several years on this composite material system and its laminates never indicated the vast presence of AE-signals due to rubbing of damaged areas (frictional noise). All signals retained for analysis could be attributed to the initiation and growth of damage.

This way of analysing the acoustic emission signals and correlating their energy content with the physical fatigue damage, called the **Energy Discriminating Acoustic Emission Method** (EDAEM), results in the allotment of an energy interval to each specific damage mode and clearly indicates the possibilities of the AE-technique to identify individual damage modes. Using a strain energy approach to calculate the energy released at flaw extension (being a matrix crack, a delamination, a fibre fracture or a debonded length) one can prove the relative positions of the energy intervals found with this calibration work on this composite system. In the scope of this paper further details however cannot be given but they can be found in ref. 3.

#### Tests on the cross plied $(0^\circ_2, 90^\circ_2)_s$ carbon fibre reinforced epoxy laminates

To prove the quantitative possibilities of the EDAEM, the fatigue tests on the cross plied  $(0^\circ_2, 90^\circ_2)_s$  laminates will be discussed. For the same maximum stress, two different test series were carried out: one with  $R = 0.03$  and another with  $R = 0.5$ . The former tests were carried out for 280000 cycles, the latter for 500 000 cycles.

For each test the total length of the delaminated area was measured on the edge replicas and the total length of matrix cracks was measured on the penetrant enhanced X-ray radiographs. These lengths are given in TABLE 1.

TABLE 1 -- Information on the damage extent of matrix cracks and delaminations.

	Matrix cracks L (mm) (X-ray graph)	Delamination L (mm) (replica)	Matrix cracks growth value: # AE-signals/ intervallength	Delamination growth value: # AE-signals/ intervallength
R = 0.03 280 000 c.	570 477	394 330	2299 1928	2063 1738
R = 0.5 507 150 c.	165	53	1011	643

Using the EDAEM on this type of laminate, it was found that the AE-signals caused by matrix cracking were gathered in the [28,51] energy interval and that delamination emitted AE-signals of a higher energy interval namely [52,78]. By counting for each number of fatigue cycles, the number of acoustic emission signals in the energy interval of each damage mode, and by normalising this number with respect to the energy interval length, growth curves of each fatigue damage mode were obtained. From these growth curves, growth values (the total number of acoustic emission signals per energy interval divided by the interval length) for matrix cracking and delamination at the end of each fatigue test were obtained. All these data are gathered in TABLE 1.

When for each damage mode the growth value at the end of the fatigue test is then divided by the measured length of damage extent, damage factors were obtained for each test (TABLE 2).

TABLE 2 -- Damage factors of each damage mode.

	Matrix cracks # AE-signals/L (mm)	Delamination # AE-signals/L (mm)
R = 0.03 280 000 c.	4.03 4.04	5.24 5.27
R = 0.5 507 150 c.	6.12	12.13

These results indicate the quantitative possibilities of the acoustic emission method. For the tests of series 1 the same damage factors were obtained indicating a direct correlation between the extent of a specific fatigue damage mode and the number of acoustic emission signals generated by the initiation and growth of that damage mode. For the test of series 2, a smaller extent of the fatigue damage modes correlated with less acoustic emission signals measured, but the factors obtained were higher. This could be due to the much slower growth rate of the fatigue damage modes in this specimen, which was fatigued for 507150 fatigue cycles at a smaller stress amplitude. In other words, for the same damage extent more fatigue cycles are needed and hence more acoustic emission signals are measured per unit length.

So besides qualitative results, also quantitative results can be obtained when using the Energy Discriminating Acoustic Emission Method to monitor the fatigue damage growth in cfre composites.

#### CONCLUSIONS

The complex tension fatigue behaviour of typical cfre laminates produced from the Fibredux 920C-TS-5-42 prepreg material was studied. To assess the fatigue damage with the acoustic emission technique several other NDT techniques had to be called upon to calibrate the AE-measurements. The EDAEM, which was developed to identify each distinct fatigue damage mechanism and to assess the growth of each fatigue damage mode taking part in the fatigue process, however clearly produced for this composite system and its fatigue test conditions quantitative information on the extent of the real physical damage. To monitor fatigue damage in carbon fibre reinforced epoxy composites, this EDAEM is highly recommended.

#### REFERENCES

- [1] Wevers, M., Verpoest, I., Aernoudt, E., and De Meester, P., "Analysis of Fatigue Damage in CFR Epoxy Composites by Means of Acoustic Emission: Preparing a Calibration Exercise," Verbundwerkstoffe Technologie und Prufung, G. Onadreck, Ed., Oberursel, 1985.
- [2] Wevers, M., Verpoest, I., Aernoudt, E., and De Meester, P., "Analysis of Fatigue Damage in CFR Epoxy Composites by Means of Acoustic Emission: Setting up a Damage Accumulation Theory," Journal of Acoustic Emission, Vol. 4, No. 2/3, April-Sept., 1985, pp. 186-190.
- [3] Wevers, M., "Identification of Fatigue Failure Modes in Carbon Fibre Reinforced Composites," Proefschrift Voorgedragen tot het Behalen van het Doctoraat in de Toegepaste Wetenschappen, K. U. Leuven, 7 Mei, 1987.

Jerry W. Whittaker\* and William D. Brosey\*

DETECTION OF IMPACT DAMAGE IN COMPOSITE BI-AXIAL TEST SPECIMENS BY USE OF THERMALLY-ACTIVATED ACOUSTIC EMISSION

---

REFERENCE: Whittaker, J. W., and Brosey, W. D., "Detection of Impact Damage in Composite Bi-Axial Test Specimens by Use of Thermally-Activated Acoustic Emission," Acoustic Emission: Current Practice and Future Directions, ASTM STP 1077, W. Sachse, J. Roget, and K. Yamaguchi, Eds., American Society for Testing and Materials, Philadelphia, 1991.

ABSTRACT: Acoustic emission (AE) produced during thermo-mechanical loading of composite materials is known as thermo-acoustic emission (thermo-AE). When thermally cycled, coupons of various composite materials have been shown to produce quantities of AE which are directly proportional to the damage level. This work demonstrates the applicability of thermo-AE monitoring to an engineering structure.

Impact-damaged bi-axial composite test specimens were thermally cycled and their AE response recorded. An undamaged specimen produced little AE while damaged ones generated widely varying amounts. For damaged specimens, the thermo-AE was found to originate primarily in the damaged regions. Damaged specimens produced AE as a function of increasing and decreasing temperature but the effect was not repeatable. More severely damaged specimens produced copious amounts of AE. It was not possible to determine the source(s) of the emission.

KEYWORDS: acoustic emission, bi-axial specimens, composite materials, damage detection, thermo-acoustic emission.

## INTRODUCTION

Thermo-acoustic emission (thermo-AE) is the term coined by researchers [1,2] to describe the acoustic emission (AE) emanating from composite materials subjected to thermal cycling. The researchers utilized composite specimens fabricated from laminated carbon fiber/epoxy and chopped carbon fiber/polyester resin and introduced damage by mechanical loading. The specimens were subjected to uniaxial tension, bending, and

---

\*Development Division, Oak Ridge Y-12 Plant, Oak Ridge, TN 37831-2009  
Operated by Martin Marietta Energy Systems, Inc. for the U. S.  
Department of Energy under contract DE-AC05-84OR21400.

tension-tension fatigue to produce varied damage states and levels. Two coupon sizes (40mm long x 20mm wide x 3mm thick and 50mm long x 20mm wide x 3mm thick) were cut from the specimens and then subjected to uniform heating and cooling cycles. As-fabricated (i.e., undamaged) coupons were found to produce very little thermo-AE while damaged specimens produced orders-of-magnitude greater quantities. The quantity of emission produced was directly related to the stress levels achieved and/or number of fatigue cycles experienced by the specimen. Friction between damage surfaces (delaminations and cracks) was thought to be the primary AE production mechanism. The researchers proposed that thermo-AE monitoring techniques could be used as a means to detect existing damage in complex composite structures.

This work extends the concepts of thermo-AE monitoring to a common engineering structure. Test specimens originally fabricated for a study of the fabrication parameters which significantly affect composite structure quality were used. A goal of the original study was to evaluate the efficacy of various nondestructive evaluation techniques in detecting fabrication-related flaws [3]. A finding of that study was that specimens containing small levels of impact damage always failed in the damaged region but did not exhibit reduced strength when hydraulically pressurized to failure [3,4]. Additional work was then planned to determine if higher levels of impact damage would degrade specimen strength. Thermo-AE monitoring was performed to assess its ability to detect damage in a complex composite structure.

## EXPERIMENTAL CONSIDERATIONS

### Specimens

The specimens were fabricated at the same time and in the same manner as those used in the previous study [3]. Epoxy-wetted Kevlar fiber was wound over a spherical aluminum shell into which a fill tube was welded. (The epoxy glass transition temperature was 85°C.) The position of the tube was defined as the north pole. Eight specimens were used, one representing each of seven anomaly types (standard, dry windings, alternate winding pattern, alternate fiber, simulated delaminations, embedded macrosphere voids, and low fiber tension) and one fabricated during winding pattern development which had a slightly thinner composite layer. Reference 4 contains a detailed description of the specimens and the anomalies. Figure 1 is a cross-sectional view of a typical specimen.

The specimens were impacted by dropping them from known heights onto a linoleum-covered concrete floor. Angular rotation was minimized so that impact generally occurred within 5° of the equator, but always within 30°. The damage level was equated with the energy absorbed during impact (calculated from the difference in drop and rebound heights). Specimen data are summarized in Table 1. Subsequent to thermo-AE testing, the specimens were hydraulically pressurized to failure. Although not a subject of this work, specimen failure strengths [5] are included to add perspective to the thermo-AE results. The strength of undamaged specimens was  $135.7 \pm 12.6$  MPa (mean  $\pm$  2 standard deviations) [4].

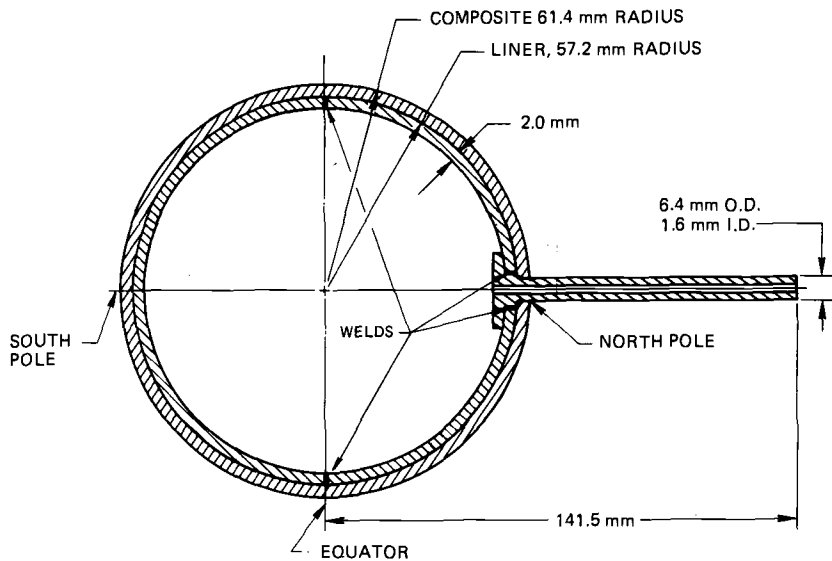


FIGURE 1 -- Cross-sectional view of test specimen showing component parts.

TABLE 1 -- Summary of specimen data.

S/N	0779	0780	0781	0782	0783	0784	0785
Type*	A	K	DW	S	M	D	L
Absorbed Energy (J)	2.40	5.00	8.02	10.02	13.06	16.21	16.24
Failure Strength (MPa)	128.2	124.0	87.9	115.8	97.1	103.4	83.4

\*A - alternate pattern, K - Kevlar 29, DW - dry windings, S - standard, M - macrospheres, D - delaminations, L - low fiber winding tension.

#### Apparatus

The experimental apparatus is shown in Figure 2. Three resonant AE transducers (PAC/Dunegan S-140A, modified to increase sensitivity by the method used by Hamstad [6]) were used to detect emission from separate regions of the specimens. The output of each transducer was amplified (40 dB) and filtered (100-300 kHz) by PAC 1220A preamplifiers. Further signal conditioning (~30 dB gain and 100-300 kHz filtering) was performed by the analog portion of a standard computer-based AE monitor (PAC 3000/3104). A threshold of 0.2V was used giving a system detection

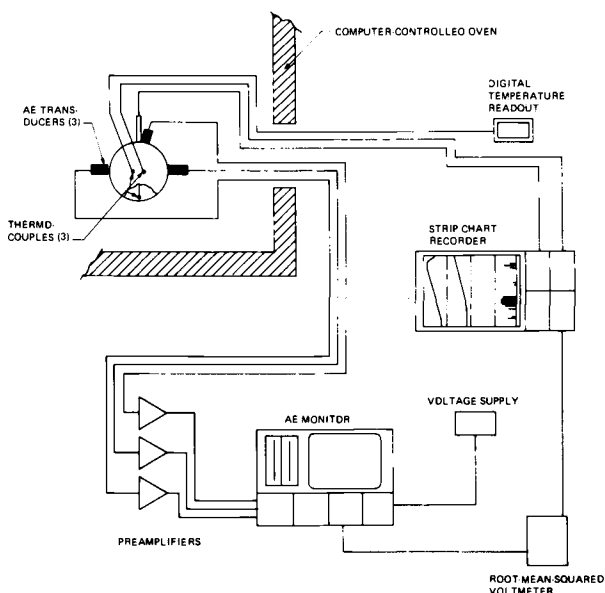


FIGURE 2 -- Experimental apparatus.

threshold of  $\sim 36$  dB (referenced to  $80$  dB =  $1$  V). System deadtime was  $100$   $\mu$  sec. The amplified and filtered analog signal from one transducer was supplied to an RMS voltmeter (Hewlett-Packard 3400A) whose output voltage was recorded on the stripchart recorder (Gould 2400).

Three chromel-alumel thermocouples were used to measure specimen temperature. Two were taped to the surface at approximately the equator. The third was inserted down the fill tube and pressed into contact with the aluminum liner. The signals from one surface-mounted and the internally-placed thermocouple were input to the stripchart recorder. The output of the remaining surface thermocouple was supplied to a digital temperature readout for visual observation. A voltage supply was manually adjusted to input a voltage level proportional to temperature to the parametric input of the AE monitor.

### Procedure

Acoustic couplant (Apiezon-M vacuum grease) was applied to the transducer faces and the transducers were taped to the specimen. One transducer (Channel 1) was mounted near the fill tube. A second (Channel 2) was applied to the equator opposite the damaged area. The third (Channel 3) was positioned within the damaged area. This transducer configuration enabled comparison of AE originating in sound material to that originating in damaged material. The specimen was placed in a computer-controlled oven on a Teflon ring which provided support and thermal isolation from the oven floor. The thermocouples were applied. All electrical connections were made and an AE system calibration performed. During calibration, mechanical pencil leads were broken in a controlled fashion at a point on the specimen equator approximately

equidistant from the three transducers. If all signal amplitudes were above 70 dB (an arbitrary level determined from lead breaks on an undamaged specimen), the specimen was considered calibrated. If the amplitudes were too low, the condition which caused the problem was corrected and the calibration repeated. Following calibration, the oven door was closed and the AE instrumentation activated. The oven was placed under computer control and the specimen heated at a rate of  $7^{\circ}\text{C}/\text{min}$  (except for the undamaged specimen which was heated at  $5^{\circ}/\text{min}$ ). Heating continued until the specimen surface temperature reached  $68^{\circ}\text{C}$ . At that point, heating ceased and the oven door was opened allowing the specimen to cool. Maximum cooling rates were  $86^{\circ}/\text{min}$ . externally and  $0.86^{\circ}/\text{min}$ . internally. After the specimen's internal temperature decreased to  $<30^{\circ}\text{C}$ , the oven door was closed and the cycle repeated. A third heating/cooling cycle was performed on one specimen to evaluate emission process repeatability. AE was monitored during the heating portion of each cycle and during cooling until AE activity ceased or was significantly diminished.



FIGURE 3 -- Surface damage indications. (S/N0785, 16.24J damage)

## RESULTS AND DISCUSSION

### Impact Damage

Figures 3 and 4 are examples of the type and extent of damage produced by impact. Surface damage (Figure 3), highlighted by optical photography, includes micro-buckling (light-colored, wavy areas), matrix cracks between fibers, and a crack transverse to the fibers. Tangential radiography of the same damaged region (Figure 4) revealed the existence of delaminations, a through-lamina crack, composite/liner disbonding, and liner plastic

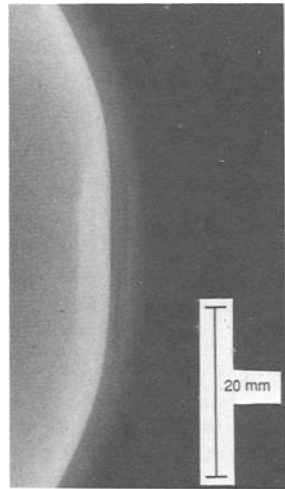


FIGURE 4 -- Radiograph showing internal damage. (S/N0785, 16.24J damage)

deformation. In the following discussion, a scenario for damage introduction is presented which is based on the observed liner deformation and composite contour. Impact pushed the composite shell inward, loading a localized area in circumferential compression until the material buckled. The composite flexed upon buckling, producing tension in the inner-surface fibers, delaminations through the thickness, and compression in the outer surface fibers. When specimen rebound began, load was removed and the composite flexed outward toward its original contour. The inner-surface fibers were again loaded in compression. As the composite returned to an equilibrium position, the outer-surface fibers were probably loaded in tension. Fiber compression should produce micro-buckling since Kevlar exhibits poor resistance to compressive



loading [7]. Micro-buckling followed by tension should further weaken or break fibers. The surface crack and internal trans-lamina crack are evidence that such micro-buckling and tensile failure did occur. Potential sources of AE in the damaged material are matrix crack and delamination extension, and interfacial friction. Any of these sources could be activated by thermal expansion and contraction and/or temperature differential-induced stresses through the composite thickness. Five of the seven damaged specimens exhibited statistically significant strength degradation [3,5] implying that the material was truly damaged.

#### Acoustic Emission

The temperature response and AE event rate recorded during the first cycle heating of three specimens damaged to various degrees are compared in Figure 5. Each graph includes all AE events with amplitudes  $\geq 38$  dB detected by all channels during the test and thus provides a picture of the overall AE activity. All specimens produced thermo-AE. AE in the undamaged specimen may have arisen from relaxation of fabrication-related stresses or matrix micro-cracking.

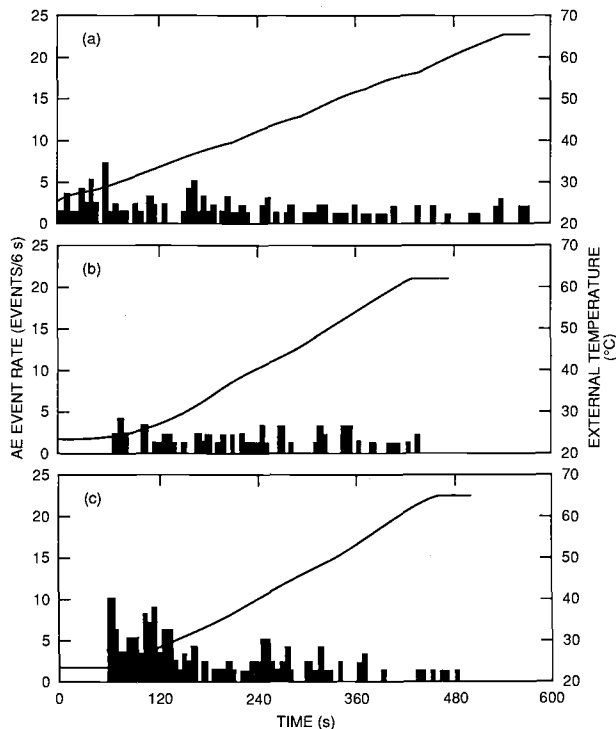


FIGURE 5 -- Total AE activity of 3 specimens. The moderately damaged specimen produced higher AE rates. (Damage levels: a. 0, b. 2.24J, c. 13.06J)

Due to the relatively small size of the specimens, AE waves propagating from a source may be detected by more than one sensor before being attenuated below the level of detectability. Wave velocity in these

structures is constant and independent of propagation direction [8], thus the sensor that detects the wave first (first hit) is closest to the source. Hence, sorting the AE events according to the first channel "hit" allows a crude determination of the origin of the emission. Accordingly, the AE data were filtered so that events detected by the individual channels could be totaled. The results are shown in Figure 6. In each case, AE is detected by all channels, implying that sources occur throughout the composite. By comparing the number of first hits at Channel 3 (transducer located within the damaged area) with that at either of the other channels, it is seen that the damaged composite produces more emission.

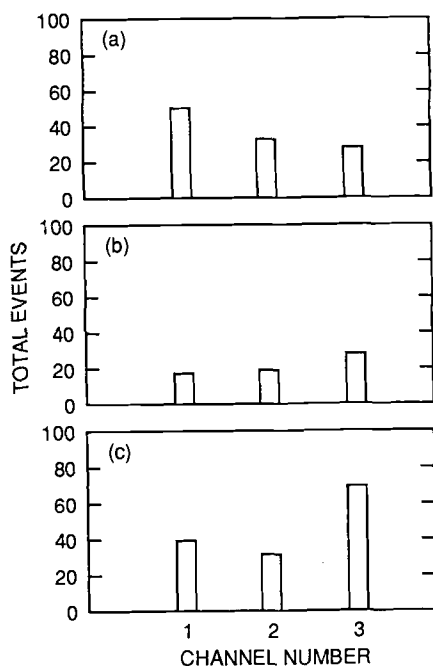


FIGURE 6 -- Comparison of origins of first cycle AE. Most emission originates in the damaged area (Channel 3.) (Damage levels Figure 5.)

Relatively little emission (tens or hundreds of events) was produced by the undamaged or low-to-moderately damaged specimens. However, for the more severely damaged specimens, periods of extremely high emission rates from the damaged area occurred (Figure 7). Rates were so high that events overlapped, continuously triggering the AE monitor. AE description on a per event basis became impossible. However, a measure of threshold crossings (counts) was possible, so the remaining results will be presented in terms of counts.

While most of the emission for damaged specimens emanates from damaged composite, the mechanism(s) for its production are not fully understood. Sato, et al [1,2] concluded that frictional processes produced the emission they observed since it was produced on all cycles

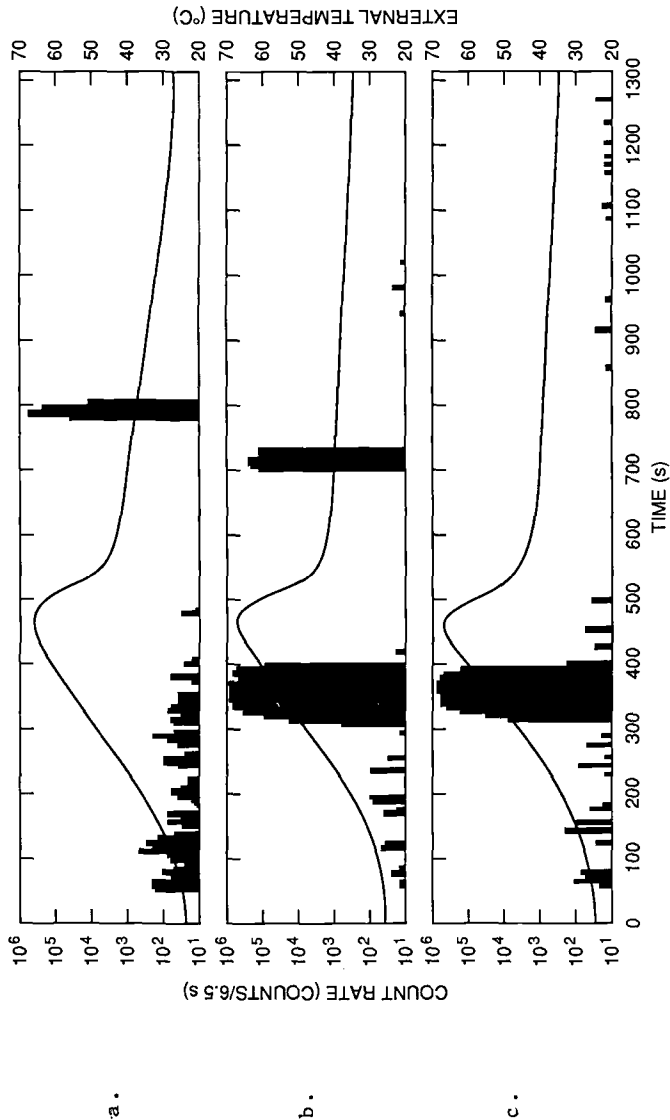


FIGURE 7 -- AE count rates from damaged area on successive cycles showing non-repeatability of AE behavior. (a. Cycle 1; b. Cycle 2; c. Cycle 3)

during heating and cooling, but at decreasing rates. They also concluded that damage growth was not a source of emission since that would imply a continuing rather than decreasing rate of emission.

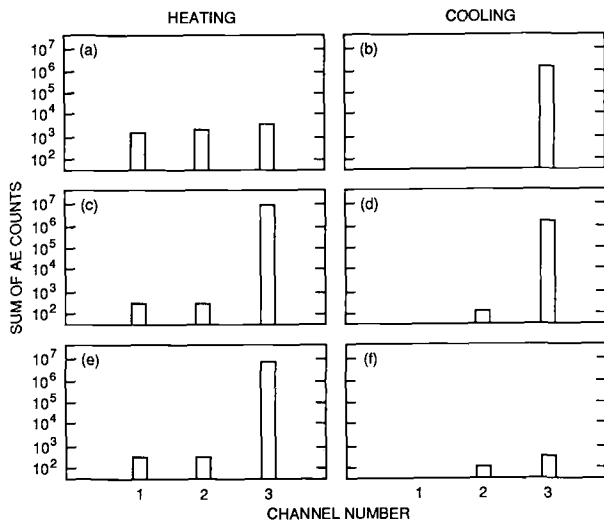


FIGURE 8 -- Comparison of origins of AE during successive thermal cycles of a single specimen. (a,b. Cycle 1; c., d. Cycle 2; e., f. Cycle 3)

In an effort to more fully understand the processes occurring in our specimens, one specimen (moderate damage level, 13.06 J absorbed energy) was subjected to an additional heating cycle. Intense periods of emission occurred during heating on Cycles 2 and 3 and on cooling in Cycles 1 and 2 (Figure 7). Significant emission did occur during Cycle 1 heating, but not the intense behavior typically observed on the first cycle of other moderately or highly damaged specimens. A comparison of the total counts registered by each channel during each cycle are shown in Figure 8. The damaged composite (Channel 3) produced orders-of-magnitude more counts on both heating and cooling. Emission from non-damage related sources (Channel 1 and/or 2) is present on all heating cycles and the last two cooling cycles but in decreasing quantities. If it is assumed that the thermo-AE mechanism(s) in Kevlar/epoxy are the same as in carbon/epoxy and carbon/polyester, and if the emission was solely from frictional processes, it should occur on all cycles but gradually decrease in quantity. This is not the case since the count rate increases more than three orders-of-magnitude from Cycle 1 to Cycle 2 (heating) and cooling emission almost vanishes on Cycle 3. The dramatic changes in emission rate from cycle to cycle imply activation of an AE source(s) (i.e. going from little AE to much) or deactivation of an AE source(s) (i.e. going from much AE to little) caused by damage growth or cessation of growth. Due to the presence of interfaces (cracks, delaminations), friction must produce some AE, but it is not possible to determine how much comes from friction and how much from damage growth. Isolation of typical event features (amplitude, energy, etc.) similar to the Friction Emission Threshold values determined by Awerbuch and Ghaffari [9] was not possible due to event overlap caused by the high event rates.

A potentially complicating factor in data analysis is that each specimen had a different fabrication anomaly. The anomalies were shown in Ref. 4 to not affect specimen strength or AE behavior due to mechanical loading, but it is possible that thermal cycling activated anomaly-related AE sources. Those sources would be distributed throughout the specimens to a greater or lesser degree and not concentrated near Transducer 3. Anomaly-related sources are considered inconsequential compared to the impact-damage related AE because of the much greater amount of AE detected by Channel 3 compared to Channels 1 and 2.

Specimens containing moderate-to-high levels of impact damage exhibited very high count rates ( $>10^5$  counts/sec) at some point during thermal cycling, whereas low-to-moderately damaged specimens did not. This implies that it might be possible to sort similar composite structures with unacceptably high levels of impact or, potentially, other types of damage from those with acceptable levels during a screening or proof test. At least two thermal cycles would be required since damage-related significant emission does not always occur on the first such cycle.

This work successfully extended the concepts of thermo-AE monitoring originally developed by Sato and his co-workers to detection of damage in complex composite structures.

#### CONCLUSIONS

Composite biaxial test specimens produce AE when subjected to thermal cycles with impact-damaged specimens producing more AE than undamaged ones. More severely damaged specimens produce significantly more emission than less damaged ones. For damaged specimens, most of the thermo-AE originates in the damaged region. It was not possible to determine sources of the emission. Thermo-AE is produced during every thermal cycle but large changes in emission rate occur from cycle to cycle. An initial thermal cycle may be required to activate emission sources which may then be detected on a subsequent cycle. With a suitably-designed test comprised of two or more thermal cycles, the thermo-acoustic emission effect may be useful as an NDE technique for detection of impact or other existing damage in composite structures.

## REFERENCES

- [1] Sato, N., Kurauchi, T., and Kamigato, O., "Detection of Damage in Composite Materials by Thermo-Acoustic Emission Technique", in Progress in Acoustic Emission III, Japanese Society of NDI, 1986, pp. 620-629.
- [2] Sato, N., Kurauchi, T., and Kamigato, O., "Thermo-Acoustic Emission from Damaged Composite", SAMPE Journal, Vol. 23, Sept.-Oct., 1987, pp. 48-52.
- [3] Brosey, W. D., Calfee, M. T., Dews, T. D., Whittaker, J. W., Bell, Z. W., Cantrell, J. L., Young, K. G., Henneke, E. G., Post, D., Reifsnider, K. L., and Blake, R. A., "Evaluation of NDE Techniques for Determination of Flawed Conditions and Mechanical Strength of Kevlar-Epoxy Filament-Wound Spherical Test Specimens", Report Y-2428, Martin Marietta Energy Systems, Y-12 Plant, Oak Ridge, TN, 1989.
- [4] Whittaker, J. W., Brosey, W. D., and Hamstad, M. A., "Felicity Ratio Behavior of Pneumatically and Hydraulically Loaded Spherical Composite Test Specimens", in Third International Symposium on Acoustic Emission from Reinforced Composites, July 1989, pp. 168-179.
- [5] Whittaker, J. W., Brosey, W. D., and Hamstad, M. A., "Correlation of Felicity Ratio and Strength Behavior of Impact-Damaged Spherical Composite Test Specimens", in Third International Symposium on Acoustic Emission from Reinforced Composites, July 1989, pp. 160-167.
- [6] Hamstad, M. A., and Patterson, R. G., "Considerations for Acoustic Emission Monitoring of Spherical Kevlar/Epoxy Composite Pressure Vessels", in Composites in Pressure Vessels and Piping, ASME Publication PVP-PB-021, American Society of Mechanical Engineers, New York, pp. 141-163.
- [7] Engineered Materials Handbook, Volume 1: Composites (Dostal, C. A., Editor), Sect. 4, pp. 196-198; ASM International, Metals Park, OH, USA (1987).
- [8] Whittaker, J. W., Brosey, W. D., Burenko, O., and Waldrop, D. A., "Acoustic Emission Propagation and Source Location in Small, Spherical Composite Test Specimens", Journal of Acoustic Emission, Vol. 7, Jan. - Mar. 1988, pp. 31-40.
- [9] Awerbuch, J. and Ghaffari, S., "Monitoring Progression of Matrix Splitting During Fatigue Loading Through Acoustic Emission in Notched Unidirectional Graphite/Epoxy Composite", in Second International Symposium on Acoustic Emission from Reinforced Composites, July 1986, pp. 51-58.

Frank C. Beall

## ACOUSTIC EMISSION MONITORING OF CONTACT DRYING OF SOUTHERN PINE VENEER

---

**REFERENCE:** Beall, F.C., "Acoustic Emission Monitoring of Contact Drying of Southern Pine Veneer," Acoustic Emission: Current Practice and Future Directions, ASTM STP 1077, W. Sachse, J. Roget, and K. Yamaguchi, Eds, American Society for Testing and Materials, Philadelphia, 1991.

**ABSTRACT:** Veneer was contact dried at two pressures and two temperatures to evaluate the formation of defects and drying characteristics as monitored by acoustic emission. The formation of excessive splits was characterized by a stepwise pattern of acoustic emission events. The effects of heat transfer and temperature on drying rate could be inferred from the rate of events or shape of the normalized total event curves.

**KEYWORDS:** splitting, checking, heat transfer, moisture content

Plywood continues to be the dominant panel material manufactured from wood-base materials. In 1988, about 20 million m<sup>3</sup> of softwood plywood was produced, representing 80% of the total structural panels [1]. Most structural plywood is made from veneer that is peeled on a lathe to about 3 or 4 mm thick. The dominant method of drying the veneer is by hot air convective heating in long dryers in which the veneer is conveyed by cables or rollers. In convective drying, shrinkage is nominally about 10% in the direction of peel with little or none in the grain direction. Contact drying was developed to dry veneer faster with less waviness and with little shrinkage in the plane of the sheet, recognizing that some additional thickness shrinkage would occur. During contact drying (between parallel heated platens), pressure and temperature are the major variables that influence the drying rate, final thickness, and quality of the dried veneer. Pressure must be high enough to obtain intimate contact with the veneer, assuring good heat transfer and minimizing shrinkage in width, but low enough to prevent excessive permanent thickness loss. The predominant effect of temperature is in controlling the drying time.

When veneer is peeled (Figure 1), the sheet fractures as it straightens over the lathe knife, causing "lathe checks" as shown. The nosebar provides the pressure

---

Dr. Beall is Professor and Director, Forest Products Laboratory, University of California at Berkeley, Richmond, California 94804.

backing to control the integrity of the cut and the veneer thickness. Lathe checks represent precursors for further checking during drying, and if the checking is severe, will lead to splitting through the sheet. It is probable that extension of lathe checks is the source of most AE in drying veneer. Nearly all of the literature related to AE in drying of wood-base materials is for lumber, in which the initial research was first reported about 10 years ago [2]. It has been clearly demonstrated that the checks (surface fractures) which occur in the normal drying process are the source of AE [3]. At this point, no work has been reported on monitoring AE in the drying of veneer by either convective or contact drying.

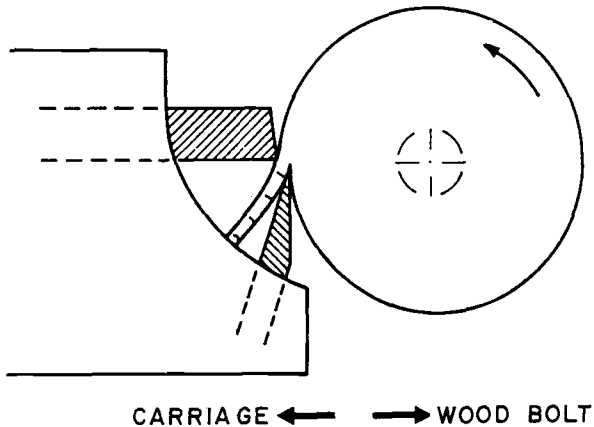


FIG. 1 -- Schematic representation of veneer peeling, showing the knife (shaded triangle), nosebar (shaded opposite knife), and lathe checks in veneer adjacent to knife (adapted from [4]).

## EQUIPMENT AND PROCEDURE

### Equipment

The veneer was dried in a single-opening Wabash press with electrically-heated platens. The upper caul was sheet aluminum; the lower was grooved steel (3 mm groove depth and width; 38 mm spacing between grooves) with a 200-mm-long waveguide welded to the center of one edge. An automatic closing system minimized the closure time and switchover to pressure control. The AE equipment consisted of an AET5000 with a 175 kHz sensor and 125-250 kHz filter and was operated at 60 dB gain with a 1.5 volt floating threshold. The sensor was mounted to the waveguide with an 18-N spring and a fluorocarbon couplant. The threshold level was set to eliminate both mechanical noise and that caused by steam escaping from the veneer during the loss of free water in drying. (Free water is defined as that portion of water existing in the liquid state in contrast to bound water, which exists within the cell walls of wood. The nominal maximum limit of bound water is about 27% of the oven-dry mass of wood, at which point the cell walls are saturated).



## **Material and Test Variables**

Square specimens, 380 by 380 mm, were cut from 3-mm-thick green southern pine held in cold storage. The green moisture contents, which were not altered prior to testing, were determined after the tests by oven-drying at 103°C. For the major portion of the study, four specimens were run at each combination of temperature (180 and 220°C) and pressure (50 and 240 kPa), for a total of 16 runs. In general, there were two clear and two knot-containing specimens in each group. An additional set of three specimens was run to determine the drying endpoint sensitivity of AE. The 180°C and 240 kPa conditions were nominal for commercial contact drying of southern pine veneer. Higher temperature was used to determine the effect on the drying rate; this temperature is close to the upper limit before the thermal degradation and discoloration. The lower pressure was chosen to see if splitting would occur and whether heat transfer was reduced.

## **RESULTS AND DISCUSSION**

### **Veneer Splitting**

The degree of splitting was assessed qualitatively after drying by placing the sheets on a light table and ranking them by severity of splits. The clear sheets were ranked separately from those with knots because of the tendency for checking within the knot. In general, the poorest sheets were from the low pressure and low temperature group and the best from the high pressure and high temperature. The other two groups were intermediate in splits and not separable from each other.

### **AE Parameters**

The AET POSTPRO software package was used to analyze the relationship of AE parameters (event rate, cumulative events, peak amplitude, energy, and event duration) and process conditions. Of the AE parameters, only event rate and cumulative events showed any trends among specimens and treatments. AE event curves were reduced in several ways. In one, the cumulative events were normalized over a nominal time period for each temperature group, about 360 s for 180°C and 240 s for 220°C, because of the effect of temperature on drying time. At the end of the nominal time period, events had essentially ceased. These plots were quantified by the half-time, time to one-half of the total events. The normalization process was used since cumulative events, which ranged from 23 to 304 for the 16 specimens, showed no relationship among the four treatments and two types of specimens. Also, the time to the maximum rate of events was determined directly from event rate curves. Where significant splitting occurred, the AE event vs time curves showed stepwise changes, however, no other AE parameters showed differences with respect to splitting. Figure 2 shows the typical pattern of a clear specimen vs one containing a knot. The AE step changes for the "defect" specimen appeared to indicate much greater severity of splitting of the "defect" specimen. This irregularity of the AE curve was the clearest and most consistent indicator of damage developing through splits.

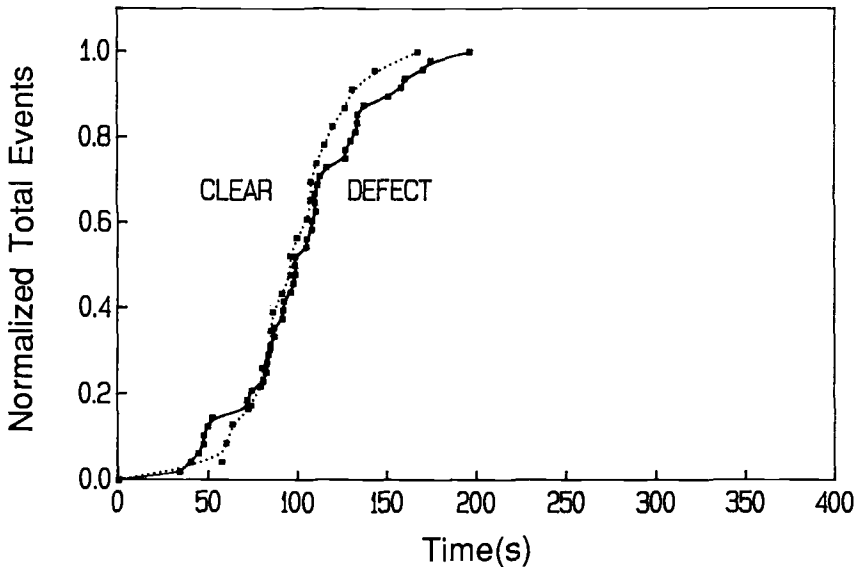


FIG. 2 -- AE events of clear vs defect-containing veneer dried at high temperature (220°C) and low pressure (50 kPa).

#### Relationship of AE Events to Pressure and Temperature

At low temperature (180°C), the half-time (of total events) correlated strongly with initial moisture content. In Figure 3, specimens having substantially different green moisture contents were dried at "commercial" conditions (180°C and 240 kPa) with the resulting time shift for the higher moisture content specimen. The relationship of half-time to moisture content for both pressures at 180°C is given in Figure 4. In the Figure, it can be seen that pressure has no apparent influence on the relationship. Regression lines for each pressure group (4 specimens) had similar regression coefficients. The high regression coefficient indicates a significant effect of moisture content level on the occurrence of AE. Since AE will be produced during drying-induced shrinkage, the shift in AE with time is a strong inferential indicator of an increase of drying time with increasing initial moisture content.

High temperature (220°C) dried specimens showed no significant relationship of half-time to moisture content, indicating that pressure-driven flow probably expels free water, evening out the initial variability in green moisture content. Although pressure effects were not significant at 180°C, they were important for the high temperature specimens. Figure 5 shows the delay in AE in the initial stages of drying at low pressure, indicative of a lag in the drying process, analogous to that for higher moisture content. On the basis of half-time at 220°C (Figure 6), the apparent drying time was up to 40% longer at 50 vs 240 kPa. Most of this increase appeared to be in the initial heat transfer stages, as indicated in Figure 5. Also, the effect of pressure on defect generation was substantial at 220°C; specimens containing knots were severely split at 50 kPa, but were acceptable at 240 kPa. The specimens that split (220°C, 50 kPa) had exaggerated step-wise cumulative AE event curves compared with smooth curves for all of the clear as well as for the 240 kPa specimens (see Figure 2).

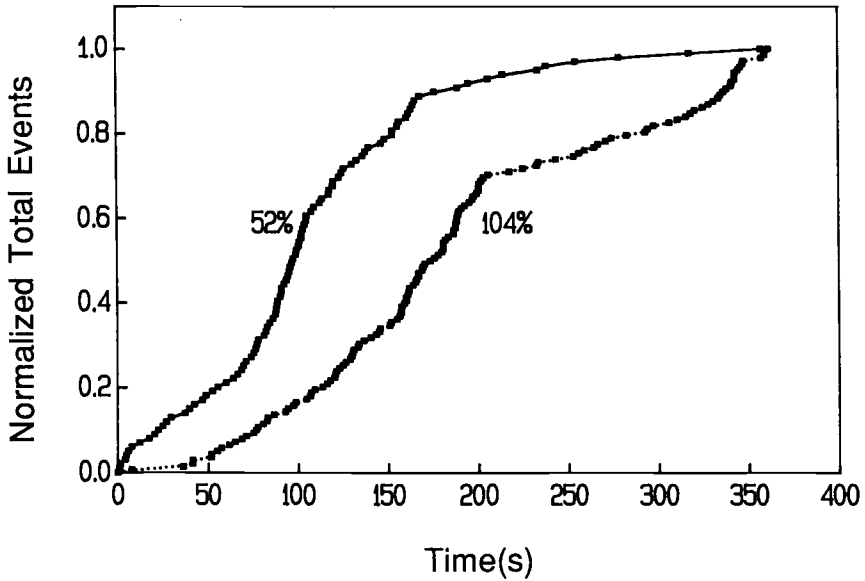


FIG. 3 -- AE events of veneer at two extremes of moisture content dried at low temperature (180°C) and high pressure (240 kPa).

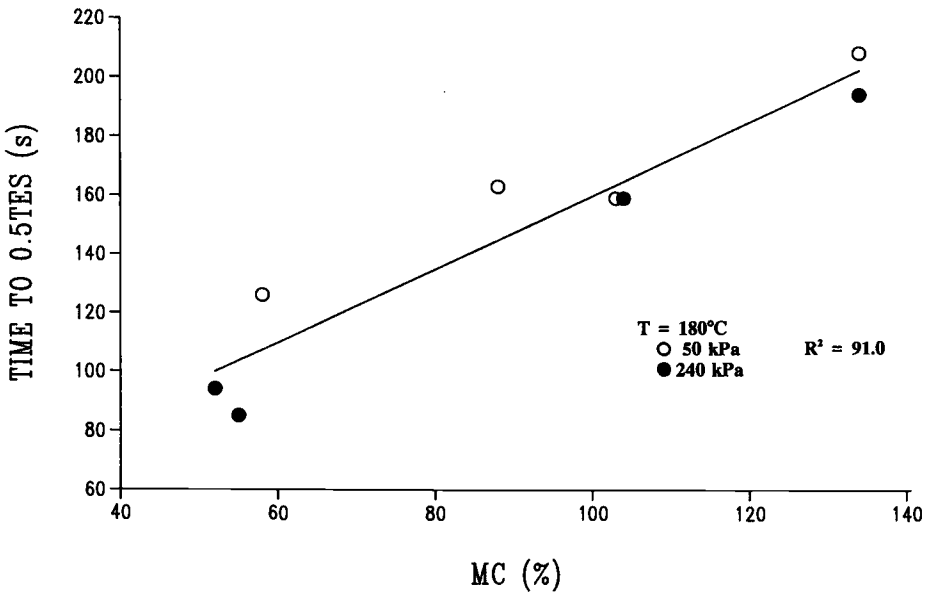


FIG. 4 -- Regression of half-time of total events vs moisture content for all specimens dried at low temperature (180°C).

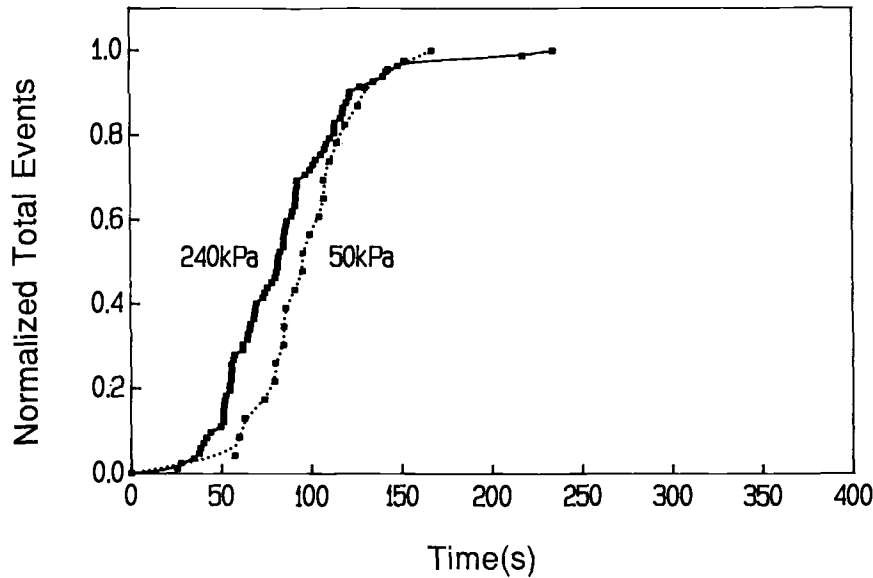


FIG. 5 -- AE events of clear veneer dried at high temperature (220°C) and both pressures.

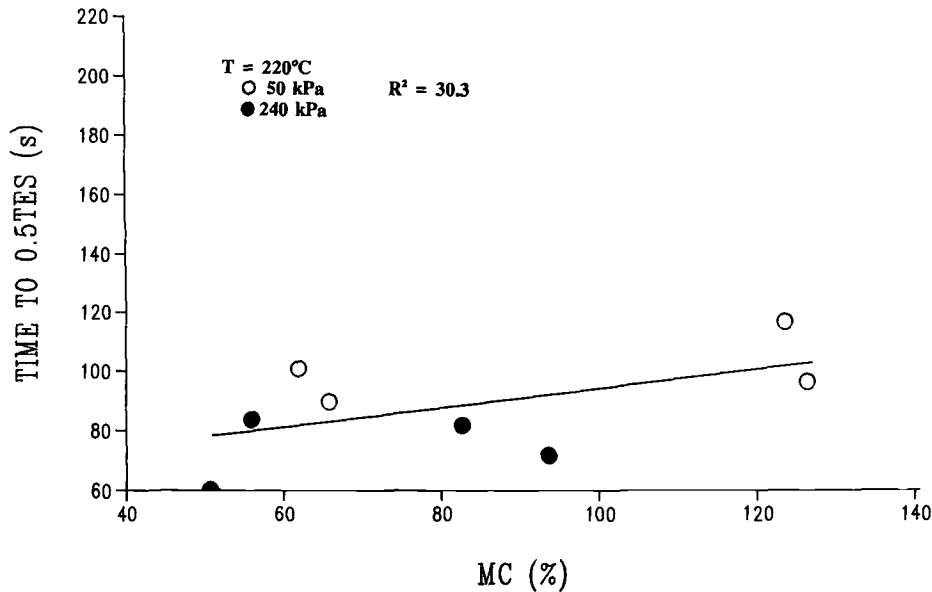


FIG. 6 -- Regression of half-time of total events vs moisture content for all specimens dried at high temperature (220°C).

In Figure 7, two specimens having similar initial moisture contents show an initial lag in AE for 220°C, followed by a much more rapid increase than for 180°C. This appeared to confirm pressure-driven flow of moisture initially at 220°C (evidenced by steam evolution), followed by more rapid drying (as suggested by the high AE rate). The relationship is clearer in Figure 8, where the dependence of half-time for 180°C on moisture content is clearly shown, as contrasted by the independence at 220°C. At low pressure (Figure 9), the delay in drying at 180°C is obvious when compared with that of Figure 7.

In Table 1, the regression coefficients between two AE parameters and moisture content are summarized for the four press variables. In addition to the "half-time" analysis (first data column), regressions were also run against moisture content using time to the peak event rate (second data column). These latter correlations were essentially the same as for the half-time analysis. The high cross-correlation between half-time and maximum rate analyses (last column) verified the consistency except for the high temperature data (last row). Figure 10 shows an example of this cross-correlation for the data at 180°C. The use of half-time in this paper was for the convenience of post-processing analysis, since no visual interpretation of the data was necessary. However, if AE were used for controlling the drying process in real time, the rate of events would be the only usable AE parameter.

TABLE 1 -- Regression coefficients ( $R^2$ ) for analyzed AE parameters

		Regression vs MC		
		Time to 0.5 Total Events	Time to Max Event Rate	Cross Correlation
Low p	(50 kPa) <sup>a</sup>	18.5	33.5	92.8
High p	(240 kPa) <sup>a</sup>	66.5 (8) <sup>c</sup>	74.2	83.0
Low T	(180°C) <sup>b</sup>	91.0 (4) <sup>c</sup>	88.1	94.2 (10) <sup>c</sup>
High T	(220°C) <sup>b</sup>	30.3 (6) <sup>c</sup>	28.8	54.4

<sup>a</sup>Includes both temperatures.

<sup>b</sup>Includes both pressures.

<sup>c</sup>See corresponding Figures.

### Drying Endpoint Determination

Of the three specimens dried at 180°C and 240 kPa to test the relationship of AE to the drying endpoint, two were removed when the events just ceased at which point the moisture content was 1 to 1.5%. The third specimen was removed about 5 s after the maximum in the rate of events, and was found to be at 3% moisture content. It appears that events occur to about the oven-dry point and that the peak of event rate would be appropriate reference point for endpoint control that could prevent overdrying and reduce total drying time.

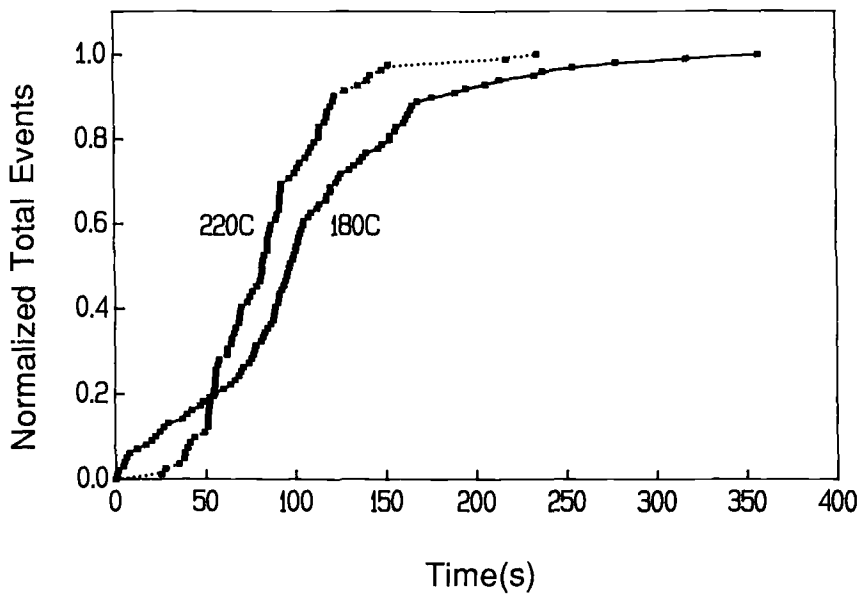


FIG. 7 -- AE events of clear veneer dried at high pressure (240 kPa) and both temperatures.

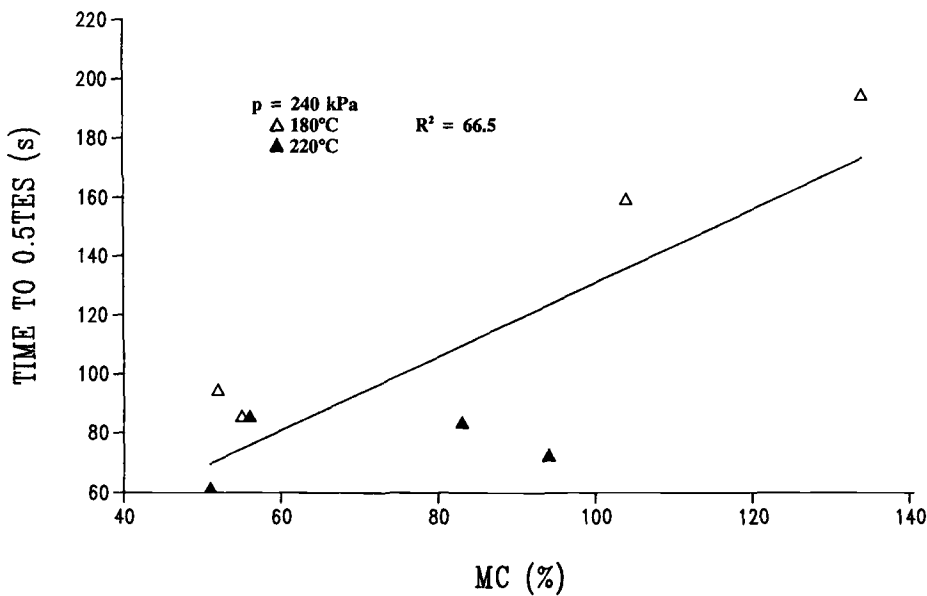


FIG. 8 -- Regression of half-time of total events vs moisture content for all specimens dried at high pressure (240 kPa).

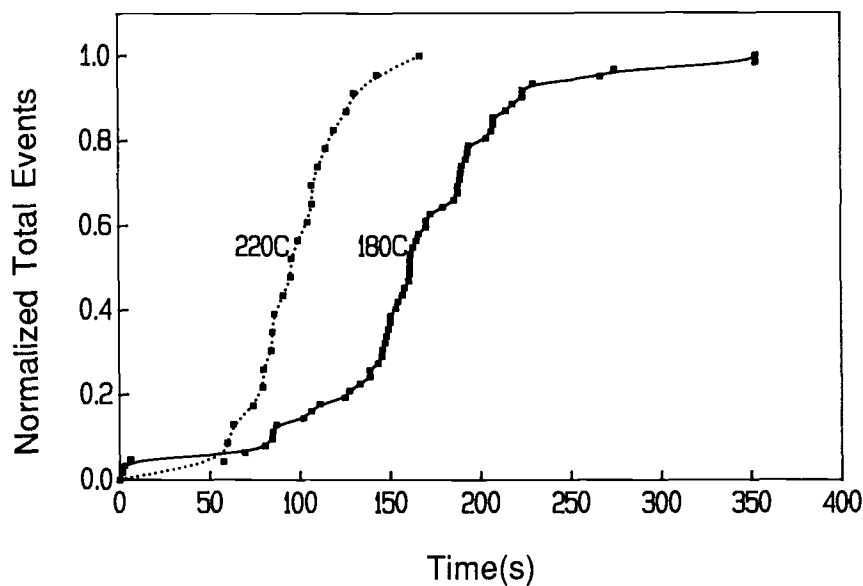


FIG. 9 -- AE events of clear veneer dried at low pressure (50 kPa) and both temperatures.

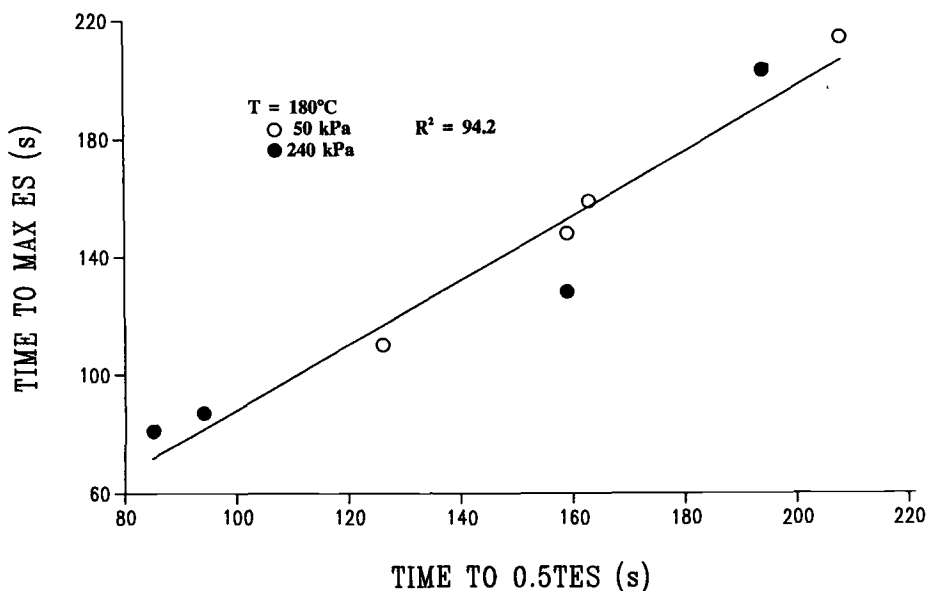


FIG. 10 -- Regression of time to the maximum rate of events vs half-time of total events for all specimens dried at low temperature (180°C).

## CONCLUSIONS

1. The delay in AE with increasing green moisture content for veneer dried at 180°C indicated a strong relationship between AE and drying rate. The lack of a delay in AE for tests at 220°C indicated that free water was expelled by pressure-driven flow, permitting a constant drying time for varying initial moisture contents.
2. Step changes in cumulative AE curves were related to the development of severe splits in the veneer.
3. Event rate data appears to be the best candidate parameter for monitoring and controlling the drying process, including endpoint determination.
4. Low pressure (50 kPa) resulted in a delay in AE, inferring reduced heat transfer to the veneer, and produced highly split material. High pressure (240 kPa) conditions produced acceptable quality material with no delay in AE.

## REFERENCES

- [1] Anon, "Booming Panel Industry Shatters Output Records", Forest Industry, 115(4) 1988, pp. 18-19.
- [2] Noguchi, M., Kagawa, Y. and Katagiri, J., "Detection of Acoustic Emissions During Hardwoods Drying", Journal of Japan Wood Research Society, Vol. 26, No. 9, 1980, pp. 637-638.
- [3] Ogino, S., Kaino, K. and Suzuki, M. "Prediction of Lumber Checking During Drying by Means of Acoustic Emission Technique", Journal of Acoustic Emission, Vol. 5, No. 2, 1986, pp. 61-65.
- [4] Lutz, J.F., Mergen, A.F. and Panzer, H.R., "Control of Veneer Thickness during Rotary Cutting," Forest Products Journal, Vol. 19, No. 12, pp. 21-28.



## Author Index

### A

Aernoudt, E., 416  
Aoki, K., 261  
Armstrong, B. H., 358  
Awerbuch, J., 404

### B

Barthélémy, H. M., 185  
Beall, F. C., 435  
Bohm, P., 35  
Bowman, P. S., 146  
Brosey, W. D., 424  
Buttle, D. J., 273

### C

Carpenter, S. H., 77, 252  
Chow, T., 381  
Christiansen, S. S., 77  
Crostack, H. A., 35

### D

De Meester, P., 416  
Derakhshan, O., 305  
Deschamps, M., 316  
Dornfeld, D. A., 328  
Duke, J. C., Jr., 105

### E

Enoki, M., 47

### F

Falls, S. D., 381

### G

Ghaffari, S., 404  
Govekar, E., 165  
Grabec, I., 165  
Gsib, N., 316

### H

Hardy, H. R., Jr., 365  
Harris, R. W., 156  
Heiple, C. R., 77  
Higo, Y., 7  
Holroyd, T. J., 25  
Houghton, J. R., 305  
Hutchins, D. A., 86, 381

### I

Inaba, H., 7

### J

Jayakumar, T., 218  
Jeng, J. S., 395  
Johkaji, J., 123  
Jones, R. K., 305

### K

Kiernan, M. T., 105  
Kim, K. Y., 67  
King, S. D., 25  
Kishi, T., 47, 242  
Kobayashi, Y., 123, 261

### M

MacPhail, J. D., 146  
March, P. A., 305  
Maxwell, S. C., 86  
McBride, S. L., 146  
Mori, Y., 242

### O

Obata, Y., 261  
Ohtsu, M., 347  
Ono, K., 395  
Oyaizu, H., 123

**P**

Peters, D. T., 146  
Pollard, M. D., 146

**R**

Raj, B., 218  
Randall, N., 25  
Rao, M. V. M. S., 365  
Roget, J., 316  
Roman, I., 213

**S**

Sachse, W., 67, 165  
Sato, I., 287  
Sato, K., 287  
Scruby, C. B., 273  
Shibata, K., 261  
Sklarczyk, C., 199  
Souquet, P., 316  
Storp, H. J., 35  
Sun, X., 365

**T**

Takikawa, K., 287  
Tanaka, T., 287  
Tracey, T. E., 25

**V**

Valdes, C. M., 358  
Vary, A., 95  
Verpoest, I., 416

**W**

Waschkies, E., 199  
Wevers, M., 416  
Whittaker, J. W., 424  
Wood, B. R. A., 156

**Y**

Yamaguchi, K., 123, 261  
Yanagibashi, M., 287  
Yang, J. M., 395  
Yoneyama, T., 287  
Young, R. P., 86, 381

**Z**

Zeides, F., 213  
Zhu, Z., 252

## Subject Index

### A

Acoustic pressure method, 7  
 Acousto-ultrasonics (See also  
   Ultrasonics), 95, 105  
 Adaptive systems, 165  
 Adhesive strength, 95  
   metal film, 67  
 Air conditioners, rotary  
   compressors, 287  
 Airframe components, 146  
 Alloy PE-16, 218  
 Aluminum, 77, 273  
 Aluminum-lithium alloys, 213  
 Amplitude distribution  
   analysis, 365  
 Arrival time data, synthetic, 86  
 Artificial flaw, 242  
 Austenitic alloys, 218

### B

Bending, three-point, 395  
 Boron, 77  
 Brazilian tests, 381  
 Bronze particles, impact test, 273

### C

Calibration source, 77  
 Carbon fibers, 395, 416  
 Cavitation, 305  
 Ceramics  
   flaw size and acoustic  
     emission, 242  
   microfracture, 47  
 Composites, 95, 105, 424  
   carbon fiber reinforced  
     laminates, 416  
   fiber, 395  
   fiber-reinforced plastics, 123  
   graphite/epoxy, 404  
   microfracture, 47  
   tensile tests, 123  
 Compressors, rotary, 287  
 Corrosion, acoustic emission test  
   for, 185

Cracks, 347  
   advanced, 146  
   detection, 185, 199, 261  
   growth, 146, 261  
   kinematics, 347  
   microcrack, 47  
   model, elliptical, 365  
   presence, 146  
   surface friction, 199  
 Cycling, thermal, 424  
 Cylinders, compressed gas, 185

### D

Damage detection, 424  
 Data acquisition system, 146  
 Decohesion, 252  
 Deconvolution, 47, 67, 273  
 Debonding, 252  
 Deformation  
   compressive, 252  
   inelastic, 365  
   tensile, 77, 213, 218  
 Delta learning rule, 165  
 Diagnostics, machine condition, 287  
 Dilatancy point, 365, 381  
 Drying characteristics, pine  
   veneer, 435  
 Dust impact process, 273

### E

Earthquakes, 347  
   preparation zone, 358  
 Elastic impact, 273  
 Elasticity, 105  
   theory, 77  
 Electromagnetic-acoustic  
   transducer, 35  
 Electron beam welding, 35  
 End-notched flexure, 395  
 Energy discriminating acoustic  
   emission method, 416  
 Erosion, 273  
   cavitation, 305  
 Event increment rate, 365  
 Expert systems, 156, 316

## F

Failure mechanisms,  
graphite/epoxy coupons, 404  
Fatigue  
crack growth, 261  
cyclic, tests, 199  
damage modes, 416  
Fiber-reinforced plastics, 123  
Film adhesive strength, 67  
Flaw size, 242  
Flight, crack detection during, 146  
Fracture, 47, 146, 218, 328, 395  
behavior, 123  
hydro-, 347  
inclusion, 77, 252  
intergranular, 261  
matrix splitting, 404  
strength, effect on flaw size, 242  
Friction emission, 404

## G

Gas cylinders, compressed, 185  
Gear, spur, 261  
Geotechnics, 347, 365  
Glass particles, impact test, 273  
Grain boundary slippage, 358  
Graphite, 252  
Graphite/epoxy composites, 404  
Green's functions, 67, 273  
dynamic, 47  
simplified, 347

## H

Hatano method, 7  
Heat transfer, 435  
Hydrogen charging, 213  
Hydrogen embrittlement, 213  
Hydrostatic test, 185  
Hydrotest, 199  
Hydroturbines, 305

## I

Imaging, ultrasonic, 86, 381  
Impact damage, 424  
Impact, elastic, 273  
Impact, particle, 273  
Impact, plastic, 273  
Inclusion fracture, 77, 252

Industrial environment, sensing, 25  
In-flight monitoring, 146  
Inspection, pressure vessel, 185,  
199  
Integrity evaluation, 156  
Intergranular fracture, 261  
Inverse problems, 47, 165  
Iron, nodular cast, 252

## J

Joule heating, 67

## L

Lamb waves, 105  
Laminates, carbon reinforced  
composites, 416  
Lead, acoustic emission signals, 7  
Line source, 67  
Lithium, aluminum-, alloys, 213  
Loading conditions, rock  
fracture, 365  
Loading, thermo-mechanical, 424  
Localization, 199  
Low strain, 358

## M

Machine condition diagnosis, 287  
Machining, 328  
Maintenance, machine, 287  
Mapping, system, 165  
Mass production products, 287  
Matrix cracking, 395  
Matrix splitting, 404  
Mechanical properties, change  
assessment, 95  
Metals, 218, 261  
coatings, 67  
films, 67  
microfracture, 47  
Microcracks, 47  
Microfracture, 47, 365, 381  
Micromechanics, 47  
Microseismics, 347, 358  
Milling, 316, 328  
Moisture content, 435  
Moment tensor analysis, 347

## Monitoring

- plant, 156, 287
- process, 35, 165
- tool, 316

## N

- Neural networks, 165, 316, 328
- Neural signal processing, 165
- Nimonic alloy, 218
- Nodular cast iron, 252
- Nondestructive evaluation, 242
  - quantitative, 47

## O

- Orowan looping, 218

## P

### Particle

- impact, 273
- shearing, 218
- second phase, 252

### Pencil lead fracture method, 7

### Pine veneer, 435

### Plant operability

- efficient, 287
- monitoring, 156

### Plastic impact, 273

### Plastics, fiber reinforced, 123

### Point source, 67

### Polyetheretherketone, 395

### Pressure vessels, 185, 199

### Process control, 35

### Process monitoring, 35, 165

## R

### Rock, 347, 358, 365, 381

### Root mean square, 305

### Rotating machinery, 287

## S

### Second phase particles, 252

### Sensitivity, sensor, 7

## Sensors, 328

- electron beam welding, for, 35
- housing, 25
- integrated, 25
- mounting condition, 7
- problems with, 7
- sensitivity, 7
- stress wave, 25
- transducers, 35, 47, 305

## Shear motion, 381

## Signal analysis, 199, 416

- development, 95

## Signal energy, 77

## Signal processing, 123, 328

## Signals, emission, 7

- fracture, 146, 242

## Silicon nitride, 242

## Source characterization, 165

- acoustic emission, 47

## Source inversion, 347

## Source location, 86, 347, 381

## Source mechanism, 381

## Splitting, matrix, 404

## Splitting, veneer, 435

## Spur gear, 261

## Steel

- carburized, 261

- stainless, 218

## Strain ageing, 218

## Strain levels, low, 358

## Stress concentration, 365

## Stress induced changes, 86, 381

## Stress, residual, 199

## Stress-strain curve, 365

## Stress waves, 95

- factor, 95

- sensing, 25

## Structural integrity function, 156

## T

## Tectonic strain, 358

## Tensile deformation, 77, 213, 218

## Tensile tests, 123, 395

## Tension fatigue, 416

## Tensor analysis, moment, 347

## Thermal cycling, 424

## Thermal shock tests, 199

## Thermo-acoustic emission, 424

## Thermoelastic generation, 67

## Thermoelastic source, 67

## Thermoplastic, 395

Thick film hybrid, 25  
Thin-film testing, 67  
Through-thickness-transverse-  
resonance (TTTR), 105  
Time data, synthetic arrival, 86  
Tomography  
    difference, 381  
    passive, 86  
Tools, cutting  
    breakage, 316  
    wear, 316, 328  
Transducers, 47, 305  
    electromagnetic-acoustic, 35  
Transport vessels, compressed  
    gas, 185  
Turbines, hydro-, 305  
Turning, 316, 328

**U**

Ultrasonics, 213  
    acoustic, 95, 105

imaging, 86, 381  
signals, 67

**V**

Velocity structure, 86  
Veneer, southern pine, 435

**W**

Water, effect on acoustic  
    emission, 213  
Wave envelope processing, 123  
Waveform parameters, 123  
Wave propagation, 105  
Waves, stress, 95  
    sensing, 25  
Wear, cutting tool, 316, 328  
Welding, electron beam, 35

ISBN 0-8031-1389-7